frontiers | Research Topics

The Atlantic Meridional Transect programme (1995-2023)

Edited by
Andrew Paul Rees, Vanda Brotas and
Timothy James Smyth

Published in
Frontiers in Marine Science

ISSN 1664-8714
ISBN 978-2-8325-4351-1
DOI 10.3389/978-2-8325-4351-1

About Frontiers

Frontiers is more than just an open access publisher of scholarly articles: it is a pioneering approach to the world of academia, radically improving the way scholarly research is managed. The grand vision of Frontiers is a world where all people have an equal opportunity to seek, share and generate knowledge. Frontiers provides immediate and permanent online open access to all its publications, but this alone is not enough to realize our grand goals.

Frontiers journal series

The Frontiers journal series is a multi-tier and interdisciplinary set of open-access, online journals, promising a paradigm shift from the current review, selection and dissemination processes in academic publishing. All Frontiers journals are driven by researchers for researchers; therefore, they constitute a service to the scholarly community. At the same time, the *Frontiers journal series* operates on a revolutionary invention, the tiered publishing system, initially addressing specific communities of scholars, and gradually climbing up to broader public understanding, thus serving the interests of the lay society, too.

Dedication to quality

Each Frontiers article is a landmark of the highest quality, thanks to genuinely collaborative interactions between authors and review editors, who include some of the world's best academicians. Research must be certified by peers before entering a stream of knowledge that may eventually reach the public - and shape society; therefore, Frontiers only applies the most rigorous and unbiased reviews. Frontiers revolutionizes research publishing by freely delivering the most outstanding research, evaluated with no bias from both the academic and social point of view. By applying the most advanced information technologies, Frontiers is catapulting scholarly publishing into a new generation.

What are Frontiers Research Topics?

Frontiers Research Topics are very popular trademarks of the *Frontiers journals series*: they are collections of at least ten articles, all centered on a particular subject. With their unique mix of varied contributions from Original Research to Review Articles, Frontiers Research Topics unify the most influential researchers, the latest key findings and historical advances in a hot research area.

Find out more on how to host your own Frontiers Research Topic or contribute to one as an author by contacting the Frontiers editorial office: frontiersin.org/about/contact

The Atlantic Meridional Transect programme (1995-2023)

Topic editors
Andrew Paul Rees – Plymouth Marine Laboratory, United Kingdom
Vanda Brotas – University of Lisbon, Portugal
Timothy James Smyth – Plymouth Marine Laboratory, United Kingdom

Citation
Rees, A. P., Brotas, V., Smyth, T. J., eds. (2024). *The Atlantic Meridional Transect programme (1995-2023)*. Lausanne: Frontiers Media SA.
doi: 10.3389/978-2-8325-4351-1

Table of contents

frontiers | Frontiers in Marine Science

TYPE Editorial
PUBLISHED 11 January 2024
DOI 10.3389/fmars.2024.1358174

Editorial: The Atlantic Meridional Transect programme (1995-2023)

Andrew P. Rees[1]*, Timothy J. Smyth[1] and Vanda Brotas[2]

[1]Plymouth Marine Laboratory, Prospect Place, The Hoe, Plymouth, United Kingdom, [2]Marine and Environmental Science Centre (MARE), Faculdade de Ciencias, Universidade de Lisboa, Lisbon, Portugal

KEYWORDS

AMT, Atlantic Meridional Transect, sustained observations, biodiversity, biogeochemistry, environmental change

Editorial on the Research Topic
The Atlantic Meridional Transect programme, (1995-2023)

OPEN ACCESS

EDITED AND REVIEWED BY
Hervé Claustre,
Centre National de la Recherche Scientifique (CNRS), France

*CORRESPONDENCE
Andrew P. Rees
✉ APRE@pml.ac.uk

RECEIVED 19 December 2023
ACCEPTED 02 January 2024
PUBLISHED 11 January 2024

CITATION
Rees AP, Smyth TJ and Brotas V (2024) Editorial: The Atlantic Meridional Transect programme (1995-2023). *Front. Mar. Sci.* 11:1358174. doi: 10.3389/fmars.2024.1358174

Introduction

Since 1995 the Atlantic Meridional Transect (AMT) has undertaken measurements of oceanographic and atmospheric variables during 30 research cruises on a passage between the UK and destinations in the South Atlantic (Aiken and Bale, 2000; Robinson et al., 2006; Robinson et al., 2009; Rees et al., 2017). The transect spans more than 100° of latitude, samples to ocean depths of up to 1000 m and crosses a range of ecosystems from sub-polar to tropical, from eutrophic shelf seas and upwelling systems, to oligotrophic mid-ocean gyres. AMT has enabled the acquisition of repeat measurements of several Essential Ocean Variables and other ecosystem parameters and rate processes at a resolution of ~160 km (over ~13000 km). In delivering these activities AMT has facilitated long-term collaborations with NASA and ESA for the calibration and validation of satellite ocean colour sensors; with the UK Met-Office, NOC, NOAA, SOCCOM and University of Washington for ARGO and Bio-ARGO float deployment; and has maintained a long-term mooring in the South Atlantic Gyre (2009 to 2023). AMT data is archived and managed by the British Oceanographic Data Centre (BODC), whilst key data are also directed to other focus specific databases (e.g. NASA SeaBASS, ESA OC-CCI, SOCAT, CDIAC, SeaDataNet).

The generation of sustained observations of ocean biogeochemical variables is invaluable in monitoring ecosystem function and health during this period of rapid climate and environmental change. Globally there are a number of initiatives which aim to make repeated observations which include ship transects such as GO-SHIP and GEOTRACES and deployment of hydrodynamical and biogeochemical sensors as part of the ARGO programme. Examples of fixed point observations in the Atlantic include: The European Station for Time-Series in the Ocean (ESTOC) which has provided observations of the eastern sub-tropical Atlantic for more than twenty five years (González-Dávila and Santana-Casiano, 2023), the Bermuda Atlantic Time Series (BATS) in the western sub-tropical Atlantic, which, since 1988 has documented increases in temperature, ocean acidification and decreasing oxygen (Bates and Johnson, 2021); In the north-east Atlantic, the Western Channel Observatory (WCO) has records dating to the early 20th century and in recent decades has further evidenced climate related shifts in plankton communities alongside increases in temperature and ocean acidification (McEvoy et al., 2023); the Estación Permanente de Estudios Ambientale (EPEA) in the western South Atlantic has evidenced increases in chlorophyll associated with an increased proportion of small celled phytoplankton (Lutz et al., 2023). The AMT offers a unique and alternative approach by making repeat measurements along a transect which incorporates the latitudinal range of all these fixed-point stations.

AMT provides an inclusive platform for multi-disciplinary ocean research with cruise berths open to the international community upon request. The thirty research expeditions to date have involved 310 sea-going scientists from 81 institutes representing 31 countries, resulting in 400 refereed papers which are available here.

Research topic preview

The collection of eleven manuscripts in the current Research Topic reflect the diversity of measurements made during AMT cruises and the multi-disciplinarity of studies performed. The topics range between bacterial biodiversity through to the surface ocean exchange of greenhouse gases, and whilst some papers synthesise data from multiple cruises others present data from a single transect.

In their investigation of the bacterioplankton biogeography of the Atlantic during the AMT25 expedition in 2015, Allen et al. used the ratio of total 16S RNA gene sequences to active 16S gene sequences in order to inform on the active microbiome of the Atlantic Ocean and to provide insights towards the ecology and life history strategies of biogeochemically and ecologically significant bacterioplankton. Reintjes et al. also used molecular tools to describe particle associated bacterial communities observed during AMT22 which provided new insights into the composition, community dynamics and the potential for catabolic activity of several polysaccharides associated with their host particles. Several of the manuscripts focus on aspects of the biodiversity of phytoplankton groups. Phongphattarawat et al. combined data from AMT and BATS in their study of phytoplankton pigments and were able to describe species specific relationships between seasonal and depth dependent variability in photosynthetic and photoprotective pigments which were often reflected in variable carbon: chlorophyll ratios (C:Chl). The C:Chl provides a widely used proxy for estimation of ocean carbon content and formed the focus of the study by Smyth et al. Here the authors used analytical flow cytometry and machine learning techniques to analyse cyanobacterial cells of *Prochlorococcus* sp. and *Synechococcus* sp. from laboratory cultures and from samples collected on AMT cruise numbers 18 to 29 in order to predict C:Chl from dissolved nutrient concentrations. Quartly et al. compared AMT measurements of chlorophyll-a from the surface and deep chlorophyll maximum with surface satellite observations, profiles from biogeochemical ARGO floats and two different biogeochemical models. Brewin et al. employed traditional and contemporary techniques to estimate phytoplankton biomass on four AMT cruises between 2013 and 2018 and compared them satellite derived measurements; a high degree of similarity was reported across all methods used giving great confidence in comparability across decades of observations. Brotas et al. took similar datasets and complimented them with microscopic analysis to provide contemporary descriptions of phytoplankton biodiversity, size structure and carbon content from AMT cruises in 2018 and 2019 which were compared to similar measurements made two decades earlier. Guerreiro et al. focused on oceanographic features, macronutrient concentrations and aerosol dust deposition in controlling distribution and abundance of the calcite containing coccolithophore phytoplankton.

Serret et al. used their data from AMT22 to further refine empirical relationships between measures of community productivity and respiration in working towards a model for satellite estimation of net community production. Li et al. examined the biogeographical distribution of the *Tintinnina*, single celled protozoa, along the AMT29 transect. They found that *Tintinnina* species were divided into four biogeographic distribution patterns constituting four sub-assemblages which could largely be characterised by a number of dominant species in each group. Brown et al., 2023 combined a latitudinal transect from AMT27 with a longitudinal transect at 24.5°N to validate a novel instrument design which provided high frequency, high precision measurements of the potent greenhouse gases nitrous oxide and methane.

The AMT project has a rich history of observations over nearly three decades, but the future outlook is uncertain. In an age when financial and carbon budgets provide a severe limitation upon large research ships and expeditions, the development and integration of autonomous vehicles and sensors offer great promise of an alternative approach to delivering sustained observations along repeat ocean transects. This paper is AMT contribution number 403.

Author contributions

AR: Writing – original draft, Writing – review & editing. TS: Writing – review & editing. VB: Writing – review & editing.

Funding

The author(s) declare financial support was received for the research, authorship, and/or publication of this article. The Atlantic Meridional Transect is funded by the UK Natural Environment Research Council through its National Capability Long-term Single Centre Science Programme, Climate Linked Atlantic Sector Science (grant number NE/R015953/1).

Conflict of interest

The authors declare that the research was conducted in the absence of any commercial or financial relationships that could be construed as a potential conflict of interest.

Publisher's note

References

Aiken, J., and Bale, A. J. (2000). An introduction to the Atlantic Meridional Transect (AMT) programme. *Prog. Oceanogr.* 45, 251–256. doi: 10.1016/s0079-6611(00)00004-5

Bates, N. R., and Johnson, R. J. (2021). Ocean observing in the north atlantic subtropical gyre. *Oceanography* 34, 32–34. doi: 10.5670/oceanog.2021.supplement.02-14

González-Dávila, M., and Santana-Casiano, J. M. (2023). Long-term trends of pH and inorganic carbon in the Eastern North Atlantic: the ESTOC site. *Front. Mar. Sci.* 10. doi: 10.3389/fmars.2023.1236214

Lutz, V., Chidiak, M., Frouin, R., Negri, R., Dogliotti, A. I., Santamaria-del-Angel, E., et al. (2023). Regulation of CO2 by the sea in areas around Latin America in a context of climate change. *Environ. Monit. Assess.* 195, 417. doi: 10.1007/s10661-023-10997-1

McEvoy, A. J., Atkinson, A., Airs, R. L., Brittain, R., Brown, I., Fileman, E. S., et al. (2023). The Western Channel Observatory: a century of oceanographic, chemical and biological data compiled from pelagic and benthic habitats in the Western English Channel. *Earth Syst. Sci. Data Discuss.* 2023, 1–42. doi: 10.5194/essd-2023-311

Rees, A. P., Nightingale, P. D., Poulton, A. J., Smyth, T. J., Tarran, G. A., and Tilstone, G. H. (2017). The atlantic meridional transect programme, (1995-2016). *Prog. Oceanogr.* 158, 3–18. doi: 10.1016/j.pocean.2017.05.004

Robinson, C., Holligan, P., Jickells, T., and Lavender, S. (2009). The atlantic meridional transect programme, (1995-2012) foreword. *Deep-Sea. Res. Part Ii-Topical. Stud. Oceanogr.* 56, 895–898. doi: 10.1016/j.dsr2.2008.10.005

Robinson, C., Poulton, A. J., Holligan, P. M., Baker, A. R., Forster, G., Gist, N., et al. (2006). The Atlantic Meridional Transect (AMT) Programme: A contextual view 1995-2005. *Deep-Sea. Res. Part Ii-Topical. Stud. Oceanogr.* 53, 1485–1515. doi: 10.1016/j.dsr2.2006.05.015

frontiers | Frontiers in Marine Science

TYPE Original Research
PUBLISHED 14 February 2023
DOI 10.3389/fmars.2023.1112177

Check for updates

OPEN ACCESS

EDITED BY
Laura Lorenzoni,
National Aeronautics and Space Administration (NASA), United States

REVIEWED BY
François Ribalet,
University of Washington, United States
Alex J. Poulton,
Heriot-Watt University, United Kingdom

*CORRESPONDENCE
Sornsiri Phongphattarawat
sornsiri.p@phuket.psu.ac.th

SPECIALTY SECTION
This article was submitted to Ocean Observation, a section of the journal Frontiers in Marine Science

RECEIVED 30 November 2022
ACCEPTED 30 January 2023
PUBLISHED 14 February 2023

CITATION
Phongphattarawat S, Bouman HA, Lomas MW, Sathyendranath S, Tarran GA, Ulloa O and Zubkov MV (2023) Ecophysiological basis of spatiotemporal patterns in picophytoplankton pigments in the global ocean. *Front. Mar. Sci.* 10:1112177. doi: 10.3389/fmars.2023.1112177

Ecophysiological basis of spatiotemporal patterns in picophytoplankton pigments in the global ocean

Sornsiri Phongphattarawat[1,2]*, Heather A. Bouman[1], Michael W. Lomas[3], Shubha Sathyendranath[4], Glen A. Tarran[4], Osvaldo Ulloa[5,6] and Mikhail V. Zubkov[7]

[1]Department of Earth Sciences, University of Oxford, Oxford, United Kingdom, [2]Faculty of Technology and Environment, Prince of Songkla University, Phuket, Thailand, [3]Bigelow Laboratory for Ocean Sciences, East Boothbay, ME, United States, [4]Plymouth Marine Laboratory, Plymouth, United Kingdom, [5]Department of Oceanography, University of Concepción, Concepción, Chile, [6]Millenium Institute of Oceanography, Concepción, Chile, [7]Scottish Association for Marine Science, Oban, United Kingdom

Information on the intracellular content and functional diversity of phytoplankton pigments can provide valuable insight on the ecophysiological state of primary producers and the flow of energy within aquatic ecosystems. Combined global datasets of analytical flow cytometry (AFC) cell counts and High-Performance Liquid Chromatography (HPLC) pigment concentrations were used to examine vertical and seasonal variability in the ratios of phytoplankton pigments in relation to indices of cellular photoacclimation. Across all open ocean datasets, the weight-to-weight ratio of photoprotective to photosynthetic pigments showed a strong depth dependence that tracked the vertical decline in the relative availability of light. The Bermuda Atlantic Time-series Study (BATS) dataset revealed a general increase in surface values of the relative concentrations of photoprotective carotenoids from the winter-spring phytoplankton communities dominated by low-light acclimated eukaryotic microalgae to the summer and early autumn communities dominated by high-light acclimated picocyanobacteria. In *Prochlorococcus*-dominated waters, the vertical decline in the relative contribution of photoprotective pigments to total pigment concentration could be attributed in large part to changes in the cellular content of photosynthetic pigments (PSP) rather than photoprotective pigments (PPP), as evidenced by a depth-dependent increase of the intracellular concentration of the divinyl chlorophyll-*a* (DVChl-*a*) whilst the intracellular concentration of the PPP zeaxanthin remained relatively uniform with depth. The ability of *Prochlorococcus* cells to adjust their DVChl-*a* cell^{-1} over a large gradient in light intensity was reflected in more highly variable estimates of carbon-to-Chl-*a* ratio compared to those reported for other phytoplankton groups. This cellular property is likely the combined result of photoacclimatory changes at the cellular level and a shift in dominant ecotypes. Developing a mechanistic understanding of sources of variability in pigmentation of picocyanobacteria is critical if the pigment markers and bio-optical properties of these cells are to be used to map their biogeography and serve as indicators of photoacclimatory state of subtropical phytoplankton communities more broadly. It would also allow better assessment of effects on, and adaptability of phytoplankton communities in the tropical/subtropical ocean due to climate change.

KEYWORDS

picocyanobacteria, *Prochlorococcus*, pigments, photoacclimation, phytoplankton, carbon-to-chlorophyll ratio

1 Introduction

Picophytoplankton (cell diameter< 2-3 µm) are the dominant primary producers in the largest biomes on Earth - the subtropical/tropical gyres. It has been estimated that marine picophytoplankton account for ~30% of global phytoplankton carbon biomass (~1 Pg C) (Le Quéré et al., 2005; Buitenhuis et al., 2012), and at least 10% of global net primary production (Visintini et al., 2021). As their oligotrophic habitats are expanding, presumably as a result of global warming (Polovina et al., 2008), it is anticipated there will be an overall shift in the size and community structure of marine phytoplankton. Highly-stratified oligotrophic waters have been shown to favour a dominance of picocyanobacteria, whereas in more dynamic, nutrient-replete environments photosynthetic picoeukaryotes tend to outcompete their cyanobacterial counterparts (Bouman et al., 2011).

Picophytoplankton also differ markedly in their vertical distribution: while *Synechococcus* often occupies the upper lit layer, *Prochlorococcus* and picoeukaryotes can be found throughout the euphotic zone in stratified oligotrophic waters (Claustre and Marty, 1995; Partensky et al., 1996; Hickman et al., 2010). The ability of *Prochlorococcus* to grow at the base of the euphotic zone has been ascribed to high light absorption efficiency resulting from its minute cell size and high concentrations of accessory pigments, in particular divinyl chlorophyll-*b* (DVChl-*b*), allowing the cells to harvest extremely low levels of blue light at depth (Moore et al., 1995; Barrera-Rojas et al., 2018). The co-existence of high light (HL) and low light-adapted (LL) ecotypes with variable ratios of DVChl-*b* to divinyl chlorophyll-*a* (DVChl-*a*) (Moore et al., 1998) can also explain the extremely large depth distribution of this genus (Campbell et al., 1994; Hickman et al., 2010). Furthermore, accessory chlorophyll-*b* and *c* and a variety of photosynthetic carotenoids with distinct light absorptive properties enable picoeukaryotes to exploit a broad range of light conditions and ensure an efficient harvesting of photons deep within the euphotic zone. The dominance of picoeukaryotes at depth is also linked to their ability to assimilate newly upwelled nitrogen (Claustre and Marty, 1995; Fawcett et al., 2011). In contrast, many strains of *Synechococcus* contain photosynthetic apparatuses rich in phycoerythrin and phycoerythrobilin which allow them to utilize orange-green photons abundant particularly near the surface of mesotrophic waters (Grébert et al., 2018) where blue light is strongly attenuated due to the presence of dissolved and particulate organic materials, including algal cells.

To derive information on the distribution, taxonomic composition, and productivity of picophytoplankton over larger spatio-temporal scales, various empirical models exploiting satellite observations of ocean color have been proposed (Hirata et al., 2008; Lange et al., 2018). In open ocean waters, variability in sea-surface reflectance is driven primarily by light absorption by phytoplankton pigments, and thus any factors that cause variability in phytoplankton pigment composition within phytoplankton groups could hinder our ability to use pigment data to infer changes in community structure. Moreover, variation in the intracellular composition of light-harvesting pigments induced by changes in environmental forcing, such as the strength of irradiance incident on the sea surface and the intensity of vertical mixing (Dusenberry et al., 1999), would complicate the conversion of pigment biomass measured by remote sensing into phytoplankton carbon (Karl, 1999) and the detection of shifts in community structure using ocean color sensors (Dutkiewicz et al., 2019).

Photoprotective pigments (PPP) have been shown to play an important role in governing the regional- and basin-scale variability in light absorptive properties of phytoplankton in the surface ocean (Babin et al., 1996; Bouman et al., 2000; Letelier et al., 2017). Variation in PPPs is closely linked with the taxonomic structure of phytoplankton communities: the PPP zeaxanthin associated with picocyanobacteria can contribute to a significant fraction of total pigment concentration in warmer, oligotrophic waters (Gieskes et al., 1988; Babin et al., 1996; Bouman et al., 2000), whereas in temperate and polar regions, PPP associated with eukaryotic cells (diadinoxanthin and diatoxanthin) tend to be more important (Johnsen et al., 2018). Within a biogeochemical province, fractional contributions of phytoplankton pigments, including PPPs, could also vary as cells physiologically respond to seasonal and/or vertical variation in available light (Uitz et al., 2008) and such light-dependent changes in pigment composition have been widely observed in cultures (Kulk et al., 2011; Stawiarski et al., 2018). Knowledge of how both photosynthetic and photoprotective pigments vary in the ocean and their relationship to dominant phytoplankton taxa is essential if we are to utilize the distribution of pigment markers and their associated bio-optical signatures to infer the flow of energy through marine ecosystems and to detect major phytoplankton groups.

Following from the points raised above, the first part of this study takes a community-level view of how variations in both the taxonomic composition and photoacclimatory status of phytoplankton influence the relative abundance of PPPs observed across various marine ecosystems both spatially and seasonally. By combining *in situ* pigment data and flow cytometric measurements of cell abundance, the second part of this study focuses on the photoacclimatory properties of picocyanobacterial populations. We exploit the unique divinyl chlorophylls of *Prochlorococcus* to examine how the intracellular pigment concentrations of this globally significant genus varies across the oligotrophic open ocean. By converting cell abundances obtained by flow cytometry to carbon biomass using published carbon conversion factors, we estimate the carbon-to-(DV) Chl-*a* ratio of *Prochlorococcus* (θ_{Pro}), and compare these values with those obtained from both bulk estimates of POC : Chl-*a* obtained in field measurements and from laboratory cultures. Our estimates of θ_{Pro} are then compared to published values of other picophytoplankton groups to determine whether the pigment-based responses of this model cyanobacterium can serve as an indicator of the photoacclimatory status of open-ocean phytoplankton communities in general.

2 Methods

2.1 Data

Pigment concentrations and cell abundance data used in this study were compiled from measurements carried out during oceanographic campaigns that focused primarily on the tropical and subtropical waters of the Atlantic and Pacific basins (Table 1 and Figure 1). Seawater samples were collected using a conductivity-temperature-depth (CTD) profiler equipped with a rosette of Niskin bottles. Further details on sampling strategies for individual oceanographic datasets can be found in the references provided in Table 1.

2.2 Phytoplankton pigment analysis

Phytoplankton pigments were identified and quantified using High-Performance Liquid Chromatography (HPLC). For each of the datasets, the filtration volumes, organic solvents used for pigment extraction, and corresponding references are summarized in Table 2. Note that DVChl-*a* and DVChl-*b*, pigment markers unique to *Prochlorococcus*, are not available for the Bermuda Atlantic Time-series Study (BATS) as the HPLC method employed did not allow for these pigments to be completely separated from their monovinyl derivatives (Steinberg et al., 2001). A quality check on the HPLC-determined pigment data was conducted using linear regressions (model I) of total accessory pigment concentration on total chlorophyll-*a* concentration (monovinyl + divinyl Chl-*a*; TChl-*a*) (Trees et al., 2000). Outliers with estimated standard deviations greater than 3 in absolute value (Uitz et al., 2006) were removed (final slope = 0.82, R^2 = 0.90), reducing the pigment database to 2,960 observations, which was 83% of the original data.

2.3 Estimation of picocyanobacteria abundance

Cell counts of the picocyanobacteria *Prochlorococcus* and *Synechococcus* were determined by Analytical Flow Cytometry (AFC) on either freshly collected or preserved samples. *Synechococcus* populations were identified from the orange fluorescence emitted by their characteristic phycoerythrin pigment-protein complex (Moore et al., 1995), and *Prochlorococcus* populations were distinguished based on their red fluorescence associated with DVChl-*a* and right-angle light scattering properties (Zubkov et al., 1998). However, *Prochlorococcus* cells collected from the surface layer of the subtropical gyres typically contain a very low concentration of DVChl-*a*, which makes it difficult to enumerate the cells accurately using their natural fluorescence signal (Zubkov et al., 1998; Grob et al., 2007a). Therefore, alternative approaches have been developed at different laboratories to estimate the abundance of surface *Prochlorococcus* populations that are weakly fluorescent as summarized below.

For the BIOSOPE project, Grob et al. (2007a); Grob et al. (2007b) determined the concentration of *Prochlorococcus* cells with low fluorescence by using the software Cytowin to fit a normal curve to the signal distribution plot. In cases where the fluorescence signal was too dim, the cell number was derived from the pigment DVChl-*a* assuming an average cell-specific concentration 0.23 fg DVChl-*a* cell^{-1} which was intracellular pigment concentration collected within the surface layer above the 5% level of the incident light and corresponded to the lowest possible values reported in Blanchot and Rodier (1996) and Partensky et al. (1999) for surface, HL *Prochlorococcus* populations. The BIOSOPE samples with *Prochlorococcus* cell abundances indirectly estimated from DVChl-*a* (N = 23) were included in our analyses, and they appeared to agree well with the general trends observed for other datasets.

For the AMT (Zubkov et al., 1998; Hartmann et al., 2014; Lange et al., 2018) and DCM datasets (Veldhuis and Kraay, 2004), *Prochlorococcus* in surface water samples were DNA-stained with fluorescent dyes, such as TOTO-1 (Zubkov et al., 1998), or SYBR Green (Hartmann et al., 2014), or PicoGreen (Veldhuis and Kraay, 2004), prior to analysis by flow cytometry. The staining technique allows for better visualization of the dim *Prochlorococcus* cells based on the green fluorescence originating from the DNA-binding dyes in addition to their chlorophyll (red) fluorescence and scattering signals.

Flow cytometric measurements for the HOT program between 1990 and 2005, which corresponds to the period when most of the HOT data used in this study were collected, were carried out using a flow cytometer fitted with a 1-W 488-nm laser as described in Campbell and Vaulot (1993). However, the authors noted that the flow cytometer configuration often failed to detect surface populations of *Prochlorococcus*. Thus, under these circumstances, a laser that generates an excitation beam in the range 457-515 nm was used instead (Olson et al., 1990) so that the excitation energy more closely matches the absorption bands of the DVChl-*a* and DVChl-*b* (Olson et al., 1990). This flow cytometer set-up was also optimized to increase the sensitivity of the instrument to detect surface assemblages of *Prochlorococcus* at the BATS station (DuRand et al., 2001).

2.4 Computation of mixed-layer and euphotic depths

For each of the datasets, the depth of the mixed layer (z_m) was calculated from vertical profiles of the potential density (σ_θ) [kg m^{-3}]

TABLE 1 Summary of oceanographic campaigns included in the database.

Dataset	Dates	N		Regions	Relevant publications
		HPLC	FCM		
Atlantic Meridional Transect (AMT)		1856	2684	North Atlantic Drift Province, South Atlantic Subtropical Convergence Province, North and South Atlantic Subtropical Gyres, Eastern and Western Tropical Atlantic Provinces, Canary Coastal Province, Benguela Current Coastal Province (upwelling system)	
AMT-3	22 Sep – 25 Oct 1996	298	209		Zubkov et al. (1998); Zubkov et al. (2000)
AMT-4	27 Apr – 21 May 1997	219	232		Zubkov et al. (2000)
AMT-6	15 May – 16 Jun 1998	508	170		Barlow et al. (2004)
AMT-12	12 May – 17 Jun 2003	236	371		Poulton et al. (2006); Lange et al. (2018)
AMT-13	8 Sep – 13 Oct 2003	172	277		Poulton et al. (2006); Lange et al. (2018)
AMT-14	28 Apr – 1 Jun 2004	208	942		Poulton et al. (2006); Lange et al. (2018)
AMT-15	17 Sep – 29 Oct 2004	215	483		Poulton et al. (2006); Zwirglmaier et al. (2007); Hickman et al. (2010); Lange et al. (2018)
Bermuda Atlantic Time-series Study (BATS)	2002 – 2007	698	761	Western North Atlantic Subtropical Gyre	Steinberg et al. (2001); Malmstrom et al. (2010)
BIogeochemistry and Optics SOuth Pacific Experiment (BIOSOPE)	26 Oct – 11 Dec 2004	615	1170	Transect from Marquesas Islands to the Coast of Chile (South Pacific Subtropical Gyre and Humboldt Current Coastal Province)	Grob et al. (2007a); Grob et al. (2007b)
Deep Chlorophyll Maximum Study (DCM)	Jul – Aug 1996	75	75	North Atlantic Subtropical Gyre	Bouman et al. (2000); Veldhuis and Kraay (2004)
Hawaii Ocean Time-series (HOT)	2002 – 2008	301	138	North Pacific Subtropical Gyre	Malmstrom et al. (2010); Letelier et al. (2017); Thompson et al. (2018)

N is the number of samples collected from each campaign for determination of pigment concentration using HPLC analysis (HPLC) and cell enumeration using flow cytometry (FCM). Biogeochemical provinces are defined according to Longhurst (1998).

obtained from online data repositories. When the online information of σ_θ was not readily available, the σ_θ was calculated from temperature and salinity profiles using the '*swSigmaTheta*' function in the R statistical package '*oce*' (Kelly, 2018). The z_m was defined as the depth at which the σ_θ was offset from the near surface (10 m) reference value by a threshold value of 0.125 kg m^{-3} (Bouman et al., 2006).

The euphotic depth (z_e) is often considered as the maximum depth in the water column where phytoplankton photosynthesis takes place, and typically corresponds to the depth at which the downwelling irradiance of photosynthetically-available radiation (PAR) decrease to 1% of its surface value (Kirk, 2011). Assuming that the spectrally non-resolved vertical attenuation coefficient for PAR, K_d (PAR) [m^{-1}], is constant with depth, the z_e can be estimated from K_d (PAR) using the relation (Kirk, 2011):

$$z_e = \frac{4.6}{K_d\,(\mathrm{PAR})} \; . \tag{1}$$

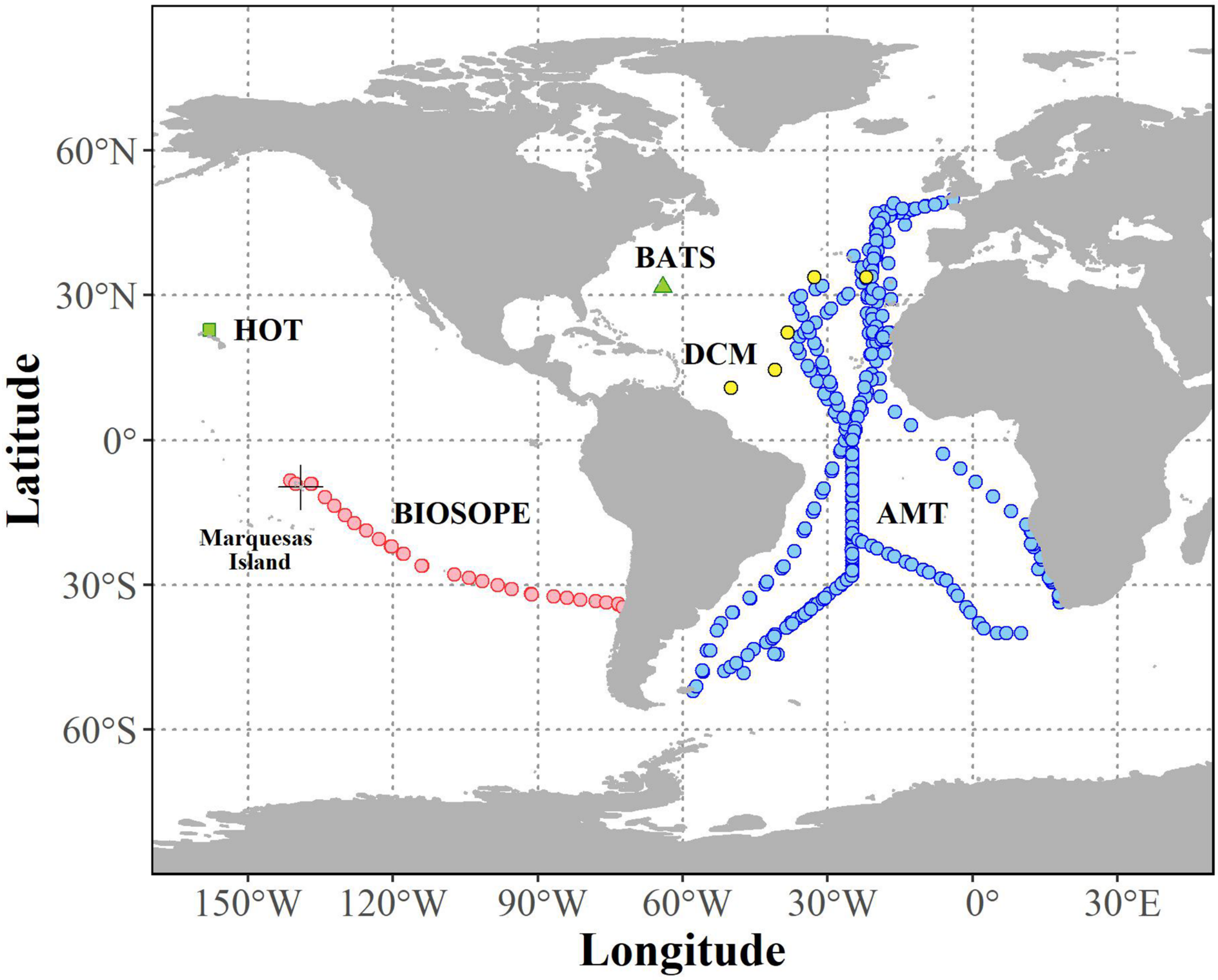

FIGURE 1
Map showing the distribution of oceanographic datasets of simultaneous measurements of phytoplankton pigment and picocyanobacteria abundance that passed quality assurance (N = 1,934).

TABLE 2 Summary of the filtration volume (V), organic solvent used for pigment extraction, and reference for each method used for HPLC pigment analysis for each oceanographic campaign.

Campaign	HPLC pigment analysis			Reference
	Methodology	V	Solvent	
AMT-3	Barlow et al. (1997)	0.5-2 L	90% acetone	Aiken et al. (2009)
AMT-4	Barlow et al. (1997)	2 L	90% acetone	Aiken et al. (2009)
AMT-6	Barlow et al. (1997)	0.5-4 L	90% acetone	Barlow et al. (2004); Aiken et al. (2009)
AMT 12-15	Barlow et al. (1997)	1-4.2 L	90% acetone	Poulton et al. (2006); Aiken et al. (2009)
BATS	Bidigare (1991)	4 L	90% acetone	Steinberg et al. (2001)
BIOSOPE	van Heukelem and Thomas (2001)	1-5.6 L	100% methanol	Ras et al. (2008)
DCM	Veldhuis and Kraay (1990)	20 L	100% methanol	Bouman et al. (2000); Veldhuis and Kraay (2004)
HOT	Bidigare et al. (2005)	4-10 L	100% acetone	Letelier et al. (2017)

K_d (PAR) was converted from the attenuation coefficient at 490 nm, K_d (490) [m^{-1}], using the relationship reported in Morel et al. (2007) for open-ocean (Case I) waters:

$$K_d\,(PAR) = 0.0665 + 0.874\ K_d\,(490) - \frac{0.00121}{K_d(490)} . \qquad (2)$$

The K_d (490) was calculated from TChl-*a* based on an empirical relationship derived by Morel and Maritorena (2001):

$$K_d\,(490) = K_w\,(490) + 0.07242\ Chl^{0.68955} \quad , \ (3)$$

where K_w (490) = 0.0166 m^{-1} is the attenuation coefficient for pure water at 490 nm, and Chl is the average TChl-*a* [mg Chl-*a* m^{-3}] in the mixed layer (Grébert et al., 2018).

Profiles of pigment ratios and intracellular pigment concentrations of picocyanobacteria are presented here as a function of optical depth (the nominal depth divided by the estimated euphotic depth, z/z_e). The advantages of using the dimensionless z/z_e index rather than nominal depths are twofold. First, it provides an approximation of ambient light conditions at a given depth when *in situ* vertically-resolved measurements of irradiance were not available (Uitz et al., 2008). Second, as pointed out in Lange et al. (2018), it implicitly carries information about attenuation of light through the water column, which has been shown to be a more effective predictor of long-term changes in phytoplankton pigments and cell abundance in the open ocean than does the instantaneous variation of light intensity expressed in absolute units.

3 Results

3.1 Changes in pigment composition of surface assemblages across contrasting nutrient regimes

Spatial distribution of pigment composition of phytoplankton populations in surface waters across different trophic domains encountered during the BIOSOPE transect in the South Pacific is illustrated in Figure 2. There is a clear relationship between the shoaling of the mixed layer and increased nutrient supply which likely reinforced changes in the relative contribution of PPPs as a result of the combined effect of taxonomic changes and photoacclimation. When we focus on depth-dependent changes in the ratio of PPPs (sum of zeaxanthin (ZEA), diadinoxanthin (DIAD), diatoxanthin (DIAT), violaxanthin (VIOL), alloxanthin (ALLO), and carotenes (CARO)) to the sum of all pigments (referred to in this study as the PPP index) within the oligotrophic samples, we observed a striking systematic increase from productive, upwelling stations to mesotrophic conditions, and to the high-nutrient, low-chlorophyll (HNLC) regions and the (hyper)oligotrophic central gyres (Figure 3A). These trophic-dependent changes that are evident throughout the euphotic zone are likely the result of corresponding shifts in both the photoacclimatory status and the taxonomic composition of phytoplankton communities.

Given that the BIOSOPE data were all collected within a restricted time period and latitudinal range, variation in incident solar radiation

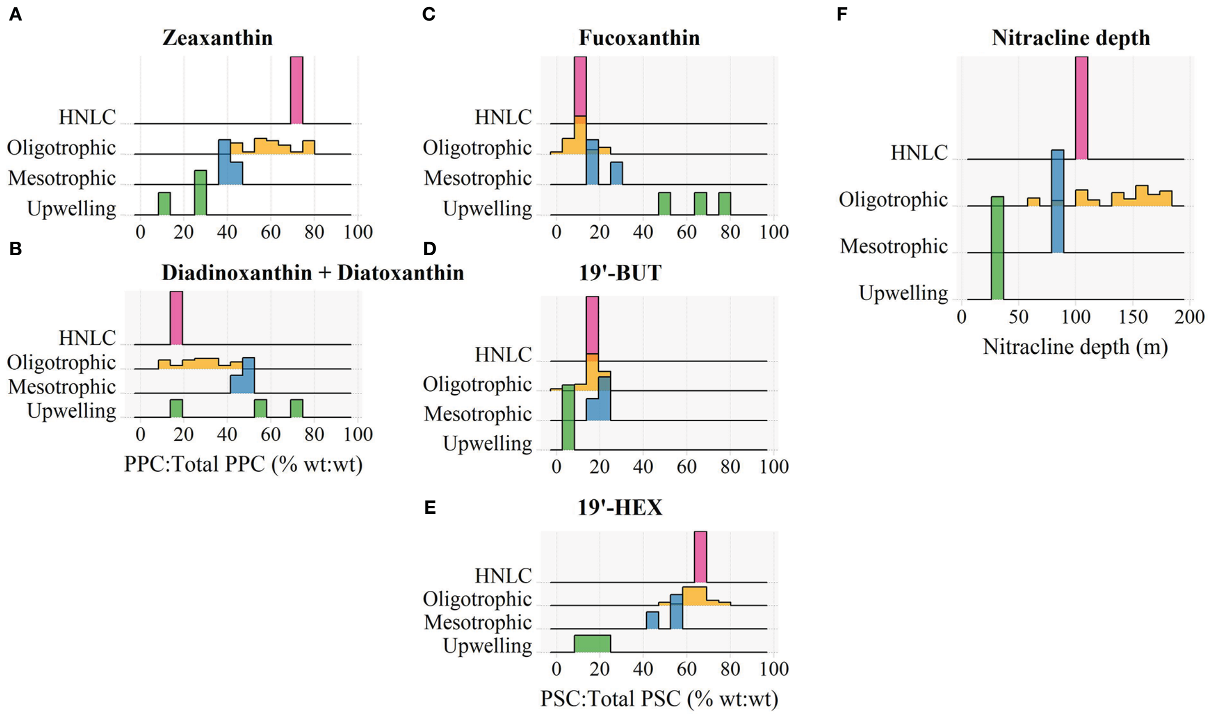

FIGURE 2
Frequency distributions of the percent contribution of **(A)** zeaxanthin and **(B)** diadinoxanthin + diatoxanthin to the total concentration of photoprotective carotenoids (PPC), and the percent contribution of **(C)** fucoxanthin, **(D)** 19′-butanoyloxyfucoxanthin (19′-BUT), and **(E)** 19′-hexanoyloxyfucoxanthin (19′-HEX) to the total concentration of photosynthetic carotenoids (PSC), and **(F)** the estimated nitracline depth for different trophic domains encountered during the BIOSOPE transect. Pigment contributions were measured in surface waters where $z/z_e < 0.1$.

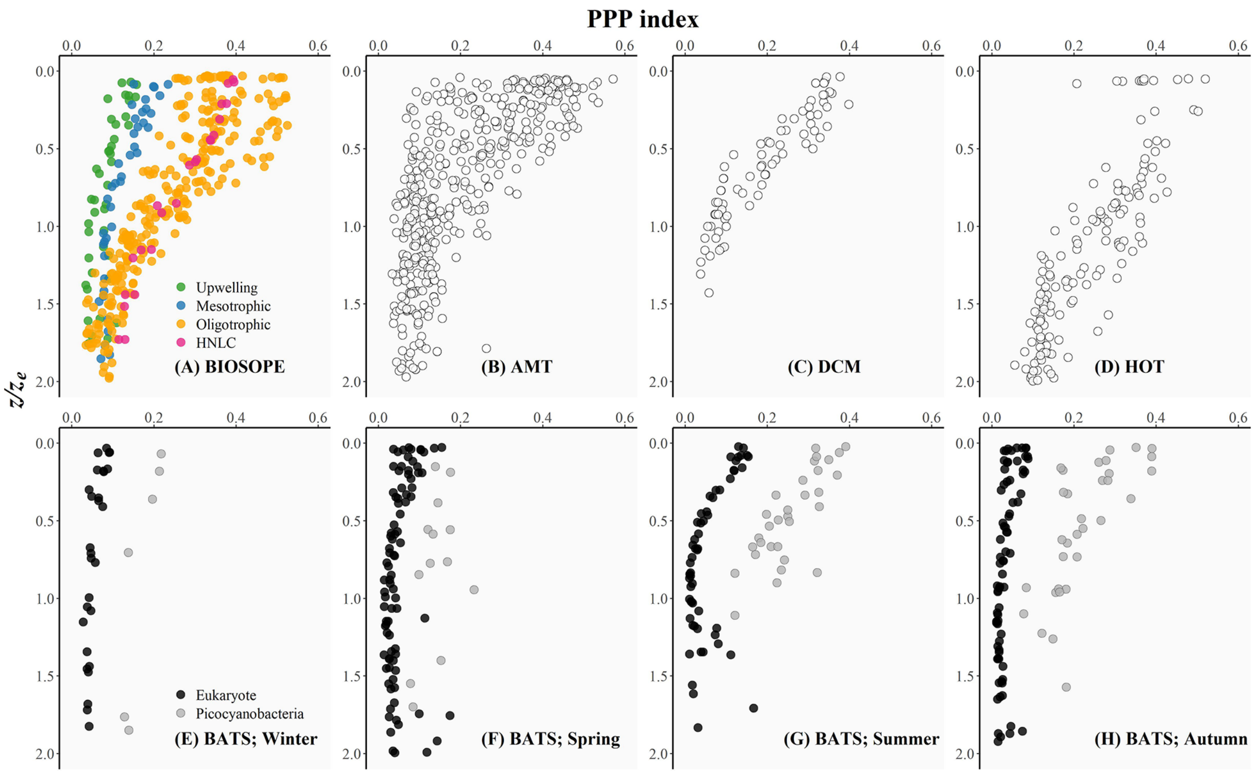

FIGURE 3
The photoprotective pigment index (PPP index: the ratio of PPPs to the sum of all pigments) plotted as a function of the depth of sampling divided by the depth of the euphotic zone (z/z_e) as an index of the underwater light availability for each oceanographic dataset included in this study: **(A)** BIOSOPE, **(B)** AMT, **(C)** DCM, **(D)** HOT, and **(E-H)** BATS (see the Methods section for details of each cruise). The BIOSOPE dataset was partitioned into the coastal upwelling, mesotrophic, oligotrophic, and high-nutrient, low-chlorophyll (HNLC) regions as described in Grob et al. (2007a). The BATS time series was roughly divided into seasons: **(E)** winter (21 December – 20 March), **(F)** spring (21 March – 20 June), **(G)** summer (21 June – 20 September), and **(H)** autumn (21 September – 20 December). For each season, phytoplankton communities were classified into those dominated by eukaryotic taxa (no detectable zeaxanthin; black circles) and those dominated by picocyanobacteria (ratio of zeaxanthin to the sum of all PPPs $\geq$ 0.6; grey circles).

should be minimal and thus differences in the pigment composition of surface phytoplankton communities are most likely primarily caused by shifts in taxonomic structure. Thus, we used the BIOSOPE dataset to explore the relative importance of cyanobacterial- versus eukaryotic-associated pigments in controlling the overall variation in the PPP index covering four major nutrient regimes (eutrophic, mesotrophic, oligotrophic and HNLC). In the HNLC and oligotrophic stations, ZEA, a diagnostic pigment of the picocyanobacteria *Synechococcus* and *Prochlorococcus*, accounted for more than half of the total PPP concentration (Figure 2A). On the other hand, DIAD and DIAT, associated with eukaryotic phytoplankton including photosynthetic picoeukaryotes (Dimier et al., 2009), contributed a low percentage ($\lesssim$ 30%) to the total PPP budget in these regions (Figure 2B). The relative abundance of ZEA decreased, while that of DIAD + DIAT increased as trophic conditions progressed toward a more productive state, indicating a domain shift from a prokaryote-dominated to a eukaryote-dominated surface phytoplankton community (Karl, 1999; Bouman et al., 2011).

The domain shift in pigment composition was also reflected in a progressive increase in the relative proportion of the photosynthetic pigment (PSP) fucoxanthin (FUCO), which is a pigment marker for diatoms, from oligotrophic open-ocean region to the coastal upwelling zone (Figure 2C). The PSPs chlorophyll-*b* (Chl-*b*) and prasinoxanthin (PRAS) along with the PPPs VIOL and neoxanthin (NEOX) were in significant quantities at several upwelling sites (data not shown) and indicated the presence of picoeukaryotic green algae (Ras et al., 2008), such as those in the genus *Ostreococcus* which has been reported to thrive in various coastal environments (Tragin and Vaulot, 2019). The near ubiquity of 19′-hexanoyloxyfucoxanthin (19′-HEX) throughout the transect (Figure 2E) reflects the cosmopolitan nature of haptophytes (Liu et al., 2009; Swan et al., 2016), and the elevated fraction of this carotenoid observed under oligotrophic conditions and in HNLC waters suggests that some of these cells may fall within the picophytoplankton size fraction (Ras et al., 2008; Liu et al., 2009).

The HNLC stations have surface TChl-*a* values (0.2-2 mg Chl-*a* m^{-3}) similar to those of the mesotrophic sites (i.e., near the Marquises Islands, Figure 1), yet they exhibited a markedly higher abundance of picocyanobacteria, especially *Prochlorococcus* (average of ~200×10^{3} cells mL^{-1}) in surface waters (0-80 m) of the HNLC region compared to ~60 × 10^{3} cells mL-$^{-1}$ at other mesotrophic sites (see also Grob et al., 2007a). This was reflected clearly in a markedly higher relative proportion of ZEA (Figure 2A). The numerical dominance of *Prochlorococcus* in these low-latitude HNLC waters was associated with highly stable water columns which were likely influenced by the South Pacific Tropical Water (Ras et al., 2008). Molecular studies (Rusch et al., 2010; Malmstrom et al., 2013) have revealed that *Prochlorococcus* isolated from HNLC regions of the tropical Pacific and Indian Oceans are adapted to iron limitation by reducing their iron requirements through the loss of several genes encoding iron-containing proteins which are mostly involved in the electron transport chain. These HNLC isolates also possess genes that enable them to efficiently acquire iron bound to organic ligands in seawater (Rusch et al., 2010; Malmstrom et al., 2013; Larkrin et al., 2020).

The taxonomic composition of open-ocean phytoplankton communities is governed largely by the supply of nutrients (Cullen et al., 2002). The region in the water column where there is a sharp increase in nitrate concentration is commonly referred to as the nitracline, and its depth, termed the nitracline depth, is widely regarded as an indicator of the supply of the deep-ocean nitrate to the upper mixed layer (Cullen et al., 2002; Cermeño et al., 2008). Along the BIOSOPE transect, the depth of the nitracline was found to increase steadily from the productive upwelling system nearshore to the more oligotrophic open ocean (Figure 2F). In the gyres, the deep nitracline and the corresponding reduced nutrient supply to surface waters resulted in a high abundance of picocyanobacteria indicated by higher values of the PPP index (Figure 3A). As the nitracline shoaled, the surface phytoplankton community structure shifted toward a eukaryote-dominated ecosystem (i.e., higher relative contributions of DIAD + DIAT and FUCO (Figures 2B, C), and lower PPP index values (Figure 3A)) supported by entrainment of new nutrients from depth.

3.2 Vertical changes across oceanic provinces and its seasonal variability

Figure 3 shows that the PPP index decreased vertically coinciding with a reduction in the relative availability of light in the water column as indexed by z/z_e (Uitz et al., 2008). For all of the datasets, the magnitude of the PPP index varied appreciably within the surface layer (i.e. $z/z_e < 0.5$), and the values appeared to converge to a minimum below the ~$1.5z_e$ depth.

HPLC data from the BATS time series revealed that the PPP index at the sea surface varied seasonally with consistently low and less variable values in winter and spring, and higher and more variable PPP index values observed during the summer-autumn months (Figures 3E–H). The uniformly low PPP index observed during winter (late December to mid-March) (Figure 3E) could be attributed to the combined effect of deep vertical mixing typical of the Sargasso Sea (Steinberg et al., 2001) and a seasonal reduction in incident solar radiation leading to a weakly-stratified water column. Nutrient-replete conditions established previously by deep winter mixing allowed eukaryotic phytoplankton to dominate within the surface layer until early spring (late March to mid-April). The relative similarities in the ambient nutrient and light conditions during winter and spring likely resulted in surface populations dominated by low light-acclimated cells and thus were reflected in the PPP indices for both seasons falling within a relatively similar range (Figures 3E, F). As the upper water column became thermally stratified due to intense solar heating, and the intensity of the wind-driven surface mixing was weakened during the late spring and summer months (late June to mid-September), the mixed layer shoaled such that phytoplankton were confined within the upper mixed layer and thereby continuously exposed to high UV and visible radiation. Photoacclimation of phytoplankton to high-light conditions resulted in an overall increase in the PPP index observed for both eukaryote-dominated and picocyanobacteria-dominated populations (Figure 3G). Picocyanobacterial cells continued to dominate the surface phytoplankton as surface waters became more nutrient-limited during the early autumn (late September to early October) when the sea-surface temperature remained relatively high (> 25°C) and the water-column was strongly stratified. However, as the autumn progressed, surface cooling and a deepening of the mixed layer allowed for the upper water column to be replenished with nutrients and resulted in a phytoplankton community dominated by larger eukaryotic cells acclimated to low-light intensities. This prokaryote-to-eukaryote domain shift occurring intraseasonally between early and late autumn was supported by the contrasting profiles of the PPP index (Figure 3H).

3.3 Photoacclimatory changes in the intracellular pigment content of picocyanobacteria

The BIOSOPE dataset illustrates that domain-specific (prokaryotic to eukaryotic) shifts in gross phytoplankton community structure governs horizontal changes in the relative contribution of photoprotective pigments to total pigment biomass in the surface ocean. However, the strong vertical decline in the PPP index was a striking feature exhibited across the various datasets that span a range of spatial and temporal scales (Figure 3). Since picocyanobacteria have been shown to exhibit tremendous variation in their pigment composition in response to both seasonal and vertical changes in light conditions, we examined the photoacclimatory characteristics of this group at the cellular level *via* the intracellular content of their diagnostic pigments. Our analyses were focused primarily on the picocyanobacteria-dominated waters of the subtropical and tropical oligotrophic gyres where simultaneous measurements of abundance determined by flow cytometry and pigment concentrations measured using the HPLC method were widely available.

In picocyanobacteria, photoacclimatory changes in the magnitude of the PPP index could be attributed to variation in the intracellular concentration of either photoprotective (Kulk et al., 2011; Mella-Flores et al., 2012), or photosynthetic pigments (Kana et al., 1988; Moore et al., 1995), or both. To assess the relative influences that each of these two major pigment groups has on variation in the PPP index, intracellular concentration of ZEA (Figure 4) found in both picocyanobacterial genera *Synechococcus* and *Prochlorococcus* and DVChl-*a*, which is the major photosynthetic pigment for the genus *Prochlorococcus* (Figure 5) were plotted against the z/z_e index as a proxy for the relative light availability. When calculating the intracellular concentration of ZEA, we partitioned this pigment between the two cyanobacteria groups based on culture observations that have shown that ZEA per cell for *Synechococcus* is approximately three-times higher than that of *Prochlorococcus* when grown over a similar range of light intensities (Moore et al., 1995).

The intracellular concentration of ZEA remained relatively uniform from the well-lit surface layer down to the bottom of the euphotic zone (Figure 4), whereas the amount of DVChl-*a* cell^{-1} gradually increased with depth (Figure 5). However, for the BIOSOPE

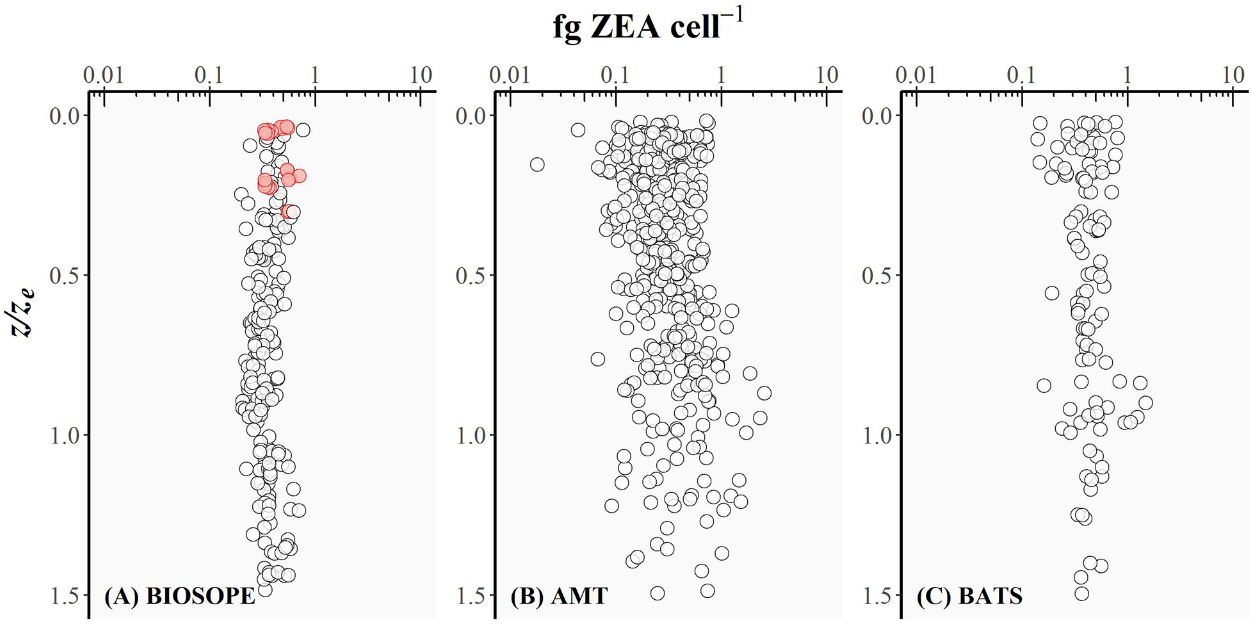

FIGURE 4
The intracellular concentration of zeaxanthin (fg ZEA cell^{-1}) for picocyanobacteria plotted as a function of the depth of sampling divided by the depth of the euphotic zone (z/z_e) for **(A)** BIOSOPE, **(B)** AMT, and **(C)** BATS datasets. Red circles represent the cases where the *Prochlorococcus* cell number was derived from DVChl-*a* concentration as the fluorescence signal measured in flow cytometry was too weak.

dataset, the calculated DVChl-*a* cell^{-1} was relatively constant within the top 0-0.5z_e layer with most values falling between 0.2-0.3. This is partially the result of the authors estimating *Prochlorococcus* abundance based on pigment data assuming 0.23 fg DVChl-*a* cell^{-1} for surface samples (Figure 5, red circles) where the natural fluorescence of these cells was too low to detect them using flow cytometry (Grob et al., 2007a). In addition, mesotrophic stations sampled during the BIOSOPE cruise off the Marquesas Islands exhibited intracellular concentrations of DVChl-*a* that were substantially higher (nearly 1.0 fg DVChl-*a* cell^{-1}) and more

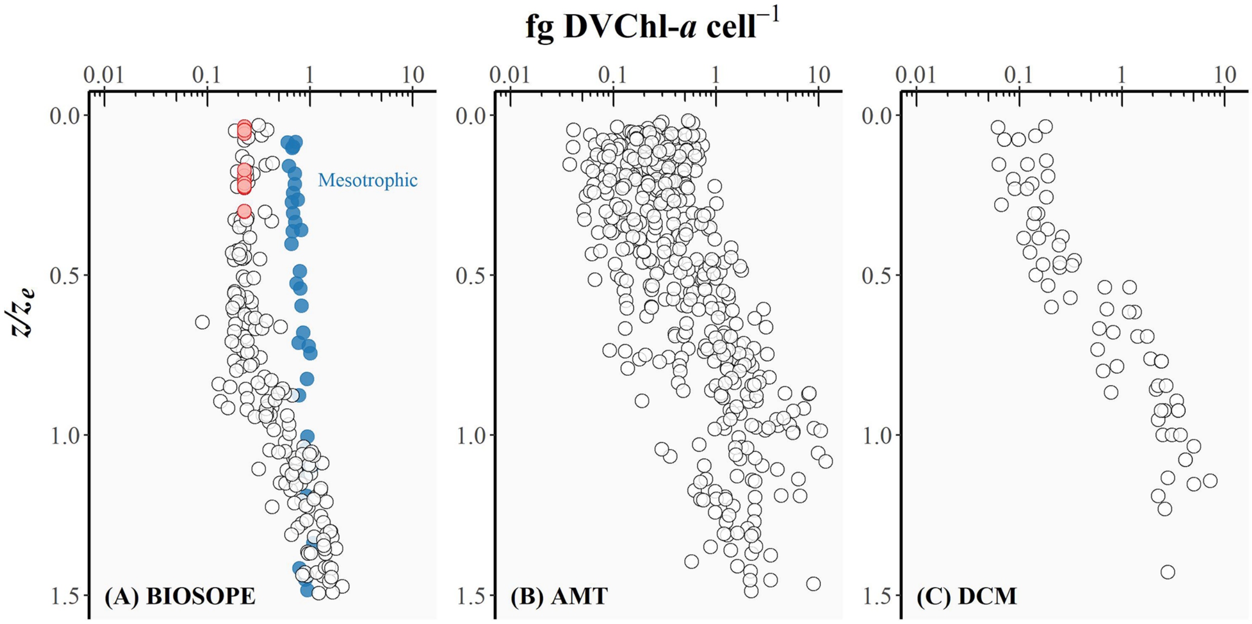

FIGURE 5
The intracellular concentration of divinyl chlorophyll-*a* (fg DVChl-*a* cell^{-1}) for *Prochlorococcus* plotted as a function of the depth of sampling divided by the depth of the euphotic zone (z/z_e) for **(A)** BIOSOPE, **(B)** AMT, and **(C)** DCM datasets. Red circles represent the cases where the *Prochlorococcus* cell number was derived from DVChl-*a* concentration as the fluorescence signal measured in flow cytometry was too weak.

uniform over the vertical profile than the rest of the transect (Figure 5, blue circles). Vertical density profiles revealed that these stations were more deeply mixed (mixed layer depths of ~70-100 m compared to< 50 m typically observed at other stations), which would reduce the average daily mixed-layer irradiance for phytoplankton communities. If we assume that *Prochlorococcus* cells were uniformly mixed throughout the mixed layer, the reduction in the average mixed-layer irradiance would result in an increase in the intracellular concentration of their major light-harvesting pigments and therefore explain the relatively high and uniform DVChl-*a* cell^{-1} and low PPP index (Figure 3A, blue circles) measured throughout the water column at these stations.

Uniform ZEA cell^{-1} values over a range of z/z_e values (Figure 4) are reflected in the linear relationship between bulk ZEA concentration and the number of picocyanobacterial cells (Pico) depicted in Figure 6 ($\log_{10}$ Pico = 0.90 $\log_{10}$ ZEA + 3.65, R^2 = 0.61). Upper and lower envelopes shown in Figure 6 correspond, respectively, to the maximum (q_{max}) and minimum (q_{min}) quantiles (Sathyendranath et al., 2009). Quantile regressions facilitated constraining the variability in values of ZEA cell^{-1} by allowing outliers that fell outside the computed maximum and minimum quantiles to be identified and removed. The lower and upper bounds could be viewed as being representatives of extremely high-light (surface) and low-light (bottom of the euphotic zone) conditions, respectively. Note that higher ZEA cell^{-1} values could result from the presence of other cyanobacterial populations not accounted for in the flow cytometry counts, in particular the colonial diazotroph *Trichodesmium* that is known to be abundant in the North Atlantic Subtropical Gyre.

Quantile regressions were also fitted to the plot of DVChl-*a* concentration against *Prochlorococcus* cell abundance (Pro) (Figure 7A; $\log_{10}$ Pro = 0.82 $\log_{10}$ DVChl-*a* + 3.53, R^2 = 0.40). In this case, the physiological interpretation of the upper and lower envelopes is the opposite to that for the ZEA-cell abundance relationship (Figure 6): the lower boundary (q_{min} = 0.01) corresponds to the upper limit of DVChl-*a* cell^{-1} for *Prochlorococcus* cells acclimated to extremely low light, whereas the upper boundary (q_{max} = 0.99) represents the lower limits of DVChl-*a* cell^{-1} resulting from cells photoacclimated to maximum surface irradiances. The overall variability in the relationship between DVChl-*a* and cell abundance (Figure 7A) was far greater than that of ZEA and cell abundance (Figure 6). This highlights the significance of the photosynthetic pigment fraction in driving changes in the PPP index in picocyanobacterial-dominated systems.

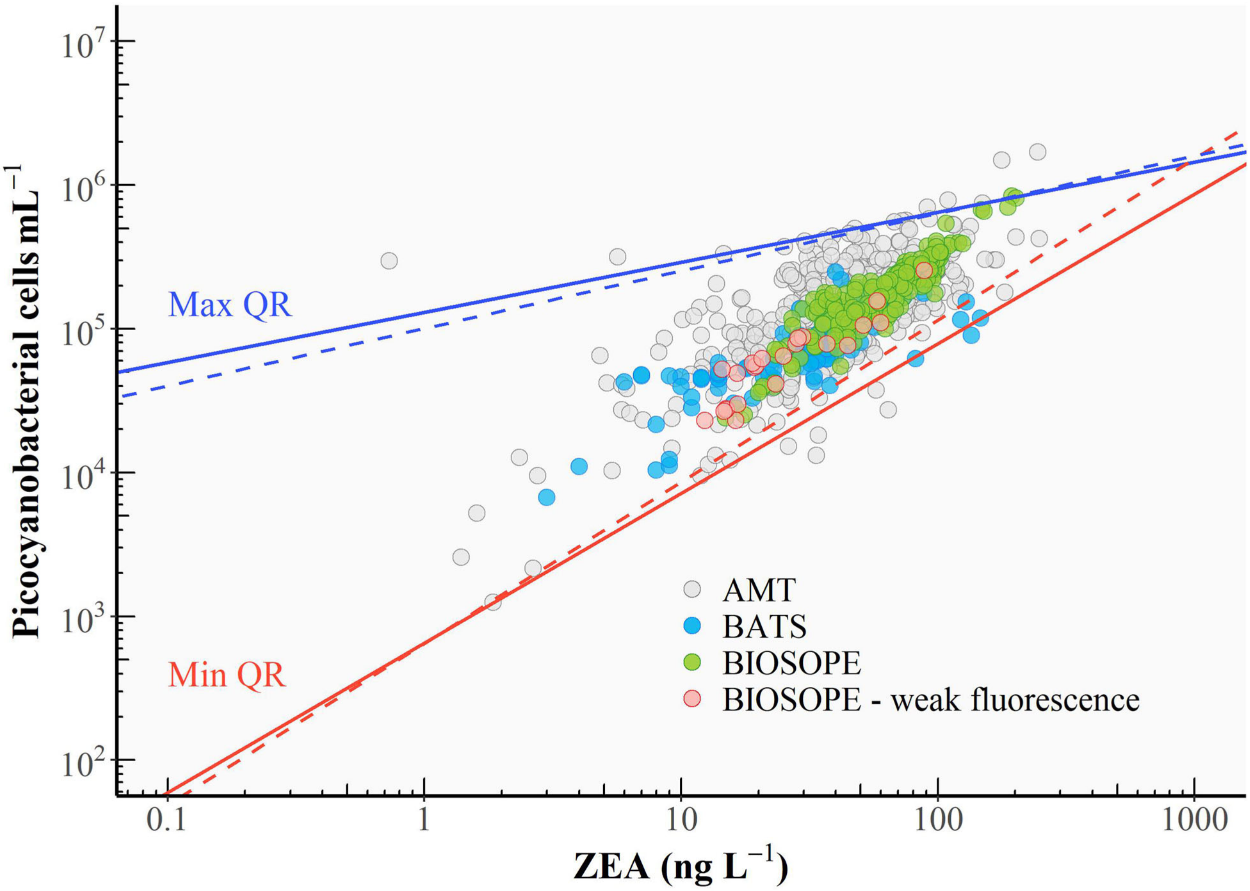

FIGURE 6
Relationship between cell abundance of picocyanobacteria and the concentration of zeaxanthin (ZEA). A linear regression was performed (black line), and the 95% confidence interval for the linear regression line is shaded in grey. The upper (solid blue line) and lower (solid red line) boundaries correspond to the maximum (99th) and minimum (1st) quantiles, respectively (see text for the calculation). Dashed lines represent the re-fitted quantile regressions after identified outliers were excluded. Red circles represent the cases where the *Prochlorococcus* cell number was derived from DVChl-*a* concentration as the fluorescence signal measured in flow cytometry was too weak.

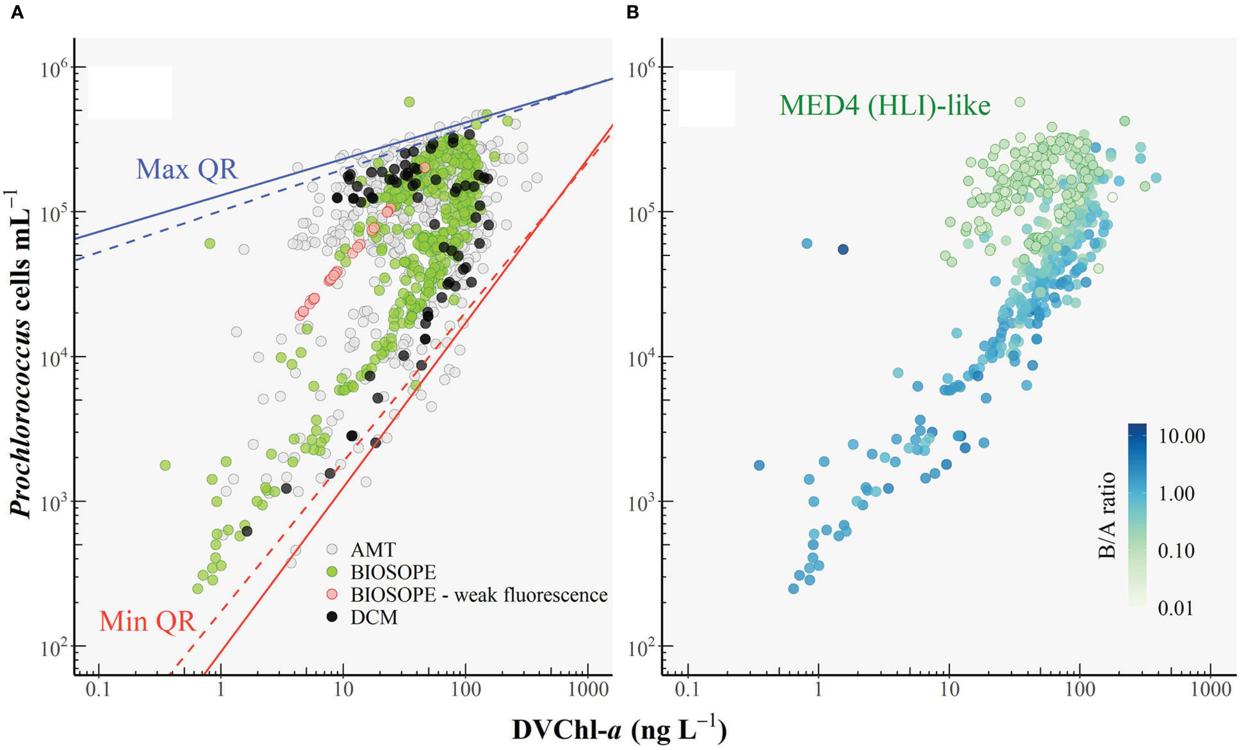

FIGURE 7
(A) Relationship between *Prochlorococcus* cell abundance and the concentration of divinyl chlorophyll-*a* (DVChl-*a*). The black line represents the line of best fit, and the grey shaded area indicates the 95% confidence interval. The upper (solid blue line) and lower (solid red line) boundaries correspond to the maximum (99th) and minimum (1st) quantiles, respectively. Dashed lines represent the re-fitted quantile regressions after outliers were removed. Red circles represent the cases where the *Prochlorococcus* cell number was derived from DVChl-*a* concentration as the fluorescence signal measured in flow cytometry was too weak. **(B)** As in **Figure 7A** with symbols coloured according to the weight-to-weight ratio of divinyl chlorophyll-*b* to divinyl chlorophyll-*a* (B/A ratio). *Prochlorococcus* samples with B/A ratios of<0.14 were classified as the MED4 (HLI)-like populations. Note that only a subset of the HPLC dataset could be used for this analysis since for some datasets DVChl-*b* was not separated from monovinyl Chl-*b*.

3.4 Estimation of the carbon-to-DVChl-*a* ratio of *Prochlorococcus*

The carbon-to-DVChl-*a* ratio of *Prochlorococcus* (θ_{Pro}) was estimated based on simultaneous measurements of cell abundance and the concentration of DVChl-*a* illustrated in Figure 8. *Prochlorococcus* cell carbon was estimated from abundances (determined by flow cytometry) using two sets of conversion factors. The first conversion factor of 49 fg C cell^{-1} (Cailliau et al., 1996) based on the assumption that both HL- and LL-ecotypes have similar carbon contents. In non-axenic cultures of a *Prochlorococcus* strain, Cailliau and colleagues (1996) derived the cellular carbon contents from flow cytometric cell counts and measurements of particulate organic carbon (POC) that were corrected for the presence of heterotrophic bacteria. Their study found that the values obtained for *Prochlorococcus* under low and high light were not statistically different, suggesting that this value may be applied to both HL and LL cells.

We also applied conversion factors of 52 and 158 fg C cell^{-1} (Casey et al., 2013) to *Prochlorococcus* populations residing within the euphotic (0-120 m) and sub-euphotic zone (> 120 m), respectively, during the period of water-column stratification which is reflected in the presence of a deep chlorophyll maximum. Casey and colleagues (2013) derived the carbon biomass of *Prochlorococcus* at the BATS stations based on an empirical relationship between flow cytometric forward light scatter and cellular carbon content. Their study found that *Prochlorococcus* carbon content increases significantly with depth as cells acclimate to low-light conditions potentially by increasing the number of thylakoid membranes to allow increased synthesis of PSPs (Casey et al., 2013).

Values of the cellular carbon content of surface *Prochlorococcus* populations obtained by both Cailliau et al. (1996) from cultures and Casey et al. (2013) from field samples are comparable to published estimates from other studies [e.g. 53 fg C cell^{-1} reported in DuRand et al. (2001); 54 fg C cell^{-1} in Campbell et al. (1994) and Grob et al. (2007b)], although it is important to stress that determination of the carbon content from cell volume has a significant degree of uncertainty since, as pointed out in Bertilsson et al. (2003), the amount of carbon per unit cell volume observed in marine bacteria can vary both between and within species in response to changes in growth conditions. Our choice of conversion factors is therefore based on estimates of *Prochlorococcus* cellular carbon content derived from direct measurements of POC (Partensky et al., 1999; Bertilsson et al., 2003) and the conversion factors used in this study fall within those obtained from studies of natural picophytoplankton populations.

3.5 Constraining the variability in the estimated θ_{Pro}

When samples collected from below the 1.5z_e depth and potential outliers (Figure 8) were removed, our estimates of θ_{Pro} varied from 9

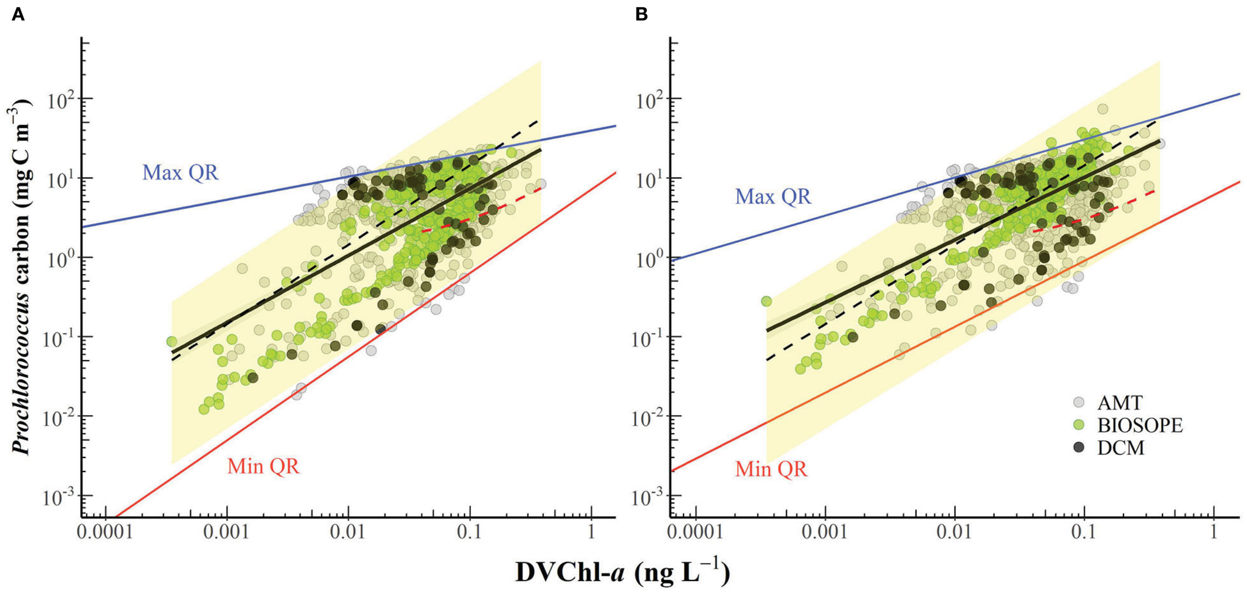

FIGURE 8
The cell carbon biomass of *Prochlorococcus* plotted against the concentration of divinyl chlorophyll-*a* (DVChl-*a*). Carbon content was converted from cell abundances using the conversion factor of **(A)** 49 fg C cell^{-1} (Cailliau et al., 1996) and **(B)** 52 and 158 fg C cell^{-1} for euphotic and sub-euphotic populations, respectively (Casey et al., 2013). The black line represents the line of best fit (panel A: $\log y = 0.843 \log x + 1.711$, $R^2 = 0.41$; panel B: $\log y = 0.788 \log x + 1.798$, $R^2 = 0.47$), and the grey shaded area indicates the 95% confidence interval. The upper (solid blue line) and lower (solid red line) boundaries correspond to the maximum (99th) and minimum (1st) quantiles, respectively. The black dashed line corresponds to the carbon-to-DVChl-*a* of *Prochlorococcus* (θ_{Pro}) of 145 g C (g DVChl-*a*)$^{-1}$ reported in Sathyendranath et al. (2009). The red dashed line represents the relationship observed by Latasa et al. (2022) in the northwestern Mediterranean Sea in September 2009 when the measured DVChl-*a* concentrations were always greater than 0.04 mg m^{-3}. The yellow-shaded area represents the possible range of θ_{Pro} values reported in the literature.

to 499 g C (g DVChl-*a*)$^{-1}$ for all samples, and θ_{Pro} values for surface populations ($z/z_e < 0.1$) ranged from 66-361 g C (g DVChl-*a*)$^{-1}$. To assess whether the extent of the observed variability in θ_{Pro} was reasonable, these results were compared with θ_{Pro} measured in various culture experiments and field studies using an approach outlined in Marañón (2005). Given that (1) the intracellular carbon content of *Prochlorococcus* previously reported in the literature ranged from about 29 to 158 fg C cell^{-1} (Casey et al., 2013 and references therein), and (2) the intracellular content of DVChl-*a* of *Prochlorococcus* cells subject to extremely high irradiances typical of the subtropical surface ocean (e.g. > 1,000 µmol quanta m^{-2} s^{-1}) can be as low as ~0.2 fg DVChl-*a* cell^{-1} (Blanchot and Rodier, 1996; Grob et al., 2007a) and that of *Prochlorococcus* growing under very low irradiances (e.g. 7 µmol quanta m^{-2} s^{-1}) is up to 4.0 fg DVChl-*a* cell^{-1} (Partensky et al., 1993; Blanchot et al., 2001), the resulting upper boundary of θ_{Pro} values should be in the range of 145-790 g C (g DVChl-*a*)$^{-1}$ and the lower boundary in the range of 7-40 g C (g DVChl-*a*)$^{-1}$. In general, our estimated values of θ_{Pro} fell within these derived upper and lower limits.

Using open-ocean samples collected from the Northwest Atlantic and the Arabian Sea, Sathyendranath et al. (2009) indirectly estimated an upper bound on θ for different groups of phytoplankton in the field based on quantile linear regressions of POC and Chl-*a* concentration and obtained an average θ_{Pro} value of 145 g C (g DVChl-*a*)$^{-1}$ for stations classified as *Prochlorococcus*-dominated. When this average value was superimposed on the scatterplot of *Prochlorococcus* cell carbon content and DVChl-*a* concentration (Figure 8), the line of best fit from the Sathyendranath et al. (2009) study lies remarkably closed to the best equation obtained in this study, despite being derived from independent datasets. It should be noted that most of the data used in Sathyendranath et al. (2009) were from samples collected within the top 40 m of the water column, and therefore their estimate likely applies to cells acclimated to mixed-layer light intensities. The estimated value of θ_{Pro} obtained in the Sathyendranath et al. (2009) study was higher than the average θ_{Pro} values reported by Blanchot et al. (2001) for surface (0-40 m) *Prochlorococcus* samples from the oligotrophic (66 g C (g DVChl-*a*)$^{-1}$) and HNLC (93 g C (g DVChl-*a*)$^{-1}$) regions of the equatorial Pacific (Table 3). It has been shown that *Prochlorococcus* samples from mesotrophic regions contain more carbon biomass relative to chlorophyll pigment than samples associated with oligotrophic environments (Wei et al., 2019) and this may explain the higher θ_{Pro} values in the Sathyendranath et al. (2009) study.

4 Discussion

4.1 Photoacclimatory changes in the cellular content of photoprotective and photosynthetic pigments

The vertical patterns in the cellular content of PPPs and PSPs observed in this study are consistent with those obtained by Matsumoto and Ando (2009) who examined vertical profiles of picocyanobacterial pigments in the nutrient-limited western Pacific and found a steady vertical increase in the intracellular Chl-*a* concentration but no obvious variation in ZEA content. Our findings are also supported by culture experiments. Kana et al.

TABLE 3 Published estimates of carbon-to-(DV)Chl-*a* ratio (θ) for *Prochlorococcus* (Pro) and photosynthetic picoeukaryotes (PPE).

Reference	Study area (sampling depth)	θ (g C (g Chl-*a*)$^{-1}$)	
		Pro[a]	PPE
Blanchot et al. (2001)	Equatorial Pacific (0-50 m) - Oligotrophic (warm pool) region - HNLC region	67 93	43 84
Kulk et al. (2011)	Culture experiments (light intensities: 50-125 µmol quanta m^{-2}s^{-1})	14-43 (HLI)	39-40[b]
Latasa et al. (2022)	Open northwestern Mediterranean Sea (Average, 0-100 m) - During the spring bloom (Mar.) - Post-bloom period (Apr.-May) - Fully developed stratification period (mid Sep.)	29.8-49.3	6.9-16.7[c] 15.8-28.7[c] 11.4-73.2[c]
Sathyendranath et al. (2009)	Northwest Atlantic and the Arabian Sea (0-40 m)	143-147	
Stawiarski et al. (2018)	Culture experiments (13-150 µmol quanta m^{-2} s^{-1})	12-36 (HLII) 15-56 (LLII)	19-24[d] 19-28[e]
Veldhuis and Kraay (2004)	Subtropical North Atlantic (0-150 m)	15-450	30-80
This study		9-499	

[a] HL and LL = High light and low light-adapted ecotypes.
[b] *Ostreococcus sp.*
[c] Green algae contribute substantially to the picoeukaryote biomass pool (Latasa et al., 2022).
[d] *Micromonas pusilla*, [e] *Nannochloropsis granulata*.

(1988) were amongst the first to observe the constant ZEA cell^{-1} in nutrient-replete batch cultures of *Synechococcus* WH7803 grown under different irradiance levels. Similarly, Moore et al. (1995) found that *Synechococcus* WH8103 and *Prochlorococcus* MED4 maintained relatively constant cellular content of ZEA under varying irradiances, although for the *Prochlorococcus* SS120 strain, there was a slight increase with the increased light level. In contrast, the intracellular concentration of (DV)Chl-*a* was found to decrease significantly at high light for all picocyanobacterial isolates, with the DVChl-*a* cell^{-1} of *Prochlorococcus* being up to six times lower than the Chl-*a* cell^{-1} of *Synechococcus*. A molecular study by Mella-Flores et al. (2012) revealed that *Synechococcus* WH8103 possess more genes involved in photoprotection and the dissipation of excess energy as heat than *Prochlorococcus* PCC9511 (very close to the MED4 strain), and that there was a close correlation between expression levels of these genes and diel variations of growth irradiances for *Synechococcus* which was not always the case for *Prochlorococcus*. The study also suggested that, rather than intensively inducing a variety of photoprotective mechanisms (including the production of ZEA) as observed in *Synechococcus*, high light-acclimated *Prochlorococcus* reduces their energy demand by temporarily down-regulating the synthesis of light-harvesting pigment proteins, ATP formation, and the light-independent reactions of photosynthesis. This is not only to avoid photodamage during a period of high irradiance, but also allows *Prochlorococcus* cells to generate the energy from photosynthesis that is sufficient to satisfy their minimized energy requirement despite having only low amounts of PSPs to carry out light absorption for photochemistry (Hartmann et al., 2014).

The large dynamic range of DVChl-*a* cell^{-1} values observed in our dataset appears to be indicative of the ability of *Prochlorococcus* to acclimate to a broad range of light conditions (Partensky et al., 1999). Yet, culture experiments by Moore et al. (1995) on *Prochlorococcus* strains MED4 and SS120 suggested that plasticity in the intracellular content of DVChl-*a* in different ecotypes may be restricted to a range of light levels not greater than ~2.5 orders of magnitude (Moore et al., 1995; Partensky et al., 1999). The high dynamic range in the DVChl-*a* cell^{-1} in the field data can be explained by the combined result of both photoacclimation and a vertical shift in dominant (HL and LL) ecotypes, given the limited range of intracellular pigment content observed in cultures.

Figure 7A shows that data points tended to separate into two clusters: one above the line of best fit corresponding to lower cell-specific DVChl-*a* concentration, and another below the line of best fit which corresponded to samples exhibiting higher DVChl-*a* content per cell. These clusters represent two distinct populations of *Prochlorococcus* cells occupying different vertical niches in the water column. The occurrence of a double or bimodal population is a common feature in flow cytometric studies that have examined the intensity of cellular fluorescence in the red due to DVChl-*a* (Campbell et al., 1994; Blanchot and Rodier, 1996; Thompson et al., 2018). Dim populations have a lower intracellular concentration of DVChl-*a* and thus lower cellular fluorescence, and tend to be found within the surface mixed layer. On the other hand, bright populations have markedly higher DVChl-*a* cell^{-1} and thus a much stronger fluorescence signal, and typically dominate near the bottom of the euphotic zone. Previous studies (Moore et al., 1998; Moore and Chisholm, 1999) on cultured isolates distinguished the dim and bright *Prochlorococcus* as HL- and LL-adapted ecotypes, respectively, according to the observation that the dim isolates have lower ratios of DVChl-*b* to DVChl-*a* (B/A ratios) than the bright ones over a range of growth irradiances. Molecular studies (Partensky and Garczarek, 2010 and references therein) later confirmed that the two ecotypes differentiated by B/A ratios are, in several ways, genetically distinct.

As illustrated in Figure 7B, ecotype differentiation in *Prochlorococcus* could account for variation in the intracellular DVChl-*a* concentration measured in this study. In the absence of genetic information for most of our datasets, B/A ratios were used instead to distinguish ecotypes in *Prochlorococcus* assemblages, with an increase in B/A ratios indicating a shift from HL ecotype-dominated populations toward populations dominated by LL-adapted strains. Note that only a subset of the HPLC dataset could be used for this analysis since for some datasets, DVChl-*b* was not separated from monovinyl Chl-*b*.

Figures 7A, B show a clear separation of HL (lower B/A ratios) and LL ecotypes (higher B/A ratios) based on their DVChl-*a* cell^{-1}, highlighting how the two *Prochlorococcus* ecotypes are readily distinguished from each other on the basis of their intracellular pigment concentration. Note, however, that this rather crude pigment criterion for classifying HL and LL ecotype-dominated populations does not reflect the fact that both ecotypes can co-exist. A study by Thompson et al. (2018) conducted at station ALOHA reported the presence of the LL-adapted strain NATL (with relatively high B/A ratios; Rocap et al., 2002) in the surface *Prochlorococcus* populations characterized by low intracellular chlorophyll concentration. This was likely to be the result of deep vertical mixing of the water column that brought LL ecotype into the surface layer (Bouman et al., 2006; Thompson et al., 2018). The physiological and genetic characteristics that are intermediate between HL and LL ecotypes (Partensky and Garczarek, 2010) and the ability to be better acclimated to high light relative to other members of the same LL ecotype (Rocap et al., 2002; Malmstrom et al., 2010) allow the *Prochlorococcus* NATL to occupy a larger depth range than other clades (Partensky and Garczarek, 2010).

To examine the impact of shifts in ecotype diversity on variation in DVChl-*a* cell^{-1} requires that ecotype abundances were measured using molecular methods for each sample. Since this information was not available for many of the datasets, the B/A ratios were used to assist in the identification of certain *Prochlorococcus* strains. Comparative culture experiments by Partensky et al. (1993) on the isolates MED4 (HLI), SARG (LLI), and NATL (LLI) grown at different irradiance levels (~7.5-133.0 µmol quanta (white light) m^{-2} s^{-1}) showed that the relationship between intracellular concentration of DVChl-*a* and DVChl-*b* (Figure 2 in Partensky et al., 1993) for the MED4 strain had a regression slope that was markedly different from those for SARG and NATL1 strains. Also, although B/A ratios for all strains exhibited a general decreasing trend with increasing growth irradiances, the B/A ratio of the MED4 strain was always less than 0.14, while those of the SARG and NATL1 strains were never found to fall below this value. The range of B/A ratios of the MED4 isolate reported in Partensky et al. (1993) is comparable to the results of Moore and colleagues (1995) who observed the range between 0.05 and 0.20 (growth irradiance >10-400 µmol quanta (white light) m^{-2} s^{-1}), and of Rocap et al. (2002) who reported that the MED4 strain acclimating to low light at 18 µmol quanta (white light) m^{-2} s^{-1}) (~1% of typical surface irradiance at subtropical gyres) had a B/A ratio of 0.20, which is the lowest among the 32 *Prochlorococcus* strains examined.

Based on the culture study of Partensky et al. (1993), *Prochlorococcus* samples which were likely to be dominated by the MED4 strain (B/A ratio< 0.14) were identified. As shown in Figure 7B (green outline circles), populations dominated by the MED4-like cells exhibited very low intracellular concentrations of DVChl-*a*, typical of HLI ecotypes, although the values were somewhat variable. Vertical profiles (data not shown) showed that DVChl-*a* cell^{-1} for samples identified as resembling *Prochlorococcus* HLI populations increased from *ca* 0.1 near the well-lit surface to up to 1.0 fg DVChl-*a* cell^{-1} below the euphotic depth ($z/z_e > 1$). This increase was similar to the range previously observed in culture studies (Moore et al., 1995; Moore and Chisholm, 1999) and suggested photoacclimation in this ecotype.

Thus, the results presented in this study show that variability in DVChl-*a* cell^{-1} is likely to be the result of (1) changes in vertical distribution of genetically distinct HL and LL-adapted *Prochlorococcus* ecotypes, (2) photoacclimation of each ecotype to the local light environment through regulation of the intracellular concentration of the major light-harvesting pigment. The apparent link between genetic diversity and the inherent photophysiological characteristics of *Prochlorococcus* provides important insight to its ecological success (Johnson and Lin, 2009). *Prochlorococcus* is able to occupy a broad range of ocean niches from the sea surface to the bottom of the euphotic zone, and as a result, is a significant contributor to global marine primary production (Lange et al., 2018; Visintini et al., 2021). Because of its small and highly-sequenced genome, unique pigmentation, and its rapid identification based on its unique optical signature, *Prochlorococcus* has been widely used as a model organism for understanding relationships between environmental forcing and microbial processes across vast scales of organization (Partensky and Garczarek, 2010). However, several studies have pointed to differences in photoprotective mechanisms among picocyanobacterial taxa as well as when compared with eukaryotic phytoplankton (e.g. Key et al., 2010; Kulk et al., 2011; Mella-Flores et al., 2012). The question then arises whether *Prochlorococcus* can serve as an appropriate model for elucidating phytoplankton photoacclimation in general. In other words, are the photoacclimatory characteristics of *Prochlorococcus* similar to, or different from, those of eukaryotic species, including photosynthetic picoeukaryotes? Since, in many global ocean biogeochemical models, *Prochlorococcus* is normally classified together with *Synechococcus* and picoeukaryotes as a 'pico-autotroph' functional type (Le Quéré et al., 2005) based on their shared characteristics of being highly effective in nutrient and photon acquisition (Raven, 1998; Le Quéré et al., 2005), it is important to be able to compare photoacclimatory properties of picophytoplankton groups so that it can be justified, from a physiological point of view, whether it is appropriate to combine them into a common biogeochemical functional type.

4.2 Variability in derived carbon-to-DVChl-*a* ratios for *Prochlorococcus*

The carbon-to-Chl-*a* ratio (θ) of phytoplankton is widely used in phytoplankton growth models to represent the photophysiological status of microalgae and to convert Chl-*a* concentration to estimates of carbon standing stock (Geider, 1987; Geider et al., 1996; Geider et al., 1997; Sathyendranath et al., 2009; Sathyendranath et al., 2020). Studies (Geider, 1987; MacIntyre et al., 2002) have shown that, for various phytoplankton species grown under constant temperature and nutrient-replete conditions, θ increases linearly with increasing light level. Light-dependent variability in θ is the result of photophysiological mechanisms used by the cell to avoid the harmful overexcitation of photosystems under high light by lowering the cellular content of Chl-*a* and accumulating more carbon reflecting the increase in the photosynthetic utilization of the absorbed light energy. However, when cultures are maintained under constant light levels, θ decreases significantly with increased temperature, suggesting that high temperature may inhibit phytoplankton growth and thus reduce the demand for energy in the form of fixed carbon (Geider et al., 1997). Variation in θ is also regulated strongly by the availability of nutrients, particularly nitrogen which is a major component of the light-harvesting apparatus (Halsey and Jones, 2015). In addition, since the cellular quota of Chl-*a* differ widely between phytoplankton taxa (MacIntyre et al., 2002), it can be expected that θ also varies across taxa.

The choices of the carbon conversion factor used to convert phytoplankton cell density to carbon biomass could introduce unconstrained variance in our estimates of θ_{Pro}. The conversion factors used in this study were either directly measured on cultures (Cailliau et al., 1996) or on oligotrophic populations (Casey et al., 2013). In a different approach, Grob et al. (2007a) independently derived the cellular carbon content of *Prochlorococcus* from total particle beam attenuation coefficient measurements conducted in the South Pacific Subtropical Gyre and obtained a much lower value of 29 fg C cell^{-1} which is in line with that determined by Zubkov et al. (2000) based on cell volume (by size fractionating filtration) on field samples. Later, Zubkov (2014) carried out alternative measurements of cellular biomass using the $^{14}CO_2$-tracer method and acquired a considerably low value of 11 fg C cell^{-1} for surface *Prochlorococcus* populations in the equatorial and temperate South Atlantic. This suggests that there is no universal cell-specific carbon conversion factor (Veldhuis and Kraay, 2004) and shows that such conversion factors vary widely depending on the method as well as the natural and experimental growth conditions of the cells. Attempts have been made, particularly in culture studies on axenic strains (Bertilsson et al., 2003), to refine taxon-specific conversion factors to aid the assessment of the contribution of the phytoplankton standing stock to the ocean carbon pool. Independent information including the genome size and optical properties (Veldhuis and Kraay, 2004) will also help to improve phytoplankton carbon conversion factors for use in marine biogeochemical studies. As the divergence between clusters of the surface and deep populations lessens when applying a higher conversion factor to deeper samples (Figure 8B) and as the explained amount of variance increases at the same time, we feel that further effort is required to measure the carbon content on natural *Prochlorococcus* populations in general, and within and below the deep chlorophyll maximum, in particular. Differences in the size distribution of surface and deep *Prochlorococcus* populations suggest that applying conversion factors based on biovolume may help address the problem of converting cell abundances into carbon standing stocks (Casey et al., 2013).

The high and variable values of θ_{Pro} observed in this study clearly demonstrate that *Prochlorococcus* has tremendous physiological plasticity to acclimate to the wide range of environmental conditions in which it lives. In general, picocyanobacteria tend to have higher and more variable θ than eukaryotic micro- and nanophytoplankton (i.e. diatoms, dinoflagellates, and nano-prymnesiophytes (Veldhuis and Kraay, 2004; Sathyendranath et al., 2009). Larger eukaryotes, notably diatoms which are known to be successful in fluctuating light environments (more deeply mixed waters) (Claustre et al., 1994), have been shown to be intrinsically less sensitive to photodamage not only owing to their large cell size and corresponding high pigment packaging (Key et al., 2010), but also because they are able to maintain their constitutive resource investments in photoprotection under varying light regimes (Talmy et al., 2013; Halsey and Jones, 2015), which in turn is reflected in a relatively stable θ. In contrast, small picocyanobacteria, which are adapted to more stable water columns, can adjust the proportion of cellular resources allocated to light-harvesting apparatus in response to shifts in irradiance (Talmy et al., 2013), resulting in highly variable intracellular concentrations of photosynthetic pigments (Moore et al., 1995) and thus θ. However, within the picoplankton size range, it remains unclear whether cyanobacteria significantly differ from photosynthetic eukaryotes with respect to variation in θ since studies that directly compare the θ values of the two picophytoplankton groups under similar growth conditions are rare (Table 3).

In comparison to picocyanobacteria, picoeukaryotes have been found to be better adapted to grow in ocean habitats characterized by more extreme physical dynamics (Bouman et al., 2011). Laboratory studies (Kulk et al., 2011; Stawiarski et al., 2018) have demonstrated that photosynthetic picoeukaryotes are able to maintain the high growth rates over a wide range of irradiances and are less affected by photoinhibition at high light. Therefore, it is reasonable to anticipate that our estimates of θ_{Pro} should be higher and more variable than those of picoeukaryotes. This expectation is consistent with the findings of Veldhuis and Kraay (2004) who examined flow cytometry samples from oligotrophic subtropical waters of the North Atlantic using an independent approach for converting cellular DNA content to phytoplankton carbon biomass. The study showed that θ_{Pro} decreased substantially from a maximum of 450 g C (g DVChl-*a*)$^{-1}$ at the surface to a minimum of 15 g C (g DVChl-*a*)$^{-1}$ at 150 m, whereas θ of the collective pico- and nanoeukaryote communities also decreased with depth, although to a much lesser extent (3-7 fold variation) with surface values of 30-80 g C (g Chl-*a*)$^{-1}$. The reduced vertical variation in θ observed for photosynthetic eukaryotes was likely due in part to a co-variation of cell pigment content and size as reflected by the increases in both the intracellular concentration of Chl-*a* and the genome size (proportional to cell size) with depth. A culture experiment by Kulk et al. (2011) also showed that θ_{Pro} varied from 14 ± 1.27 to 43 ± 1.17 g C (g DVChl-*a*)$^{-1}$ under variable light intensities (50-125 µmol quanta m^{-2} s^{-1}), while the observed range for the picoeukaryote *Ostreococcus* sp. was only between 39 ± 1.89 and 40 ± 0.99 g C (g DVChl-*a*)$^{-1}$. Determining whether the observed differences in the overall variability in θ between picophytoplankton populations reported here is the result of changes in the inherent difference in photoadaption or an artifact of not accounting for shifts in cell size within natural populations should be a focus of future research as it will allow us to leverage the wealth of global data on their abundance and pigment markers in order to better represent these globally-significant primary producers in the ocean carbon cycle.

5 Conclusions

The wealth of pigment and flow cytometry data obtained from a range of open-ocean environments allowed examination of the vertical variation in the photoprotective pigment (PPP) index and relation to photoacclimatory responses of individual phytoplankton cells through changes in their intracellular pigment complement, in particular the relative concentrations of PPPs and photosynthetic pigments (PSP).

The PPP index varied significantly in response to depth-dependent changes in the underwater light conditions (indexed by the dimensionless depth z/z_e), photoacclimatory status, and gross phytoplankton community structure (determined by pigment markers and cell counts). Vertical variability in the PPP index was especially pronounced in the subtropical gyres and low-latitude HNLC regions, and observations from the BATS time series showed that there is also a seasonal component to changes in the PPP index: the summer and early autumn surface communities dominated by high-light acclimated picocyanobacteria were characterized by a higher PPP index, which was largely caused by the presence of a strongly stratified water column.

At the cellular level, variation in the PPP index in *Prochlorococcus* was found to be associated primarily with changes in the intracellular concentration of DVChl-*a* rather than PPPs. The marked increase in DVChl-*a* cell^{-1} with depth was the result of both a photoacclimatory response to low light through increasing the intracellular concentration of DVChl-*a* in order to harvest sufficient light to support net growth and a shift from high light-acclimated (HL) to low light-acclimated (LL) ecotypes which are inherently more pigmented as a result of evolutionary adaptation to low-light conditions.

The vertical partitioning of ecotypes allows this marine picocyanobacterium to adapt to a wide range of light and nutrient conditions which is also reflected by the observed variability in derived values of θ_{Pro} computed from flow cytometry counts, pigment data, and published conversion factors. Estimates of θ_{Pro} appeared to be far more variable than θ values for eukaryotic phytoplankton reported in the literature, implying that *Prochlorococcus* is more sensitive to changes in growth irradiance and must therefore regulate the cellular constituents involved in light harvesting and photoprotection, whereas microalgae have been shown to be more resilient to changes in light history (Claustre et al., 1994) and less vulnerable to photodamage at high light (Key et al., 2010).

These results serve to underscore the importance of considering the physiological plasticity of different phytoplankton groups when using pigments and cell counts as proxies of phytoplankton biomass or chemotaxonomic markers. The unique pigment signatures of *Prochlorococcus* can be used to not only map their distribution but also provide insight into variation in the physiological status of the natural populations of this globally-significant cyanobacterium, which can, in turn, aid us in understanding how the long-term effect of global warming and its anticipated impact on upper ocean stratification may affect this genus that dominates a large fraction of the global ocean. Developing a mechanistic understanding of how Chl-*a*, PSPs, and PPPs change relative to one another at the cellular level across different taxa and how they change in response to environmental forcing is required if these pigments are to be used to derive estimates of phytoplankton carbon biomass, taxa, and θ from *in situ* and satellites observations.

Data availability statement

Publicly available datasets were analyzed in this study. This data can be found here: https://www.bodc.ac.uk/data/bodc_database/samples/ (pigment and AFC data; AMT dataset); http://batsftp.bios.edu/BATS/bottle/ (pigment and AFC data; BATS dataset); http://www.obs-vlfr.fr/proof/php/x_datalist.php?xxop=biosope&xxcamp=biosope (pigment and AFC data; BIOSOPE dataset) https://doi.org/10.1594/PANGAEA.93815 (pigment data, DCM dataset); https://doi.org/10.1594/PANGAEA.761718 (AFC data, DCM dataset); https://www.bodc.ac.uk/data/bodc_database/ctd/search/ (CTD profiles; AMT dataset); http://batsftp.bios.edu/BATS/prelim/ctd/ (CTD profiles; BATS dataset); http://www.obs-vlfr.fr/proof/php/bio_log_basicfiles.php (CTD profiles; BIOSOPE dataset); https://doi.org/10.1594/PANGAEA.761693 (CTD profiles; DCM dataset).

Author contributions

HB conceived the study. SP analyzed the data. HB and SP drafted the manuscript. All authors contributed to the writing of the manuscript, and approved the submitted version.

Funding

SP's studentship at the University of Oxford was funded by the Ministry of Education, Royal Thai Government through the Development and Promotion of Science and Technology Talents (DPST) Project. HB's work was supported by the European Space Agency's BICEP Project. BATS program recognizes support from the National Science Foundation Chemical and Biological Oceanography Programs through the following awards: OCE 0326885, OCE 0752366, and OCE- 0801991. GT's involvement was supported through the Atlantic Meridional Transect Program, funded by the UK Natural Environment Research Council through its National Capability Long-term Single Centre Science Programme, Climate Linked Atlantic Section Science (grant number NE/R015953/1). The BIOSOPE project is part of the LEFE-CYBER program and is funded by the Centre National de la Recherche Scientifique (CNRS), the Insitut des Science de l'Univers (INSU), the Centre National d'Etudes Saptiales (CNES), ESA, NASA, and the Natural Science and Engineering Research Council of Canada (NSERC). SS also acknowledges support from Simons. Foundation Project Collaboration on Computational Biogeochemical Modeling of Marine Ecosystems (CBIOMES; 549947, SS). The Atlantic Meridional Transect is funded by the UK Natural Environment Research Council through its National Capability Longterm Single Centre Science Programme, Climate Linked Atlantic Sector Science (grant number NE/R015953/1). This study contributes to the international IMBeR project and is contribution number 387 of the AMT program.

Conflict of interest

The authors declare that the research was conducted in the absence of any commercial or financial relationships that could be construed as a potential conflict of interest.

Publisher's note

References

Aiken, J., Pradhan, Y., Barlow, R. G., Lavender, S. J., Poulton, A., and Hardman-Mountford, N. J. (2009). Phytoplankton pigments and functional types in the Atlantic ocean: a decadal assessment 1995-2005. *Deep. Sea. Res. Part II: Top. Stud. Oceanogr.* 56 (15), 899–917. doi: 10.1016/j.dsr2.2008.09.017

Babin, M., Morel, A., Claustre, H., Bricaud, A., Kolber, Z., and Falkowski, P. G. (1996). Nitrogen- and irradiance-dependent variations of the maximum quantum yield of carbon fixation in eutrophic, mesotrophic and oligotrophic marine systems. *Deep-Sea Res. I: Oceanogr. Res. Pap.* 43 (8), 1241–1272. doi: 10.1016/0967-0637(96)00058-1

Barlow, R. G., Aiken, J., Moore, G. F., Holligan, P. M., and Lavender, S. J. (2004). Pigment adaptations in surface phytoplankton along the eastern boundary of the Atlantic ocean. *Mar. Ecol. Prog. Ser.* 281, 13–26. doi: 10.3354/meps281013

Barlow, R. G., Cummings, D. G., and Gibb, S. W. (1997). Improved resolution of mono- and divinyl chlorophylls *a* and *b* and zeaxanthin and lutein in phytoplankton extracts using reverse phase c-8 HPLC. *Mar. Ecol. Prog. Ser.* 161, 303–307. doi: 10.3354/meps161303

Barrera-Rojas, J., de la Vara, L. G., Ríos-Castro, E., Leyva-Castillo, L. E., and Gómez-Lojero, C. (2018). The distribution of divinyl chlorophylls *a* and *b* and the presence of ferredoxin-NADP$^+$ reductase in *Prochlorococcus marinus* MIT9313 thylakoid membranes. *Heliyon.* 4, e01100. doi: 10.1016/j.heliyon.2018.e01100

Bertilsson, S., Berglund, O., Karl, D. M., and Chisholm, S. W. (2003). Elemental composition of marine *Prochlorococcus* and *Synechococcus*: implications for the ecological stoichiometry of the sea. *Limnol. Oceanogr.* 48 (5), 1721–1731. doi: 10.4319/lo.2003.48.5.1721

Bidigare, R. R. (1991). "Analysis of algal chlorophylls and carotenoids," in *Marine particles: Analysis and characterization*. Eds. D. C. Hurd and D. W. Spencer (Washington D.C: American Geophysical Union), 119–123.

Bidigare, R. R., Van Heukelem, L., and Trees, C. C. (2005). "Analysis of algal pigments by high-performance liquid chromatography," in *Algal culturing techniques*. Ed. R. A. Andersen (Burlington, MA: Academic Press), 432–435.

Blanchot, J., André, J. M., Navarette, C., Neveux, J., and Radenac, M. H. (2001). Picophytoplankton in the equatorial pacific: vertical distributions in the warm pool and in the high nutrient low chlorophyll conditions. *Deep-Sea Res. I: Oceanogr. Res. Pap.* 48 (1), 297–314. doi: 10.1016/S0967-0637(00)00063-7

Blanchot, J., and Rodier, M. (1996). Picophytoplankton abundance and biomass in the western tropical pacific ocean during the 1992 El nino year: results from flow cytometry. *Deep-Sea Res. I: Oceanogr. Res. Pap.* 43 (6), 877–895. doi: 10.1016/0967-0637(96)00026-X

Bouman, H. A., Platt, T., Kraay, G. W., Sathyendranath, S., and Irwin, B. D. (2000). Bio-optical properties of the subtropical north atlantic. i. vertical variability. *Mar. Ecol. Prog. Ser.* 200, 3–18. doi: 10.3354/meps200003

Bouman, H. A., Ulloa, O., Barlow, R. G., Li, W. K. W., Platt, T., Zwirglmaier, K., et al. (2011). Water-column stratification governs the community structure of subtropical marine picophytoplankton. *Environ. Microbiol. Rep.* 3 (4), 473–482. doi: 10.1111/j.1758-2229.2011.00241.x

Bouman, H. A., Ulloa, O., Scanlan, D. J., Zwirglmaier, K., Li, W. K. W., Platt, T., et al. (2006). Oceanographic basis of the global surface distribution of *Prochlorococcus* ecotypes. *Science.* 312 (5775), 918–921. doi: 10.1126/science.1122692

Buitenhuis, E. T., Li, W. K. W., Vaulot, D., Lomas, M. W., Landry, M. R., Partensky, F., et al. (2012). Picophytoplankton biomass distribution in the global ocean. *Earth Syst. Sci. Data.* 4 (1), 37–46. doi: 10.5194/essd-4-37-2012

Cailliau, C., Claustre, H., Vidussi, F., Marie, D., and Vaulot, D. (1996). Carbon biomass, and gross growth rates as estimated from ^{14}C pigment labelling, during photoacclimation in *Prochlorococcus* CCMP 1378. *Mar. Ecol. Prog. Ser.* 145, 209–221. doi: 10.3354/meps145209

Campbell, L., Nolla, H. A., and Vaulot, D. (1994). The importance of *Prochlorococcus* to community structure in the central north pacific ocean. *Limnol. Oceanogr.* 39 (4), 954–961. doi: 10.4319/lo.1994.39.4.0954

Campbell, L., and Vaulot, D. (1993). Photosynthetic picoplankton community structure in the subtropical north pacific ocean near Hawaii (station ALOHA). *Deep-Sea Res. I: Oceanogr. Res. Pap.* 40 (10), 2043–2060. doi: 10.1016/0967-0637(93)90044-4

Casey, J. R., Aucan, J. P., Goldberg, S. R., and Lomas, M. W. (2013). Changes in partition of carbon amongst photosynthetic pico- and nano-plankton groups in the Sargasso Sea in response to changes in the north Atlantic oscillation. *Deep-Sea Res. Part II: Top. Stud. Oceanogr.* 93, 58–70. doi: 10.1016/j.dsr2.2013.02.002

Cermeño, P., Dutkiewicz, S., Harris, R. P., Follows, M. J., Schofield, O. M., and Falkowski, P. G. (2008). The role of nutricline depth in regulating the ocean carbon cycle. *Proc. Natl. Acad. Sci. U.S.A.* 105 (51), 20344–20349. doi: 10.1073/pnas.0811302106

Claustre, H., Kerhervé, P., Marty, J.-C., and Prieur, L. (1994). Phytoplankton photoadaptation related to some frontal physical processes. *J. Mar. Syst.* 5 (3–5), 251–265. doi: 10.1016/0924-7963(94)90050-7

Claustre, H., and Marty, J.-C. (1995). Specific phytoplankton biomasses and their relation to primary production in the subtropical north Atlantic. *Deep-Sea Res. I: Oceanogr. Res. Pap.* 42 (8), 1475–1493. doi: 10.1016/0967-0637(95)00053-9

Cullen, J. J., Franks, P. J. S., Karl, D. M., and Longhurst, A. R. (2002). "Physical influences on marine ecosystem dynamics," in *The Sea*, vol. Vol. 12 . Eds. A. R. Robinson, J. J. McCarthy and B. J. Rothschild (New York: John Willey & Sons), 297–336.

Dimier, C., Giovanni, S., Ferdinando, T., and Brunet, C. (2009). Comparative ecophysiology of the xanthophyll cycle in six marine phytoplanktonic species. *Protist.* 160 (3), 397–411. doi: 10.1016/j.protis.2009.03.001

DuRand, M. D., Olson, R. J., and Chisholm, S. W. (2001). Phytoplankton population dynamics at the Bermuda Atlantic time-series station in the Sargasso Sea. *Deep. Sea. Res. Part II: Top. Stud. Oceanogr.* 48 (8–9), 1983–2003. doi: 10.1016/S0967-0645(00)00166-1

Dusenberry, J. A., Olson, R. J., and Chisholm, S. W. (1999). Frequency distributions of phytoplankton single-cell fluorescence and vertical mixing in the surface ocean. *Limnol. Oceanogr.* 44 (2), 431–435. doi: 10.4319/lo.1999.44.2.0431

Dutkiewicz, S., Hickman, A. E., Jahn, O., Henson, S., Beaulieu, C., and Monier, E. (2019). Ocean colour signature of climate change. *Nat. Commun.* 10, 578. doi: 10.1038/s41467-019-08457-x

Fawcett, S. E., Lomas, M. W., Casey, J. R., Ward, B. B., and Sigman, D. M. (2011). Assimilation of upwelled nitrate by small eukaryotes in the Sargasso Sea. *Nat. Geosci.* 4 (10), 717–722. doi: 10.1038/ngeo1265

Geider, R. J. (1987). Light and temperature dependence of the carbon to chlorophyll a ratio in microalgae and cyanobacteria: implications for physiology and growth of phytoplankton. *New Phytol.* 106 (1), 1–34. doi: 10.1111/j.1469-8137.1987.tb04788.x

Geider, R. J., MacIntyre, H. L., and Kana, T. M. (1996). A dynamic model of photoadaptation in phytoplankton. *Limnol. Oceanogr.* 41, 1–15. doi: 10.4319/lo.1996.41.1.0001

Geider, R. J., MacIntyre, H. L., and Kana, T. M. (1997). Dynamic model of phytoplankton growth and acclimation: responses of the balanced growth rate and the chlorophyll a:carbon ratio to light, nutrient-limitation and temperature. *Mar. Ecol. Prog. Ser.* 148, 187–200. doi: 10.3354/meps148187

Gieskes, W. W. C., Kraay, G. W., Nontji, A., Setiapermana, D., and Sutomo, (1988). Monsoonal alternation of a mixed and a layered structure in the phytoplankton of the euphotic zone of the banda Sea (Indonesia): a mathematical analysis of algal pigment fingerprints. *Neth. J. Sea Res.* 22, 123–137. doi: 10.1016/0077-7579(88)90016-6

Grébert, T., Doré, H., Partensky, F., Farrant, G. K., Boss, E. S., Picheral, M., et al. (2018). Light color acclimation is a key process in the global ocean distribution of *Synechococcus* cyanobacteria. *Proc. Natl. Acad. Sci. U.S.A.* 115 (9), E2010–E2019. doi: 10.1073/pnas.1717069115

Grob, C., Ulloa, O., Claustre, H., Huot, Y., Alarcón, G., and Marie, D. (2007a). Contribution of picoplankton to the total particulate organic carbon (POC) concentration in the eastern south pacific. *Biogeosciences.* 4, 837–852. doi: 10.5194/bgd-4-1461-2007

Grob, C., Ulloa, O., Li, W. K. W., Alarcón, G., Fukasawa, M., and Watanabe, S. (2007b). Picoplankton abundance and biomass across the eastern south pacific ocean along latitude 32.5°S. *Mar. Ecol. Prog. Ser.* 332, 53–62. doi: 10.3354/meps332053

Halsey, K. H., and Jones, B. M. (2015). Phytoplankton strategies for photosynthetic energy allocation. *Annu. Rev. Mar. Sci.* 7 (1), 265–297. doi: 10.1146/annurev-marine-010814-015813

Hartmann, M., Gomez-Pereira, P., Grob, C., Ostrowski, M., Scanlan, D. J., and Zubkov, M. V. (2014). Efficient CO_2 fixation by surface *Prochlorococcus* in the Atlantic ocean. *ISME J.* 8 (11), 2280–2289. doi: 10.1038/ismej.2014.56

Hickman, A. E., Dutkiewicz, S., Williams, R. G., and Follows, M. J. (2010). Modelling the effects of chromatic adaptation on phytoplankton community structure in the oligotrophic ocean. *Mar. Ecol. Prog. Ser.* 406, 1–17. doi: 10.3354/meps08588

Hirata, T., Aiken, J., Hardman-Mountford, N. J., Smyth, T. J., and Barlow, R. G. (2008). An absorption model to determine phytoplankton size classes from satellite ocean colour. *Remote Sens. Environ.* 112 (6), 3153–3159. doi: 10.1016/j.rse.2008.03.011

Johnsen, G., Norli, M., Moline, M. A., Robbins, I., Quillfeldt, C., Von Sørensen, K., et al. (2018). The advective origin of an under-ice spring bloom in the Arctic ocean using multiple observational platforms. *Polar Biol.* 41, 1197–1216. doi: 10.1007/s00300-018-2278-5

Johnson, Z. I., and Lin, Y. (2009). *Prochlorococcus*: approved for export. *Proc. Natl. Acad. Sci. U.S.A.* 106 (26), 10400–104001. doi: 10.1073/pnas.0905187106

Kana, T. M., Glibert, P. M., Goericke, R., and Welschmeyer, N. A. (1988). Zeaxanthin and β-carotene in *Synechococcus* WH7803 respond differently to irradiance. *Limnol. Oceanogr.* 33 (6), 1623–1627. doi: 10.4319/lo.1988.33.6part2.1623

Karl, D. M. (1999). A sea of change: biogeochemical variability in the north pacific subtropical gyre. *Ecosystems.* 2 (3), 181–214. doi: 10.1007/s100219900068

Kelly, D. E. (2018). *Oceanographic analysis with r* (New York: Springer).

Key, T., McCarthy, A., Campbell, D. A., Six, C., Roy, S., and Finkel, Z. V. (2010). Cell size trade-offs govern light exploitation strategies in marine phytoplankton. *Environ. Microbiol.* 12 (1), 95–104. doi: 10.1111/j.1462-2920.2009.02046.x

Kirk, J. T. O. (2011). *Light and photosynthesis in aquatic ecosystems (3rd ed.)* (Cambridge: Cambridge University Press). doi: 10.1017/CBO9781139168212

Kulk, G., de Poll, W. H., Visser, R. J. W., and Buma, A. G. J. (2011). Distinct differences in photoacclimation potential between prokaryotic and eukaryotic oceanic phytoplankton. *J. Exp. Mar. Biol. Ecol.* 398 (1–2), 63–72. doi: 10.1016/j.jembe.2010.12.011

Lange, P. K., Brewin, R. J. W., Dall'Olmo, G., Tarran, G. A., Sathyendranath, S., Zubkov, M. V., et al. (2018). Scratching beneath the surface: a model to predict the vertical distribution of *Prochlorococcus* using remote sensing. *Remote Sens.* 10 (6), 847. doi: 10.3390/rs10060847

Larkrin, A. A., Moreno, A. R., Fagan, A. J., Fowlds, A., Ruiz, A., and Martinty, A. C. (2020). Persistent El niño driven shifts in marine cyanobacteria populations. *PLos One* 15 (9), e0238405. doi: 10.1371/journal.pone.0238405

Latasa, M., Scharek, R., Morán, X. A. G., Gutiérrez-Rodríguez, A., Emelianov, M., Salat, J., et al. (2022). Dynamics of phytoplankton groups in three contrasting situations of the open NW Mediterranean Sea revealed by pigment, microscopy, and flow cytometry analyses. *Prog. Oceanogr.* 201, 102737. doi: 10.1016/j.pocean.2021.102737

Le Quéré, C., Harrison, S. P., Colin Prentice, I., Buitenhuis, E. T., Aumont, O., Bopp, L., et al. (2005). Ecosystem dynamics based on plankton functional types for global ocean biogeochemistry models. *Glob. Change Biol.* 11, 2016–2040. doi: 10.1111/j.1365-2486.2005.1004.x

Letelier, R. M., White, A. E., Bidigare, R. R., Barone, B., Church, M. J., and Karl, D. M. (2017). Light absorption by phytoplankton in the north pacific subtropical gyre. *Limnol. Oceanogr.* 62, 1526–1540. doi: 10.1002/lno.10515

Liu, H., Probert, I., Uitz, J., Claustre, H., Aris-Brosou, S., Frada, M., et al. (2009). Extreme diversity in noncalcifying haptophytes explains a major pigment paradox in the open oceans. *Proc. Nat. Acad. Sci.* 106, 12803–12808. doi: 0.1073/pnas.0905841106

Longhurst, A. R. (1998). *Ecological geography of the Sea.* (London: Academic Press).

MacIntyre, H. L., Kana, T. M., Anning, T., and Geider, R. J. (2002). Photoacclimation of photosynthesis irradiance response curves and photosynthetic pigments in microalgae and cyanobacteria. *J. Physiol.* 38 (1), 17–38. doi: 10.0000/135184797337543

Malmstrom, R. R., Coe, A., Kettler, G. C., Martiny, A. C., Frias-Lopez, J., Zinser, E. R., et al. (2010). Temporal dynamics of *Prochlorococcus* ecotypes in the Atlantic and pacific oceans. *ISME J.* 4, 1252–1264. doi: 10.1038/ismej.2010.60

Malmstrom, R. R., Rodrigue, S., Huang, K. H., Kelly, L., Kern, S. E., Thompson, A., et al. (2013). Ecology of uncultured *Prochlorococcus* clades revealed through single-cell genomics and biogeographic analysis. *ISME J.* 7 (1), 184–198. doi: 10.1038/ismej.2012.89

Marañón, E. (2005). Phytoplankton growth rates in the Atlantic subtropical gyres. *Limnol. Oceanogr.* 50 (1), 299–310. doi: 10.4319/lo.2005.50.1.0299

Matsumoto, K., and Ando, K. (2009). Use of cyanobacterial pigments to characterize the ocean surface mixed layer in the western pacific warm pool. *J. Mar. Syst.* 75, 245–252. doi: 10.1016/j.jmarsys.2008.10.007

Mella-Flores, D., Six, C., Ratin, M., Partensky, F., Boutte, C., Le Corguille, G., et al. (2012). *Prochlorococcus* and *Synechococcus* have evolved different adaptive mechanisms to cope with light and UV stress. *Front. Microbiol.* 3 (285). doi: 10.3389/fmicb.2012.00285

Moore, L. R., and Chisholm, S. W. (1999). Photophysiology of the marine cyanobacterium *Prochlorococcus*: ecotypic differences among cultured isolates. *Limnol. Oceanogr.* 44, 628–638. doi: 10.4319/lo.1999.44.3.0628

Moore, L. R., Goericke, R., and Chisholm, S. W. (1995). Comparative physiology of *Synechococcus* and *Prochlorococcus*: influence of light and temperature on growth, pigment, fluorescence and absorptive properties. *Mar. Ecol. Prog. Ser.* 116, 259–275. doi: 10.3354/meps116259

Moore, L. R., Rocap, G., and Chisholm, S. W. (1998). Physiology and molecular phylogeny of coexisting *Prochlorococcus* ecotypes. *Nature.* 393, 464–467. doi: 10.1038/30965

Morel, A., Huot, Y., Gentili, B., Werdell, P. J., Hooker, S. B., and Franz, B. A. (2007). Examining the consistency of products derived from various ocean color sensors in open ocean (Case I) waters in the perspective of a multi-sensor approach. *Remote Sens. Environ.* 111, 69–88. doi: 10.1016/j.rse.2007.03.012

Morel, A., and Maritorena, S. (2001). Bio-optical properties of oceanic waters: a reappraisal. *J. Geophys. Res. Oceans.* 106 (C4), 7163–7180. doi: 10.1029/2000JC000319

Olson, R. J., Chisholm, S. W., Zettler, E. R., Altabet, M. A., and Dusenberry, J. A. (1990). Spatial and temporal distributions of prochlorophytes picoplankton in the north Atlantic ocean. *Deep-Sea Res. I: Oceanogr. Res. Pap.* 37 (6), 1033–1051. doi: 10.1016/0198-0149(90)90109-9

Partensky, F., Blanchot, J., Latoine, F., Neveux, J., and Marie, D. (1996). Vertical structure of picophytoplankton at different trophic sites of the tropical northeastern Atlantic ocean. *Deep-Sea Res. I: Oceanogr. Res. Pap.* 43 (8), 1191–1213. doi: 10.1016/0967-0637(96)00056-8

Partensky, F., and Garczarek, L. (2010). *Prochlorococcus*: advantages and limits of minimalism. *Annu. Rev. Mar. Sci.* 2, 305–331. doi: 10.1146/annurev-marine-120308-081034

Partensky, F., Hess, W. R., and Vaulot, D. (1999). *Prochlorococcus*, a marine photosynthetic prokaryote of global significance. *Microbiol. Mol. Biol. Rev.* 63 (1), 106–127. doi: 10.1128/MMBR.63.1.106-127.1999

Partensky, F., Hoepffner, N., Li, W. K. W., Ulloa, O., and Vaulot, D. (1993). Photoacclimation of *Prochlorococcus* sp. (Prochlorophyta) strains isolated from the north Atlantic and the Mediterranean Sea. *Plant Physiol.* 101, 285–296. doi: 10.1104/pp.101.1.285

Polovina, J. J., Howell, E. A., and Abecassis, M. (2008). Ocean's least productive waters are expanding. *Geophys. Res. Lett.* 35 (3), L03618. doi: 10.1029/2007GL031745

Poulton, A. J., Holligan, P. M., Hickman, A. E., Kim, Y.-N. K., Adey, T. R., Stinchcombe, M. C., et al. (2006). Phytoplankton carbon fixation, chlorophyll-biomass and diagnostic pigments in the Atlantic ocean. *Deep. Sea. Res. Part II: Top. Stud. Oceanogr.* 53, 1593–1610. doi: 10.1016/j.dsr2.2006.05.007

Ras, J., Claustre, H., and Uitz, J. (2008). Spatial variability of phytoplankton pigment distributions in the subtropical south pacific ocean: comparison between *in situ* and predicted data. *Biogeosciences.* 5, 353–369. doi: 10.5194/bg-5-353-2008

Raven, J. A. (1998). The twelfth tansley lecture. small is beautiful: the picophytoplankton. *Funct. Ecol.* 12 (4), 503–513. doi: 10.1046/j.1365-2435.1998.00233.x

Rocap, G., Distel, D. L., Waterbury, J. B., and Chisholm, S. W. (2002). Resolution of *Prochlorococcus* and *Synechococcus* ecotypes by using 16S-23S ribosomal DNA internal transcribed spacer sequences. *Appl. Environ. Microbiol.* 68 (3), 1180–1191. doi: 10.1128/AEM.68.3.1180-1191.2002

Rusch, D. B., Martiny, A. C., Dupont, C. L., Halpern, A. L., and Venter, J. C. (2010). Characterization of *Prochlorococcus* clades from iron-depleted oceanic regions. *Proc. Natl. Acad. Sci. U.S.A.* 107 (37), 16184–16189. doi: 10.1073/pnas.1009513107

Sathyendranath, S., Platt, T., Kovač, Ž., Dingle, J., Jackson, T., Brewin, R. J. W., et al. (2020). Reconciling models of primary production and photoacclimation. *Appl. Opt.* 59 (10), 100–114. doi: 10.1364/AO.386252

Sathyendranath, S., Stuart, V., Nair, A., Oka, K., Nakane, T., Bouman, H. A., et al. (2009). Carbon-to-chlorophyll ratio and growth rate of phytoplankton in the sea. *Mar. Ecol. Prog. Ser.* 383, 73–84. doi: 10.3354/meps07998

Stawiarski, B., Buitenhuis, E. T., and Fallens, M. (2018). The physiological response of seven strains of picophytoplankton to light, and its representation in a dynamic photosynthesis model. *Limnol. Oceanogr.* 63, S367–S380. doi: 10.1002/lno.10745

Steinberg, D. K., Carlson, C. A., Bates, N. R., Johnson, R. J., Michaels, A. F., and Knap, A. H. (2001). Overview of the US JGOFS Bermuda Atlantic time-series study (BATS): a decade-scale look at ocean biology and biogeochemistry. *Deep. Sea. Res. Part II: Top. Stud. Oceanogr.* 48, 1405–1447. doi: 10.1016/S0967-0645(00)00148-X

Swan, C. M., Vogt, M., Gruber, N., and Laufkoetter, C. (2016). A global seasonal surface ocean climatology of phytoplankton types based on CHEMTAX analysis of HPLC pigments. *Deep-Sea Res. I: Oceanogr. Res. Pap.* 109, 137–156. doi: 10.1016/j.dsr.2015.12.002

Talmy, D., Blackford, J., Hardman-Mountford, N. J., Dumbrell, A. J., and Geider, R. J. (2013). An optimality model of photoadaptation in contrasting aquatic light regimes. *Limnol. Oceanogr.* 58 (5), 1802–1818. doi: 10.4319/lo.2013.58.5.1802

Thompson, A. W., van den Engh, G. J., Ahlgren, N. A., Kouba, K., Ward, S., Wilson, S. T., et al. (2018). Dynamics of *Prochlorococcus* diversity and photoacclimation during short-term shifts in water column stratification at station ALOHA. *Front. Mar. Sci.* 5. doi: 10.3389/fmars.2018.00488

Tragin, M., and Vaulot, D. (2019). Novel diversity within marine mamiellophyceae (Chlorophyta) unveiled by metabarcoding. *Sci. Rep.* 9, 5190. doi: 10.1038/s41598-019-41680-6

Trees, C. C., Clark, D. K., Bidigare, R. R., Ondrusek, M. E., and Mueller, J. L. (2000). Accessory pigments versus chlorophyll a concentrations within the euphotic zone: a ubiquitous relationship. *Limnol. Oceanogr.* 45 (5), 1130–1143. doi: 10.4319/lo.2000.45.5.1130

Uitz, J., Claustre, H., Morel, A., and Hooker, S. B. (2006). Vertical distribution of phytoplankton communities in open ocean: an assessment based on surface chlorophyll. *J. Geophys. Res. Oceans.* 111 (8), C08005. doi: 10.1029/2005JC003207

Uitz, J., Huot, Y., Bruyant, F., Babin, M., and Claustre, H. (2008). Relating phytoplankton photophysiological properties to community structure on large scales. *Limnol. Oceanogr.* 53 (2), 614–630. doi: 10.4319/lo.2008.53.2.0614

van Heukelem, L., and Thomas, C. S. (2001). Computer-assisted high performance liquid chromatography method development with applications to the isolation and analysis of phytoplankton pigments. *J. Chromatogr. A.* 910 (1), 31–49. doi: 10.1016/S0378-4347(00)00603-4

Veldhuis, M. J. W., and Kraay, G. W. (1990). Vertical distribution and pigment composition of a picoplanktonic prochlorophyte in the subtropical north Atlantic: a combined study of HPLC-analysis of pigments and flow cytometry. *Mar. Ecol. Prog. Ser.* 68, 121–127. doi: 10.3354/MEPS068121

Veldhuis, M. J. W., and Kraay, G. W. (2004). Phytoplankton in the subtropical Atlantic ocean: towards a better assessment of biomass and composition. *Deep-Sea Res. I: Oceanogr. Res. Pap.* 51 (4), 507–530. doi: 10.1016/j.dsr.2003.12.002

Visintini, N., Martiny, A. C., and Flombaum, P. (2021). *Prochlorococcus*, *Synechococcus*, and picoeukaryotic phytoplankton abundances in the global ocean. *Limnol. Oceanogr. Lett* 6, 207–215. doi: 10.1002/lol2.10188

Wei, Y., Sun, J., Zhang, X., Wang, J., and Huang, K. (2019). Picophytoplankton size and biomass around equatorial eastern Indian ocean. *MicrobiologyOpen.* 8 (2), e629. doi: 10.1002/mbo3.629

Zubkov, M. V. (2014). Faster growth of the major prokaryotic versus eukaryotic CO_2 fixers in the oligotrophic ocean. *Nat. Commun.* 5, 3376. doi: 10.1038/ncomms4776

Zubkov, M. V., Sleigh, M. A., Burkill, P. H., and Leakey, R. J. G. (2000). Picoplankton community structure on the Atlantic meridional transect: a comparison between seasons. *Prog. Oceanogr.* 45, 369–386. doi: 10.1016/S0079-6611(00)00008-2

Zubkov, M. V., Sleigh, M. A., Tarran, G. A., Burkill, P. H., and Leakey, R. J. G. (1998). Picoplanktonic community structure on an Atlantic transect from 50°N to 50°S. *Deep-Sea Res. I: Oceanogr. Res. Pap.* 45, 1339–1355. doi: 10.1016/S0967-0637(98)00015-6

Zwirglmaier, K., Heywood, J. L., Chamberlain, K., Woodward, E. M. S., Zubkov, M. V., and Scanlan, D. J. (2007). Basin-scale distribution patterns of picocyanobacterial lineages in the Atlantic ocean. *Environ. Microbiol.* 9 (5), 1278–1290. doi: 10.1111/j.1462-2920.2007.01246.x

frontiers | Frontiers in Marine Science

TYPE Original Research
PUBLISHED 23 February 2023
DOI 10.3389/fmars.2023.1082495

EDITED BY
Punyasloke Bhadury,
Indian Institute of Science Education and Research Kolkata, India

REVIEWED BY
Ruth S. Eriksen,
Oceans and Atmosphere (CSIRO), Australia
Genuario Belmonte,
University of Salento, Italy
Lanlan Zhang,
South China Sea Institute of Oceanology (CAS), China

*CORRESPONDENCE
Wuchang Zhang
✉ wuchangzhang@qdio.ac.cn

SPECIALTY SECTION
This article was submitted to Ocean Observation, a section of the journal Frontiers in Marine Science

RECEIVED 28 October 2022
ACCEPTED 13 February 2023
PUBLISHED 23 February 2023

CITATION
Li H, Tarran GA, Dall'Olmo G, Rees AP, Denis M, Wang C, Grégori G, Dong Y, Zhao Y, Zhang W and Xiao T (2023) Organization of planktonic Tintinnina assemblages in the Atlantic Ocean. *Front. Mar. Sci.* 10:1082495. doi: 10.3389/fmars.2023.1082495

Organization of planktonic Tintinnina assemblages in the Atlantic Ocean

Haibo Li[1,2,3], Glen A. Tarran[4], Giorgio Dall'Olmo[4,5], Andrew P. Rees[4], Michel Denis[6], Chaofeng Wang[1,2,3], Gérald Grégori[6], Yi Dong[1,2,3], Yuan Zhao[1,2,3], Wuchang Zhang[1,2,3]* and Tian Xiao[1,2,3]

[1]CAS Key Laboratory of Marine Ecology and Environmental Sciences, Institute of Oceanology, Chinese Academy of Sciences, Qingdao, China, [2]Laboratory for Marine Ecology and Environmental Science, Qingdao National Laboratory for Marine Science and Technology, Qingdao, China, [3]Centre for Ocean Mega-Science, Chinese Academy of Sciences, Qingdao, China, [4]Plymouth Marine Laboratory, Plymouth, United Kingdom, [5]National Institute for Oceanography and Applied Geophysics- OGS, Trieste, Italy, [6]Aix-Marseille University, Toulon University, CNRS, IRD, Mediterranean Institute of Oceanography UM110, Marseille, France

Marine plankton have different biogeographical distribution patterns. However, it is not clear how the entire plankton assemblage is composed of these species with distinct biogeographical patterns. Tintinnina (tintinnids) is single-celled planktonic protozoa commonly used as model organisms in planktonic studies. In this research, we investigated the organization of Tintinnina assemblages along the Atlantic Meridional Transect (AMT) spanning over 90 degrees of latitude during the 29th AMT cruise (2019). Tintinnina with high frequency of occurrence was classified into four biogeographic distribution patterns (equatorial, gyre, frontal, and deep Chl *a* maximum) according to their vertical and horizontal distribution. All species falling within each distribution pattern formed a sub-assemblage. Equatorial sub-assemblage dominated in upper waters of the equatorial zone and gyre centres. Equatorial and frontal sub-assemblages co-dominated in upper waters of the frontal zones. Deep Chlorophyll a maximum Layer (DCM) sub-assemblage dominated in the DCM waters. Some Tintinnina species with high abundance could be used as indicator species of sub-assemblages. The Tintinnina assemblages in the northern and southern hemispheres exhibited asymmetry in terms of species composition. The latitudinal gradient of Tintinnina species richness was bimodal, which was shaped by the superposition of the species number of the four sub-assemblages with latitude. The result of this study contributes to the understanding of Tintinnina assemblage in the equatorial zone and subtropical gyres of the Pacific and Indian Ocean. It is also valuable for predicting the influence of global warming on changes in Tintinnina distribution and species richness.

KEYWORDS

Ciliophora Tintinnina, microzooplankton, biogeographic pattern, latitudinal gradient, Atlantic Meridional Transect (AMT)

Introduction

Tintinnina (tintinnids in ecological studies) is planktonic ciliates with shells called loricae. In taxonomic terms they belong to the suborder order Oligotrichida, subclass Choreotrichia, class Spirotrichea, phylum Ciliophora (Lynn, 2008) with a size range of approx. 20-200 μm (microzooplankton). The smallest recorded species is *Stenosemella perpusilla* with a body size of 13 μm (Hada, 1970). As important components of plankton, Tintinnina plays a pivotal role in material circulation and energy flow (Pierce and Turner, 1992). Because of the loricae, Tintinnina is one of the best-known groups of planktonic ciliates and have been recorded in oceans all around the world. More than 900 Tintinnina species have been recorded up to now (Zhang et al., 2012). They were regarded as model organisms in plankton studies (Dolan et al., 2013) and suggested as bioindicators of marine ecological status (Feng et al., 2015; Rakshit et al., 2017a; Rakshit et al., 2017b; Li et al., 2021).

Although biogeography is based on the distribution of species, the study of Tintinnina biogeographic distribution at the species level is poorly documented. At the genus level, Tintinnina is divided into five biogeographic distribution patterns (cosmopolitan, neritic, warm-water, boreal, and austral) according to their distribution in the global ocean (Pierce and Turner, 1993; Dolan et al., 2013). Plankton biogeography showed that there are equatorial belt and central belts (Longhurst, 2007) in the vast warm water areas between about 40°N and 40°S. However, it is not clear which warm-water Tintinnina species belong to these belts, whether there is difference in Tintinnina species between northern and southern hemispheres and how the Tintinnina assemblage was organized by species with different distribution pattern.

The general paradigm for latitudinal gradients of biodiversity is that a species richness peak appears at the equator and decreases from the lower to higher latitudes, which is considered unimodal (Gaston, 2000; Hillebrand, 2004). However, more and more studies have indicated that latitudinal species richness of marine plankton has asymmetric bimodality with a tropical species richness depression near the equator (Chaudhary et al., 2016; Yasuhara et al., 2020; Chaudhary et al., 2021), although the debate as to whether the equator dip of Tintinnina species richness exists continues (Dolan et al., 2013; Dolan et al., 2016; Gimmler et al., 2016; Sunagawa et al., 2020).

In order to quantify the nature and causes of ecological and biogeochemical variability in planktonic ecosystems of the Atlantic Ocean, the Atlantic Meridional Transect (AMT) project was launched in 1995 (Robinson et al., 2006; Rees et al., 2017), and 29 AMT cruises have been conducted so far. The transect crosses a range of ecosystems from subpolar to tropical and subtropical gyres (Robinson et al., 2006). Therefore, it is a suitable transect to study the biogeography of planktonic organisms. There are several of ecological studies on phytoplankton (Acevedo-Trejos et al., 2018; Balch et al., 2019; Dutkiewicz et al., 2020) and zooplankton (Isla et al., 2004; López and Anadón., 2008; Burridge et al., 2017) along the AMT. There was only one study (Rychert et al., 2014) of planktonic ciliate abundance with very little information about Tintinnina.

In the present study, we investigated the structure and composition variations of the Tintinnina assemblage along the AMT, by collecting Tintinnina samples at different depths. The aims were: 1) to classify Tintinnina sub-assemblages according to the biogeographic distribution patterns of various species; 2) to determine the dominance of each sub-assemblage in different zones; 3) to determine the latitudinal species richness gradient of Tintinnina.

Materials and methods

Sampling was performed at 45 stations (labelled as Stn. 1 to Stn. 45, Figure 1; Supplementary Table 1) during the 29th Atlantic Meridional Transect (AMT) cruise (October-November 2019) aboard the RRS "*Discovery*". The transect crossed through the middle of the Southern Atlantic Subtropical Gyre but through the west side of the Northern Atlantic Subtropical Gyre (Cruise report of AMT29). Depths of Stn. 1 and Stn. 2 were 130 m and 156 m, respectively. Other stations had depth more than 4000 m. Along the transect, the ship stopped two times every day (at about 4 Am and 12:30 Pm local time, respectively) to carry out oceanographic observations. Each stop was labelled as a research station. In every station, vertical profiles of temperature, salinity, and *in vivo* chlorophyll *a* fluorescence (Chl *a*) of the upper 200 m were determined using a conductivity-temperature-pressure (CTD) sensor (SeaBird, SBE, 911plus/917). Seawater samples were collected at 3-8 approximately equal distance depths (sampling points) usually within and above the deep chlorophyll *a* maximum (DCM) layer, using Niskin bottles (20 L) attached to a rosette CTD system. To sample Tintinnina, 5-20 L of water from each depth was gently filtered through a 10 μm mesh net. The samples (~200 mL) in the cod end of the net were transferred into plastic bottles and immediately fixed with Lugol's solution (1% final concentration). After settling for at least 48 h, supernatant water was gently siphoned out to concentrate the sample to about 50 mL. The settling and siphoning process was repeated to concentrate each sample to a final volume of approx. 15 mL. The samples were stored in the dark at approx. 4°C until analysis. A total of 235 samples were collected (Figure 2).

In the laboratory, each sample was settled in an Utermöhl counting chamber for at least 24 h and examined using an inverted microscope (Olympus IX 71, 100× or 400× magnification). As the Tintinnina protoplasts can easily detach from the lorica during sample collection and fixing (Paranjape and Gold, 1982; Alder, 1999; Gómez, 2007), empty Tintinnina loricae were counted as living cells in our study. For each species, at least 20 individuals (if possible) of each species were photographed and measured. Tintinnina was identified to the lowest possible taxonomic level (usually species level) based on lorica morphology and size according to the literature (Kofoid and Campbell, 1929; Hada, 1937; Hada, 1938; Kofoid and Campbell, 1939; Bakker and Phaff, 1976; Yoo et al., 1988; Zhang et al., 2012).

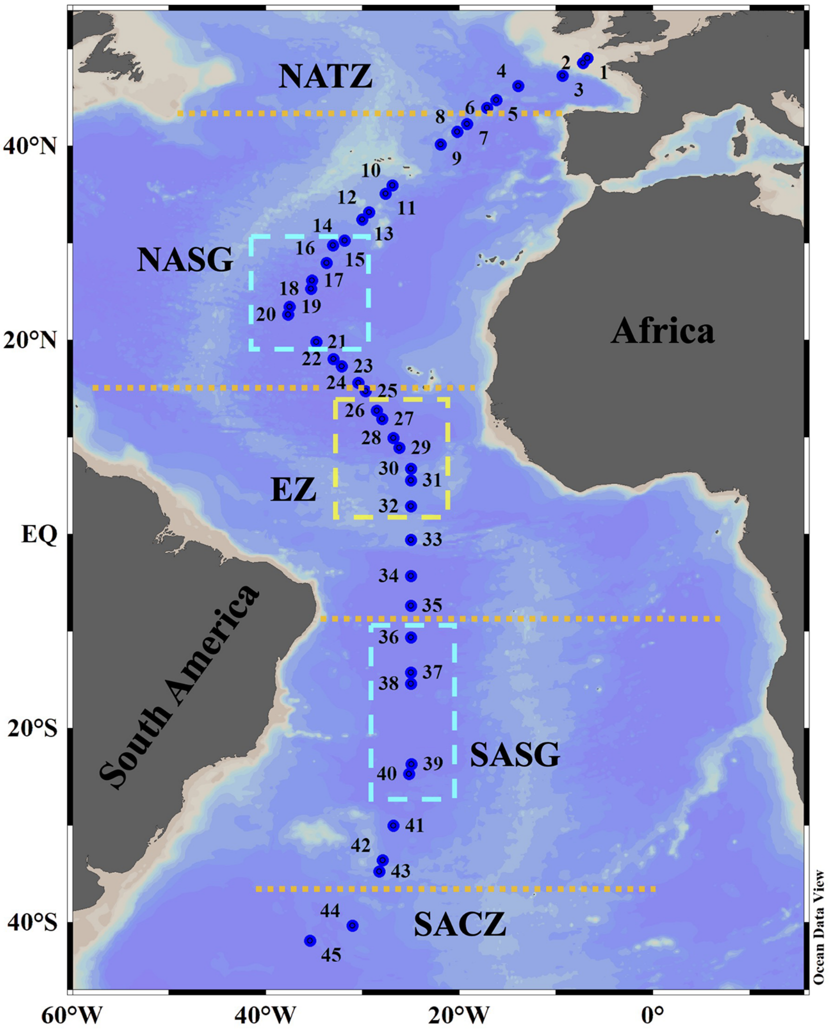

FIGURE 1
Location of sampling stations on the AMT29 cruise. The boundary positions (orange dotted lines) of the North Atlantic Transition Zone (NATZ), Northern Atlantic Subtropical Gyre (NASG), Equatorial Zone (EZ), Southern Atlantic Subtropical Gyre (SASG) and South Atlantic Convergence Zone (SACZ) were determined according to environmental factors as defined by Aiken et al. (2000), Hooker et al. (2000) and Aiken et al. (2017). The yellow box indicates the Equatorial Zone centre. The cyan boxes delimit gyre centres.

The maximum abundance of one species in all the samples was labelled as A_{max}. The dominance index (Y) was calculated using the equation:

$$Y = \frac{N_i}{N} f_i$$

where N_i was the total number of individuals of the species i, N was total individual number of all species, f_i was the occurrence frequency of species i (number of sampling points occurred/ number of all sampling points). Species with $Y > 0.02$ were defined as dominant species (Li et al., 2018). Species richness of one station is the total number of the species appeared in all the samples collected at this station.

The poleward edge positions of both Northern Atlantic Subtropical Gyre (NASG) and Southern Atlantic Subtropical Gyre (SASG) were defined as the boundary of the 0.15 μg L^{-1} surface chlorophyll isopleth (Aiken et al., 2017). The Equatorial Zone (EZ) was located between 15°N and 10°S as defined by Aiken et al. (2000). North of the NASG was the North Atlantic Transition Zone (NATZ), while south of the SASG was the South Atlantic Convergence Zone (SACZ) (Hooker et al., 2000).

Results

Hydrography and oceanic province identification

Temperature along the transect was in the range of 8.02-29.25°C in the upper 200 m (Figure 2). Water temperature was highest (28-29.25°C) in the upper 50 m between 1°N and 13°N and decreased poleward. We defined waters with temperature > 28°C as tropical waters. The prominent equatorial upwelling was observed north of the equator. Spatially, the isotherms showed obvious "W" distribution patterns along the transect (Figure 2). Taking the 18°C isotherm as an example, it appeared at about 50 m

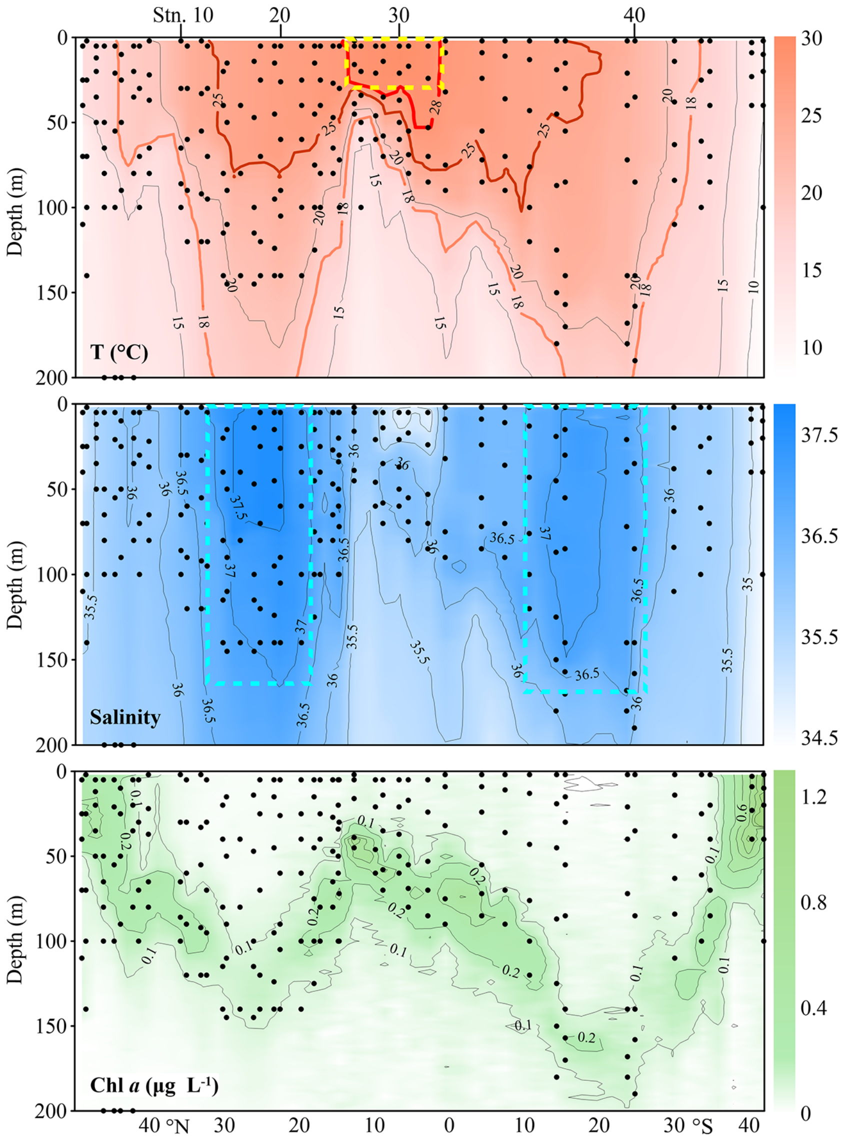

FIGURE 2
Distribution of temperature (T), salinity and *in vivo* chlorophyll fluorescence (Chl *a*) along the AMT transect. Each dot represents one sampling point. The yellow box indicates the Equatorial Zone centre. The cyan boxes delimit gyre centres. Black dots denote the locations of sample collection.

depth around 10°N and went to a depth of more than 200 m between 22-31°N and 15-24°S in the northern and southern hemispheres, respectively. The isotherm depth then became shallower poleward and reached the surface at about 43°N and 31°S, respectively. At about 5°S, the 15°C isotherm indicated a weak upwelling. The temperature changed very little vertically in the southernmost stations (Figure 2).

Salinity was in the range of 34.50-37.73. Horizontally, salinity was low at 0-12°N, it increased poleward and maintained high values in both subtropical gyres, then decreased. Vertically, the salinity varied very little with depth (Figure 2). NASG had higher salinity than SASG. The gyre centres were defined as salinity 37.5 (approximately the position of T > 25°C) in NASG and 37 in SASG, respectively. Correspondingly, waters with 15°C< T< 25°C was defined as frontal areas in both hemispheres.

Chl *a* concentration ranged from undetectable to 1.29 µg L^{-1}. The DCM layer was quite shallow in the northernmost and southernmost stations and deepened toward the equator. The DCM layer was deepest at about 24°S (170 m) and at about 26°N (132 m) (Figure 2). Consistently, the DCM was deepest in the gyre centres (Figure 2). All the stations along the transect were located in five oceanic provinces. The positions of the NASG and SASG were 15°N-43°N and 10°S-35°S, respectively (Figure 1).

Tintinnina distribution patterns

In total, 172 species were distinguished (five were unidentified species and 167 represented 40 genera) (Table 1). *Protorhabdonella curta*, *Acanthostomella minutissima*, *Dadayiella ganymedes* and

Ascampbelliella armilla were the four most common species that occurred in 172, 170, 169 and 160 samples, respectively. There were 32, 30, 50, and 29 species occurring in more than 50 samples, 30-50 samples, 10-30 samples and 5-10 samples, respectively. The remaining 31 species were observed in fewer than 5 samples.

A_{max} of Tintinnina species was positively related to their occurrence frequency (Supplementary Figure 1). *Protorhabdonella curta*, which had the highest occurrence frequency, had the highest A_{max} (69.07 ind. L^{-1}), at 40 m depth, St. 44 (Table 1). Only 15 Tintinnina species had A_{max} higher than 10.00 ind. L^{-1}. The A_{max} of most species (142 species) was lower than 5.00 ind. L^{-1}. There were 83 species with A_{max} lower than 1.00 ind. L^{-1} (Table 1).

It was also difficult to define the biogeographic distribution patterns of the 31 species observed in< 5 samples because of their low occurrence frequency. Although *Coxliella fasciata*, *Canthariella* sp. 3 and *Parundella difficilis* occurred in ≥ 5 samples, their distributions were too scattered to determine their biogeographic distribution patterns. Thus, those 34 species were considered as rare species (Table 1). The largest A_{max} among rare species was 2.17 (ind. L^{-1}).

The neritic species *Helicostomella subulata* only occurred in the northernmost two stations, while the cold-water species *Acanthostomella norvegica* only appeared in the southernmost two stations (Figure 3; Supplementary Figure 2).

All the other 136 species were warm water species. Based on their high abundance regions, they were classified into 4 biogeographic types: equatorial species, gyre species, frontal species (these three types had high abundance in the upper water< 75 m) and deep Chl *a* maximum species with high abundance in deeper water (> 75 m) (Figure 4; Supplementary Figures 3-10). Because some species showed slightly different distribution between the northern and southern hemispheres, their classification is based primarily on the distribution characteristics in the northern hemisphere.

A total of 32 species in 17 genera were considered as equatorial species (Figure 4; Supplementary Figures 3, 4 and Table 1) occurring in upper waters with temperature > 28°C. Among them, only some occurred in a narrow latitudinal range near the equator (such as *Eutintinnus tenuis*, *Amphorellopsis tetragona*, *Amphorides infundibulum*, *Metacylis corbula* and *Coxliella*

TABLE 1 Number of samples (N) where a given Tintinnina species was observed and maximum abundance (A_{max}, ind. L^{-1}) for each Tintinnina species along the Atlantic Meridional Transect.

Species	N	A_{max}	Species	N	A_{max}	Species	N	A_{max}
Neritic species								
Helicostomella subulata	7	3.69						
Cold-water species								
Acanthostomella norvegica	6	4.12						
Equatorial species								
Protorhabdonella curta	172	69.07	*Proplectella ellipsoida*	89	3.25	*Eutintinnus pacificus*	36	13.81
Acanthostomella minutissima	170	42.56	*Codonella perforata*	69	1.71	*Metacylis sanyahensis*	25	0.57
Dadayiella ganymedes	169	31.31	*Epiplocylis undella*	69	2.30	*Epiplocyloides reticulata*	24	3.63
Ascampbelliella armilla	160	9.74	*Eutintinnus fraknoii*	66	3.96	*Amphorides infundibulum*	23	3.39
Protorhabdonella simplex	130	2.84	*Ascampbelliella urceolata*	61	13.81	*Metacylis corbula*	22	3.23
Amphorides minor	110	11.90	*Rhabdonella valdestriata*	60	9.05	*Metacylis mereschkowskii*	16	0.28
Amphorides quadrilineata	109	9.62	*Rhabdonella amor*	56	5.09	*Rhabdonella cornucopia*	13	1.01
Proplectella perpusilla	103	6.15	*Eutintinnus stramentus*	55	2.83	*Eutintinnus* sp. 1	8	0.57
Rhabdonellopsis apophysata	103	4.50	*Rhabdonella brandti*	53	6.00	*Eutintinnus tenuis*	5	0.50
Eutintinnus apertus	101	6.22	*Coxliella ampla*	52	41.59	*Amphorellopsis tetragona*	5	1.22
Steenstrupiella gracilis	91	7.23	*Climacocylis scalaroides*	36	0.85			
Gyre species								
Xystonella treforti	70	1.41	*Rhabdonella chiliensis*	39	1.50	*Eutintinnus perminutus*	16	1.81
Eutintinnus medius	51	5.71	*Rhabdonella indica*	32	0.50	*Undella hemispherica*	15	0.19
Salpingella subconica	48	2.30	*Eutintinnus elongatus*	31	1.33	*Undella turgida*	8	0.13
Epiplocylis constricta	40	0.35	*Daturella angusta*	30	0.38			
Epiplocylis calyx	39	0.63	*Xystonellopsis cyclas*	22	0.60			

(Continued)

TABLE 1 Continued

Species	N	A_{max}	Species	N	A_{max}	Species	N	A_{max}
Frontal species								
Proplectella parva	86	3.75	*Parundella aculeata*	31	7.17	*Eutintinnus elegans*	15	4.29
Salpingella acuminata	82	16.30	*Steenstrupiella robusta*	28	16.90	*Salpingella* sp. 3	14	2.26
Dictyocysta reticulata	71	22.18	*Proplectella ovata*	28	8.50	*Proplectella grandis*	13	0.89
Acanthostomella conicoides	56	16.97	*Undella clevei*	28	4.14	*Epiplocylis acuminata*	12	0.63
Codonella elongata	53	5.33	*Proplectella cuspidata*	27	0.89	*Xystonella lohmanni*	12	2.99
Salpingella decurtata	53	2.40	*Cyttarocylis eucecryphalus*	27	0.38	*Xystonella lanceolata*	12	0.42
Steenstrupiella steenstrupii	47	1.73	*Epicancella nervosa*	24	1.13	*Bursaopsis striata*	12	1.13
Acanthostomella lata	45	3.96	*Salpingella faurei*	22	2.26	*Proplectella amphora*	11	1.70
Dictyocysta polygonata	43	3.45	*Petalotricha major*	22	0.38	*Proplectella angustior*	9	0.57
Eutintinnus tubulosus	42	55.03	*Ascampbelliella protuberans*	21	9.06	*Salpingella* sp. 4	9	1.15
Climacocylis scalaria	41	0.89	*Salpingella curta*	20	3.46	*Protorhabdonella striatura*	8	0.69
Dictyocysta mitra	37	13.81	*Codonellopsis contracta*	19	1.54	*Xystonellopsis cymatica*	7	0.50
Dictyocysta pacifica	35	1.63	*Dictyocysta elegans*	18	5.59	*Rhabdonella* sp.	6	35.92
Xystonellopsis brandti	34	1.13	*Rhabdonella conica*	18	26.00	*Eutintinnus* sp. 2	6	0.38
Eutintinnus lusus-undae	33	1.15	*Eutintinnus macilentus*	17	0.51	*Codonella nationalis*	5	1.36
Undella hyalina	31	3.80	*Coxliella laciniosa*	16	0.50			
Deep Chl *a* Maximum (DCM) species								
Parundella inflata	61	2.81	*Xystonella clavata*	22	0.38	*Salpingella* sp. 2	10	1.41
Acanthostomella obtusa	59	3.52	*Dictyocysta mulleri*	19	1.01	*Epiplocylis ralumensis*	9	0.75
Salpingella laminata	58	8.05	*Epiplocylis blanda*	18	0.36	*Proplectella ostenfeldi*	9	0.85
Salpingella sp. 1	49	1.13	*Xystonellopsis dicymatica*	18	0.50	*Salpingella attenuata*	9	0.38
Dictyocysta spinosa	47	1.30	*Canthariella* sp. 1	16	0.75	*Proplectella pentagona*	8	1.15
Proplectella claparedei	46	1.70	*Poroecus curtus*	16	0.57	*Salpingella acuminatoides*	8	0.57
Dadayiella pachytoecus	40	3.68	*Rhabdonella exilis*	14	0.58	*Cyttarocylis acutiformis*	8	0.14
Canthariella pyramidata	39	1.88	*Canthariella brevis*	13	1.00	*Undellopsis marsupialis*	7	0.19
Salpingacantha unguiculata	33	0.75	*Poroecus apiculatus*	13	0.25	*Xystonellopsis heros*	7	0.20
Xystonellopsis paradoxa	31	0.44	*Proplectella biorbiculata*	13	0.81	*Amplectella monocollaria*	6	0.13
Proplectella urna	30	1.70	Unidentified sp. 1	13	1.08	*Proplectella praelonga*	5	0.56
Salpingella rotundata	30	1.15	*Brandtiella palliata*	11	0.73	*Canthariella* sp. 2	5	0.33
Eutintinnus haslae	30	2.25	*Codonella amphorella*	11	0.25	*Codonellopsis meridionalis*	5	0.25
Steenstrupiella intumescens	24	2.26	*Salpingella minutissima*	11	0.27	Unidentified sp. 2	5	1.52
Ormosella bresslaui	22	1.00	*Amphorides laackmanni*	11	0.40			
Rare species								
Coxliella fasciata	8	0.28	*Climacocylis elongata*	2	0.20	*Parundella attenuata*	1	0.06
Canthariella sp. 3	8	2.17	*Proplectella acuta*	2	0.34	*Parundella aciculifera*	1	0.06
Parundella difficilis	5	0.18	*Rhabdonella sanyahensis*	2	0.19	*Xystonellopsis pulchra*	1	0.43
Coxliella pelagica	4	0.28	*Eutintinnus procurrerens*	2	0.06	*Rhabdonella hydria*	1	0.08
Amplectella collaria	4	0.13	*Eutintinnus pinguis*	2	0.35	*Salpingella gracilis*	1	0.04

(Continued)

TABLE 1 Continued

Species	N	A_{max}	Species	N	A_{max}	Species	N	A_{max}
Metacylis conica	4	0.12	*Amphorides amphora*	2	0.28	*Amphorides brandti*	1	0.19
Ormosella apsteini	4	0.13	*Amphorellopsis quinquealata*	2	0.13	*Albatrossiella agassizi*	1	0.09
Codonaria oceanica	3	0.13	Unidentified sp. 3	2	0.10	*Daturella emarginata*	1	0.06
Coxliella mariana	3	0.25	*Codonaria cistellula*	1	0.38	Unidentified sp. 4	1	0.06
Parundella lohmanni	3	0.17	*Tintinnopsis* sp.	1	0.06	Unidentified sp. 5	1	0.06
Codonella olla	2	0.19	*Undella lachmanni*	1	0.31			
Codonellopsis robusta	2	0.28	*Parundella lachmanni*	1	0.31			

Species are listed inside each group, according to their occurrence frequency.

ampla). These species were concentrated in the EZ with high surface temperature and also appeared in deep Chl *a* maximum waters with relatively low temperature. However, they were not detected in adjacent stations where the temperature was still high.

Some equatorial species had a high abundance in the equatorial region and their abundance decreased poleward (such as *Eutintinnus stramentus*, *E. fraknoii*, *Protorhabdonella simplex* and *Steenstrupiella gracilis*). *Acanthostomella minutissima*, *Dadayiella ganymedes*, *P. curta* had the widest temperature ranges. They were in high abundance not only in the EZ stations, but also in the northernmost and southernmost stations. These species had a wide temperature range and were noted over almost all the transect. Some equatorial species had very high A_{max}. For example, the A_{max} of four species (*P. curta*, *A. minutissima*, *Coxliella ampla*, *D. ganymedes*) were higher than 30 ind. L^{-1}.

A total of 13 Tintinnina species in 7 genera mainly observed in upper waters near the gyre centres and restricted to the NASG and SASG were defined as gyre species (Figure 4; Supplementary Figures 5, 6 and Table 1). They seldom occurred in waters with temperature outside the interval 18-28°C. Gyre species usually had low maximum abundance (A_{max}< 5.71 ind. L^{-1}).

A total of 47 species in 18 genera were frontal species and were mainly observed in upper waters of the gyres but not in the gyre centres themselves, being absent in waters with temperature > 28°C (Figure 4; Supplementary Figures 7, 8 and Table 1). Those species had high abundance in the frontal area where different water masses met and interacted, both horizontally and vertically. They formed a narrow band in the frontal area. For example, *Xystonellopsis brandti* occurred between 20-25°C in the northern hemisphere. Similarly, *Proplectella parva* occurred between 18-20°C and *Parundella aculeata* between 15-18°C (Figure 4). The largest A_{max} was 55.03 ind. L^{-1} for *Eutintinnus tubulosus*. Eight species had A_{max} > 10 ind. L^{-1}. Some species (e.g., *P. parva*, *Salpingella acuminata*, *Acanthostomella lata*, *A. conicoides*) showed obvious tropical submergence phenomenon: occurring throughout the water in high latitude but in deeper layers of tropical waters where temperatures are lower than in the upper layers.

Deep Chl *a* maximum species included 44 species in 21 genera occurring in deep waters but disappeared in upper (< 75 m) warmer waters (Figure 4; Supplementary Figures 9, 10 and Table 1). All of the deep Chl *a* maximum species had A_{max} lower than 10 ind. L^{-1}.

Asymmetric geographic distribution in northern and southern hemispheres

Asymmetric distribution of Tintinnina species along the latitudinal gradient was a frequent phenomenon, especially in the NASG and SASG zones (Supplementary Figures 3, 5, 7, 9). Some species were restricted to only one hemisphere. Some frontal species (e.g., *Codonella nationalis*, *Rhabdonella conica*, *Xystonella lohmanni*, *Steenstrupiella robusta* and *Proplectella ovata*) only appeared in the northern hemisphere in this study, while *Epiplocylis acuminata*, *Proplectella angustior*, *Proplectella amphora*, *Bursaopsis striata*, *Protorhabdonella striatura* and

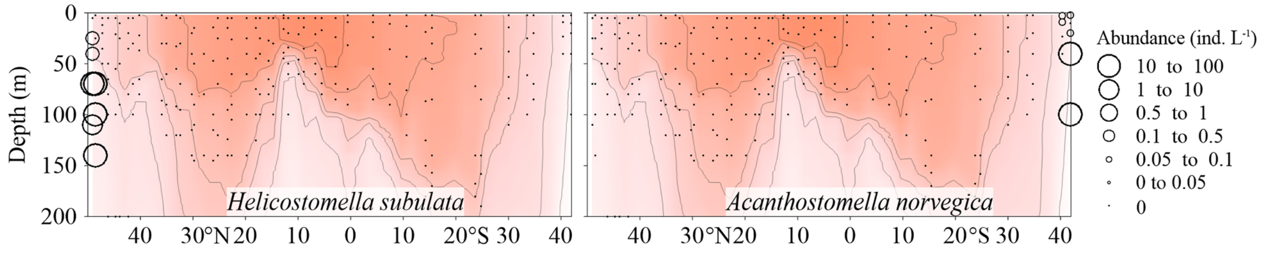

FIGURE 3
Vertical abundance (ind. L^{-1}) distribution of *Helicostomella subulata* and *Acanthostomella norvegica* along the AMT transect. The red color and isothermal lines are temperature (°C) as in Figure 2. Black dots denote the locations of sample collection.

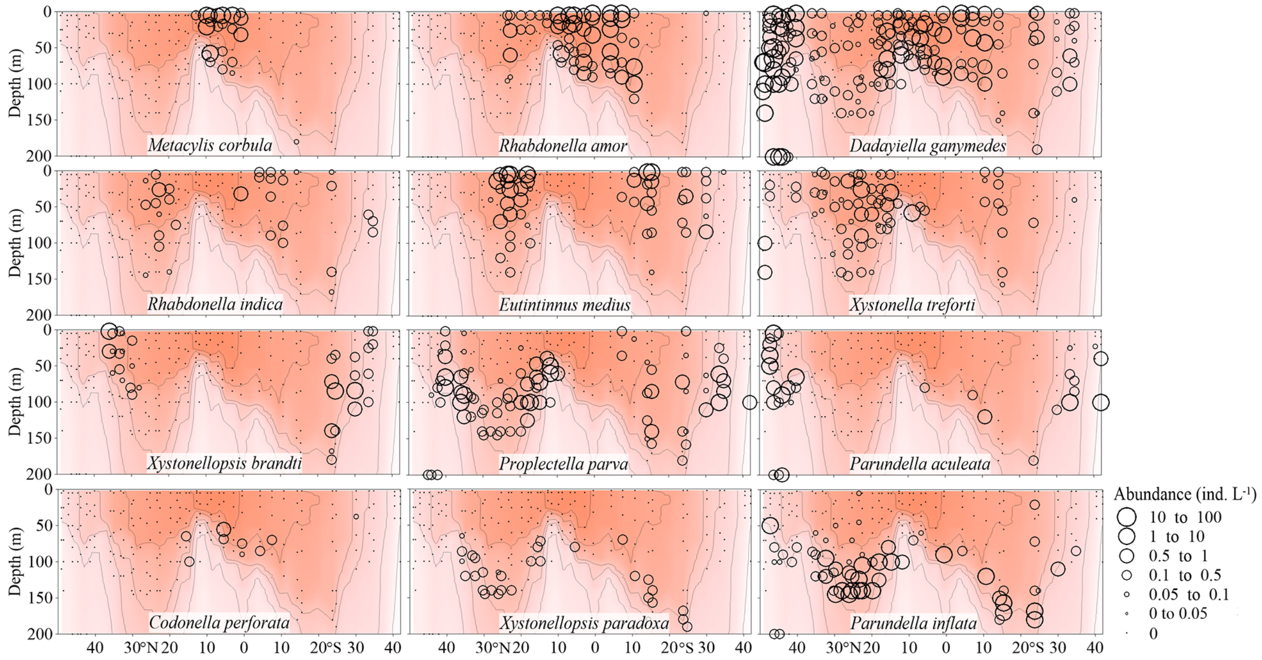

FIGURE 4
Vertical abundance (ind. L^{-1}) distribution of typical Tintinnina species in each biogeographic region along the AMT transect: from top to bottom, equatorial species, gyre species, frontal species and Deep Chl *a* Maximum species. The red color and isothermal lines are temperature (°C) as in Figure 2. Black dots denote the locations of sample collection.

Protorhabdonella sp. only occurred in the southern hemisphere (Supplementary Figure 7).

Some species showed different temperature range tolerance between the two hemispheres, such as *Acanthostomella conicoides* and *Proplectella urna*. Abundance of *A. conicoides* was high when the temperature was in the range of 15-18°C in the northern hemisphere, but almost disappeared in the same temperature range in the southern hemisphere (Supplementary Figure 7). *P. urna* exhibited high abundance when the temperature was about 25°C in the southern hemisphere, but its high abundance in the northern hemisphere appeared when the temperature was about 20° C (Supplementary Figure 9). Other examples were *P. perpusilla*, *Amphorides quadrilineata* (Supplementary Figure 3), *Rhabdonella chiliensis* (Supplementary Figure 5). Together with differences in the temperature range, the bandwidth of the vertical distributions of some frontal species (e.g., *Xystonellopsis brandti*, *P. parva*, *Parundella aculeata*) (Figure 4) was narrower in the northern hemisphere than in the southern hemisphere.

The vertical distribution of some species was likewise different in the two hemispheres. *Proplectella claparedei* and *Acanthostomella obtusa* occurred in surface waters in the southern hemisphere. In contrast, they were not observed in surface waters in the northern hemisphere (Supplementary Figure 9).

The relative locations of some species were dissimilar between the two hemispheres. For example, *Eutintinnus perminutus*, *Epiplocylis calyx* were on the poleward side of *E. medius* in the northern hemisphere, but vice versa in the southern hemisphere (Supplementary Figure 5).

Tintinnina species richness and abundance

Total abundance of equatorial species was highest in the EZ, decreased poleward and then increased at both boundaries of the transect, especially the northern one (Figure 5). The number of equatorial species at each sampling point decreased from the warm centre to both sides (Figure 6). The Gyre Species exhibited high values in the gyre centres regarding both abundance and number, with a declining trend toward the equator and poles (Figures 5, 6). The frontal species were present in high abundance and number in the AMT frontal areas (Figures 5, 6). In the DCM layer, the deep Chl *a* maximum species were also observed in high abundance (Figures 5, 6).

Tintinnina species richness was in the range of 3-45, with elevated values mainly belonging to the 50-150 m layer between 40°N and 35°S, at most stations. The highest value (45) was determined for the 110 m sample of Stn. 41. In the upper 50 m, Tintinnina species richness was relatively low (Figure 7).

Tintinnina abundance varied between 0.33 and 185.11 ind. L^{-1}, and was characterized by a distribution pattern completely different from that of their species richness. Tintinnina abundance was< 50 ind. L^{-1} in most samples, high values mainly belonged to the upper 100 m in the northernmost and southernmost stations, as well as regions around the equator. Tintinnina abundance was extremely low in the centres of both NASG and SASG (Figure 7).

Tintinnina species richness increased with temperature, reaching peak value at about 20°C, then decreased slightly when the temperature exceeded 20°C. In contrast, Tintinnina abundance did not vary much with temperature. Species richness increased

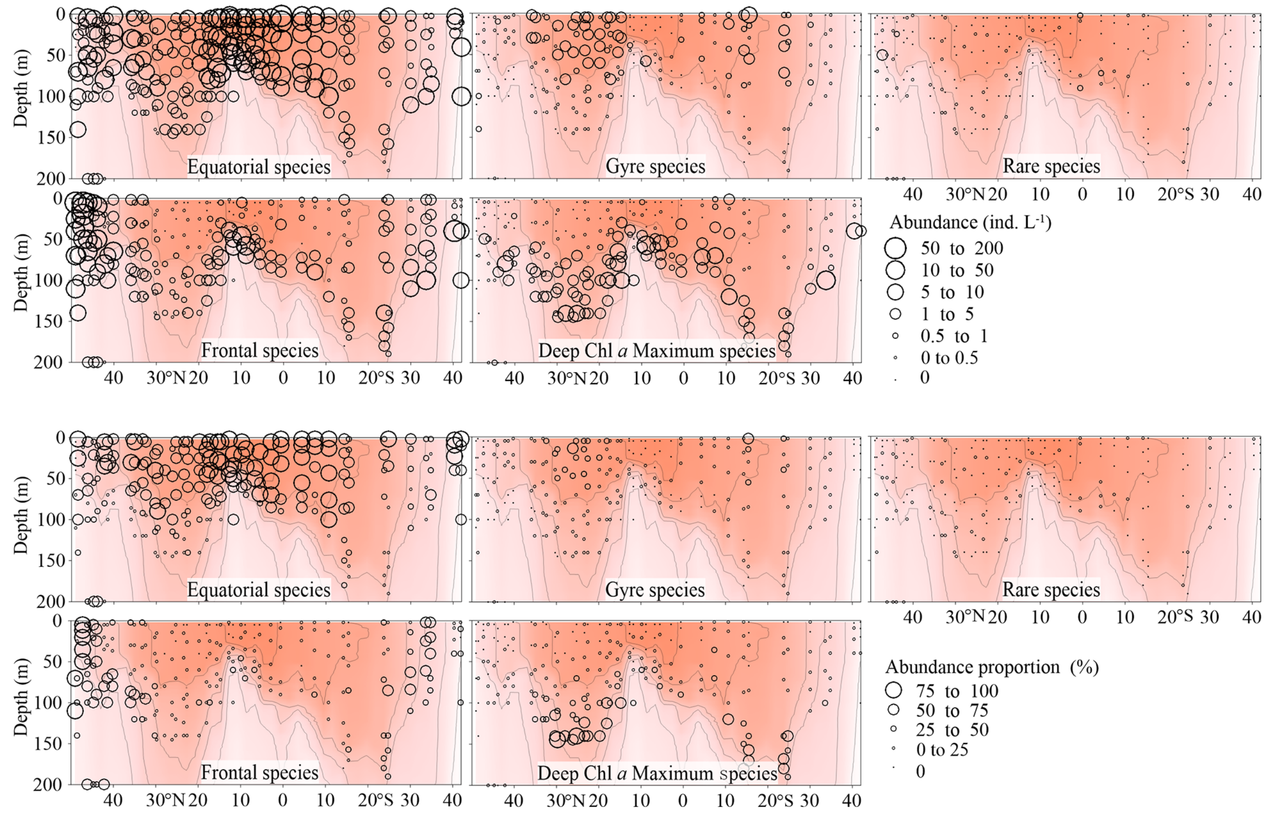

FIGURE 5
Vertical Tintinnina abundance (ind. L^{-1}, upper panel) and abundance proportion (%, lower panel) distribution in each biogeographic region along the AMT transect. The red color and isothermal lines are temperature (°C) as in Figure 2. Black dots denote the locations of sample collection.

with salinity and peaked at a salinity of about 36.5. On the other hand, Tintinnina abundance decreased when salinity increased. Tintinnina species richness and abundance increased when Chl *a* was lower than 0.4 µg L^{-1}, and decreased sharply when the Chl *a* exceeded 0.4 µg L^{-1} (Figure 8).

Organization of Tintinnina assemblage by sub-assemblages

Since all the species were mainly classified into 4 biogeographic types, all the species in a particular biogeographic type could be considered as a sub-assemblage. Therefore, the Tintinnina assemblage could be deemed as the superposition of four sub-assemblages: equatorial, gyre, frontal and deep Chl *a* maximum sub-assemblages. The dominance of each sub-assemblage in the different parts of the transect was evaluated by means of the abundance percentage and species number percentage of each sub-assemblage in the Tintinnina assemblage (Figures 5, 6). Deep Chl *a* maximum sub-assemblage was the dominant assemblage in waters below 100 m depth because it occupied > 50% in both Tintinnina abundance and species number.

In the waters shallower than 100 m, equatorial sub-assemblage abundance occupied >50% of total Tintinnina abundance in most stations. Its species number occupied >50% of total Tintinnina species number in equatorial and gyre zones and decreased in frontal zones. Therefore, equatorial sub-assemblage dominated the equatorial and gyre zone upper 100 m waters. Frontal sub-assemblage abundance and species number were >50% of respectively Tintinnina abundance and species number in the frontal zone upper waters. Since equatorial species also showed values >50% in this area, we concluded that the frontal and equatorial sub-assemblages co-dominated in the frontal zones. Gyre sub-assemblage distributed in the upper waters of the gyres. Their abundance exceeded 50% in only two samples and their species number exceeded 50% in only one sample. Therefore, gyre sub-assemblage seldom dominated in the transect.

To further compare the influence of the sub-assemblages in the equatorial centre and gyre centres, the dominant species and their abundance contribution to total Tintinnina abundance was estimated (Table 2). In equatorial centre, all of the dominant species were equatorial species. In the gyre centres, the gyre species *Eutintinnus medius* was the first dominant species in the NASG and SASG centres. The frontal species *Rhabdonella brandt*

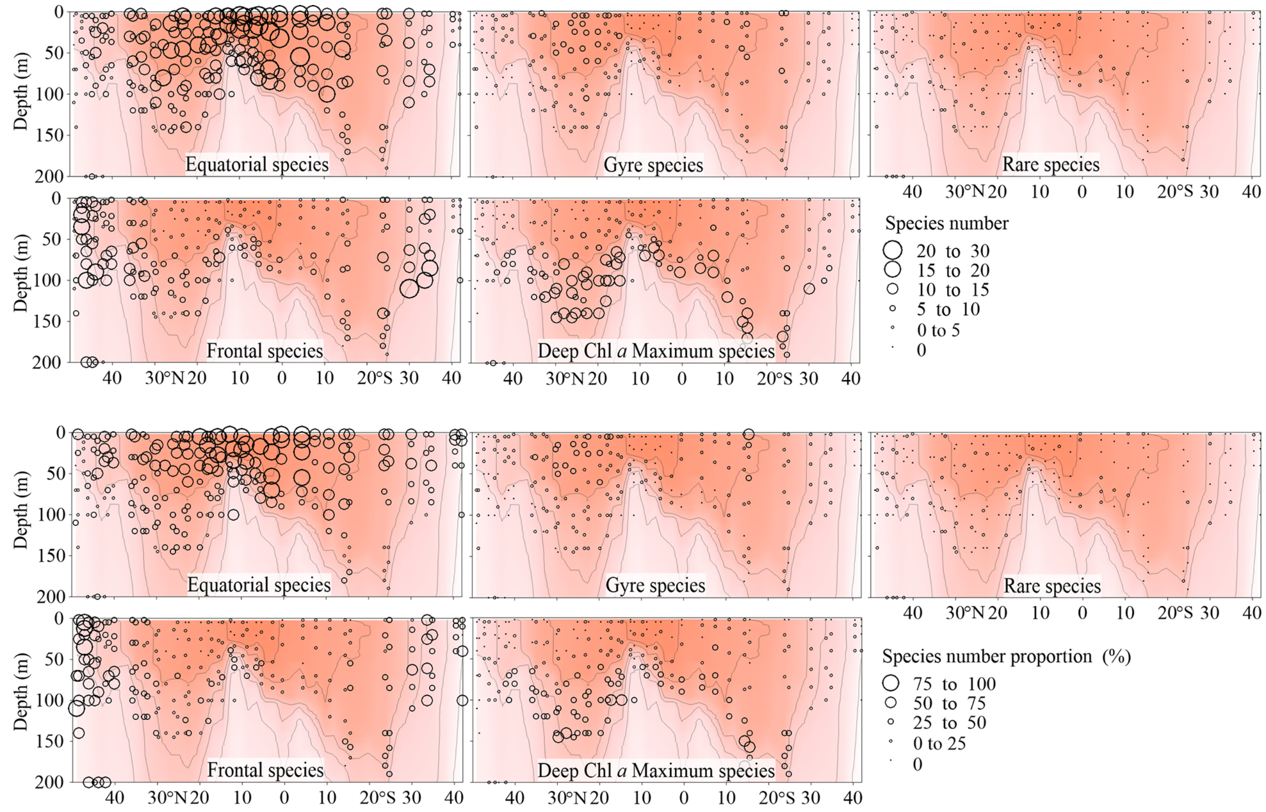

FIGURE 6
Vertical distribution of Tintinnina species number (upper panel) and proportion (%, lower panel) in each biogeographic region along the AMT transect. The red color and isothermal lines are temperature (°C) as in Figure 2. Black dots denote the locations of sample collection.

and *Proplectella cuspidata* were dominant in the NASG and SASG centres, respectively.

Tintinnina assemblage in different zones along the transect

The transect completely crossed the NASG, EZ and SASG, enabling us to reliably describe the Tintinnina assemblage structures in these regions. The number of Tintinnina species in each biogeographic region was highest in the NASG (142 species), followed by the SASG (124 species), EZ (110) and NATZ (75). Only 23 species were recorded in the SACZ. In total, 14 Tintinnina species occurred in all 5 regions, and 37, 53 and 29 species appeared in 4, 3 and 2 regions, respectively. Numbers of species which were specific in the NATZ, NASG, EZ, SASG and SACZ were 6, 14, 8, 8 and 3, respectively. The NASG and SASG assemblages shared 111 Tintinnina species. Thirty-one species that occurred in the NASG were not observed in the SASG, while 13 species occurring in the SASG were absent in the NASG (Figure 9).

There were 8, 4, 7, 7 and 6 dominant species in the NATZ, NASG, EZ, SASG and SACZ, respectively. *Eutintinnus tubulosus* and *Dadayiella ganymedes* were the top 2 dominant species in the NATZ with dominance index > 0.1. The dominance index of all the dominant species was< 0.1 in the NASG and SASG. In the EZ, *Acanthostomella minutissima* was the most dominant, while *Coxliella ampla* was the second most dominant species, with dominance index of 0.18 and 0.11, respectively. Finally, *A. minutissima*, *Protorhabdonella curta*, *D. ganymedes* and *A. armilla* were the dominant species in all the samples along the transect (Table 3).

The dominant species composition varied with different biogeographic regions. Most dominant species in the NATZ disappeared or had extremely low dominance indexes in other regions except for *Dadayiella ganymedes*, which was also dominant in the NASG, EZ and SASG and it was not observed in the SACZ. *Eutintinnus tubulosus* was the first dominant species in the NATZ, but its dominance index was extremely low in NASG and EZ and could not be determined in SASG and SACZ. *Rhabdonella conica* was the dominant species in the NATZ but was absent in the other four regions (Table 3).

The 4 dominant species in the NASG were also dominant in the EZ and SASG. *Acanthostomella minutissima* and *Protorhabdonella curta* were dominant in the NASG, EZ, SASG and SAC; their dominance index was< 0.005 in the NATZ. *Ascampbelliella armilla* was the dominant species in the NASG, EZ and SASG, but its dominance index was very low in the NATZ and did not appear in the SACZ. The EZ, SASG and SAC contained 3, 3 and 4 specific dominant species, respectively (Table 3).

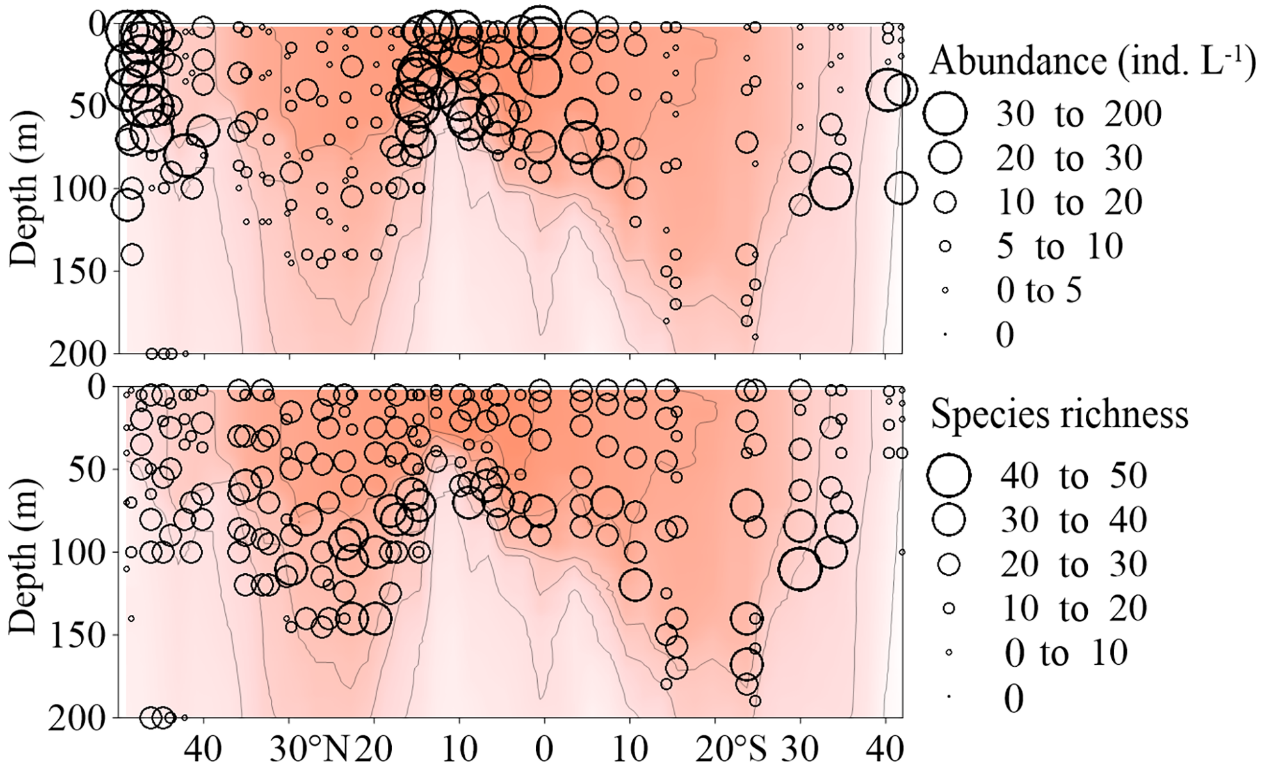

FIGURE 7
Vertical distribution of Tintinnina abundance (ind. L^{-1}) and species richness along the AMT transect. The red color and isothermal lines are temperature (°C) as in Figure 2. Black dots denote the locations of sample collection.

Latitudinal species richness gradient of Tintinnina

Latitudinally, Tintinnina species richness ranged from 6 to 71 (Figure 10) and showed an asymmetric bimodality with a dip near the equator. The northernmost and southernmost stations in both hemispheres, Stn. 1 at about 49°N and Stn. 45 at about 42°S, had the lowest species richness. The Tintinnina species richness increased towards the equator, peaking at Stns. 18 and 20 (about 20°N), and Stns. 39 and 41 (23°S and 30°S), respectively (Figure 10).

Along the transect, the number of equatorial species showed a unimodal peak in the equatorial zone. Frontal species had a high species number at both ends of the transect. Gyre species and deep Chl *a* maximum species showed bimodal peaks at the gyre centres. The total number of Tintinnina species, i.e., the superposition of the four types and rare species, showed bimodal peaks at the gyre centres (Figure 10).

Discussion

Biogeography of Tintinnina species

Previous knowledge of the geographic distribution of most Tintinnina species is largely incomplete, especially in regions of intricate and costly accessibility (Menegotto and Rangel, 2018). Dolan et al. (2013) and Pierce and Turner (1993) classified Tintinnina into 5 biogeographic distribution patterns at the genus level. Although some genera were considered as cosmopolitan, there appears to be no species that is truly cosmopolitan (Dolan et al., 2013). However, information on Tintinnina biogeographic distribution at the species level was scarce (Dolan et al., 2013; Li et al., 2019; Li et al., 2021). Tintinnina abundance was extremely low in tropical and subtropical open waters (Dolan et al., 2007; Gómez, 2007; Zhang et al., 2017; Li et al., 2018). In this study, we found that the maximum abundance of 83 Tintinnina species were lower than 1 ind. L^{-1}. Thus, sampling only 1 litre of water sample may miss many Tintinnina species with low abundance. It is worth noting that, in this study, the same person identified the Tintinnina species in all the collected samples and counted under the same protocol to minimize any potential human impact. Therefore, the method in this study could highlight the distribution pattern of most Tintinnina species except the rare ones. To our knowledge, this is the first species-level study on Tintinnina distribution and assemblage composition in the Atlantic Ocean.

In order to explore the biogeographic distribution patterns of Tintinnina in warm waters, we collected samples across a large spatial span from about 50°N to 40°S. *Helicostomella subulata* was a neritic species and commonly reported in coastal waters of the Arctic and subarctic regions (Dolan et al., 2021; Li et al., 2021). *Acanthostomella norvegica* was usually found in high-latitude waters of both hemispheres (Li et al., 2016; Liang et al., 2020; Li et al., 2021). The occurrence of *H. subulata* in the two northernmost stations and *A. norvegica* in the two southernmost stations,

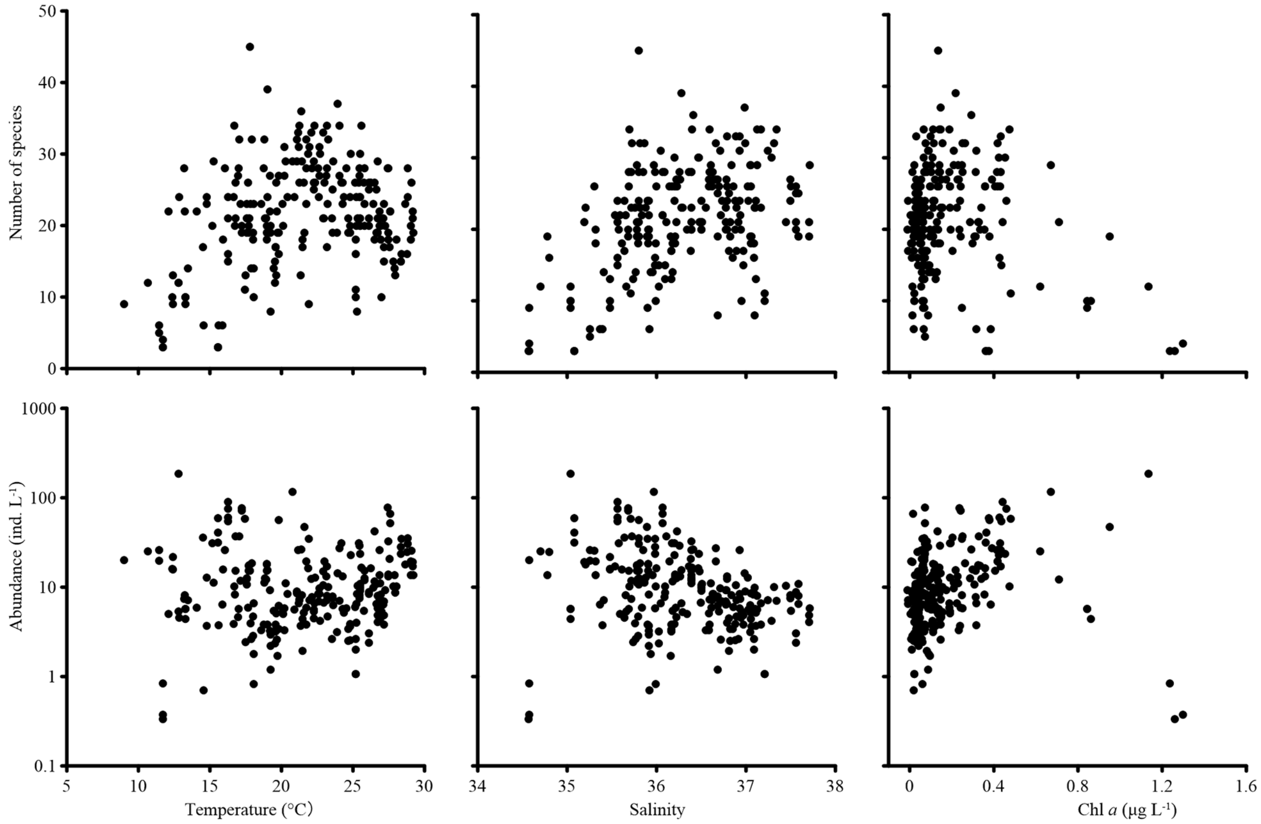

FIGURE 8
Tintinnina species richness and abundance variation with temperature, salinity, and *in vivo* chlorophyll *a* fluorescence (Chl *a*).

TABLE 2 Dominance index (*Y*) and abundance proportion (AP, %) of each dominant species in the upper 40 m of the Equatorial Zone (EZ), Northern Atlantic Subtropical Gyre (NASG) centre and Southern Atlantic Subtropical Gyre (SASG) centre shown in Figure 1.

EZ			NASG centre			SASG centre		
Species	*Y*	AP		*Y*	AP		*Y*	AP
Acanthostomella minutissima	0.1470	15.62	*Eutintinnus medius*	0.1215	13.26	*Eutintinnus medius*	0.1325	14.36
Coxliella ampla	0.1308	14.83	*Protorhabdonella curta*	0.0948	10.34	*Ascampbelliella armilla*	0.0910	9.10
Ascampbelliella armilla	0.1133	11.33	*Rhabdonellopsis apophysata*	0.0674	8.08	*Protorhabdonella simplex*	0.0726	7.86
Eutintinnus apertus	0.0518	5.50	*Ascampbelliella armilla*	0.0546	5.96	*Steenstrupiella gracilis*	0.0574	6.21
Protorhabdonella curta	0.0467	4.96	*Protorhabdonella simplex*	0.0505	5.51	*Protorhabdonella curta*	0.0504	5.96
Eutintinnus fraknoii	0.0277	4.28	*Rhabdonella chiliensis*	0.0494	5.93	*Dadayiella ganymedes*	0.0364	4.73
Eutintinnus stramentus	0.0275	3.60	*Steenstrupiella gracilis*	0.0437	5.24	*Rhabdonellopsis apophysata*	0.0329	5.35
Steenstrupiella gracilis	0.0272	3.85	*Rhabdonella valdestriata*	0.0390	5.85	*Acanthostomella minutissima*	0.0245	3.54
Amphorides infundibulum	0.0252	3.90	*Rhabdonella brandti*	0.0345	3.77	*Proplectella perpusilla*	0.0234	3.38
Rhabdonella valdestriata	0.0233	3.05	*Xystonella treforti*	0.0338	4.05	*Proplectella cuspidata*	0.0214	2.79
			Eutintinnus stramentus	0.0220	2.94			
Total		70.92			70.93			63.28

Orange color: Equatorial species; Green color: Gyre species; Blue color: Frontal species.

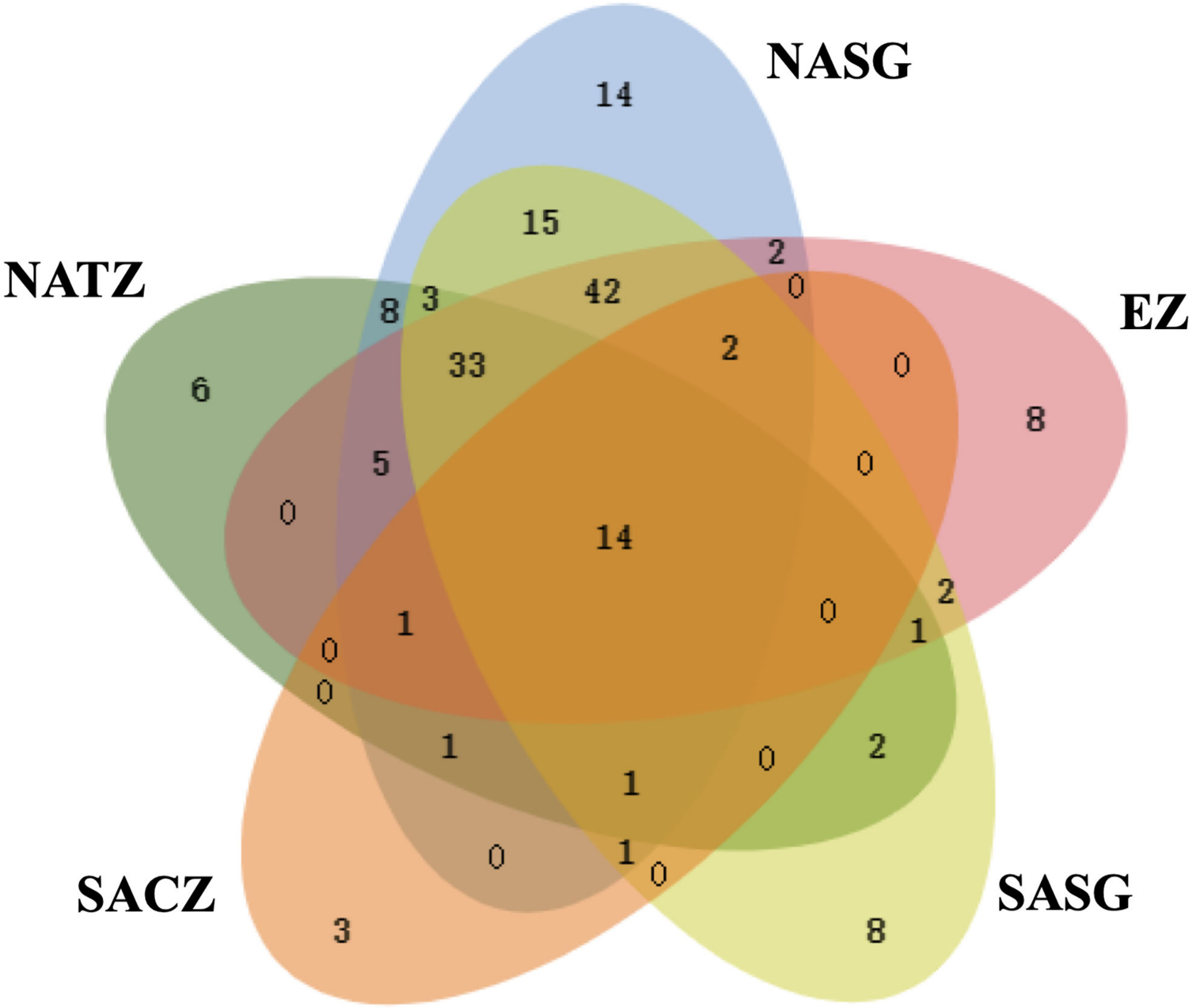

FIGURE 9
Venn diagram showing the number of Tintinnina species that are unique and shared among the five oceanic provinces. NATZ, North Atlantic Transition Zone; NASG, Northern Atlantic Subtropical Gyre; EZ, Equatorial Zone; SASG, Southern Atlantic Subtropical Gyre; SACZ, South Atlantic Convergence Zone.

indicated that the sampled transect crossed the full span of both NASG and SASG. Thus, the data in this study allowed us to analyse the Tintinnina biogeographic distribution over a large span of warm waters.

Most species identified in our study belonged to warm-water and cosmopolitan genera according to Dolan et al. (2013). *Metacylis* was considered as a neritic genus by Dolan et al. (2013). Li et al. (2016) classified *Metacylis* as a cosmopolitan genus. In the present study, four species of the genus *Metacylis* were recorded. None of them occurred in the northernmost two coastal stations. *Metacylis sanyahensis*, *M. corbula* and *M. mereschkowskii* were considered as equatorial species. *M. conica* was a rare species occurring in only 4 out of 235 samples in our study.

Li et al. (2021) investigated surface Tintinnina assemblage variation along transects across the North Pacific Transition Zone in summertime. They grouped 41 Tintinnina species into boreal, warm water type I, warm water type II, transition zone and cosmopolitan groups, according to the region where they were recorded and their abundance distribution patterns along the temperature gradient. *Dadayiella ganymedes* and *Eutintinnus tubulosus* were classified as warm water type I species, their abundance was high at the transition zone and decreased towards the equator (Li et al., 2021). In the East China Sea, high abundance of *D. ganymedes* appeared in the frontal area generated by the interaction between the Kuroshio current and coastal waters (Li et al., 2016). Those studies were based on the surface Tintinnina distribution. In the present study, the surface abundances of *D. ganymedes* and *E. tubulosus* were extremely high in the northern boundary of NASG, decreased towards the equator and had a slight increase in the EZ. However, *D. ganymedes* and *E. tubulosus* had high abundance at the subsurface waters in the EZ. Thus, we classified *D. ganymedes* and *E. tubulosus* as equatorial species.

TABLE 3 Dominant species and their dominance index (*Y*) in each biogeographic region and the total transect.

NATZ		NASG		EZ		SASG		SACZ		Total transect	
Species	*Y*	Species	*Y*	Species	*Y*	Species	*Y*	Species	*Y*	Species	*Y*
Eutintinnus tubulosus	0.16	*Ascampbelliella armilla*	0.07	*Acanthostomella minutissima*	0.18	*Ascampbelliella armilla*	0.04	*Protorhabdonella curta*	0.25	*Acanthostomella minutissima*	0.07
Dadayiella ganymedes	0.12	*Acanthostomella minutissima*	0.07	*Coxliella ampla*	0.11	*Proplectella perpusilla*	0.03	*Rhabdonella* sp.	0.10	*Protorhabdonella curta*	0.04
Steenstrupiella robusta	0.07	*Protorhabdonella curta*	0.06	*Ascampbelliella armilla*	0.08	*Acanthostomella minutissima*	0.03	*Eutintinnus pacificus*	0.05	*Dadayiella ganymedes*	0.04
Salpingella acuminata	0.05	*Dadayiella ganymedes*	0.03	*Protorhabdonella curta*	0.04	*Protorhabdonella simplex*	0.02	*Acanthostomella minutissima*	0.04	*Ascampbelliella armilla*	0.04
Dictyocysta reticulata	0.05			*Rhabdonella valdestriata*	0.02	*Eutintinnus medius*	0.02	*Proplectella perpusilla*	0.03		
Rhabdonella conica	0.04			*Rhabdonella amor*	0.02	*Dadayiella ganymedes*	0.02	*Dictyocysta mitra*	0.03		
Proplectella ovata	0.02			*Dadayiella ganymedes*	0.02	*Protorhabdonella curta*	0.02				
Amphorides minor	0.02										

NATZ, North Atlantic Transition Zone; NASG, Northern Atlantic Subtropical Gyre; EZ, Equatorial Zone; SASG, Southern Atlantic Subtropical Gyre; SACZ, South Atlantic Convergence Zone.

Vertically, the present study showed that some species had surface abundance peaks, whereas others exhibited abundance peaks at the DCM layer. These characteristics are consistent with Tintinnina in the tropical Pacific Ocean (Wang et al., 2019). Phytoplankton species were likewise classified into shallow (upper 30 m) and deep (DCM) groups in the Pacific Ocean, which offered suitable food supplies for ciliates to prey on (Venrick, 1988). Our research only sampled waters above the DCM, except at some stations in the north end of the transect. Tintinnina abundance decreased sharply below the DCM in the tropical Pacific waters (Li et al., 2018). Therefore, it is likely that the Tintinnina abundance in the AMT transect peaks at the DCM and decreases sharply below DCM.

Tropical submergence of transition zone species

Some equatorial and gyre species showed wide temperature tolerance, horizontally and vertically. They appeared in deeper colder waters but did not expand poleward. In contrast, tropical submergence was common for frontal species whose distribution coincided with the isotherm downward trend, occurring in high-latitude surface waters and detected in deep waters of the equatorial zone. Tropical submergence (Chaudhary et al., 2021) plays a significant role in the composition of low and mid-latitude plankton assemblages. Some species present near the surface at mid-high latitudes are well known to follow isothermal pathways into intermediate and abyssal water depths at low latitudes (Trubovitz et al., 2020). To our knowledge, it is the first time that Tintinnina tropical submergence is reported.

More and more researchers have realised the importance of investigating the vertical distribution of plankton species, like in the central Atlantic Ocean where four mesozooplankton groups were vertically distinguished (Vedenin et al., 2022). Preliminary studies have also shown that Tintinnina can be vertically distributed according to different groups (Wang et al., 2020; Wang et al., 2021). The fact that Tintinnina species observed in high latitude surface waters can be detected in low latitude deep waters forces one to consider the roles of both depth and latitude when investigating Tintinnina biogeographic distribution patterns.

Thanks to the large latitudinal coverage and vertical sampling, we found a lot of frontal Tintinnina species, which occurred in narrow bands between subtropical gyre centre and subarctic gyre. Some plankton species found in the transitional zone between subarctic and subtropical gyres are called transitional zone species. Our study showed that frontal zone species had wider temperature range (approx. 15-25°C) than transitional zone (15-20°C) (Li et al., 2021). *Undella clevei* and *U. californiensis* were considered as transition zone species, mainly observed in the North Pacific Transition Zone in the 15-20°C temperature range (Li et al., 2021). This Tintinnina biogeographic characterisation was only based on surface data. In the present study, *U. clevei* showed an asymmetric distribution pattern between both hemispheres and was linked to the frontal systems of different water masses. In the southern hemisphere, the *U. clevei* distribution was associated with the 15-20°C isotherms. In the northern hemisphere, it was mainly present in NASG deep waters in the temperature range 20-25°C. This is the reason why *U. clevei* was identified as a frontal species in the present study. Although *U. californiensis* was not detected in our study, it was observed in the open Pacific Ocean (Gómez, 2007). We speculate that *U. californiensis* may also be subject to a tropical submergence phenomenon and might occur in waters deeper than the DCM layer in low latitudes.

Transition zone species were reported in some phytoplankton (Venrick, 1971) and macrozooplankton (Brinton, 1962; McGowan, 1971). However, the mechanism responsible for their presence in

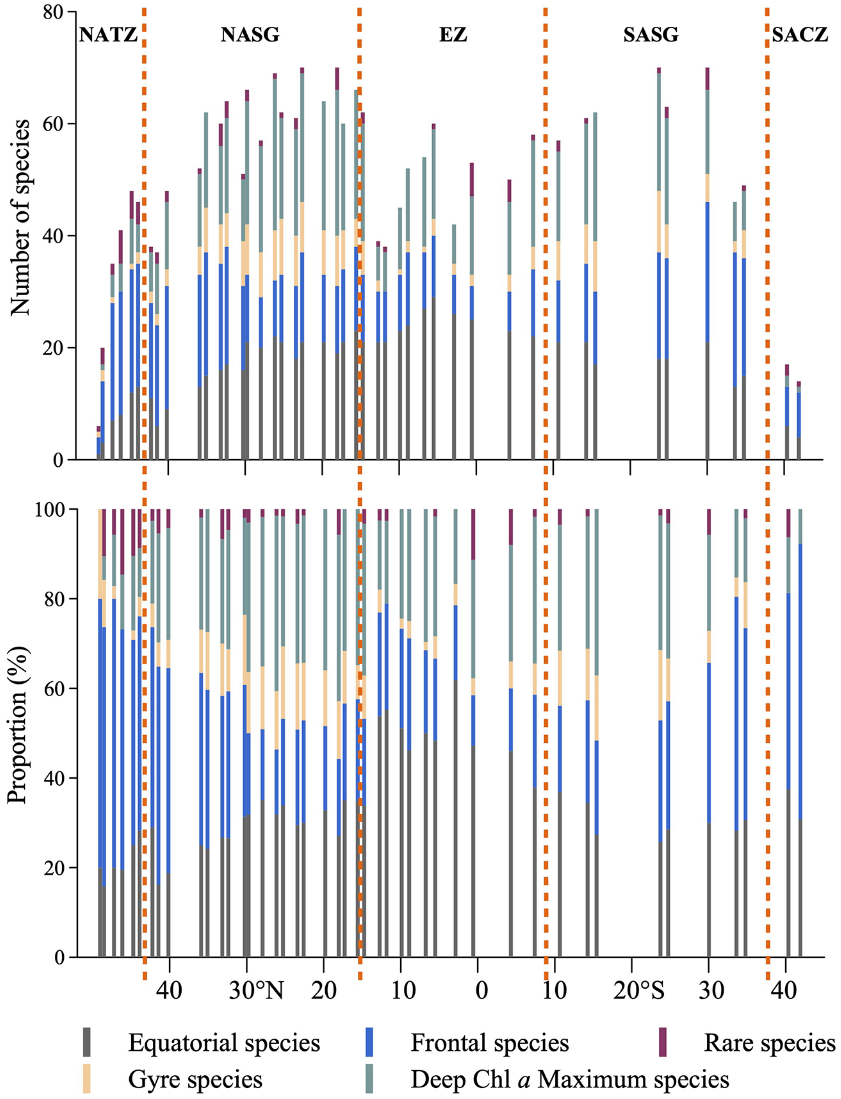

FIGURE 10
Latitudinal variation of Tintinnina species-number in each biogeographic pattern along the AMT transect. NATZ, North Atlantic Transition Zone; NASG, Northern Atlantic Subtropical Gyre; EZ, Equatorial Zone; SASG, Southern Atlantic Subtropical Gyre; SACZ, South Atlantic Convergence Zone.

the eastward flow had no obvious explanation. Olson (2001) proposed that mesoscale eddies would transport some organisms counter current. Boltovskoy (1998) and Longhurst (2007) did not agree with this mechanism. Our data suggest that tropical submergence might be the mechanism accounting for the existence of transition zone species. Circular current is the base of plankton distribution (Longhurst, 2007). Some individuals submerged to the bottom of the gyre could survive the full cycle of the gyre flow and serve as seeds when they are released to the colder area, where vertical mixing brings them back to the upper water. However, these submerged individuals had low abundance and were neglected in biogeography studies. As a result, such species might in fact be frontal species but have been mistakenly regarded as transition zone species.

Conceptual model of organization of planktonic Tintinnina assemblage

According to the plankton biogeography theory of circular current distribution (Longhurst, 2007), except for the frontal sub-assemblage, the other three sub-assemblages could be divided into core areas with high abundance and species number, and pioneer areas as per Li et al. (2016). Species confined to the core area were called core species. Correspondingly, the species that had expanded out of the core area were referred to as pioneer species. Species belonging to the deep Chl *a* maximum sub-assemblage core area were found in the gyre deep waters, whereas pioneer species expanded out to the edge of the gyres. Some pioneer species could be brought into shallow waters by vertical mixing on the polar side of the gyre.

The core area of the gyre sub-assemblage was in the upper water around the gyre centre. Pioneer species expanded to both the warm and cold sides of the gyre, but they could not exist in waters warmer than 28°C and colder than 20°C (except *Xysttonella treforti*).

In the equatorial sub-assemblage, the distribution of the species was kept in the equatorial zone by the tropical gyre which is composed of equatorial current and equatorial counter current. Core species (*Amphorides infundibulum*, *Metacylis corbula*) were in waters warmer than 28°C. Some species have been recorded poleward as pioneer species due to their large suitable temperature range. Some of them were entrained poleward by the mixing between tropical gyre and subtropical gyre. Some species (e.g., *Steenstrupiella gracilis*, *Rhabdonella brandti*) died out when they are moved into cold waters.

Some equatorial species (e.g., *Dadayiella ganymedes*, *Protorhabdonella curta*) were strong enough to exist and flourish at the edge of the subtropical gyre. These species are so special that they could also be considered frontal species which could flourish in equatorial waters. But we artificially classify them as equatorial species.

The organization of the Tintinnina assemblage resulted from the superposition of the four sub-assemblages as in the conceptual model of Figure 11. Although different biogeographical patterns were identified in previous studies, the influence of the species of a particular biogeographical pattern was not evaluated (Longhurst, 2007). Since our study is the first of its kind, we could not compare Tintinnina with other plankton. However, we speculate that the single-celled protist plankton might have similar organization mechanism because of their lack of life history.

Woods (1999) proposed a question: what is the change of plankton assemblage in a water-mass moving around the centre of north Atlantic Subtropical Gyre. Water-mass traveling from the Azores to the Antilles could take six years. It will take about five years to finish Sargasso-Sea circuit (Supplementary Figure 11). Our conceptual model suggests that, when a water-mass moves southward from Azores, individuals of frontal species in the upper water will gradually die out but some individuals in the deep water will remain alive to serve as seeds for the surface population. Some equatorial species will slowly get into the water-

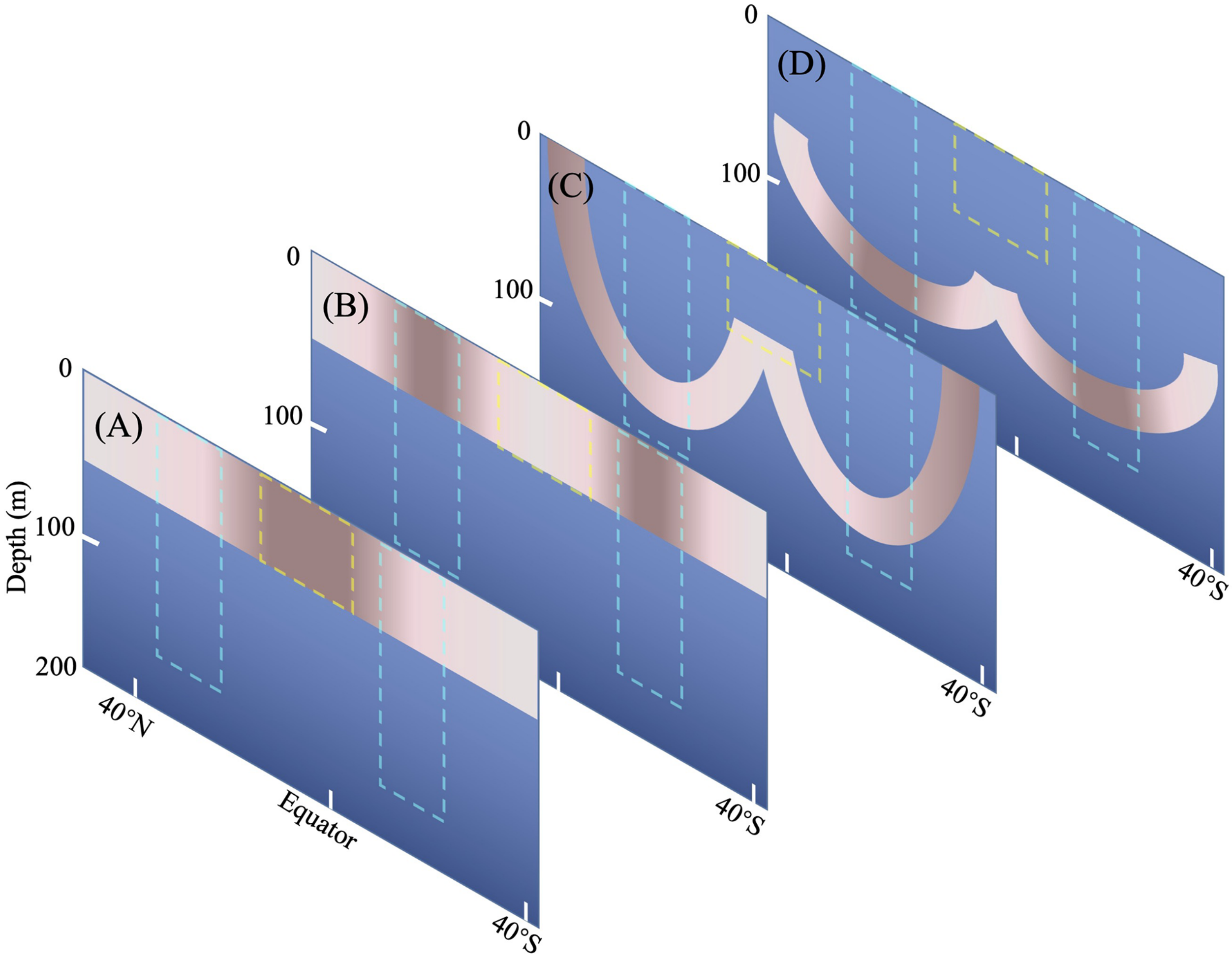

FIGURE 11
Conceptual model of Tintinnina communities composed of four sub-communities. **(A)** Equatorial sub-community, **(B)** Gyre sub-community, **(C)** Frontal sub-community, **(D)** Deep Chl *a* Maximum sub-community. The yellow box indicates the Equatorial Zone centre. The cyan boxes delimit gyre centres. Coral and rose color indicate the core and pioneer areas, respectively: the darker the color, the higher abundance and species richness.

mass as it warms up. When the water-mass moves northward from Antilles, the seeds of frontal species might be mixed upward to upper water column and flourish again.

Differences of Tintinnina assemblages in NASG and SASG

Understanding the differences and similarities between the northern and southern hemispheres is necessary to monitor the changes that are occurring and are expected in the coming decades (Timmermann et al., 2015; Rodriguez et al., 2022). In the present study, Tintinnina diversity in both NASG and SASG was very high, encompassing 142 and 124 Tintinnina species, respectively. Both gyres shared 111 species which indicated a high similarity of the Tintinnina assemblage compositions in them.

Despite of the similarity of the Tintinnina compositions, 44 species were present in one gyre but not in the other. This non-symmetrical situation was also reported for Bacteria distribution by Sul et al. (2013), who observed fewer bacteria taxa in both hemispheres but more taxa than expected were only present in a single hemisphere. The Atlantic equatorial upwelling region (with a narrow vertical temperature range between 15°C to 25°C) has been identified as a strong ecological barrier for zooplankton dispersal, such as Copepoda (Goetze et al., 2017; Mcginty et al., 2021) and Mollusca Pteropoda (Burridge et al., 2015; Choo et al., 2021). Meanwhile, oceanic barriers are species-specific (Mcginty et al., 2021). As Tintinnina mobility is much weaker than that of mesozooplankton, it was not surprising that some Tintinnina species were separated by the EZ in the Atlantic Ocean. This may also be a universal phenomenon in warm waters of the open Pacific and Indian Oceans but need more investigations to be established.

The 111 shared species also showed different distribution patterns in NASG and SASG. Tintinnina distribution has been demonstrated to have notable seasonal differences (Camacho et al., 2015; Li et al., 2016; Rekik et al., 2020). This may be linked to the fact that some species have distinct temperature ranges in the two hemispheres.

The AMT transect crossed different part of the two subtropical gyres: through the middle of SASG but through the east side of NASG. This difference in transect relative position with the gyre centre might be the reason why some frontal species occupied narrower bands in the northern hemisphere than in the south. The weak upwelling at about 5°S might account for the relative difference in position between *Eutintinnus perminutus*, *Rhabdonella indica* and *E. medius* in the two hemispheres (Supplementary Figure 3). This upwelling might also cause the surface occurrence of *Proplectella claparedei* and *Acanthostomella obtusa* in the southern hemisphere (Supplementary Figure 5) as in Prydz Bay, Antarctic (Liang et al., 2018).

Latitudinal species richness gradient of Tintinnina

Integrating Tintinnina occurrence in the world at different times of year, Dolan et al. (2013) established that Tintinnina species richness displays a latitudinal gradient where the species number peaked at about 20°N or 30°S, with the northern hemisphere peak being higher than that in the southern hemisphere. We used the same protocol to collect seawater along the AMT transect to eliminate the influence of sampling bias. At each station, large water volumes were collected at different depths and the total number of Tintinnina species at each station was the object of detailed analysis. This was the first time that Tintinnina distribution was investigated over such a large latitudinal range at the same time of the year. The latitudinal variation in the Tintinnina species richness in our study coincided with that of Dolan et al. (2013), the tiny difference being that the peak values in both hemispheres were similar in our study. This may result from the preferential data collection in the northern hemisphere and coastal areas by Dolan et al. (2013). Their weaker sampling in the southern hemisphere may have missed a lot of species (Menegotto and Rangel, 2018).

Temperature was considered to be the main driver of plankton species richness (Abirami et al., 2021; Benedetti et al., 2021; Chaudhary et al., 2021; Raven and Beardall, 2021), whose peak values are mainly associated with a temperature of about 20°C (Chaudhary et al., 2021). In the present study, the Tintinnina species richness along the temperature gradient reached its peak value at about 20°C and was thus in agreement with previous reports.

In the literature there was a debate concerning the causes of the dip in species richness at the equator. Some ecologists have argued that sampling bias is the main factor responsible for the gap in species richness, being a consequence of reduced sampling efforts at low latitudes whose access is difficult and costly (Menegotto and Rangel, 2018). In contrast, some other zooplankton experts consider the dip a natural phenomenon (Chaudhary et al., 2016; Yasuhara et al., 2020; Chaudhary et al., 2021). The present study would suggest a natural phenomenon following a new mechanism in which the species richness peaks at the gyre centre expresses the superposition of the four sub-assemblages with different latitudinal trends of species number.

The inability of Tintinnina to tolerate high temperatures may induce their latitudinal poleward shift upon global warming (Yasuhara et al., 2020). Optimum growth temperature varies with Tintinnina species, inducing differences in their tolerance to higher temperatures (Li et al., 2021). It is therefore speculated that ongoing global warming will cause a more pronounced dip in Tintinnina species richness in the equatorial zone. Indeed, once the temperature goes above the temperature tolerance of a Tintinnina species, this species may disappear in the equatorial zone and move poleward (Thomas et al., 2012; Chaudhary et al., 2021). According to the distinct four distribution patterns we observed, equatorial species might remain in deeper water where temperatures are cooler while surface temperatures increase above tolerable limits. However, the gyre species and frontal species might leave the equatorial zone that is not the centre of their distribution. Some Tintinnina species with high abundance could be used as indicator species of sub-assemblages to study their distribution shift in response to global warming.

Extrapolation of AMT data

In this study, Stns. 16-19 (Figure 1) represented the northern gyre centre along the AMT 29 transect. Geographically, these stations are in the eastern part of the NASG (Steinberg et al., 2001; Putman and He, 2013). It seems reasonable to consider that the Tintinnina assemblages observed at Stns. 16-19 as being representative of the Tintinnina assemblages in the gyre centre. The Bermuda Atlantic Time-Series (BATS) in the western part of the gyre centre, where no Tintinnina data are available, might have Tintinnina assemblages similar to those of Stns. 16-19.

The highest temperature in the present study was 29.25°C. Areas with surface temperature higher than 28.5°C are called the Atlantic Warm Pool which is centred in the Caribbean Sea, west of the AMT 29 transect (Wang et al., 2008; Aiken et al., 2017). Therefore, we hypothesised that the Caribbean Sea might have Tintinnina assemblages similar to tropical assemblages.

There was similarity in the occurrence of *Dadayiella ganymedes* and *Eutintinnus tubulosus* in the northern edges of the North Pacific Subtropical Gyre and NASG. No Arctic and subarctic species were observed in our study because the northern end of the AMT transect was outside of the subarctic region. Assuming that the interaction of warm water and subarctic assemblages in the Atlantic Ocean would be similar to that in the north Pacific Ocean (Li et al., 2021), we would predict that the abundance of both *D. ganymedes* and *E. tubulosus* would sharply decrease, rapidly reaching detection limit northward in Atlantic Ocean. With their small size and short life span, Tintinnina might have a weak viability when they are entrained northward. Consequently, Tintinnina assemblages could not move northward in response to global warming as Copepoda assemblages did (Beaugrand et al., 2002). The sudden disappearance of *D. ganymedes* as well as *Epiplocylis undella*, *Rhabdonellopsis apophysata*, *Ascampbelliella armilla* in narrow bands (biological front as defined by Le Fèvre, 1986) could be used to monitor any northward Tintinnina shift induced by global warming.

Although there were Tintinnina assemblage studies in the tropical zones of the Pacific and Indian Oceans (e.g., Zhang et al., 2017; Li et al., 2018), these studies did not divide Tintinnina species into biogeographical types due to limited spatial coverage. The organisation of Tintinnina assemblages in the AMT transect (Atlantic) might also be extrapolated to the tropical zones and subtropical gyres in the Pacific and Indian Ocean.

Conclusion

We investigated Tintinnina distribution patterns in the surface waters along the large-scale AMT transect, crossing two subtropical gyres in the Atlantic Ocean. Tintinnina species were divided into four biogeographic distribution patterns (equatorial, gyre, frontal, and deep Chl *a* maximum), which constitutes four sub-assemblages, respectively. Tintinnina assemblages along the transect were organized by the superposition of these four sub-assemblages. The tropical submergence phenomenon (i.e., Tintinnina in surface waters in high latitudes are found deeper waters in low latitudes) was observed for some frontal Tintinnina species. Tintinnina species richness gradient showed a distinct bimodal latitudinal pattern: increasing from high to low latitudes, reaching a maximum at about 20°N and 30°S, then having a slight decrease towards the equator. The latitudinal bimodality mode of species richness is resulted from the superposition of the four sub-assemblages. In response to global warming, equatorial species might remain in the equatorial zone but in deeper and cooler water while the gyre species and frontal species might leave the equatorial zone. Tintinnina species with high abundance and narrow latitudinal range could be chosen as indicators to study the influence of global warming on their distribution shift. These findings on the organization of Tintinnina assemblages might also apply to other single cell protists in the pelagic oceans.

Data availability statement

The original contributions presented in the study are included in the article/Supplementary Materials. Further inquiries can be directed to the corresponding author.

Author contributions

HL: Tintinnina taxonomy and counting, data analysis, writing-original draft. GT: field sampling, writing-original draft. GD'O: conceptualization field sampling, writing-original draft. AR, GG, and TX: conceptualization. MD: conceptualization, writing-original draft. YD and YZ: writing-original draft, figure drawing. CW: data analysis. WZ: conceptualization, field sampling, Tintinnina taxonomy, writing-original draft. All authors contributed to the article and approved the submitted version.

Funding

The Atlantic Meridional Transect is funded by the UK Natural Environment Research Council through its National Capability Long-term Single Centre Science Programme, Climate-Linked Atlantic Sector Science (CLASS) (grant number NE/R015953/1). This study contributes to the international IMBeR project and is contribution number 382 of the AMT programme. This work was supported by the Strategic Priority Research Program of the Chinese Academy of Sciences (Grant No. XDB42000000), National Natural Science Foundation of China (Grant Numbers 41706192, 42076139 and 41806178); the International Cooperation Project-Dynamics and Function of Marine Microorganisms (IRP-DYF2M): insight from physics and remote sensing, CNRS-CAS. GD'O has received funding from the European Union's Horizon 2020 research and innovation programme under grant agreement No 862923. This output reflects only the author's view, and the European Union cannot

be held responsible for any use that may be made of the information contained therein.

Acknowledgments

We are grateful to the captain and crew of RRS "*Discovery*" for their support and assistance during sampling.

Conflict of interest

The authors declare that the research was conducted in the absence of any commercial or financial relationships that could be construed as a potential conflict of interest.

Publisher's note

Supplementary material

The Supplementary Material for this article can be found online at: https://www.frontiersin.org/articles/10.3389/fmars.2023.1082495/full#supplementary-material

References

Abirami, B., Radhakrishnan, M., Kumaran, S., and Wilson, A. (2021). Impacts of global warming on marine microbial communities. *Sci. Total Environ.* 791, 147905. doi: 10.1016/j.scitotenv.2021.147905

Acevedo-Trejos, E., Marañón, E., and Merico, A. (2018). Phytoplankton size diversity and ecosystem function relationships across oceanic regions. *P Roy Soc. B-Biol Sci.* 285, 20180621. doi: 10.1098/rspb.2018.0621

Aiken, J., Brewin, R. J. W., Dufois, F., Polimene, L., Hardman-Mountford, N. J., Jackson, T., et al. (2017). A synthesis of the environmental response of the north and south Atlantic Sub-tropical gyres during two decades of AMT. *Prog. Oceanogr* 158, 236–254. doi: 10.1016/j.pocean.2016.08.004

Aiken, J., Rees, N., Hooker, S., Holligan, P., Bale, A., Robins, D., et al. (2000). The Atlantic meridional transect: overview and synthesis of data. *Prog. Oceanogr* 45, 257–312. doi: 10.1016/S0079-6611(00)00005-7

Alder, V. A. (1999). "Tintinnoinea," in *South Atlantic zooplankton*. Ed. D. Boltovskoy (Leiden: Backhuys), 321–384.

Bakker, C., and Phaff, W. J. (1976). Tintinnida from coastal waters of the S.W.-Netherlands i. the genus *Tintinnopsis* stein. *Hydrobiologia* 50, 101–111. doi: 10.1007/BF00019812

Balch, W. M., Bowler, B. C., Drapeau, D. T., Lubelczyk, L. C., Lyczkowski, E., Mitchell, C., et al. (2019). Coccolithophore distributions of the north and south Atlantic ocean. *Deep-Sea Res. Pt I* 151, 103066. doi: 10.1016/j.dsr.2019.06.012

Beaugrand, G., Reid, P. C., Ibanez, F., Lindley, J. A., and Edwards, M. (2002). Reorganization of north Atlantic marine copepod biodiversity and climate. *Science* 296, 1692–1694. doi: 10.1126/science.1071329

Benedetti, F., Vogt, M., Elizondo, U. H., Righetti, D., Zimmermann, N. E., and Gruber, N. (2021). Major restructuring of marine plankton assemblages under global warming. *Nat. Commun.* 12, 5226. doi: 10.1038/s41467-021-25385-x

Boltovskoy, D. (1998). "Pelagic biogeography: background, gaps and trends," in *Pelagic biogeography ICoPB II: Proceedings of the 2nd international conference. final report of SCOR/IOC working group 93. IOC workshop report 142*, vol. 53-64 . Eds. A. C. Pierrot-Bults and S. van der Spoel (Paris: UNESCO).

Brinton, E. (1962). The distribution of *Pacific euphausiids. Bull. Scripps Institution Oceanography* 8, 51–270.

Burridge, A. K., Goetze, E., Raes, N., Huisman, J., and Peijnenburg, K. T. C. A. (2015). Global biogeography and evolution of *Cuvierina* pteropods. *BMC Evol. Biol.* 15, 39. doi: 10.1186/s12862-015-0310-8

Burridge, A. K., Goetze, E., Wall-Palmer, D., Double, S. L. L., Huisman, J., and Peijnenburg, K. T. C. A. (2017). Diversity and abundance of pteropods and heteropods along a latitudinal gradient across the Atlantic ocean. *Prog. Oceanogr* 158, 213–223. doi: 10.1016/j.pocean.2016.10.001

Camacho, S., Connor, S., Asioli, A., Boski, T., and Scott, D. (2015). Testate amoebae and tintinnids as spatial and seasonal indicators in the intertidal margins of guadiana estuary (southeastern Portugal). *Ecol. Indic* 58, 426–444. doi: 10.1016/j.ecolind.2015.05.041

Chaudhary, C., Richardson, A. J., Schoeman, D. S., and Costello, M. J. (2021). Global warming is causing a more pronounced dip in marine species richness around the equator. *P Natl. Acad. Sci. U.S.A.* 118, e2015094118. doi: 10.1073/pnas.2015094118

Chaudhary, C., Saeedi, H., and Castello, M. J. (2016). Bimodality of latitudinal gradients in marine species richness. *Trends Ecol. Evol.* 31, 670–676. doi: 10.1016/j.tree.2016.06.001

Choo, L., Bal, T. M. P., Goetze, E., and Peijnenburg, K. T. C. A. (2021). Oceanic dispersal barriers in a holoplanktonic gastropod. *J. Evol. Biol.* 34, 224–240. doi: 10.1111/jeb.13735

Dolan, J. R., Montagnes, D. J. S., Agatha, S., Coats, D. W., and Stoecker, D. K. (2013). *The biology and ecology of tintinnid ciliates: Models for marine plankton* (Chichester: JohnWiley & Sons).

Dolan, J. R., Moon, J. K., and Yang, E. J. (2021). Notes on the occurrence of tintinnid ciliates, and the nasselarian radiolarian *Amphimelissa setosa* of the marine microzooplankton, in the chukchi Sea (Arctic ocean) sampled each august from 2011 to 2020. *Acta Protozool* 60, 1–11. doi: 10.4467/16890027AP.21.001.14061

Dolan, J. R., Ritchie, M. E., and Ras, J. (2007). The "neutral" community structure of planktonic herbivores, tintinnid ciliates of the microzooplankton, across the SE tropical pacific ocean. *Biogeosciences* 4, 297–310. doi: 10.5194/bg-4-297-2007

Dolan, J. R., Yang, E. J., Kang, S. H., and Rhee, T. S. (2016). Declines in both redundant and trace species characterize the latitudinal diversity gradient in tintinnid ciliates. *Isme J.* 10, 2174–2183. doi: 10.1038/ismej.2016.19

Dutkiewicz, S., Cermeno, P., Jahn, O., Follows, M. J., Hickman, A. E., Taniguchi, D. A. A., et al. (2020). Dimensions of marine phytoplankton diversity. *Biogeosciences* 17, 609–634. doi: 10.5194/bg-17-609-2020

Feng, M., Zhang, W., Wang, W., Zhang, G., Xiao, T., and Xu, H. (2015). Can tintinnids be used for discriminating water quality status in marine ecosystems? *Mar. pollut. Bull.* 101, 549–555. doi: 10.1016/j.marpolbul.2015.10.059

Gaston, K. J. (2000). Global patterns in biodiversity. *Nature* 405, 220–227. doi: 10.1038/35012228

Gimmler, A., Korn, R., Vargas, C. D., Audic, S., and Stoeck, T. (2016). TheTara oceans voyage reveals global diversity and distribution patterns of marine planktonic ciliates. *Sci. Rep.* 6, 33555. doi: 10.1038/srep33555

Goetze, E., Hudepohl, P. T., Chang, C., Lauren, W., Iacchei, M., and Peijnenburg, K. T. C. A. (2017). Ecological dispersal barrier across the equatorial Atlantic in a migratory planktonic copepod. *Prog. Oceanogr* 158, 203–212. doi: 10.1016/j.pocean.2016.07.001

Gómez, F. (2007). Trends on the distribution of ciliates in the open pacific ocean. *Acta Oecol* 32, 188–202. doi: 10.1016/j.actao.2007.04.002

Hada, Y. (1937). The fauna of akkeshi bay IV. the pelagic ciliata. *J. Faculty Science Hokkaido Imperial University Ser. VI Zoology* 4, 143–216.

Hada, Y. (1938). Studies on the tintinnoinea from the western tropical pacific. *J. Faculty Science Hokkaido Imperial University Ser. VI Zoology* 6, 87–190.

Hada, Y. (1970). The protozoan plankton of the Antarctic and subantarctic seas. *JARE Sci. Rep Ser. E* 31, 1–51.

Hillebrand, H. (2004). Strength, slope and variability of marine latitudinal gradients. *Mar. Ecol. Prog. Ser.* 273, 251–267. doi: 10.3354/meps273251

Hooker, S. B., Rees, N. W., and Aiken, J. (2000). An objective methodology for identifying oceanic provinces. *Prog. Oceanogr* 45, 313–338. doi: 10.1016/S0079-6611(00)00006-9

Isla, J. A., Llope, M., and Anadon, R. (2004). Size-fractionated mesozooplankton biomass, metabolism and grazing along a 50 degrees n-30 degrees s transect of the Atlantic ocean. *J. Plankton Res.* 26, 1301–1313. doi: 10.1093/plankt/fbh121

Kofoid, C. A., and Campbell, A. S. (1929). A conspectus of the marine fresh-water ciliate belonging to the suborder tintinnoinea, with descriptions of new species principally from the agassiz expedition to the eastern tropical pacific 1904-1905. *Univ Calif publ zool* 34, 1–403.

Kofoid, C. A., and Campbell, A. S. (1939). The ciliata: the tintinnoinea. *Bull. Mus Comp. Zool Harvard Coll.* 84, 1–473.

Le Fèvre, J. (1986). Aspects of the biology of frontal systems. *Adv. Mar. Biol.* 23, 163–299. doi: 10.1016/S0065-2881(08)60109-1

Li, H., Wang, C., Liang, C., Zhao, Y., Zhang, W., Grégori, G., et al. (2019). Diversity and distribution of tintinnid ciliates along salinity gradient in the pearl river estuary in southern China. *Estuar. Coast. Shelf S* 226, 106268. doi: 10.1016/j.ecss.2019.106268

Li, H., Xuan, J., Wang, C., Chen, Z., Grégori, G., Zhao, Y., et al. (2021). Summertime tintinnid community in the surface waters across the north pacific transition zone. *Front. Microbiol.* 12, 697801. doi: 10.3389/fmicb.2021.697801

Li, H., Zhang, W., Zhao, Y., Zhao, L., Dong, Y., Wang, C., et al. (2018). Tintinnid diversity in the tropical West pacific ocean. *Acta Oceanol Sin.* 37, 218–228. doi: 10.1007/s13131-018-1148-x

Li, H., Zhao, Y., Chen, X., Zhang, W., Xu, J., Li, J., et al. (2016). Interaction between neritic and warm water tintinnids in surface waters of East China Sea. *Deep-Sea Res. Pt II* 124, 84–92. doi: 10.1016/j.dsr2.2015.06.008

Liang, C., Li, H., Dong, Y., Zhao, Y., Tao, Z., and Li, C. (2018). Planktonic ciliates in different water masses in open waters near prydz bay (East Antarctic) during austral summer, with an emphasis on tintinnid assemblages. *Polar Biol.* 41, 2355–2371. doi: 10.1007/s00300-018-2375-5

Liang, C., Li, H., Zhang, W., Tao, Z., and Zhao, Y. (2020). Changes in tintinnid assemblages from subantarctic zone to Antarctic zone along transect in amundsen Sea (West Antarctica) in early austral autumn. *J. Ocean U China* 19, 339–350. doi: 10.1007/s11802-020-4129-6

Longhurst, A. R. (2007). *Ecological geography of the Sea. 2nd Edn* (San Diego, CA: Academic Press).

López, E., and Anadón., R. (2008). Copepod communities along an Atlantic meridional transect: Abundance, size structure and grazing rates. *Deep-Sea Res. Pt I* 55, 1375–1391. doi: 10.1016/j.dsr.2008.05.012

Lynn, D. H. (2008). *The ciliated Protozoa: Characterization, classification, and guide to the literature* (Dordrecht: Springer).

Mcginty, N., Barton, A. D., Finkel, Z. V., Johns, D. G., and Irwin, A. J. (2021). Niche conservation in copepods between ocean basins. *Ecography* 44, 1653–1664. doi: 10.1111/ecog.05690

McGowan, J. A. (1971). "Oceanic biogeography of the pacific," in *The micropaleontology of oceans: Proceedings of the symposium held in Cambridge, 10th-17th September 1967 under the title "Micropalaeontology of marine bottom sediments.* Eds. B. M. Funnel and W. R. Riedel (Cambridge, MA: Cambridge University Press), 3–74.

Menegotto, A., and Rangel, T. F. (2018). Mapping knowledge gaps in marine diversity reveals a latitudinal gradient of missing species richness. *Nat. Commun.* 9, 4713. doi: 10.1038/s41467-018-07217-7

Olson, D. B. (2001). Biophysical dynamics of western transition zones: a preliminary synthesis. *Fish Oceanogr* 10, 133–150. doi: 10.1046/j.1365-2419.2001.00161.x

Paranjape, M., and Gold, K. (1982). Cultivation of marine pelagic protozoa. *Ann. Inst Oceanogr Paris* 58, 143–150.

Pierce, R. W., and Turner, J. T. (1992). Ecology of planktonic ciliates in marine food webs. *Rev. Aquat. Sci.* 6, 139–181

Pierce, R. W., and Turner, J. T. (1993). Global biogeography of marine tintinnids. *Mar. Ecol. Prog. Ser.* 94, 11–26. doi: 10.3354/meps094011

Putman, N. F., and He, R. (2013). Tracking the long-distance dispersal of marine organisms: sensitivity to ocean model resolution. *J. R Soc. Interface* 10, 20120979. doi: 10.1098/rsif.2012.0979

Rakshit, D., Murugan, K., Biswas, J. K., Satpathy, K. K., Ganesh, P. S., and Sarkar, S. K. (2017a). Environmental impact on diversity and distribution of tintinnid (Ciliata: Protozoa) along hooghly estuary, India: A multivariate approach. *Reg. Stud. Mar. Sci.* 12, 1–10. doi: 10.1016/j.rsma.2017.02.007

Rakshit, D., Sahu, G., Mohanty, A. K., Satpathy, K. K., Jonathan, M. P., Murugan, K., et al. (2017b). Bioindicator role of tintinnid (Protozoa: Ciliophora) for water quality monitoring in kalpakkam, Tamil nadu, south east coast of India. *Mar. Pollut. Bull.* 114, 134–143. doi: 10.1016/j.marpolbul.2016.08.058

Raven, J. A., and Beardall, J. (2021). Influence of global environmental change on plankton. *J. Plankton Res.* 43, 779–800. doi: 10.1093/plankt/fbab075

Rees, A. P., Nightingale, P. D., Poulton, A. J., Smyth, T. J., Tarran, G. A., and Tilstone, G. H. (2017). The Atlantic meridional transect programme, (1995-2016). *Prog. Oceanogr* 158, 3–18. doi: 10.1016/j.pocean.2017.05.004

Rekik, A., Ayadi, H., and Elloumi, J. (2020). Spatial and seasonal variability of the planktonic ciliates assemblages along the Eastern Mediterranean coast (Sfax coast, Tunisia). *Reg. Stud. Mar. Sci.* 40, 101529. doi: 10.1016/j.rsma.2020.101529

Robinson, C., Poulton, A. J., Holligan, P. M., Baker, A. R., Forster, G., Gist, N., et al. (2006). The atlantic meridional transect (AMT) programme: A contextual view 1995-2005. *Deep-Sea Res. Pt II* 53, 1485–1515. doi: 10.1016/j.dsr2.2006.05.015

Rodriguez, I. D., Marina, T. I., Schloss, I. R., and Saravia, L. A. (2022). Marine food webs are more complex but less stable in sub-Antarctic (Beagle channel, Argentina) than in Antarctic (Potter cove, Antarctic peninsula) regions. *Mar. Environ. Res.* 174, 105561. doi: 10.1016/j.marenvres.2022.105561

Rychert, K., Nawacka, B., Majchrowski, R., and Zapadka, T. (2014). Latitudinal pattern of abundance and composition of ciliate communities in the surface waters of the Atlantic ocean. *Oceanol Hydrobiol St* 43, 436–441. doi: 10.2478/s13545-014-0161-8

Steinberg, D. K., Carlson, C. A., Bates, N. R., Johnson, R. J., Michaels, A. F., and Knap, A. H. (2001). Overview of the US JGOFS Bermuda Atlantic time-series study (BATS): a decade-scale look at ocean biology and biogeochemistry. *Deep-Sea Res. Pt II* 48, 1405–1447. doi: 10.1016/S0967-0645(00)00148-X

Sul, W. J., Oliver, T. A., Ducklow, H. W., Amaral-Zettler, L. A., and Sogin, M. L. (2013). Marine bacteria exhibit a bipolar distribution. *P Natl. Acad. Sci. U.S.A.* 110, 2342–2347. doi: 10.1073/pnas.1212424110

Sunagawa, S., Acinas, S. G., Bork, P., Bowler, C., Tara Oceans, C., Eveillard, D., et al. (2020). Tara Oceans: towards global ocean ecosystems biology. *Nat. Rev. Microbiol.* 18, 428–445. doi: 10.1038/s41579-020-0364-5

Thomas, M. K., Kremer, C. T., Klausmeier, C. A., and Litchman, E. (2012). A global pattern of thermal adaptation in marine phytoplankton. *Science* 338, 1085–1088. doi: 10.1126/science.1224836

Timmermann, A., Damgaard, C., Strandberg, M. T., and Svenning, J. C. (2015). Pervasive early 21st-century vegetation changes across Danish semi-natural ecosystems: more losers than winners and a shift towards competitive, tall-growing species. *J. Appl. Ecol.* 52, 21–30. doi: 10.1111/1365-2664.12374

Trubovitz, S., Lazarus, D., Renaudie, J. , and Noble, P. J. (2020). Marine plankton show threshold extinction response to neogene climate change. *Nat. Commun.* 11, 5069. doi: 10.1038/s41467-020-18879-7

Vedenin, A., Musaeva, E., Vereshchaka, A., and Waring, B. G. (2022). Three-dimensional distribution of mesoplankton assemblages in the central Atlantic. *Global Ecol. Biogeogr* 31, 1345–1365. doi: 10.1111/geb.13509

Venrick, E. L. (1971). Recurrent groups of diatom species in the north pacific. *Ecology* 52, 614–625. doi: 10.2307/1934149

Venrick, E. L. (1988). The vertical distributions of chlorophyll and phytoplankton species in the north pacific central environment. *J. Plankton Res.* 10, 987–998. doi: 10.1093/plankt/10.5.987

Wang, C. Z., Lee, S. K., and Enfield, D. B. (2008). Climate response to anomalously large and small Atlantic warm pools during the summer. *J. Climate* 21, 2437–2450. doi: 10.1175/2007JCLI2029.1

Wang, C., Li, H., Dong, Y., Zhao, L., Gregori, G., Zhao, Y., et al. (2021). Planktonic ciliate trait structure variation over yap, Mariana, and Caroline seamounts in the tropical western pacific ocean. *J. Oceanol Limnol* 39, 1705–1717. doi: 10.1007/s00343-021-0476-4

Wang, C., Li, H., Xu, Z., Zheng, S., Hao, Q., Dong, Y., et al. (2020). Difference of planktonic ciliate communities of the tropical West pacific, the Bering Sea and the Arctic ocean. *Acta Oceanol Sin.* 39, 9–17. doi: 10.1007/s13131-020-1541-0

Wang, C., Li, H., Zhao, L., Zhao, Y., Dong, Y., Zhang, W., et al. (2019). Vertical distribution of planktonic ciliates in oceanic and slope area in the tropical west pacific ocean. *Deep-Sea Res. Pt II* 167, 70–78. doi: 10.1016/j.dsr2.2018.08.002

Woods, J. (1999). Understanding the ecology of plankton. *Eur. Rev.* 7, 371–384. doi: 10.1017/S1062798700004154

Yasuhara, M., Wei, C. L., Kucera, M., Costello, M. J., Tittensor, D. P., Kiessling, W., et al. (2020). Past and future decline of tropical pelagic biodiversity. *P Natl. Acad. Sci. U.S.A.* 117, 12891–12896. doi: 10.1073/pnas.1916923117

Yoo, K. I., Kim, Y. O., and Kim, D. Y. (1988). Taxonomic studies on tintinnids (Protozoa: Ciliata) in Korean coastal waters. 1. chinhae bay. *Korean J. Systematic Zoology* 4, 67–90.

Zhang, W., Feng, M., Zhang, C., and Xiao, T. (2012). *An illustrated guide to contemporary tintinnids in the world* (Beijing: Science Press).

Zhang, C., Sun, J., Wang, D., Song, S., Zhang, X., and Munir, S. (2017). Tintinnid community structure in the eastern equatorial Indian ocean during the spring inter-monsoon period. *Aquat Biol.* 26, 87–100. doi: 10.3354/ab00677

frontiers | Frontiers in Marine Science

TYPE Original Research
PUBLISHED 07 March 2023
DOI 10.3389/fmars.2023.1051510

EDITED BY
Timothy James Smyth,
Plymouth Marine Laboratory,
United Kingdom

REVIEWED BY
Brandon Kieft,
University of British Columbia, Canada
Clarissa Karthäuser,
Woods Hole Oceanographic Institution,
United States
Anthony Bertagnolli,
Montana State University, United States

*CORRESPONDENCE
Greta Reintjes
✉ greintje@mpi-bremen.de

SPECIALTY SECTION
This article was submitted to
Ocean Observation,
a section of the journal
Frontiers in Marine Science

RECEIVED 22 September 2022
ACCEPTED 17 February 2023
PUBLISHED 07 March 2023

CITATION
Reintjes G, Heins A, Wang C and Amann R
(2023) Abundance and composition of
particles and their attached microbiomes
along an Atlantic Meridional Transect.
Front. Mar. Sci. 10:1051510.
doi: 10.3389/fmars.2023.1051510

Abundance and composition of particles and their attached microbiomes along an Atlantic Meridional Transect

Greta Reintjes[1]*, Anneke Heins[1], Cheng Wang[1,2]
and Rudolf Amann[1]

[1]Department of Molecular Ecology, Max Planck Institute for Marine Microbiology, Bremen, Germany,
[2]Sun Yat-sen University, Guangzhou, Guangdong, China

Particulate organic matter plays a significant role in the marine carbon cycle. Its sinking exports organic carbon from the surface to deep oceans. Using fractionated filtration, we analysed particles of 3 – 10 µm and >10 µm and their microbiomes in thirty-five stations along a latitudinal transect of the Atlantic Ocean and provide new insights into the composition, community dynamics, and catabolic potential of particle-attached bacteria. Samples were taken during an Atlantic Meridional Transect (AMT22), which traversed six distinctive ocean provinces. Using 16S rRNA amplicon sequencing and fluorescence *in situ* hybridisation, we could show a strong variation between particle-attached and free-living bacterial communities at each station and across the biogeographical provinces – a dynamic likely driven by chlorophyll *a* concentrations, temperature, and the oxygen content of the respective biogeographical provinces. Whereas the <3 µm fraction was primarily composed of SAR11, SAR86, *Prochlorococcus* and *Bacteroidetes* of the NS9 and NS5 clades, particle-attached communities were dominated by other *Bacteroidetes* (*Polaribacter* spp.), diverse *Gammaproteobacteria* including members of the genera *Alteromonas* and *Vibrio*, *Alphaproteobacteria*, *Planctomycetes*, OM27 and *Verrucomicrobia*. In three provinces, we quantified particle abundance and analysed their glycan composition using four lectins targeting fucose, galactose, N-acetylgalactosamine and mannose. Particles were mainly composed of fucose glycans with only a minor abundance of the other glycans, and particle abundance was directly correlated with the chlorophyll *a* concentrations. Functional analysis of 54 metagenome-assembled genomes retrieved from bacterial communities attached to small particles showed that particle-attached *Bacteroidetes*, *Planctomycetes* and *Verrucomicrobia* displayed key roles in the degradation of sulfated fucose-containing polysaccharides. We also identified gene clusters potentially encoding the utilisation of mannan and laminarin, suggesting an adaptation to the glycan composition of the particles, potentially resulting in niche diversification. Together, our results provide insights into particle-attached bacteria and their ecological strategies in the Atlantic.

KEYWORDS

MAGs: metagenome assembled genomes (MAGs), particle-attached and free-living microbes, particle composition, fucose-containing polysaccharide, CAZy (carbohydrate-active enzymes), bacterial cell abundance.

Introduction

In the vast nutrient-limited expanses of the world's oceans, there exist temporary nutrient-rich "hot spots", namely marine particles. Marine particles are the primary vehicles of organic carbon flux from the surface to the deep sea (Azam and Malfatti, 2007). As a point source of organic matter in an otherwise largely oligotrophic environment, they are rapidly colonised by specialised bacteria from the surrounding water column (Datta et al., 2016). Particle-attached bacteria show high hydrolytic activity of extracellular enzymes - a prerequisite to the extracellular degradation of particles - and are therefore important for the reduction of particle half-life, significantly impacting global nutrient and carbon cycling (Huston and Deming, 2002; Simon et al., 2002; Grossart et al., 2007; Ziervogel and Arnosti, 2008; Ziervogel et al., 2010; Lyons and Dobbs, 2012).

However, whether and how fast a particle is broken down depends not only on the associated bacteria but also on the particle's composition. Particles are composed predominantly of organic material produced by photosynthetic organisms, such as phytoplankton. Hence, they are more abundant during and after phytoplankton blooms in upwelling areas and close to the coast (Passow, 2002; Behrenfeld et al., 2005). Soluble glycans like laminarin and mannan are more readily degradable compared to particles rich in fucoidan. Whereas the former are degradable within days to weeks, the latter, the highly complex and sulfated polysaccharide fucoidan, can take months to be fully broken down (Sichert et al., 2020; Vidal-Melgosa et al., 2021).

Due to the scarcity of particles, attached bacteria are low in abundance and often make up only 1% of the total community (Alldredge et al., 1986; Heins et al., 2021). Nevertheless, attached bacteria show a high respiration rate (Grossart et al., 2007), have large cells and large genomes (Smith et al., 2013), and show extensive gene repertoires for polysaccharide degradation (Smith et al., 2013; Rieck et al., 2015; Kappelmann et al., 2019; Schultz et al., 2020). Particle-attached bacteria can function both as particle degraders and as their builders, thereby supporting both carbon sequestration and carbon remineralisation (Smith et al., 1992; Heissenberger and Herndl, 1994; Azam and Malfatti, 2007).

Alphaproteobacteria, especially of the family *Rhodobacteraceae*, *Bacteroidetes, Gammproteobacteria*, and *Planctomycetes* are typically the most dominant bacteria attached to particles (Salazar et al., 2015). In-depth analyses suggest that they fill different niches within the particle microenvironment provided by the substrate's complexity. *Alphaproteobacteria* are more efficient in the incorporation of monomers and amino acids, whereas *Bacteroidetes*, especially *Flavobacteriia*, can utilise a selfish uptake mechanism and degrade high molecular weight compounds without losing energy to their surroundings and to scavenging bacteria (Cottrell and Kirchman, 2000; Reintjes et al., 2019). Genomes of particle-attached *Bacteroidetes* showed genes potentially involved in the degradation of complex organic matter (Kappelmann et al., 2019). In contrast, in metagenome-assembled genomes of free-living *Bacteroidetes* these genes were rare (Krüger et al., 2019), indicating different adaption between members of the particle-attached and free-living fraction.

Gammaproteobacteria possess homologs to the selfish uptake mechanism. Like *Flavobacteriia* they can upregulate TonB-dependent transporters, when the nutrient concentration rises, for example during phytoplankton blooms (Reintjes et al., 2020b; Francis et al., 2021).

Planctomycetes are predominantly present in the larger particle fractions (DeLong et al., 1993; Fuchsman et al., 2012) and especially the classes *Rhodopirellula*, *Blastopirellula*, *Pirellula*, and *Planctomyces* were shown to be capable of breaking down complex organic matter (Wegner et al., 2013). They are part of the *Planctomycetes-Verrucomicrobia-Chlamydia* (PVC) superphylum, which contains a large number of bacteria, capable of degrading complex sugars like fucoidan (Glockner et al., 2003; Van Vliet et al., 2019; Orellana et al., 2022). Since it is hypothesised that these complex sulfated sugars are mostly remineralised through these bacteria, *Planctomycetes* and other members of the PVC serve an important ecological function (Glockner et al., 2003; Wegner et al., 2013; Spring et al., 2018; Orellana et al., 2022).

In this study, we pursued a genomic, glycobiological, and ecological investigation of marine particles and their attached microbial communities in a north-south transect of the Atlantic Ocean (AMT22). The study included samples from six Longhurst provinces (Longhurst, 2010), the North Atlantic Drift (NADR), North Atlantic Subtropical (NAST), North Atlantic Tropical Gyre (NATR), Western Tropical Atlantic (WTRA), South Atlantic Gyre (SATL), and South Subtropical Convergence (SSTC) (Figure 1). In these provinces, we investigated particle-attached microbial communities using a combination of 16S tag sequencing and fluorescence *in situ* hybridisation. Furthermore, in three provinces, we assessed the prevailing glycans in particles using fluorescent-lectin-binding-analysis, (Bennke et al., 2013), and investigated the potential of attached bacteria to degrade these glycans using metagenomic analysis. We hypothesised that glyco-conjugate distributions in marine aggregates will shift across the different provinces of the Atlantic Ocean and directly affect the composition of the particle-attached bacterial community. Our study aims to advance the knowledge of the ecological functioning of the ocean carbon cycle as mediated by particle-attached bacteria.

Methods

Sample collection and physicochemical measurement of sites

Samples were taken along the 22nd Atlantic Meridional Transect (AMT22) cruise on the Royal Research Ship James Cook (October-November 2012) from Southampton, United Kingdom, to Punta Arenas, Chile. Seawater was collected from 35 stations at solar noon with 20 L Niskin bottles mounted on the sampling rosette of a conductivity-temperature-depth (CTD) profiler (Sea-Bird Electronics, Washington, USA) from a depth of 20 m (Figure 1).

For microbial cell counts and CARD-FISH, 1 L of surface seawater was sampled from 35 stations for the free-living fraction

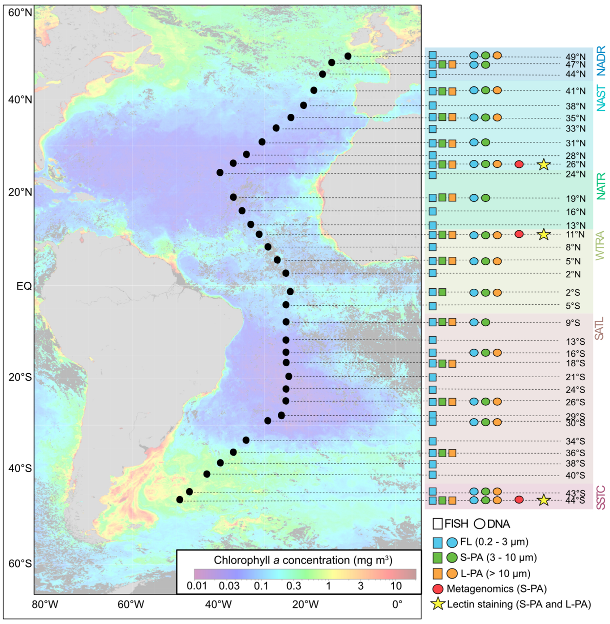

FIGURE 1
Sampling map and analysis list from AMT22. Map shows satellite-based chlorophyll a concentration during the time of sampling (Oct-Nov 2012) obtained from Aqua MODIS (Ocean Biology Processing Group, 2014). Stations are labeled according to latitude 49°N to 44°S and indicated as black dots across the map. Individual samples are shown in blue (FL), green (S-PA fraction), and orange (L-PA fraction) and indicate with FISH (boxes) and DNA (circles) analyses. Red dots indicate metagenomics samples from the S-PA fraction, stars indicate lectin staining from the S-PA and L-PA fraction. NADR North Atlantic Drift, NAST North Atlantic Subtropical, NATR North Atlantic Tropical Gyre, WTRA Western Tropical Atlantic, SATL South Atlantic Gyre, and SSTC South Subtropical Convergence.

(FL, 0.2 – 3 µm), 14 stations for the small particle fraction (S-PA, 3 – 10 µm) and 13 stations for the large particle fraction (L-PA, > 10 µm). All samples were fixated using formaldehyde to a final concentration of 1% for 1 h at room temperature and subsequently filtered in triplicate through a 47 mm diameter polycarbonate filter with a pore size of 10 µm, 3 µm, and 0.2 µm, respectively, applying a gentle vacuum of < 200 mbar. These filters were left to air dry and stored at -20°C until further analysis.

For microbial diversity analysis, between 15 L to 45 L of seawater were collected from 16 stations and sequentially filtered onto 142 mm diameter polycarbonate filters with pore sizes of 10 µm, 3 µm and 0.2 µm (Supplementary Table 1D). Different volumes of seawater were sampled to prevent filter clogging, the volume was determined from previous cell counts (Zubkov et al., 2000; Schattenhofer et al., 2009). All filters were stored at -80°C until further analysis.

The AMT22 passed through several oceanic provinces (Longhurst, 2010). The biogeographical provinces were identified using their physical, chemical and biological characteristics (Supplementary Table 1). Chlorophyll-*a* (Chl *a*) fluorescence was measured on board by a CTG FAST track Fast Repetition Rate fluorometer (Chelsea Technologies Group, UK) and calibrated against extracted Chl *a* measurements of seawater samples collected from 9 depths at each station. The main nutrient analyser was a 5-channel Bran and Luebbe AAIII segmented flow autoanalyser. The analytical chemical methodologies used were according to Brewer and Riley (1965) for nitrate, Grasshoff (1976) for nitrite, Kirkwood (1996) for phosphate and silicate. Salinity (PSU) was measured using a Guideline Autosal 8400B salinometer (OSIL, UK) and calibrated against bench salinometer measurements from 4 samples collected from each cast. Dissolved oxygen (ml L^{-1}) was measured using the Sea-Bird 43 dissolved oxygen sensor (Sea Bird Scientific) and calibrated against Winkler titration measurements from 9 samples collected at the pre-dawn CTD. Temperature (°C) was measured using a Sea-Bird 3 premium temperature sensor (Sea Bird Scientific) (all metadata is available *via* the BODC website (https://www.bodc.ac.uk/data/documents/cruise/11427/). The physico-chemical data were analysed using the ODV4 software (www.odv.awi.de).

Total cell counts, FISH and microscopy

The total cellular abundance and abundance of specific bacterial phylogenetic groups (Supplementary Table 2) was determined using the CARD-FISH procedure according to (Pernthaler et al., 2004). Hybridisations were done with horseradish peroxidase-labelled oligonucleotides probes (Biomers, Ulm, Germany) at varying formamide concentrations depending on the probe used (Supplementary Table 2). Working solutions of probes and competitors (both at 50 ng μl^{-1}) were mixed with hybridisation buffer in a 1:1:300 proportion and hybridisation was carried out 2.5 h at 46°C. The probe-delivered horseradish peroxidase was detected with tyramides that were custom labelled with fluorescein (Molecular Probes, Eugene, OR, USA). After the procedure the samples were counterstained with 4',6-diamidino-2-phenylindole (1 µg ml^{-1}).

Cell quantification was done using an automated image acquisition and cell enumeration system (Bennke et al., 2016). For our evaluation FISH positive signals for each probe were determined by an overlapping (30% minimum overlap) signal of both DAPI (360 nm) and FISH (488 nm), with a minimum area of 17 (DAPI) or 30 (FISH) pixels (0.17 - 0.3 μm^2) and minimal signal background ratio of 1 (DAPI) or 2.5 (FISH). Specific cellular abundance of aggregate associated samples were manually enumerated on a Zeiss Axioskop 2 motplus fluorescence microscope.

Within this study we designed new FISH probes targeting the *Sphingopyxis*, *Erythrobacter*, *Opitutae* and OM27 clade (Supplementary Table 2), using the probe design tool of the ARB software (Ludwig et al., 2004). Probe specificity was checked using the actual data set and SILVA release_119. For the newly designed subgroup-specific probes, optimal conditions in FISH were established by evaluating the fluorescence intensities of the target cells after hybridisation with Cy3-labeled probes at increasing concentrations of the formamide in the hybridisation buffer (Pernthaler et al., 2001).

Lectin-staining and super-resolution structured illumination microscopy

To quantify particle abundance and identify the particles carbohydrate composition we performed lectin staining (Bennke et al., 2013). We applied the lectins Aleuria Aurantia Lectin (AAL), Concanavalin A (ConA), Wheat Germ Agglutinin (WGA) and Soybean Agglutinin (SBA). We tested varying lectin concentrations ranging from 1 to 100 µg µl^{-1}. Optimised dilutions were determined microscopically and defined as strong fluorescent specific binding signals in aggregates without nonspecific background staining. The sugar specificity and working concentration of all lectins used in this study are given in Supplementary Table 3.

For glyco-conjugate staining of the aggregates, filters with formaldehyde-fixed cells were washed with filter-sterilised tap water and subsequently incubated with lectins for 20 min at room temperature. Afterwards, stained samples were carefully washed three times with filter-sterilised tap water to remove unbound lectins. For combined visualisations with particle-attached bacterial cells, CARD-FISH was performed prior to lectin staining (see protocol above).

Particles were visualised using a Zeiss ELYRA PS.1 (Carl Zeiss) with 561, 488 and 405 nm lasers and BP 573-613, BP 502-538 and BP 420-480+LP 750 optical filters (Carl Zeiss, Jena, Germany). Z-stack images were taken with a Plan-Apochromat 63 ×/1.4 Oil objective using an iXON897 EM-CCD camera. The images were reconstructed using ZEN software (Black edition, 2011, Carl Zeiss, Germany). Further analysis was performed on reconstructed super-resolution images in ZEN software blue edition (2012, Carl Zeiss, Germany).

DNA extraction and 16S rRNA sequencing

Microbial DNA was extracted using the MoBio Ultra Clean Soil DNA Extraction Kit (MoBio Laboratories) as recommended by the manufacturer with the following alterations. A 150 mm x 250 mm piece of polycarbonate filter was directly added to the Bead Solution Tubes. Sequencing was carried out on a 454 Titanium FLX (ROCHE, CT, USA) and Ion Torrent PGM (Thermo Fisher). Two sequencing platforms were used to reduce possible biases between the two systems. The 454 Titanium FLX is a pyrosequencing method. In contrast, the Ion Torrent PGM measures pH changes from the release of a proton during the incorporation of a dNTP into a DNA polymer. Where possible, samples were sequenced on both platforms to increase the accuracy (reduce sequencing bias) and yield per sample.

PCR was carried out for both platforms, using the primers S-D-Bact-0341-b-S-17 (5′-CCTACGGGNGGCWGCAG-3′) and S-D-Bact-0785-a-A-21 (5′-GACTACHVGGGTATCTAATCC -3’) targeting the V3 - V4 variable region of the 16S rRNA, evaluated by (Klindworth et al., 2013). For 454 Titanium FLX sequencing, PCR was carried out in a total volume of 50 µl. The PCR products were visualised by gel electrophoresis (1% LE agarose, Biozyme), the amplicon bands were cut out with a sterile scalpel and purified using the QiagenMinElute kit (Qiagen). If bimodal amplicon bands were detected, both bands were cut out of the gel and combined (range 430 – 490). The purified PCR products were pooled into libraries with a minimum DNA concentration of 1 µg DNA as measured using a Qubit assay (Invitrogen, Darmstadt, Germany), and sequenced on a ROCHE 454 titanium FLX (ROCHE) at the Max Planck Institute for Plant Breeding Research in Cologne.

PCR for Ion Torrent PGM was carried out using the Platinum PCR SuperMix High Fidelity polymerase kit (Thermo Fisher). PCR amplicons were size selected on 2% E-Gel size select gels using the E-Gel iBase Power System and E-Gel Safe Imager Real Time Transilluminator (Thermo Fisher), and cleaned up and concentrated over silica column using the Qiagen QIAquick PCR purification kit (Qiagen). Amplicon concentrations and quality were quantified using a Fragment Analyser (AATI) and the DNF - 472 standard sensitivity NGS fragment analysis kit (1 bp – 6,000 bp). Subsequently, the amplicons were pooled as described in the Ion Amplicon Library Preparation (Fusion Method) Manual (Thermo Fisher).

Ion Torrent sequencing was carried out as recommended by the manufacturer using an ION 314 v2 chips (Thermo Fisher). Briefly, emulsion PCR and enrichment of template-positive ion sphere particles (ISP) was done using the Ion PGM Hi-Q OT2 Kit (Thermo Fisher) on the Ion OneTouch 2 Instrument (Thermo Fisher) and Ion OneTouch ES instrument (Thermo Fisher) following the Ion Torrent user manual. Subsequently, the ISP were sequenced using the Ion PGM Hi-Q Sequencing Kit (Thermo Fisher) following the user manual on an Ion PGM system (Thermo Fisher) with a total of 1200 flows. The Torrent Suite software, which converts the raw signals (raw pH values) into incorporation measurements and ultimately into basecalls for each read, was used for initial quality trimming. We applied the following settings for base calling: Basecaller –barcode-mode 1 –barcode-cutoff 0 –trim-qual-cutoff 15 –trim-qual-window-size 10 –trim-min-read-len 250.

Sequence processing using SilvaNGS and statistical analyses

The sequence reads for each sample from the Ion Torrent PGM (Thermo Fisher) and 454 Titanium FLX (Roche) were further processed using the bioinformatics pipeline of the SilvaNGS project (Quast et al., 2013). This involved quality controls for sequence length (> 200 bp) and the presences of ambiguities (< 2%) and homopolymers (< 2%). The remaining reads were aligned against the SSU rRNA seed of the SILVA database release 125 (Quast et al., 2013). The classification was done by a local BLAST search against the SILVA SSURef 123 NR database using blast -2.2.22 + with standard settings.

Statistical analyses were carried out using normalised read abundances and classification to genus level. Normalised read abundances were calculated using within-sample relative abundances.

These were calculated using the R (R Development Core Team) function decostand(method=total) from the Vegan package (Oksanen et al., 2013). Community alpha diversity (Simpson Index) and beta diversity (dissimilarity calculated using Bray-Curtis) was calculated using R and subsequently plotted using NMDS plots. Simpsons Index was chosen for alpha diversity calculation as it provides more weight to evenness and accounts for differences in units. The Bray-Curtis Index was used for beta diversity analysis as it gives weight to species' presence and absence, and abundance. Significance tests, analyses of site-specific community composition differences and correlations to environmental factors, were done using ANOSIM and Mantel tests.

Metagenomic sequencing, assembly and binning

High-molecular-weight genomic DNA from three S-PA representative samples in the Northern Gyre (NAST, N26°), Equator (WTRA, N11°) and Southern Temperate (SSTC, S44°) region were shotgun-sequenced on an Illumina HiSeq2500 sequencer at the Max Planck Genome Center (MPGC, Cologne, Germany) after library construction using the Ovation Ultralow Library system kit (NuGen, San Carlos CA, USA). Approximately 54.7, 60.6 and 58.8 million reads were obtained for one Gyre, Equator and Temperate sample, respectively (Supplementary Table 4). Phylogenetic analysis of the reads by MetaPhlAn indicated that 56 - 68% were associated to Bacteria, 13-26% to Eukaryote, and only ~2% of the reads were Archaea related (Beghini et al., 2021).

Raw sequence reads were quality-trimmed and error-corrected using BBtools (BBmap package v. 33.57 http://sourceforge.net/projects/bbmap/) with default parameters. Bulk assembly of the metagenomes was separately performed with IDBA_UD v1.1.1 with k-mer sizes from 21 to 124 in steps of 10, and SPAdes v3.9 with k-mer sizes from 21 to 127 in steps of 10. This yielded a total of 561,913 scaffolds from all three aggregates, and the largest scaffold length was 545,657 bp (Supplementary Table 4). To obtain coverage profile of contigs from each aggregate metagenomic assembly, the trimmed reads were mapped back to contigs using BWA-MEM (v. 0.7.12) (Li, 2013). Full-length 16S rRNA genes were reconstructed from the raw reads using PhyloFlash 2.0 (http://github.com/HRGV/phyloFlash).

Genome binning was performed using CONCOCT (Alneberg et al., 2014) within the Anvi'o package (v. 2.0.2) (Eren et al., 2015). The metagenomic workflow employed here is described online (merenlab.org/2015/05/02/anvio-tutorial). CheckM was used to evaluate the accuracy of the binning approach by determining the percentage of completeness and contamination (Parks et al., 2015) using the lineage-specific workflow. The statistics of each MAG recovered from aggregates-associated microbial community is given in Supplementary Table 5. These metagenome-assembled genomes included 35 - 1,065 scaffolds with a scaffold largest length between 15,377 and 545,657 bp. Average nucleotide identities (ANIs) between the assemblies and to the next sequenced relative were calculated with JSpeciesWS web service (Richter et al., 2016). Genes were called using Prodigal (Hyatt et al., 2010). The generated assemblies were automatically annotated with the standard RAST annotation pipeline (Aziz et al., 2008) and the functions of predicted genes were curated and revised by a comparison of homology between databases including KEGG (release 94.2), Pfam-A (version 32.0), and NCBI-nr database (version of 25 August 2020). Specifically, the results of the KEGG annotations using DIAMOND (version 2.0.11) and BLASTP were compared to hidden Markov models-based HMMER3 searches against Pfam-A database and BLASTP searches against the NCBI-nr database. All predicted genes were used to query the TransportDB database (Elbourne et al., 2017), and matches were assigned to transporter families within the TransportDB database (www.membranetransport.org).

Phylogenetic analyses

For phylogenetic analyses, the reconstructed genomes were placed within the reference genome tree of CheckM (v. 0.9.7) (Parks et al., 2015) and then visualised in ARB (Ludwig et al., 2004). In addition to analysing ribosomal proteins, partial 16S rRNA genes were retrieved from reconstructed genomes and then aligned by SINA (v. 1.3.0) (Pruesse et al., 2012) to a curated SILVA SSU123 NR99 database, where all sequences with a pintail value below 50 and alignment quality below 70 were excluded from further analyses. Phylogenetic trees were calculated with various algorithms: neighbour-joining (Ludwig et al., 2004) and PhyML (v. 3.1) (Guindon, 2010) to check the stability of the basic topology. The phylogeny of the assembled metagenomic bins were determined according to both the ribosomal protein and 16S rRNA genes alignments.

Carbohydrate-active enzymes (CAZymes) and peptidases annotation

Annotation for CAZymes were performed as described in (Liu et al., 2013). Briefly, protein coding genes identified in each genomes were searched against the HMM profile-based database of carbohydrate-active enzymes obtained from dbCAN (Yin et al., 2012) in December 2012 using hmmsearch in the HMMER software package (v.3.0; http://hmmer.janelia.org/help) (Finn et al., 2011). Results were filtered using an *e*-value cut-off $< 10^{-5}$. Additionally, all returned hits were manually evaluated based on their functional annotation in RAST and pfam. Sulfatase encoding genes were identified with HMMER scans versus the PFAM database 33.1 (Mistry et al., 2021) using an *e*-value cut-off $< 10^{-5}$. Presence of extracellular peptidases was evaluated by MEROPS using an *e*-value cut-off $< 10^{-10}$ (Rawlings et al., 2012).

Data availability

The metagenomic data from this project can be found in ENA under the BioProject accession no. PRJNA421797 and drafts of genomes are available with accession no. PKCH00000000-

PKEK00000000. The raw metagenomic reads were deposited to NCBI SRA under accession number SRP126598. The 16S rRNA sequencing and FISH data was deposited using the GFBio platform (Diepenbroek et al., 2014) and can be found under the INSDC accession number: PRJEB2516 and in Pangaea https://doi.pangaea.de/10.1594/PANGAEA.878060 and https://doi.pangaea.de/10.1594/PANGAEA.891265, respectively.

Results

During the AMT22 we performed a comprehensive analysis of the free-living (FL 0.2 – 3 µm) and particle-attached (S-PA 3 – 10 µm and L-PA > 10 µm) bacterioplankton across a north-south Atlantic transect (Figure 1). Thirty-five stations were sampled, covering six Longhurst ocean provinces (Longhurst, 2010). The biogeographical provinces varied in their physical, chemical, and biological characteristics (Supplementary Table 1). The primary production was generally low, especially in the gyre regions and increased in the temperate provinces, especially the SSTC, where an active phytoplankton bloom was occurring. Across the transect, Chl *a* concentrations ranged from 0.03 mg m^3 (gyres) to up to 1.51 mg m^3 (SSTC) (Figure 1; Supplementary Table 1). Oxygen concentration remained with 231 ± 28 µmol L^{-1} more similar across the transect, but increased amidst the active bloom at S44°, alongside nitrate, nitrite and phosphate (Supplementary Table 1).

Particle quantification and biochemical identification

In three contrasting stations, N26°, N11°, and S44°, chosen based on differences in productivity and Chl *a* concentrations (N26°: 0.09 mg m^3 NATR, N11°: 0.28 mg m^3 WTRA, and S44°: 1.51 mg m^3 SSTC), we performed particle quantification and biochemical identification by lectin staining. Many particles were strongly stained with the fucose-binding lectin AAL, and showed only minor staining with the lectins ConA, WGA, and SBA (Supplementary Table 3), indicating a high presence of fucose-containing glycans (Figure 2).

Particle abundance correlated with the Chl *a* concentration and was 4-times as high in the SSTC (206 particles L^{-1}), compared to 48 particles L^{-1} in the NATR and 58 particles L^{-1} in the WTRA. Additionally, the number of bacterial cells per particle was higher in the more productive region, with 1435 cells $particle^{-1}$ in the SSTC and 47 cells $particle^{-1}$ in the WTRA (Figure 2).

Bacterial cell numbers

Absolute bacterial cellular abundances were quantified in all size fractions across the 35 stations (Figure 1). The counts in the FL fraction were three to four orders of magnitude higher than those in the S-PA and L-PA, with a mean of $7.6{\times}10^5 \pm 3.1x10^5$ and $9.3x10^2 \pm 1.4x10^3$ cells ml^{-1}, respectively (Figure 3). Concentrations of the FL and the S-PA fraction were lowest in the gyres (average $5.9x10^5$ and $4.8x10^2$ cells ml^{-1}, respectively), increased in the temperate and equatorial regions (average $8.2x10^5$ and $9.2x10^2$ cells ml^{-1}) and peaked in the phytoplankton bloom encountered in SSTC (average $1.5x10^6$ and $4.1x10^3$ cells ml^{-1}). The L-PA fraction was less affected by the bloom condition and remained the lowest across all stations ($3.2x10^2 \pm 2.5x10^2$ cells ml^{-1}, Figure 3).

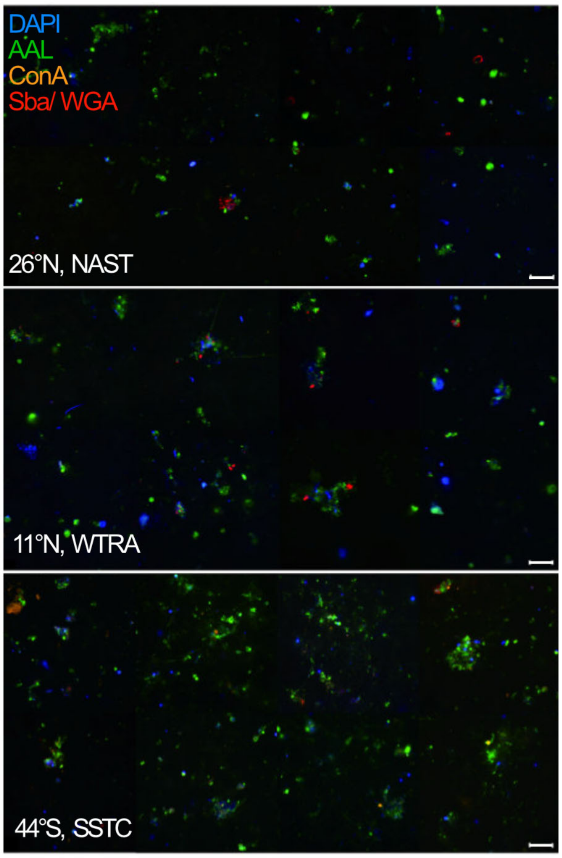

FIGURE 2
Epifluorescence microscope image of marine particles obtained from the S-PA fraction in the North Atlantic Subtropical (NAST), Western Tropical Atlantic (WTRA), and South Subtropical Convergence (SSTC) province of the Atlantic Ocean at 40 × magnification with the super-resolution microscope. Each sample was simultaneously stained by DAPI (blue), specific to DNA, and the lectins AAL (green), specific to fucose, ConA (orange), specific to a-mannopyranosyl and a-glucopyranosyl residues, as well as SBA and WGA (red), specific to Galactose/N-acetylgalactosamine. Scale bars: 20 µm.

16S tag sequencing

The community composition varied considerably between the FL and PA fractions. In the FL (0.2 - 3 µm) fraction, the most abundant clades were the *Prochlorococcus*, SAR11, SAR116, AEGEAN 169 marine group, and uncultured *Rhodobacteraceae*. The SAR86 clade was the most significant gammaproteobacterial group and *Ca.* Actinomarina the most prominent *Actinobacteria* (Figure 4).

The most significant biogeographical distribution pattern across latitudes was in the highly productive southern temperate region. At the

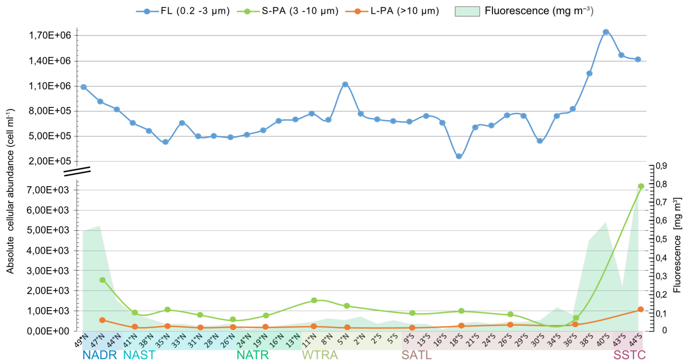

FIGURE 3
Total bacterial cellular abundance determined by CARD-FISH using the EUB I-III general bacteria probes of the free-living (FL, blue),small particle(S-PA, green),and large particle (L-PA, orange) fraction across the Atlantic Ocean sampled during the AMT22 cruise in 2012. Fluorescence is shown in green and is based on chlorophyll a calibration. NADR North Atlantic Drift, NAST North Atlantic Subtropical, NATR North Atlantic Tropical Gyre, WTRA Western Tropical Atlantic, SATL South Atlantic Gyre, and SSTC South Subtropical Convergence.

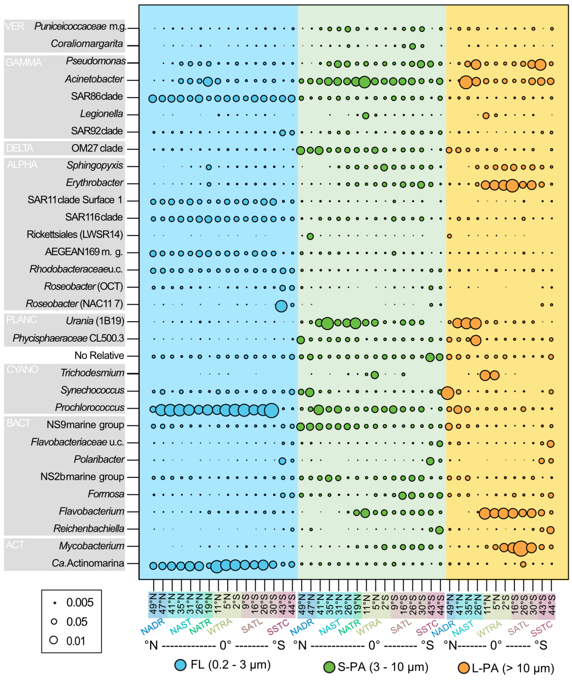

FIGURE 4
Bubble plot of bacterial taxa that reached a minimum of 5% relative read abundance from samples taken across the Atlantic Ocean during the AMT22 cruise in 2012. Colors indicate the size fraction: Blue free-living (FL), green small particle-attached (S-PA), and orange large particle-attached (L-PA) fraction. ACT Actinobacteria, ALPHA Alphaproteobacteria, BACT Bacteroidetes, CYANO Cyanobacteria, DELTA Deltaproteobacteria, GAMMA Gammaproteobacteria, PLANC Planctomycetes, VER Verrucomicrobia. NADR North Atlantic Drift, NAST North Atlantic Subtropical, NATR North Atlantic Tropical Gyre, WTRA Western Tropical Atlantic, SATL South Atlantic Gyre, and SSTC South Subtropical Convergence.

last two stations, sampled during the phytoplankton bloom, the relative read abundance of SAR11 and SAR116, *Prochlorococcus*, and *Ca.* Actinomarina were lower. Comparatively, the gammaproteobacterial SAR92 clade, uncultured *Rhodobacteraceae*, NAC11-7 and OCT *Roseobacters* had a higher abundance (Figure 4). Additionally, the *Bacteroidetes* showed a distinct response to the bloom, in both the FL and PA community, with an increased abundance of *Ulvibacter (*now *Ca.* Prociliicoccus (Francis et al., 2019)*)*, *Polaribacter, Formosa, Reichenbachiella, Owenweeksia*, NS10, *Fluviicola and* uncultured *Flavobacteriaceae* (Supplementary Figure 1).

Other bacterial groups showed smaller biogeographical distribution patterns; for example, *Acinetobacter* was more abundant at the equator in the S-PA. Comparatively, they showed a bimodal distribution in the L-PA, with a higher abundance in both gyres. A similar bimodal pattern in the L-PA was also seen in *Pseudomonas*. The *Planctomycetes* group *Urania* was more abundant in the S-PA and L-PA fraction of the northern gyre. *Erythrobacter* was higher in abundance in the equator of the L-PA fraction. Finally, several *Bacteroidetes* groups showed distinct distribution patterns in addition to their increase in the southern temperate region. NS9 was more abundant in both particle fractions in the northern samples, whereas *Flavobacterium* was more abundant in the equator and southern samples.

Across the Atlantic, members of the *Bacteroidetes* (e.g., NS9, *Flavobacterium* and *Formosa*), *Planctomycetes* (e.g. *Urania* and *Phycisphaerae*), and *Verrucomicrobia* (e.g. *Puniceicoccaceae* marine group and *Coraliomargarita*) were more prevalent on particles (Figure 4). Other taxa with higher read abundances in the PA fraction, than in the FL communities, were yet uncultured bacteria related to the genera *Pseudomonas, Acinetobacter*, and *Legionella* (all *Gammaproteobacteria*), OM27 (Deltaproteobacteria), *Shingopyxis, Erythrobacter* and *Rickettsiales* (LWSR 14) (all *Alphaproteobacteria*), and *Mycobacterium* (*Actinobacteria*).

CARD-FISH

Based on the 16S rRNA sequencing data we chose specific FISH probes to quantify the absolute abundance of the key bacterial groups. Samples clearly corresponding to a specific province were chosen. Their averaged cell count was considered representative for each respective province.

FISH counts and 16S tag sequencing were largely consistent. However, some groups showed discrepancies, most strikingly SAR11 that comprised less than 13 ± 3% of the reads in the FL fraction, but more than half of the absolute bacterial abundance, in line with repeated counter-selection by the PCR primers used (Parada et al., 2016).

The FL and PA communities had different bacterial compositions. The majority of the bacteria in the FL community, across all provinces, were *Alphaproteobacteria*, specifically SAR11 and *Roseobacter*, followed by *Cyanobacteria, specifically Prochlorococcus* and *Synechococcus*, and diverse *Bacteroidetes* (Figure 5). Comparatively, the PA bacteria were composed of *Bacteroidetes*, specifically NS5, *Polaribacter* and *Formosa, Gammaproteobacteria*, specifically *Pseudoalteromonas*, *Alteromonas*, *Vibrio* and *Balneatrix*, diverse *Alphaproteobacteria*, as well as *Planctomycetes*, specifically *Phycisphaeraceae* and *Rhodopirellula*. In the highly productive southern temperate station (S44°, SSTC) there was a high abundance of *Bacteroidetes* in both the FL and PA community. *Gammaproteobacteria* were more abundant in the L-PA community, compared to the S-PA.

Cells were counted with specific probes of the subphyla and genera to determine the absolute cell number in cases where cells showed high relative read abundance in a specific fraction. OM27 for example comprised between $6.8x10^1$ to $2.6x10^2$ cells ml^{-1} (3 - 9% relative to EUBI-III counts) of the total cell counts in the S-PA community and was also abundant in relative read abundance (Figure 4). Other important groups, based on abundances, in the S-PA were members of the family *Puniceicoccaceae* (*Verrucomicrobia, Opitutae*) with $1.8x10^1$ - $6.6x10^2$ cells ml^{-1} (1 - 9%), as well as members of the genus *Phycisphaera* (*Planctomycetes, Phycisphaerae*) with $3.4x10^1$ - $6.9x10^2$ cells ml^{-1} (3 - 10%).

To understand the finer-scale spatial organisation of PA bacteria, we used probes targeting the *Bacteroidetes*, *Planctomycetes* and *Cyanobacteria* to visualise cells directly attached to particles with a super-resolution microscope (Supplementary Figure 2D-F). The probes showed a striking degree of spatial organisation within the particle with brightly stained cells not only as surface colonisers, but also embedded within the particles (Supplementary Figure 2D-F). Dual hybridisation also showed that bacteria of at least two different taxa were intermingled within the fucose-enriched particles instead of forming large single-taxon clusters (Supplementary Figure 2E, F).

Community diversity and dissimilarity analysis based on 16s tag sequencing

The FL, S-PA, and L-PA bacterial communities had a similarly high within-sample diversity (alpha diversity, Supplementary Table 1D). The alpha diversity only showed a slight decrease in the L-PA and FL within the Southern Gyre. Cross-community analysis (beta diversity) showed a significant difference between size fractions (ANOSIM: $r^2 = 0.67$, $P = 0.001$, Figure 6A). Additionally, there was a

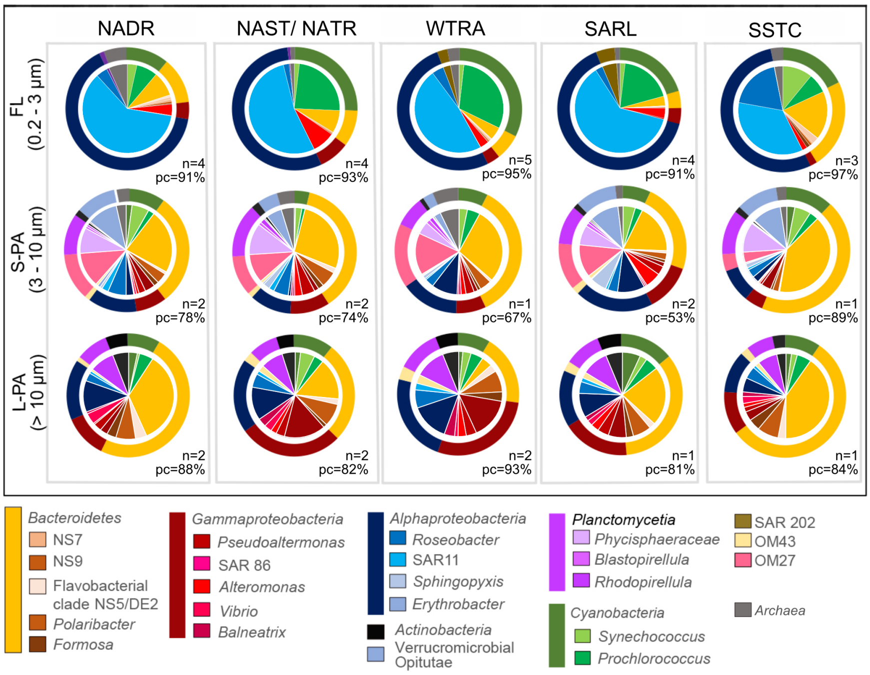

FIGURE 5
Pie chart of total bacterial cellular abundances counted using specific CARD-FISH probes (Supplement Table 2) during the AMT22 cruise in 2012. The abundance of representative stations was averaged from multiple samples for each region. All fish data is available in Pangaea. The outer rings of the chart indicate the bacterial phylum, and the inner part indicates the taxon to genus level where determined. The samples were taken across five regions, NADR North Atlantic Drift, NAST North Atlantic Subtropical, NATR North Atlantic Tropical Gyre, WTRA Western Tropical Atlantic, SATL South Atlantic Gyre, and SSTC South Subtropical Convergence, and fractionated into a free-living (FL), small particle-attached (S-PA) and large particle-attached (L- PA) fraction. n number of stations, PC probe coverage of total bacterial cell counts (EUBI-III).

significant biogeographical difference across the oceanic provinces (ANOSIM: $r^2 = 0.23$, $P = 0.001$), with the highly productive southern temperate stations being separated from the others independent of the size fraction (Figure 6A). The FL and PA bacterial communities of the northern and southern temperate sites were more similar to each other, as were the L-PA communities of the two gyre regions and the equator. The similarity within FL and PA communities became more prominent with increasing Chl *a* concentrations (Figure 6B).

Metagenome-assembled-genomes

Sequencing of whole community DNA extracted from three S-PA samples from three stations (N26°, N11°, S44°) (Figure 1) yielded a total of 151,454,079 reads after quality filtering. *De novo* genomic assembly and binning resulted in the reconstruction of 54 draft bacterioplankton metagenome-assembled-genomes (MAGs) (Supplement Table 4). Fifty-four MAGs had predicted completeness > 80% and only four had predicted contamination > 6%. The genomic bins were 1.4 – 6.7 Mb in size and contained 1,276 – 6,560 genes. Phylogenies based on concatenated marker genes and 16S rRNA genes showed that these MAGs were assigned to six bacterial phyla. MAGs reconstructed from PA microbial communities were taxonomically diverse and included members of the *Actinobacteria*, *Planctomycetes* (Urania-1B-19 and CL500-3, both *Phycisphaerae*, and *Planctomycetaceae*), *Verrucomicrobia (Opitutae* and *Verrucomicrobiaceae), Bacteroidetes* (*Flavobacterium*, NS4 and NS9 marine groups), *Gammaproteobacteria* (*Acinetobacter* and *Legionella* lineage), and *Alphaproteobacteria (Sphingopyxis)* (Supplementary Figure 3). Most of the recovered MAGs, like *Opitutae*, NS9, or members of the OM27 had also been identified as prevalent clades in the PA fractions by amplicon sequencing (Figure 4), and CARD-FISH (Figure 5).

Functional analysis

The metabolic potential of the PA communities to utilise polysaccharides was assessed by screening the MAGs of the *Actinobacteria, Planctomycetes, Verrucomicrobia, Bacteroidetes, Alpha-* and *Gammaproteobacteria* against the dbCAN database (Yin et al., 2012) and classified according to the carbohydrate-active enzymes (CAZy) database (Cantarel et al., 2009). All genomic bins contained genes relevant for carbohydrate degradation (Figure 7), mostly glycosyl transferases (GTs), glycoside hydrolases (GHs) and carbohydrate esterases (CEs), while carbohydrate binding modules (CBMs), auxiliary activities (AAs) and polysaccharide lyases (PLs) made up for a smaller proportion (Figure 7). GHs and GTs showed the highest diversity with, respectively, up to 20 and 18 different kinds across all MAGs. The most numerous glycoside hydrolase across all MAGs was GH109. Also highly abundant were GH13 (second most numerous), as well as GH23 and GH74 (Supplementary Figure 4).

Verrucomicrobia, Planctomycetaceae *(Planctomycetes)* and *Flavobacteriaceae (Bacteroidetes)* had a high frequency of sulfatases (Figure 7). These phyla also showed a GHs preference with on average 2.0 - 2.4% GH genes per MAG (Supplementary Table 5). Annotation indicated that the encoded enzymes likely targeted a diverse array of glycans (Figure 7, Supplementary Figure 3). GH16 and 30, used for the degradation of laminarin, were particularly high in the MAGs of Bacter3, 11, and 1 all affiliating with NS9 marine group. The highest abundance for the degradation of mannan (e.g. GH92) was found in Bacter3, 11 (both NS9 marine group), and Bacter2 (*Flavobacterium* sp.). The degradation capability for fucoidan was highest in the MAGs of Verruco1 and 2 (*Puniceicoccaceae* and *Verrucomicrobiales*, respectively), as well as Plancto9 (*Planctomycetaceae*) (Figure 7).

Since single GH genes provide only a preliminary view of degradation potential, we also extracted from the MAGs the polysaccharide utilisation loci (PULs), PUL-like structures, as well as co-localized genes for the degradation of polysaccharides of three substrates of interest: laminarin, mannan, and fucoidan. PULs and PUL-like structures rarely comprised all GHs, binding sites and transporters associated with the degradation and incorporation of oligo- or polysaccharides (Supplementary Figure 5). Bacter1 (NS9 marine group) for example was the only PUL that contained genes for the SusCD heteromer, including the porin type TonB-dependent transporter (SusC) and the glycan binding site/lid of the transporter

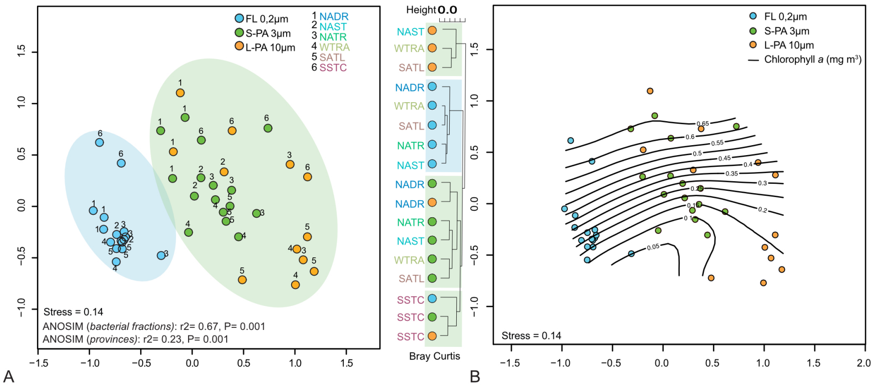

FIGURE 6
NMDS plots of 16S tag data showing bacterial communities sampled during the AMT22 cruise in 2012. **(A)** Communities clustering into significantly different groups of free-living (FL, blue background) and a small and large particle-attached (S-PA, L-PA, green background) fraction. **(B)** Communities shown across chlorophyll a as isotherm. NADR North Atlantic Drift, NAST North Atlantic Subtropical, NATR North Atlantic Tropical Gyre, WTRA Western Tropical Atlantic, SATL South Atlantic Gyre, and SSTC South Subtropical Convergence.

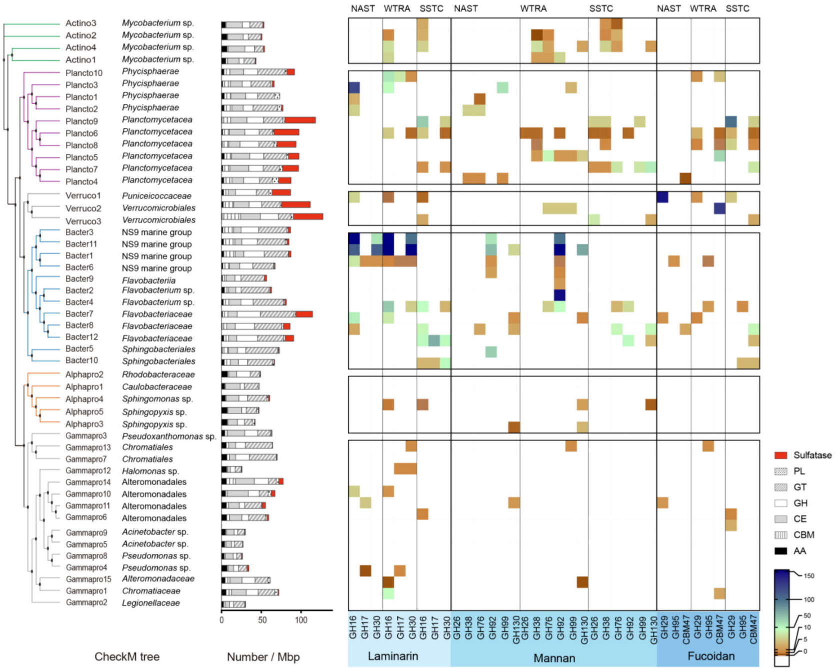

FIGURE 7
Carbohydrate-degradation enzyme profile across reconstructed genomes (MAGs). Heatmap visualises the abundance profiles, the number of CAZymes found in a particular MAG related to bin coverage, of glycoside hydrolases responsible for degrading various glycans in each MAG. GT glycosyl transferases, GH glycoside hydrolases, CE carbohydrate esterases, CBM carbohydrate binding modules, AA auxiliary activities, PL polysaccharide lyases.

protein (SusD). Most MAGs contained only the gene for the SusD protein in close proximity to the other genes important for polysaccharide degradation. More than one copy of a particular GH family was seen in several MAGs, for example Bacter1, 4, 7 (Supplementary Figure 5.1), Bacter5 (Supplementary Figure 5.2), and Plancto6, 8, and Verruco1 (Supplementary Figure 5.3).

Discussion

In the marine environment, particulate organic matter (POM) is a primary vector of carbon export to the deep sea, resulting in long-term storage. The chemical composition of particles and the associated microbial community, specifically their degradation potential, are critical factors for the level of carbon export. In this study, we present a comprehensive analysis of the microbial particle-attached community, in diversity and abundance, from diverse open ocean regions across the Atlantic Ocean (49°N-44° S). Our findings decipher ecological functioning in marine carbon cycling by expanding our understanding of the particle-attached microbiomes.

Similar to previous research, we found that PA bacteria make up only a small fraction of the microbial community (Alldredge et al., 1986; Heins et al., 2021). However, despite a lower cellular abundance, PA bacteria showed a high diversity and distinct dissimilarity from the free-living community, indicating that particles offer a high number of selective niches.

In line with previous studies, the particle-attached bacterial communities consisted primarily of OM27 (*Deltaproteobacteria*), *Opitutae* (*Verrucomicrobia*), *Phycisphaera* (*Planctomycetes*), *Gammaproteobacteria*, and several *Bacteroidetes* groups (e.g. NS9, *Flavobacterium* and *Formosa).* Members of these groups have been associated with attachment and organic matter degradation before (Buchan et al., 2014; Milici et al., 2017), except for OM27, which is considered a member of the oligotrophic gyre community (Yilmaz et al., 2012).

Despite higher abundance in the particle fractions, some taxa, like *Roseobacter (Alphaproteobacteria)*, the flavobacterial NS5 clade *(Bacteroidetes)*, and *Alteromonas (Gammaproteobacteria)*, were present in both fractions. Reasons for this could be a "stick-or-swim" lifestyle switch, as shown for *Roseobacter* (Michael et al., 2016), *Gammaproteobacteria* and *Flavobacteriia* (Fernández-Gómez et al., 2013; Marín, 2014); as well as stickiness of the particles (Passow, 2002); or micro-niching within clades (Dadon-Pilosof et al., 2017; Mestre et al., 2020), genera (Thompson et al., 2005; Hunt et al., 2008), and species (Moormann et al., 1997). We show, using FISH, that the abundant attached bacterial groups were not only attached to the particle surface but also embedded within the particle, indicating a tight linkage.

Particles were analysed across a broad geographic range and showed differences in abundance, as well as bacterial colonisation density. This finding could be related to the particle production time point or age (inferred by the level of primary production, e.g., within a gyre compared to an active phytoplankton bloom) and the glycan composition of the particles. We found that most particles were largely fucose-based, with only a minor fraction of mannose, galactose and N-acetylgalactosamine residues. It should be noted that lectin staining requires washing steps during the preparation of the particle and cell staining, which can lead to the unspecific removal of less persistent sugars.

Our finding corresponds with the finding from Huang et al. (2021), who showed that only a fraction of the secreted polysaccharides by microalgae promote particle formation. Specifically, 1,4-xylan and β-1,4-mannan are predominant in POM. At the same time, fucose-containing polysaccharides are mainly secreted but subsequently tend to enrich in POM, indicating that they promote particle formation. Furthermore, it has been proposed that fucoidans are quite resistant to degradation (Sichert et al., 2020), and that through their accumulation and aggregation, they drive carbon sequestration (Huang et al., 2021; Vidal-Melgosa et al., 2021). Sequestration is also affected by the particle sinking rate, because it affects whether particle-associated bacteria can react to the particle's nutrient plume and stay in its proximity long enough for degradation to set in (Stocker et al., 2008; Seymour et al., 2017). How fast particles sink is related to a particle's shape, size, composition and density (Bach et al., 2012; Turner, 2015), however, keeping the 3D particle structure intact requires other means for particle extraction than filtration, for example, with syringes, which was not done in this study.

The presence of bacteria potentially capable of using fucose-containing sulfated polysaccharides in the particle fraction in our study – 24% of the MAG's contain GH29 or GH95 – supports a prevalence of these glycans in particles. However, their degradation must be slower than the production because these organisms showed moderately high cellular abundance. *Verrucomicrobia* and *Planctomycetes* had 7 - 16% and 1 – 9% relative abundance in the S-PA fraction, respectively, and *Planctomycetes* had an abundance of 9 – 16%in the L-PA fraction. Potentially the complexity of the required enzymes (Sichert et al., 2020), and the compositional complexity of the particles are preventing the degradation. Based on previous results, *Verrucomicrobia* are particularly well-adapted for fucose-containing polysaccharide degradation(Orellana et al., 2022).

Several MAGs in this study showed a partial mannan degradation pathway by targeting α-mannosidic linkages, including lineages of *Actinobacteria*, *Planctomycetes*, NS9, *Flavobacteriaceae* as well as *Deltaproteobacteria*. We found that of 54 MAGs 30 had predictive α-mannan glycoside hydrolases (GH38, GH76, GH92, and GH99). GH38 (α-mannosidase) and GH76 (α-1,6-mannanase) were mainly enriched in *Mycobacterium* and *Planctomycetes* clades, while GH92 (α-1,2/3-mannosidase) was abundantly found in most genomes in *Bacteroidetes*. Only the *Planctomycetes*, *Verrucomicrobia* and *Gammaproteobacteria* genomes encoded the gene for endo-α-1,2-mannosidase (GH99). Notably, one of the *Planctomycetes* genomes (Plancto5) contained the whole subset of glycoside hydrolases for the complete degradation of mannan. The incomplete pathways indicate a potential partitioning of mannan degradation pathways to individual community members and suggest that a complete degradation of mannan could be mediated through synergistic interactions. However, the particles 3D structure must be considered in the hypothesis. The individual organisms must be located near each other to profit from the degradation potential of others. Such cross-feeding on particles has been experimentally shown by (Enke et al., 2018). Although we did not visualise diverse organisms in co-localisation with mannan on a single particle, we could show that some groups, with partial mannan degrading potential, are located on and within the particles (Supplementary Figure 2D-F). Some of this degradation could also appear as selfish uptake – surface binding, partial hydrolysis, and direct uptake of hydrolysis products without loss to the environment –, driven by *Bacteroidetes* and *Gammaproteobacteria* as was shown for yeast α-mannan in rumen bacteria (Klassen et al., 2021). Recent research also showed the degradation of fungal α-mannan by a *Salegentibacter* sp. (*Bacteroidota*) strain isolated during a phytoplankton bloom in the North Sea (Solanki et al., 2022).

In the PA bacteria a lineage-specific pattern for GHs was observed; *Verrucomicrobia*, *Planctomycetes* and *Bacteroidetes* generally contained more GHs (on average 2.0-2.4% genes per genome), while *Proteobacteria*, *Actinobacteria* and *Cyanobacteria* showed the relatively lower GHs (0.8-1.1% genes per genome). The most numerous glycoside hydrolase across all genomes was GH109 (Supplementary Figure 4). An α-*N*-acetylgalactosaminidase activity is described for GH109, despite more functions assigned to this family. α-*N*-acetylgalactosaminidase can cleave *N*-acetylgalactosamine residues from glycoproteins and glycolipids (Desnick, 2001). GH13 is the second most abundant and contains many hydrolyzing enzymes with diverse functions, and it was originally established as the α-amylase family (Jespersen et al., 1993). GH23 and GH74 also appear to be abundantly present within the reconstructed genomes. These two enzymes generally act on the β-1,4-linkages in peptidoglycans and glucans, respectively. Together, these observations suggest that the most apparent nutrient sources might be α-glucan storage molecules such as glycogen or peptidoglycans.

Newly formed biomass, which contains more simple sugars like the storage polysaccharide laminarin, was encountered at the SSTC stations where an active phytoplankton bloom occurred. There was a high concentration of laminarin in the particle of the SSTC and WTRA (4mg/L) comparatively; the NAST/NTRA had only 0-1mg/L (Becker et al., 2020). Compared to fucose-containing sulfated polysaccharides, bacteria quickly break down laminarin when available (Arnosti et al., 2018; Reintjes et al., 2020a; Vidal-Melgosa et al., 2021). Correspondingly, the formation of fresh algal material in the SSTC supported a surge in bacterial cell numbers for both the free-living and the particle-attached bacterial community. These communities were highly similar, indicating that free-living bacteria were colonizing the POM, and that either similar selection forces were acting on all bacteria or an active exchange between communities occurred.

Equally, as mentioned above, bacteria are not necessarily fixed to a particle but can exhibit hop-on, hop-off behavior (McCarter, 1999; Kiorboe et al., 2003) or alternate between lifestyles, as was shown for some *Bacteroidetes* species (*Polaribacter dokdonensis* (MED 134) and *Leeuwenhoekiella blandensis* (MED217)) and are therefore present in multiple size fractions. They can attach to surfaces and use complex organic matter such as polysaccharides and proteins (Fernández-Gómez et al., 2013), and during times of organic matter limitation, they can switch to a free-living lifestyle using proteorhodopsins to obtain energy from light (Béjà et al., 2000; González et al., 2008; Fernández-Gómez et al., 2013). The apparent interchangeability of bacteria between different size fractions would explain the overlap in community composition between different size fractions found in our study and multiple others (Hollibaugh et al., 2000; Crespo et al., 2013; Mestre et al., 2017; Milici et al., 2017).

The potential differences in the nature of particles, whether they are of an abiotic or biotic source (live cells, diatomaceous earth, sand, chitin and cellulose), affect the colonisation by bacteria (López-Pérez et al., 2016). The "new" particles produced at the SSTC stations were predominantly phytoplankton-derived organic matter and selected for specific heterotrophs in both the free-living and particle-attached fraction. Specifically, there was an increase in the abundance of *Bacteroidetes*, which are often associated with phytoplankton-derived organic matter (Teeling et al., 2012). The high dissimilarity between the SSTC particle-attached community and the particle-attached communities of the other stations indicated that particles in different oceanic provinces may vary in chemical composition and therefore select for different bacterial groups.

Another reason for the high variability between the particle-attached communities could be due to succession patterns occurring during particle colonization (Datta et al., 2016). Analysis of bacterial colonization of chitin particles demonstrated that particle-attached bacteria undergo rapid succession patterns (Datta et al., 2016). Motile bacteria that can use the particles as a resource are the initial colonizers. Subsequently, secondary consumers colonize the particle, likely because they are attracted by the metabolites produced by the primary colonizers rather than the particle composition (Datta et al., 2016). The colonization of "new" particles at the SSTC stations by predominantly *Bacteroidetes* may represent an initial colonization by organisms using the particle as a resource (i.e. polysaccharides, proteins). The communities of particles in other regions, such as in the gyres, represent a more established but variable community of secondary colonizers.

Our study shows biogeographical differences in bacterial communities, especially the PA fraction, caused by differences in age and composition of particles. The results stress the importance of transect campaigns, such as the AMT22.

Data availability statement

The datasets presented in this study can be found in online repositories. The names of the repository/repositories and accession number(s) can be found below: https://www.ebi.ac.uk/ena, PRJNA421797, https://www.ebi.ac.uk/ena, PKCH00000000-PKEK00000000, https://www.ncbi.nlm.nih.gov/, SRP126598, https://www.ebi.ac.uk/ena, PRJEB2516, https://doi.pangaea.de/10.1594/PANGAEA.878060, PANGAEA.878060, https://doi.pangaea.de/10.1594/PANGAEA.891265, PANGAEA.891265, https://www.bodc.ac.uk/data/documents/cruise/11427/, 11427.

Author contributions

The project was designed by GR and RA. GR performed the sampling, FISH of the FL and 16S rRNA sequencing of all samples. CW performed the particle-associated FISH, lectin staining and metagenomic analysis. Statistical analysis was performed by GR and CW. The figures were prepared by GR and AH. The manuscript was written and reviewed by GR, AH, CW and RA. All authors contributed to the article and approved the submitted version.

Funding

This work was supported by the Max Planck Society. This study is a contribution to the international IMBER project and was also supported by the National Oceanography Centre, Southampton. The Atlantic Meridional Transect is funded by the UK Natural Environment Research Council through its National Capability Long-term Single Centre Science Programme, Climate Linked Atlantic Sector Science (grant number NE/R015953/1). This study contributes to the international IMBeR project and is contribution number 389 of the AMT programme.

Acknowledgments

We thank Jörg Wulf, Martha Schattenhoffer, Dimitri Meier, Karen Krüger, and Andreas Ellrott for technical assistance and helpful discussions. We thank the captain and crew of the RRS James Cook, as well as the principle scientist Glen Tarran (Plymouth Marine Laboratories) for assistance at sea. We are grateful to Bernhard M. Fuchs for helpful suggestions during the planning and realization of this study.

Conflict of interest

Publisher's note

Supplementary material

The Supplementary Material for this article can be found online at: https://www.frontiersin.org/articles/10.3389/fmars.2023.1051510/full#supplementary-material

References

Alldredge, A. L., Cole, J. J., and Caron, D. A. (1986). Production of heterotrophic bacteria inhabiting macroscopic organic aggregates (marine snow) from surface waters. *Limnol. Oceanogr.* 31 (1), 68–78. doi: 10.4319/lo.1986.31.1.0068

Alneberg, J., Bjarnason, B. S., de Bruijn, I., Schirmer, M., Quick, J., Ijaz, U. Z., et al. (2014). Binning metagenomic contigs by coverage and composition. *Nat Methods* 11, 1144–1146. doi: 10.1038/nmeth.3103

Arnosti, C., Reintjes, G., and Amann, R. (2018). A mechanistic microbial underpinning for the size-reactivity continuum of dissolved organic carbon degradation. *Mar. Chem.* 206, 93–99. doi: 10.1016/j.marchem.2018.09.008

Azam, F., and Malfatti, F. (2007). Microbial structuring of marine ecosystems. *Nat. Rev. Microbiol.* 5 (10), 782–791. doi: 10.1038/nrmicro1747

Aziz, R. K., Bartels, D., Best, A. A., DeJongh, M., Disz, T., Edwards, R. A., et al. (2008). The RAST server: rapid annotations using subsystems technology. *BMC Genomics* 9 (1), 1–15. doi: 10.1186/1471-2164-9-75

Bach, L. T., Riebesell, U., Sett, S., Febiri, S., Rzepka, P., and Schulz, K. G. (2012). An approach for particle sinking velocity measurements in the 3–400 μm size range and considerations on the effect of temperature on sinking rates. *Mar. Biol.* 159 (8), 1853–1864. doi: 10.1007/s00227-012-1945-2

Becker, S., Tebben, J., Coffinet, S., Wiltshire, K., Iversen, M. H., Harder, T., et al. (2020). Laminarin is a major molecule in the marine carbon cycle. *PNAS.* 117. 6599–6607.

Beghini, F., McIver, L. J., Blanco-Míguez, A., Dubois, L., Asnicar, F., Maharjan, S., et al. (2021). Integrating taxonomic, functional, and strain-level profiling of diverse microbial communities with bioBakery 3. *Elife* 10, e65088. doi: 10.7554/eLife.65088.sa2

Behrenfeld, M. J., Boss, E., Siegel, D. A., and Shea, D. M. (2005). Carbon-based ocean productivity and phytoplankton physiology from space. *Global Biogeochem. Cycles* 19 (1), GB1006. doi: 10.1029/2004GB002299

Béjà, O., Suzuki, M. T., Koonin, E. V., Aravind, L., Hadd, A., Nguyen, L. P., et al. (2000). Construction and analysis of bacterial artificial chromosome libraries from a marine microbial assemblage. *Environ. Microbiol.* 2 (5), 516–529. doi: 10.1046/j.1462-2920.2000.00133.x

Bennke, C. M., Neu, T. R., Fuchs, B. M., and Amann, R. (2013). Mapping glycoconjugate-mediated interactions of marine *Bacteroidetes* with diatoms. *Syst. Appl. Microbiol.* 36 (6), 417–425. doi: 10.1016/j.syapm.2013.05.002

Bennke, C. M., Reintjes, G., Schattenhofer, M., Ellrott, A., Wulf, J., Zeder, M., et al. (2016). Modification of a high-throughput automatic microbial cell enumeration system for shipboard analyses. *Appl. Environ. Microbiol.* 82 (11), 3289–3296. doi: 10.1128/AEM.03931-15

Brewer, P.G., and Riley, J.P. (1965). The automatic determination of nitrate in sea water. *Deep Sea Research and Oceanographic Abstracts* 12 (6), 765–772. doi: 10.1016/0011-7471(65)90797-7

Buchan, A., LeCleir, G. R., Gulvik, C. A., and González, J. M. (2014). Master recyclers: Features and functions of bacteria associated with phytoplankton blooms. *Nat. Rev. Microbiol.* 12 (10), 686–698. doi: 10.1038/nrmicro3326

Cantarel, B. L., Coutinho, P. M., Rancurel, C., Bernard, T., Lombard, V., and Henrissat, B. (2009). The carbohydrate-active EnZymes database (CAZy): An expert resource for glycogenomics. *Nucleic Acids Res.* 37 (Database issue), 233–238. doi: 10.1093/nar/gkn663

Cottrell, M. T., and Kirchman, D. L. (2000). Natural assemblages of marine *Proteobacteria* and members of the *Cytophaga-flavobacter* cluster consuming low- and high-molecular-weight dissolved organic matter. *Appl. Environ. Microbiol.* 66 (4), 1692–1697. doi: 10.1128/AEM.66.4.1692-1697.2000

Crespo, B. G., Pommier, T., Fernandez-Gomez, B., and Pedros-Alio, C. (2013). Taxonomic composition of the particle-attached and free-living bacterial assemblages in the Northwest Mediterranean Sea analyzed by pyrosequencing of the 16S rRNA. *Microbiologyopen* 2 (4), 541–552. doi: 10.1002/mbo3.92

Dadon-Pilosof, A., Conley, K. R., Jacobi, Y., Haber, M., Lombard, F., Sutherland, K. R., et al. (2017). Surface properties of SAR11 bacteria facilitate grazing avoidance. *Nat. Microbiol.* 2 (12), 1608–1615. doi: 10.1038/s41564-017-0030-5

Datta, M. S., Sliwerska, E., Gore, J., Polz, M. F., and Cordero, O. X. (2016). Microbial interactions lead to rapid micro-scale successions on model marine particles. *Nat. Commun.* 7 (1), 11965. doi: 10.1038/ncomms11965

DeLong, E. F., Franks, D. G., and Alldredge, A. L. (1993). Phylogenetic diversity of aggregate-attached vs free-living marine bacterial assemblages. *Limnol. Oceanogr.* 38 (5), 924–934. doi: 10.4319/lo.1993.38.5.0924

Desnick, R. (2001). α-n-acetylgalactosaminidase deficiency: Schindler disease. *Metab. Mol. bases inherit. Dis.*, 3483–3505.

Diepenbroek, M., Glöckner, F. O., Grobe, P., Güntsch, A., Huber, R., König-Ries, B., et al. (2014). "Towards an integrated biodiversity and ecological research data management and archiving platform: The German federation for the curation of biological data (GFBio)," in *Informatik 2014.* Eds. E. Plödereder, L. Grunske, E. Schneider and D. Ull (Bonn: Gesellschaft für Informatik e.V), S.1711–1721.

Elbourne, L. D., Tetu, S. G., Hassan, K. A., and Paulsen, I. T. (2017). TransportDB 2.0: A database for exploring membrane transporters in sequenced genomes from all domains of life. *Nucleic Acids Res.* 45 (1), 320–324. doi: 10.1093/nar/gkw1068

Enke, T. N., Leventhal, G. E., Metzger, M., Saavedra, J. T., and Cordero, O. X. (2018). Microscale ecology regulates particulate organic matter turnover in model marine microbial communities. *Nat. Commun.* 9, 2743. doi: 10.1038/s41467-018-05159-8

Eren, A. M., Esen, Ö.C., Quince, C., Vineis, J. H., Morrison, H. G., Sogin, M. L., et al. (2015). Anvi'o: an advanced analysis and visualization platform for 'omics data. *PeerJ* 3, e1319. doi: 10.7717/peerj.1319

Fernández-Gómez, B., Richter, M., Schüler, M., Pinhassi, J., Acinas, S. G., González, J. M., et al. (2013). Ecology of marine *Bacteroidetes*: A comparative genomics approach. *ISME J.* 7 (5), 1026–1037. doi: 10.1038/ismej.2012.169

Finn, R. D., Clements, J., and Eddy, S. R. (2011). HMMER web server: interactive sequence similarity searching. *Nucleic Acids Res.* 39 (2), 29–37. doi: 10.1093/nar/gkr367

Francis, T. B., Bartosik, D., Sura, T., Sichert, A., Hehemann, J.-H., Markert, S., et al. (2021). Changing expression patterns of TonB-dependent transporters suggest shifts in polysaccharide consumption over the course of a spring phytoplankton bloom. *ISME J.* 15, 2336–2350. doi: 10.1038/s41396-021-00928-8

Francis, B., Krüger, K., Fuchs, B. M., Teeling, H., and Amann, R. I. (2019). *Candidatus* prosiliicoccus vernus, a spring phytoplankton bloom associated member of the *Flavobacteriaceae*. *Syst. Appl. Microbiol.* 42 (1), 41–53. doi: 10.1016/j.syapm.2018.08.007

Fuchsman, C. A., Staley, J. T., Oakley, B. B., Kirkpatrick, J. B., and Murray, J. W. (2012). Free-living and aggregate-associated *Planctomycetes* in the black Sea. *FEMS Microbiol. Ecol.* 80 (2), 402–416. doi: 10.1111/j.1574-6941.2012.01306.x

Glockner, F. O., Kube, M., Bauer, M., Teeling, H., Lombardot, T., Ludwig, W., et al. (2003). Complete genome sequence of the marine planctomycete pirellula sp. strain 1. *PNAS.* 100. 8298–8303.

González, J. M., Fernández-Gómez, B., Fernàndez-Guerra, A., Gómez-Consarnau, L., Sánchez, O., Coll-Lladó, M., et al. (2008). Genome analysis of the proteorhodopsin-containing marine bacterium polaribacter sp. MED152 (*Flavobacteria*). *PNAS.* 105, 8724–8729.

Grasshoff, K. (1976). *Determination of nitrate and nitrite. methods of seawater analysis* (Weinheim, New York: Verlag Chemie).

Grossart, H. P., Tang, K. W., Kiorboe, T., and Ploug, H. (2007). Comparison of cell-specific activity between free-living and attached bacteria using isolates and natural assemblages. *FEMS Microbiol. Lett.* 266 (2), 194–200. doi: 10.1111/j.1574-6968.2006.00520.x

Guindon, S., Lethiec, F., Duroux, P., and Gascuel, O. (2005). PHYML Online—a web server for fast maximum likelihood-based phylogenetic inference. *Nucleic Acids Research* 33(suppl_2), W557–W559. doi: 10.1093/nar/gki352

Heins, A., Reintjes, G., Amann, R. I., and Harder, J. (2021). Particle collection in imhoff sedimentation cones enriches both motile chemotactic and particle-attached bacteria. *Front. Microbiol.* 12 (619), 1–17. doi: 10.3389/fmicb.2021.643730

Heissenberger, A., and Herndl, G. J. (1994). Formation of high molecular weight material by free-living marine bacteria. *Mar. Ecol. Prog. series. Oldendorf.* 111 (1), 129–135. doi: 10.3354/meps111129

Hollibaugh, J. T., Wong, P. S., and Murrell, M. C. (2000). Similarity of particle-associated and free-living bacterial communities in northern San Francisco bay, California. *Aquat. Microbial. Ecol.* 21 (2), 103–114. doi: 10.3354/ame021103

Huang, G., Vidal-Melgosa, S., Sichert, A., Becker, S., Fang, Y., Niggemann, J., et al. (2021). Secretion of sulfated fucans by diatoms may contribute to marine aggregate formation. *Limnol. Oceanogr.* 66 (10), 3768–3782. doi: 10.1002/lno.11917

Hunt, D. E., David, L. A., Gevers, D., Preheim, S. P., Alm, E. J., and Polz, M. F. (2008). Resource partitioning and sympatric differentiation among closely related bacterioplankton. *Science* 320 (5879), 1081–1085. doi: 10.1126/science.1157890

Huston, A., and Deming, J. (2002). Relationships between microbial extracellular enzymatic activity and suspended and sinking particulate organic matter: Seasonal transformations in the north water. *Deep Sea Res. Part II: Topical Stud. Oceanogr.* 49 (22-23), 5211–5225. doi: 10.1016/S0967-0645(02)00186-8

Hyatt, D., Chen, G.-L., LoCascio, P. F., Land, M. L., Larimer, F. W., and Hauser, L. J. (2010). Prodigal: Prokaryotic gene recognition and translation initiation site identification. *BMC Bioinf.* 11 (1), 1–11. doi: 10.1186/1471-2105-11-119

Jespersen, H. M., Ann MacGregor, E., Henrissat, B., Sierks, M. R., and Svensson, B. (1993). Starch- and glycogen-debranching and branching enzymes: Prediction of structural features of the catalytic (β/α)8-barrel domain and evolutionary relationship to other amylolytic enzymes. *J. Protein Chem.* 12 (6), 791–805. doi: 10.1007/BF01024938

Kappelmann, L., Krüger, K., Hehemann, J.-H., Harder, J., Markert, S., Unfried, F., et al. (2019). Polysaccharide utilization loci of north Sea *Flavobacteriia* as basis for using SusC/D-protein expression for predicting major phytoplankton glycans. *ISME J.* 13 (1), 76–91. doi: 10.1038/s41396-018-0242-6

Kiorboe, T., Tang, K., Grossart, H. P., and Ploug, H. (2003). Dynamics of microbial communities on marine snow aggregates: Colonization, growth, detachment, and grazing mortality of attached bacteria. *Appl. Environ. Microbiol.* 69 (6), 3036–3047. doi: 10.1128/AEM.69.6.3036-3047.2003

Kirkwood, D. (1996). *Nutrients: Practical notes on their determination in sea water* (Copenhagen, Denmark: ICES).

Klassen, L., Reintjes, G., Tingley, J. P., Jones, D. R., Hehemann, J.-H., Smith, A. D., et al. (2021). Quantifying fluorescent glycan uptake to elucidate strain-level variability in foraging behaviors of rumen bacteria. *Microbiome* 9 (1), 23. doi: 10.1186/s40168-020-00975-x

Klindworth, A., Pruesse, E., Schweer, T., Peplies, J., Quast, C., Horn, M., et al. (2013). Evaluation of general 16S ribosomal RNA gene PCR primers for classical and next-generation sequencing-based diversity studies. *Nucleic Acids Res.* 41 (1), e1. doi: 10.1093/nar/gks808

Krüger, K., Chafee, M., Ben Francis, T., Glavina del Rio, T., Becher, D., Schweder, T., et al. (2019). In marine *Bacteroidetes* the bulk of glycan degradation during algae blooms is mediated by few clades using a restricted set of genes. *ISME J.* 13 (11), 2800–2816. doi: 10.1038/s41396-019-0476-y

Li, H. (2013). Aligning sequence reads, clone sequences and assembly contigs with BWA-MEM. *arXiv: Genomics*. 1303. doi: 10.48550/arXiv.1303.3997

Liu, G., Zhang, L., Wei, X., Zou, G., Qin, Y., Ma, L., et al. (2013). Genomic and secretomic analyses reveal unique features of the lignocellulolytic enzyme system of *Penicillium decumbens*. *PloS One* 8 (2), e55185. doi: 10.1371/journal.pone.0055185

Longhurst, A. R. (2010). *Ecological geography of the sea* (Academic press).

López-Pérez, M., Kimes, N. E., Haro-Moreno, J. M., and Rodriguez-Valera, F. (2016). Not all particles are equal: the selective enrichment of particle-associated bacteria from the mediterranean sea. *Front. Microbiol.* 7, 996. doi: 10.3389/fmicb.2016.00996

Ludwig, W., Strunk, O., Westram, R., Richter, L., Meier, H., Yadhukumar,, et al. (2004). ARB: a software environment for sequence data. *Nucleic Acids Res.* 32 (4), 1363–1371. doi: 10.1093/nar/gkh293

Lyons, M., and Dobbs, F. (2012). Differential utilization of carbon substrates by aggregate-associated and water-associated heterotrophic bacterial communities. *Hydrobiologia* 686 (1), 181–193. doi: 10.1007/s10750-012-1010-7

Marín, I. (2014). “Proteobacteria,” in *Encyclopedia of astrobiology*. Eds. R. Amils, M. Gargaud, J. Cernicharo Quintanilla, H. J. Cleaves, W. M. Irvine, D. Pinti and M. Viso (Berlin, Heidelberg: Springer Berlin Heidelberg), 1–2.

McCarter, L. (1999). The multiple identities of *Vibrio parahaemolyticus*. *J. Mol. Microbiol. Biotechnol.* 1 (1), 51–57.

Mestre, M., Ferrera, I., Borrull, E., Ortega-Retuerta, E., Mbedi, S., Grossart, H.-P., et al. (2017). Spatial variability of marine bacterial and archaeal communities along the particulate matter continuum. *Mol. Ecol.* 26 (24), 6827–6840. doi: 10.1111/mec.14421

Mestre, M., Höfer, J., Sala, M. M., and Gasol, J. M. (2020). Seasonal variation of bacterial diversity along the marine particulate matter continuum. *Front. Microbiol.* 11, 1590. doi: 10.3389/fmicb.2020.01590

Michael, V., Frank, O., Bartling, P., Scheuner, C., Göker, M., Brinkmann, H., et al. (2016). Biofilm plasmids with a rhamnose operon are widely distributed determinants of the ‘swim-or-stick’ lifestyle in roseobacters. *ISME J.* 10 (10), 2498–2513. doi: 10.1038/ismej.2016.30

Milici, M., Vital, M., Tomasch, J., Badewien, T. H., Giebel, H. A., Plumeier, I., et al. (2017). Diversity and community composition of particle-associated and free-living bacteria in mesopelagic and bathypelagic southern ocean water masses: evidence of dispersal limitation in the bransfield strait. *Limnol. Oceanogr.* 62 (3), 1080–1095. doi: 10.1002/lno.10487

Mistry, J., Chuguransky, S., Williams, L., Qureshi, M., Salazar, G. A., Sonnhammer, E. L. L., et al. (2021). Pfam: The protein families database in 2021. *Nucleic Acids Res.* 49 (1), 412–419. doi: 10.1093/nar/gkaa913

Moormann, M., Zähringer, U., Moll, H., Kaufmann, R., Schmid, R., and Altendorf, K. (1997). A new glycosylated lipopeptide incorporated into the cell wall of a smooth variant of *Gordona hydrophobica*. *J. Biol. Chem.* 272, 10729–10738. doi: 10.1074/jbc.272.16.10729

Oksanen, J., Blanchet, F. G., Kindt, R., Legendre, P., Minchin, P. R., O'hara, R., et al. (2013). “Package ‘vegan’,” in *Community ecology package, version 2*, 1–295.

Orellana, L. H., Francis, T. B., Ferraro, M., Hehemann, J.-H., Fuchs, B. M., and Amann, R. I. (2022). *Verrucomicrobiota* are specialist consumers of sulfated methyl pentoses during diatom blooms. *ISME J.* 16, 630–641. doi: 10.1038/s41396-021-01105-7

Parada, A. E., Needham, D. M., and Fuhrman, J. A. (2016). Every base matters: assessing small subunit rRNA primers for marine microbiomes with mock communities, time series and global field samples. *Environ. Microbiol.* 18, 1403–1414. doi: 10.1111/1462-2920.13023

Parks, D. H., Imelfort, M., Skennerton, C. T., Hugenholtz, P., and Tyson, G. W. (2015). CheckM: assessing the quality of microbial genomes recovered from isolates, single cells, and metagenomes. *Genome Res.* 25, 1043–1055. doi: 10.1101/gr.186072.114

Passow, U. (2002). Transparent exopolymer particles (TEP) in aquatic environments. *Prog. Oceanogr.* 55, 287–333. doi: 10.1016/S0079-6611(02)00138-6

Pernthaler, J., Glöckner, F.-O., Schönhuber, W., and Amann, R. (2001). Fluorescence *in situ* hybridization (FISH) with rRNA-targeted oligonucleotide probes. *Methods Microbiol.* 30, 207–226. doi: 10.1016/S0580-9517(01)30046-6

Pernthaler, A., Pernthaler, J., and Amann, R. (2004). “Sensitive multi-color fluorescence in situ hybridization for the identification of environmental microorganisms,” in *Molecular microbial ecology manual*. Eds. G. Kowalchuk, F. J. De Bruijn, I. M. Head, A. D. Akkermans and J. D. Van Elsas (Dordrecht, the Netherlands: Kluwer Academic Publishers), 711–726.

Pruesse, E., Peplies, J., and Glöckner, F. O. (2012). SINA: Accurate high-throughput multiple sequence alignment of ribosomal RNA genes. *Bioinformatics* 28, 1823–1829. doi: 10.1093/bioinformatics/bts252

Quast, C., Pruesse, E., Yilmaz, P., Gerken, J., Schweer, T., Yarza, P., et al. (2013). The SILVA ribosomal RNA gene database project: improved data processing and web-based tools. *Nucleic Acids Res.* 41, 590–596. doi: 10.1093/nar/gks1219

Rawlings, N., Barrett, A., and Bateman, A. (2012). MEROPS. the www. jbc. org downloaded from database of proteolytic enzymes, their substrates and inhibitors. *Nucleic Acids Res.* 40, D343–D350. doi: 10.1093/nar/gkx1134

Reintjes, G., Arnosti, C., Fuchs, B., and Amann, R. (2019). Selfish, sharing and scavenging bacteria in the Atlantic ocean: a biogeographical study of bacterial substrate utilisation. *ISME J.* 13, 1119–1132. doi: 10.1038/s41396-018-0326-3

Reintjes, G., Fuchs, B. M., Amann, R., and Arnosti, C. (2020a). Extensive microbial processing of polysaccharides in the south pacific gyre *via* selfish uptake and extracellular hydrolysis. *Front. Microbiol.* 11. doi: 10.3389/fmicb.2020.583158

Reintjes, G., Fuchs, B. M., Scharfe, M., Wiltshire, K. H., Amann, R., and Arnosti, C. (2020b). Short-term changes in polysaccharide utilization mechanisms of marine bacterioplankton during a spring phytoplankton bloom. *Environ. Microbiol.* 22, 1884–1900. doi: 10.1111/1462-2920.14971

Richter, M., Rosselló-Móra, R., Oliver Glöckner, F., and Peplies, J. (2016). JSpeciesWS: a web server for prokaryotic species circumscription based on pairwise genome comparison. *Bioinformatics* 32, 929–931. doi: 10.1093/bioinformatics/btv681

Rieck, A., Herlemann, D. P. R., Jürgens, K., and Grossart, H.-P. (2015). Particle-associated differ from free-living bacteria in surface waters of the Baltic Sea. *Front. Microbiol.* 6, 1297. doi: 10.3389/fmicb.2015.01297

Salazar, G., Cornejo-Castillo, F. M., Borrull, E., Díez-Vives, C., Lara, E., Vaqué, D., et al. (2015). Particle-association lifestyle is a phylogenetically conserved trait in bathypelagic prokaryotes. *Mol. Ecol.* 24, 5692–5706. doi: 10.1111/mec.13419

Schattenhofer, M., Fuchs, B. M., Amann, R., Zubkov, M. V., Tarran, G. A., and Pernthaler, J. (2009). Latitudinal distribution of prokaryotic picoplankton populations in the Atlantic ocean. *Environ. Microbiol.* 11, 2078–2093. doi: 10.1111/j.1462-2920.2009.01929.x

Schultz, D., Zühlke, D., Bernhardt, J., Francis, T. B., Albrecht, D., Hirschfeld, C., et al. (2020). An optimized metaproteomics protocol for a holistic taxonomic and functional characterization of microbial communities from marine particles. *Environ. Microbiol. Rep.* 12, 367–376. doi: 10.1111/1758-2229.12842

Seymour, J. R., Amin, S. A., Raina, J.-B., and Stocker, R. (2017). Zooming in on the phycosphere: the ecological interface for phytoplankton–bacteria relationships. *Nat. Microbiol.* 2 (7), 17065. doi: 10.1038/nmicrobiol.2017.65

Sichert, A., Corzett, C. H., Schechter, M. S., Unfried, F., Markert, S., Becher, D., et al. (2020). Verrucomicrobia use hundreds of enzymes to digest the algal polysaccharide fucoidan. *Nat. Microbiol.* 5, 1026–1039. doi: 10.1038/s41564-020-0720-2

Simon, M., Grossart, H. P., Schweitzer, B., and Ploug, H. (2002). Microbial ecology of organic aggregates in aquatic ecosystems. *Aquat. Microbial. Ecol.* 28, 175–211. doi: 10.3354/ame028175

Smith, D. C., Simon, M., Alldredge, A. L., and Azam, F. (1992). Intense hydrolytic enzyme-activity on marine aggregates and implications for rapid particle dissolution. *Nature* 359, 139–142. doi: 10.1038/359139a0

Smith, M., Zeigler Allen, L., Allen, A., Herfort, L., and Simon, H. (2013). Contrasting genomic properties of free-living and particle-attached microbial assemblages within a coastal ecosystem. *Front. Microbiol.* 4, 120. doi: 10.3389/fmicb.2013.00120

Solanki, V., Krüger, K., Crawford, C. J., Pardo-Vargas, A., Danglad-Flores, J., Hoang, K. L. M., et al. (2022). Glycoside hydrolase from the GH76 family indicates that marine salegentibacter sp. Hel_I_6 consumes alpha-mannan from fungi. *ISME J.* 16, 1818–1830. doi: 10.1038/s41396-022-01223-w

Spring, S., Bunk, B., Spröer, C., Rohde, M., and Klenk, H. P. (2018). Genome biology of a novel lineage of *Planctomycetes* widespread in anoxic aquatic environments. *Environ. Microbiol.* 20, 2438–2455. doi: 10.1111/1462-2920.14253

Stocker, R., Seymour, J. R., Samadani, A., Hunt, D. E., and Polz, M. F. (2008). Rapid chemotactic response enables marine bacteria to exploit ephemeral microscale nutrient patches. *PNAS.* 105. 4209–4214.

Teeling, H., Fuchs, B. M., Becher, D., Klockow, C., Gardebrecht, A., Bennke, C. M., et al. (2012). Substrate-controlled succession of marine bacterioplankton populations induced by a phytoplankton bloom. *Science* 336, 608–611. doi: 10.1126/science.1218344

Thompson, J. R., Pacocha, S., Pharino, C., Klepac-Ceraj, V., Hunt, D. E., Benoit, J., et al. (2005). Genotypic diversity within a natural coastal bacterioplankton population. *Science* 307, 1311–1313. doi: 10.1126/science.1106028

Turner, J. T. (2015). Zooplankton fecal pellets, marine snow, phytodetritus and the ocean's biological pump. *Prog. Oceanogr.* 130, 205–248. doi: 10.1016/j.pocean.2014.08.005

Van Vliet, D. M., Palakawong Na Ayudthaya, S., Diop, S., Villanueva, L., Stams, A. J., and Sánchez-Andrea, I. (2019). Anaerobic degradation of sulfated polysaccharides by two novel *Kiritimatiellales* strains isolated from black Sea sediment. *Front. Microbiol.* 10, 253. doi: 10.3389/fmicb.2019.00253

Vidal-Melgosa, S., Sichert, A., Francis, T. B., Bartosik, D., Niggemann, J., Wichels, A., et al. (2021). Diatom fucan polysaccharide precipitates carbon during algal blooms. *Nat. Commun.* 12, 1150. doi: 10.1038/s41467-021-21009-6

Wegner, C.-E., Richter-Heitmann, T., Klindworth, A., Klockow, C., Richter, M., Achstetter, T., et al. (2013). Expression of sulfatases in rhodopirellula baltica and the diversity of sulfatases in the genus rhodopirellula. *Mar. Genomics* 9, 51–61. doi: 10.1016/j.margen.2012.12.001

Yilmaz, P., Iversen, M. H., Hankeln, W., Kottmann, R., Quast, C., and Glöckner, F. O. (2012). Ecological structuring of bacterial and archaeal taxa in surface ocean waters. *FEMS Microbiol. Ecol.* 81, 373–385. doi: 10.1111/j.1574-6941.2012.01357.x

Yin, Y., Mao, X., Yang, J., Chen, X., Mao, F., and Xu, Y. (2012). dbCAN: a web resource for automated carbohydrate-active enzyme annotation. *Nucleic Acids Res.* 40, 445–451. doi: 10.1093/nar/gks479

Ziervogel, K., and Arnosti, C. (2008). Polysaccharide hydrolysis in aggregates and free enzyme activity in aggregate-free seawater from the north-eastern gulf of Mexico. *Environ. Microbiol.* 10, 289–299. doi: 10.1111/j.1462-2920.2007.01451.x

Ziervogel, K., Steen, A. D., and Arnosti, C. (2010). Changes in the spectrum and rates of extracellular enzyme activities in seawater following aggregate formation. *Biogeosciences* 7, 1007–1015. doi: 10.5194/bg-7-1007-2010

Zubkov, M. V., Sleigh, M. A., Burkill, P. H., and Leakey, R. J. (2000). Picoplankton community structure on the Atlantic meridional transect: a comparison between seasons. *Prog. oceanogr.* 45, 369–386. doi: 10.1016/S0079-6611(00)00008-2

frontiers | Frontiers in Marine Science

TYPE Original Research
PUBLISHED 07 March 2023
DOI 10.3389/fmars.2023.1111416

OPEN ACCESS

EDITED BY
Vanda Brotas,
University of Lisbon, Portugal

REVIEWED BY
Emmanuel Boss,
University of Maine, United States
Shengqiang Wang,
Nanjing University of Information Science and Technology, China

*CORRESPONDENCE
Robert J. W. Brewin
✉ r.brewin@exeter.ac.uk

SPECIALTY SECTION
This article was submitted to Ocean Observation, a section of the journal Frontiers in Marine Science

RECEIVED 29 November 2022
ACCEPTED 26 January 2023
PUBLISHED 07 March 2023

CITATION
Brewin RJW, Pitarch J, Dall'Olmo G, van der Woerd HJ, Lin J, Sun X and Tilstone GH (2023) Evaluating historic and modern optical techniques for monitoring phytoplankton biomass in the Atlantic Ocean.
Front. Mar. Sci. 10:1111416.
doi: 10.3389/fmars.2023.1111416

Evaluating historic and modern optical techniques for monitoring phytoplankton biomass in the Atlantic Ocean

Robert J. W. Brewin[1,2]*, Jaime Pitarch[3], Giorgio Dall'Olmo[2,4,5], Hendrik J. van der Woerd[6], Junfang Lin[2], Xuerong Sun[1] and Gavin H. Tilstone[2]

[1]Centre for Geography and Environmental Science, Faculty of Environment, Science and Economy, University of Exeter, Penryn, United Kingdom, [2]Plymouth Marine Laboratory, Plymouth, United Kingdom, [3]Consiglio Nazionale delle Ricerche (CNR), Istituto di Scienze Marine (ISMAR), Rome, Italy, [4]National Centre for Earth Observation, Plymouth Marine Laboratory, Plymouth, United Kingdom, [5]Istituto Nazionale di Oceanografia e di Geofisica Sperimentale - OGS, Trieste, Italy, [6]Department of Water and Climate Risk, Institute for Environmental Studies (IVM), Vrije Universiteit, Amsterdam, Netherlands

Traditional measurements of the Secchi depth (z_{SD}) and Forel-Ule colour were collected alongside modern radiometric measurements of ocean clarity and colour, and *in-situ* measurements of chlorophyll-a concentration (Chl-a), on four Atlantic Meridional Transect (AMT) cruises. These data were used to evaluate historic and modern optical techniques for monitoring Chl-a, and to evaluate remote-sensing algorithms. Historic and modern optical measurements were broadly consistent with current understanding, with Secchi depth inversely related to Forel-Ule colour and to beam and diffuse attenuation, positively related to the ratio of blue to green remote-sensing reflectance and euphotic depth. The relationship between Secchi depth and Forel-Ule on AMT was found to be in closer agreement to historical relationships when using data of the Forel-Ule colour of infinite depth, rather than the Forel-Ule colour of the water above the Secchi disk at half z_{SD}. Over the range of 0.03-2.95 mg m^{-3}, Chl-a was tightly correlated with these optical variables, with the ratio of blue to green remote-sensing reflectance explaining the highest amount of variance in Chl-a (89%), closely followed by the Secchi depth (85%) and Forel-Ule colour (71-81%, depending on the scale used). Existing algorithms that predict Chl-a from these variables were evaluated, and found to perform well, albeit with some systematic differences. Remote sensing algorithms of Secchi depth were in good agreement with *in-situ* data over the range of values collected (8.5 - 51.8 m, r^2>0.77, unbiased root mean square differences around 4.5 m), but with a slight positive bias (2.0 - 5.4 m). Remote sensing algorithms of Forel-Ule agreed well with Forel-Ule colour data of infinite water (r^2>0.68, mean differences <1). We investigated the impact of environmental conditions and found wind speed to impact the estimation of z_{SD}, and propose a path forward to include the effect of wind in current Secchi depth theory. We discuss the benefits and challenges of collecting measurements of the Secchi depth and Forel-Ule colour and propose future directions for research. Our dataset is made publicly available to support the research community working on the topic.

KEYWORDS

Forel-Ule colour scale, radiometry, chlorophyll-a, Atlantic Meridional Transect, phytoplankton, Secchi disk

1 Introduction

Phytoplankton play a central role in the Earth System, contributing to around half the world's organic carbon and oxygen production (Longhurst et al., 1995; Field et al., 1998). They act as a conduit for propagating solar energy into the marine ecosystem, supporting marine life and sustaining fisheries (Chassot et al., 2010). They are intimately linked to the biogeochemical cycles of many key elements and compounds in the ocean, helping to regulate the climate of our planet (Falkowski, 2012).

Climate change is considered one of the greatest threats to life on Earth (Dow and Downing, 2011). Sea surface temperatures are rising, sea-level increasing, parts of the ocean are becoming more stratified, oxygen minimum zones are expanding, and the oceans are becoming more acidic (IPCC, 2019), with consequences for marine life. While many studies have investigated the impact of climate variability and change on marine phytoplankton (e.g., Behrenfeld et al., 2006; Martinez et al., 2009; Boyce et al., 2010; Wernand and van der Woerd, 2010a; Behrenfeld, 2011; Boyce et al., 2012; Brewin et al., 2012b; Wernand et al., 2013b; Behrenfeld, 2014; Boyce et al., 2014; Dutkiewicz et al., 2019; Henson et al., 2021) results are not always in agreement, with differences thought to be related to variations in the methods used for data collection, differences in data processing, and dealing with spatial and temporal biases in data collection (Gregg and Conkright, 2002; Antoine et al., 2005; Boyce et al., 2010; Mackas, 2011; McQuatters-Gollop et al., 2011; Rykaczewski and Dunne, 2011; Wernand et al., 2013b; Raitsos et al., 2014).

Phytoplankton may respond to climate change in different ways. For example, through changes in community composition, phenology, metabolic rates, geographical distribution, and vertical structure (Sathyendranath et al., 2017; Brewin et al., 2022) to name a few. Arguably one of the most important metrics to monitor is phytoplankton biomass, considering this metric is explicitly linked to many of these responses. Though not a perfect measure of phytoplankton biomass, since it can change independently through processes like photo-acclimation, the total chlorophyll-a concentration (Chl-a) is one of the most commonly-used metrics of phytoplankton biomass, owing to the fact it is present in all of phytoplankton (in one form or another), is relatively easy to measure (both *in situ* (directly and visually) and remotely (e.g., satellite)) at a sufficient accuracy and precision, with data being available over long periods needed to monitor change. Consequently, the Global Climate Observing System programme (GCOS) consider Chl-a to be an Essential Climate Variable (GCOS, 2011).

A key requirement for monitoring the response of phytoplankton biomass to climate change is to have a global dataset of a sufficient length to separate anthropogenic climate change from natural climate variability (e.g., >40 years in length; Henson et al., 2010). Though it is clear that satellites will become the main source of data used in the future for monitoring the response of phytoplankton to climate change (e.g., Siegel and Franz, 2010; Sathyendranath et al., 2019), the continuous ocean-colour data record is not yet at a sufficient length to do so. Ocean robotic platforms are increasing in number (Chai et al., 2020) and can measure deeper into the water column than the satellites, but have only been operating widely for a few decades. Time-series stations are critical (Henson, 2014), and in some cases have data available for >40 years (e.g., Bermuda Atlantic Time-series Study (BATS), Hawaii Ocean Time-series (HOT), Stončica), but are only available at discrete locations. At present, our only means to understand the global response of phytoplankton to climate change, at appropriate time scales (e.g., centennial), is to bridge modern measurements of Chl-a with historic proxies estimated by visual means, such as those collected using a Secchi disk, Forel-Ule colour scale, or the Continuous Plankton Recorder's (CPR) phytoplankton colour index (Lewis et al., 1988; Falkowski and Wilson, 1992; Boyce et al., 2010; Wernand et al., 2013b; Raitsos et al., 2014).

Among the oldest instruments used in optical oceanography are the Secchi disk (Secchi, 1864) and Forel-Ule colour scale (Forel, 1890; Ule, 1892). A Secchi disk is a white (typically) disk one lowers into the water and the depth at which it disappears/reappears from sight is proportional to water clarity or transparency (Tyler, 1968; Preisendorfer, 1986; Wernand, 2010; Wernand and Gieskes, 2012; Pitarch, 2020). The Forel-Ule colour scale is a visual scale of 21 colours, ranging from blue to green to yellow to brown, that can be used alongside the Secchi disk with the observer typically recording the colour of a submerged Secchi disk at around roughly half the Secchi depth (Wernand and Gieskes, 2012). This visual index of colour can reflect information on the composition of optically active constituents in the water, such as sediment, phytoplankton and yellow substances (Wernand and van der Woerd, 2010b; Wang et al., 2019; Ye and Sun, 2022). In open-ocean case-1 waters (around 70% of the ocean surface; Hu et al., 2012), where optically active water constituents covary in a predictable manner with phytoplankton (Morel and Prieur, 1977), these visual indices can be a powerful predictor of Chl-a concentration (Boyce et al., 2010). In case-2 waters, where optically active water constituents do not covary in a predictable manner with phytoplankton (Morel and Prieur, 1977), relating Secchi depth and Forel-Ule colour readings to a Chl-a concentration can be more challenging.

In open-ocean case-1 waters, converting Secchi depth and Forel-Ule readings to a Chl-a concentration typically requires establishing statistical, empirical or analytical relationships (Boyce et al., 2012; Lee et al., 2015; Lee et al., 2018c). When searching for long-term trends, it is essential to quantify the accuracy of these conversions and their uncertainties (Boyce et al., 2012; Boyce et al., 2014), to minimise systematic biases between methods (Rykaczewski and Dunne, 2011), and to bridge these historic datasets with modern radiometric measurements used to derive Chl-a, considering satellite radiometry will soon become the main source of data for monitoring the impact of climate change on phytoplankton (Siegel and Franz, 2010; Wernand et al., 2013a; Lee et al., 2018b; Pitarch et al., 2019; Sathyendranath et al., 2019; Pitarch et al., 2021). To achieve these requirements, a comprehensive, consistent, co-located *in-situ* dataset of Secchi depth, Forel-Ule colour, Chl-a concentration and radiometric measurements is required, that covers the range of conditions representative of open-ocean waters. At present, the distribution of *in-situ* data available is biased toward coastal and eutrophic waters, with few measurements collected in the less accessible open-ocean (Brewin et al., 2016; Lee et al., 2018a)

The Atlantic Meridional Transect (AMT) is an open-ocean research programme that collects oceanographic data through the centre of the Atlantic Ocean, across a transect of >12,000 km, covering shelf seas and upwelling systems, and the mid-ocean oligotrophic gyres (Aiken et al., 2000; Robinson et al., 2006; Rees et al., 2017). The programme has been operating since 1995, with 29 cruises completed to date. Additional details of the AMT programme can be found on the AMT website (https://amt-uk.org). Among the current objectives of AMT, there is a requirement to construct a multi-decadal, multidisciplinary ocean time-series, and to provide essential sea-truth validation for current and next-generation satellite missions (Rees et al., 2015). In-line with these two objectives, and with a view towards using AMT data to help toward constructing time-series data of phytoplankton at a length longer than that collected during the programme, we collected a dataset of concurrent and co-located measurements of Secchi depth, Forel-Ule colour, Chl-a, hyperspectral remote-sensing reflectance (R_{rs}), diffuse attenuation (K_d) and beam attenuation (c), on four AMT cruises (AMTs 23, 25, 26 and 28, a total of 127 stations). In this paper, we use this dataset to evaluate techniques that convert Secchi depth, Forel-Ule colour and R_{rs} data to measurements of Chl-a, that have been used for constructing centennial scale time-series data on phytoplankton biomass, and to evaluate satellite algorithms designed to monitor these variables.

2 Methods

2.1 Statistical tests

To compare variables, we used the Pearson linear correlation coefficient (r), the squared Pearson linear correlation coefficient (r^2), the centre-patterned (or unbiased) root mean square difference (Δ) and the bias (δ). The latter two statistics representing an index of precision and accuracy of a model, respectively. The root mean square difference (Ψ), which contains information on both accuracy and precision, can be reconstructed from Δ and δ, according to, $\Psi = \sqrt{\Delta^2 + \delta^2}$. The value of Δ and δ were computed according to

$$\Delta = \left(\frac{1}{N}\sum_{i=1}^{N}\left\{\left[X_{i,1} - \left(\frac{1}{N}\sum_{j=1}^{N}X_{j,1}\right)\right] - \left[X_{i,2} - \left(\frac{1}{N}\sum_{k=1}^{N}X_{k,2}\right)\right]\right\}^2\right)^{1/2}, \quad (1)$$

$$\delta = \frac{1}{N}\sum_{i=1}^{N}(X_{i,1} - X_{i,2}), \quad (2)$$

where X is the variable and N is the number of samples. The subscripts 1 and 2 represent different estimates of the same variable, with 1 typically representing the estimated variable and 2 the measured variable. In many cases, statistical tests were performed in $\log_{10}$ space, depending on whether the distribution of the data was closer to log-normal. Linear models relating two variables (e.g., Secchi depth and Chl-a) were fitted (often after $\log_{10}$-transformation of one or both variables, depending on their distribution) using a outlier-resistant fitting function (IDL function ROBUST_LINEFIT.pro) and non-linear models were fitted using least-square minimisation (Levenberg-Marquardt, IDL function MPFITFUN.pro (Moré, 1978; Markwardt, 2008), MatLab function fit.m).

2.2 AMT cruises

Data used in this study were collected at 127 stations on four AMT cruises (Figure 1) that took place onboard the RRS *James Clark Ross* (Figure 2), each one departing the UK and arriving in Port Stanley, Falkland Islands, including: AMT cruise 23 (AMT23) that took place between the 7th October and 8th November 2013 (25 stations sampled); AMT cruise 25 (AMT25) that took place between the 11th September and 4th November 2015 (35 stations sampled); AMT cruise 26 (AMT26) that took place between the 20th September and 4th November 2016 (37 stations sampled); and AMT cruise 28 (AMT28) that took place between the 23rd September and 30th October 2018 (30 stations sampled). Stations were sampled primarily around local noon, with a few stations sampled on AMT26 around mid-morning, so as to align with the passing of ESA's Sentinel 3A satellite.

2.3 Datasets collected

Table 1 lists all datasets collected and used in the study, providing acronyms, units and number of stations sampled.

2.3.1 Chlorophyll-a concentration

Surface seawater samples (2-5 m depth) were collected from the CTD casts (Figure 2B, 117 stations) and from the ship underway system (six stations, where CTD casts were unavailable). Seawater was sampled into 9.5 L polypropylene carboys covered in black plastic to protect from light. Seawater samples were well mixed to avoid issues with sedimentation. Between 1-4 L samples (depending on phytoplankton biomass, e.g. 1 L in productive waters and 4 L in oligotrophic waters) were measured using the rinsed measuring cylinders, and then decanted into rinsed polypropylene bottles with siphon tubes and inverted into a six port vacuum filtration rig. Using forceps, Whatman glass fibre filters (pore size of 0.7 μm) were placed on the filter rig with the smoother side facing down. Filter papers were covered

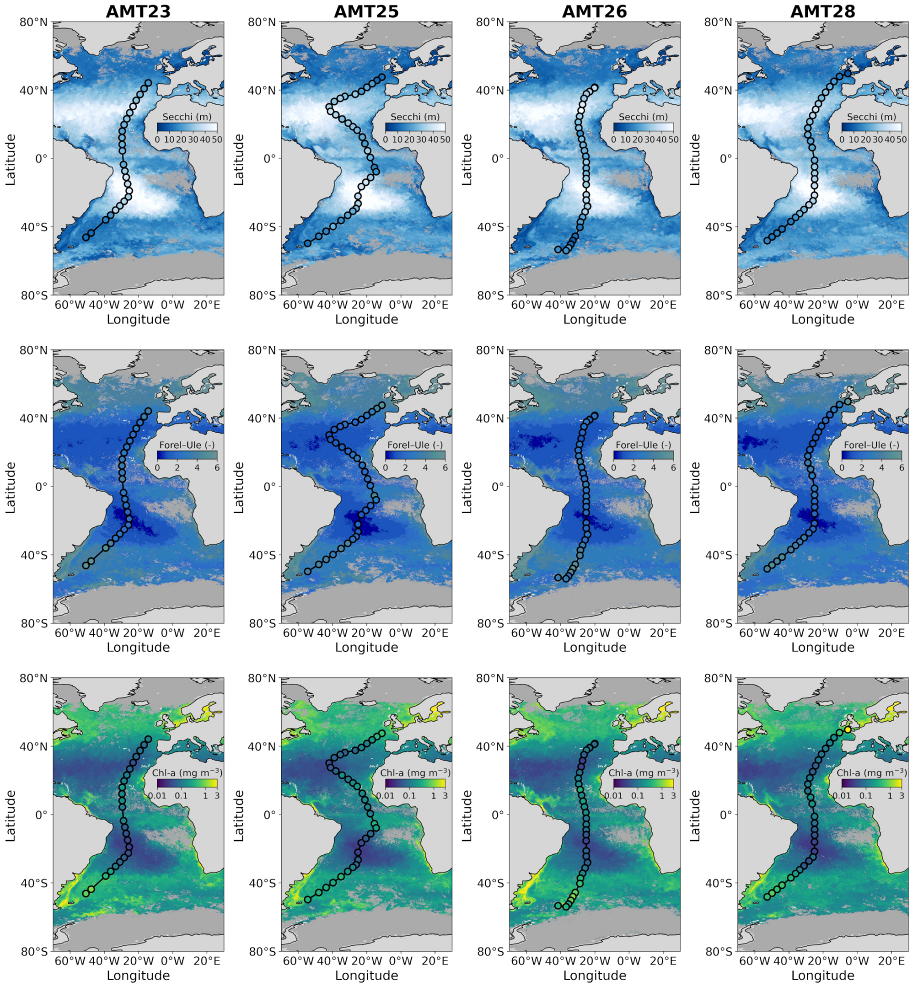

FIGURE 1

Locations of the 127 AMT stations where Secchi depth, Forel-Ule colour (using the LaMotte scale, for the colour of the disk at half the Secchi depth converted to infinite colour using the method of Pitarch (2017)) and Chl-a data were collected, on the four AMT cruises. The transects are overlain onto satellite estimates of Secchi depth (Pitarch et al., 2021), Forel-Ule colour (Pitarch et al., 2021), and Chl-a concentration (Sathyendranath et al., 2019), for the month of October (during which the AMT cruises took place), for each of the respective years that the cruises took place (AMT23 October 2013, AMT25 October 2015, AMT26 October 2016, AMT28 October 2018). Satellite data are from version 4.2 of the Ocean Colour Climate Change Initiative (Sathyendranath et al., 2019). The stations are coloured using the *in-situ* data, using the same colour scale as the satellite data, to illustrate how the two independent estimates of Secchi depth, Forel-Ule colour and Chl-a compare visually.

over sintered glass circles such that there were no gaps and water could only pass through the filters. Samples were filtered using a low-medium vacuum setting on the vacuum pump. When the last of the water passed through the filter paper, taps on the vacuum pump were closed and the sample filters were folded into 2 mL cryovials and either flash frozen in liquid nitrogen and transferred to the −80°C freezer (on AMT23, AMT26 and AMT28), or transferred directly to the −80°C freezer, for cases where liquid nitrogen was unavailable (AMT25).

Following each AMT campaign, High Performance Liquid Chromatography (HPLC) was used to determine total Chl-a (estimated from the sum of monovinyl chlorophyll-a, divinyl chlorophyll-a, and chlorophyllide-a). Details of the HPLC protocols and pigment extraction methods used on AMT23 and AMT25 are provided in Brotas et al. (2022), and those used on AMT26 and AMT28 are provided in Tilstone et al. (2021). At stations where neither CTD casts or underway samples were collected (four stations, one on AMT25, three on AMT26), Chl-a was estimated from underway spectrophotometric measurements of particulate absorption collected at the stations using the line-height method as described in Dall'Olmo et al. (2012), a technique proven to provide very accurate estimates of Chl-a on AMT cruises (see Dall'Olmo et al., 2012; Brewin et al., 2016; Rasse et al., 2017; Tilstone et al., 2021).

2.3.2 Secchi depth

For all four AMT cruises, a 30 cm Secchi disk was attached to the profiling rig that was deployed from the aft-deck winch of the RRS *James Clark Ross* (Figure 2A). Attaching the disk to the profiling rig minimised drift in all but extreme circumstances (e.g. very strong currents at the equator). The profiling rig was lowered from the surface down to around 250 m depth, and brought up from this depth to the surface, at a constant speed (that sometimes varied between down and up casts). In all but a few cases (where only one up and down cast was conducted), the profiling rig was deployed twice (two casts), and consequently, the depth of the disappearance and reappearance of the disk were measured twice (four measurements of Secchi depth at each station).

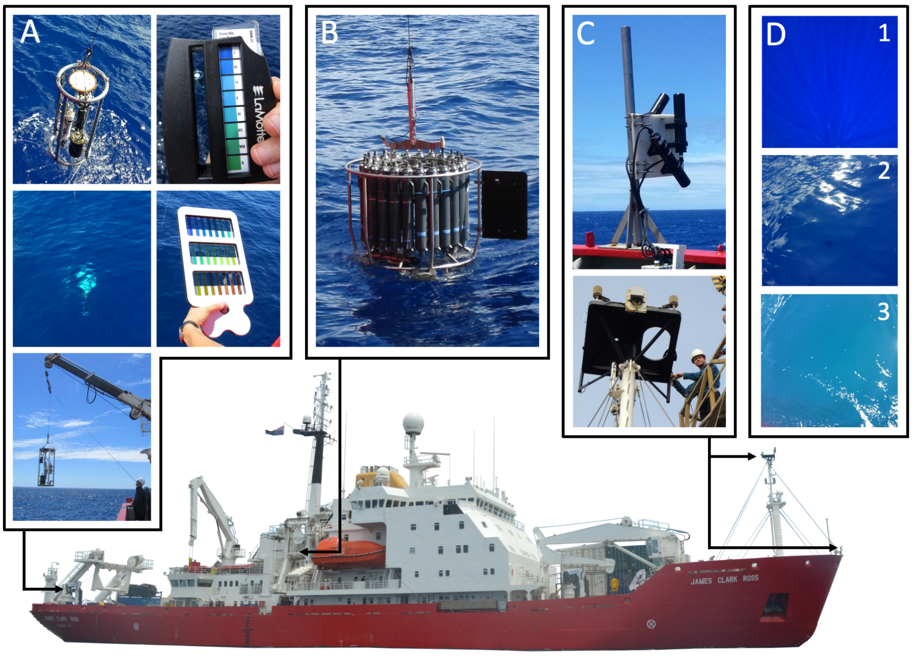

FIGURE 2
Instrumentation used on-board the RRS *James Clark Ross*. **(A)** Secchi disk attached to the optics rig and deployed from the aft-deck winch, with the Forel-Ule colour scales, the LaMotte scale used on AMT23-28, and that described in Novoa et al. (2014) and used on AMT25-28. **(B)** Conductivity, Temperature and Depth (CTD) Niskin Rossette used to collect water samples of Chl-a, measure PAR and beam attenuation, deployed on the CTD winch located towards the centre of the ship. **(C)** Satlantic Hyperspectral (HyperSAS) radiometer set-up (photos from AMT23), with the two radiance sensors positioned on the very bow of the ship (and tilt and heading sensor is shown vertically), and the downwelling irradiance sensor positioned vertically on the met-platform on the ship's foremast (bottom figure showing it being attached on AMT23). **(D)** Photos of water colour collected on AMT23, in (1) the centre of the South Atlantic gyre, (2) the edge of the North Atlantic gyre, and (3) in the South Subtropical Convergence Zone, illustrating visual transitions from blue to blue-green waters.

Over the four AMT cruises, the Secchi depth was measured using three different techniques. When available (principally on AMT26 and 28), a Wire Length Measurement sensor (WLM) was attached to the aft-deck winch that calculated the length of wire released by the winch. This was zeroed when the disk was at the surface, and when the disk disappeared and reappeared the observer shouted out to the winch operator who shouted back the depth, which was logged. For cases where the WLM was not available (principally on AMT23 and AMT25), the Secchi depth was measured using two alternative techniques. Firstly, and considering the profiling rig was lowered and retrieved at a set speed, the observer logged the time when the disk was at the surface, when it disappeared (or reappeared), and when the 50 m, 100 m and 150 m tags on the wire were at the surface, and did a linear interpolation to get the Secchi depth. Secondly, a watch was calibrated to the same time on a pressure sensor (CTD) on the profiling rig, and the Secchi depths were extracted by matching the time of disappearance and reappearance, with the depth from pressure sensor, correcting for distance between pressure sensor and disk. Both methods were found to agree well with a mean difference of 0.48 m (Figure 3A).

At each station, all Secchi depth data collected were averaged (denoted z_{SD}) and a standard deviation computed as a proxy of the uncertainty in the Secchi depth (average was 2.7 m, with an average percent deviation (standard deviation divided by z_{SD}) of 10%). Where possible, different participants (scientists and crew) contributed to data collection (see acknowledgements to this paper) so as to include variability between individuals. When measuring the Secchi depth, and for clear sky conditions, the measurement was often conducted on the sunny side of the ship, as there was a preference to deploy the profiling rig on the sunny side (for the Photosynthetically Available Radiation (PAR) sensor on the main CTD). At low latitudes in the tropics (especially near the equator), the sun zenith angle was very low at the noon stations (sun high in the sky), making it difficult to avoid the sun (i.e. both sides of the ship were sunny). The observer often took notes of the conditions, that were subsequently used to indicate if the sky was fully overcast or clear/partial cloud (when reported, denoted VCI), and when sun glint was reported as a problem when collecting data (denoted VGI).

2.3.3 Forel-Ule colour

Two different Forel-Ule (F) scales were used in the study (shown in Figure 2A). A LaMotte scale was used on all four AMT cruises, which consists of a simple printed scale encased in perspex, showing F colours 1, 3, 4, 5, 6, 7, 8, and 9 (missing 2). Additionally, on AMT25, AMT26 and AMT28, the Forel-Ule scale presented in Novoa et al. (2014), and kindly provided by Marcel Wernand, was also used (with all F numbers). At the majority of stations, four F measurements were collected, for the two up and down casts (at stations where only one cast was made, two measurements were collected). The measurements were collected by comparing the colour of the disk at roughly half the Secchi depth (approximated based on *a priori* knowledge). As with the Secchi depth, many participants (scientists and crew) contributed to Forel-Ule data collection (see acknowledgements to this paper), many at the same time using the different scales, so as to include

TABLE 1 A summary of the datasets collected and used in the study.

Variable	Acronym	Units	Section description	*N* stations sampled
Chlorophyll-a concentration	Chl-a	mg m^{-3}	2.3.1	127
Secchi depth	z_{SD}	m	2.3.2	127
Visual cloud index	VCI	dimensionless	2.3.2	127
Visual glint index	VGI	dimensionless	2.3.2	127
Forel-Ule colour (LaMotte, 1/2 z_{SD})	$F_{D,L}$	dimensionless	2.3.3	127
Forel-Ule colour (N14*, 1/2 z_{SD})	$F_{D,N}$	dimensionless	2.3.3	102
Forel-Ule colour (LaMotte, infinite)	$F_{I,L}$	dimensionless	2.3.3	127
Forel-Ule colour (N14*, infinite)	$F_{I,N}$	dimensionless	2.3.3	102
Forel-Ule colour (App, infinite)	$F_{I,A}$	dimensionless	2.3.3	37
Diffuse attenuation for PAR (10%)	K_d	m^{-1}	2.3.4	106
Euphotic depth	z_p	m	2.3.4	118
Beam attenuation (650 nm)	c	m^{-1}	2.3.4	119
Remote sensing reflectance	R_{rs}	sr^{-1}	2.3.5	101
Maximum blue-green R_{rs} ratio	$\frac{R_{rs}(MB)}{R_{rs}(G)}$	dimensionless	2.3.5	101
HyperSAS cloud index	$\frac{L_i(750)}{E_s(750)}$	sr^{-1}	2.3.5	125
Wind speed	w_s	m s^{-1}	2.3.6	125
Sea surface temperature	SST	degrees C	2.3.6	127
Sea surface salinity	SSS	PSU	2.3.6	127
Solar zenith angle	θ	degrees	2.3.6	127
Pitch standard deviation	PSD	degrees	2.3.6	125
Roll standard deviation	RSD	degrees	2.3.6	125
Photosynthetically Available Radiation	PAR	μmol m^{-2} s^{-1}	2.3.6	124

* N14 refers to the Novoa et al. (2014) Forel-Ule colour scale.

variability between individuals. At each station, and separately for each scale, all measurements collected were averaged and a standard deviation computed as a proxy of the uncertainty. Comparisons between the colour of the disk using the LaMotte scale ($F_{D,L}$) and the colour of the disk using the Novoa et al. (2014) scale ($F_{D,N}$) are shown in Figure 3B, and are in reasonable agreement ($r^2 = 0.75$), but with the LaMotte scale generally higher than the Novoa et al. (2014) scale ($\delta = 0.64$). These measurements were also converted from the colour of the water above the disk at half the Secchi depth, to the colour of infinite water ($F_{I,L}$ and $F_{I,N}$, where I refers to the conversion to infinite colour), using the algorithm of Pitarch (2017) and a lower boundary of $F = 0$ (Pitarch et al., 2019). This method consists of converting F to hue angle, applying a polynomial relationship to convert the hue angle of the water above the disk at half the Secchi depth to the hue angle of infinite water, then converting back to F (Pitarch, 2017). For stations on AMT26, the F colour was also measured using the EyeOnWater-Colour mobile phone app (www.eyeonwater.org; Novoa et al., 2015; Busch et al., 2016; Malthus et al., 2020), for infinite water (not using the disk, denoted $F_{I,A}$), which gave a single number for each station. The measurement was collected in a direction away from sun glint (typically between 100-170 degrees azimuth). Comparisons between $F_{I,A}$ and $F_{I,N}$ on AMT26 are shown in Figure 3C. The $F_{I,N}$ data are in good agreement with $F_{I,A}$, with a mean difference of −0.3 compared with −1.4 for the unconverted data ($F_{D,N}$), supporting the conversion method.

2.3.4 Diffuse and beam attenuation

On all four AMT cruises, a WET Labs C-Star, designed to measure beam attenuation (c) at 650 nm, was attached to the base of the main CTD, and a Biospherical QCD-905L sensor, designed to measure downwelling PAR, was attached to the top of the CTD (Figure 2B). Both sensors provided vertical profiles of c and PAR, for stations where the main CTD was deployed. Data for downcasts were extracted from the CTD logger, which was preferred over upcast data when bottles were fired (CTD stopped to shut the Niskin bottles at discrete depths on the upcast).

Data for c were processed as follows: firstly, a cruise specific minimum value of c derived from all profiles used for each cruise, were subtracted from the profile, this minimum value (which varied among cruises) represented that of pure water beam attenuation [c_w(650)] and any residual biases in the calibration; secondly, values of c_w(650) (c_w=b_w+a_w, where a_w is the absorption coefficient of pure water,

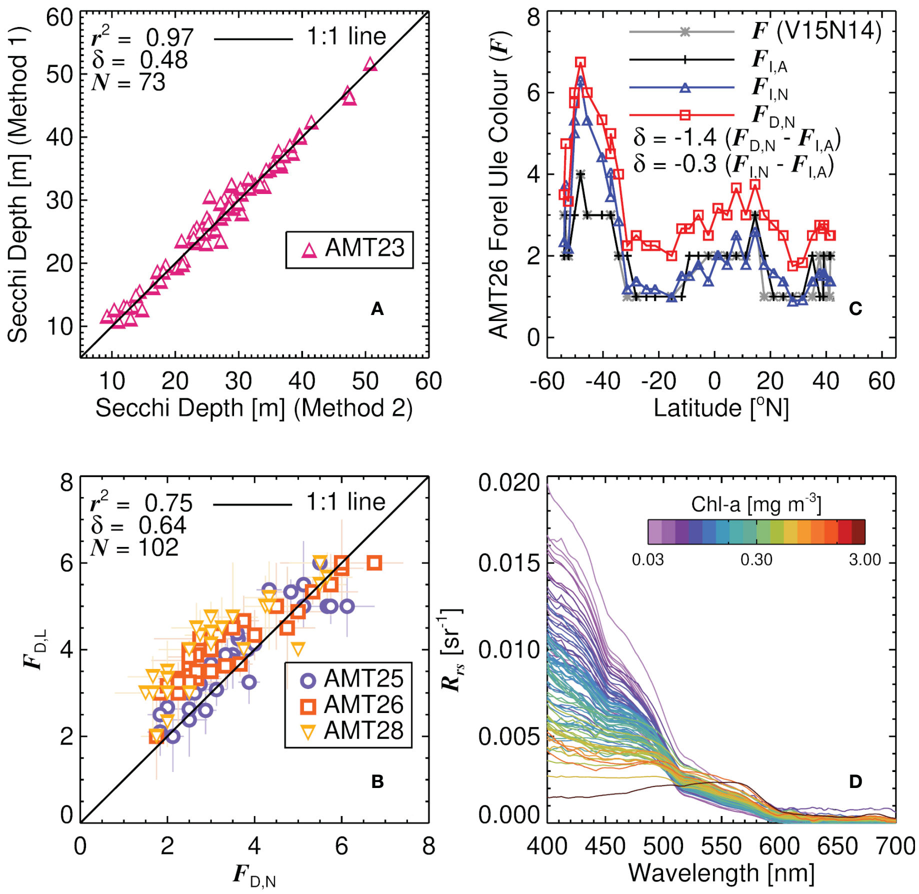

FIGURE 3

(A) Comparison between two methods for measuring the Secchi depth on AMT23. Method 1 involved linear interpolation, logging the time when the disk was at the surface, when it disappeared (or reappeared), and when the 50 m, 100 m and 150 m tags on wire were at the surface. Method 2 involved using a watch which was calibrated to the same time of a pressure sensor (CTD) on the profiling rig, and logging the time of disappearance and reappearance (see Section 4.3.2 for further details). Note that data are shown for all the reappearances and disappearances logged (hence there are more samples (*N*) than stations on AMT23). **(B)** Comparison between the Forel-Ule colour (*F*) using the method of Novoa et al. (2014) ($F_{D,N}$) and the LaMotte method ($F_{D,L}$), for the colour of the disk at half the Secchi depth on AMT25, AMT26 and AMT28. **(C)** AMT26 latitudinal transects of *F* using the method of Novoa et al. (2014), for the colour of the disk at half the Secchi depth ($F_{D,N}$), for the colour of the disk at half the Secchi depth but converted to infinite colour using the method of Pitarch (2017) ($F_{I,N}$), the Forel-Ule colour of infinite water measured using the EyeOnWater-Colour mobile phone app (Busch et al., 2016) ($F_{I,A}$), and estimated *F* from R_{rs} using the methods of van der Woerd and Wernand (2015) and Novoa et al. (2014) (V15N14). **(D)** Remote sensing reflectance data used in the study (101 stations) plotted as a function of wavelength and coloured according to the Chl-a concentration at the station. r^2 is the squared Pearson correlation coefficient, δ the mean difference (bias) and *N* the number of samples.

taken from Pope and Fry (1997), and b_w the scattering coefficient of pure water, which was computed as a function of sea surface temperature (SST) and salinity (SSS) at each station following Zhang and Hu (2009) and Zhang et al. (2009), see Section 4.3.6 for details on how SST and SSS were collected) were added back to the profile, which resulted in calibrated profiles of *c*. Data were extracted from between the surface and Secchi depth, and median values of *c* and standard deviations (range of distribution that lies within the percentiles of one standard deviation) were computed. Data for *c* were only retained if the coefficient of variation for the samples in the Secchi depth layer was less than 0.04. Considering this method assumes $c_p(650)$ and $c_y(650)$ are close to zero at depth (*y* representing coloured dissolved organic matter), which may not always hold, it is possible the *c* values are slightly biased low.

Vertical profiles of PAR were used to compute the diffuse attenuation coefficient of PAR (K_d). Two values of K_d were derived for each profile, $K_d(10\%)$ in the layer between the surface and the 10% light level (defined as $2.3/K_d$), and $K_d(1\%)$ in the layer between the surface and the 1% light level (defined as $4.6/K_d$). The latter was used to compute the euphotic depth (z_p=4.6/K_d(1%)), and the former was used to represent K_d (i.e., $K_d = K_d(10\%)$) in the Secchi depth layer (Lee et al., 2018c). Both were computed as follows: firstly, the 10% and 1% light depth levels were approximated from the surface Chl-a concentration using an AMT-calibrated model (Brewin et al., 2017); PAR data above these depth levels were extracted and initial values of K_d for the two depth levels were derived by fitting a Beer-Lambert law (acknowledging this assumes inherent optical properties to be constant in the layer) to the PAR and depth data (using IDL function ROBUST_LINEFIT.pro, an outlier-resistant fitting function); next, these initial values were used to recompute the 10% land 1% light depth levels, and the data were re-fitted to PAR and depth data above these light depth levels, to derive final values for K_d and z_p. Standard deviations for K_d were also extracted from the fits. To remove dubious data (from unusual profiles), K_d and z_p for a given profile were only retained if the r^2 between log(PAR) and depth, above the respective light level, was greater than 0.85.

2.3.5 Remote sensing reflectance data and ocean colour models

The same Satlantic/Seabird Hyperspectral (HyperSAS) radiometer package was installed on the RRS *James Clark Ross* for all four AMT cruises. Sensors were calibrated prior to the start of each cruise. The hyperspectral downwelling irradiance (E_s) sensor was attached to the met-station on the ship's foremast (Figure 2C), to minimise obstructions from the ship shading the sensor. The two radiance sensors, measuring total water leaving radiance (L_t) and sky radiance (L_i), were mounted at the identical azimuth angle, and pointed at the water surface at an angle of 40° from nadir and zenith respectively (Figure 2C). Data were collected at a frequency of 1-5 seconds, during day light hours.

Hyperspectral (at 2 nm resolution) remote sensing reflectance data (R_{rs}) were computed using the method described in Lin et al. (2022). Briefly, this involved: interpolating the dark counts (collected at 10-minute intervals) for each sensor, to the times of the light data, and subtracting them from the light measurements; interpolating the (dark-count-corrected) light data to a common set of wavelengths (350 to 860, at 2 nm resolution) and a common time (based on the sensor with the slowest integration time); interpolating auxiliary ship data (wind, latitude, longitude, time, wind, heading, tilt, pitch, and roll) used for data filtering to the same time as the light measurements; filtering data according to a set criteria (<5° tilt, removing sun glint using the near-infrared signal, discarding data with high solar zenith angle (>80°) and relative azimuth angles <100 and >170°, and any spectra with negative values at 443 nm); and computing R_{rs} by first computing water leaving radiance according to L_w=L_t−ρL_i−ΔL, where ρ is the sea-surface reflectance used to correct for the sun and sky light reflected by the sea surface, and ΔL is a spectrally-flat residual term representing contributions due to glint, foam, sea spray and whitecaps (both derived using an non-linear optimization technique), then dividing L_w by E_s to get R_{rs}. Further details of the processing are provided in Lin et al. (2022). In addition to R_{rs}, the method of Lin et al. (2022) also included a full uncertainty propagation method, following the Law of Propagation of Uncertainty, and provides robust uncertainty estimates with each R_{rs} measurement (see Lin et al. (2022) for further details).

At each station for which R_{rs} data passed the filtering criteria, data were extracted between 20 minutes prior to and 60 minutes after the start time of the station (stations were typically >1 hour in duration). Data 20 minutes prior were included, as at this point, the ship slows down to arrive at the station and reorientates its position, allowing data to be available (during the orientation process) for cases where the ship's final position (relative azimuth angle) at the station was not ideal for data collection. All 2-min binned R_{rs} data available during this period at each station were analysed and the spectra with the lowest average R_{rs} uncertainty between 400-600 nm were selected (data outside the range of 0 and 20% uncertainty were excluded). This resulted in R_{rs} data at 101 stations. R_{rs} data were bidirectionally corrected using the method of Lee et al. (2011) and are plotted in Figure 3D and coloured according to the Chl-a concentration at the station. A proxy of sky conditions was also derived using the ratio of $L_i(750)/E_s(750)$, using data processed over a one hour duration after the start of the station following the method of Brewin et al. (2016), removing any unrealistic data where the ratio was $\geq 1/\pi$. Median values of $L_i(750)/E_s(750)$ were extracted from each station as were standard deviations (defined as the range of distribution that lies within the percentiles of one standard deviation). Clear skies are known to be approximately 0.02 (Mobley, 1999) and fully overcast in the order 0.3 (Ruddick et al., 2006). To cross-check with the notes from the Secchi disk observations, we computed the median of all $L_i(750)/E_s(750)$ data where the observer had reported overcast skies and found that to be 0.264 (± 0.083) and the median of all other stations to be 0.046 (± 0.068), showing consistency in the two datasets.

The *in-situ* R_{rs} data were used to compute the maximum blue-green band ratio ($\max\{R_{rs}(443), R_{rs}(490), R_{rs}(510)\}/R_{rs}(555)$), hereafter denoted $R_{rs}(\mathrm{MB})/R_{rs}(\mathrm{G})$ that was subsequently used to show changes in the relationship between the maximum band ratio and Chl-a concentration, using the NASA OC4v6 algorithm (NASA, 2010). Additionally, Secchi depth (z_{SD}) was estimated from R_{rs} and the solar zenith angle (see Section 2.3.6) data using the algorithms of Lee et al. (2015) and Jiang et al. (2019). An initial step in the computation of z_{SD} using both algorithms, is the estimation of inherent optical properties from R_{rs}, using the Quasi-Analytical Algorithm (QAA) (Lee et al., 2002, 2009). Here, we incorporated a Raman scattering correction on R_{rs} prior to inversion, following Pitarch et al. (2020), and used updates on the parameters that relate non-water absorption at 555 nm to R_{rs}, as described in Pitarch and Vanhellemont (2021). The Forel-Ule colour (F) was estimated from hyperspectral R_{rs} data by computing the hue angle using the approach of van der Woerd and Wernand (2015) and then converting the hue angle into F following Novoa et al. (2014).

2.3.6 Auxiliary observations

A series of auxiliary measurements were averaged (mean of 90 percentile distribution) over the duration of each station (1 h after the start time of the station), and standard deviations computed (range of distribution that lies within the percentiles of one standard deviation). These data include: wind speed (w_s) measurements, which were collected continuously from the anemometer located on the met-platform of the ship's foremast (Figure 2C), and corrected for ship direction, course and speed (following https://www.coaps.fsu.edu/woce/truewind/true-IDL.html); SST and SSS, when not available from the main CTD (taken as the median temperature and salinity values in layer between surface and z_{SD}), were extracted from continuous measurements collected by the ships underway CTD (SBE45); solar zenith angles (θ) were computed as a function of time and location of the stations; standard deviations in the pitch (PSD) and roll (RSD) of the ship were taken from continuous measurements collected by the ship's gyro system; and above-surface PAR data were collected from the PAR sensor (Kipp & Zonen) located on the met-platform of the ship's foremast.

In addition to AMT observations, we also used two databases of Secchi depth and Forel-Ule colour measurements, collected globally since 1890, from the US National Oceanographic Data Center (NODC) and from CalCOFI. NODC data were taken from the dataset assembled by Boyce et al. (2012) and are designed to represent global, case-1 (open ocean) conditions. Boyce et al. (2012) describe the NODC data mining and processing. Briefly, nearshore, shallow and unrealistic data were eliminated, and remaining data binned into one-by-one degree geographical cells. High sediment and CDOM-laden measurements were removed by eliminating Secchi disk depth measurements less than 6 m. Forel-Ule measurements were constrained to values between 2 and 10. The total amount of NODC Secchi disk and Forel-Ule data used was 46,180 data points. The data are available through the NODC website (https://www.ncei.noaa.gov/data/oceans/woa/WOD/DATA_SUBSETS/). The CalCOFI site is in clear waters off the Californian coastline, and has been operating since 1949. Sampling was made following a defined grid geographically distributed between 20°N and 40°N, and measurements were collected at a relatively consistent rate across the seasons. Data are downloadable from the project site (https://calcofi.org/). Matched Secchi disk and Forel-Ule data exists between 1969 and 1972 and then from 1986 to 1998, and amounts to a total of 2046 matched data points.

3 Results and discussion

3.1 Comparison of optical measurements on AMT

Figure 4 shows a comparison of optical measurements collected on the four AMT cruises. Consistent with previous understanding (e.g., Wernand, 2011), we see tight inverse relationships between Secchi depth (z_{SD}) and Forel-Ule colour (F), with F explaining between 73-83% of the variance in z_{SD}, depending on the colour scale used (see Figures 4A–D). For the colour of the disk (at 1/2 the Secchi depth, $F_{D,L}$ and $F_{D,N}$), and over the range of data collected, there appears to be a log-linear relationship between variables (Figures 4A, B). For infinite depth, the LaMotte scale ($F_{D,L}$) also show a log-linear relationship (Figure 4C), but the Novoa et al. (2014) scale ($F_{I,N}$) is closer to a log-log relationship, consistent with earlier models (Wernand, 2011, see Figure 4D), albeit with differences in parameters. Figure 5 overlays the AMT data collected using the Novoa et al. (2014) scale onto historical datasets from NODC and

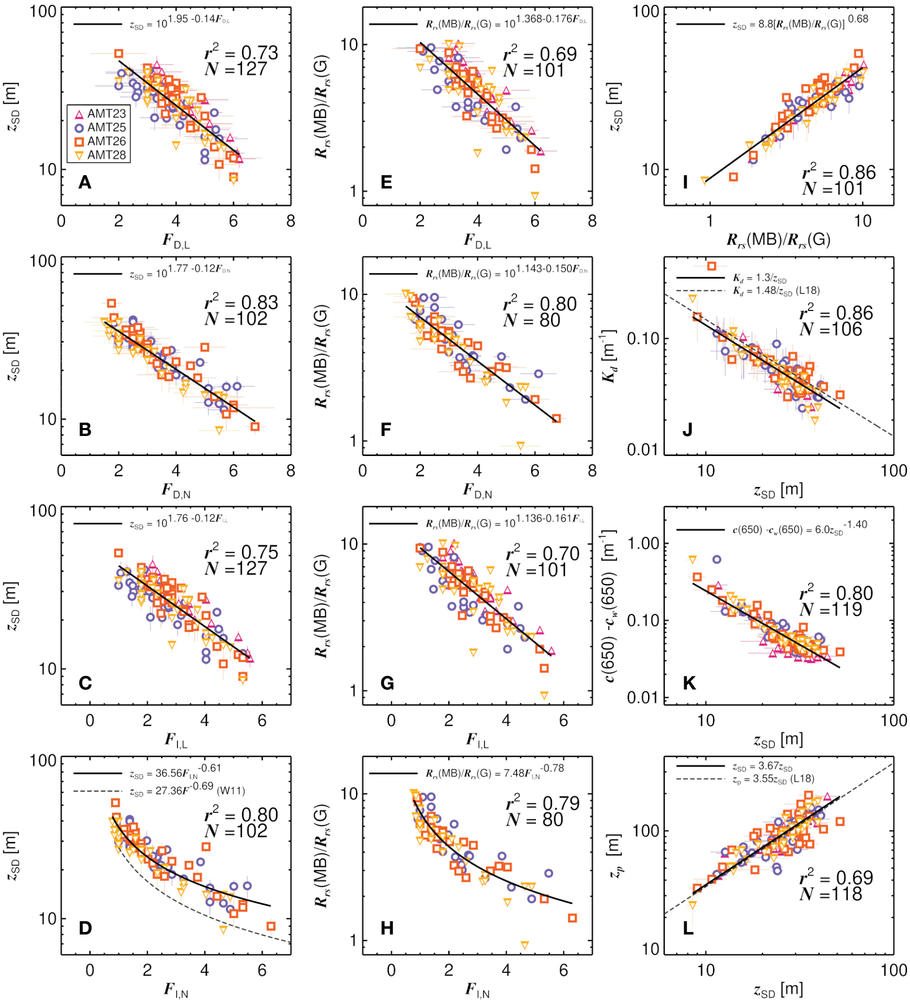

FIGURE 4
Comparison of optical measurements collected on the four AMT cruises. **(A–D)** Secchi depth (z_{SD}) versus Forel-Ule colour (F), with subscripts D being colour of disk, I colour of infinite waters, L the LaMotte scale, and N the scale of Novoa et al. (2014). **(E–H)** Maximum blue-green R_{rs} ratio (R_{rs}(MB)/R_{rs}(G)) versus Forel-Ule colour (F). **(I)** Secchi depth (z_{SD}) versus R_{rs}(MB)/R_{rs}(G). **(J)** Diffuse attenuation for PAR (10% light level, K_d) versus Secchi depth (z_{SD}). **(K)** Beam attenuation (650 nm) (c) minus that of pure water (c_W) versus Secchi depth (z_{SD}). **(L)** Euphotic depth (z_p) versus Secchi depth (z_{SD}). Solid lines are models fitted to the data. Dashed lines are earlier models, with W11 referring to the model of Wernand (2011) and L18 referring to models from Lee et al. (2018c).

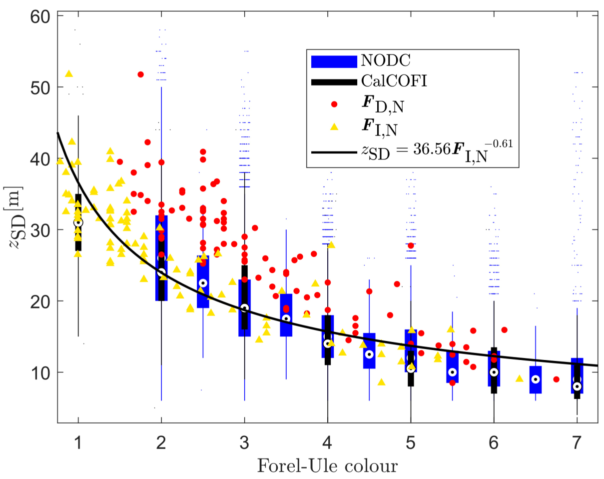

FIGURE 5
Comparison of Secchi depth (z_{SD}) versus Forel-Ule colour (F) data collected on AMT (red circles and yellow triangles) with historical datasets from NODC and CalCOFI. Note that $F_{I,N}$ is a synthetic quantity that derives from $F_{D,N}$ and the model in Pitarch (2017).

CalCOFI. We find the relationship between z_{SD} and infinite colour ($F_{I,N}$) on AMT to be in closer agreement with relationships between z_{SD} and F seen in both historical datasets, when compared with data on z_{SD} and the colour of the disk at 1/2 the Secchi depth ($F_{D,N}$). Particularly for lower F values (1-3). This result suggests that the majority of the Forel-Ule historical data may have been collected by looking directly at the colour of the water, rather than at the colour of the water above the disk at $1/2z_{SD}$, as other literature has implied (Wernand and van der Woerd, 2010a). Further investigation is needed to ascertain if this is in fact correct, perhaps by reviewing historical information on the protocols used for collecting these earlier Forel-Ule measurements.

On AMT, relationships between the maximum band ratio (R_{rs}(MB)/R_{rs}(G)) and F (Figures 4E–H) are remarkably consistent with the relationships seen between z_{SD} and F (Figures 4A–D), with F explaining between 69-80% of the variance in R_{rs}(MB)/R_{rs}(G). This is due to a tight relationship observed between z_{SD} and R_{rs}(MB)/R_{rs}(G) (Figure 4I). Inverse relationships between both diffuse and beam attenuation and z_{SD} were also observed (Figures 4J, K), with the former (K_d=1.3/z_{SD}) in good agreement with the relationship proposed by Lee et al. (2018c), (Figure 4J, K_d = 1.48/z_{SD}), with differences possibly related to environmental conditions, considering the Lee et al. (2018c) relationship is for a fixed solar zenith angle (θ) of 30 degrees, and a fixed wind speed (w_s) of 5 ms^{-1}. We also see good agreement between the euphotic depth (z_p) and z_{SD} (Figure 4L, z_p=3.67z_{SD}), with no significant difference to the relationship proposed by Lee et al. (2018c) (where z_p is equal to 3.55 (± 0.15) times z_{SD}).

3.2 Relationships between surface Chl-a and optical properties on AMT

Figure 6 shows a comparison of Chl-a and optical measurements collected on the four AMT cruises. We find z_{SD} to be tightly correlated with Chl-a, explaining around 85% of its variance (r^2 =0.85, on log$_{10}$-transformed variables). The relationship between z_{SD} and Chl-a is in good agreement with published models (Table 2; Morel et al., 2007; Boyce et al., 2012; Lee et al., 2018c). Systematic differences (accuracy, δ) are close to zero for the models of Morel et al. (2007) and Lee et al. (2018c), with the a small bias for the model of Boyce et al. (2012) (Table 2). The models of Boyce et al. (2012) and Lee et al. (2018c) have slightly better precision (Δ, Table 2) than the Morel et al. (2007) model. Fitting a power-law model to the data [Table 2, the same mathematical model to that of Lee et al. (2018c) and Boyce et al. (2012)] reduces the bias (δ) to zero, with no improvement in precision (Δ), and obtained parameters are found not to be significantly different to those of Lee et al. (2018c) (Table 2). Statistical tests indicate that the retrieval of surface Chl-a from z_{SD} is comparable, in precision and accuracy, to retrievals of Chl-a using satellite ocean colour algorithms in the Atlantic Ocean (Brewin et al., 2016; Tilstone et al., 2021). Residuals in log$_{10}$(Chl-a), between the fitted power model and Chl-a data, were positively correlated with wind speed and R_{rs}(MB)/R_{rs}(G), and inversely correlated with log$_{10}$(Chl-a) (Table 3). The latter two (which are inversely related, see Figure 6B) perhaps suggesting the mathematical formulation of the relationship (power function) may need further consideration, with there being a slight tendency for the model to overestimate log$_{10}$(Chl-a) at lower concentrations and underestimate it at higher concentrations. Other fitting functions were explored, including log-linear and polynomial fits (data not shown), but they also showed the same tendency, suggesting this may be related to the distribution of the dataset. The positive correlation between residuals and wind speed (Table 3), suggested that for the same Chl-a, as the wind speed increases, the observer sees a shallower Secchi depth. This is consistent with theory on the impact of wind speed on the apparent contrast of the disk (Preisendorfer, 1986). However, multi-linear regression (not shown) of log$_{10}$(Chl-a) as a function of both log$_{10}$(z_{SD}) and wind speed, yielded no significant increase in r^2 over log$_{10}$(z_{SD}) alone (Z-test, p>0.05), suggesting any such effect is minor. No relationship was found between the VGI and VCI, and the residuals in log$_{10}$(Chl-a), between the fitted power model and Chl-a data.

Of all the optical proxies tested, R_{rs}(MB)/R_{rs}(G) was found to explain the greatest variance in Chl-a (Figure 6B, r^2 = 0.89, on log$_{10}$-transformed variables). The NASA OC4v6 algorithm was found to have a tendency to underestimate Chl-a in the Atlantic (Table 2, δ = −0.109), consistent with earlier work (Szeto et al., 2011). A retuning of the OC4v6 algorithm removed this bias, and showed improvements in both precision (Δ) and r^2 (Table 2). The retuning was also found to show a strong linear dependency (on log$_{10}$-transformed data) between variables, suggesting a simpler (more parsimonious) linear model to be more appropriate than a 4th order polynomial on this AMT dataset, which yielded statistically similar results to the retuned polynomial (OC4 Table 2). We found a small dependency in the residuals of this linear model and log$_{10}$(Chl-a), similar to the z_{SD} fits and likely related to data distribution, but no other dependency between residuals and other environmental variables were observed (Table 3). R_{rs}(MB)/R_{rs}(G) was shown to produce the highest r^2 and lowest Δ of all variables tested (Table 2). R_{rs}(MB)/R_{rs}(G) only performs marginally better as a predictive variable of Chl-a, than z_{SD} (Table 2), on the AMT.

All four Forel-Ule datasets ($F_{D,L}$, $F_{D,N}$, $F_{I,L}$ and $F_{I,N}$) were positively correlated with Chl-a, explaining between 71-81% of the variance in log$_{10}$-transformed Chl-a (Figures 6C–F). The Novoa et al.

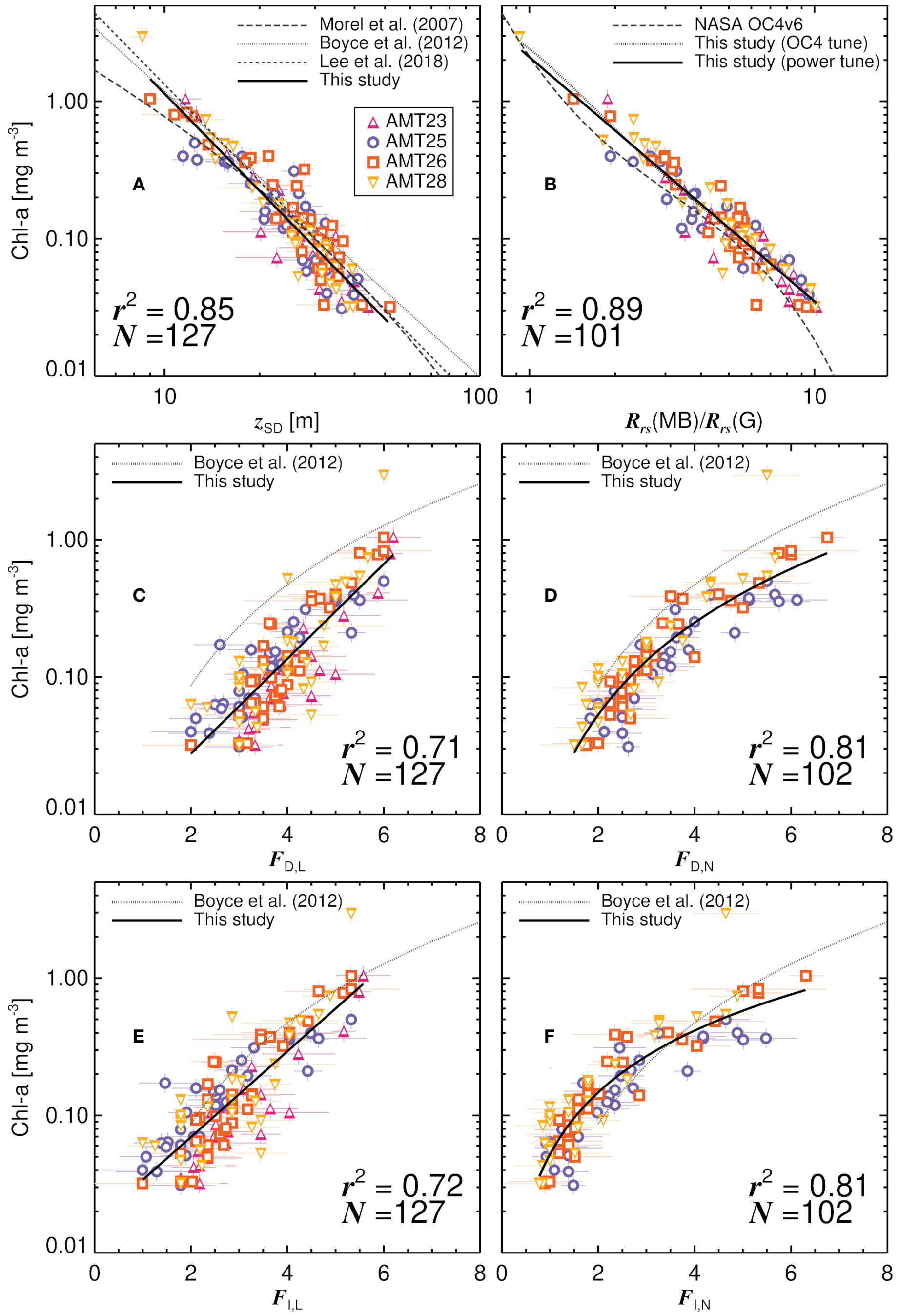

FIGURE 6

Relationship between historical and modern optical properties and the chlorophyll-a concentration (Chl-a) on the four AMT cruises. **(A)** Comparison of Chl-a and Secchi depth (z_{SD}). **(B)** Comparison of Chl-a and maximum blue-green R_{rs} ratio (R_{rs}(MB)/R_{rs}(G)). **(C)** Comparison of Chl-a and Forel-Ule colour using the LaMotte scale and with reference to the colour of the disk at 1/2z_{SD} ($F_{D,L}$). **(D)** Comparison of Chl-a and Forel-Ule colour using the Novoa et al. (2014) scale and with reference to the colour of the disk at 1/2z_{SD} ($F_{D,N}$). **(E)** Comparison of Chl-a and Forel-Ule colour using the LaMotte scale and with reference to infinite water ($F_{I,L}$). **(F)** Comparison of Chl-a and Forel-Ule colour using the Novoa et al. (2014) scale and with reference to infinite water ($F_{I,N}$).

(2014) scale data ($F_{D,N}$, $F_{I,N}$) were found to correlate more tightly to Chl-a (explaining around 81% of the variance) than the LaMotte scale data (explaining around 71% of the variance), with the Novoa et al. (2014) scale data predicting Chl-a with the highest accuracy using a power function (linear-function in $\log_{10}$ space), consistent with the model of Boyce et al. (2012), with the LaMotte scale data best described using a log-linear relationship (Figures 6C–F; Table 2). For Forel-Ule data greater than 2, the lower limit of the range of data in which the Boyce et al. (2012) model was trained on, the Boyce et al. (2012) model is seen to overestimate Chl-a when using $F_{D,L}$ and $F_{D,N}$ as input (Figures 6C, D; Table 2), with better agreement (biases (δ) closer to zero) when using $F_{I,L}$ and $F_{I,N}$ as input (Figures 6E, F; Table 2). This is consistent with the Forel-Ule infinite colour data collected on AMT being in closer agreement with historical datasets than data collected on the colour of the water above the disk at 1/2z_{SD} (Figure 5), considering the Boyce et al. (2012) model was parameterised on these historical data. As with the z_{SD} and R_{rs}(MB)/R_{rs}(G) models, there is a dependency in Forel-Ule model

TABLE 2 Algorithms tested to predict Chl-a [mg m^{-3}] (dependent variable) from historic and modern optical measurements (independent variable, models tuned to data, denoted "This Study" in Table 2).

Independent variable	Reference	Algorithm	r^{2} *	Δ *	δ *	N
z_{SD}	Morel et al. (2007)$^{\$}$	$z_{SD} = 10^{8.5-12.6\log_{10}(\text{Chl}-\text{a})+7.36\log_{10}(\text{Chl}-\text{a})^2-1.43\log_{10}(\text{Chl}-\text{a})^3}$	0.85	0.162	0.026	127
z_{SD}	Boyce et al. (2012)	Chl-a $= \alpha {z_{SD}}^{\beta}$ $(\alpha = 143.29,\ \beta = -2.082)$	0.85	0.157	0.124	127
z_{SD}	Lee et al. (2018c)	Chl-a $= \alpha {z_{SD}}^{\beta}$ $(\alpha = 293.9,\ \beta = -2.345)$	0.85	0.152	0.068	127
z_{SD}	This Study$^{\#}$	Chl-a $= \alpha {z_{SD}}^{\beta}$ $(\alpha = 253.7[201.7 \leftrightarrow 319.1],\ \beta = -2.349[-2.432 \leftrightarrow -2.265])$	0.85	0.152	−0.001	127
$\frac{R_{rs}(MB)}{R_{rs}(G)}$	NASA (2010, OC4v6)	Chl-a $= 10^{0.3272-2.9940\log_{10}(\frac{R_{rs}(MB)}{R_{rs}(G)})+2.7218\log_{10}(\frac{R_{rs}(MB)}{R_{rs}(G)})^2-1.2259\log_{10}(\frac{R_{rs}(MB)}{R_{rs}(G)})^3-0.5683\log_{10}(\frac{R_{rs}(MB)}{R_{rs}(G)})^4}$	0.87	0.139	−0.109	101
$\frac{R_{rs}(MB)}{R_{rs}(G)}$	This Study (OC4)$^{\#}$	Chl-a $= 10^{0.3822-1.6372\log_{10}(\frac{R_{rs}(MB)}{R_{rs}(G)})-1.8880\log_{10}(\frac{R_{rs}(MB)}{R_{rs}(G)})^2+3.4805\log_{10}(\frac{R_{rs}(MB)}{R_{rs}(G)})^3-1.8068\log_{10}(\frac{R_{rs}(MB)}{R_{rs}(G)})^4}$	0.89	0.128	0.000	101
$\frac{R_{rs}(MB)}{R_{rs}(G)}$	This Study$^{\#}$	Chl-a $= \epsilon\left(\frac{R_{rs}(MB)}{R_{rs}(G)}\right)^{\gamma}(\epsilon = 2.10[1.87 \leftrightarrow 2.37],\ \gamma = -1.78[-1.84 \leftrightarrow -1.72])$	0.89	0.129	0.003	101
$F_{D,L}$	Boyce et al. (2012)$^{\%}$	Chl-a $= \tau {F_{D,L}}^{\eta}(\tau = 0.016,\ \eta = 2.44)$	0.65	0.243	0.510	127
$F_{D,L}$	This Study$^{\#}$	Chl-a $= 10^{\upsilon+\varepsilon F_{D,L}}(\upsilon = -2.246[-2.289 \leftrightarrow -2.203], \xi = 0.345[0.326 \leftrightarrow 0.364])$	0.71	0.215	−0.001	127
$F_{D,N}$	Boyce et al. (2012)$^{\%}$	Chl-a $= \tau {F_{D,N}}^{\eta}(\tau = 0.016, \eta = 2.44)$	0.79	0.176	0.260	93
$F_{D,N}$	This Study$^{\#}$	Chl-a $= \tau {F_{D,N}}^{\eta}(\tau = 0.0114, [0.0103 \leftrightarrow 0.0126], \eta = 2.23[2.21 \leftrightarrow 2.25])$	0.81	0.176	−0.003	102
$F_{I,L}$	Boyce et al. (2012)$^{\%}$	Chl-a $= \tau {F_{I,L}}^{\eta}(\tau = 0.016, \eta = 2.44)$	0.70	0.213	0.189	101
$F_{I,L}$	This Study$^{\#}$	Chl-a $= 10^{\upsilon+\upsilon F_{I,L}}(\upsilon = -1.781[-1.824 \leftrightarrow -1.738], \xi = 0.345[0.292 \leftrightarrow 0.331])$	0.72	0.210	−0.001	127
$F_{I,N}$	Boyce et al. (2012)$^{\%}$	Chl-a $= \tau {F_{I,N}}^{\eta}(\tau = 0.016, \eta = 2.44)$	0.59	0.221	−0.035	41
$F_{I,N}$	This Study$^{\#}$	Chl-a $= \tau {F_{I,N}}^{\eta}(\tau = 0.0522, [0.0473 \leftrightarrow 0.0576], \eta = 1.49[1.48 \leftrightarrow 1.51])$	0.81	0.173	−0.003	102

*Statistical tests performed on log$_{10}$-transformed Chl-a, owing to the distribution of Chl-a on AMT being close to log-normal (Brewin et al., 2016), as typically found in open ocean waters (Campbell, 1995).

$^{\$}$Look-Up Table (LUT) of model made for every 0.001 mg m^{-3} Chl-a, from 0.001 to 5.0 mg m^{-3}. z_{SD} compared with LUT and closest match used to extract modelled Chl-a.

$^{\#}$Model is tuned to the data (not independent of the dataset). Square brackets are upper and lower confidence limit based on one standard deviation.

$^{\%}$Model tested only on data within the range for which it was parametrised (only designed for >=2 Forel-Ule).

residuals (log$_{10}$(Chl-a) model minus data) on log$_{10}$(Chl-a) (Table 3, positive for $F_{D,L}$ and negative for $F_{D,N}$), likely related to data distribution. The LaMotte model residuals were also correlated with $L_i(750)/E_s(750)$, $R_{rs}(MB)/R_{rs}(G)$ and z_{SD} (Table 3). Residuals in both models were also found to be correlated with solar zenith angle (Table 3). This may suggest the sky conditions had some impact on data collection, possibly influencing the apparent colour of the disk, although no relationship was found between residuals and the VGI and VCI. Whereas measuring Forel-Ule of infinite water directly is useful for testing the Pitarch (2017) conversion, and more in-line with the historical observations (Figure 5), it is difficult to observe subtle variations in Chl-a at low concentrations, since the Forel-Ule saturates at the lowest value (Figure 3C). In fact, this is a key reason Boyce et al. (2012) excluded Forel-Ule data less than two in their algorithm. Instead, by measuring the colour of the disk at $1/2z_{SD}$, the observer can track these subtle changes in colour at very low Chl-a (Figure 6), as the scale has not saturated at its lowest value.

Whereas it is clear from this analysis that modern optical tools for estimating Chl-a ($R_{rs}(MB)/R_{rs}(G)$) performed the best (Table 2), it is nonetheless remarkable how well the historical tools performed, with some (e.g., z_{SD}) only marginally lower in performance than the modern method, and with a higher number of observations (less effected by environmental constrains in data collection). These results supports the merging of historical data with modern methods (e.g., satellite remote sensing) in search of long term trends in Chl-a, providing systematic differences can be identified, and acknowledging the challenges in bridging data collected at very different temporal and spatial scales (Boyce et al., 2010; Rykaczewski and Dunne, 2011; Boyce et al., 2012; Boyce et al., 2014). Models proposed here are nonetheless limited to the range of data they have been calibrated with, to case-1 open-ocean waters, and to the Atlantic Ocean. Caution is also needed when applying such models, developed between 2013-2018, to data collected in the past, since the relationships among Secchi depth, Forel-Ule colour, R_{rs}, and Chl-a, could themselves be sensitive to climate change.

3.3 Evaluating algorithms for estimating Secchi depth and Forel-Ule colour from remote-sensing reflectance on AMT

The AMT is, and has been, widely used as a platform for evaluating Chl-a remote-sensing algorithms (O'Reilly et al., 1998; Brewin et al., 2016; Tilstone et al., 2021), owing to the fact the transect samples such a wide variety of biogeochemical provinces. Here, we extend the range of remote-sensing variables evaluated on AMT, to include the Secchi depth and Forel-Ule colour.

Figure 7A and Table 4 show results from a statistical comparison between Forel-Ule data derived using the R_{rs}-based methods of van der Woerd and Wernand (2015) and Novoa et al. (2014) and that from the four *in-situ* datasets collected on AMT. The R_{rs}-based method performs well in the comparison, with r^2 values ranging

TABLE 3 Residuals between estimated $\log_{10}$(Chl-a), from Z_{SD}, $F_{D,L}$, $F_{D,N}$ and R_{rs}(MB)/R_{rs}(G) (independent variables), and measured $\log_{10}$(Chl-a), correlated with environmental variables (EV).

EV	z_{SD}		$F_{D,L}$		$F_{D,N}$		$\frac{R_{rs}(MB)}{R_{rs}(G)}$	
	r *	p *	r *	p *	r *	p *	r *	p *
$\frac{L_i(750)}{E_s(750)}$	0.046	0.609	**–0.185**	**0.039**	–0.082	0.417	–0.067	0.507
w_s	**0.238**	**0.008**	0.142	0.114	–0.019	0.850	–0.066	0.510
θ	–0.112	0.208	**–0.303**	**0.001**	**–0.247**	**0.012**	0.057	0.572
PSD	0.053	0.557	–0.018	0.841	0.106	0.296	–0.160	0.110
RSD	–0.007	0.934	–0.002	0.985	0.043	0.668	–0.131	0.193
PAR	0.031	0.031	0.156	0.084	0.113	0.266	–0.001	0.989
z_{SD}	–0.001	0.989	**0.362**	**<0.001**	0.115	0.250	0.118	0.241
$F_{D,L}$	–0.127	0.153	0.002	0.986	–0.02	0.831	–0.09	0.350
$F_{D,N}$	–0.110	0.270	–0.305	0.002	0.115	0.248	–0.137	0.225
$\frac{R_{rs}(MB)}{R_{rs}(G)}$	**0.234**	**0.018**	**0.367**	**<0.001**	0.098	0.385	–0.019	0.847
$\log_{10}$(Chl-a)	**–0.376**	**<0.001**	**0.540**	**<0.001**	**–0.297**	**0.002**	**–0.331**	**<0.001**

*Bold text indicates significant correlation at the 95% level (p<0.05).

from 0.64 to 0.70, and unbiased root mean square differences (Δ) ranging from 0.48 to 0.71 (Table 4). As expected, the R_{rs}-based method is in better agreement with the infinite colour *in-situ* datasets, with biases (δ) closer to zero for $F_{I,L}$, $F_{I,N}$ and $F_{I,A}$, than for $F_{D,L}$, $F_{D,N}$ (Table 4). Linear regression between data shows the biases to vary systematically over the range of Forel-Ule data, with the $F_{I,L}$ and $F_{I,N}$ in better agreement with the R_{rs}-based method at lower values (<4), but deviating significantly at higher values (>4, Figure 7A; Table 4), with differences (residuals) between the R_{rs}-based method and $F_{I,N}$ data inversely correlated with changes in Forel-Ule (Table 5). These residuals were also found to be correlated with wind speed, the pitch and roll of the vessel, the Secchi depth and $\log_{10}$(Chl-a) (Table 5). Interestingly, the slope of the regression in the statistical comparison between the R_{rs}-based method and $F_{I,A}$ (phone app) data was closer to one, and the bias (δ) closer to zero, when compared with other data (Table 4). Furthermore, differences (residuals) between the R_{rs}-based method and $F_{I,A}$ data were not significantly correlated with any environmental variables (data not shown), acknowledging that only one cruise (AMT26) of $F_{I,A}$ data were available in the analysis. Figure 3C shows the transect of F data for AMT26. All infinite F data are in good agreement at low values, but at higher values towards the end of the cruise (in the South Atlantic), the $F_{I,L}$ and $F_{I,N}$ are significantly higher than both the $F_{I,A}$ (phone app) data and the R_{rs}-based method, with the latter two in very good agreement. It may be that the conversion between the colour of the disk and infinite colour used here (Pitarch, 2017) to derive $F_{I,L}$ and $F_{I,N}$, which performs very well at lower values (<4) (Figure 3C), requires revaluation at higher F values (>4).

A statistical comparison between *in-situ* z_{SD} and the R_{rs}-based algorithms of Lee et al. (2015) and Jiang et al. (2019) are shown in Figures 7B, C. Within the range of *in-situ* z_{SD} collected on the AMT cruises (8.5 - 51.8 m), both algorithms perform reasonably at

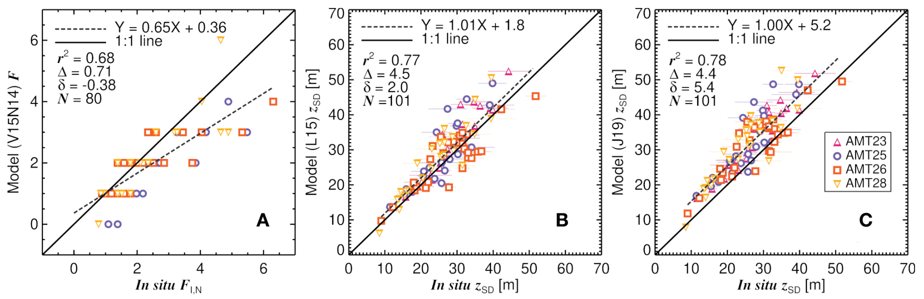

FIGURE 7
Comparison of R_{rs}-derived Forel-Ule colour (F) and Secchi depth (z_{SD}) with *in-situ* data. **(A)** R_{rs}-derived F using the methods of van der Woerd and Wernand (2015) and Novoa et al. (2014) (V15N14) with *in-situ* $F_{I,N}$ (F measured using the scale of Novoa et al. (2014) for the colour of the disk at half the Secchi depth, but converted to infinite colour using the method of Pitarch (2017)). **(B)** R_{rs}-derived z_{SD} using the model of Lee et al. (2015) (L15) against *in-situ* z_{SD}. **(C)** R_{rs}-derived z_{SD} using the model of Jiang et al. (2019) (J19) against *in-situ* z_{SD}. r^2 is the squared Pearson correlation coefficient, δ the mean difference (bias), Δ the unbiased root mean square difference, and N the number of samples.

TABLE 4 Comparison of R_{rs}-derived *F* using the R_{rs}-based methods of van der Woerd and Wernand (2015) and Novoa et al. (2014) with various *in-situ F* datasets collected on AMT.

In-situ F dataset	Linear regression*	r^2	Δ	δ	*N*
$F_{D,L}$	$Y = 0.82X - 1.49$	0.64	0.63	−2.17	101
$F_{I,L}$	$Y = 0.75X - 0.42$	0.65	0.64	−1.10	101
$F_{D,N}$	$Y = 0.69X - 0.44$	0.70	0.66	−1.43	80
$F_{I,N}$	$Y = 0.65X + 0.36$	0.68	0.71	−0.38	80
$F_{I,A}$	$Y = 0.88X + 0.14$	0.68	0.48	−0.10	29

**Y* represents the data from the R_{rs}-based methods of van der Woerd and Wernand (2015) and Novoa et al. (2014) and *X* the *in-situ* F data.

retrieving z_{SD} from R_{rs}, with r^2 values ranging from 0.77 to 0.78, unbiased root mean square differences (Δ) ranging from 4.4 to 4.5 m, and linear regression slopes close to one. Both R_{rs}-based algorithms show slightly higher estimates than the *in-situ* z_{SD} data (positive biases (δ)), but biases for the Lee et al. (2015) algorithm are closer to zero ($\delta = 2.0$) than for the Jiang et al. (2019) algorithm, where there is a systematic overestimation of z_{SD} of around five meters (δ = 5.4). Interestingly, there was no significant change in model performance when removing stations with overcast conditions (VCI = 1). However, it is important to recognise both models were calibrated with Hydrolight simulations using cloudless skies (Lee et al., 2002, 2005, 2009).

3.4 On the dependency of Secchi depth on solar zenith angle and wind speed

Differences (residuals) between the Lee et al. (2015) and Jiang et al. (2019) algorithms, and the *in-situ* z_{SD} data, were both found to be positively correlated with $R_{rs}(\mathrm{MB})/R_{rs}(\mathrm{G})$ and inversely correlated with $\log_{10}$(Chl-a) (Table 5). Residuals between the Lee et al. (2015) algorithm and the *in-situ* z_{SD} data were inversely correlated with solar zenith angle (θ), but not in the case of the Jiang et al. (2019) algorithm (Table 5 and Figure 8). Both algorithms incorporate a dependency on θ in the conversion of IOPs [derived analytically from R_{rs} following Lee et al. (2002, 2005, 2009)] to $K_d(\lambda)$, and both algorithms subsequently derive z_{SD} according to

$$z_{SD} = \frac{1}{\omega \min\left(K_d(\lambda)\right)} \ln\left(\frac{\left|0.14 - R_{rs}^{pc}\right|}{C_t^r}\right), \tag{3}$$

where R_{rs}^{pc} represents remote sensing reflectance at the corresponding wavelength to $\min(K_d(\lambda))$, C_t^r is the threshold contrast for sighting a white Secchi disk, and ω converts $\min(K_d(\lambda))$ to the sum of downwelling diffuse attenuation (K_d^{tr}) and upwelling diffuse attenuation (K_T^{tr}), in the transparent window. The Lee et al. (2015) algorithm fixes ω at 2.5, whereas the Jiang et al. (2019) algorithm has a variable ω, itself dependent on θ according to

$$\omega = 1 + \frac{1.04(1 + 5.4u)^{0.5}}{1/(1 - \frac{sin(\theta)^2}{{n_w}^2})^{0.5}}, \tag{4}$$

where u is the ratio of the backscattering coefficient to the sum of absorption and backscattering coefficients (derived from R_{rs} following

TABLE 5 Residuals between estimated z_{SD} or *F* using R_{rs}-based models and *in-situ* data correlated with environmental variables (EV).

EV	z_{SD} (L15)		z_{SD} (J19)		$F_{I,N}$ (V15N14)	
	r^*	p^*	r^*	p^*	r^*	p^*
$\frac{L_i(750)}{E_s(750)}$	0.043	0.673	0.065	0.515	−0.071	0.532
w_s	**0.286**	**0.004**	**0.197**	**0.048**	**−0.243**	**0.030**
θ	**−0.398**	**<0.001**	−0.133	0.186	0.147	0.193
PSD	0.148	0.139	0.112	0.263	**−0.387**	**<0.001**
RSD	0.048	0.635	0.130	0.194	**−0.230**	**0.040**
PAR	0.128	0.203	0.005	0.959	−0.055	0.629
z_{SD}	0.010	0.922	0.007	0.942	**0.278**	**0.012**
$F_{D,L}$	−0.151	0.130	−0.174	0.082	**−0.316**	**0.004**
$F_{D,N}$	−0.115	0.309	−0.172	0.127	**−0.539**	**<0.001**
$\frac{R_{rs}(MB)}{R_{rs}(G)}$	**0.434**	**<0.001**	**0.412**	**<0.001**	0.166	0.142
$\log_{10}$(Chl-a)	**−0.243**	**0.014**	**−0.238**	**0.017**	**−0.237**	**0.034**

* Bold text indicates significant correlation at the 95% level (p=<0.05).
L15 = Lee et al. (2015), J19 = Jiang et al. (2019), and V15N14 = combined methods of van der Woerd and Wernand (2015) and Novoa et al. (2014).

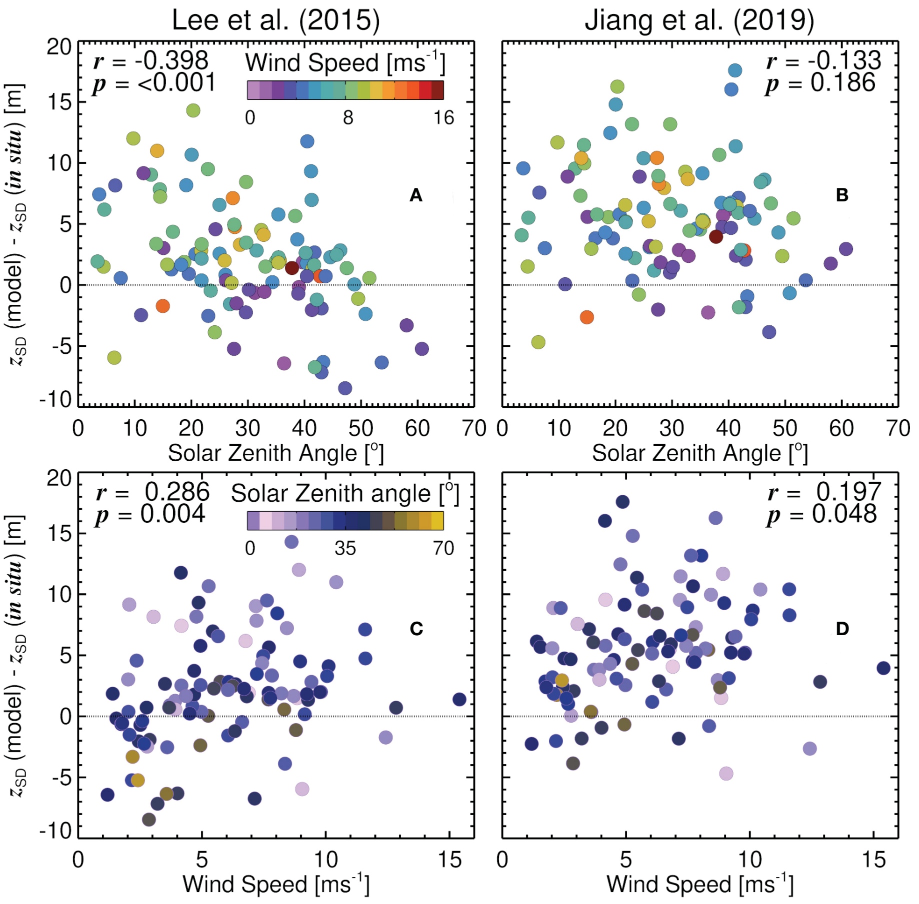

FIGURE 8
Differences (residuals) between R_{rs}-derived Secchi depth (z_{SD}) and *in-situ* z_{SD}, using the algorithms of Lee et al. (2015) **(A, C)** and Jiang et al. (2019) **(B, D)**, plotted as a function of solar zenith angle (θ) **(A, B)** and wind speed (w_s) **(C, D)**. Dotted line represents residuals of zero.

Lee et al. (2002; 2005; 2009)), and n_w is the refractive index of water (1.34). For the same backscattering and absorption coefficient, as θ increases, $K_d(\lambda)$ increases in model of Lee et al. (2005) (used in both Jiang et al. (2019) and Lee et al. (2015) models), which subsequently decreases z_{SD} in Eq. 3. However, in the Jiang et al. (2019) algorithm, as θ increases, ω decreases (Eq. 4), which counterbalances the increase in ($K_d(\lambda)$) with θ. The resulting effect is that z_{SD} estimated using the Jiang et al. (2019) algorithm is less dependent on θ than for the Lee et al. (2015) model.

Differences (residuals) between the Lee et al. (2015) and Jiang et al. (2019) algorithms, and the *in-situ* z_{SD} data, were also found to be positively correlated with wind speed (Table 5 and Figure 8). At very low wind speed (<3 ms^{-1}), there is better agreement between models and *in-situ* data, with δ closer to zero ($\delta = -1.03$ for Lee et al. (2015) and $\delta = 2.79$ for Jiang et al. (2019)). These biases increased with increasing wind speed (Figure 8) Neither models incorporate a dependency of z_{SD} on wind speed, but our results are broadly consistent with theory of Preisendorfer (1986) that assumes an increase in wind speed causes a reduction in the apparent contrast of the disk at the surface, and a subsequent reduction in z_{SD}.

Though the Preisendorfer (1986) and Lee et al. (2015) Secchi disk theory define contrast differently, the Preisendorfer (1986) approach could be used to introduce some relationship between contrast and wind speed in the theory of Lee et al. (2015). The inherent contrast (C_0) is defined not as a relative difference in irradiance reflectance between the disk and the surrounding water (as in Preisendorfer, 1986), but as an absolute difference between the radiance reflectance of the disk (r_0) and the surrounding water (r_∞), such that

$$C_0 = |r_0 - r_\infty| . \tag{5}$$

The derived theory states that the contrast is modified as the distance (z) from the observer to the disk increases, such that

$$C(z) = C_0 \exp\left(-(K_d^{tr} + K_T^{tr})z\right). \tag{6}$$

Following Preisendorfer (1986), a contrast reduction factor ($\bar{\tau}_0$) could be introduced, such that Eq. 6 becomes

$$C(z) = \bar{\tau}_0 C_0 \exp\left(-(K_d^{tr} + K_T^{tr})z\right). \tag{7}$$

If we make the assumption that $\bar{\tau}_0$ is controlled by wind speed (w_s), acknowledging that other factors (which may or may not covary with w_s) are likely to impact $\bar{\tau}_0$, we could relate $\bar{\tau}_0$ to w_s empirically. To do that, we define $x(z)=C_0/C(z)$, and for $z=z_{SD}$, it follows that $C(z_{SD})$ =0.013. Then, as the measurement is made from above the surface, it has to include another contrast reduction factor due to surface reflection effects, leading to $x(z_{SD}) = x_{SD} = |0.14 - R_{rs}|/0.013$ (see Section 4 of Lee et al., 2015). To have an operational expression to solve for $\bar{\tau}_0$, we make the ratio of Secchi depth with ($z_{SD,ws}$) and without ($z_{SD,ws=0}$) wind, such that

$$\frac{z_{SD,ws}}{z_{SD,ws=0}} = \frac{\ln(\bar{\tau}_0 x_{SD})}{\ln(x_{SD})}. \tag{8}$$

Rearranging the equation following some algebra, we obtain

$$\bar{\tau}_0 = x_{SD}^{\frac{z_{SD,ws}}{z_{SD,ws=0}}-1}, \tag{9}$$

and derive $\bar{\tau}_0$ by making the assumption $z_{SD,ws=0}$ is equal to the Jiang et al. (2019) algorithm output, and $z_{SD,ws}$ represents the *in-situ* data. Next we model $\bar{\tau}_0$ as a function of wind speed (w_s) and $z_{SD,ws=0}$ (Jiang et al. (2019) algorithm), according to

$$\bar{\tau}_0 = q_0 \exp\left[-q_1 w_s (1 + q_2 z_{SD,ws=0})\right], \tag{10}$$

with the expression chosen carefully to follow the observed trend in which wind explains most of the variation, but it is modulated by $z_{SD,ws=0}$. Fitting of Eq. 10 to the data resulted in $q_0 = 0.901$ ($0.805 \leftrightarrow 0.998$), $q_1 = 0.022$ ($-0.007 \leftrightarrow 0.051$), and $q_2 = 0.03$ ($-0.045 \leftrightarrow 0.106$). Once $\bar{\tau}_0$ is known, $z_{SD,ws}$ can be estimated from

$$z_{SD,ws} = \frac{\ln(\bar{\tau}_0 x_{SD})}{\ln(x_{SD})} z_{SD,ws=0}. \tag{11}$$

Using the modelled $z_{SD,ws}$ (Jiang et al., 2019) removes the significant positive correlation between wind speed and model residuals (r=−0.135, p=0.179) apparent in original (Jiang et al., 2019) algorithm ($z_{SD,ws=0}$, Figure 8D). Additional datasets are need to independently validate this approach, but it certainly offers a way to incorporate the influence of wind speed into the Secchi depth theory of Lee et al. (2015), and could be useful for standardising *in-situ* z_{SD} data to a common wind speed.

3.5 Experiences and recommendations from collecting optical measurements using historical techniques on AMT

Our experience of collecting Secchi depth and Forel-Ule colour data on the Atlantic Meridional Transect revealed a number of insights. With the exception of a few sceptical scientists on-board the ship, there were many (scientists and members of the ship's crew) that loved visually inspecting the colour and clarity of the water using the Secchi disk and Forel-Ule colour scales (see acknowledgements). It was the only time of the day where these participants had the opportunity to visually connect and interact with the ocean. The AMT transect was the perfect cruise to do this, as it transects through a ranges of conditions, with the clarity and colour of the water changing (sometimes rapidly) over the duration of the cruise. Visually inspecting the water also resulted in an increased number of sightings of marine wildlife and oceanic phenomena, including (and to name a few) observations of dolphins, sharks, whales, dolphinfish, rays, penguins, squid, turtles, icebergs, all manner of seabirds, as well as some of the more negative features (e.g., marine litter). For some, this had a positive influence on mental health, important to consider when on-board a research vessel for an extended period of time. Considering the nature of the measurement of Secchi depth and Forel-Ule colour, in that the observer is intrinsically part of the measurement process, it was a useful activity for teaching the concepts of ocean colour and clarity to non-scientists, and scientists working on other aspects of oceanography, on the AMT cruises.

Despite these positives, it was evident that measuring the Secchi depth in oligotrophic waters is challenging. After unsuccessfully attempting to deploy a Secchi disk using the traditional technique (rope and weighted Secchi disk), hindered by the disk drifting quickly away from the vessel (which was kept stationary), we followed the recommendations of the late Marcel Wernand, who in his 2010 paper states "*…the author recommends a reintroduction of the Secchi disc to expand the historical Secchi depth database to facilitate climate change research. One option is to mount a Secchi disc on an instrumental or CTD frame…*" (Wernand, 2010, p5). Once the disk was mounted on the optics rig (Figure 2A) it became feasible to do the measurements, as part of routine data collection.

A major challenge with conducting Secchi depth measurements in oligotrophic waters, is the fact that the disk disappears at a depth far greater than in mesotrophic and eutrophic waters. The angular subtense of the disk's radius ($\Phi = r_{SD}/z_{SD}$, r_{SD} is the disk's radius, the first order approximation of the MacLaurin expansion of the arctan function), for a 30 cm diameter disk at a z_{SD} of 50 m, is 0.003. To put this into perspective (and something that could easily be tested in inland water), the target viewed is equivalent to lowering a 1 cm diameter disk to 1.7 m. One solution could be to increase the disk size for oligotrophic waters. Although a 30 cm diameter disk is standard for measuring the Secchi depth in the ocean, Angelo Secchi himself used disks as big as 2.5 m in diameter in his early work (Pitarch et al., 2021), and others have modified the disk size to be smaller in more turbid waters (e.g., Brewin et al., 2019a). However, the exact impact of disk size on Secchi depth is still a matter of research (Hou et al., 2007). Another possible artefact of a very low angular subtense (Φ) in oligotrophic waters, could be an increasing impact of environmental factors on the detection threshold of the human eye (in air) seeing the disk, since the target is so small. Additionally, there may be other optical effects that occur, that are not currently accounted for in the theory. For example, with a very small target in a moving ocean, there may be some kind of adjacency effect, caused by the spectrum near the edge of the disk being a mixture of reflectance of the disk and the infinitely deep waters.

The dataset collected on AMT is freely available (Brewin et al. 2023), courtesy of the British Oceanographic Data Centre (BODC), for use in future research on the topic. In this paper, we have compared and evaluated broad relationships between historic and modern optical techniques for monitoring phytoplankton biomass. Future work could use these data to examine in greater detail the influence of varying concentrations of different optically-active constituents on the relationships between Secchi depth, Forel-Ule colour, R_{rs}, and Chl-a. For example, variations in coloured dissolved organic matter (CDOM) will have an impact on water colour, and consequently the relationships between bulk variables (Van der Woerd and Wernand, 2018). For some AMT cruises, underway CDOM absorption data (Dall'Olmo et al., 2017), as well as underway and profile particulate absorption and scattering measurements (Dall'Olmo et al., 2012; Brewin et al., 2016; Tilstone et al., 2021), have been collected, and could be useful for studying relationships between Secchi depth, Forel-Ule colour, R_{rs}, and Chl-a.

Measuring PAR on a profiling package and the Secchi depth from a large oceanographic vessel could lead to cases of ship shadow. For PAR, this was somewhat minimised by only using profiles where depth and log(PAR) were tightly correlated and (where possible) deploying the profiling package on the sunny side of the vessel. Our K_d values for oligotrophic waters (varying between 0.02 – 0.08) are consistent with values from satellite data in the region (e.g., Son and Wang, 2015) and consistent with BGC-Argo float data (see Demeaux and Boss (2022)). AMT K_d data also agreed well with K_d estimates from a BGC-Argo float WMO:3902121 in the South Atlantic gyre, (results not shown).

Another factor that may influence relationships between Secchi depth, Forel-Ule colour, R_{rs}, and Chl-a, are shifts in the community composition of phytoplankton. It is well know that the chl-specific absorption and backscattering coefficients vary with phytoplankton community composition (e.g., Ciotti et al., 2002; Sathyendranath et al., 2004; Kostadinov et al., 2010; Brewin et al., 2011; Devred et al., 2011; Brewin et al., 2012a; Brewin et al., 2019b). Although the median ratio of Secchi-depth to mixed-layer depth (computed using temperature criterion of de Boyer Montégut et al. (2004)) was found to be 0.49 (standard deviation 0.44), suggesting on average the mixed-layer depth was twice that of the Secchi depth, there were a few cases where the Secchi depth was shallower than the mixed-layer depth. Vertical variability in Chl-a and phytoplankton community structure in the region (Mojica et al., 2015), and within the Secchi depth layer, may exist (e.g., in very clear waters, with very shallow mixed-layers) which may complicate relationships between Secchi depth, Forel-Ule colour, R_{rs}, and Chl-a.

We chose to use surface Chl-a, rather than depth-averaged Chl-a within the Secchi depth layer, in our analysis, as it has been recommended by the community to use surface Chl-a when developing surface optical models (Sathyendranath et al., 2019; Lee et al., 2020), and it allowed us to compare relationships in our dataset with earlier algorithms (Boyce et al., 2012; Lee et al., 2018c). However, datasets on vertical variations in Chl-a and community composition (e.g. through flow cytometry and HPLC analysis) have been collected on AMT cruises, and could be useful for studying impact of vertical variability in water constituents on proposed models. Future efforts in collecting vertically-resolved inherent optical properties, alongside Secchi depth and FU measurements, would help further. Considering issues with direct observations of Forel-Ule colour of infinite waters not resolving subtle variations in low Chl-a in oligotrophic waters, we recommend measuring Forel-Ule colour in oligotrophic waters using the colour of the Secchi disk at $1/2z_{SD}$.

4 Summary

On four AMT cruises (23, 25, 26 and 28), we collected a dataset of both modern (radiometric) and traditional (Secchi depth and Forel-Ule colour) measurements of ocean clarity and colour, together with *in-situ* measurements of Chl-a, with the aim to evaluate relationships between historic and modern methods for monitoring phytoplankton biomass, and evaluate satellite ocean colour remote-sensing algorithms, two key goals of the AMT programme. Historic and modern optical measurements were in good agreement and consistent with current understanding, with the Secchi depth inversely correlated to the Forel-Ule colour, beam and diffuse attenuation, and positively correlated to the euphotic depth and $R_{rs}(MB)/R_{rs}(G)$. The relationship between Secchi depth and Forel-Ule on AMT was also in good agreement with historical data, but only when using data of the Forel-Ule colour of infinite water (estimated using Pitarch (2017)), rather than the Forel-Ule colour of the Secchi disk at half the Secchi depth. $R_{rs}(MB)/R_{rs}(G)$ explained the highest amount of variance in Chl-a (89%), closely followed by the Secchi depth (85%) and the Forel-Ule colour (71-81%, depending on scale used). Overall, algorithms that predict Chl-a from these optical proxies were found to perform well, with some systematic differences. Algorithms that estimate Forel-Ule and Secchi depth from remote sensing reflectance were found to be in good agreement with the *in-situ* data, albeit with a positive bias (2.0 - 5.4 m, ~8-22%) in Secchi depth, and differences in performance depending on which Forel-Ule scale and method were used (infinite colour or colour of water above disk at $1/2z_{SD}$). The impact of different environmental variables on relationships between optical proxies was investigated, and varied depending on the optical proxies analysed. We found wind speed to impact the estimation of z_{SD}, and proposed a path forward to include the effect of wind in current Secchi depth theory, based on the classical work of Preisendorfer (1986). We highlight some of the benefits and challenges in collecting optical measurements using traditional methods on AMT, and highlight future directions for research. Our dataset is made publicly available to support the research community (see Brewin et al., 2023).

Data availability statement

The dataset used for this study is openly available through the British Oceanographic Data Centre (see https://doi.org/10.5285/f3198e10-faf3-1525-e053-6c86abc0d2f6).

Author contributions

RB and GD organised and participated in the collection of all the Secchi disk and Forel-Ule colour data. RB, GD, and GT organised and participated in the collection of all modern optical datasets used (e.g., radiometry). RB wrote an initial plan for the paper with input from GD, JP, and HW. JL and XS contributed to data processing and figure production. RB and JP synthesised the data, ran the analysis and prepared the figures. RB wrote the first version of the manuscript, with input from JP. All authors contributed to the article and approved the submitted version.

Funding

This work was supported by grants from the European Space Agency (ESA), including the Changing Earth Science Network initiative funded by the STSE programme (DECIPHER project), AMT4SentinelFRM (ESRIN/RFQ/3-14457/16/I-BG) and AMT4OceanSatFlux (4000125730/18/NL/FF/gp). Additional support from the UK National Centre for Earth Observation is acknowledged. The work was supported by UK Natural Environment Research Council (NERC) National Capability funding for AMT to Plymouth Marine Laboratory. AMT is funded by the NERC through its National Capability Long-term Single Centre Science Programme, Climate Linked Atlantic Sector Science (grant number NE/R015953/1). This study contributes to the international IMBeR project and is contribution number 384 of the AMT programme. RB is funded by a UKRI Future Leader Fellowship (MR/V022792/1).

Acknowledgments

We thank Marcel Wernand for providing Forel-Ule scale used on AMT25, AMT26 and AMT28, and for his support for collecting Forel-Ule and Secchi depth data on AMT. We are indebted to the all the scientists, the captain's and crew of the RRS *James Clark Ross*, on AMT23, AMT25, AMT26, and AMT28, who helped make this work happen. Especially those who were kind enough to come out on deck at the noon station, look at the ocean, and help us collect the Forel-Ule and Secchi depth data, specific thanks goes to: Arwen Bargery, Carolina Beltran, Kimberley Bird, Ian Brown, Catherine Burd, Priscilla Lange, Phyllis Lam, Ankita Misra, Catherine Mitchell, Mónica Moniz, Clifford Mullaney, Francesco Nencioli, John O'Duffy, Emanuele Organelli, Paul Provost, Rafael Rasse, Andy Rees, Nick Rundle, Bita Sabbaghzadeh, Chata Seguro, Charlotte Smith, Tim Smyth, Madeline Steer, Glen Tarran, Robyn Tuerena, Natalie Wager, and Simon Wright. We thank Tom Jackson for help in data transfer and Afonso Ferreira and Andreia Tracana for help filtering water for HPLC analysis on AMT28. We thank Arwen Bargery, Priscilla Lange and Phyllis Lam, for use of photos in Figure 2. We thank all those that contributed to the CalCOFI and NODC datasets.

Conflict of interest

The authors declare that the research was conducted in the absence of any commercial or financial relationships that could be construed as a potential conflict of interest.

The handling editor VB declared a past co-authorship with the authors RB and XS.

Publisher's note

References

Aiken, J., Rees, N., Hooker, S., Holligan, P., Bale, A., Robins, D., et al. (2000). The Atlantic Meridional Transect: Overview and synthesis of data. *Prog. Oceanography* 45, 257–312. doi: 10.1016/S0079-6611(00)00005-7

Antoine, D., Morel, A., Gordon, H. R., Banzon, V. F., and Evans, R. H. (2005). Bridging Ocean Color observations of the 1980s and 2000s in search of long-term trends. *J. Geophysical Research: Oceans* 110, 1–22. doi: 10.1029/2004JC002620

Behrenfeld, M. (2011). Uncertain future for ocean algae. *Nat. Climate Change* 1, 33–34. doi: 10.1038/nclimate1069

Behrenfeld, M. J. (2014). Climate-mediated dance of the plankton. *Nat. Climate Change* 4, 880–887. doi: 10.1038/nclimate2349

Behrenfeld, M. J., O'Malley, R. T., Siegel, D. A., McClain, C. R., Sarmiento, J. L., Feldman, G. C., et al. (2006). Climate-driven trends in contemporary ocean productivity. *Nature* 444, 752–755. doi: 10.1038/nature05317

Boyce, D. G., Dowd, M., Lewis, M. R., and Worm, B. (2014). Estimating global chlorophyll changes over the past century. *Prog. Oceanography* 122, 163–173. doi: 10.1016/j.pocean.2014.01.004

Boyce, D. G., Lewis, M. R., and Worm, B. (2010). Global phytoplankton decline over the past century. *Nature* 466, 591–596. doi: 10.1038/nature09268

Boyce, D. G., Lewis, M., and Worm, B. (2012). Integrating global chlorophyll data from 1890 to 2010. *Limnology Oceanography Methods* 10, 840–852. doi: 10.4319/lom.2012.10.840

Brewin, R. J. W., Brewin, T. G., Phillips, J., Rose, S., Abdulaziz, A., Wimmer, W., et al. (2019a). A printable device for measuring clarity and colour in lake and nearshore waters. *Sensors* 9, 1–26. doi: 10.3390/s19040936

Brewin, R. J. W., Ciavatta, S., Sathyendranath, S., Skákala, J., Bruggeman, J., Ford, D., et al. (2019b). The influence of temperature and community structure on light absorption by phytoplankton in the north Atlantic. *Sensors* 19, 1–25. doi: 10.3390/s19194182

Brewin, R. J. W., Dall'Olmo, G., Gittings, J., Sun, X., Lange, P. K., Raitsos, D. E., et al. (2022). A conceptual approach to partitioning a vertical profile of phytoplankton biomass into contributions from two communities. *J. Geophysical Researech: Oceans* 127, e2021JC018195. doi: 10.1029/2021JC018195

Brewin, R. J. W., Dall'Olmo, G., Pardo, S., van Dongen-Vogel, V., and Boss, E. S. (2016). Underway spectrophotometry along the Atlantic Meridional Transect reveals high performance in satellite chlorophyll retrievals. *Remote Sens. Environ.* 183, 82–97. doi: 10.1016/j.rse.2016.05.005

Brewin, R. J. W., Dall'Olmo, G., Sathyendranath, S., and Hardman-Mountford, N. J. (2012a). Particle backscattering as a function of chlorophyll and phytoplankton size structure in the open-ocean. *Optics Express* 20, 17632–17652. doi: 10.1364/OE.20.017632

Brewin, R. J. W., Devred, E., Sathyendranath, S., Lavender, S. J., and Hardman-Mountford, N. J. (2011). Model of phytoplankton absorption based on three size classes. *Appl. Optics* 50, 4535–4549. doi: 10.1364/AO.50.004535

Brewin, R. J. W., Hirata, T., Hardman-Mountford, N. J., Lavender, S., Sathyendranath, S., and Barlow, R. (2012b). The influence of the Indian ocean dipole on interannual variations in phytoplankton size structure as revealed by Earth Observation. *Deep Sea Res. II* 77-80, 117–127. doi: 10.1016/j.dsr2.2012.04.009

Brewin, R. J.W., Pitarch, J., Dall'Olmo, G., van der Woerd, H. J., Lin, J., Sun, X., and Tilstone, G. H. (2023). Modern and traditional optical measurements, and environmental data, collected on four Atlantic Meridional Transect cruises between 2013 and 2018. *NERC EDS British Oceanographic Data Centre NOC*. doi: 10.5285/f3198e10-faf3-1525-e053-6c86abc0d2f6

Brewin, R. J. W., Tilstone, G., Jackson, T., Cain, T., Miller, P., Lange, P. K., et al. (2017). Modelling size-fractionated primary production in the Atlantic ocean from remote sensing. *Prog. Oceanography* 158, 130–149. doi: 10.1016/j.pocean.2017.02.002

Brotas, V., Tarran, G. A., Veloso, V., Brewin, R. J. W., Woodward, E. M. S., Airs, R., et al. (2022). Complementary approaches to assess phytoplankton groups and size classes on a long transect in the Atlantic ocean. *Front. Mar. Sci.* 8. doi: 10.3389/fmars.2021.682621

Busch, J. A., Bardaji, R., Ceccaroni, L., Friedrichs, A., Piera, J., Simon, C., et al. (2016). Citizen bio-optical observations from coast-and ocean and their compatibility with ocean colour satellite measurements. *Remote Sens.* 8, 1–19. doi: 10.3390/rs8110879

Campbell, J. W. (1995). The lognormal distribution as a model for bio-optical variability in the sea. *J. Geophysical Res.* 100 (C7), 13237–13254. doi: 10.1029/95JC00458

Chai, F., Johnson, K. S., Claustre, H., Xing, X., Wang, Y., Boss, E., et al. (2020). Monitoring ocean biogeochemistry with autonomous platforms. *Nat. Rev. Earth Environ.* 1, 315–326. doi: 10.1038/s43017-020-0053-y

Chassot, E., Bonhommeau, S., Dulvy, N. K., Mélin, F., Watson, R., Gascuel, D., et al. (2010). Global marine primary production constrains fisheries catches. *Ecol. Lett.* 13, 495–505. doi: 10.1111/j.1461-0248.2010.01443.x

Ciotti, A. M., Lewis, M. R., and Cullen, J. J. (2002). Assessment of the relationships between dominant cell size in natural phytoplankton communities and the spectral shape of the absorption coefficient. *Limnology Oceanography* 47, 404–417. doi: 10.4319/lo.2002.47.2.0404

Dall'Olmo, G., Boss, E., Behrenfeld, M., and Westberry, T. K. (2012). Particulate optical scattering coefficients along an Atlantic Meridional Transect. *Optics Express* 20, 21532–21551. doi: 10.1364/OE.20.021532

Dall'Olmo, G., Brewin, R. J. W., Nencioli, F., Organelli, E., Lefering, I., McKee, D., et al. (2017). Determination of the absorption coefficient of chromophoric dissolved organic matter from underway spectrophotometry. *Optics Express* 25, A1079–A1095. doi: 10.1364/OE.25.0A1079

de Boyer Montégut, C., Madec, G., Fischer, A. S., Lazar, A., and Iudicone, D. (2004). Mixed layer depth over the global ocean: An examination of profile data and a profile-based climatology. *J. Geophysical Reserach: Oceans* 109, 1–20. doi: 10.1029/2004JC002378

Demeaux, C. B., and Boss, E. (2022). Validation of remote-sensing algorithms for diffuse attenuation of downward irradiance using BGC-argo floats. *Remotre Sens.* 14, 4500. doi: 10.3390/rs14184500

Devred, E., Sathyendranath, S., Stuart, V., and Platt, T. (2011). A three component classification of phytoplankton absorption spectra: Applications to ocean-colour data. *Remote Sens. Environ.* 115, 2255–2266. doi: 10.1016/j.rse.2011.04.025

Dow, K., and Downing, T. E. (2011). *The atlas of climate change: mapping the world's greatest challenge* (Univ of California Press, Oakland, California).

Dutkiewicz, S., Hickman, A. E., Jahn, O., Henson, S., Beaulieu, C., and Moneir, E. (2019). Ocean colour signature of climate change. *Nat. Commun.* 10, 578. doi: 10.1038/s41467-019-08457-x

Falkowski, P. G. (2012). Ocean science: The power of plankton. *Nature* 483, S17–S20. doi: 10.1038/483s17a

Falkowski, P. G., and Wilson, C. (1992). Phytoplankton productivity in the North Pacific ocean since 1900 and implications for absorption of anthropogenic co_2. *Nature* 358, 741–743. doi: 10.1038/358741a0

Field, C. B., Behrenfeld, M. J., Randerson, J. T., and Falkowski, P. G. (1998). Primary production of the biosphere: integrating terrestrial and oceanic components. *Science* 281, 237–240. doi: 10.1126/science.281.5374.237

Forel, F. A. (1890). "Une nouvelle forme de la gamme de couleur pour l'étude de l'eau des lacs," in *Archives des sciences physiques et Naturelles/Société de physique et d'Histoire naturelle de genève*, vol. 6. , 25.

GCOS (2011). "Systematic observation requirements from satellite-based data products for climate," in *Tech. rep* (7 bis, avenue de la Paix, CH-1211 Geneva 2, Switzerland: World Meteorological Organisation (WMO).

Gregg, W. W., and Conkright, M. E. (2002). Decadal changes in global ocean chlorophyll. *Geophysical Res. Lett.* 29, 20–1–20–4. doi: 10.1029/2002GL014689

Henson, S. A. (2014). Slow science: the value of long ocean biogeochemistry records. *Philos. Trans. R. Soc. A* 372, 1–22. doi: 10.1098/rsta.2013.0334

Henson, S. A., Cael, B. B., Allen, S. R., and Dutkiewicz, S. (2021). Future phytoplankton diversity in a changing climate. *Nat. Commun.* 12, 1–8. doi: 10.1038/s41467-021-25699-w

Henson, S. A., Sarmiento, J. L., Dunne, J. P., Bopp, L., Lima, I., Doney, S. C., et al. (2010). Detection of anthropogenic climate change in satellite records of ocean chlorophyll and productivity. *Biogeosciences* 7, 621–640. doi: 10.5194/bg-7-621-2010

Hou, W., Lee, Z., and Weidemann, A. D. (2007). Why does the Secchi disk disappear? an imaging perspective. *Optics Express* 15, 2791–2802. doi: 10.1364/OE.15.002791

Hu, C., Lee, Z., and Franz, B. (2012). Chlorophyll a algorithms for oligotrophic oceans: A novel approach based on three-band reflectance difference. *J. Geophysical Res.* 117, C01011. doi: 10.1029/2011JC007395

IPCC (2019). "*IPCC Special Report on the Ocean and Cryosphere in a Changing Climate*," Eds, H.-O. Pörtner, D.C. Roberts, V. Masson-Delmotte, P. Zhai, M. Tignor, E. Poloczanska, et al. Cambridge University Press, Cambridge, UK and New York, NY, USA, 755 pp. doi: 10.1017/9781009157964.

Jiang, D., Matsushita, B., Setiawan, F., and Vundo, A. (2019). An improved algorithm for estimating the Secchi disk depth from remote sensing data based on the new underwater visibility theory. *ISPRS J. Photogrammetry Remote Sens.* 152, 13–23. doi: 10.1016/j.isprsjprs.2019.04.002

Kostadinov, T. S., Siegel, D. A., and Maritorena, S. (2010). Global variability of phytoplankton functional types from space: assessment *via* the particle size distribution. *Biogeosciences* 7, 3239–3257. doi: 10.5194/bgd-7-4295-2010

Lee, Z., Arnone, R., Boyce, D., Franz, B., Greb, S., Hu, C., et al. (2018a). Global water clarity: Continuing a century-long monitoring. *Eos* 99. doi: 10.1029/2018EO097251

Lee, Z., Carder, K. L., and Arnone, R. A. (2002). Deriving inherent optical properties from water color: a multiband quasi-analytical algorithm for optically deep waters. *Appl. Optics* 41, 5755–5772. doi: 10.1364/AO.41.005755

Lee, Z., Du, K., and Arnone, R. (2005). A model for the diffuse attenuation coefficient of downwelling irradiance. *J. Geophysical Res.* 110, C02016. doi: 10.1029/2004JC002275

Lee, Z., Lubac, B., Werdell, P. J., and Arnone, R. (2009). An update of the quasi-analytical algorithm (QAA_v5). In: *Tech. rep* (International Ocean Colour Coordinating Group (IOCCG). Available at: http://www.ioccg.org/groups/software.html (Accessed assessed 07/11/2022).

Lee, Z., Shang, S., Du, K., Liu, B., Lin, G., Wei, J., et al. (2018b). Enhance field water-color measurements with a Secchi disk and its implication for fusion of active and passive ocean-color remote sensing. *Appl. Optics* 57, 3463–3473. doi: 10.1364/AO.57.003463

Lee, Z., Shang, S., Du, K., and Wei, J. (2018c). Resolving the long-standing puzzles about the observed Secchi depth relationships. *Limnology Oceanography* 63, 2321–2336. doi: 10.1002/lno.10940

Lee, Z., Shang, S., Hu, C., Du, K., Weidemann, A., Hou, W., et al. (2015). Secchi disk depth: A new theory and mechanistic model for underwater visibility. *Remote Sens. Environ.* 169, 139–149. doi: 10.1016/j.rse.2015.08.002

Lee, Z., Wang, Y., Yu, X., Shang, S., and Luis, K. (2020). Evaluation of forward reflectance models and empirical algorithms for chlorophyll concentration of stratified waters. *Appl. Optics* 59, 9340–9352. doi: 10.1364/AO.400070

Lee, Z., Du, K., Voss, K. J., Zibordi, G., Lubac, B., Arnone, R., et al. (2011). An inherent-optical-property-centered approach to correct the angular effects in water-leaving radiance. *Appl. Optics* 50, 3155–3167. doi: 10.1364/AO.50.003155

Lewis, M. R., Kuring, N., and Yentsch, C. (1988). Global patterns of ocean transparency: Implications for the new production of the open ocean. *Jounral Geophysical Res.* 93, 6847–6856. doi: 10.1029/JC093iC06p06847

Lin, J., Dall'Olmo, G., Tilstone, G. H., Brewin, R. J. W., Vabson, V., Ansko, I., et al. (2022). Derivation of uncertainty budgets for continuous above-water radiometric measurements along an Atlantic Meridional Transect. *Optics Express*. doi: 10.1364/OE.470994

Longhurst, A., Sathyendranath, S., Platt, T., and Caverhill, C. (1995). An estimate of global primary production in the ocean from satellite radiometer data. *J. Plankton Res.* 17, 1245–1271. doi: 10.1093/plankt/17.6.1245

Mackas, D. L. (2011). Does blending of chlorophyll data bias temporal trend? *Nature* 472, E4–E5. doi: 10.1038/nature09951

Malthus, T. J., Ohmsen, R., and van der Woerd, H. J. (2020). An evaluation of citizen science smartphone apps for inland water quality assessment. *Remote Sensing.* 12, 1578. doi: 10.3390/rs12101578

Markwardt, C. B. (2008). "Non-linear least squares fitting in IDL with MPFIT," in *Proceedings of the astronomical data analysis software and systems XVIII*, vol. 411 . Eds. D. Bohlender, P. Dowler and D. Duran (Quebec, Canada: Astronomical Society of the Pacific, San Francisco).

Martinez, E., Antoine, D., D'ortenzio, F., and Gentili, B. (2009). Climate-driven basin-scale decadal oscillations of oceanic phytoplankton. *Science* 326, 1253–1256. doi: 10.1126/science.1177012

McQuatters-Gollop, A., Reid, P., Edwards, M., Burkill, P. H., Castellani, C., Batten, S., et al. (2011). Is there a decline in marine phytoplankton? *Nature* 472, E6–E7. doi: 10.1038/nature09950

Mobley, C. D. (1999). Estimation of the remote-sensing reflectance from above-surface measurements. *Appl. Optics* 38, 7442–7455. doi: 10.1364/AO.38.007442

Mojica, K. D. A., van de Poll, W. H., Kehoe, M., Huisman, J., Timmermans, K. R., Buma, A. G. J., et al. (2015). Phytoplankton community structure in relation to vertical stratification along a north-south gradient in the northeast Atlantic ocean. *Limnolology Oceanography* 60, 1498–1521. doi: 10.1002/lno.10113

Moré, J. (1978). "The levenberg-marquardt algorithm: implementation and theory," in *Numerical analysis* (Berlin: Springer-Verlag).

Morel, A., Huot, Y., Gentili, B., Werdell, P. J., Hooker, S. B., and Franz, B. A. (2007). Examining the consistency of products derived from various Ocean Color sensors in open ocean (case 1) waters in the perspective of a multi-sensor approach. *Remote Sens. Environ.* 111, 69–88. doi: 10.1016/j.rse.2007.03.012

Morel, A., and Prieur, L. (1977). Analysis of variations in Ocean Color. *Limnology Oceanography* 22, 709–722. doi: 10.4319/lo.1977.22.4.0709

NASA (2010). Ocean Color chlorophyll (OC) v6. In: *Tech. rep*. Available at: https://oceancolor.gsfc.nasa.gov/reprocessing/r2009/ocv6/ (Accessed 23/11/2022).

Novoa, S., Wernand, M., and van der Woerd, H. J. (2015). WACODI: A generic algorithm to derive the intrinsic color of natural waters from digital images. *Limnology Oceanography Methods* 13, 697–711. doi: 10.1002/lom3.10059\

Novoa, S., Wernand, M. R., and van der Woerd, H. J. (2014). The modern Forel-Ule scale: a 'do-it-yourself' colour comparator for water monitoring. *J. Eur. Optical Soc. - Rapid Publications* 9, 1–10. doi: 10.2971/jeos.2014.14025

O'Reilly, J. E., Maritorena, S., Mitchell, B. G., Siegel, D. A., Carder, K. L., Garver, S. A., et al. (1998). Ocean chlorophyll algorithms for SeaWiFS. *J. Geophysical Res.* 103, 24,937–24,953. doi: 10.1029/98JC02160

Pitarch, J. (2017). Biases in Ocean Color over a Secchi disk. *Optics Express* 25, A1124–A1131. doi: 10.1364/OE.25.0A1124

Pitarch, J. (2020). A review of Secchi's contribution to marine optics and the foundation of Secchi disk science. *Oceanography* 33, 26–37. doi: 10.5670/oceanog.2020.301

Pitarch, J., Bellacicco, M., Marullo, S., and van der Woerd, H. J. (2021). Global maps of Forel–Ule index, hue angle and Secchi disk depth derived from 21 years of monthly ESA ocean colour climate change initiative data. *Earth System Sci. Data* 13, 481–490. doi: 10.5194/essd-13-481-2021

Pitarch, J., Bellacicco, M., Organelli, E., Volpe, G., Colella, S., Vellucci, V., et al. (2020). Retrieval of particulate backscattering using field and satellite radiometry: Assessment of the QAA algorithm. *Remote Sens.* 12, 77. doi: 10.3390/rs1201007

Pitarch, J., van der Woerd, H. J., Brewin, R. J. W., and Zielinski, O. (2019). Optical properties of Forel-Ule water types deduced from 15 years of global satellite Ocean Color observations. *Remote Sens. Environ.* 231, 111249. doi: 10.1016/j.rse.2019.111249

Pitarch, J., and Vanhellemont, Q. (2021). The QAA-RGB: A universal three-band absorption and backscattering retrieval algorithm for high resolution satellite sensors. development and implementation in ACOLITE. *Remote Sens. Environ.* 265, 112667. doi: 10.1016/j.rse.2021.112667

Pope, R., and Fry, E. (1997). Absorption spectrum (380-700 nm) of pure water. II. integrating cavity measurements. *Appl. Optics* 36, 8710–8723. doi: 10.1364/AO.36.008710

Preisendorfer, R. W. (1986). Secchi disk science: Visual optics of natural waters. *Limnology Oceanography* 31, 909–926. doi: 10.4319/lo.1986.31.5.0909

Raitsos, D. E., Pradhan, Y., Lavender, S. J., Hoteit, I., McQuatters-Gollop, A., Reid, P. C., et al. (2014). From silk to satellite: half a century of ocean colour anomalies in the northeast Atlantic. *Global Change Biol.* 20, 2117–2123. doi: 10.1111/gcb.12457

Rasse, R., Dall'Olmo, G., Graff, J., Westberry, T. K., van Dongen-Vogels, V., and Behrenfeld, M. J. (2017). Evaluating optical proxies of particulate organic carbon across the surface Atlantic ocean. *Front. Mar. Sci.* 4, 1–18. doi: 10.3389/fmars.2017.00367

Rees, A. P., Nightingale, P. D., Poulton, A. J., Smyth, T., Tarran, G. A., and Tilstone, G. (2017). The Atlantic Meridional Transect programme, (1995–2016). *Prog. Oceanography* 158, 3–18. doi: 10.1016/j.pocean.2017.05.004

Rees, A. P., Robinson, C., Smyth, T., Aiken, J., Nightingale, P., and Zubkov, M. (2015). 20 years of the Atlantic Meridional Transect – AMT. *Limnology Oceanography Bull.* 24, 101–127. doi: 10.1002/lob.10069

Robinson, C., Poulton, A. J., Holligan, P. M., Baker, A. R., Forster, G., Gist, N., et al. (2006). The Atlantic Meridional Transect (AMT) programme: a contextual view 1995-2005. *Deep Sea Res. II* 53, 1485–1515. doi: 10.1016/j.dsr2.2006.05.015

Ruddick, K. G., De Cauwer, V., Park, Y.-J., and Moore, G. (2006). Seaborne measurements of near infrared water-leaving reflectance: The similarity spectrum for turbid waters. *Limnology Oceanography* 51, 1167–1179. doi: 10.4319/lo.2006.51.2.1167

Rykaczewski, R., and Dunne, J. (2011). A measured look at ocean chlorophyll trends. *Nature* 472, E5–E6. doi: 10.1038/nature0995

Sathyendranath, S., Brewin, R. J. W., Brockmann, C., Brotas, V., Calton, B., Chuprin, A., et al. (2019). An ocean-colour time series for use in climate studies: The experience of the Ocean-Colour Climate Change Initiative (OC-CCI). *Sensors* 19, 4285. doi: 10.3390/s19194285

Sathyendranath, S., Brewin, R. J. W., Jackson, T., Mélin, F., and Platt, T. (2017). Ocean-colour products for climate-change studies: What are their ideal characteristics? *Remote Sens. Environ.* 203, 125–138. doi: 10.1016/j.rse.2017.04.017

Sathyendranath, S., Watts, L., Devred, E., Platt, T., Caverhill, C., and Maass, H. (2004). Discrimination of diatoms from other phytoplankton using ocean-colour data. *Mar. Ecol. Prog. Ser.* 272, 59–68. doi: 10.3354/meps272059

Secchi, P. A. (1864). Relazione delle esperienze fatte a bordo della pontificia pirocorvetta l'*Immacolata concezione* per determinare la trasparenza del mare; memoria del P. A. Secchi. *Il Nuovo Cimento* 1855-1868) 20, 205–238. doi: 10.1007/BF02726911

Siegel, D. A., and Franz, B. A. (2010). Century of phytoplankton change. *Nature* 466, 569–571. doi: 10.1038/466569a

Son, S., and Wang, M. (2015). Diffuse attenuation coefficient of the photosynthetically available radiation K_d(par) for global open ocean and coastal waters. *Remote Sens. Environ.* 159, 250–258. doi: 10.1016/j.rse.2014.12.011

Szeto, M., Werdell, P. J., Moore, T. S., and Campbell, J. W. (2011). Are the world's oceans optically different? *J. Geophysical Res. - Oceans* 116, C00H04. doi: 10.1029/2011JC007230

Tilstone, G. H., Pardo, S., Dall'Olmo, G., Brewin, R. J. W., Nencioli, F., Dessailly, D., et al. (2021). Performance of ocean colour chlorophyll a algorithms for sentinel-3 OLCI, MODIS-aqua and suomi-VIIRS in open-ocean waters of the Atlantic. *Remote Sens. Environ.* 260, 112444. doi: 10.1016/j.rse.2021.112444

Tyler, J. E. (1968). The Secchi disc. *Limnology Oceanography* 13, 1–6. doi: 10.4319/lo.1968.13.1.0001

Ule, W. (1892). "Die bestimmung der wasserfarbe in den seen," in *Kleinere mittheilungen. dr. a. petermanns mittheilungen aus justus perthes geographischer anstalt* (Gotha: Justus Perthes), 70–71. 1892.

van der Woerd, H. J., and Wernand, M. (2015). True colour classification of natural waters with medium-spectral resolution satellites: SeaWiFS, MODIS, MERIS and OLCI. *Sensors* 15, 25663–25680. doi: 10.3390/s151025663

Van der Woerd, H. J., and Wernand, M. R. (2018). Hue-angle product for low to medium spatial resolution optical satellite sensors. *Remote Sens.* 10, 1–18. doi: 10.3390/rs10020180

Wang, S., Lee, Z., Shang, S., Li, J., Zhang, B., and Lin, G. (2019). Deriving inherent optical properties from classical water color measurements: Forel-Ule index and Secchi disk depth. *Optics Express* 27, 7642–7655. doi: 10.1364/OE.27.007642

Wernand, M. (2011). Poseidon's paintbox: historical archives of ocean colour in global-change perspective. Phd thesis, Utrecht University, Netherlands.

Wernand, M. R. (2010). On the history of the Secchi disc. *J. Eur. Optical Soc. - Rapid Publications* 5, 10013s. doi: 10.2971/jeos.2010.10013s

Wernand, M. R., and Gieskes, W. W. C. (2012). *Ocean optics from 1600 (Hudson) to 1930 (Raman): Shifting interpretation of natural water colouring* (Union des Océanographes de France).

Wernand, M. R., Hommersom, A., and van der Woerd, H. J. (2013a). MERIS-based ocean colour classification with the discrete Forel-Ule scale. *Ocean Sci.* 9, 477–487. doi: 10.5194/os-9-477-2013

Wernand, M. R., and van der Woerd, H. J. (2010a). Ocean colour changes in the North Pacific since 1930. *J. Eur. Optical Soc. - Rapid Publications* 5, 10015s. doi: 10.2971/jeos.2010.10015s

Wernand, M. R., and van der Woerd, H. J. (2010b). Spectral analysis of the Forel-Ule ocean colour comparator scale. *J. Eur. Optical Soc. - Rapid Publications* 5, 10014s. doi: 10.2971/jeos.2010.10014s

Wernand, M. R., van der Woerd, H. J., and Gieskes, W. W. C. (2013b). Trends in ocean colour and chlorophyll concentration from 1889 to 2000, worldwide. *PloS One* 8, e63766. doi: 10.1371/journal.pone.0063766

Ye, M., and Sun, Y. (2022). Review of the Forel–Ule index based on *in situ* and remote sensing methods and application in water quality assessment. *Environ. Sci. pollut. Res.* 29, 13024–13041. doi: 10.1007/s11356-021-18083-0

Zhang, X., and Hu, L. (2009). Estimating scattering of pure water from density fluctuation of the refractive index. *Optics Express* 17, 1671–1678. doi: 10.1364/OE.17.001671

Zhang, X., Hu, L., and He, M.-X. (2009). Scattering by pure seawater: Effect of salinity. *Optics Express* 17, 5698–5710. doi: 10.1364/OE.17.005698

frontiers | Frontiers in Marine Science

TYPE Original Research
PUBLISHED 04 April 2023
DOI 10.3389/fmars.2023.1119488

OPEN ACCESS

EDITED BY
Gilles Reverdin,
Centre National de la Recherche Scientifique (CNRS), France

REVIEWED BY
Stella Psarra,
Hellenic Centre for Marine Research (HCMR), Greece
Alex J. Poulton,
Heriot-Watt University, United Kingdom

*CORRESPONDENCE
Catarina V. Guerreiro
✉ cataguerreiro@fc.ul.pt

SPECIALTY SECTION
This article was submitted to Ocean Observation, a section of the journal Frontiers in Marine Science

RECEIVED 08 December 2022
ACCEPTED 06 March 2023
PUBLISHED 04 April 2023

CITATION
Guerreiro CV, Ferreira A, Cros L, Stuut J-B, Baker A, Tracana A, Pinto C, Veloso V, Rees AP, Cachão MAP, Nunes T and Brotas V (2023) Response of coccolithophore communities to oceanographic and atmospheric processes across the North- and Equatorial Atlantic. *Front. Mar. Sci.* 10:1119488. doi: 10.3389/fmars.2023.1119488

Response of coccolithophore communities to oceanographic and atmospheric processes across the North- and Equatorial Atlantic

Catarina V. Guerreiro[1,2,3]*, Afonso Ferreira[1], Lluisa Cros[4], Jan-Berend Stuut[5,6], Alex Baker[7], Andreia Tracana[1], Catarina Pinto[1,2], Vera Veloso[1], Andrew P. Rees[8], Mário A. P. Cachão[9], Telmo Nunes[3] and Vanda Brotas[1,3]

[1]Marine and Environmental Science Centre (MARE)/Aquatic Research Network (ARNET), Faculdade de Ciências, Universidade de Lisboa, Lisbon, Portugal, [2]Instituto Dom Luiz (IDL), Faculdade de Ciências, Universidade de Lisboa, Lisbon, Portugal, [3]Department of Plant Biology, Faculty of Sciences of the University of Lisbon, Lisbon, Portugal, [4]Institut de Ciencies del Mar (CSIC), Passeig Marítim de la Barceloneta, Barcelona, Spain, [5]Department of Ocean Systems, NIOZ Royal Netherlands Institute for Sea Research, Texel, Den Burg, Netherlands, [6]Faculty of Earth and Life Sciences, Vrije Universiteit (VU), Amsterdam, Netherlands, [7]School of Environmental Sciences, University of East Anglia, Norwich, United Kingdom, [8]Plymouth Marine Laboratory (PML), Plymouth, United Kingdom, [9]Departament of Geology, Faculty of Sciences of the University of Lisbon, Lisbon, Portugal

Changes in coccolithophore productivity in response to climate-driven ocean warming are likely to have cascading biogeochemical effects that feed back to the changing climate. This paper investigates the role (and interplay) of large-scale oceanographic and atmospheric processes across the North- and Equatorial Atlantic, including Saharan dust deposition, on the distribution of coccolithophore communities. The study is based on biological and hydrological data collected across the photic zone of the ocean, and aerosol data collected from the lower atmosphere, across 50°N–1°S during the Atlantic Meridional Transect in boreal Autumn of 2018 (AMT28), in synergy with Earth Observations. Results confirm existing understanding of the distribution of coccolithophore communities which are related to major meridional hydrological gradients across the North Atlantic. Dynamic, oxygenated and microphytoplankton-enriched waters at higher-latitudes were characterized by less diverse coccolithophore populations, dominated by placolith-bearing r-selected coccolithophores. In contrast, the heavily stratified and picoplankton-enriched waters of the subtropical gyre revealed more diverse populations, dominated by umbelliform coccolithophores and holococcolithophores at the surface, and by floriform taxa in the lower photic zone. Mean concentrations of 14.4×10^3 cells/L present in the North Atlantic Tropical Gyre Province (30–12°N), only slightly lower compared to 17.7×10^3 cells/L produced in the North Atlantic Drift province (50–40°N), provide a snapshot perspective on the importance of coccolithophore production in heavily stratified gyre conditions. Higher concentrations of 19'-Hexanoyloxyfucoxanthin (HexFuco) in regions of enhanced production of r-selected placolith-bearing species suggest that this pigment should not be generalized as a proxy for the entire coccolithophore community. Enhanced abundances of fast-blooming *Emiliania huxleyi* and *Gephyrocapsa oceanica*, and of cyanobacteria (including both picoplankton and N_2-fixing *Trichodesmium* spp.) at the surface of the region of more persistent Saharan dust deposition (at ~12-10°N) appeared to result from dust-born nutrient input. Underneath this stratified surface layer, enhanced productivity in the deep chlorophyll maximum (DCM) appeared decoupled from that on the surface, fueled by geostrophic eastward shoaling of the nutricline across the tropical North Atlantic. As this was the region of highest macronutrient concentrations measured along and below the nutricline, our data suggest that the NE tropical Atlantic may act as a permanent dust-born nutrient depocenter as previously hypothesized.

KEYWORDS

coccolithophores, phytoplankton, ecological gradients, nutricline, Westerly Wind Biome, Trade Wind Biome, Saharan dust, Atlantic Meridional Transect

1 Introduction

Ongoing climate warming is likely to hamper the efficiency of the biological carbon pump through altering the latitudinal distribution of temperature, light, and nutrient concentrations in the upper ocean, all synergistically interplaying to modulate the productivity and composition of phytoplankton communities (e.g., Laufkötter et al., 2015). According to the most recent IPCC report (2021), enhanced ocean warming and high latitude freshening over the last decades have weakened the overturning of surface ocean waters, which has inevitable consequences for nutrient cycling in the open ocean and associated primary production. Several studies report a decrease of global phytoplankton productivity over the past century due to reduced nutrient availability driven by increasing thermal stratification (e.g., Behrenfeld et al., 2006; Polovina et al., 2008; Boyce et al., 2010; Krumhardt et al., 2017; Moore et al., 2018). This overall warming-driven decrease in global primary production has been projected to continue over the mid-21st century, particularly in tropical and subtropical regions, and in most of the Atlantic (Krumhardt et al. (2017). While some studies suggest that phytoplankton communities can adapt physiologically and evolutionarily to climate change (Irwin et al., 2015), others indicate a sharp decline in tropical phytoplankton diversity and a poleward shift in species' thermal niches (e.g., Thomas et al., 2012). This includes an abundance increase and northward expansion of small-sized phytoplankton species (e.g., Dutkiewicz et al., 2013), including N2-fixing diazotrophic cyanobacteria (Krumhardt et al., 2016; Krumhardt et al., 2017) and calcifying nanoplankton (Winter et al., 2013; Rivero-Calle et al., 2015; Oziel et al., 2020), possibly reflecting their capacity to thrive at low nutrient levels compared to microphytoplankton, e.g., diatoms (e.g., Boyd et al., 2010; Lancelot, 2012; Krumhardt et al., 2017).

A mechanism that has been hypothesized to counteract the negative effects from ocean stratification is the deposition of atmospheric nutrients by dust outbreaks triggered by ongoing climate-induced land desertification (Moulin and Chiapello, 2006; Mirzabaev et al., 2019) and biomass burning (Turco et al., 2019; Ruffault et al., 2020; Ito et al., 2021). In fact, mineral dust is considered the dominant source of Fe and other trace metals to the global ocean (e.g., Martin, 1990; Coale et al., 1996; Boyd et al., 2007; Baker et al., 2013). This matters because dissolved (bioavailable) Fe is often only present at trace concentrations in oxygenated open ocean surface waters (e.g., Ussher et al., 2013), thereby limiting primary production in up to 30–40% of the global ocean (Moore et al., 2002; Boyd and Ellwood, 2010). Guieu et al. (2014) report the importance of strong and short-term (pulse-like) dust-born nutrient deposition events for marine productivity at High Nutrient Low Chlorophyll regions, up to one order of magnitude larger than vertical supply from the sub-surface in oligotrophic regions. In addition, dust also acts as mineral ballast to increase the sinking velocities of carbon-enriched marine snow aggregates, critical for the export and sequestration of particulate organic carbon (POC) produced by phyto- and zooplankton (van der Jagt et al., 2018).

Of all the continental deserts, the Sahara Desert is the world's largest source of atmospheric soil dust (Figure 1). Megatons of Saharan-dust blown into and over the Atlantic every year are thought to supply macronutrients and trace metals for marine

---

Abbreviations: AOT, Aerosol Optical Thickness; AzC, Azores Current; TChl-*a*, Total Chlorophyll-*a;* DCM, Deep Chlorophyll Maximum; ENACW, Eastern North Atlantic Central Water; Fuco, Fucoxanthin; HexFuco, 19'Hexanoyloxyfucoxanthin; ITCZ, Intertropical Convergence Zone; LPZ, Lower Photic Zone; MLD, Mixed Layer Depth; NAC, North Atlantic Current; NADR, North Atlantic Drift Province; NAST, North Atlantic Subtropical Province; NATR, North Atlantic Tropical Province; NEC, North Equatorial Current; NECC, North Equatorial Counter Current; OMZ, Oxygen Minimum Zone; PAR, Photosynthetically Available Radiance; Perid, Peridinin; POC, Particulate Organic Carbon; SACW, South Atlantic Central Water; SSS, Sea Surface Salinity; SST, Sea Surface Temperature; TSW, Tropical Surface Water; UPZ, Upper Photic Zone; WTRA, Western Tropical Atlantic Province; Zea, Zeaxanthin.

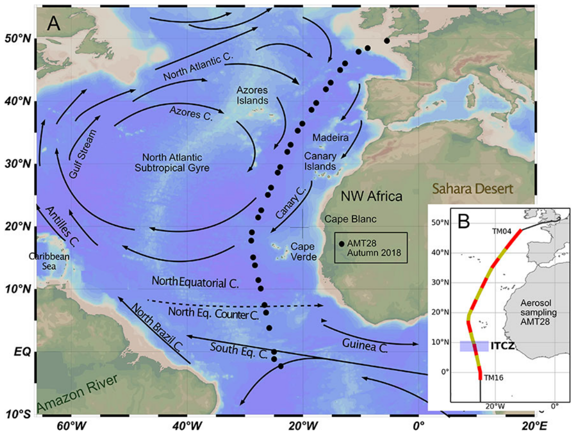

FIGURE 1
Location of the CTD sampling stations across the North- and equatorial Atlantic, collected during AMT28, and a schematic representation of the main surface currents in the region **(A)**; location of aerosol sampling and approximate position of the ITCZ during the expedition **(B)**.

phytoplankton in the tropical North Atlantic (Goudie and Middleton, 2001; Jickells et al., 2005). Being adjacent to NW Africa, a region affected by ongoing desertification (Mirzabaev et al., 2019), the North Atlantic provides a unique opportunity to investigate the effects of Saharan dust outbreaks on ocean productivity and biogeochemistry. This process is likely to be especially important for organisms living in the subtropical gyre and in the tropical region outside the equatorial upwelling, where nearly permanently stratified Low Nutrient Low Chlorophyll waters result in low productivity during most of the year (see Mann and Lazier, 2006; Moore et al., 2018). Fixed nitrogen in the remote open North Atlantic is largely delivered by *in situ* diazotrophic N2-fixation (Mahaffey et al., 2014). This process is co-limited by Fe and P (Mills et al., 2004), with these limitations being partially alleviated by the deposition of atmospherically processed African dust (e.g., Baker et al., 2006; Buck et al., 2010). In turn, dust-stimulated N_2-fixation may fuel up to 50% of the export production (Mills et al., 2004 and refs. therein) through promoting the growth of other phytoplankton groups for which N_2-limitation is relieved by diazotrophic N_2-release (Moore et al., 2002; Pabortsava et al., 2017). This is the case for *Trichodesmium* spp. which are reportedly most abundant in areas of higher Saharan dust input (Mills et al., 2004 and refs. therein; Pabortsava et al., 2017; Shelley et al., 2017). However, little is known about the effects of Saharan dust on other major phytoplankton groups.

Among the main groups of marine phytoplankton, coccolithophores are the main primary producers able to biomineralize calcite platelets (coccoliths) around their cell surface to form an exoskeleton (coccosphere) (Pienaar, 1994; Monteiro et al., 2016) through a biogeochemical process that incorporates carbon in calcite and releases CO_2 into the environment (Rost and Riebesell, 2004). This means that coccolithophores influence the carbon cycle both *via* photosynthesis (while producing POC – CO_2 sink); *via* calcification (while producing particulate inorganic carbon, PIC – CO_2 source); and *via* carbon-burial in oceanic sediments through coccolith-ballasting POC (Rost and Riebesell, 2004; Ziveri et al., 2007; Guerreiro et al., 2021). Hence, coccolithophores contribute crucially to modulate biogenic PIC/POC export from the surface down to the deep ocean (also termed "rain ratio"), which is largely what determines the efficiency of the biological carbon pump in sequestering atmospheric CO_2 (Rost and Riebesell, 2004; Cermeño et al., 2008).

As a group, coccolithophores are more diverse and contribute higher percentages to the phytoplankton community in open-ocean, stratified oligotrophic waters from low- to mid-latitude regions (e.g., Winter et al., 1994), hence displaying features more typical of K-selected taxa (Margalef, 1978), compared to eutrophic environments (e.g., coastal-neritic and upwelling waters) where they are less diverse and surpassed by more opportunistic groups (r-selected taxa, Margalef, 1978), e.g., diatoms. Still, the group also includes more opportunistic species that quickly respond to short-term change, able to produce massive blooms in the open-ocean (e.g., Knappertsbusch and Brummer, 1995; Souza et al., 2011) and within coastal and upwelled waters (e.g., Baumann et al., 2000; Guerreiro et al., 2013) that are often optically reflective enough and close enough to the ocean's surface to be detected by remote sensing (e.g., Balch, 2018).

Despite their lower nutrient requirements compared to, for instance, diatoms (e.g., Margalef, 1978; Boyd et al., 2010), coccolithophores are also susceptible to ocean nutrient depletion. Their limitation to Fe and Zn has been evidenced from incubation experiments suggesting that changes in dust deposition may affect their calcification in regions marked by trace-metal limitation (Schulz et al., 2004), and result in higher coccolithophore-based biomass and carbonate production (Crawford et al., 2003). Recent work based on coccolith species fluxes from four sediment-trap time-series across the tropical North Atlantic report evidence supporting the hypothesis of Saharan dust acting as a fertilizer for marine phytoplankton, including opportunistic coccolithophore species (Guerreiro et al., 2017; Guerreiro et al., 2019). A striking flux increase of POC and of coccolith fluxes by fast-blooming surface-dwelling species *E. huxleyi* and *G. oceanica* during times of enhanced dust deposition and Amazon water dispersal was seen promoting a more efficient coccolith-ballasting and resulting in lower rain ratios (Korte et al., 2020; Guerreiro et al., 2021). Whether these species have grown by directly consuming nutrients supplied by dust, or indirectly by consuming N_2 released from dust-stimulated N_2-fixation, and whether these events mostly reflected an ecological response and/or a higher export efficiency due to dust- and coccolith-ballasting (see Pabortsava et al., 2017), remain as open questions.

To tackle these issues, we have investigated links between biological, oceanographic, and atmospheric processes influencing coccolithophore communities across the entire North- and Equatorial Atlantic, including Saharan dust deposition. The study is based on multidisciplinary *in situ* data collected during the Atlantic Meridional Transect (AMT28 – Figure 1), in synergy with a range of satellite and modelled data and contributes to distinguishing the effects of distinct drivers of coccolithophore productivity in the North Atlantic. Our goal is to provide robust baseline information of modern ecological analogues to inform how oceanographic processes and dust deposition will impact ocean productivity in a future ocean.

2 Regional settings

2.1 Water masses

Water masses of the uppermost 500 m in the temperate and subtropical regions of our study area (50°–20°N, sites 1–19), mostly consist of Eastern North Atlantic Central Water (ENACW) marked by large temperature (T) and salinity (S) ranges (T: 8–18 °C; S: 35.2–36.7) and low nutrient concentrations (Emery, 2001; Liu and Tanhua, 2021), formed in the inter-gyre region at latitudes between 39–48° N during the winter subduction (Pollard et al., 1996). To the south of 20° N (sites 20–31), the uppermost 100 m mostly consist of salty and nutrient-depleted Tropical Surface Water (TSW) (T: ~27°C, S: 36.7–37) above the cooler, less salty and relatively nutrient-enriched South Atlantic Central Water (SACW) at depths down to ~500 m (T: 6.0–18°C, S: 34.3–35.8) (Emery and Meincke, 1986; Reid, 1994; Stramma and England, 1999). Within the eastern tropical North Atlantic, SACW waters are found at < 100 m, shallow enough to reach the ephotic zone through the action of the surface winds, and with substantial contributions of the saltier and warmer ENACW in its lower part (300–550 m) (Pelegrí et al., 2017).

2.2 Surface circulation and biogeographic provinces

Surface water circulation in the study area, involving ENACW along 50–20°N, and TSW and SACW along 20°N–1°S, is mostly forced by the overlying anticyclonic wind system that occurs north of the Equator (~45–15°N), driving a clockwise circular ocean current system across the entire North Atlantic, termed North Atlantic Subtropical Gyre (Figure 1). On the west, the gyre is bounded by the strong and narrow northward-flowing Gulf Stream, which bifurcates over the Newfoundland Basin to feed into the northeastward flowing North Atlantic Current (NAC, at ~45–40°N), and into the southeastward-flowing Azores Current (AzC, at 36–33°N) directly into the gyral circulation. Part of the NAC recirculates into the gyre when encountering the European continental shelf, feeding into the broader and slower Portugal/Canary Current continuum that flows southwards along the Iberian Peninsula and NW coast of Africa. At ~21°N, the Canary Current detaches from the continental shelf and starts flowing westwards, feeding into the westward-flowing North Equatorial Current (NEC) which, in turn, connects back to the Gulf Stream through the northwestward-flowing Antilles Current (Aiken et al., 2017 and refs. therein) (Figure 1).

Such wind-forced gyral circulation has direct effects on the mixed layer depth (MLD) dynamics and, subsequently, on the biogeographic distribution of phytoplankton communities. According to Longhurst (2007), our meridional transect crosses two important circulation-driven biomes: the North Atlantic Westerly Wind Biome (60–30°N), where the MLD is markedly modulated by seasonal variations in westerly wind stress and solar insolation; and the Trade Wind Biome (30°N–5°S) where the MLD is much less seasonal, modulated by variations in the magnitude and latitudinal position of the trade winds.

Each of the two biomes are divided in two biogeographic provinces, reflecting smaller-scale variations in terms of MLD dynamics, ocean temperature and nutrient availability (Longhurst, 2007). The Westerly Wind Biome is divided into the North Atlantic Drift Province (NADR) at 60–40°N (Sites 1-7), and the North Atlantic Subtropical Gyre Province (NAST-E) at 40–30°N (Sites 8–13). The Trade Wind Biome is, in turn, divided into the North Atlantic Tropical Gyre Province (NATR) at 30–12°N (Sites 14-23); and the Western Tropical Atlantic Province (WTRA) at 12/14°N–5° S and to the west of 15°W (Sites 24-31). Between the NEC and the Equator is the North Equatorial Counter Current (NECC), flowing against the wind in eastward direction, and with no influence on the gyre equatorial edge (Stramma and England, 1999; Aiken et al., 2017), both of which are subjected to the latitudinal migrations of the Intertropical Convergence Zone (ITCZ) (Basha et al., 2015).

2.3 Saharan dust deposition in the open Atlantic Ocean

Despite the highly variable and intermittent nature of atmospheric dust deposition, the Saharan dust plume region is characterized by well-marked spatiotemporal gradients (Powell et al., 2015), which are seasonally modulated by the ITCZ (Ben-Ami et al., 2012; Yu et al., 2019; van der Does et al., 2021). Highest dust fluxes in winter occur in the eastern tropical North Atlantic, closer to the dust sources in Africa (Skonieczny et al., 2013; Fomba et al., 2014; Fischer et al., 2016), and mainly transported by the Harmattan winds at lower altitudes in the atmosphere (0–3 km). During summer, the highest dust fluxes occur closer to the Caribbean in the western tropical North Atlantic (Prospero et al., 2014), mainly transported by the Saharan Air Layer at higher altitudes in the atmosphere (5–7 km) (Stuut et al., 2005; Adams et al., 2012; Tsamalis et al., 2013). Highest surface dissolved iron (dFe) and total dFe concentrations in waters of the oligotrophic tropical North Atlantic (~5–30° N) reflect the latitudinal extent of the Saharan dust plume (Bergquist and Boyle, 2006; Measures et al., 2008; Ussher et al., 2013; Shelley et al., 2017).

3 Material and methods

3.1 *In situ* sampling

Sampling was conducted between 25 September and 10 October 2018, on board of RRS James Clark Ross during the Atlantic Meridional Transect (AMT28). Coccolithophore communities were inspected in 150 seawater samples collected from 31 predawn and noon CTD (conductivity, temperature, depth) casts along a track crossing the Atlantic from ~50°N to 1°S (Figure 1 and Table 1).

Hydrological data (i.e., temperature, salinity, oxygen, fluorometry and nutrients) and seawater samples for the coccolithophore and photosynthetic pigment analysis were collected using OTE (Ocean Test Equipment) Niskin bottles (24 x 20L) mounted on a stainless-steel rosette and a Seabird CTD system. Samples were collected at discrete water depth levels between 5 and 200 m depth to assess the distribution of coccolithophore species along the photic zone of the ocean. Pigment markers were analysed from samples collected at 5 m and DCM, while nutrient samples were collected at every depth from each CTD cast following GO-SHIP protocols (Becker et al., 2020). CTD data are represented as contour plots constructed with the inverse distance to power gridding method of Surfer Version 8.

Aerosol samples were collected using an Anderson high volume (1 m^3 min^{-1}) sampler, which operated under control from an automatic wind sector controller in order to avoid contamination from the ship's stack. This device interrupted pumping if the relative wind speed was below 2 $m\ s^{-1}$, or if the wind direction was between 150 and 280 degrees relative to the ship's bow. Samples were collected onto single

TABLE 1 Metadata information regarding the sites sampled during AMT28 used in this study. MLD determined following the temperature criterion (Levitus, 1982).

Date	Site	LAT	LONG (W)	Depths Sampled (m)	DCM (m)	MLD (m)
25/09/2018	1	49° 38.285' N	05° 30.096'	80; 60; 22; 12; 5	12	18
26/09/2018	2	48° 28,.65' N	08° 50.193'	100; 60; 20; 10; 5	60	62
26/09/2018	3	47° 54.073'N	10° 23.884	150; 50; 30; 20; 5	30	52
27/09/2018	4	46° 01.745' N	12° 43.950	150; 70; 20; 10; 5	70	43
27/09/2018	5	44° 58.715' N	13° 35.363	150; 50; 40; 20; 5	40	35
28/09/2018	6	42° 58.022'N	15° 12.784	150; 60; 52; 20; 5	52	43
28/09/2018	7	41°54,700' N	16°02.179	150; 56; 50; 20; 5	56	39
29/09/2018	8	39° 43.158'N	17° 42.968'	150; 81; 71; 20; 5	71	30
29/09/2018	9	38° 37.851' N	18° 31.541'	150; 70; 50; 20; 5	70	30
30/09/2018	10	36° 24.836' N	20° 07.287'	150; 115; 105; 20; 5	105	43
30/09/2018	11	35° 18.121' N	20° 54.912'	150; 105; 50; 20; 5	105	34
01/10/2018	12	33° 2.816' N	22° 08.206'	150; 100; 90; 50; 5	90	23
01/10/2018	13	31° 55.442' N	22° 42.611'	150; 120; 85; 50; 5	85	37
02/10/2018	14	29° 29.299'N	23° 55.948'	200; 150; 114; 50; 5	114	34
02/10/2018	15	28° 36.544' N	24° 21.650'	200; 150; 135; 50; 5	135	26
03/10/2018	16	26° 12.227' N	25° 31.264'	200; 150; 107; 50; 5	105	23
03/10/2018	17	25° 03.461' N	26° 03.408'	200; 140; 120; 50; 5	120	17
04/10/2018	18	22° 35.980' N	27° 12.800'	200; 150; 93; 50; 5	93	42
04/10/2018	19	21° 26.830' N	27° 44.720'	200; 140; 120; 50; 5	120	22
05/10/2018	20	19° 04.664' N	28° 49.004'	200; 150; 90; 50; 5	90	41
05/10/2018	21	17° 44.837' N	28° 55.814'	200; 100; 65; 50; 5	65	44
06/10/2018	22	15° 04.566' N	28° 36.756'	150; 100; 57; 20; 5	57	27
06/10/2018	23	13° 48.630' N	28° 17.763'	150; 85; 60; 50; 5	60	29
07/10/2018	24	11° 26.819'N	27° 42.524'	150; 100; 50; 20; 5	50	20
07/10/2018	25	10° 05.894'N	27° 17.629'	150; 70; 40; 20; 5	40	21
08/10/2018	27	07° 28.277' N	26° 39.007'	150; 100; 72; 50; 5	72	29
08/10/2018	28	06° 15.359' N	26° 22.796'	150; 85; 64; 30; 5	64	39
09/10/2018	29	03° 48.465' N	25° 50.148'	200; 150; 89; 50; 5	89	41
10/10/2018	30	00° 00.031' S	24° 59.953'	150; 70; 60; 50; 5	60	34
10/10/2018	31	01° 09.109' S	24° 59.435'	120; 90; 75; 30; 5	75	61

203 x 254 mm Whatman 41 cellulose filters which had been washed prior to use with dilute (0.5 M and 0.1 M) hydrochloric acid solution. Sample collection times were generally 24 hours, although pumping times were occasionally shorter due to the operation of the wind sector controller (see Table 2). After collection, filters were sealed in zip-lock polyethylene bags and frozen (detailed description on sampling procedures in Rickli et al., 2010).

3.2 Laboratory and microscope analysis

3.2.1 Coccolithophores

For the study of coccolithophores, seawater samples of around 2 to 5 L were filtered onto cellulose acetate filters (0.45 µm pore size, 47 mm diameter) using a low-pressure vacuum system directly on board. The filters were then rinsed with a buffered solution to remove salt, dried at room temperature, and stored in petri dishes. A randomly chosen section (approx. 30°–45°) of each filter (radius of ~16 mm) was cut and permanently mounted on a glass slide. Coccospheres (cells) were identified and counted under polarized light microscope (Zeiss Ortholux II-POL-BK) at 1250× magnification. The examined area per filter varied between 9×10^5 and 9.8×10^6 mm^2, depending on the general cell density. The number of cells per litre (cells/l) was estimated from the number of counted coccospheres in the examined area, multiplied by the ratio of total filter area to examined area, and divided by the volume of filtered water (Cros, 2001).

Coccolithophores taxonomy followed Jordan et al. (2004), Cros and Fortuño (2000), Frada et al. (2010) and Young et al. (2011). To refine the differentiation of *Syracosphaera* spp., *Ophiaster* spp., *Michaelsarsia* spp., *Acanthoica* spp. and holococcolithophores, Ca 26 samples selected to be inspected using the Scanning Electron Microscope (SEM, JEOL JSM5200-LV at FCUL, mostly at 15kV), containing higher numbers of rare species and holoccocolithophores. A randomly chosen section of the selected filters was fixed with carbon tape on a SEM stub and sputtered with an Au coating.

Coccolithophore taxa were further grouped according to their similarities in terms of meridional and in-depth distribution during AMT28, following similar criteria to those of Young (1994). Alterations to Young (1994) are described in the Supplementary Material (Figures II-IV). The ratio between upper photic zone (UPZ) r-selected species and lower photic zone (LPZ) species was used as a proxy for inferring regions of surface nutrient-enrichment vs. enhanced stratification (i.e., higher UPZ/LPZ ratios indicate more productive surface conditions). The ratio was calculated for each studied discrete sampling depth as the sum of the abundances of *E. huxleyi* and Gephyrocapsid species divided by the sum of the abundances of *Florisphaera profunda* and *Gladiolithus flabellatus* (e.g., Molfino and McIntyre, 1990; Beaufort et al., 1997; Stoll et al., 2007; Guerreiro et al., 2019). Finally, the Shannon–Wiener diversity index (H' exp) (e.g., Tuomisto, 2013) was calculated from the cell counts using the polarizing light microscope, for assessing the coccolithophore species diversity at each sampling site.

3.2.2 Phytoplankton cells and photosynthetic pigments

For the photosynthetic pigment analysis, a volume of 1 to 4 L of seawater was vacuum-filtered through GF/F glass fibre filters (Whatman) of pore size 0.7 µm and 25 mm diameter, which were further folded into 2 mL cryovials, flash frozen in liquid nitrogen and stored at -80°C. Pigments were later determined using High Performance Liquid Chromatography, following Zapata et al. (2000); the column used was a Waters C8 Symmetry with 150 x 2.1 mm and 3.5 µm particle size, and a flow rate of 200 µL min^{-1}. The HPLC was calibrated using a suite of standards purchased from DHI (Denmark). Pigments were identified based on retention time and spectral match using a photo-diode array.

TABLE 2 Summary of aerosol collection periods and pump operation times during AMT28. See Figure 1B for the location of the aerosol collection periods.

Sample Number	Start Date	Start Lat (°N)	Start Lon (°E)	End Date	End Lat (°N)	End Lon (°E)	Pump Time (hr)
TM04	26/09/2018	47.36	-11.62	28/09/2018	40.97	-16.76	8.00
TM05	28/09/2018	40.97	-16.76	29/09/2018	37.78	-19.14	10.49
TM06	29/09/2018	37.76	-19.16	30/09/2018	34.49	-21.39	22.49
TM07	30/09/2018	34.46	-21.41	01/10/2018	31.13	-23.12	23.23
TM08	01/10/2018	31.13	-23.12	02/10/2018	27.76	-24.77	19.14
TM09	02/10/2018	27.76	-24.77	03/10/2018	23.95	-26.59	23.35
TM10	03/10/2018	23.95	-26.59	04/10/2018	20.62	-28.13	10.97
TM11	04/10/2018	20.53	-28.17	05/10/2018	16.79	-28.98	14.03
TM12	05/10/2018	16.76	-28.98	06/10/2018	12.51	-27.97	22.81
TM13	06/10/2018	12.51	-27.97	07/10/2018	8.98	-26.98	22.64
TM14	07/10/2018	8.91	-26.97	08/10/2018	5.41	-26.19	21.31
TM15	08/10/2018	5.20	-26.14	09/10/2018	1.46	-25.32	23.27
TM16	09/10/2018	1.46	-25.32	10/10/2018	-2.01	-24.99	23.30

To obtain an overview of the distribution of major taxonomic groups, a marker-pigment approach was used. Fucoxanthin (Fuco) was used as pigment marker for diatoms, peridinin (Perid) for autotrophic dinoflagellates, 19'hexanoyloxyfucoxanthin (HexFuco) for coccolithophores (Haptophyta Type 6), and zeaxanthin (Zea) for marine cyanobacteria *sensu latu* (s.l.), i.e., including picoplankton and N_2-fixing filamentous diazotrophs (detailed description of the pigment analysis in Brotas et al., 2022). While HexFuco is an exclusive pigment of coccolithophores, fucoxanthin is not exclusive of diatoms, nor zeaxanthin of Cyanobateria, nor is peridinin present in all Dinoflagellate species. Nevertheless, this simplistic approach was considered the most appropriate for our studied region since the phytoplankton community has been reported to change significantly across the large hydrological gradients as those covered by the AMT, therefore less suitable for implementing other pigment analysis approaches (e.g. CHEMTAX), as discussed in Brotas et al. (2022)

For the phytoplankton cells count and identification, samples of 200 mL were collected at each sampling site, placed put in amber glass bottles, and fixed with acidic Lugol's iodine solution. Taxonomic analysis and abundance quantification of filamentous cyanobacteria (e.g., *Trichodesmium* spp.) were made with a Zeiss Axiovert 200 inverted microscope over a 50 mL chamber (see Utermöhl, 1958).

3.2.3 Macronutrients and mixed layer depth

To determine the concentration of macronutrients, water samples taken at each CTD cast were sub-sampled into clean (acid-washed) 60 mL HDPE (Nalgene) sample bottles, which were rinsed three times with sample seawater prior to filling and capping. The samples were analysed on the ship as soon as possible after sampling and were not stored or preserved. Micro-molar nutrient analysis was carried out on board using a four channel SEAL analytical AAIII segmented flow nutrient auto-analyser. The colorimetric analysis methods used were: nitrate (Brewer and Riley, 1965, modified), nitrite (Grasshoff, 1976), and phosphate and silicate (Kirkwood, 1989). The MLD was determined following the temperature criterion defined by Levitus (1982), according to which the mixed layer is the depth at which the difference in temperature from the surface value is 0.5° C.

3.2.4 Aerosol concentration, composition and deposition fluxes

The Whatman 41 aerosol filters were cut into four equal portions, with separate portions used for analysis of dust, water-soluble and ammonium acetate-soluble components. For dust analysis, the filter portion was ashed in a low temperature asher (e.g., van der Does et al., 2018) to isolate the aeolian dust collected during AMT28 (Tarran, 2018, cruise report). The amount of dust that remained after ashing was measured on a Toledo micro balance. Dust concentrations were calculated using the mass total dust per filter (mg) and the volumes of filtered air (m^3) per filter.

Soluble nutrients were determined in aerosol samples following extraction of portions of each sample into ultrapure water for nitrate (NO_3^-) and ammonium (NH_4^+) ions (Yodle and Baker, 2019) and into ~ 1 M ammonium acetate solution for soluble phosphorus (s-P) and iron (s-Fe) (Baker et al., 2007), with the extraction solutions being passed through 0.2 mm cellulose acetate cartridge filters (Sartorius). Analysis was by ion chromatography for nitrogen species (Baker et al., 2007) and inductively coupled plasma – mass spectrometry for s-P and s-Fe, with P and Fe determined as their oxygen adducts ($^{31}P^{16}O$ and $^{56}Fe^{16}O$ respectively) in triple-quad mode (iCAP TQ, Thermo). Estimations of wet and dry dust deposition fluxes from the measured atmospheric concentrations are described in the Supplementary Material.

3.3 Earth observation data

Time series of relevant hydrological and meteorological parameters were obtained from satellite data and used to assess the environmental conditions during the in-situ sampling conducted whilst at sea. The full list of parameters includes the sea surface temperature (SST; °C), sea surface salinity (SSS; unitless), Chl-*a* concentration (Chl-*a*; mg m^{-3}), the aerosol optical thickness at 865 nm (AOT; unitless), the photosynthetically available radiance (PAR; µEinstein m^{-2} d^{-1}), the wind speed (m s^{-1}) and wind direction (degrees) and the daily rain rate (mm d^{-1}). Data were downloaded from various sources and processed for the study period and for 1998-2020 (list and description in the Supplementary Material - Table I).

4 Results

4.1 Meteorological and hydrological conditions

Mean surface ocean conditions changed along the transect, with cooler, of lower salinities and higher Chl-*a* concentrations waters under the windier conditions in the NADR (> 40°N), from which they gradually changed to increasingly warmer, saline and Chl-poor waters towards the gyre central region (~30–25°N) where SSS was highest and Chl-*a* was lowest across the transect (Figures 2A–C). From there, SST continued to increase southwards while SSS gradually decreased until reaching its lowest values in the WTRA equatorial region (Figures 2A, B). Weaker winds and higher rain rates at ~12–5°N indicated the influence of the ITCZ (Figures 2D, E). A warm lens of very low SSS and high Chl-*a* concentrations was expanding from the Amazon and Orinoco River mouths into the open equatorial North Atlantic to form a Chl-enriched continuum across the tropical NE Atlantic (i.e., along ~22–5°N, to the east of 30°W) (Figures 2A–C). South of this region, a band of lower SST, higher SSS and low Chl-*a* concentrations extended across the entire ocean basin. Chl-*a* increased to slightly higher concentrations along the Equator. Chl-enrichment along the NATR-WTRA transition to the east of 30°W (at ~22–10°N) occurred under strong NE winds and the highest mean AOT of the study area (Figures 2C, D, F),

Hydrological parameters measured within the uppermost 200 m of the ocean (Figures 3, 4) confirmed the meridional

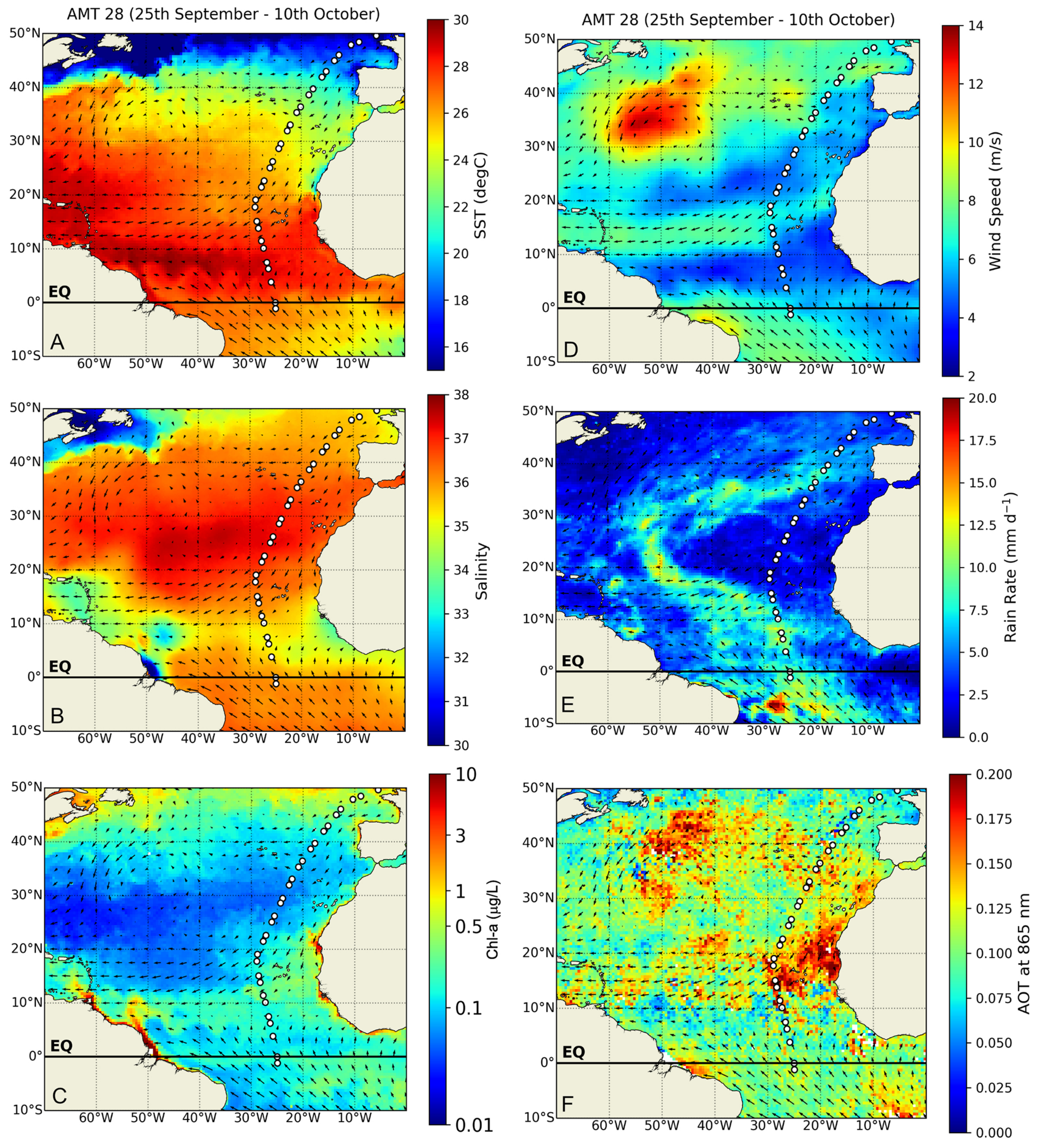

FIGURE 2
Satellite-derived atmospheric and surface ocean conditions averaged for the entire North- and Equatorial Atlantic during the AMT 28 sampling period (25 September to 10 October 2018): **(A)** sea surface temperature (SST, °C), **(B)** sea surface salinity, **(C)** Chl-*a* concentrations (µg/L) **(D)** wind speed (m/s), **(E)** rain rates (mm/day), and **(F)** aerosol optical thickness (AOT). Arrows shown in all figures represent spatial variations on the averaged wind direction during AMT28.

surface patterns described above. Colder and denser water masses in the NADR were characterized by the highest Chl-fluorescence and oxygen levels along the transect, and a DCM extending from 12 m depth at Site 1 to 30–71 m along Sites 2–9. To the south of the NADR, a gradient of increasing temperature and decreasing density and oxygen occurred along the uppermost 30–40 m depth, with a region of highest salinity along ~39–20°N related to the gyre (Figures 3A, C, D). Here, high salinities and warm temperatures deepened the most across the transect (down to >200 m) (Figures 3A, B), as well as the DCM (down to 135 m at site 15), while Chl-fluorescence was minimum at the surface (Figure 4E). To the south of the gyre, salinity dropped until reaching a surface minimum at sites 27–28 (Figure 3B), signalling contributions from the Amazon River plume and from ITCZ-related rainfall prior to

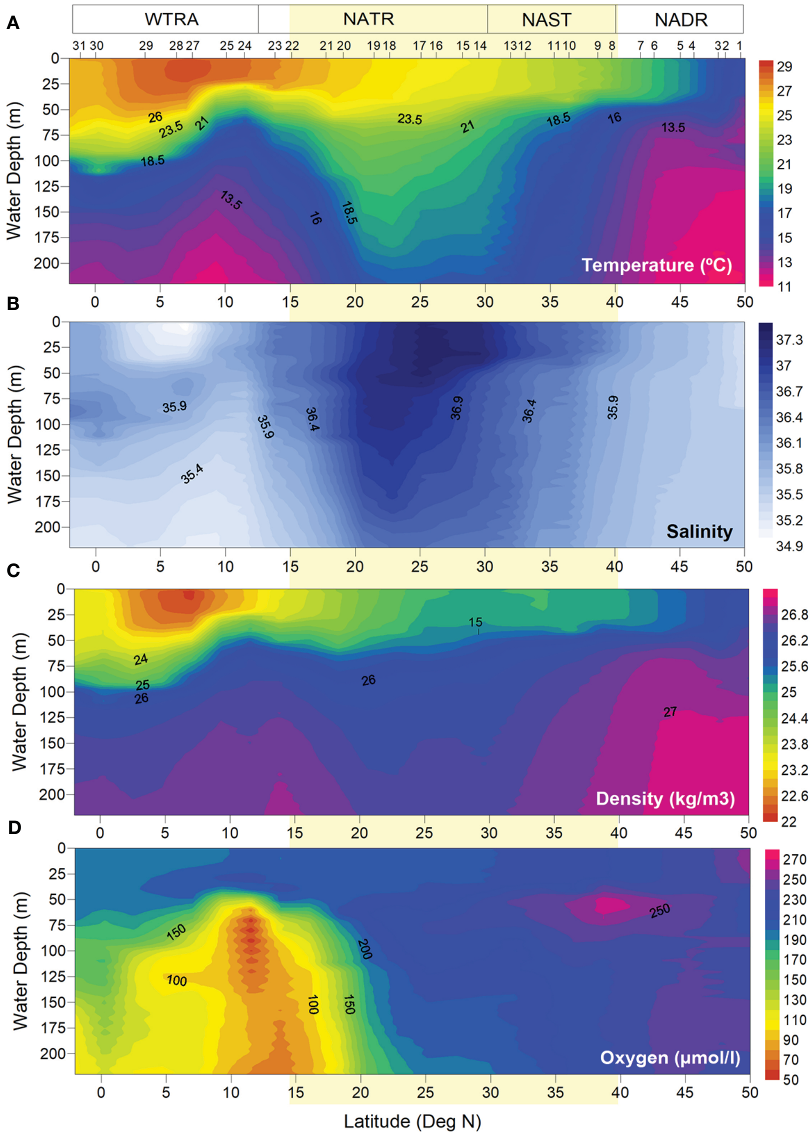

FIGURE 3
Hydrological conditions measured *in situ* at AMT 28 sampling sites: **(A)** temperature (°C), **(B)** salinity, **(C)** density (kg/m^3), and **(D)** dissolved oxygen concentration (µmol/L). Light-yellow band indicates the approximate location of the North Atlantic Subtropical Gyre at ~15-40° N (Aiken et al., 2017).

the expedition (Figures 2B, E). At 18–5°N, a 25 m uppermost layer of heavily stratified tropical water was overlaid over a colder and less saline water mass which was upwelling between the Equator and 15° N (Figures 3A–C), and coinciding with a sub-surface Oxygen Minimum Zone (OMZ) (Figure 3D). The DCM was shallower in this region (50–40 m at Sites 24–25), following the rising of the pycnocline (Figure 4E).

MLDs were often greater under stronger wind-stress conditions, more notably in the southern part of the transect (Figures 4C, D), although this was not always the case. A good example of one such exception concerns the windier conditions in the AzC region (centred at ~33°N) under which no deepening of the MLD was observed. The lowest MLDs across the transect were observed at the centre of the gyre (Site 17, at 25°N), followed by the northernmost end of the transect (Site 1, at 49°N) and northern part of the WTRA (Sites 24–25, at ~11–10° N). During the sampling period, rain only occurred in the NADR and, to a much lesser extent, in the southern part of the gyre (~22–19° N), but not in the region underneath the ITCZ (Figure 4C).

4.2 Atmospheric dust deposition

The occurrence of two dust outbreak events during AMT28 was depicted from daily images of the atmosphere taken by NASA Worldview (Figure 5). While the first event began at the start of the expedition, the dust plume only crossed our transect by 27–30 September (between Sites 4 and 11, 46–36°N), in line with the AOT increase observed in the NADR and northern NAST (Figure 4C). The second event was during 3–7 October (between Sites 16 and 25, 26–10°N), thereby coinciding with the period during which the photic zone was sampled across the NATR-WTRA (Figure 5). This

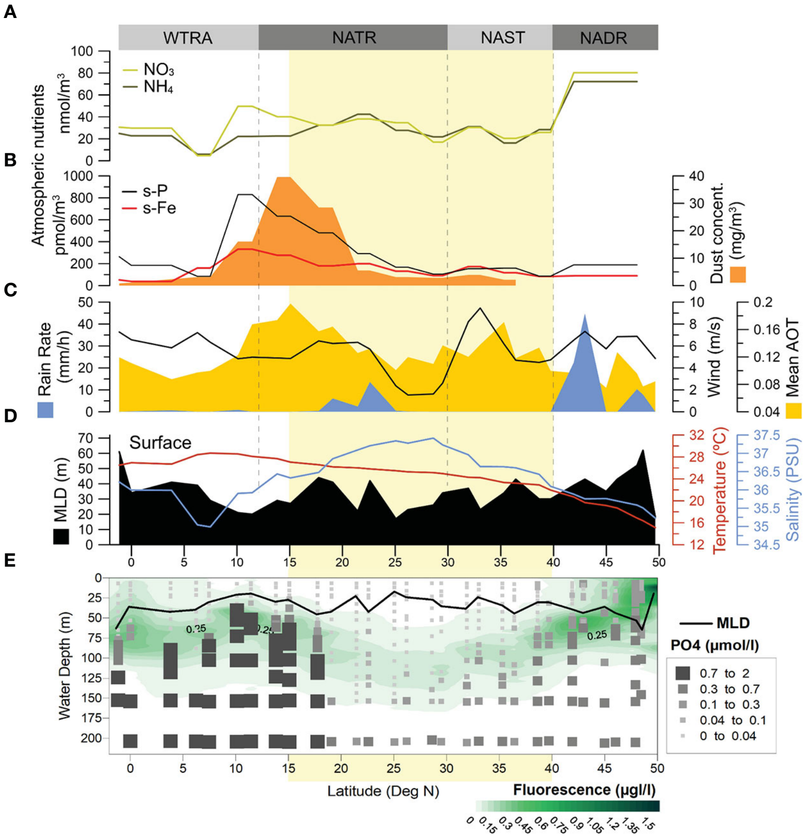

FIGURE 4
Environmental conditions during AMT28: **(A)** concentrations of atmospheric NO_3 and NH_4, **(B)** concentrations of atmospheric dust (dark orange), and of atmospheric soluble phosphorus (s-P) and iron (s-Fe); **(C)** remotely sensed rain rate (blue), wind strength (black line) and mean aerosol optical thickness (AOT – light orange); **(D)** in-situ measured MLD (black), surface temperature (red line), surface salinity (blue line), and **(E)** in-situ measured MLD (black curve), Chl-fluorescence (green) and PO_4 concentrations. Light-yellow band indicates the approximate location of the North Atlantic Subtropical Gyre at ~40-15° N (Aiken et al., 2017.

was also the region of highest dust concentrations measured in-situ (Figure 4B), and where high AOT levels extended the most to the west (Figures 2F), suggesting transport of African dust by the trade winds.

Concentrations of atmospheric soluble Fe and P increased strikingly across the NATR-WTRA, pointing to the occurrence of dust-born nutrient input at the surface of the ocean. S-Fe also showed a slight increase in the NAST, while s-P increased in the NADR, NAST, and in the equatorial North Atlantic, but to a much lesser extent compared to the NATR-WTRA transition (Figure 4B). While atmospheric nitrates also increased in this region, particularly NO_3, concentrations were much higher than s-Fe and s-P within the gyre region, and highest to the north of 45° N (Figure 4A).

4.3 Macronutrient concentrations in the upper ocean

All macronutrients measured across the photic zone revealed a similar meridional and in-depth distribution, consistently higher below the surface and usually coinciding with the DCM. Highest concentrations occurred across the NATR-WTRA transition (Sites 21–27 at 17–7°N) (e.g., Figure 4E), coinciding with the sub-surface OMZ (Figure 4D), and with the region of highest atmospheric dust concentrations and mean AOT (Figures 4B, C). NOx had the highest range of concentrations (~0–36 µmol/L), followed by SiO_2 (~0–20 µmol/L), and PO_4 (0–2 µmol/L, Figure 4E) (NOx and SiO_2 are shown in Figure I - Supplementary Material). A surficial and relatively diluted nutricline at the northernmost part of the transect gradually deepened and sharpened towards the south, down to ~160–200 m depth at the gyre central-southern region (Sites 14–19, ~30–21°N). From there, the nutricline (i.e., ocean layer where the greatest change in the nutrient concentration occurs with depth) became gradually shallower southwards, up to ~40–50 m depth at the NATR–WTRA transition. Southwards, the nutricline for NOx and PO_4 gradually deepened to ~80–120 m, becoming increasingly more diluted towards the Equator (Sites 30–31). SiO_2 concentrations had a similar meridional pattern but were more broadly vertically distributed to the south of 18°N compared to NOx and PO_4. SiO_2 concentrations were higher in the uppermost 50 m at the ITCZ-influenced region (8–3°N) compared to NOx and PO_4.

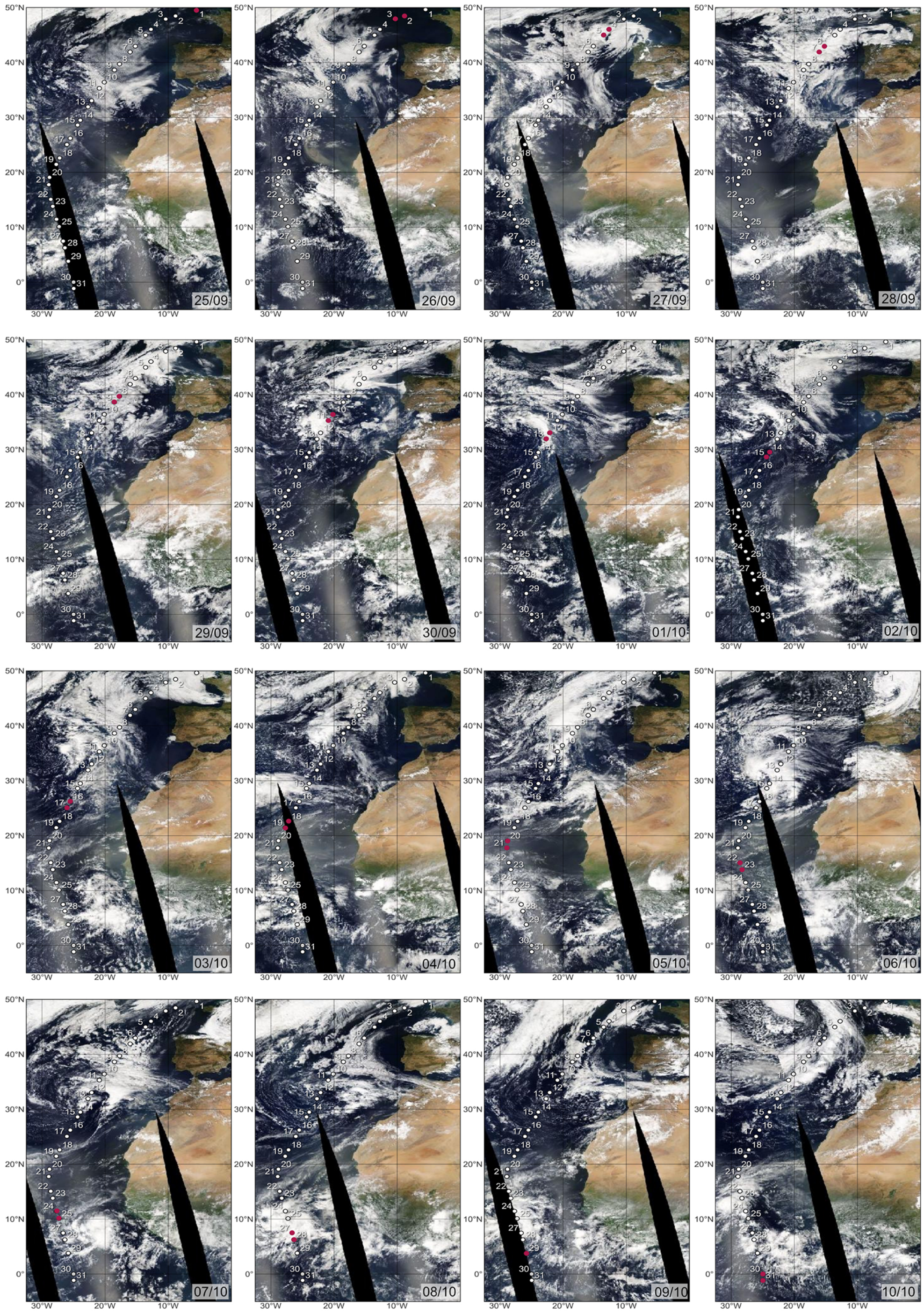

FIGURE 5
True colour daily satellites images from NASA MODIS AQUA (https://worldview.earthdata.nasa.gov) showing dust plumes blowing from NW Africa into the adjacent NE Atlantic during AMT28. White circles indicate the sampling sites during the expedition, whereas the red circles indicate where the ship was in each sampling day.

4.4 Coccolithophore total cells concentrations, UPZ/LPZ ratios and species diversity

Coccolithophores produced a mean of 23×10^3 cells/L (1×10^3–111×10^3cells/L) at the NADR, followed by 18×10^3 cells/L (2×10^3–60×10^3cells/L) at the WTRA, 14×10^3 cells/L (1×10^3–49×10^3cells/L) at the NATR, and finally 11×10^3 cells/L (2×10^3–23×10^3cells/L) at the NAST (Table II – Supplementary Material).

A degree of variability was driven by the heterogeneous distribution of ecologically distinct taxa, but higher cell densities generally followed the meridional distribution of the DCM (Figure 6A). Coccolithophores were most abundant along the uppermost 30 m in the NADR. High but comparably lower cell

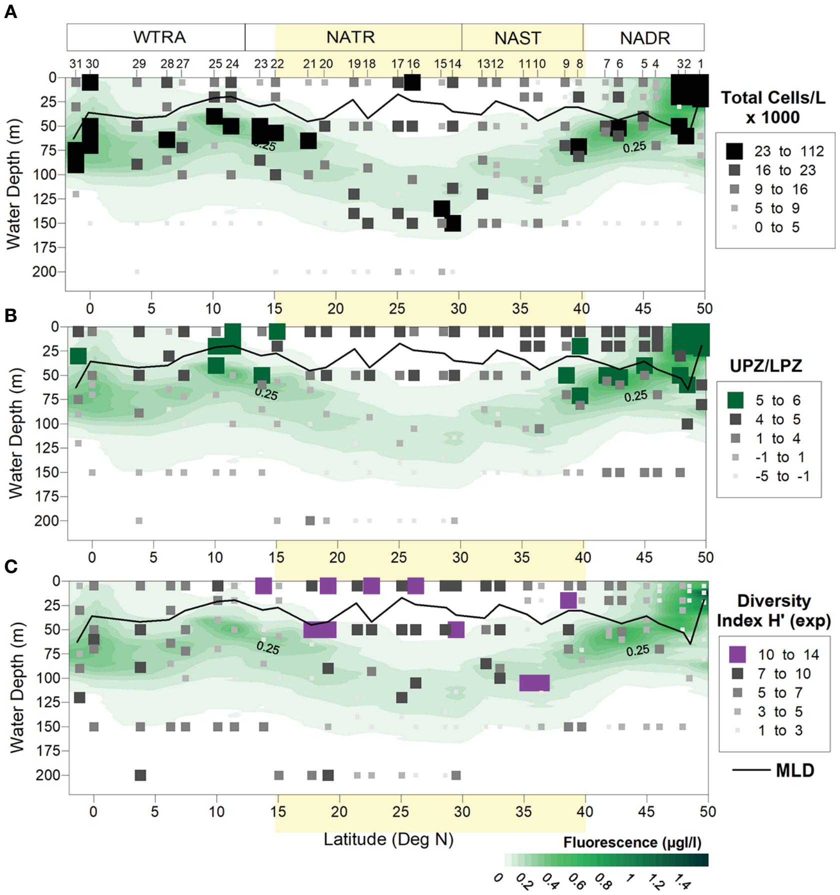

FIGURE 6
Meridional and vertical distribution of **(A)** coccolithophore total cell densities (cells/L), **(B)** UPZ/LPZ ratios calculated from the ratio between the cell concentrations by UPZ-species *E. huxleyi* and Gephyrocapsid species, and LPZ-species *F. profunda* and *G. flabellatus*, and **(C)** Shannon-Weaver species diversity index (H' Exp). UPZ and LPZ stand for upper- and lower photic zone. Light-yellow band indicates the approximate location of the North Atlantic Subtropical Gyre at ~15-40° N (Aiken et al., 2017).

densities also occurred: in the gyre region, both at the surface and at ~135 m depth (Sites 16 and 15, respectively); in the southern part of the NATR (Site 22, at 57 m); across the NATR-WTRA transition (Sites 24 and 25, at 40–50 m); and at the Equator (Site 30, at 60 m). Lowest cell densities usually occurred below ~125 m depth along the transect, except in the gyre where coccolithophores were more abundant along and below the DCM. Lower concentrations occurred at the surface occurred in the gyre and in the ITCZ-influenced region (Sites 27–28) (Figure 6A).

Higher UPZ/LPZ ratios, indicative of more nutritious conditions in the upper- compared to the lower photic zone, occurred in the NADR (i.e., at the surface at >47°N, and in sub-surface waters at 47-40°N), near the Equator (at 25 m depth of Site 31), and across the NATR-WTRA transition (both at the highly stratified uppermost 20 m and along the shallow DCM underneath) (Figure 6B).

In terms of species richness, a total of 87 heterococcolithophore taxa were identified in this study, of which 45 species and five genera (*Michaelsarsia* spp., *Ophiaster* spp., *Syracosphaera* spp., *Alisphaera* spp. and *Pontosphaera* spp.) were identified using the polarizing light microscope, while the SEM analysis allowed the identification of 42 additional species. In terms of holococcolithophores, three taxa (*S. pulchra* HOL, *S. anthos* HOL, and *Syracolithus* spp.) were identified with the polarizing light microscope, while the SEM confirmed these genera and revealed 29 more species, of which *Helladosphaera cornifera*, *Homozygosphaera triarcha*, and *Syracosphaera pulchra* HOL *oblonga* type were the most abundant. The full list of identified taxa is in the Taxonomic Appendix.

Coccolithophore species diversity inferred from the Shannon–Weaver diversity index was clearly higher along the uppermost ~50 m depth within the gyre, and lower at higher latitudes in the NADR (> 45°N), and in the gyre's lower photic zone (> 150 m). A diversity peak occurred at ~100 m in the AzC region (Sites 10–11) (Figure 6C).

4.5 Coccolithophore species' abundances and meridional distribution

Placolith-bearing r-selected taxa, including *E. huxleyi*, *G. oceanica*, *G. ericsonii* and *G. muellerae*, were by far the most abundant group during AMT28. Higher cell concentrations occurred along the uppermost 60–80 m across the transect

(Figure 7A), contributing highest mean percentages to the coccolithophore community in the NADR (69%) and WTRA (42%), and the lowest in the gyre (28% and 23% in the NAST and NATR, respectively) (Table II – Supplementary Material). *E. huxleyi* was the most abundant, often following the DCM but also thriving at the surface. Its highest concentrations occurred in the northernmost part of the transect (max. 96% at 60 m of Site 1), but also across the NATR-WTRA transition and at the Equator (max. 67% at 20m of Site 24 and 64% at 75m of Site 31).

G. muellerae was mostly thriving in the NADR, reaching its maximum in the AzC Front region (up to 78% at 71 m of Site 8). *G. ericsonii* was also abundant across in the AzC Front region (Sites 8–9) but also across the NATR-WTRA transition (up to 68% at 50 m of Site 23). Finally, *G. oceanica* was the least abundant and most persistently surficial of the gephyrocapsids, with maxima in the NADR (at 47–44°N), in the WTRA (up to 14% at 20 m of Site 25 at 11°N), and to a lesser extent, at the Equator (Figure II - Supplementary Material).

Deep-dwelling floriform taxa were the second most abundant group, usually distributed along- and below the DCM (down to 200 m at 29–22°N), but also occurring at shallower levels (~75–100 m) across the NATR-WTRA transition (Figure 7D). Highest mean percentages occurred in the gyre (28% and 41% in the NAST and NATR, respectively) and in the WTRA (24%), but nearly absent in the NADR. *F. profunda* was by far the dominant species, reaching up to 99% of the total coccolithophore assemblage at 140 m of Site 17, but also thriving in more productive conditions across the NATR-WTRA transition (Site 22 at 15°N) and at the Equator (Site 30). Albeit less abundant, *G. flabellatus* and *A. robusta* showed a similar meridional distribution, except that *G. flabellatus* was thriving deeper and more restricted to the gyre (Table II and Figure III - Supplementary Material).

The miscellaneous group produced up to 21% mean percentage at the NADR, compared to only 10–15% in the other provinces. These taxa were more abundant in the LPZ of the NADR (> 40° N), reaching up to >76% at 150 m of Sites 5 and 7 (Figure 7E), and showing a broader meridional and vertical distribution range compared to the previous groups. *Syracosphaera* spp. and *S. pulchra* were the most abundant taxa, generally thriving in the uppermost 75-80 m depth, but also producing high cell concentrations at more surficial levels within the gyre (Table II and Figure V - Supplementary Material).

Rhabdosphaera and Umbelliform taxa were notably more abundant in the gyre, producing mean percentages of 17–20% in the NAST and NATR compared to only 8% in the NADR and 11% in the WTRA. These taxa were consistently more abundant above the DCM (i.e., uppermost 50 m), coinciding with the gyre surface regions of lowest Chl-fluorescence and highest H'(exp). Increases in their abundance also occurred in the ITCZ-influenced stratified region (~7–6°N, Sites 27–28) (Figure 7C). *Umbellosphaera* spp. were dominant, presenting a broad distribution along 45–5°N, while *Discosphaera tubifera* was more restricted to the gyre (Table II and Figure IV - Supplementary Material).

Like the umbelliform taxa, holococcolithophores were also more abundant in the uppermost 25-50 m of the gyre, contributing mean percentages of 6% at NAST and NATR, compared to < 3% in the other provinces (Figure 7F and Table II - Supplementary Material). Given the reportedly higher susceptibility of holococcoliths to dissolution (Kleijne, 1991; Cros, 2001), their high abundance and diversity testify upon the quality of our samples in terms of coccolith-carbonate preservation and related freshness of the assemblages.

Finally, the other placolith-bearing taxa comprised the least abundant group along the transect. Highest mean percentages of 6% occurred in the WTRA, compared to only 0-2% in the other provinces, and more abundant in the DCM underneath the highly stratified equatorial North Atlantic (up to 11% at 64 m of Site 28, at 6°N) (Figure 7B). *Umbilicosphaera* spp. and *Oolitothus* spp. were more abundant to the south of 25°N, while *Calcidiscus leptoporus* was more broadly distributed to the south of 40°N. None of these species showed a specific vertical distribution (Table II and Figure VI - Supplementary Material).

4.6 Phytoplankton pigments meridional distribution

TChl-*a* concentrations presented low values in all stations, both in surface and DCM, except for the northern station at 49°, where it reached (2.85 µg/L). As for Chla-fluorescence, measured across the entire photic zone, values at the DCM were generally higher compared to the surface; minimum values were found in the gyre region. (Figure 8A). Of the five pigment/TChl-*a* ratios used as proxies for the phytoplankton groups, cyanobacteria s.l. (Zea) were the highest across the transect, followed by coccolithophores (HexFuco), dinoflagellates (Perid), and finally diatoms (Fuco).

Cyanobacteria s.l. were most abundant at the surface along 30–5°N, but also peaking at the DCM in the gyre and near the Equator (Sites 14 and 31) (Figure 8B). Diatoms were more abundant in the NADR, both at the surface and DCM, with sporadic increases at the surface across the NADR-NAST transition (39°N, Site 8) and NATR (25–20°N); and at the DCM in the gyre central region and, to a lesser extent, across the NATR–WTRA transition (Figure 8C). Dinoflagellates strikingly peaked at the northernmost end of transect, both at the surface and DCM (Site 1 at 49°N), and slightly increased across the NATR-WTRA transition (Figure 8D). Finally, pigment-inferred coccolithophores biomass revealed similar range of values and meridional distributions at the surface and DCM, albeit more variable at the surface. HexFuco/TChl-*a* ratios were highest in NADR and northern part of NAST, occasionally increasing at ~30°N, at ~15°N, and at the Equator (Figure 8E). These findings are further exploited and discussed in Brotas et al. (this special issue).

The meridional distribution of HexFuco concentrations had a similar pattern to that of the mean cells abundances of placolith-bearing r-selected species, i.e., in the NADR, and to the south of 20° N, as shown in Figure 9. Lowest HexFuco concentrations in the gyre coincided with communities dominated by umbelliform and holococcolithophore taxa in the UPZ, and by floriform taxa in the LPZ. Similarly, coccolithophore cell densities and HexFuco/

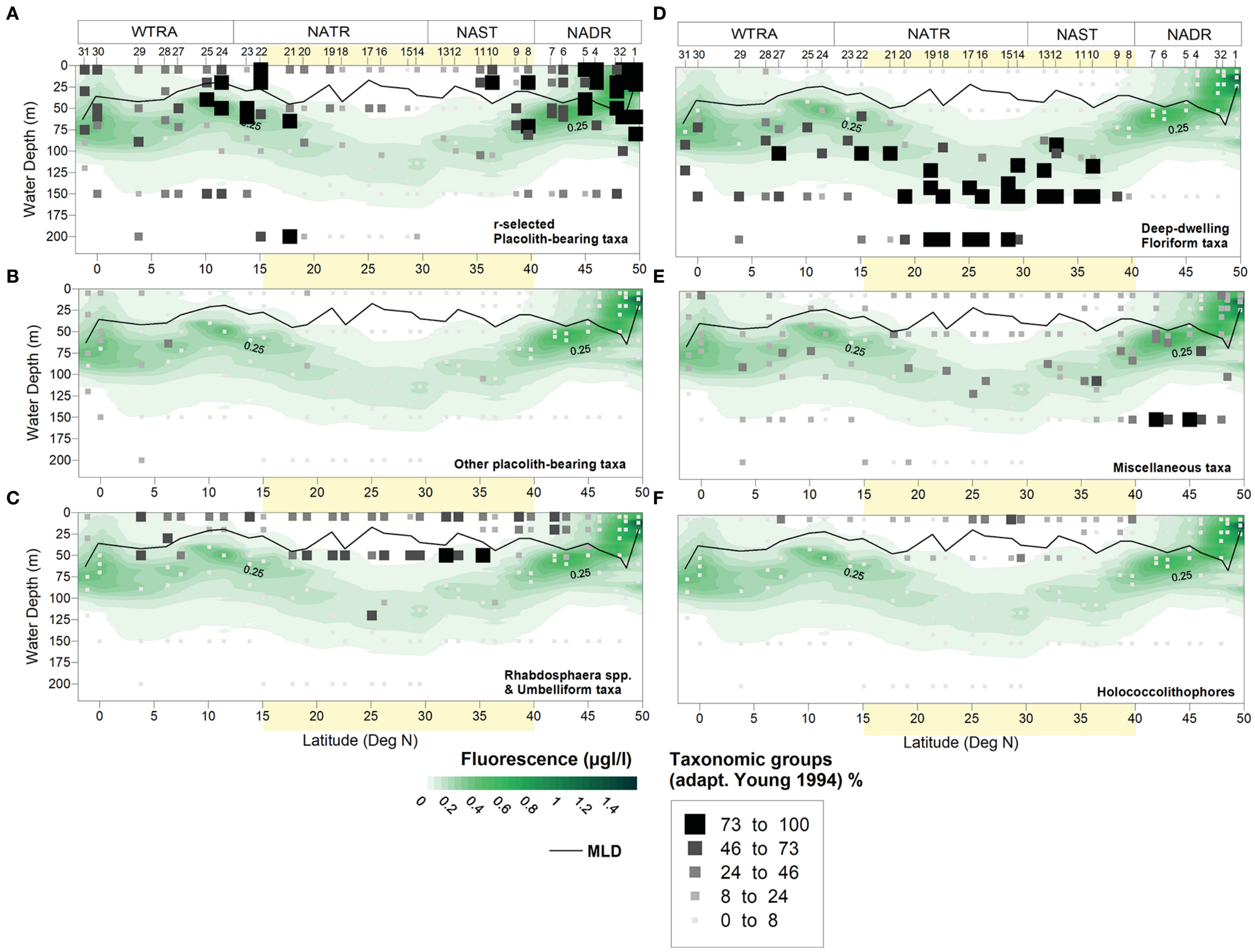

FIGURE 7
Meridional and vertical distribution of cell concentrations produced by the main coccolithophore taxonomic groups (adapted from Young, 1994) living along the photic zone during across the North Atlantic during AMT28: **(A)** r-selected placolith-bearing taxa including *E. huxleyi*, *G. oceanica*, *G. ericsonii*, *G. muellerae*; **(B)** other placolith-bearing taxa including *Umbilicosphaera* spp., *Oolithotus* spp. and *C. leptoporus*; **(C)** species within *Rhabdosphaera* spp. and umbelliform taxa including *Umbellosphaera* spp. and *D. tubifera*; **(D)** deep-dwelling floriform taxa including *F. profunda*, *G. flabellatus* and *A. robusta*; **(E)** miscellaneous taxa including (ordered from more to less abundant) *Syracosphaera* spp., *Ophiaster* spp., *S. pulchra*, *Calciosolenia* spp., *Helicosphaera* spp., *Coronosphaera* spp., Acanthoica spp., *Michaelsarsia* spp., *R. sessilis*, other taxa contributing < 5% to the coccolithophore assemblage, and indetermined taxa; **(F)** holococcolithophore species. Light-yellow band indicates the approximate location of the North Atlantic Subtropical Gyre at ~15-40° N (Aiken et al., 2017).

TChl-*a* ratios nicely and substantially co-increased at the surface of Sites 3 and 30, where *E. huxleyi* had maxima along the transect (Figures 8E, F, J). Both HexFuco and HexFuco/TChl-*a* increased along 21-10°N, roughly coinciding the increase of r-selected placolith-bearing taxa off NW Africa (Figures 8, 9).

5 Discussion

Ecologically-relevant morphological differences among coccolithophore species at the ends of the ecological succession spectrum (e.g., r–K differentiation, Brand, 1994; Young, 1994; Balch, 2004) have long been considered to reflect evolutionary ecological adaptations to a broad range of environmental niches in the global ocean. This concept of morphologically distinct coccolithophore assemblages having different biogeographic distributions (Winter et al., 1994; Young, 1994) is well illustrated in our AMT28 data and is closely linked to large-scale hydrographic and atmospheric forcing across the North- and Equatorial Atlantic, as discussed in the following sections.

5.1 North Atlantic coccolithophore communities during boreal Autumn 2018

5.1.1 North Atlantic Drift Province

The NADR (60–40°N) was the province of highest production of coccolithophores and Chl-*a*, related to the dominance of more opportunistic species in more dynamic and seasonally nutrient-enriched mixed layer conditions, typical of high latitude regions. This is evidenced by the shallowest DCM (up to 12–30 m) and the highest UPZ/LPZ ratio across the transect (Figures 6A, B), reflecting

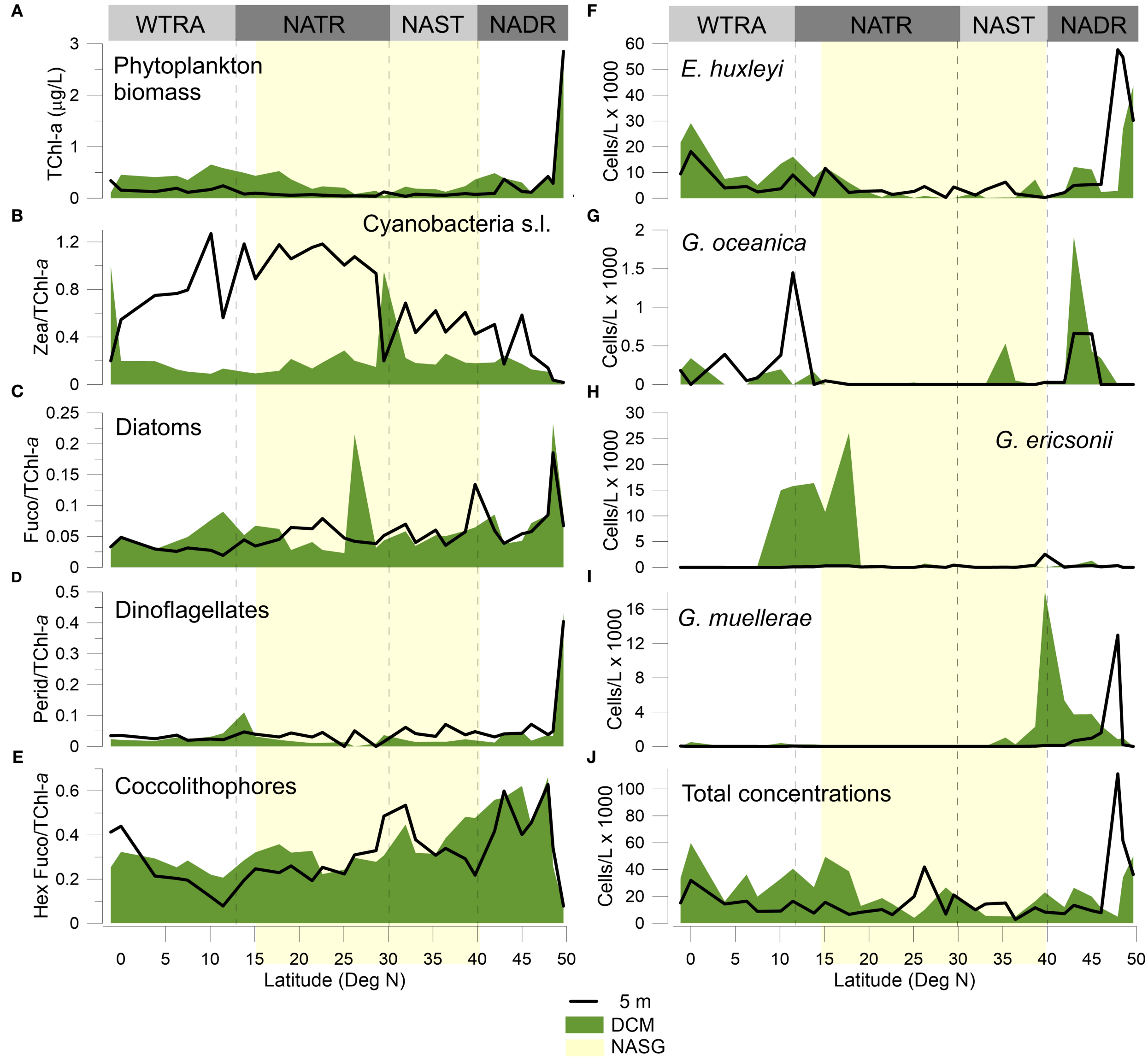

FIGURE 8

Meridional distribution of pigment-derived phytoplankton biomass and species groups measured at the surface and DCM: **(A)** TChl-*a* concentrations, **(B)** cyanobacteria s.l. (Zea/TChl-*a*), **(C)** diatoms (Fuco/TChl-*a*), **(D)** dinoflagellates (Perid/TChl-*a*), and **(E)** coccolithophores (HexFuco/TChl-*a*); and of **(F)** *E. huxleyi*, **(G)** *G. oceanica*, **(H)** *G. ericsonii*, **(I)** *G. muellerae*, and **(J)** total coccolithophore cell densities.

a 77% of cells production contributed by r-selected placolith-bearing species (Table II – Supplementary Material). Higher productivity in colder and with deeper mixed layer conditions coupled to the windier atmospheric conditions at > 40°N (Figures 2A, C, D, 4C–E) reflects the role of the westerlies in inducing seasonal nutrient-enrichments through the mixing and cooling of the upper ocean. Given the shallow location of Sites 1 and 2 (sampled at 87 m and 147 bottom depths, respectively – Figure 1), high nutrient concentrations and enhanced productivity in this area were probably also related to intensified coastal-neritic oceanographic processes, including upwelling and lateral advection of nutrient-rich waters. Although the NADR featured the deepest MLDs during the expedition, it was only down to a maximum of 62 m (at Site 2) compared to the anomalous mixed layer deepening reported earlier by Longhurst (2007) (down to 300 m during autumn and winter). Therefore, the combination of moderate MLDs, nutrient-enrichment and favorable PAR levels in the NADR (Figures 4D, E, 10E, F) induced favorable conditions for coccolithophores to reach their highest productivity during the boreal autumn in this area. Highest proportion of pigments associated with diatoms and dinoflagellates in the northernmost part of the NADR (Figures 8C, D) is in line with AMT pigment studies from previous years (Brotas et al., 2022), and earlier descriptions of NADR as the region of highest productivity by all eukaryotic phytoplankton (Tarran et al., 2006). Our data confirm existing notions of larger cell-sized microphytoplankton being dominant at higher latitude regions (e.g., Marañón et al., 2000; Marañón et al., 2001; Marañón et al., 2003; Brotas et al., 2022), with

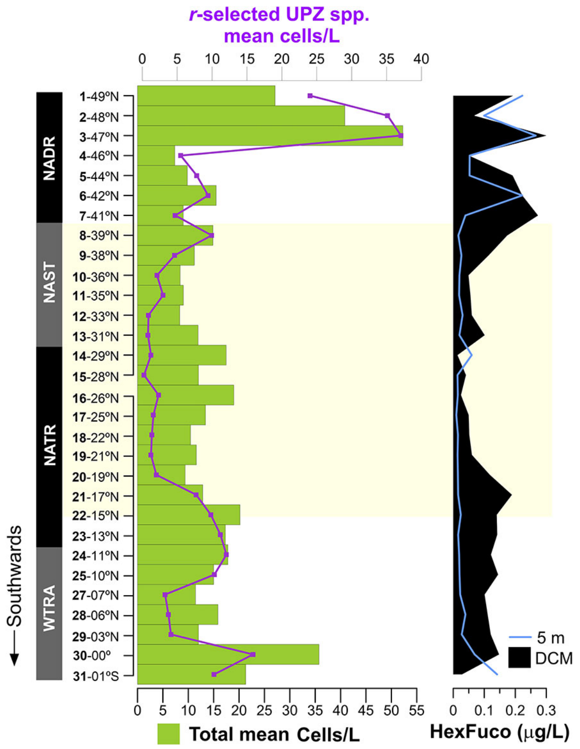

FIGURE 9
Meridional distribution of coccolithophore mean concentrations (cells/L) in the photic zone (green bars – total; purple line – r-selected UPZ species), and of 19'-Hexanoyloxyfucoxanthin concentration (HexFuco; µg/L) at the surface and DCM.

which r-selected coccolithophores species are more likely to compete, reflecting their ability to thrive in light-nutrient conditions that are favourable for rapid population growth (e.g., Winter et al., 1994; Young, 1994; Baumann et al., 2000; Guerreiro et al., 2013; Poulton et al., 2017). This probably contributed to the high levels of oxygen concentrations found near the surface in this region (Figure 3D), in line with existing understanding on the importance of marine phytoplankton for oxygen production. The deepening of the MLD and the drop of PAR from Site 3 to Site 4 (Figure 10), in parallel with a drastic decrease in cell concentrations, Chl-*a* and pigments produced by microphytoplankton (Figure 8), suggests less favorable conditions for growth at these latitudes compared to further northeast.

Our data support the notion of species producing robust and interlocking coccospheres made up of disc-shaped "placolith" coccoliths, and usually having higher cell division rates, as being faster at exploiting intermittent nutrient input in dynamic environments (Winter et al., 1994; Young, 1994). This is especially the case of *E. huxleyi* which was by far the most productive species in the NADR (Figure I - Supplementary Material), in line with its recognized capacity of growing rapidly in more dynamic mixed layer conditions (e.g., Andruleit and Rogalla, 2002; Sprengel et al., 2002; Andruleit, 2007; Guerreiro et al., 2013), and the most common bloom-forming coccolithophore in at higher latitudes (e.g., Holligan et al., 1993). Of the gephyrocapsid species, *G. muellerae* was the most abundant and geographically more restricted to the NADR, in line with previous studies describing it as a cold-water species that often dominates *Gephyrocapsa* assemblages in temperate latitude regions (Boeckel and Baumann, 2008; Guerreiro et al., 2013).

5.1.2 North Atlantic Subtropical Gyre Province

Towards the NAST (40–30°N), the gradual deepening of the nutricline and DCM induced a decrease of TChl-*a*, UPZ/LPZ ratios and of the total coccolithophore concentrations at the surface, in parallel with an increasingly diverse coccolithophore assemblage (Figures 4E, 6A, B, 10). Despite the westerly winds influencing this region, the weaker intensity at these latitudes resulted in shallower MLDs and, subsequently lower phytoplankton productivity (Longhurst, 2007; Aiken et al., 2017). Coccolithophore assemblages showed more marked vertical ecological gradients in this province, likely in response to the progressively higher thermal stratification towards the center of the gyre. Increasingly more abundant light-dependent *Rhabdosphaera* spp., umbelliform taxa and holococcolithophores in the UPZ, and nutrient-dependent floriform taxa along and below the DCM (Figures 7C, D) reflected such enhanced vertical niche partitioning in the gyre. The transition towards a more oligotrophic setting was also evidenced from a decrease in pigments produced by microphytoplankton, and concurrent increasing proportions of pigments by picophytoplankton (i.e., cyanobacteria s.l.) (Figure 8), in line with previous studies (Marañón et al., 2000; Marañón et al., 2001; Marañón et al., 2003; Tarran et al., 2006; Brotas et al., 2022).

Enhanced UPZ/LPZ ratios at 39–38°N (Sites 8–9), to which r-selected gephyrocapsid species largely contributed (Figures 6B, 7A; Figure II - Supplementary Material), are likely linked to the AzC Front. This is a region of reportedly locally enhanced productivity, to which enhanced vorticity driven by mesoscale eddies formed from the Gulf Stream and along the NAC is thought to contribute (Frazão et al., 2022 and refs. therein). *G. muellerae* was the most abundant r-selected species in this region, reaching up to 69% at Site 8 (20 m) (Figure II - Supplementary Material), suggesting a preference for more moderately nutritious transitional conditions where competition with *E. huxleyi* is lower (e.g., Giraudeau and Bayley, 1995; Boeckel et al., 2006; Guerreiro et al., 2013).

5.1.3 North Atlantic Tropical Gyre Province

The entire section that includes the southern part of the NAST and most of the NATR (30–12°N) was the region of lowest Chl-*a* concentrations, coccolithophore concentrations and UPZ/LPZ ratios at the surface, while the coccolithophore species diversity was highest (Figure 6). Our data are consistent with the uniformly oligotrophic and seasonally invariable mixed layer conditions described for "Typical Tropical Profile" settings (Aiken et al., 2017; Longhurst, 2007). Surface phytoplankton assemblages were similar to those of the southern NAST, i.e., dominated by cyanobacteria s.l., *Rhabdosphaera* spp., umbelliform species and holococcolithophores (Figures 7C, F, 8). Cyanobacteria in this region were mostly dominated by picoplankton as evidenced by cell counts obtained by flow cytometry and from microscope

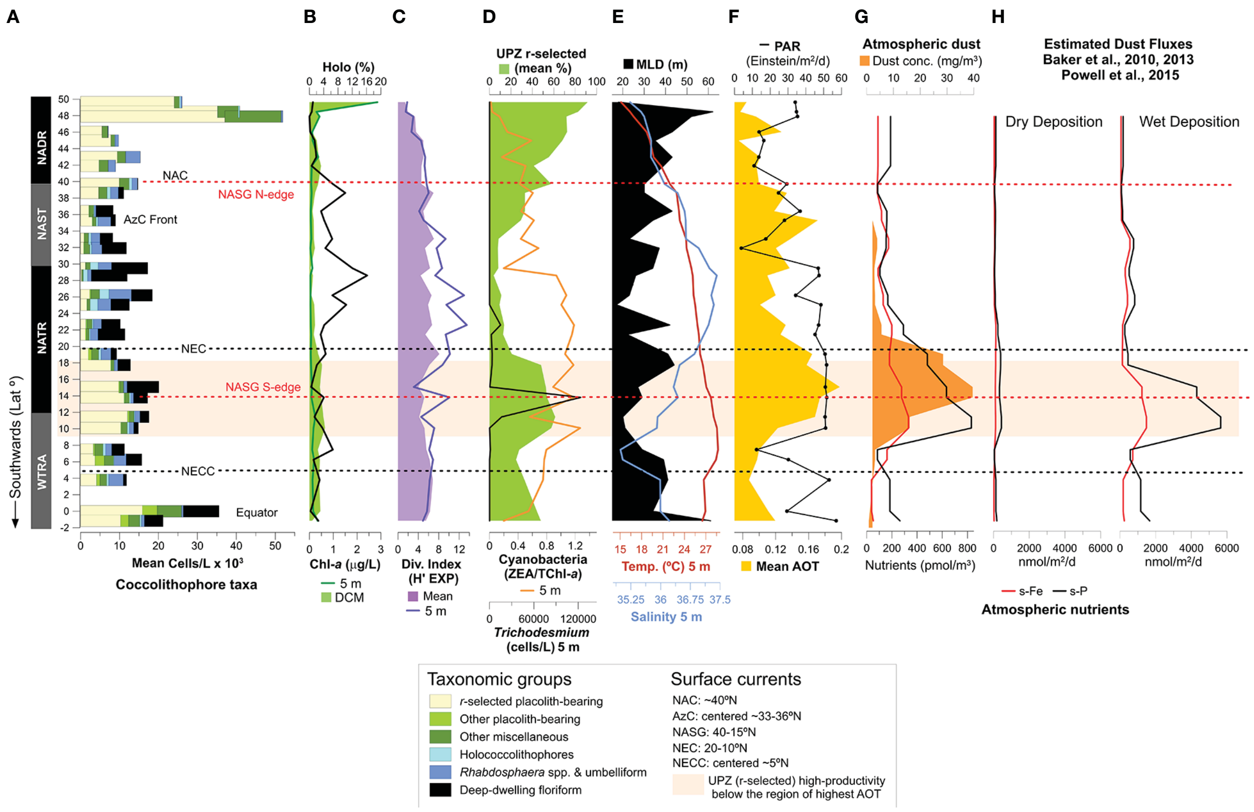

FIGURE 10
Meridional distribution of coccolithophore communities in relation to other phytoplankton groups and hydrological and atmospheric conditions: **(A)** mean cell concentrations of the main coccolithophore taxonomic groups determined from each site (adapted from Young, 1994); **(B)** holococcolithophore mean percentages (black line) and Chl-*a* concentration measured at the surface (light green) and DCM (dark green); **(C)** Shannon-Weaver diversity index (exp), averaged to the photic zone (light purple) and at the surface (dark purple); **(D)** mean percentages of by r-selected placolith-bearing coccolithophores (green), cell concentrations of N_2-fixing *Trichodesmium* sp. at the surface (black line), and pigment-derived cyanobacteria s.l. (i.e., zea/TChl-*a*); **(E)** mixed layer depth (MLD – black), temperature (red line) and salinity (blue) at the surface; **(F)** photosynthetically available radiation (PAR – black line), and aerosol optical thickness (AOT – orange); **(G)** concentrations of dust (dark orange) and of atmospheric soluble Fe (red) and soluble P (black); **(H)** estimated fluxes of dry- and wet dust deposition, calculated according to Baker et al. (2010, 2013) and Powell et al. (2015). NAC=North Atlantic Current, AzC=Azores Current; NASG=North Atlantic Subtropical Gyre, NEC=North Equatorial Current, NECC=North Equatorial Counter-Current. Concerning the taxonomic groups, r-selected placolith-bearing taxa include *E. huxleyi*, *G. oceanica*, *G. ericsonii*, *G. muellerae*; other placolith-bearing taxa include *C. leptoporus*, *Oolithotus* spp. and *Umbilicosphaera* spp.; Umbelliform taxa include *Umbellosphaera* spp. and *D. tubifera*; deep-dwelling floriform taxa include *F. profunda*, *G. flabellatus* and *A. robusta*; miscellaneous taxa include *R. sessilis*, *Calciosolenia* spp., *Acanthoica* spp., *Ophiaster* spp., *Michaelsarsia* spp., *Syracosphaera* spp., *S. pulchra*, *Coronosphaera* spp., *Helicosphaera* spp. and other taxa with abundances < 5%. Orange band indicates the region of highest dust deposition during AMT28 (along ~18–10°N).

analysis (data not shown; see Brotas et al. this issue). This reflects the capacity of pico- and K-selected nannoplankton species to thrive in heavily stratified, well-illuminated and oligotrophic conditions, typical of the gyre (e.g., Marañón et al., 2000; Marañón et al., 2001; Marañón et al., 2003; Tarran et al., 2006; Brotas et al., 2022). Floriform taxa living along and below the DCM (down to a maximum of 135-200 m Site 15) were the dominant species within the coccolithophore community in this province (Figure 7D), confirming their ability to grow under the nutrient-enriched and low light conditions of the deep euphotic and subeuphotic zones of the ocean (Winter et al., 1994; Young, 1994; Poulton et al., 2017; Balch et al., 2019) (discussed in section 5.2).

The increase of more opportunistic coccolithophores and of pigment markers of microphytoplankton towards the gyre's southern edge indicates a change towards more nutritious ocean conditions across the NATR–WTRA transition (Figures 7A, 8, 10). Locally enhanced productivity in the heavily stratified uppermost 20 m in this area appeared decoupled from productivity in the shallow DCM (40–50 m) underneath (Figures 3A, C, 4E), possibly reflecting the effects from distinct environmental drivers (discussed in section 5.4).

5.1.4 Western tropical Atlantic Province

The WTRA (12/14°N–5°S) was marked by a shallower DCM and nutricline (Figure 4E), and by less striking vertical ecological gradients compared to the gyre. Umbelliform and floriform species were inhabiting the regions of stronger stratification, while placolith-bearing species were more abundant in locally nutrient-enriched conditions at the Equator (Figures 7, 10), consistent with Poulton et al. (2017).

Enhanced SiO_2 concentrations along the ITCZ-influenced region (Figure IV - Supplementary Material) were possibly linked to the warm water lens of low SSS and high Chl-*a* that was extending from the Amazon and Orinoco River mouths across the tropical North Atlantic (Figures 2A–C). Indeed, enhanced Chl-*a* production related to seasonal changes in the NEC and to nutrient-enriched Amazon and Orinoco water inflow into the eastward-flowing NECC have been previously reported (Longhurst, 1993; Signorini et al., 1999; Aiken et al., 2000; Signorini et al., 2015; Guerreiro et al., 2017). However, our *in situ* observations of low pigment-derived diatoms and dinoflagellates (Figures 8C, D), and the markedly oligotrophic coccolithophore signature along the NECC/ITCZ region (i.e., increase of umbelliform species at the surface; Figure 7C) point otherwise. This is in line with the generally oligotrophic conditions in the WTRA north of the Equator reported by Aiken et al. (2017). While the Amazon River plume has been recognized to fuel phytoplankton in the western tropical North Atlantic, including r-selected coccolithophores (Guerreiro et al., 2017; Korte et al., 2020), the low salinity plume was largely nutrient-depleted and unfavorable to clades of high nutrient requiring coccolithophore groups at the positions sampled during this study.

At the Equator, the shoaling of the DCM up to 60 m and the increase of the UPZ/LPZ ratios and of coccolithophore concentrations along the uppermost 75–100 m (Figures 6A, B) suggest the transition towards more nutritious conditions related to equatorial upwelling. The observed deepening of the MLD in the colder and denser surface waters in this area (Figures 3, 4C) supports a scenario of phytoplankton growth at the expense of nutrients supplied by enhanced vertical mixing driven by divergent upwelling. While lower coccolithophore production and diversity have been reported from equatorial divergence regions (O'Brien et al., 2016; Balch et al., 2019), the Equator was the second most productive region across the transect, with several taxa with distinct ecological preferences increased in this area. Despite the lower H' (exp) at the surface compared to the heavily stratified gyre, both regions revealed similar H'(exp) averaged for the entire photic zone. This reflects the significant contribution by both r-selected species *E. huxleyi* and *G. oceanica*, but also by other placolith-bearing taxa, as well as deep-dwelling floriform species, and several taxa within the miscellaneous group (Figure V - Supplementary Material). Our data are consistent with Kinkel et al. (2000) who also reported enhanced coccolithophore productivity in the equatorial upwelling area, dominated by *E. huxleyi*. Our data suggest that coccolithophores with variable nutrient-requirements were being stimulated along the photic zone and/or that upwelling-related enhanced vertical mixing was weakening the vertical ecological partitioning in this area. While Chl-*a* concentrations were not high at the Equator during AMT28, coccolithophores are likely to have significantly contributed to phytoplankton biomass in this region, together with cyanobacteria s.l. (Figure 8) which were dominated by picoplankton (data not shown; see Brotas et al. this issue). Although seasonal changes in coccolithophore species composition across the North Atlantic have been reported to be stronger compared to inter-annual differences (Poulton et al., 2017 and refs. therein), differences between our observations and those of Balch et al. (2019) may reflect some degree of interannual variability in the equatorial upwelling region.

5.2 On the resilience of subtropical gyre coccolithophore communities

Highest coccolithophore species richness and diversity along the uppermost ~50 m of the gyre (comprising the NAST and the NATR) (Figures 6C), the region of highest environmental stability and stronger vertical ecological gradients across the transect, are in line with previous plankton studies (Winter et al., 1994; Cermeño et al., 2008; Charalampopoulou et al., 2011; O'Brien et al., 2016; Poulton et al., 2017). The negative relationship between species diversity and Chl-*a* in the oligotrophic and picoplankton cyanobacteria-enriched surface gyre region (Figure 8) probably reflects the greater ability of more coccolithophore species to successfully compete in regions where faster-growing microphytoplankton and r-selected coccolithophores are less abundant. O'Brien et al. (2016) reports this pattern to occur on a global scale, with several species having a more even biomass distribution and contributing more to the total phytoplankton community at low latitudes, to which light and temperature are suggested as the most important drivers. Poulton et al. (2017) highlights the combination of nutrient limitation and enhanced vertical ecological niche partitioning as crucially favouring coccolithophore diversity in the gyre compared to higher latitude regions. This pattern is also described for non-calcifying haptophytes (Liu et al., 2009), as well as other calcifying planktonic phyla (e.g., foraminifera) (Rutherford et al., 1999; Dolan et al., 2006), reportedly crucial for maintaining the ecosystem functioning and linked biogeochemical processes (Caron and Countway, 2009).

Highest abundances and diversity of holococcolithophores at the surface of the gyre confirm their K-selected ecological affinity (e.g., Kleijne, 1991; Kleijne, 1993; Houdan et al., 2006; Dimiza et al., 2008; Cros and Estrada, 2013; Godrijan et al., 2018). Our data support existing notions of coccolithophores' heteromorphic life cycle (alternating between diploid and often non-mobile, i.e., without flagellates, to haploid mobile and flagellate) enhancing their ability of exploiting extreme ranges of light and nutrient ocean conditions. On one hand, the presence of flagella in holococcolithophores prevents the cell from sinking out of the photic zone within heavily stratified ocean conditions (Houdan et al., 2006). In addition, holococcoliths have a higher capacity to reflect UV light while minimizing the loss of photosynthetically active light, thereby protecting the cell from photodamage under the high surface light levels in the gyre (Monteiro et al., 2016 and refs. therein).

Umbelliform K-selected species also have lower nutrient requirements, as well as slower cell division rates, compared to r-selected coccolithophores. Their ability to produce large, low-density coccospheres around smaller organic cells is also thought to increase their resilience to the stable but difficult gyre conditions (Young, 1994). Several species reportedly form double-layered coccospheres, with which they trap a layer of seawater, thereby enhancing chemical buffering and nutrient absorption in highly oligotrophic conditions (Young, 1994). *D. tubifera* was particularly restricted to the UPZ in gyre region, suggesting a lower tolerance for colder and more dynamic mixed layer conditions compared to the more broadly distributed *Umbellosphaera* spp. and *Rhabdosphaera* spp. (Figure IV – Supplementary Material).

The gyre was also the region where floriform taxa reached their highest cell concentrations in the deep euphotic and subeuphotic zones of the ocean, down to 200 m at Sites 15–17 (Figure 7D), in line with previous studies (e.g., Poulton et al. (2017). These taxa typically produce small to medium size coccospheres built of distinctive blade-like coccoliths which, in the case of *F. profunda*, are organized in a "radar dish" coccosphere architecture. The latter is thought to funnel photons into the cell towards increasing light availability onto the chloroplasts to improve photosynthesis at very low light conditions (Young, 1994; Monteiro et al., 2016 and refs. therein). The absence of floriform species in the colder and more dynamic mixed layer conditions of the NADR reflects their dependency on thermal stratification and water column stability for light to penetrate deeper into the lower photic zone (e.g., Young, 1994; Aiken et al., 2017). *G. flabellatus* was the most meridionally confined to the gyre region and the most productive at greater depths, suggesting that *F. profunda* and *A. robusta* are comparably "ecologically broader". Nevertheless, the observation that all three deep-dwelling species also increased at up to ~60 m in the Equator (Figure III – Supplementary Material) suggests a certain capacity to withstand some degree of turbulence and/or competition with other species in more mixed conditions.

In addition to the morphological/physiological advantages referred above, gyre coccolithophore communities are also likely to overcome the extreme vertical light/nutrient ranges in this stratified region through displaying nutritional strategies other than photosynthesis. Poulton et al. (2017) have argued that deep-dwelling coccolithophores probably present mixotrophy (i.e., physiological ability of combining autotrophy and heterotrophy – osmotrophy and/or phagotrophy), given that light conditions at <1% surface irradiance in the photic zone are not sufficient to support photosynthesis. They further hypothesize that mixotrophy may also be useful for umbelliform species living at the surface, where nutrient-depletion limits their growth. These hypotheses are supported by the very high coccolith export production *by F. profunda* and *G. flabellatus* in the western tropical North Atlantic, as reported from a recent transatlantic sediment trap study by Guerreiro et al. (2019). According to these authors, the two species contributed up to 3–5 times higher coccolith fluxes in this heavily and permanently stratified region compared to the easternmost traps, where the nutricline was geostrophically shoaled and ocean conditions are influenced by the Canary Current upwelling system (Guerreiro et al., 2019 and refs. therein). This testifies to the capacity of floriform taxa being highly productive in the LPZ of heavily stratified ocean conditions, typical of tropical and subtropical open ocean settings.

Additional arguments favoring mixotrophy as an alternative nutritional strategy in coccolithophores include the potential function of the haptonema (flagella) as a food gathering organelle (Billard and Inouye, 2004), and the existence of heterotrophic species in polar waters (Thomsen et al., 1991). Recent culture experiments report the ability of several species (including placolith-bearing *E. huxleyi*, *G. oceanica* and *C. leptoporus*) to use osmotrophy as a mode of mixotrophic acquisition of a wide array of carbon-enriched organic compounds in dark conditions (Godrijan et al., 2020; Godrijan et al., 2021). Avrahami and Frada (2020) also provided evidence of mixotrophy and phagotrophy (i.e., the ability to ingest prey) as nutritional strategies widespread in coccolithophores. Holococcolithophores are also thought to be more likely to use mixotrophy towards efficiently exploiting stable and oligotrophic niches (Worden et al., 2015; Caron, 2016).

Our data suggest that enhanced species diversity linked to a possibly broader range of nutritional strategies, and the ability of undergoing life cycle changes, are good indicators of gyre coccolithophore species having an ecological advantage in the context of ongoing gyre expansion due to ocean warming. Their resilience is well illustrated by the up to 28-41% contributions by floriform taxa, 17–20% by umbelliforms, and 6% by holococcolithophores, together contributing to mean total of 11–14×10^3 cells/L in the gyre (NAST and NATR), only slightly lower compared to mean total of 17.7×10^3 cells/L produced by r-selected species in the highly productive NADR (Table II – Supplementary Material).

Our observations provide a snapshot perception on the importance of coccolithophore productivity in typical gyre conditions, considered as a modern analog for future productivity in the context of an increasingly stratified upper ocean. While this provides good perspectives for their survival in the face of ocean warming, a growing use of mixotrophy in detriment of autotrophy could significantly alter the role of coccolithophore communities in the organic and inorganic carbon pumps, with implications for both O_2 production and atmospheric CO_2 sequestration (e.g., Hutchins, 2011; Guerreiro et al., 2019; Godrijan et al., 2020; Guerreiro et al., 2021).

5.3 Coccolithophore production and HexFuco concentrations

Despite the diversity of the distribution of the currently known pigment markers among coccolithophore species, the carotenoid 19'-hexanoyloxyfucoxanthin (HexFuco) has been considered a straightforward marker for coccolithophore (Haptophytes Type 6) distribution in open coastal and oceanic settings (Van Lenning et al., 2004; Wright and Jeffrey, 2006). In this study, HexFuco concentrations were mostly coincident with the distribution of coccolithophores along the regions of higher cell concentrations, higher TChl-*a* and enhanced productivity by r-selected placolith-bearing coccolithophore species, i.e., in the NADR, in the AzC Front region, and to the south of 20°N. This is in line with reported species within the HexFuco-synthetizing genera, including *C. pelagicus*, *E. huxleyi* and *G. oceanica*, all characteristic of more open-ocean regions compared to diatoms, but also blooming in nutrient-enriched conditions (Kees Van Lenning et al., 2004). Our data are also consistent with Zapata et al. (2004) who reported 11 strains of *E. huxleyi* to have a high correlation to pigment Type 6 composition.

Our observations confirm that HexFuco may be produced towards maximizing the use of light in nutritious ocean conditions, both within well mixed- and heavily stratified surface ocean conditions, in line with its reported light-harvesting role (Siefermann-Harms, 1985; Zapata et al., 2004). This is supported by the fact that HexFuco concentrations were lowest in the gyre (near the detection limit; Figure 9), where coccolithophore populations were dominated by deep dwelling floriform taxa (Figure 7). Given that the gyre region was not light-limited, the observed meridional patterns suggest that the production of HexFuco is somehow used to maximizing photosynthesis in the presence of higher nutrient availability. Dandonneau et al. (2006) also reported slightly improved agreement between HexFuco and coccolithophore cell concentrations in regions/seasons of higher coccolithophore standing stocks in the North Atlantic (i.e., Gulf Stream province) and of populations dominated by *G. oceanica* (i.e., Pacific North Equatorial Current region). The same authors justify the observed poor agreement between total cell concentrations and HexFuco as probably reflecting changes in pigment ratios among distinct coccolithophore species and/or in other phytoplankton groups containing this carotenoid. This suggests that coccolithophore species composition should be considered when using HexFuco as a pigment marker of coccolithophores, consistent with our AMT28 observations. The fact that HexFuco was not correlated to the gyre coccolithophore communities could be related with their greater use of mixotrophy to survive within its extremely stratified ocean conditions (discussed in Section 5.2).

5.4 Enhanced r-selected productivity underneath the largest Saharan dust plume

Though Saharan dust fluxes during boreal autumn tend to be highest in the western tropical North Atlantic (e.g., Prospero et al., 2014) our data point to the occurrence of dust-born nutrient deposition in the eastern part of the ocean basin. In addition to being the region of highest and most persistent dust input during the expedition, the NATR-WTRA transition was also where high AOT values extended the most towards the west (Figures 2F, 4A, 10, 11), reflecting its location under the largest Saharan dust plume. Being adjacent to NW Africa, the tropical NE Atlantic is subjected to some of the highest inputs of atmospheric dust (Yu et al., 2019) which are yearlong transported by the westward-blowing trade winds (Duce et al., 1991; Chiapello et al., 1999; Prospero et al., 2002; Jickells et al., 2005; Scheuvens et al., 2013; van der Does et al., 2020). The striking increase in the concentrations of s-Fe and s-P in dust samples collected across the NATR-WTRA transition (Figures 4A, 10) is consistent with the notion of Saharan dust plumes acting as long-range vehicles for the transport of nutrient-enriched particles towards the Atlantic (Jickells et al., 2005).

The increase of s-Fe and s-P in dust samples strikingly coincided with the increase of cell concentrations by *E. huxleyi* and *G. oceanica* in the heavily stratified and oligotrophic uppermost 20 m of the ocean across the NATR-WTRA transition (Figure II – Supplementary Material), resulting in a significant increase of the UPZ/LPZ ratios at the surface (Figure 6B). Low concentrations of all macronutrients measured at the surface in this region (Figure 4D) suggest that dust-born nutrients were only enough to fuel fast-blooming species but not to change the nutrient stocks at the surface. *E. huxleyi* produced up to 9–16×10^3 cells/L at Site 24, only surpassed by densities recorded in the NADR (max. 58×10^3 cells/L at 5 m of Site 3) and in the Equator (total of 29×10^3 cells/L at 60 m of Site 30). *G. oceanica* had one of its maximum occurrences at Site 25 (3×10^3 cells/L at 20 m) (Figure II – Supplementary Material). Despite being considered less productive compared to the opportunistic *E. huxleyi*, *G. oceanica* is often referred to as an upwelling indicator, based on its quick response to nutrient input (Winter et al., 1994; Giraudeau and Bayley, 1995; Broerse et al., 2000; Andruleit and Rogalla, 2002; Sprengel et al., 2002; Andruleit et al., 2003; Guerreiro et al., 2013). *G. oceanica* has also been reported to be faster and more efficient in responding to intermittent "bursts" of nutrient input compared to other gephyrocapsids (see Guerreiro et al., 2013; Guerreiro et al., 2017). Our data are consistent with previous sediment-trap observations of *E. huxleyi* and *G. oceanica* producing coccolith flux maxima during two events of enhanced Saharan dust deposition in 2013 in the open tropical North Atlantic (Guerreiro et al., 2017). According to this study, fluxes produced by these species in this highly stratified region were almost as high as those produced in the mesotrophic region off the coast of Mauritania for the same period. The resulting striking flux increase of POC and coccoliths was seen promoting a more efficient coccolith-ballasting and resulting in lower rain ratios (Korte et al., 2020; Guerreiro et al., 2021).

Enhanced cell concentrations produced by *Trichodesmium* spp. at 14°N (Figure 10) and increased proportions of pigments produced by cyanobacteria s.l. (i.e., including both smaller cell-sized picophytoplankton and filamentous N_2-fixing species) along 29–10°N (Figure 8) also support the hypothesis of phytoplankton growth at the expense of Saharan dust-driven nutrients. Pigments produced by cyanobacteria s.l. show a meridional distribution at the surface that coincides remarkably with the region of highest dust-driven dFe and total dFe surface concentrations along 30–5°N recently reported by Shelley et al. (2017), and in line with previous studies (Bowie et al., 2002; Bergquist and Boyle, 2006; Measures et al., 2008; Ussher et al., 2013). The median N:P (67 mol/mol) and N:Fe (144 mol/mol) ratios of the deposition in the 30–5°N latitude band (Samples TM08-14) are both lower (and thus more favorable for N_2-fixation) than in the samples outside of this band (medians 98 mol/mol and 317 mol/mol, respectively). This pattern is also present when considering the period of 1998-2020, during which the mean surface Chl-*a* concentrations were seen to increase in the region of highest mean AOT (at 15–10°N), much lower compared to Chl-*a* concentrations in the NADR, but comparable to those near the Equator (Figure 11). These results support existing notions of African dust acting to alleviate Fe- and P-imitation of N_2-fixation by diazotrophic cyanobacteria, critical for stimulating the growth of other phytoplankton groups for which N_2-limitation is relieved by diazotrophic N_2-release (Moore et al., 2002; Pabortsava et al., 2017). Higher abundances of e.g., *Trichodesmium* spp. and associated P-depleted waters have been reported to be typically distributed in areas of higher dust input (Capone et al., 1997; Tyrrell et al., 2003; Schlosser et al., 2013) along a latitudinal gradient that nicely follows the seasonal migrations of the ITCZ (Prospero and Carlson, 1972; Doherty et al., 2012;

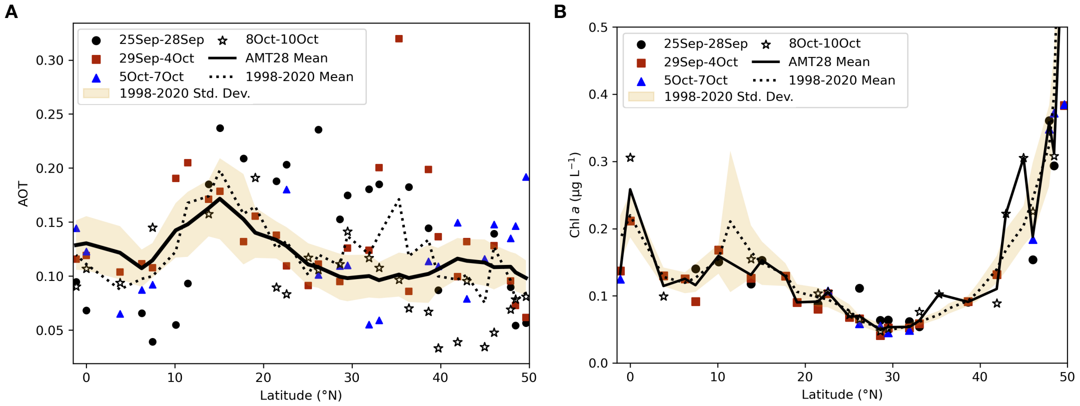

FIGURE 11
Aerosol optical depth (AOT; unitless) **(A)** and Chl-*a* concentrations (µg/L) **(B)** averaged for distinct time intervals across the studied meridional transect: 25-28 September, when the ship was crossing the high latitude regions in the NADR (sites 1-7, 50-40°N – grey circle); 29 September to 4 October, when the ship was crossing most of the gyre region, including the NAST and most of the NATR (sites 8-19, 39-21°N – purple square); 5-7 October, when the ship was crossing the region of highest and most persistent dust input during the expedition (sites 20-25, 20-10°N – green triangle); 8-10 October, when the ship was crossing the WTRA including the salinity minimum region influenced by the ITCZ and NECC, and the Equator (sites 27-31, 7°N-1°S – grey star); mean for the entire AMT28 sampling period (black line); mean and standard deviation for 1998-2020 (dashed line and yellow band, respectively).

Tsamalis et al., 2013; Doherty et al., 2014). As N_2-fixation in the tropical North Atlantic is thought to fuel up to 50% of the export production (Mills et al., 2004 and refs. therein), highest soluble Fe- and P-inputs from Saharan aerosol inputs are likely crucial for stimulating primary production (Baker et al., 2003). However, the observation that coccolithophores living in the gyre were dominantly mostly K-selected (Figure 7C; discussed in section 5.2) suggests that dust-stimulated N_2-fixation did not have a significant role in fueling r-selected coccolithophore productivity to the north of 18°N. This is consistent with previous sediment-trap observations reporting *Umbellosphaera* spp., *F. profunda* and *G. flabellatus* as apparently unaffected by dust deposition, suggesting that only opportunistic species are likely to benefit from pulsed dust-born nutrient-enrichment (Guerreiro et al., 2017).

The NATR-WTRA transition was also marked by rather striking hydrological gradients across the upper ocean, including the highest sub-surface macronutrient concentrations across the transect and the presence of a sub-surface OMZ (Figures 3D, 4E). While Saharan dust appears to have contributed to fuel productivity at the surface in this region, enhanced productivity in the shallow DCM underneath appears to have been stimulated by nutrients supplied from below. Indeed, the uplift of colder subsurface waters underneath this stratified surface region was signalling the geostrophic eastward shoaling of the thermocline/nutricline (positioned at up to ~40–50 m depth at 11–10°N) (Figures 3, 4) (see Merle, 1980a; Merle, 1980b; Katz, 1981; Guerreiro et al., 2019) (see Section 2). Unlike the intermittent nature of dust fertilization at the surface, the geostrophic shoaling of the nutricline is a permanent feature of the tropical NE Atlantic (Longhurst, 2007; Guerreiro et al., 2019) thereby acting to stimulate the phytoplankton community more sustainably across this region. This is evidenced by higher Chl-*a* concentrations and coccolithophore concentrations dominated by *E. huxleyi* and *G. ericsonii* at the DCM compared to the surface, to which higher proportions of diatoms and dinoflagellates (derived from marker-pigments for each group) also contributed (Figures 8, 10). This is in line with the increase of Chl-*a* concentrations and fluxes of biogenic silica and coccoliths produced by r-selected taxa from west to east at ~21–12°N reported by Guerreiro et al. (2019). While the shoaled nutricline is likely to be easily eroded during strong wind-forced mixing events, thereby fuelling phytoplankton along the entire photic zone, shallow and stratified mixed layer conditions at the surface (Figures 3, 4) suggest that wind was not strong enough to do so during AMT28. Therefore, our data suggests that enhanced productivity by opportunistic coccolithophore taxa, *Trichodesmium* spp. and cyanobacteria s.l. at the surface was, at least to some extent, decoupled from that occurring along/below the DCM.

While the geostrophic shoaling of the thermocline explains the shallow position of the nutricline in the NATR-WTRA transition, persistently enhanced dust inputs in this area probably contributed for the highest concentrations of all macronutrients to be observed here, along 18–7°N (Sites 21–27) (Figure 4E and Figure I – Supplementary Material). For example, high PO_4 concentrations at 37–63 m depth in this region (up to 1.4 µmol/L at Site 24 and 1.3 µmol/L at Site 25, located at 11-10°N) are comparable to the maximum of 1.2 µmol/L at ~150 m near the Equator (Site 30), and higher than the maximum of 0.6 µmol/L at ~150 m in the NADR (Sites 2–3) (see Figure 4E). High macronutrient concentrations off NW Africa are consistent with the highest s-Fe and s-P found in our dust samples collected at the same latitudes (Figures 4B, C, 10). Previous studies also report highest s-P concentrations from Saharan dust input (Baker et al., 2003) and higher sub-surface s-Fe concentrations in the tropical NE Atlantic, with persistent maxima at 18–15°N (Measures et al., 2008; Fitzsimmons et al., 2013), and coinciding with the location of the OMZ of the tropical North Atlantic (Karstensen et al., 2008), in line with our data. According to Shelley et al. (2017 and refs. therein), the OMZ is sustained to a great extent by remineralization of high Fe:C organic matter produced by enhanced N_2-fixation driven export from the overlying Fe-rich surface (Shelley et al., 2017 and refs. therein). A sub-surface plume of high dFe in the low oxygen/suboxic subsurface waters has been reported to extend from Mauritania into the center of the tropical upwelling region, fueled by high atmospheric deposition fluxes (Ussher et al., 2013 and refs. therein). Wind-forced vertical diffusive mixing in this region, in turn, is likely to provide an important source of dFe to the surface ocean, reportedly equal to, or even surpassing that of a major dust event. Relatively high phytoplankton biomass in tropical Atlantic waters have been reported to be sustained by such combination of transport of nutrient-rich water from below with atmospheric input from above (Rijkenberg et al., 2012), in line with our data. The resulting large amount of sinking organic detritus and its subsequent bacterial degradation are, in turn, thought to contribute to develop the OMZ.

Enhanced rain events in the NADR probably contributed to increase aerosol nutrient concentrations in the filters sampled in this region, which was more notably the case of atmospheric NO_3 and NH_4. Our data support Baker et al. (2006) reporting the occurrence of intermittent high concentrations of aerosol N in the northern part of the AMT section, largely originated from industrial and agricultural activities in the highly populated adjacent continental regions (e.g., fossil fuel combustion, biomass burning, intensive agriculture). While these authors also report Saharan dust aerosols as generally mixed with anthropogenic nitrates, in line with our atmospheric NO_3 data across the NATR-WTRA (Figure 4A), they argue that such nitrates are more likely to be transported southwards within relatively N-polluted European air, into the desert region, just before being transported by the trades across the Atlantic. In any case, either when directly provided by anthropogenic activities surrounding the NADR, or when transported to the NATR-WTRA transition from more remote regions within African dust plumes, atmospheric nitrates are likely to have also contributed to increase primary productivity in these regions.

In summary, while the magnitude of phytoplankton response to dust-born nutrient input may be higher during strong dust outbreak events, dust-stimulated productivity may be a relatively pervasive feature of the tropical NE Atlantic, driven by geostrophic shoaling of the dust-fueled nutricline in the region of highest and yearlong dust fluxes across the Atlantic (Figure 12). In other words, in addition to directly fueling phytoplankton species at the surface, dust is also likely to feed into a sub-surface "nutrient depocenter" (both macro- and trace metals), to which reportedly enhanced biological recycling/export fueled by dust-driven N_2-fixation likely contribute. Based on the deposition estimates presented here, wet deposition appears to be the dominant delivery mechanism of s-Fe and s-P (Figure 10), suggesting that the magnitude of coccolithophores' ecological response is likely to be much higher when nutrients are delivered with rain compared to the studied sampling period. Our data support Guerreiro et al. (2021) arguing that Saharan dust deposition is likely to, at least partly, counterbalance the effects of climate-driven ocean stratification through stimulating r-selected and ballasting-efficient coccolithophore species.

6 Conclusions

Our study provides important insights into the interplay of oceanographic and atmospheric processes modulating the meridional distribution of coccolithophore communities distributed across the North- and Equatorial Atlantic Ocean. This understanding is critical to gain improved perspectives on the

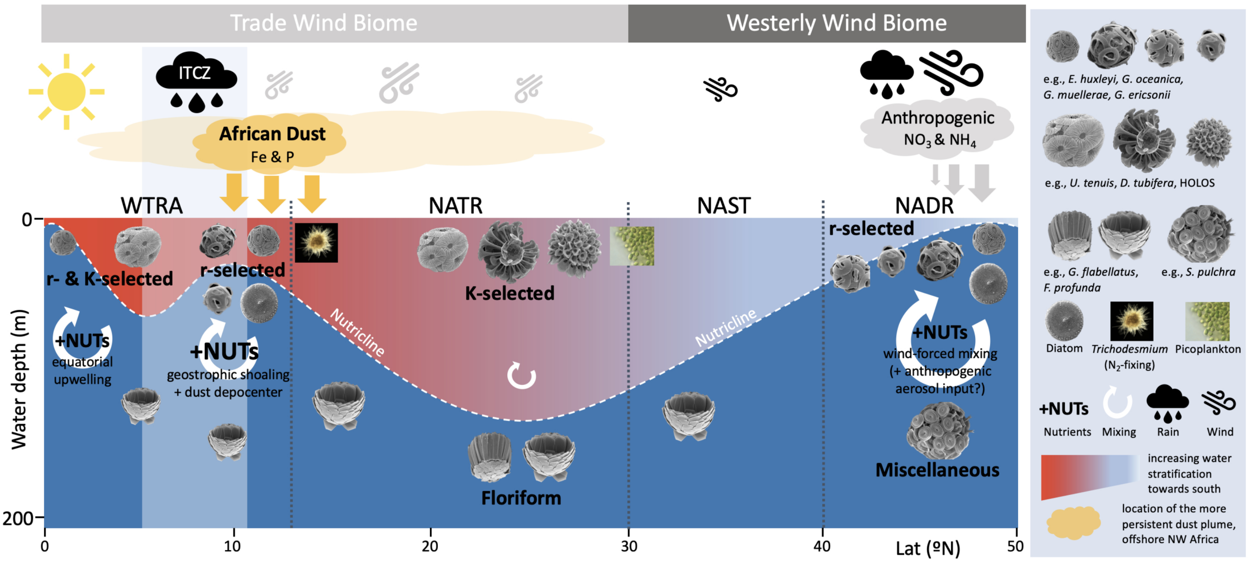

FIGURE 12
Schematic illustration of the environmental and ecological conditions across the North- and Equatorial North Atlantic during the boreal Autumn of 2018 (AMT28).

response of this biogeochemically important group to ongoing climate change. The main findings from our AMT28 study are as follows:

1. The NADR (60–40°N) had the weakest vertical ecological gradients and the highest production by larger cell-sized microphytoplankton and of r-selected placolith-bearing species (*E. huxleyi* and gephyrocapsids), reflecting their ability to thrive and compete for nutrients in more dynamic and seasonally nutritious mixed layer conditions, typical of high-latitude regions and coastal areas.
2. The subtropical gyre region, comprising the NAST and the NATR (40–12°N), had the strongest vertical ecological gradients and the highest production by smaller cell-sized picophytoplankton and by K-selected umbelliform taxa and holococcolithophores living at the surface, and by deep-dwelling florifom living in the deep euphotic and subeuphotic zones of the ocean.
3. The WTRA (12°N–5°S) presented heavily stratified and oxygen-poor surface water conditions over a shallower nutricline, and a shallow DCM which was associated to the eastward geostrophic shoaling of the thermocline. Umbelliform and floriform species were inhabiting the regions of stronger stratification, while placolith-bearing species were more abundant in locally nutrient-enriched areas. The Equator region was the second most productive region across the transect, next to the NADR, with several ecologically distinct taxa (both r- and K-selected) increasing.
4. High coccolithophore species richness and diversity linked to a possibly broader range of nutritional strategies (e.g., mixotrophy), and the ability of undergoing life cycle changes, are good indicators of gyre coccolithophore communities being more resilient to climate-driven ongoing ocean warming. This is illustrated by mean concentrations of 11-14×10^3 cells/L contributed by floriform taxa, umbelliforms and holococcolithophores in the gyre, only slightly lower compared to 17.7×10^3 mean cells/L dominated by r-selected species in the NADR.
5. Higher HexFuco concentrations along the regions of enhanced productivity by r-selected placolith-bearing coccolithophore species suggest that this pigment is produced towards maximizing the use of light in nutritious ocean conditions, and that species composition should be considered when using HexFuco as a pigment marker of coccolithophores.
6. The striking coincidence between the increase of atmospheric s-Fe and s-P across the NATR-WTRA transition, and the increase of cell concentrations by r-selected *E. huxleyi* and *G. oceanica*, and of the N_2-fixing *Thrichodesmium* spp. in the stratified oligotrophic surface layer underneath, point to the occurrence of Saharan-dust fertilization at the surface of the ocean, off NW Africa. This process appeared decoupled from the enhanced productivity in the shallow DCM underneath, which was probably stimulated by nutrients supplied from below, linked to the geostrophic shoaling of the thermocline/nutricline (up to ~40–50 m depth at 11–10°N).
7. Persistently enhanced Saharan-dust inputs off NW Africa across the NATR-WTRA transition probably contributed for this region presenting the highest macronutrient sub-surface concentrations across the transect (along 18–7°N, Sites 21–27), consistent with the highest s-Fe and s-P found in dust samples collected at the same latitudes, and with previous studies.
8. While the magnitude of phytoplankton response to dust-born nutrient input at the surface might be higher during strong dust outbreak events, our data suggest that dust-stimulated productivity may be a relatively pervasive feature of the tropical NE Atlantic, driven by geostrophic shoaling of the dust-fueled shallow nutricline in the region of highest dust fluxes across the Atlantic.8.

Data availability statement

The original contributions presented in the study are included in the article/Supplementary Material. Further inquiries can be directed to the corresponding author.

Author contributions

CG was responsible for the conceptual development and writing of the manuscript, with contributions of all authors. CG and CP performed the coccolithophore light microscope analysis. CG was responsible for the SEM taxonomic analysis, with contributions from LC and TN. VV performed the microscope identification and enumeration of *Trichodesmium* spp. AT and AF performed all the in-situ sampling during AMT28. AT and VB performed the pigment analysis *via* High Performance Liquid Chromatography. AF performed the processing of all the satellite remote sensing. J-BS did the quantification of dust concentrations. AB was responsible for the quantification of atmospheric nutrients. All authors contributed to the article and approved the submitted version.

Funding

CG benefited from a Marie Sklodowska-Curie European Fellowship supported by the EU H2020-MSCA-IF-2017 (grant no. 796802) linked to project DUSTCO, and currently benefits from a research grant funded by FCT (contract CEECIND/00752/2018/CP1534/CT0011) linked to project CHASE (/www.chase-dust.com). This work also received funding from the European Union's Horizon 2020 Research and Innovation Programme under grant agreement n° 810139 Project Portugal Twinning for Innovation and Excellence in Marine Science and Earth Observation – PORTWIMS; and from the UK Natural Environment Research Council under grant agreement n° NE/V001213/1. This is contribution number 361 of the AMT programme. The Atlantic Meridional Transect is funded by the UK Natural Environment Research Council through its National Capability Long-term Single Centre Science Programme, Climate Linked Atlantic Sector Science (grant number NE/R015953/1). This publication was financed under H2020 Research and Innovation Program LC-SPACE-04-EO-2019-2020: Copernicus evolution – Research activities in support of cross-cutting applications between Copernicus services – CERTO.

Acknowledgments

This study contributes to the international IMBeR project. We thank the officers and crew of the British Antarctic Survey vessel James Clark Ross. We also thank Susan Becker and John R. Ballard (UC San Diego/Scripps Institution of Oceanography) for the macronutrient collection and analysis; to Dominic Handscomb (University of East Anglia) for the aerosol nutrient analysis; and to Bror Jonsson (Plymouth Marine Laboratory) for the helpful discussion about the physical oceanographic processes at play in the tropical Atlantic. Quantification of dust concentrations was performed at the Royal Netherlands Institute for Sea Research, NL, and the quantification of atmospheric nutrients was performed at the University of East Anglia, UK. Lab preparation and polarizing-light microscope analysis of the coccolithophore samples were performed at the Laboratory of Calcareous Nannofossils, Instituto Dom Luiz (IDL-RG2/Uni-Lisbon); scanning electron microscope analysis, HPLC pigment analysis and the *Thrichodesmium* study were performed at MARE and Dep. Plant Biology, at the Faculty of Sciences of the University of Lisbon, Portugal.

Conflict of interest

The authors declare that the research was conducted in the absence of any commercial or financial relationships that could be construed as a potential conflict of interest

Publisher's note

Supplementary material

The Supplementary Material for this article can be found online at: https://www.frontiersin.org/articles/10.3389/fmars.2023.1119488/full#supplementary-material

References

Adams, A. M., Prospero, J. M., and Zhang, C. (2012). CALIPSO-derived three-dimensional structure of aerosol over the Atlantic basin and adjacent continents. *J. Climate* 25 (19), 6862–6879. doi: 10.1175/JCLI-D-11-00672.1

Aiken, J., Brewin, R. J. W., Dufois, F., Polimene, L., Hardman-Mountford, N. J., and Jackson, T. (2017). A synthesis of the environmental response of the north and south Atlantic sub-tropical gyres during two decades of AMT. *Prog. Oceanogr.* 158, 236–254. doi: 10.1016/j.pocean.2016.08.004

Aiken, J., Rees, N., Hooker, S., Holligan, P., Bale, A., Robins, D., et al. (2000). The Atlantic meridional transect: overview and synthesis of data. *Prog. Oceanogr.* 45 (3–4), 257–312. doi: 10.1016/S0079-6611(00)00005-7

Andruleit, H. (2007). Status of the Java upwelling area (Indian ocean) during the oligothrophic northern hemisphere winter monsoon season as revealed by coccolithophores. *Mar. Micropaleontol.* 64, 36–51. doi: 10.1016/j.marmicro.2007.02.001

Andruleit, H., and Rogalla, U. (2002). Coccolithophores in surface sediments of the Arabian Sea in relation to environmental gradients in surface waters. *Mar. Geol.* 186, 505–526. doi: 10.1016/S0025-3227(02)00312-2

Andruleit, H., Stager, S., Rogalla, U., and Cepek, P. (2003). Living coccolithophores in the northern Arabian Sea: ecological tolerances and environmental control. *Mar. Micropaleontol.* 49, 157–181. doi: 10.1016/S0377-8398(03)00049-5

Avrahami, Y., and Frada, M. J. (2020). Detection of phagotrophy in the marine phytoplankton group of the coccolithophores (Calcihaptophycidae, haptophyta) during nutrient-replete and phosphate-limited growth. *J. Phycol.* 56 (4), 1103–1108. doi: 10.1111/jpy.12997

Baker, A. R., Adams, C., Bell, T. G., Jickells, T. D., and Ganzeveld, L. (2013). Estimation of atmospheric nutrient inputs to the Atlantic ocean from 50°N to 50°S based on large-scale field sampling: Iron and other dust-associated elements. *Global Biogeochem. Cycles* 27, 755–767. doi: 10.1002/gbc.20062

Baker, A. R., Jickells, T. D., Biswas, K. F., Weston, K., and French, M. (2006). Nutrients in atmospheric aerosol particles along the Atlantic meridional transect, deep-Sea res. *Pt. II 53* 1706– 1719, 2006. doi: 10.1016/j.dsr2.2006.05.012

Baker, A. R., Kelly, S. D., Biswas, K. F., Witt, M., and Jickells, T. D. (2003). Atmospheric deposition of nutrients to the Atlantic ocean, geophys. *Res. Lett.* 30 (24), 2296. doi: 10.1029/2003GL018518

Baker, A. R., Lesworth, T., Adams, C., Jickells, T. D., and Ganzeveld, L. (2010). Estimation of atmospheric nutrient inputs to the Atlantic ocean from 50°N to 50°S based on large-scale field sampling: Fixed nitrogen and dry deposition of phosphorus. *Global Biogeochem. Cycles* 24, GB3006. doi: 10.1029/2009GB003634

Baker, A. R., Weston, K., Kelly, S. D., Voss, M., Streu, P., and Cape, J. N. (2007). Dry and wet deposition of nutrients from the tropical Atlantic atmosphere: links to primary productivity and nitrogen fixation. *Deep Sea Res. Part I* 54, 1704–1720. doi: 10.1016/j.dsr.2007.07.001

Balch, W. M. (2004). "Re-evaluation of the physiological ecology of coccolithophores," in *Coccolithophores: From molecular processes to global impact*. Eds. H. R. Thierstein and J. R. Young (Berlin: Springer), 165–190.

Balch, W. M. (2018). The ecology, biogeochemistry, and optical properties of coccolithophores. *Annu. Rev. Mar. Sci.* 10, 71–98. doi: 10.1146/annurev-marine-121916-063319

Balch, W. M., Bowler, B. C., Drapeau, D. T., Lubelczyk, L. C., Lyczkowski, E., Mitchell, C., et al. (2019). Coccolithophore distributions of the north and south Atlantic ocean. *Deep Sea Res. Part I: Oceanogr. Res. Pap.* 151, 103066. doi: 10.1016/j.dsr.2019.06.012

Basha, G., Kishore, P., Venkat Ratnamc, M., Ouarda, T. B. M. J., Velicogna, I., and Sutterley, T. (2015). Vertical and latitudinal variation of the intertropical convergence zone derived using GPS radio occultation measurements. *Remote Sens. Environ.* 163, 262–269. doi: 10.1016/j.rse.2015.03.024

Baumann, K.-H., Andruleit, H. A., and Samtleben, C. (2000). Coccolithophores in the Nordic seas: comparison of living communities with surface sediment assemblages. *Deep-Sea Res. II* 47, 1743–1772. doi: 10.1016/S0967-0645(00)00005-9

Beaufort, L., Lancelot, Y., Camberlin, P., Cayre, O., Vincent, E., Bassinot, F., et al. (1997). Insolation cycles as a major control of equatorial Indian ocean primary production. *Science* 278, 1451–1454. doi: 10.1126/science.278.5342.1451

Becker, S., Aoyama, M., Woodward, E. M. S., Bakker, K., Coverly, S., Mahaffey, C., et al. (2020). GO-SHIP repeat hydrography nutrient manual: the precise and accurate determination of dissolved inorganic nutrients in seawater, using continuous flow analysis methods. *Front. Mar. Sci.* 7. doi: 10.3389/fmars.2020.581790

Behrenfeld, M. J., O'Malley, R. T., Siegel, D. A., McClain, C. R., Sarmiento, J. L., Feldman, G. C., et al. (2006). Climate-driven trends in contemporary ocean productivity. *Nature* 444, 752–755. doi: 10.1038/nature05317

Ben-Ami, Y., Koren, I., Altaratz, O., Kostinski, A., and Lehahn, Y. (2012). Discernible rhythm in the spatio/temporal distributions of transatlantic dust, atmos. *Chem. Phys.* 12, 2253–2262. doi: 10.5194/acp-12-2253-2012

Bergquist, B. A., and Boyle, E. A. (2006). Dissolved iron in the tropical and subtropical Atlantic ocean. *Global Biogeochem. Cycles* 20, 1–14. doi: 10.1029/2005GB002505

Billard, C., and Inouye, I. (2004). "What is new in coccolithophore biology?," in *Coccolithophores*. Eds. H. R. Thierstein and J. R. Young (Berlin, Heidelberg: Springer). doi: 10.1007/978-3-662-06278-4_1

Boeckel, B., and Baumann, K.-H. (2008). Vertical and lateral variations in coccolithophore community structure across the subtropical frontal zone in the south Atlantic ocean. *Mar. Micropaleontol.* 76, 255–273. doi: 10.1016/j.marmicro.2008.01.014

Boeckel, B., Baumann, K.-H., Henrich, R., and Kinkel, H. (2006). Coccolith distribution patterns in south Atlantic and southern ocean surface sediments in relation to environmental gradients. *Deep-Sea Res. Pt. I* 53, 1073–1099. doi: 10.1016/j.dsr.2005.11.006

Bowie, A. R., Whitworth, D. J., Achterberg, E. P., Mantoura, R. F. C., and Worsfold, P. J. (2002). Biogeochemistry of fe and other trace elements (Al, Co, Ni) in the upper Atlantic ocean. *Deep Sea Res. Part I* 49, 605–636. doi: 10.1016/S0967-0637(01)00061-9

Boyce, D. G., Lewis, M. R., and Worm, B. (2010). Global phytoplankton decline over the past century. *Nature* 466 (29), 591–596. doi: 10.1038/nature09268

Boyd, P. W., and Ellwood, M. J. (2010). The biogeochemical cycle of iron in the ocean. *Nat. Geosci.* 3, 675–682. doi: 10.1038/ngeo964

Boyd, P. W., Jickells, T., Law, C. S., Blain, S., Boyle, E. A., Buesseler, K. O., et al. (2007). Mesoscale iron enrichment experiments 1993-2005: Synthesis and future directions. *Science* 315, 612–617. doi: 10.1126/science.1131669

Boyd, P. W., Strzepek, R., Fu, F.-X., Hutchins, D. A., Hutchins, D. A., et al. (2010). Environmental control of open-ocean phytoplankton groups: now and in the future. *Limn. Ocean.* 55, 1353–1376. doi: 10.4319/lo.2010.55.3.1353

Brand, L. E. (1994). "Physiological ecology of marine coccolithophores," in *Coccolithophores*. Eds. A. Winter and W. G. Siesser (Cambridge: Cambridge University Press), 39–49.

Brewer, P. G., and Riley, J. P. (1965). The automatic determination of nitrate in sea water. *Deep Sea Research and Oceanographic Abstracts* 12 (6), 765–772.

Broerse, A. T. C., Ziveri, P., van Hinte, J. E., and Honjo, S. (2000). Coccolithophore export pro- duction, species composition and coccolith- CaCO3 fluxes in the NE Atlantic (34°N 21°W and 48°N 21°W). *Deep-Sea Res. Pt. II* 47, 1877–1906. doi: 10.1016/S0967-0645(00)00010-2

Brotas, V., Tarran, G., Veloso, V., Brewin, R. J. W., Woodward, E. M. S., Airs, R., et al. (2022). Complementary approaches to assess phytoplankton groups and size classes on a long transect in the Atlantic ocean. *Front. Mar. Sci.* 8. doi: 10.3389/fmars.2021.682621

Buck, C. S., Landing, W. M., Resing, J. A., and Measures, C. I. (2010). The solubility and deposition of aerosol fe and other trace elements in the north Atlantic ocean: observations from the A16N CLIVAR/CO2 repeat hydrography section. *Mar. Chem.* 120, 57–70. doi: 10.1016/j.marchem.2008.08.003

Capone, D. G., Zehr, J., Paerl, H., Bergman, B., and Carpenter, E. J. (1997). Trichodesmium: A globally significant marine cyanobacterium. *Science* 276, 1221–1229. doi: 10.1126/science.276.5316.1221

Caron, D. A. (2016). Mixotrophy stirs up our understanding of marine food webs. *Proc. Natl. Acad. Sci. U.S.A.* 113, 2806–2808. doi: 10.1073/pnas.1600718113

Caron, D. A., and Countway, P. D. (2009). Hypotheses on the role of protistan rare biosphere in a changing world. *Aquat. Microb. Ecol.* 57, 227–238. doi: 10.3354/ame01352

Cermeño, P., Dutkiewicz, S., Harris, R. P., Follows, M., Schofield, O., and Falkowski, P. G. (2008). The role of nutricline depth in regulating the ocean carbon cycle. *PNAS* 105 (51), 20344–20349. doi: 10.1073/pnas.0811302106

Charalampopoulou, A., Poulton, A. J., Tyrrell, T., and Lucas, M. I. (2011). Irradiance and pH affect coccolithophore community composition on a transect between the north Sea and the Arctic ocean. *Mar. Ecol. Prog. Ser.* 431, 25–43. doi: 10.3354/meps09140

Chiapello, I., Prospero, J. M., Herman, J. R., and Hsu, N. C. (1999). Detection of mineral dust over the north Atlantic ocean and Africa with the nimbus 7 TOMS. *J. Geophys. Res.* 104, 9277–9291. doi: 10.1029/1998JD200083

Coale, K. H., Johnson, K. S., Fitzwater, S. E., Gordon, R. M., Tanner, S., and Chavez, F. P. (1996). A massive phytoplankton bloom induced by an ecosystem-scale iron fertilization experiment in the equatorial pacific ocean. *Nature* 383, 495–501. doi: 10.1038/383495a0

Crawford, D., Lipsen, M. S., Purdie, D. A., Lohan, M. C., Statham, P. J., Whitney, F. A., et al. (2003). Influence of zn and fe enrichments on phytoplankton growth in the northeastern subarctic pacific. *Limnol. Ocean.* 48, 1583–1600. doi: 10.4319/lo.2003.48.4.1583

Cros, L. (2001). *Planktonic coccolithophores of the NW Mediterranean* (Universitat de Barcelona: PhD Thesis), 181.

Cros, L., and Estrada, M. (2013). Holo-heterococcolithophore life cycles: ecological implications. *Mar. Ecol. Progr Ser.* 492, 57–68. doi: 10.3354/meps10473

Cros, L., and Fortuño, J.-M. (2000). Atlas of northwestern Mediterranean coccolithophores. *Sci. Mar.* 66, 7–182. doi: 10.3989/scimar.2002.66s11

Dandonneau, Y., Montel, Y., Blanchot, J., Giraudeau, J., and Neveux, J. (2006). Temporal variability in phytoplankton pigments, picoplankton and coccolithophores along a transect through the north Atlantic and tropical southwestern pacific. *Deep Sea Res. Part I* 53 (4), 689–712. doi: 10.1016/j.dsr.2006.01.002

Dimiza, M. D., Triantaphyllou, M. V., and Dermitzakis, M. D. (2008). Seasonality and ecology of living coccolithophores in e. Mediterranean coastal environments (Andros island, middle Aegean Sea). *Micropaleontology* 54 (1), 59–75.

Doherty, O. M., Riemer, N., and Hameed, S. (2012). Control of Saharan mineral dust transport to Barbados in winter by the intertropical convergence zone over West Africa. *J. Geophys. Res. Atmos.* 117, 1–13. doi: 10.1029/2012JD017767

Doherty, O. M., Riemer, N., and Hameed, S. (2014). Role of the convergence zone over West Africa in controlling Saharan mineral dust load and transport in the boreal summer. *Tellus B* 66, 23191. doi: 10.3402/tellusb.v66.23191

Dolan, J. R., Lemée, R., Gasparini, S., Mousseau, L., and Heyndrickx, C. (2006). Probing diversity in the plankton: using patterns in tintinnids (planktonic marine ciliates) to identify mechanisms. *Hydrobiologia* 555 (1), 143–157. doi: 10.1007/s10750-005-1112-6

Duce, R. A., Liss, P., Merrill, J., Atlas, E., Buat-Ménard, P., Hicks, B., et al. (1991). The atmospheric input of trace species to the world ocean. *Global Biogeochem. Cycles* 5, 193–259. doi: 10.1029/91GB01778

Dutkiewicz, S., Scott, J. R., and Follows, M. J. (2013). Winners and losers: Ecological and biogeochemical changes in a warming ocean. *Global Biogeochem. Cycle.* 27, 463–477. doi: 10.1002/gbc.20042

Emery, W. J. (2001). "Water types and water masses," in *Encyclopedia of ocean sciences*, *3rd ed.* Eds. J.K. Cochran, H. J. Bokuniewicz and P. L. Yager (Elsevier: Academic Press), 169–179.

Emery, W. J., and Meincke, J. (1986). Global water masses: Summary and review, oceanol. *Acta* 9, 383–391. 1986.

Fischer, G., Romero, O., Merkel, U., Donner, B., Iversen, M., Nowald, N., et al. (2016). Deep ocean mass fluxes in the coastal upwelling off Mauritania from 1988 to 2012: variability on seasonal to decadal time-scales. *Biogeosciences* 13, 3071–3090. doi: 10.5194/bg-13-3071-2016

Fitzsimmons, J. N., Zhang, R., and Boyle, E. A. (2013). Dissolved iron in the tropical north Atlantic ocean. *Mar. Chem.* 154, 87–99. doi: 10.1016/j.marchem.2013.05.009

Fomba, K. W., Müller, K., van Pinxteren, D., Poulain, L., van Pinxteren, M., and Herrmann, H. (2014). Long-term chemical characterizationof tropical and marine aerosols at the cape Verde atmospheric observatory (CVAO) from 2007 to 2011. *Atmospheric Chem. Phys.* 14 (17), 8883–8904. doi: 10.5194/acp-14-8883-2014

Frada, M., Young, J., Cachão, M., Lino, S., Martins, A., Narciso, A., et al. (2010). A guide to extant coccolithophores (Calcihaptophycidae, haptophyta) using light microscopy. *J. Nannoplankton Res.* 31 (2), 58–112.

Frazão, H. C., Prien, R. D., Schulz-Bull, D. E., Seidov, D., and Waniek, J. J. (2022). The forgotten Azores current: A long-term perspective. *Front. Mar. Sci.* 9. doi: 10.3389/fmars.2022.842251

Giraudeau, J., and Bayley, G. W. (1995). Spatial dynamics of coccolithophore communities during an upwelling event in the southern benguela system, cont. *Shelf Res.* 15, 1825–1852. doi: 10.1016/0278-4343(94)00095-5

Godrijan, J., Drapeau, D., and Balch, W. M. (2020). Mixotrophic uptake of organic compounds by coccolithophores. *Limnol. Oceanogr.* 65, 1410–1421. doi: 10.1002/lno.11396

Godrijan, J., Drapeau, D. T., and Balch, W. M. (2021). Osmotrophy of dissolved organic carbon by coccolithophores in darkness. *New Phytol.* 233, 781–794. doi: 10.1111/nph.17819

Godrijan, J., Young, J. R., Maric Pfannkuchen, D., Precali, R., and Pfannkuchen, M. (2018). Coastal zones as important habitats of coccolithophores: a study of species diversity, succession, and life-cycle phases. *Limnol. Oceanogr.* 63, 1692–1710. doi: 10.1002/lno.10801

Goudie, A. S., and Middleton, N. J. (2001). Saharan Dust storms: nature and consequences, earth-sci. *Rev.* 56, 179–204.

Grasshoff, K. (1976). *Methods of Sea-water analysis* (Weiheim: Verlag Chemie), 317.

Guerreiro, C. V., Baumann, K.-H., Brummer, G.-J. A., Fischer, G., Korte, L. F., Merkel, U. S. C., et al. (2017). Coccolithophore fluxes in the open tropical north Atlantic: influence of thermocline depth, Amazon water, and Saharan dust. *Biogeosciences* 14, 4577–4599. doi: 10.5194/bg-14-4577-2017

Guerreiro, C. V., Baumann, K.-H., Brummer, G.-J. A., Fischer, G., Korte, L. F., and Stuut, J.-B. W. (2019). Wind-forced transatlantic gradients in coccolithophore species fluxes. *Prog. Oceanogr.* 176, 102140. doi: 10.1016/j.pocean.2019.102140

Guerreiro, C. V., Baumann, K.-H., Brummer, G.-J. A., Valente, A., Fischer, G., Ziveri, P., et al. (2021). Carbonate fluxes by coccolithophore species between NW Africa and the Caribbean: implications for the biological carbon pump. *Limnol. Oceanogr.* 9999, 1–19. doi: 10.1002/lno.11872

Guerreiro, C., Oliveira, A., Cachão, M., de Stigter, H., Sá, C., Borges, C., et al. (2013). Late winter coccolithophore bloom off central Portugal in response to river discharge and upwelling. *Cont. Shelf Res.* 59, 65–83. doi: 10.1016/j.csr.2013.04.016

Guieu, C., Aumont, O., Paytan, A., Bopp, L., Law, C. S., Mahowald, N., et al. (2014). The significance of the episodic nature of atmospheric deposition to low nutrient low chlorophyll regions. *Global Biogeochem. Cy.* 28, 1179–1198. doi: 10.1002/2014GB004852

Holligan, P. M., Fernandez, E., Aiken,, et al. (1993). Biogeochemical study of the coccolithophore, emiliania huxleyi, in the north Atlantic. *Global Biogeochem. Cycles* 7, 879–900. doi: 10.1029/93GB01731

Houdan, A., Billard, C., Marie, D., Not, F., Sá, A., Young, J., et al. (2006). Holococcolithophore- heterococcolithophore (Haptophyta) life cycles: Flow cytometric analysis of relative ploidy levels. *Syst. Biodivers.* 1 (4), 453–465. doi: 10.1017/S1477200003001270

Hutchins, D. (2011). Forecasting the rain ratio. *Nature* 476, 41–42. doi: 10.1038/476041a

Irwin, A. J., Finkel, Z. V., Müller-Karger, F. E., and Ghinaglia, L. T. (2015). Phytoplankton adapt to changing ocean environments. *PNAS* 112 (18), 5762–5766. doi: 10.1073/pnas.1414752112

Ito, A., Ye, Y., Baldo, C., and Shi, Z. (2021). Ocean fertilization by pyrogenic aerosol iron. *Climate Atmospheric Sci.* 4 (30), 1–20. doi: 10.1038/s41612-021-00185-8

Jickells, T. D., An, Z. S., Andersen, K. K., Baker, A. R., Bergametti, G., Brooks, N., et al. (2005). Global iron connections between desert dust, ocean biogeochemistry, and climate. *Science* 308, 67–71. doi: 10.1126/science.1105959

Jordan, R., Cros, L., and Young, J. (2004). A revised classification scheme for living haptophytes. *Micropaleontology* 50 (1), 55–79. doi: 10.2113/50.Suppl_1.55

Karstensen, J., Stramma, L., and Visbeck, M. (2008). Oxygen minimum zones in the eastern tropical Atlantic and pacific oceans. *Prog. Oceanogr.* 77, 331–350. doi: 10.1016/j.pocean.2007.05.009

Katz, E. J. (1981). Dynamic topography of the sea surface in the equatorial Atlantic. *J. Mar. Res.* 39, 53–63.

Kinkel, H., Baumann, K.-H., and Cepek, M. (2000). Coccolithophores in the equatorial Atlantic ocean: response to seasonal and late quaternary surface water variability. *Mar. Micropaleontol.* 39, 87–112. doi: 10.1016/S0377-8398(00)00016-5

Kirkwood, D. S. (1989). *Simultaneous determination of selected nutrients in seawater, ICES CM 1989/C* (Washington, DC: ICES), 29.

Kleijne, A. (1991). Holococcolithophorids from the Indian ocean, red Sea, Mediterranean Sea and north Atlantic ocean. *Mar. Micropaleontol.* 17 (1–2), 1–76. doi: 10.1016/0377-8398(91)90023-Y

Kleijne, A. (1993). *Morphology, taxonomy and distribution of extant coccolithophorids (calcareous nannoplankton)* (Vrije Universiteit, Amsterdam: Ph.D. Thesis).

Knappertsbusch, M., and Brummer, G.-J. A. (1995). A sediment trap investigation of sinking coccolithophores in the north Atlantic. *Deep-Sea Res. I* 42, 1083–1109. doi: 10.1016/0967-0637(95)00036-6

Korte, L. F., Brummer, G.-J., van der Does, M., Guerreiro, C. V., Mienis, F., Munday, C. I., et al. (2020). Multiple drivers of production and particle export in the western tropical north Atlantic. *Limnol. Oceanogr.* 9999, 1–17. doi: 10.1002/lno.11442

Krumhardt, K. M., Lovenduski, N. S., Freeman, N. M., and Bates, N. R. (2016). Apparent increase in coccolithophore abundance in the subtropical north Atlantic from 1990 to 2014. *Biogeosciences* 13, 1163–1177. doi: 10.5194/bg-13-1163-2016

Krumhardt, K. M., Lovenduski, N. S., Long, M. C., and Lindsay, K. (2017). Avoidable impacts of ocean warming on marine primary production: Insights from the CESM ensembles. *Global Biogeochem. Cycl.* 31, 114–133. doi: 10.1002/2016GB005528

Lancelot, C. (2012). Marine nutrient cycling – how will the ocean's capacity of biological carbon pumping change? *PAGES News* 20 (1), 16. doi: 10.22498/pages.20.1.16

Laufkötter, C., Vogt, M., Gruber, N., Aita-Noguchi, M., Aumont, O., Bopp, L., et al. (2015). Drivers and uncertainties of future global marine primary production in marine ecosystem models. *Biogeosciences* 12, 6955–6984. doi: 10.5194/bg-12-6955-2015,2015

Levitus, S. (1982). Climatological atlas of the world ocean. *NOAA Prof. Paper* 13, 173.

Liu, H., Probert, I., Uitz, J., Claustre, H., Aris-Brosou, S., Frada, M., et al. (2009). Extreme diversity in noncalcifying haptophytes explains a major pigment paradox in open oceans. *PNAS* 106 (31), 12803–12808. doi: 10.1073/pnas.0905841106

Liu, M., and Tanhua, T. (2021). Water masses in the Atlantic ocean: characteristics and distributions. *Ocean Sci.* 17, 463–486. doi: 10.5194/os-17-463-2021

Longhurst, A. (1993). Seasonal cooling and blooming in tropical oceans. *Deep-Sea Res. I* 40, 2145–2165. doi: 10.1016/0967-0637(93)90095-K

Longhurst, A. (2007). *Ecological geography of the Sea. 2nd Ed* (San Diego: Academic Press), ISBN: .

Mahaffey, C., Reynolds, S., Davis, C. E., and Lohan, M. C. (2014). Alkaline phosphatase activity in the subtropical ocean: Insights from nutrient, dust and trace metal addition experiments. *Front. Mar. Sci.* 1. doi: 10.3389/fmars.2014.00073

Mann, K. H., and Lazier, J. R. (2006). *Dynamics of marine ecosystems, biological-physical interactions in the oceans. 3rd ed.* (Malden, MA, Oxford, UK: Black-well Publishing), 512.

Marañón, E., Behrenfeld, M. J., Gonzalez, N., Mourino, B., and Zubkov, M. V. (2003). High variability of primary production in oligotrophic waters of the Atlantic ocean: uncoupling from phytoplankton biomass and size structure. *Mar. Ecol. Prog. Ser.* 257, 1–11. doi: 10.3354/meps257001

Marañón, E., Holligan, P. M., Barciela, R., Gonzalez, N., Mourino, B., Pazo, M. J., et al. (2001). Patterns of phytoplankton size structure and productivity in contrasting open-ocean environments. *Mar. Ecol. Prog. Ser.* 216, 43–56. doi: 10.3354/meps216043

Marañón, E., Holligan, P. M., Varela, M., Mourino, B., and Bale, A. J. (2000). Basin-scale variability of phytoplankton biomass, production and growth in the Atlantic ocean. *Deep-Sea Res. I* 47, 825–857. doi: 10.1016/S0967-0637(99)00087-4

Margalef, R. (1978). Life-forms of phytoplankton as survival alternatives in an unstable environment. *Oceanol. Acta* 1, 493–509.

Martin, J. H. (1990). Glacial–interglacial CO_2 change: The iron hypothesis. *Paleoceanography* 5, 1–13. doi: 10.1029/PA005i001p00001

Measures, C. I., Landing, W. M., Brown, M. T., and Buck, C. S. (2008). High-resolution Al and fe data from the Atlantic ocean CLIVAR-CO2 repeat hydrography A16N transect: extensive linkages between dust and upper ocean geochemistry. *Global Biogeochem. Cycles* 22, 1–10. doi: 10.1029/2007GB003042

Merle, J. (1980a). Seasonal heat budget in the equatorial Atlantic ocean. *J. Phys. Oceanogr.* 10, 464–469. doi: 10.1175/1520-0485(1980)010<0464:SHBITE>2.0.CO;2

Merle, J. (1980b). Seasonal variation of heat storage in the tropical Atlantic ocean. *Oceanol. Acta* 3, 455463.

Mills, M. M., Ridame, C., Davey, M., Roche, J. L., and Geider, R. J. (2004). Iron and phosphorus co-limit nitrogen fixation in the eastern tropical north Atlantic. *Nature* 429, 292–294. doi: 10.1038/nature02550

Mirzabaev, A., Wu, J., Evans, J., García-Oliva, F., Hussein, I. A. G., Iqbal, M. H., et al (2019). "Desertification," in *Climate change and land: an IPCC special report on climate change, desertification, land degradation, sustainable land management, food security, and greenhouse gas fluxes in terrestrial ecosystems*. Eds. P. R. Shukla, J. Skea, E. Calvo Buendia, V. Masson-Delmotte, H.-O. Pörtner, D. C. Roberts, P. Zhai, R. Slade, S. Connors, R. van Diemen, M. Ferrat, E. Haughey, S. Luz, S. Neogi, M. Pathak, J. Petzold, J. Portugal Pereira, P. Vyas, E. Huntley, K. Kissick, M. Belkacemi and J Malley.

Molfino, B., and McIntyre, A. (1990). Precessional forcing of nutricline dynamics in the equatorial Atlantic. *Science* 249, 766–769. doi: 10.1126/science.249.4970.766

Monteiro, F. M., Bach, L. T., Brownlee, C., Bown, P., Rickaby, R. E. M., Poulton, A. J., et al. (2016). Why marine phytoplankton calcify. *Sci. Adv.* 2, e1501822. doi: 10.1126/sciadv.1501822

Moore, J. K., Doney, S. C., Glover, D. M., and Fung, I. Y. (2002). Iron cycling and nutrient-limitation patterns in surface waters of the world ocean. *Deep Sea Res. Part II* 49, 463–507. doi: 10.1016/S0967-0645(01)00109-6

Moore, J. K., Fu, W., Primeau, F., Britten, G. L., Lindsay, K., Long, M., et al. (2018). Sustained climate warming drives declining marine biological productivity. *Science* 359, 1139–1143. doi: 10.1126/science.aao6379

Moulin, C., and Chiapello, I. (2006). Impact of human-induced desertification on the intensification of sahel dust emission and export over the last decades. *Geophys. Res. Lett.* 33, L18808. doi: 10.1029/2006GL025923. 2006.

O'Brien, C. J., Vogt, M., and Gruber, N. (2016). Global coccolithophore diversity: drivers and future change. *Prog. Oceanogr.* 140, 27–42. doi: 10.1016/j.pocean.2015.10.003

Oziel, L., Baudena, A., Ardyna, M., Massicotte, P., Randelhoff, A., Sallée, J.-B., et al. (2020). Faster Atlantic currents drive poleward expansion of temperate phytoplankton in the Arctic ocean. *Nat. Commun.* 11, 1705. doi: 10.1038/s41467-020-15485-5

Pabortsava, K., Lampitt, R. S., Benson, J., Crowe, C., McLachlan, R., Le Moigne, F. A. C., et al. (2017). Carbon sequestration in the deep Atlantic enhanced by Saharan dust. *Nat. Geosci.* 10, 189–194. doi: 10.1038/ngeo28997

Pelegrí, J. L., Peña-Izquierdo, J., Machín, F., Meiners, C., and Presas-Navarro, C. (2017). "Oceanography of the cape Verde basin and Mauritanian slope waters," in *Deep-Sea ecosystems off Mauritania, research of marine biodiversity and habitats in the Northwest African margin*. Eds. A. Ramos, F. Ramil and J. Sanz, 119–153.

Pienaar, R. N. (1994). "Ultrastructure and calcification of coccolithophores," in *Coccolithophores*. Eds. A. Winter and W. G. Siesser (Cambridge, New York, Melbourne: Cambridge University Press), 63–82.

Pollard, R. T., Griffiths, M. J., Cunningham, S. A., READ, J. F., Perez, F. F., and Rios, A. F. (1996). Vivaldi 1991 - a study of the formation, circulation and ventilation of Eastern north Atlantic central water. *Prog. Oceanog.* 37, 167–192. doi: 10.1016/S0079-6611(96)00008-0

Polovina, J. J., Howell, E. A., and Abecassis, M. (2008). Ocean's least productive waters are expanding. *Geophys. Res. Lett.* 35, L03618. doi: 10.1029/2007GL031745

Poulton, A. J., Holligan, P. M., Charalampopoulou, A., and Adey, T. R. (2017). Coccolithophore ecology in the tropical and subtropical Atlantic ocean: new perspectives from the Atlantic meridional transect (AMT) programme. *Prog. Oceanogr* 158, 150–170. doi: 10.1016/j.pocean.2017.01.003

Powell, C. F., Baker, A. R., Jickells, T. D., Bange, H. W., Chance, R., and Yodle, C. (2015). Estimation of the atmospheric flux of nutrients and trace metals to the eastern tropical north Atlantic ocean. *J. Atmospheric Sci. Am. Meteorol. Soc.* 72, 4029–4045. doi: 10.1175/JAS-D-15-0011.1

Prospero, J. M., and Carlson, T. N. (1972). Vertical and areal distribution of Saharan dust over the equatorial north Atlantic ocean. *J. Geophys. Res.* 77, 5255–5265. doi: 10.1029/JC077i027p05255

Prospero, J., Collard, F.-X., Molinié, J., and Jeannot, A. (2014). Characterizing the annual cycle of African dust transport to the Caribbean basin and south America and its impact on the environment and air quality. *Global Biogeochem. Cy.* 29, 757–773. doi: 10.1002/2013GB004802

Prospero, J. M., Ginoux, P., Torres, O., Nicholson, S. E., and Thomas, T. E. (2002). Environmental characterization of global sources of atmospheric dust identified with the nimbus 7 total ozone mapping spectrometer (TOMS) absorbing aerosol product. *Rev. Geophys.* 40, 1–24. doi: 10.1029/2000RG000095

Reid, J. L. (1994). On the total geostrophic circulation of the north Atlantic ocean: flow patterns, tracers, and transports. *Prog. Oceanogr.* 33, 1–92. doi: 10.1016/0079-6611(94)90014-0

Rickli, J., Frank, M., Baker, A. R., Aciego, S., de Souza, G., Georg, R. B., et al. (2010). Hafnium and neodymium isotope distribution in surface waters of the eastern Atlantic ocean: Implications for sources and inputs of trace metals to the ocean. *Geochimica Cosmochimica Acta* 74, 540–557. doi: 10.1016/j.gca.2009.10.006

Rijkenberg, M. J. A., Steigenberger, S., Powell, C. F., van Haren, H., Patey, M. D., Baker, A. R., et al. (2012). Fluxes and distribution of dissolved iron in the eastern (sub-) tropical north Atlantic ocean. *Global Biogeochem. Cycles* 26, 1–15. doi: 10.1029/2011gb004264

Rivero-Calle, S., Gnanadesikan, A., Del Castillo, C. E., Balch, W. M., and Guikema, S. D. (2015). Multidecadal increase in north Atlantic coccolithophores and the potential role of rising CO2. *Science* 350 (6267), 1533–1537. doi: 10.1126/science.aaa8026

Rost, B., and Riebesell, U. (2004). "Coccolithophores and the biological pump: responses to environmental changes," in *Coccolithophores: From molecular processes to global impact*. Eds. H. R. Thierstein and J. R. Young (Berlin: Springer), 99–125.

Ruffault, J., Curt, T., Moron, V., Trigo, R. M., Mouillot, F., and Koutsias, N. (2020). Increased likelihood of heat-induced large wildfires in the Mediterranean basin. *Sci. Rep.* 10, 13790. doi: 10.1038/s41598-020-70069-z

Rutherford, S., D'Hondt, S., and Prell, W. (1999). Environmental controls on the geographic distribution of zooplankton diversity. *Nature* 400 (6746), 749–753. doi: 10.1038/23449

Scheuvens, D., Schütz, L., Kandler, K., Ebert, M., and Weinbruch, S. (2013). Bulk composition of northern African dust and its source sediments–a compilation. *Earth Sci. Rev.* 116, 170–194. doi: 10.1016/j.earscirev.2012.08.005

Schlosser, C., Klar, J. K., Wake, B., Snow, J., Honey, D., Woodward, E. M. S., et al. (2013). Seasonal ITCZ migration dynamically controls the location of the (sub-)tropical Atlantic biogeochemical divide. *Proc. Natl. Acad. Sci. U.S.A.* 111, 1438–1442. doi: 10.1073/pnas.1318670111

Schulz, K. G., Zondervan, I., Gerringa, L. J.A., Timmermans, K. R., Veldhuis, M. J.W., Riebesell, U., et al. (2004). Effect of trace metal availability on coccolithophorid calcification. *Nature* 430, 673–676. doi: 10.1038/nature02631

Shelley, R. U., Wyatt, N. J., Tarran, G. A., Rees, A. P., Worsfold, P. J., and Lohan, M. C. (2017). A tale of two gyres: Contrasting distributions of dissolved cobalt and iron in the Atlantic ocean during an Atlantic meridional transect (AMT-19). *Prog. Oceanogr.* 158, 52–64. doi: 10.1016/j.pocean.2016.10.013

Siefermann-Harms, D. (1985). Carotenoids in photosynthesis. i. location in photosynthetic membranes and light-harvesting function. *Biochim. Biophys. Acta* 811, 325–355. doi: 10.1016/0304-4173(85)90006-0

Signorini, S. R., Franz, B. A., and McClain, C. R. (2015). Chlorophyll variability in the oligotrophic gyres: mechanisms, seasonality and trends. *Front. Mar. Sci.* 2. doi: 10.3389/fmars.2015.00001

Signorini, S. R., Murtugudde, R. G., McClain, C. R., Christian, J. R., Picaut, J., and Busalacchi, A. J. (1999). Biological and physical signatures in the tropical and subtropical Atlantic. *J. Geophys. Res.: Oceans* 104, 18367–18382. doi: 10.1029/1999JC900134

Skonieczny, C., Bory, A., Bout-Roumazeilles, V., Abouchami, W., Galer, S. J. G., Crosta, X., et al. (2013). A three-year time series of mineral dust deposits on the West African margin: Sedimentological and geochemical signatures and implications for interpretation of marine paleo-dust records. *Earth Planetary Sci. Lett.* 364, 145–156. doi: 10.1016/j.epsl.2012.12.039

Souza, M. S., Mendes, C. R. B., Garcia, V. M., Pollery, R., and Brotas, V. (2011). Phytoplankton community during a coccolithophorid bloom in the Patagonian shelf: Microscopic and high-performance liquid chromatography pigment analyses. *J. Mar. Biol. Assoc. United Kingdom* 106 (92), 1–15. doi: 10.1017/S0025315411000439

Sprengel, C., Baumann, K.-H., Henderiks, J., Henrich, R., and Neuer, S. (2002). Modern coccolithophore and carbonate sedimentation along a productivity gradient in the canary islands region: Seasonal export production and surface accumulation rates. *Deep-Sea Res. II* 49, 3577–3598. doi: 10.1016/S0967-0645(02)00099-1

Stoll, H. M., Arevalos, A., Burke, A., Ziveri, P., Mortyn, G., Shimizu, N., et al. (2007). Seasonal cycles in biogenic production and export in northern bay of Bengal sediment traps. *Deep-Sea Res. II* 54, 558–580. doi: 10.1016/j.dsr2.2007.01.002

Stramma, L., and England, M. (1999). On the water masses and mean circulation of the south Atlantic ocean. *J. Geophys. Res.* 104, 20863–20883. doi: 10.1029/1999JC900139

Stuut, J. B., Zabel, M., Ratmeyer, V., Helmke, P., Schefuss, E., Lavik, G., et al. (2005). Provenance of present-day eolian dust collected off NW Africa. *J. Geophys. Res.* 110, 1–14. doi: 10.1029/2004JD005161

Tarran, G. (2018). "AMT 28 cruise report," in *RRS James Clark Ross (JR18-001)* (Plymouth Marine Laboratory: Plimouth Marine Laboratory), 183. 23 September – 29 October 2018.

Tarran, G. A., Heywood, J. L., and Zubkov, M. V. (2006). Latitudinal changes in the standing stocks of nano- and picoeukaryotic phytoplankton in the Atlantic ocean. *Deep Sea Res. II Top. Stud. Oceanogr.* 53, 1516–1529. doi: 10.1016/j.dsr2.2006.05.004

Thomas, M. K., Kremer, C. T., Klausmeier, C. A., and Litchman, E. (2012). A global pattern of thermal adaptation in marine phytoplankton. *Science* 338, 1085. doi: 10.1126/science.1224836

Thomsen, H. A., Ostergaard, J. B., and Hansen, L. E. (1991). Heteromorphic life histories in Arctic coccolithophorids (Prymnesiophyceae). *J. Phycol.* 27, 634–642. doi: 10.1111/j.0022-3646.1991.00634.x

Tsamalis, C., Chedin, A., Pelon, J., and Capelle, V. (2013). The seasonal vertical distribution of the Saharan air layer and its modulation by the wind. *Atmospheric Chem. Phys.* 13 (22), 11,235–11,257. doi: 10.5194/acp-13-11235-2013

Tuomisto, H. (2013). Defining, measuring, and partitioning species diversity. *Encycloped. Biodivers.* 2, 434–446. doi: 10.1016/B978-0-12-384719-5.00378-6

Turco, M., Jerez, S., Augusto, S., Tarín-Carrasco, P., Ratola, N., Jiménez-Guerrero, J., et al. (2019). Climate drivers of the 2017 devastating fires in Portugal. *Sci. Rep.* 9 (13886), 1–8. doi: 10.1038/s41598-019-50281-2

Tyrrell, T., Marañón, E., Poulton, A. J., Bowie, A. R., Harbour, D. S., and Woodward, E. M. S. (2003). Large-Scale latitudinal distribution of trichodesmium spp. in the Atlantic ocean. *J. Plankton Res.* 25, 405–416. doi: 10.1093/plankt/25.4.405

Ussher, S. J., Achterberg, E. P., Powell, C., Baker, A. R., Jickells, T. D., Torres, R., et al. (2013). Impact of atmospheric deposition on the contrasting iron biogeochemistry of the north and south Atlantic ocean, global biogeochem. *Cycles* 27, 1096–1107. doi: 10.1002/gbc.20056

Utermöhl, H. (1958). Zur vervolkommung der quantitativen phytoplankton: methodik. mitteilungen internationale vereinigung für theoretische und angewandte. *Limnologie* 9, 1–38. doi: 10.1080/05384680.1958.11904091

van der Does, M., Brummer, G.-J. A., Korte, L. F., and Stuut, J.-B. W. (2021). Seasonality in Saharan dust across the Atlantic ocean: From atmospheric transport to seafloor deposition. *J. Geophys. Res.: Atmospheres* 126 (11), e2021JD034614. doi: 10.1029/2021JD034614

van der Does, M., Brummer, G.-J. A., van Crimpen, F. C. J., Korte, L. F., Mahowald, N. M., Merkel, U., et al. (2020). Tropical rains controlling deposition of Saharan dust across the north Atlantic ocean. *Geophys. Res. Lett.* 47 (5), e2019GL086867. doi: 10.1029/2019GL086867

van der Does, M., Pourmand, A., Sharifi, A., and Stuut, J.-B. W. (2018). North African mineral dust across the tropical Atlantic ocean: Insights from dust particle size, radiogenic Sr-Nd-Hf isotopes and rare earth elements (REE). *Aeolian Res.* 33, 106–116. doi: 10.1016/j.aeolia.2018.06.001

van der Jagt, H., Friese, C., Stuut, J.-B. W., Fischer, G., and Iversen, M. H. (2018). The ballasting effect of Saharan dust deposition on aggregate dynamics and carbon export: aggregation, settling, and scavenging potential of marine snow. *Limnol. Oceanogr.* 106 (63), 3–9. doi: 10.1002/lno.10779

Van Lenning, K., Probert, I., Latasa, M., Estrada, M., and Young, J. (2004). "Pigment diversity of coccolithophores in relation to taxonomy, phylogeny, and ecological preferences," in *Coccolithophores: From molecular processes to global impact*. Eds. H. R. Thierstein and J. R. Young (Berlin: Springer), 51–73.

Winter, A., Henderiks, J., Beaufort, L., Rickaby, R., and Brown, C. (2013). Poleward expansion of the coccolithophore emiliania huxleyi. *J. Plankton Res.* 36 (2), 1–10. doi: 10.1093/plankt/fbt110

Winter, A., Jordan, R., and Roth, P. (1994). "Biogeography of living coccolithophores in ocean waters," in *Coccolithophores*. Eds. A. Winter and W. Siesser (Cambridge, New York, Melbourne: Cambridge Univ. Press), 161–177.

Worden, A. Z., Follows, M. J., Giovannoni, S. J., Wilken, S., Zimmerman, A. E., and Keeling, P. J. (2015). Rethinking the marine carbon cycle: Factoring in the multifarious lifestyles of microbes. *Science* 347, 1257594. doi: 10.1126/science.1257594

Wright, S. W., and Jeffrey, S. W. (2006). "Pigment markers for phytoplankton production," in *Hdb env chem 2, part n*, 71–104.

Yodle, C., and Baker, A. R. (2019). Influence of collection substrate and extraction method on the speciation of soluble iodine in atmospheric aerosols. *Atmospheric Environment: X* 1, 100009. doi: 10.1016/j.aeaoa.2019.100009

Young, J. (1994). *Functions of coccoliths* (Cambridge: Cambridge Univ. Press), 63–82.

Young, J. R., Bown, P. R., and Lees, J. A. (2011). Nannotax website. international observations. *Prog. Oceanogr.* 26, 357–402.

Yu, H., Tan, Q., Chin, M., Remer, L. A., Kahn, R. A., Bian, H., et al. (2019). Estimates of African dust deposition along the trans-Atlantic transit using the decadelong record of aerosol measurements from CALIOP, MODIS, MISR, and IASI. *J. Geophys. Res.: Atmospheres* 124, 7975–7996. doi: 10.1029/2019JD030574

Zapata, M., Jeffrey, S. W., Wright, S. W., Rodríguez, F., Garrido, J. L., and Clementson, L. (2004). Photosynthetic pigments in 37 species (65 strains) of haptophyta: Implications for oceanography and chemotaxonomy. *Mar. Ecol. Prog. Ser.* 270, 83–102. doi: 10.3354/meps270083

Zapata, M., Rodriguez, F., and Garrido, J. L. (2000). Separation of chlorophylls and carotenoids from 1 marine phytoplankton: A new HPLC method using a reversed phase C8 column and pyridine-2 containing mobile phases. *Mar. Ecol. Prog.* 195, 29–45. doi: 10.3354/meps195029

Ziveri, P., de Bernardi, B., Baumann, K.-H., Stoll, H. M., and Mortyn, P. G. (2007). Sinking of coccolith carbonate and potential contribution to organic carbon ballasting in the deep ocean. *Deep-Sea Res. II* 54, 659–675. doi: 10.1016/j.dsr2.2007.01.006

Appendix A

List of taxa identified by Light- and Scanning Electron Microscopy. Holococcolithophores (HOL) indicated in bold italics.

Acantoica acanthos
Acantoica quattrospina
Algirosphaera robusta
Alisphaera spp.
Alisphaera unicornis
Anacanthoica cidaris
Braarudosphaera bigelowii
Calcidiscus leptoporus
Calcidiscus leptoporus ssp. _quadriperforatus_ HOL
Calciosolenia brasiliensis
Calciosolenia corsellii
Calciosolenia murrayi
Calyptrolithophora papillifera HOL
Calyptrosphaera cialdii HOL
Calyptrosphaera dentata HOL
Ceratolithus cristatus HET coccolithomorpha type
Cocccolithus pelagicus
Corisphaera sp. HOL
Coronosphaera binodata
Coronosphaera maxima
Coronosphaera mediterranea
Coronosphaera mediterranea HOL _hellenica_ type
Coronosphaera sp. Y
Cyrtosphaera cf. *aculeata*
Discosphaera tubifera
Emiliania huxleyi type B
Emiliania huxleyi type O
Emiliania huxleyi var. *corona*
Florisphaera profunda
Gephyrocapsa ericsonii
Gephyrocapsa muellerae
Gephyrocapsa oceanica
Gephyrocapsa ornata
Gephyrocapsa parvula
Gladiolithus flabellatus
Gliscolithus amitakareniae HOL
Hayaster perplexus
Helicosphaera carteri
Helicosphaera carteri HOL solid _("Syracolithus catilliferus")_
Helicosphaera HOL _catilliferus_ type
Helicosphaera hyalina
Helicosphaera wallichii
Helladosphaera cornifera HOL
Helladosphaera pienarii I HOL
Homozygosphaera spinosa HOL
Homozygosphaera triarcha HOL
Michaelsarsia adriaticus
Michaelsarsia elegans
Oolitothus antillarum
Oolitothus fragilis
Ophiaster formosus
Ophiaster hydroideus
Ophiaster reductus
Palusphaera probertii
Palusphaera vandelii
Papposphaera lepida
Polycrater sp.
Pontosphaera japonica
Pontosphaera multipora
Pontosphaera spp.
Poricalyptra isselii HOL
Poricalyptra magnaghii HOL
Poritectolithus maximus HOL
Rabdosphaera clavigera
Rabdosphaera stylifera
Rabdosphaera xiphos
Reticulofenestra sessilis
Scyphosphaera apsteinii
Syracolithus sp. type A HOL
Syracosphaera mediterranea HOL _wettsteinii_ type
Syracosphaera anthos
Syracosphaera anthos HOL _("Periphyllophora mirabilis"_
Syracosphaera aurisinae HOL
Syracosphaera bannockii
Syracosphaera bannockii HOL
Syracosphaera corolla (coccoliths)
Syracosphaera dilatata
Syracosphaera gaarderae
Syracosphaera gaarderae HOL
Syracosphaera halldalii
Syracosphaera histrica
Syracosphaera lamina
Syracosphaera mediterraea HOL _gracillima_ type
Syracosphaera mediterranea HOL _hellenica_ type
Syracosphaera molischii
Syracosphaera molischii type 3
Syracosphaera nana
Syracosphaera nodosa
Syracosphaera noroitica
Syracosphaera operculata
Syracosphaera ossa type 1BCs
Syracosphaera pirus
Syracosphaera prolongata
Syracosphaera protrudens
Syracosphaera pulchra
Syracosphaera pulchra HOL _oblonga_
Syracosphaera pulchra HOL _pirus_
Syracosphaera reniformis
Syracosphaera rotula
Syracosphaera sp. (C-D)
Syracosphaera sp. aff. *S. nodosa*
Syracosphaera sp. aff. to *S. orbiculus* (image B)
Syracosphaera sp. type J
Syracosphaera spp.
Syracosphaera tumularis
Turrilithus latericioides
Umbelosphaera irregularis

Umbelosphaera tenuis
Umbilicosphaera anulus
Umbilicosphaera foliosa
Umbilicosphaera hulburtiana
Umbilicosphaera sibogae
Zygosphaera amoena **HOL**
Zygosphaera **cf.** ***marsilii*** **HOL**
Zygosphaera marsilii **HOL**

Frontiers in Marine Science

TYPE Original Research
PUBLISHED 11 July 2023
DOI 10.3389/fmars.2023.1191216

OPEN ACCESS

EDITED BY
Takafumi Hirata,
Hokkaido University, Japan

REVIEWED BY
James Fox,
Oregon State University, United States
Anne W. Thompson,
Portland State University, United States

*CORRESPONDENCE
Timothy Smyth
✉ tjsm@pml.ac.uk

RECEIVED 21 March 2023
ACCEPTED 26 June 2023
PUBLISHED 11 July 2023

CITATION
Smyth T, Moffat D, Tarran G, Sathyendranath S, Ribalet F and Casey J (2023) Determining drivers of phytoplankton carbon to chlorophyll ratio at Atlantic Basin scale. *Front. Mar. Sci.* 10:1191216. doi: 10.3389/fmars.2023.1191216

Determining drivers of phytoplankton carbon to chlorophyll ratio at Atlantic Basin scale

Timothy Smyth[1]*, David Moffat[1], Glen Tarran[1], Shubha Sathyendranath[1], Francois Ribalet[2] and John Casey[4,5]

[1]Plymouth Marine Laboratory, Prospect Place, Plymouth, Devon, United Kingdom, [2]School of Oceanography, Center for Environmental Genomics, University of Washington, Seattle, WA, United States, [3]Department of Earth, Atmosphere and Planetary Sciences, Massachusetts Institute of Technology, Cambridge, MA, United States, [4]Daniel K. Inouye Center for Microbial Oceanography, School of Ocean and Earth Science and Technology, University of Hawaiʻi, Mānoa, Honolulu, HI, United States, [5]Lawrence Livermore National Laboratory, Bioscience and Biotechnology Division, Livermore, CA, United States

We demonstrate the ability of flow cytometry to determine species specific cellular carbon and chlorophyll content *in vivo* by using laboratory cultures of phytoplankton encompassing a wide range of cell sizes. When applied to the large Atlantic Meridional Transect flow cytometry dataset, we reveal patterns in the species-specific phytoplankton carbon (C), chlorophyll (Chl) and C:Chl ratio. For *Prochlorococcus* the range of C:Chl is between 2 – 604; for *Synechococcus* 0.5 – 558. Using a Random Forest machine learning approach, we show that predictability of phytoplankton C:Chl, dominated by the prevalence of *Prochlorococcus*, is largely driven by silicate and nitrite concentration in the Atlantic Ocean.

KEYWORDS

flow cytometry, carbon, chlorophyll, machine learning, random forests, Atlantic Ocean, phytoplankton, physiology

Introduction

The ocean's soft tissue carbon pump (Volk and Hoffert, 1985) removes atmospheric CO_2 through particle sinking and is governed by the balance of photosynthesis and respiration, abiotic factors such as temperature (Geider, 1987), and biogeochemical factors such as elemental stoichiometry (Collos et al., 1999). The phytoplankton carbon-to-chlorophyll-a ratio (C:Chl) is a key parameter determining photosynthetic rate (Jassby and Platt, 1976) and is widely applied in biogeochemical modeling (Behrenfeld et al., 2005) and for the quantification of phytoplankton biomass (Riemann et al., 1989; Jakobsen and Markager, 2016).

Plankton cellular C content is closely related to cell volume (Menden-Deuer and Lessard, 2000) and is therefore likely to be strongly correlated with a cell's light scattering characteristics. Phytoplankton cells are of a size (0.5 – 20 µm) relative to visible light (400 – 700 nm) which means they scatter in the Mie regime (Mie, 1908); the scattering phase function (i.e., the directionality of the scattered photons) is determined by the cell's size and refractive index (e.g., Bohren and Huffman (1983)). Flow cytometry is a proven tool in marine biology for discriminating and enumerating the smallest phytoplankton cells based on their light (forward and side) scattering and fluorescence (red, orange, green) signatures (Tarran et al., 2006) and has been previously used to determine cell size and refractive index (Ackleson and Spinrad, 1988; Green et al., 2003; Agagliate et al., 2018; Smyth et al., 2019), as well as C quotas (Garrison et al., 2000; DuRand et al., 2001; Shalapyonok et al., 2001; Landry and Kirchman, 2002; Worden et al., 2004; Grob et al., 2007; Casey et al., 2013).

In this paper laboratory phytoplankton cultures were used to estimate C quotas based on forward scatter, and chlorophyll based on side scatter. These laboratory derived relationships were then applied to a large flow cytometry time-series dataset (Smyth et al., 2019) constructed using multiple expeditions of the Atlantic Meridional Transect (AMT) (Rees et al., 2017). The nature of the AMT long-term time-series of expeditions (Rees et al., 2017) ensures that there are multiple sources of contextual (or meta) data available for each transect (Smyth et al., 2017) across multiple ocean provinces (Longhurst et al., 1995).

This work makes the following significant advances in that it:

(1) Reveals a robust relationship between flow-cytometrically measured forward scatter and phytoplankton cellular C content which is replicated on multiple instruments and is log-linear across two orders of magnitude in scatter and five orders of magnitude in C content, i.e., across several phytoplankton size classes.

(2) Reveals a similarly robust relationship between flow-cytometrically measured side scatter and phytoplankton (normalized) fluorescence (nFl) which is replicated on multiple instruments and is log-linear across four orders of magnitude in scatter and four orders of magnitude in nFl.

(3) Quantifies the depth resolved C and Chl content of different phytoplankton populations over multiple AMT expeditions throughout the length of the Atlantic Basin, over multiple ocean provinces.

(4) Determines the dominant drivers of C:Chl through the multiple Atlantic Ocean provinces using Machine Learning approaches.

Materials and methods

Flow cytometry measures the light scatter (forward and side) and fluorescence characteristics of a population of cells or particles on an individual basis by injecting fluid (seawater)-suspended samples, ideally flowing one cell at a time, through a laser beam. A combination of fluorescence (typically: green, orange and red) and side scatter properties are used to further classify the phytoplankton cells into different types and hence enumerate abundances (Tarran et al., 2006). Previous work (Ackleson and Spinrad, 1988; Green et al., 2003; Agagliate et al., 2018; Smyth et al., 2019) has shown that well characterized instruments can determine the size and refractive index of individual phytoplankton cells and populations by measuring their differential forward ($dC_{sca}/d\Omega_3$) and side ($dC_{sca}/d\Omega_4$) scatter (Bohren and Huffman, 1983) using equations for a detector i of form:

$$(dC_{sca}/d\Omega_i)_p = \frac{S(i)_p I(i)_r G(i)_r}{S(i)_r I(i)_p G(i)_p}(dC_{sca}/d\Omega_i)_r \tag{1}$$

where $S(i)$ is channel value, $I(i)$ laser intensity, $G(i)$ the detector gain, subscript r is a reference particle of known size and refractive index, for each particle p (here phytoplankton cell) of interest. In this work we relate $dC_{sca}/d\Omega_3$ and $dC_{sca}/d\Omega_4$ to cellular carbon and chlorophyll content.

Laboratory cultures

Average cellular carbon quotas (Ribalet et al., 2019) were determined for six axenic, exponentially growing cyanobacteria cultures (*Prochlorococcus* MED4, MIT9312, AS9601 and NATL12A, *Synechococcus* WH7803 and WH8012) and four different eukaryotic phytoplankton cultures (*Micromonas pusilla*, *Navicula transitans*, *T. pseudonana* 3367 and 1135) (Table 1). Cells were grown under continuous light (150 µmol quanta m^{-2} s^{-1}) in nutrient replete media (Pro99 (Moore et al., 2007) and F/2 media (Guillard et al., 1975) for cyanobacteria and eukaryote species, respectively) and harvested during late exponential phase. Cells were filtered onto pre-combusted 0.3 µm GF-75 or 0.7 µm GF/F filters and analyzed on a Carlo Erba CHNS analyzer (model NA1500) in the Oregon State University Stable Isotope Laboratory using cystine (29.99% carbon and 11.66% nitrogen by weight) as an analytical standard. For each culture, aliquots of growth media filtered through three pre-combusted GF-75 and GF/F glass fiber filters were used as blanks to correct for background carbon concentration on filters before filtration and DOC adsorption onto filters. Carbon quotas were obtained by normalizing the concentrations of blank-corrected particulate carbon to cell abundance measured with a BD Influx cell sorter (Ribalet et al., 2019).

nFl was estimated using the log amplified median values of red fluorescence measured by flow cytometry (692 ± 40 nm band-pass filter), normalized to the median values of log amplified 1 µm calibration beads (Invitrogen F8823). Regression analyses were performed between forward scattering and cellular carbon content and between side scattering and nFl (Table 2).

The samples were then preserved (0.25% Glutaraldehyde, 0.01% Pluronic F68 final concentrations (Marie et al., 2014)) and transported to the Plymouth Marine Laboratory so that an independent analysis of flow cytometer scattering could be carried out, and to test for the applicability and subsequent transferability of our methodology.

TABLE 1 Phytoplankton cultures used to derive scattering relationships shown in Figure 1.

Legend name (Figure 1)	Group	Species/genus	Strain
MICRO	Prasinophyte	*Micromonas pusilla*	unknown
EHUX	Prymnesiophyte	*Emiliania huxleyi*	CCMP1742
NAV	Diatom	*Navicula transitans*	RCC80
PT632A	Diatom	*Phaeodactylum tricornutum*	CCMP632
PT632B	Diatom	*Phaeodactylum tricornutum*	CCMP632
TAPS1335	Diatom	*Thalassiosira pseudonana*	CCMP1335
TAPS3367	Diatom	*Thalassiosira pseudonana*	CCMP3367
TW3365	Diatom	*Thalassiosira weissflogii*	CCMP3365
WH8102	Cyanobacteria	*Synechococcus* sp.	WH8102
WH7803	Cyanobacteria	*Synechococcus* sp.	WH7803
MED4	Cyanobacteria	*Prochlorococcus marinus* (HL-I)	MED4
MIT9312	Cyanobacteria	*Prochlorococcus marinus* (HL-II)	MIT9312
AS9601	Cyanobacteria	*Prochlorococcus marinus* (HL-II)	AS9601
NATL2A	Cyanobacteria	*Prochlorococcus marinus* (LL-I)	NATL2A

Light adaptation given for Prochlorococcus as high light (HL) and low light (LL), sub-divided into ecotypes (I, II) (Rocap et al., 2002).

In situ AMT samples

Two Becton Dickinson FACSort$^{\text{TM}}$ flow cytometers (serial numbers B0264 and B0043), with identical optical geometries, were used to enumerate depth-resolved vertical profiles of pico- and nano-phytoplankton for multiple AMT expeditions (AMT18 – 29). The individual samples were collected from Niskin bottles attached to an oceanographic rosette sampler into clean 250 mL polycarbonate bottles (Nalge Nunc International, USA) at multiple depths between the surface and 200 m. These were then stored at 4°C in the dark and analysed within two hours of sample collection. Samples were analysed at flow rates calibrated daily using Beckman Coulter$^{\text{TM}}$ Flowset$^{\text{TM}}$ fluorospheres (polystyrene) of known concentration, prior to the analysis of seawater samples. The polystyrene beads of known refractive index, used within the flow rate calibration, are critical for maintaining the consistency of the FACS forward and side scattering calibration and give the reference values (subscript *r* terms) necessary to implement Equation 1.

The FACS uses an air-cooled argon-ion 15 mW laser (488 nm) light source with detectors arranged to measure forward scatter (ψ_{S3}= ± 1.5-12.2°) and side scatter (ψ_{S4} = 64-116°); red (>650 nm; note the slightly different but overlapping (692 ± 42 nm) configuration to the laboratory culture flow cytometer) and orange (585 ± 21 nm) fluorescence. For individual samples, cluster analyses were carried out (Smyth et al., 2019) to enumerate abundance and mean values of $dC_{sca}/d\Omega_3$ and $dC_{sca}/d\Omega_4$. Using differential scatter (side and forward) calibrated against polystyrene beads, enables correction for any change in gain settings the individual flow cytometer operator may have used, for example to enhance manually gated species identification, and ensures continuity between multiple expeditions. The main phytoplankton types analysed were *Prochlorococcus* and

TABLE 2 Regression statistics for five flow cytometers using the laboratory cultures shown in Table 1 and Figure 2 in $\log_{10}$ space to use with equation of form $10^c(dC_{sca}/d\Omega_n)^m$ or $10^c(FS)^m$.

Instrument	c	m	R^2	N	Parameter	Property
PML B0043	-6.926	2.512	0.864	14	$dC_{sca}/d\Omega_3$	C
PML B0043	2.292	1.271	0.741	15	$dC_{sca}/d\Omega_4$ [a]	Chl
PML B0264	-5.819	2.223	0.900	21	$dC_{sca}/d\Omega_3$ [a]	C
PML B0264	1.980	1.010	0.935	21	$dC_{sca}/d\Omega_4$ [a]	Chl
PML Influx	-5.614	2.460	0.833	15	FS	C
PML Accuri C6	-6.777	1.420	0.927	15	FS[b]	C
UW Influx	0.655	1.368	0.925	15	FS[b]	C

N is the number of cultures used in the regression statistics.

[a] Referenced to polystyrene beads.

[b] Forward Scatter. Raw data output from flow cytometer.

Synechococcus; a generic *Other* phytoplankton type was also enumerated (see Smyth et al. (2019) and Tarran et al. (2006) for details). On the AMT expedition, the FACS operator typically analyses samples using two gain settings: Pico and Nano [see Table 1, Smyth et al. (2019)]. The Pico setting is used for detecting the smallest phytoplankton sizes (*Prochlorococcus* and *Synechococcus*; typically 0.5 – 2 µm) whereas the Nano for slightly larger sizes (> 2 µm; *Other*). The Pico gain setting is an order of magnitude higher (1 cf. 0.1) than Nano, and also the photomultiplier tube voltages are higher. The regressions determined for the laboratory cultured cells were then applied to the large (33 k samples) AMT FACS dataset.

For each discrete *in situ* sample the weight of carbon and the concentration of chlorophyll attributable to *Prochlorococcus*, *Synechococcus* and *Other* was calculated using the five stages shown schematically in Figure 2. Stage 1: the cluster analyses described in Smyth et al. (2019) were used to group the phytoplankton into *Prochlorococcus* (*Pro.*), *Synechococcus* (*Syn.*) and *Other* (*Oth.*) populations, the results of which (Stage 2) gave a triplet of measurements for abundance (N), mean $dC_{sca}/d\Omega_3$ and mean $dC_{sca}/d\Omega_4$. Stage 3: the flow cytometer dependent statistical fits to the logarithmic regressions for cultured cells (Figure 1; Table 2) were applied to the mean $dC_{sca}/d\Omega_3$ and mean $dC_{sca}/d\Omega_4$ to determine the weight of carbon per cell (pgC $cell^{-1}$) and nFl respectively. The total weight of carbon for each type was calculated using the abundance (cells m^{-3}) multiplied by the weight of carbon per cell to give mgC m^{-3} for C_{pro}, C_{syn} and C_{oth}. For chlorophyll, two further stages were required. Stage 4: weighting functions for abundance and normalized fluorescence were constructed based on the percentage contribution to the whole for both those parameters for each type. Stage 5: the two weighting functions were multiplied together and then multiplied by the coincidentally measured (using the rosette sampler) fluorometrically derived chlorophyll concentration (Welschmeyer, 1994) for each type. This resulted in Chl_{pro}, Chl_{syn} and Chl_{oth} in units of mgChl m^{-3}.

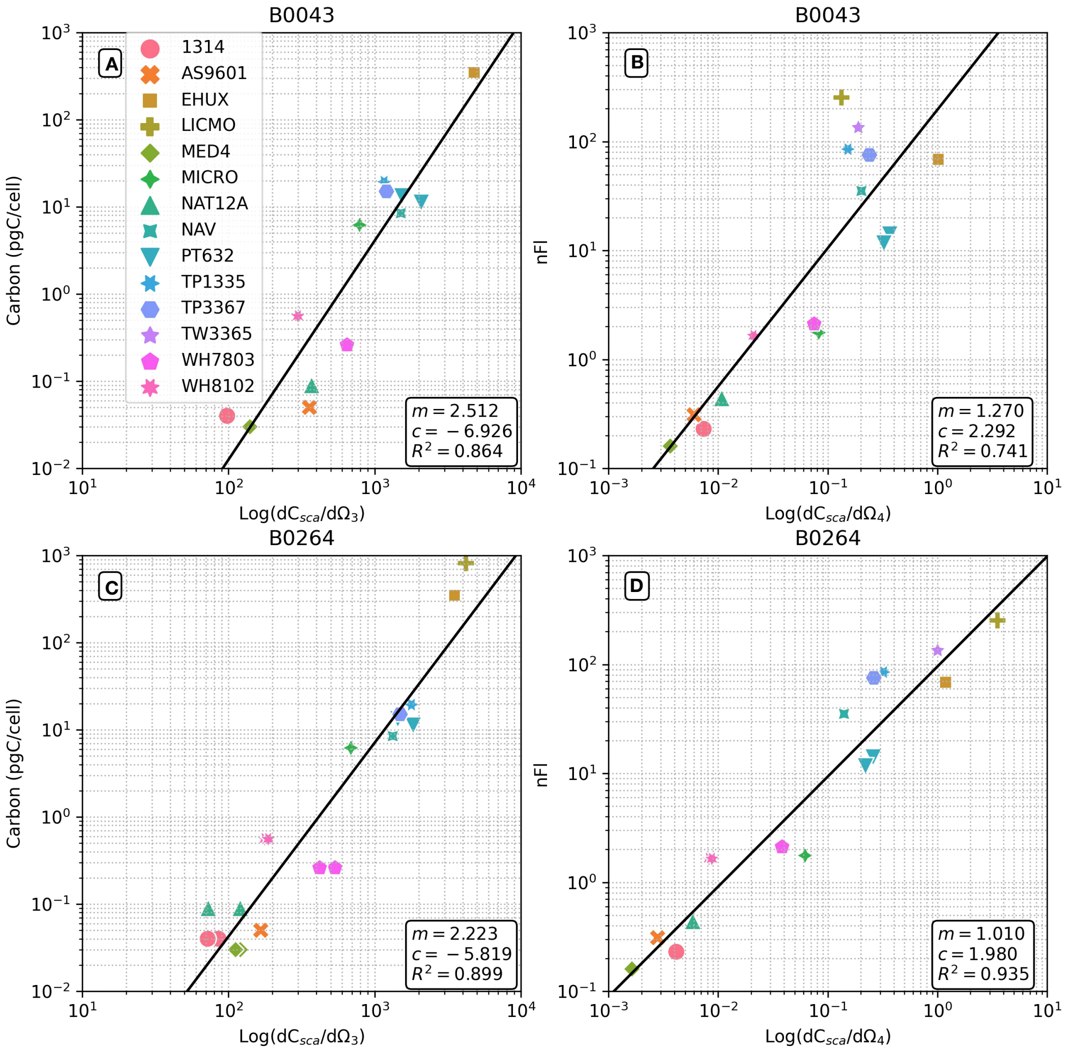

FIGURE 1

Flow cytometrically derived relationships between differential forward scatter and cellular carbon weight **(A, C)** and differential side scatter and normalized fluorescence **(B, D)** for a range of phytoplankton cells (see Table 1). Results for two Becton Dickinson FACSort^{TM} flow cytometers shown: **(A, B)** serial #B0043; **(C, D)** serial #B0264. Regression statistics shown are in $\log_{10}$ space to use with equation of form $10^c(dC_{sca}/d\Omega_n)^m$.

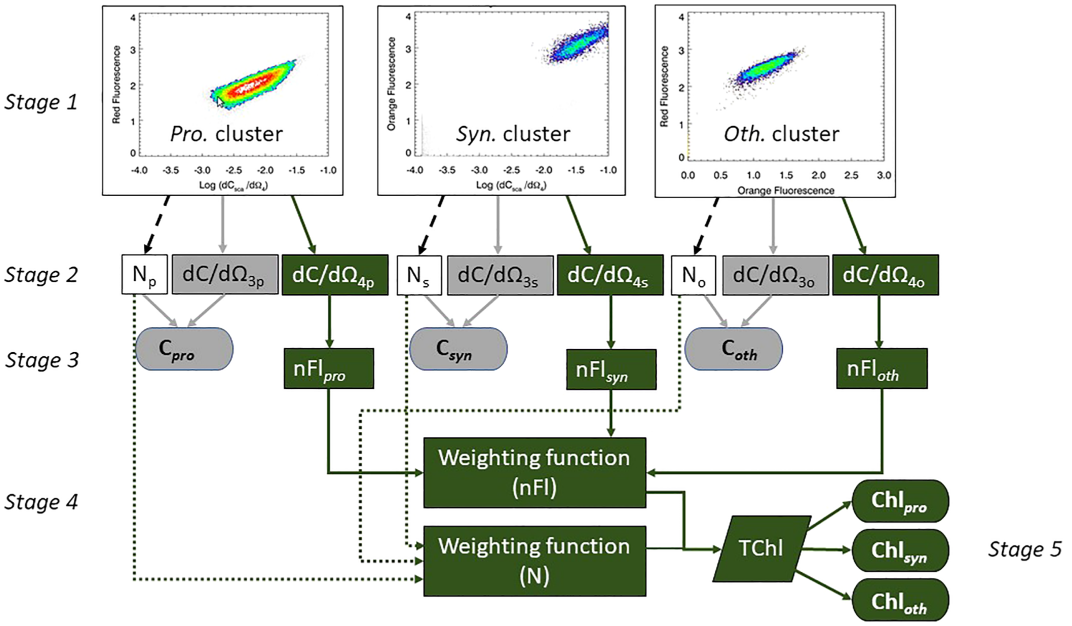

FIGURE 2
Stage 1 – cluster analyses with warmer colors showing higher density of points. Stages 2 – 4: Determination of Carbon (elements in grey) and Chlorophyll (elements in green) concentrations attributable to the different phytoplankton types, using a three and five stage process respectively.

Strict data filtering criteria were then applied to the resultant dataset for use within the Machine Learning (ML) analysis. This included: removing data points where agreement between the automatically clustered and manually gated abundances for individual species were not within 30% of each other; any instances of NaN in the FACS or ancillary datasets (e.g., nutrients); where the species-specific chlorophyll was ≤ 0.05 mg m^{-3} or ≤ 25% of the total chlorophyll concentration and minimization of the variability of the $dC_{sca}/d\Omega_3$ in the sample. The latter was set to ±400 $m^2\ sr^{-1}$ for *Prochlorococcus*; ± 800 $m^2\ sr^{-1}$ for *Synechococcus* and ±1000 $m^2\ sr^{-1}$ for the Nano setting species. This resulted in 1066 *Prochlorococcus*, 198 *Synechococcus* and 73 Nano (*Other*) samples. Table 3 shows a basic C:Chl statistical analysis of the filtered dataset based on the above criteria.

Machine learning analyses

A Random Forest (RF) machine learning approach (Breiman, 2001) was used in order to gain an understanding of the environmental factors which influence phytoplankton carbon and chlorophyll. RF is an ensemble learning method for growing decision trees using subsets of the training data, known as bootstrap aggregation. The data were collected, and several predictor variables identified. The possible predictors identified from across the nine different AMT cruises were: Latitude, Depth, Temperature, Salinity, Oxygen, Nitrite, Nitrate, Phosphate, Silicate, and Species (*Prochlorococcus, Synechococcus* etc.). (Although Irradiance would be an obvious choice as a predictor variable, the dataset is dominated by pre-dawn samples, which subsequently precluded its use). The input variables were then standardized to scale each variable to a zero mean and unit variance, except the species information, as this is a categorical variable, encoded as a number. The data were then randomly separated into a training (70%) and a test (30%) data subset stratified across the nine AMT expeditions. This resulted in the training set being 1079 data samples, and test set as 463 data samples.

The RF model was then trained to predict phytoplankton C:Chl. A model was first trained to make the prediction based on all combined data, where phytoplankton species was included as a predictor variable. Then, further models were trained to make predictions on the individual northern and southern Atlantic

TABLE 3 Statistical analysis for the filtered C:Chl dataset.

Species	N	C:Chl			
		min	max	mean	median
Prochlorococcus	1066	2.5	604.5	77.1	46.9
Synechococcus	198	0.5	557.8	138.5	98.8
Nano (Other)	73	0.8	863.6	50.2	25.3

N is the number of samples used.

gyres (see e.g., Smyth et al. (2017)) defined by their Longhurst province (Longhurst et al., 1995). The northern gyre is defined as the regions North Atlantic Subtropical - West (NASW), North Atlantic Subtropical - East (NASE) and North Atlantic Trades (NATR). The southern gyre is defined as region South Atlantic Trades gyraL (SATL). Test and training data set separation was performed using the exact same process for the separate northern gyre (training: 255; test: 110) and southern gyre (training: 394; test: 170) regions. This left 613 samples not included within either gyral region.

A SHAP (Shapley Additive exPlanations) analysis (Lundberg and Lee, 2017) was performed on the RF predictors. SHAP analysis compensates for any collinearity of multiple variables by using a game theory approach to variable analysis (Lundberg and Lee, 2017). SHAP analysis manages the interdependence and correlations of variables, thereby producing an insightful variable importance metric. SHAP analysis enables a value to be assigned to each variable (i.e. Latitude, Depth, Temperature, Salinity, Oxygen, Nitrite, Nitrate, Phosphate, Silicate, and Species) which indicates how much that variable will change the output predicted (i.e., C:Chl) value. Positive SHAP values indicate an increase in the C:Chl ratio, and vice versa; a SHAP value of zero means no impact on the predicted C:Chl ratio. A ranking by SHAP value allows a better insight into which environmental variables are the drivers for the C:Chl ratio.

Results

Laboratory culture determined C and nFl

Figure 1 shows that there are strong relationships ($R^2 = 0.864$ and 0.899 for B0043 and B0264 respectively) between cellular carbon content and $dC_{sca}/d\Omega_3$ for different cultures over five and two orders of magnitude respectively for two different flow cytometers (Figures 1A, C). Similarly, robust relationships ($R^2 = 0.741$ and 0.935 for B0043 and B0264 respectively) were found between cellular nFl and $dC_{sca}/d\Omega_4$ for different cultures over four orders of magnitude in both axes (Figures 1B, D). Table 2 shows that for three other flow cytometers, similar robust ($R^2 > 0.8$) relationships hold between the FACS measured forward scatter and cellular carbon content.

AMT field determined C:Chl

Figure 3 shows the physical (Figures 3A, B) and biogeochemical (Figures 3C–F) conditions throughout all the AMT (18 – 29) transects (50°N – 50°S) over the depths 0 – 200 m. The major features of the AMT transect are the northern and southern gyre regions, characterized by warm (> 25°C), high salinity (>37 PSU)

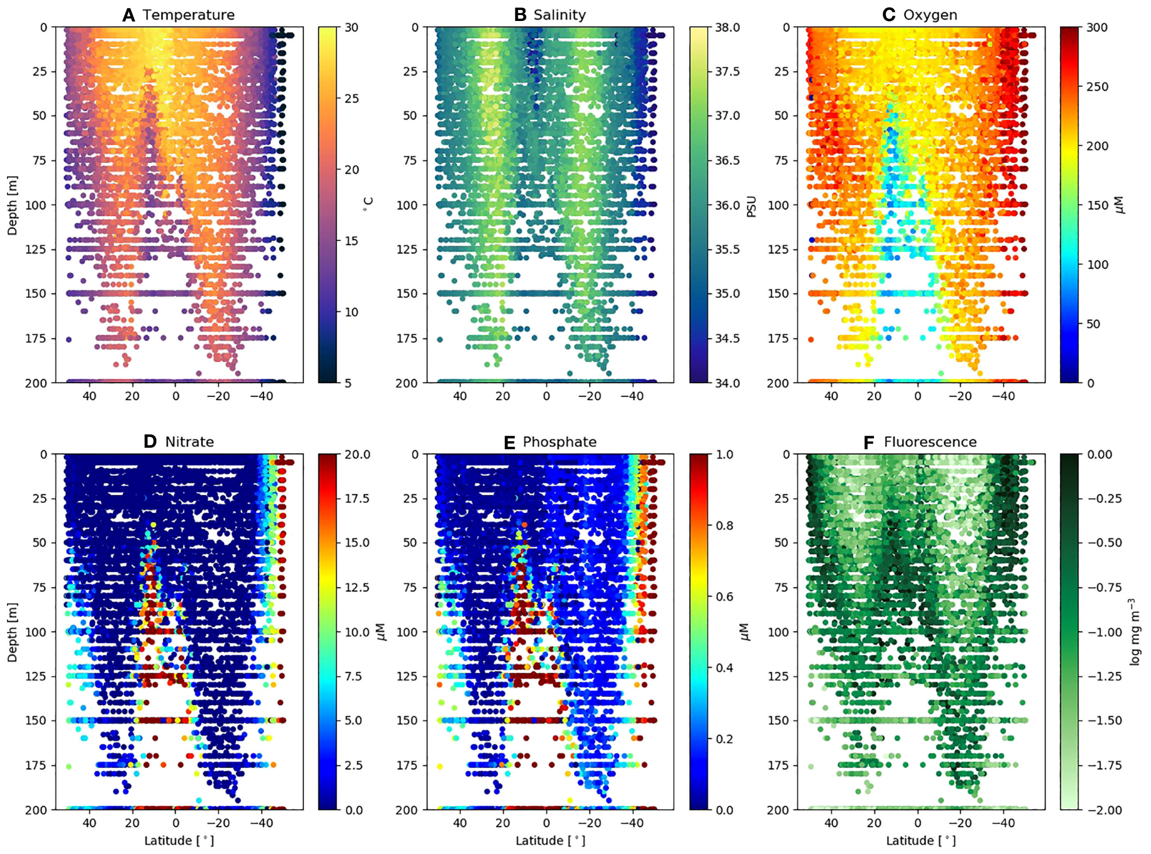

FIGURE 3
Environmental variables for AMT18 – 29 plotted as a function of latitude and depth. Individual values of **(A)** Temperature (°C); **(B)** Salinity (PSU); **(C)** Oxygen (μM); **(D)** Nitrate (μM); **(E)** Phosphate (μM) and **(F)** Fluorescence (log mg m^{-3}), extracted as points where discrete FACS samples obtained.

deep surface mixed layer (>100 m) cores, separated by the warm (>27°C) but fresher (<36 PSU) equatorial upwelling zone (~10°N). The gyres are biogeochemically characterized by lower surface mixed layer oxygen (Figure 3C: 180 – 220 µM), nitrate (Figure 3D) approaching or below the limit of detection (<0.01 µM) and a deep (Figure 3F: up to 150 – 200 m) chlorophyll maximum (0.1 – 0.3 mg m^{-3}). Other features of note are the higher phosphate concentrations (Figure 3E: 0.3 µM) in the southern compared with the northern gyre (<0.2 µM) with implications for nutrient stoichiometry, and the lower oxygen zone (<120 µM) in the equatorial upwelling region (Figure 3C). For a further analysis of the biogeochemical traits of the AMT transect see Smyth et al. (2017).

The FACS measured *Prochlorococcus* differential forward and side scatter (Figures 4A, B) shows regions of enhanced scattering which clearly follow the depth of the thermocline (base of the surface mixed layer), with clear differences between the northern and southern gyres. The range of maximum $dC_{sca}/d\Omega_3$ and $dC_{sca}/d\Omega_4$ of 300 – 450 m^2 sr^{-1} and 0.01 – 0.03 m^2 sr^{-1} respectively is at a depth of >75 m in the northern gyre, but >125 m in the southern. When converted to total carbon (Figure 4C) using the regression statistics (Figure 1A or C) and multiplied by the abundance (Stage 2 of Figure 2) the patterns show a tendency for *Prochlorococcus* carbon (C_{pro}) to increase with depth towards the thermocline (typical values<5 mg m^{-3} in the surface; 20 – 50 mg m^{-3} close to the base of the mixed layer). The species-specific Chl (Chl_{pro}) also show an increase with depth towards the thermocline (Figure 4E), in some cases exceeding 0.1 mg m^{-3}. Taking the ratio of C_{pro} : Chl_{pro} results in a range of values between 1 – 600 (Figures 4F, 5A; Table 3). For a similar visualization of *Synechococcus* and the generic *Other* class, see Figures S1, S2.

Environmental drivers of C:Chl

Using all the species data combined over all provinces the trained RF model (Figure 5A) can predict C:Chl with a high percentage of variance explained (R^2 = 0.931). For the independent test dataset (N=463) (Figure 5B) the predictions of C:Chl are markedly poorer (R^2 = 0.359). The ML model tends to predict C:Chl most accurately over a range between 20 – 200 for both the training and test datasets (Figures 5A, B); the prediction is less reliable for C:Chl< 15. This is partly caused by an imbalance within the sampling, as lower carbon and chlorophyll values are less common and hence more challenging to represent. The corresponding SHAP analysis (Figure 5C) identifies that

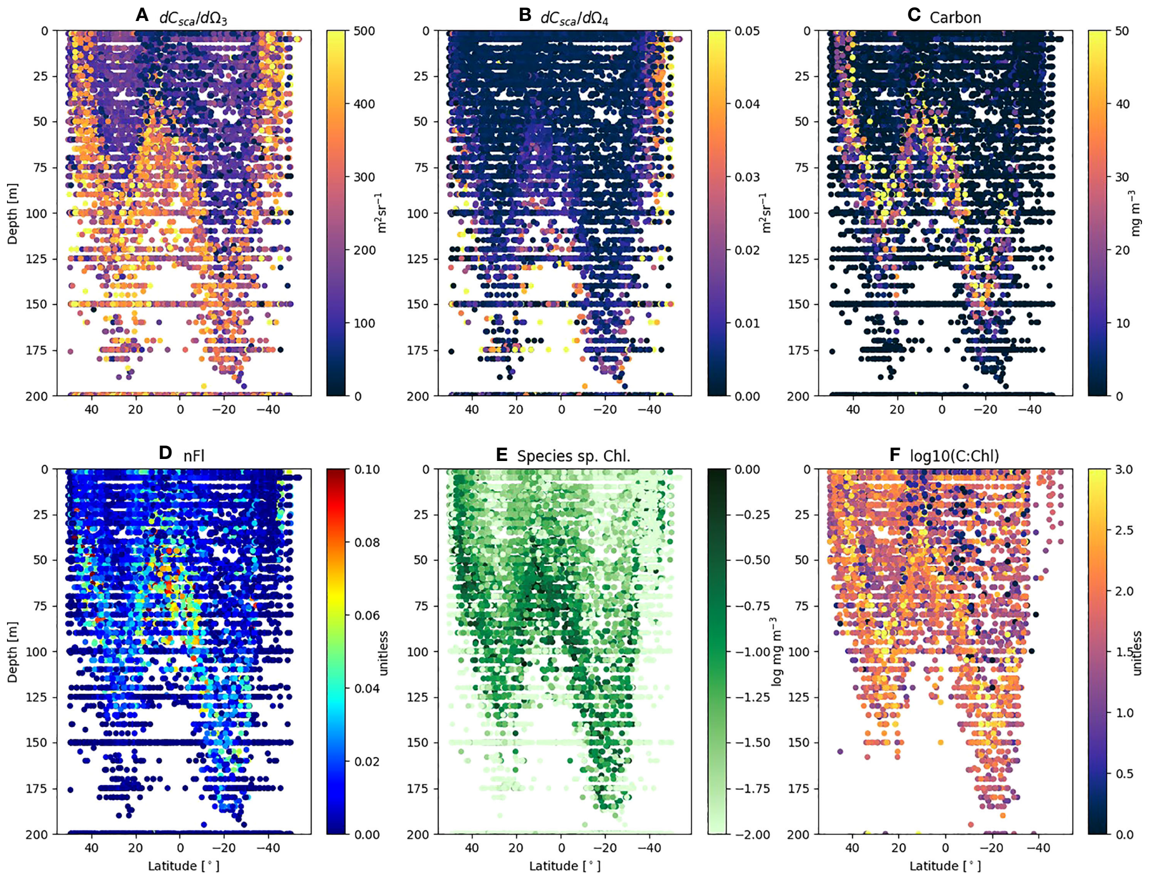

FIGURE 4
FACS scattering and derived variables for *Prochlorococcus* from AMT18 − 29 plotted as a function of latitude and depth. Individual sample values of **(A)** mean differential forward scatter ($dC_{sca}/d\Omega_3$); **(B)** mean differential side scatter ($dC_{sca}/d\Omega_4$); **(C)** Total Carbon (mg m^{-3}); **(D)** normalized Fluorescence (nFl); **(E)** Species specific Chl (log mg m^{-3}); **(F)** log carbon to chlorophyll ratio (C:Chl).

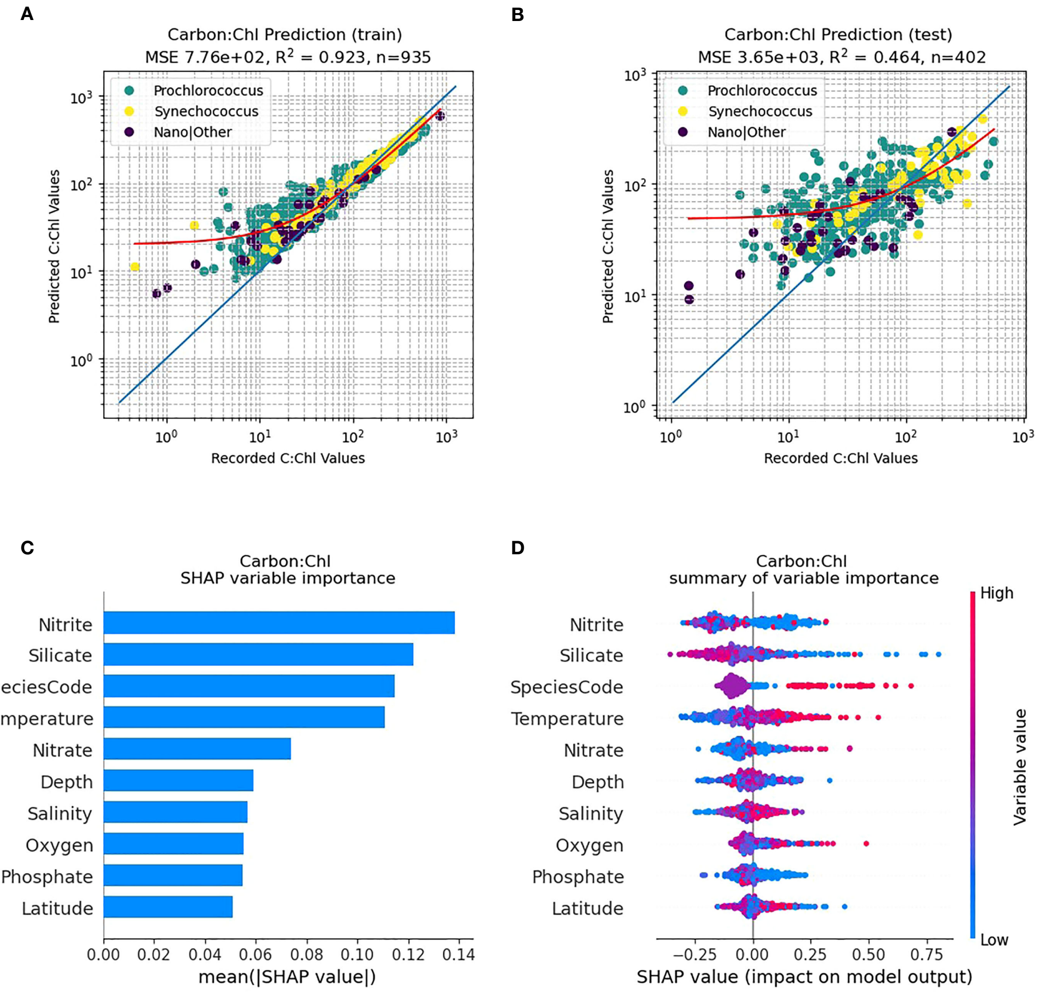

FIGURE 5
RF model prediction and analysis of C:Chl for all AMT provinces. **(A)** The RF prediction results for the training dataset, identified per species, with the red line representing the best fit and the blue line the 1:1 (perfect prediction). **(B)** The RF prediction results for the test dataset. **(C)** The SHAP variable importance of each predictor variable. **(D)** Impact of the variable on the predicted output, based on the value of the variable. The colours represent whether the variable is high or low, and the horizontal axis represents a positive or negative change on the predicted output C:Chl.

phytoplankton species (*Prochlorococcus*, *Synechococcus* etc.) are the most important predictor of C:Chl, followed by nitrite, silicate and temperature. Figure 5D shows the impact that high and low variable values will have on the model output. Silicate tends to have a negative correlation with the prediction of C:Chl, and low values of nitrite will have either a strong positive or negative impact on the results, whereas high nitrate levels have minimal impact on the C:Chl values over the AMT transect.

The northern gyral provinces (Figure 6), are dominated by *Prochlorococcus*. The RF predictive capability of C:Chl using the training dataset (N=255) renders a good fit to the data (Figure 6A; R^2 = 0.89), however the independent test data set has a poorer fit (Figure 6B; N=110, R^2 = 0.27). The SHAP analysis shows that silicate is one of the dominant drivers of C:Chl in the northern gyre, followed by oxygen and nitrite (Figure 6C). As in Figure 5D for all ocean provinces, silicate tends to have a negative correlation with the prediction of C:Chl in the northern gyre (Figure 6D), and low values of nitrite have a slightly positive impact. In contrast, the RF predictivity of C:Chl in the southern gyre is markedly improved (Figure 7). The training data (Figure 7A, N=394) has a good fit (R^2 = 0.94) and the independent test data (Figure 7B, N=170) has a moderate fit (R^2 = 0.68). The SHAP analysis shows that C:Chl predictability in the southern gyre is driven by silicate and species type (Figure 7C). For further analyses of other species see Figures S3–S7.

Discussion

This paper effectively highlights the use of FACS for *in vivo* determination of cellular carbon content across a variety of phytoplankton species with sizes ranging from 0.5 to 10 µm. This is particularly powerful as FACS can distinguish different phytoplankton species using automated (Smyth et al., 2019) or manual (Tarran et al., 2006) clustering techniques. This removes the need for size fractionated filtering and subsequent elemental analysis e.g., using a CHNS analyser, and can distinguish the contribution from individual cells (Pallon et al., 1999). FACS has

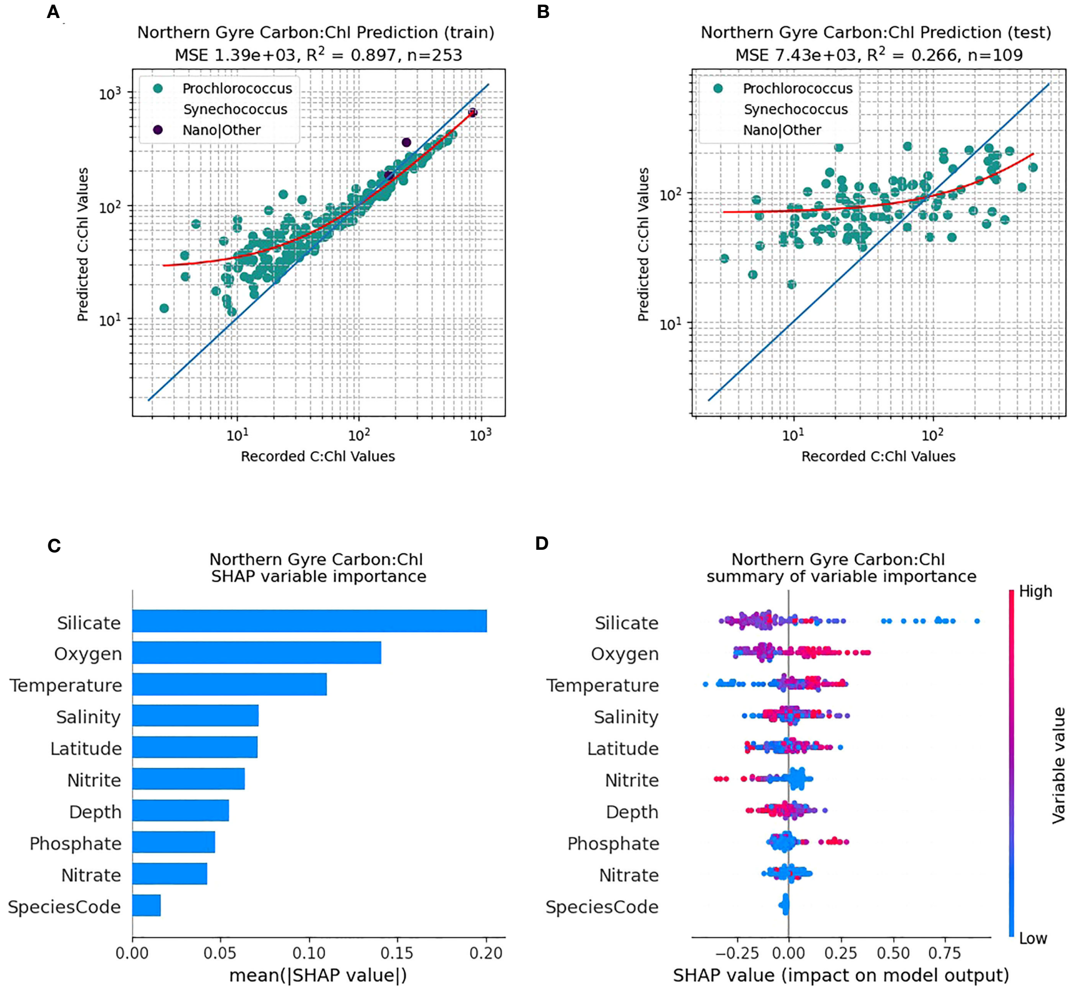

FIGURE 6
RF model prediction and analysis of C:Chl for the Northern Gyre provinces. **(A)** The RF prediction results for the training dataset, identified per species, with the red line representing the best fit and the blue line the 1:1 (perfect prediction). **(B)** The RF prediction results for the test dataset. **(C)** The SHAP variable importance of each predictor variable. **(D)** Impact of the variable on the predicted output, based on the value of the variable. The colours represent whether the variable is high or low, and the horizontal axis represents a positive or negative change on the predicted output C:Chl.

the additional benefit of being high throughput in comparison to other techniques such as light microscopy and is readily applicable to machine learning tools and methodologies (Thomas et al., 2018). Advances in miniaturization, and electro-optical techniques may soon make *in situ* measurements of cellular carbon using platforms such as moorings (Olson et al., 2017) and gliders a reality. Further work is needed in addressing issues concerning cellular shape and heterogeneous internal structure (Smyth et al., 2021), particularly for the smaller size classes of phytoplankton such as *Prochlorococcus*. We have attempted to overcome these typical limitations imposed by light scattering approaches by taking the geometric mean values of $dC_{sca}/d\Omega_3$ and $dC_{sca}/d\Omega_4$ and removing data from the RF analysis where there is an associated large standard deviation. Figures 1, 4; Table 2.

The high values of C_{proc} (Figure 4C) at the deep chlorophyll maximum (DCM) seem counterintuitive given the well-documented high abundances of *Prochlorococcus* in the surface layers of the tropical Atlantic (Johnson et al., 2006; Tarran et al., 2006; Smyth et al., 2019). Cultured *Prochlorococcus* strains (MIT9312, MED4, AS9601, NAT12A) typically display $dC_{sca}/d\Omega_3$ values in the range of 100 – 400 m^2 sr^{-1} (Figure 1); consistent with field observations of 50 – 500 m^2 sr^{-1} (Figure 4A). However, when these data are translated into cellular carbon content (Table 2), we observe a range from 0.002 – 0.72 pgC cell^{-1}, spanning 2.5 orders of magnitude. This contrasts significantly with the more modest variations in *Prochlorococcus* cellular carbon content observed from the surface to the deep chlorophyll maximum (DCM) at BATS (0.05 pgC surface; 0.15 pgC DCM - Casey et al. (2013)) and HOT (0.02 pgC surface; 0.114 pgC DCM - Casey et al. (2019)) time-series stations. This discrepancy may underline a potential limitation in our methodology, as the log-log transformation from differential forward scattering to carbon might exacerbate any uncertainties in differential forward scatter and those linked to a log-log regression, especially for smaller cells. Our regression between differential forward scatter and cellular carbon resulted in slopes of 2.51 and 2.22, depending on the instrument used (Figure 1). These values are noticeably higher than the 1.74 value derived from a similar instrument (Burbage and Binder, 2007). The

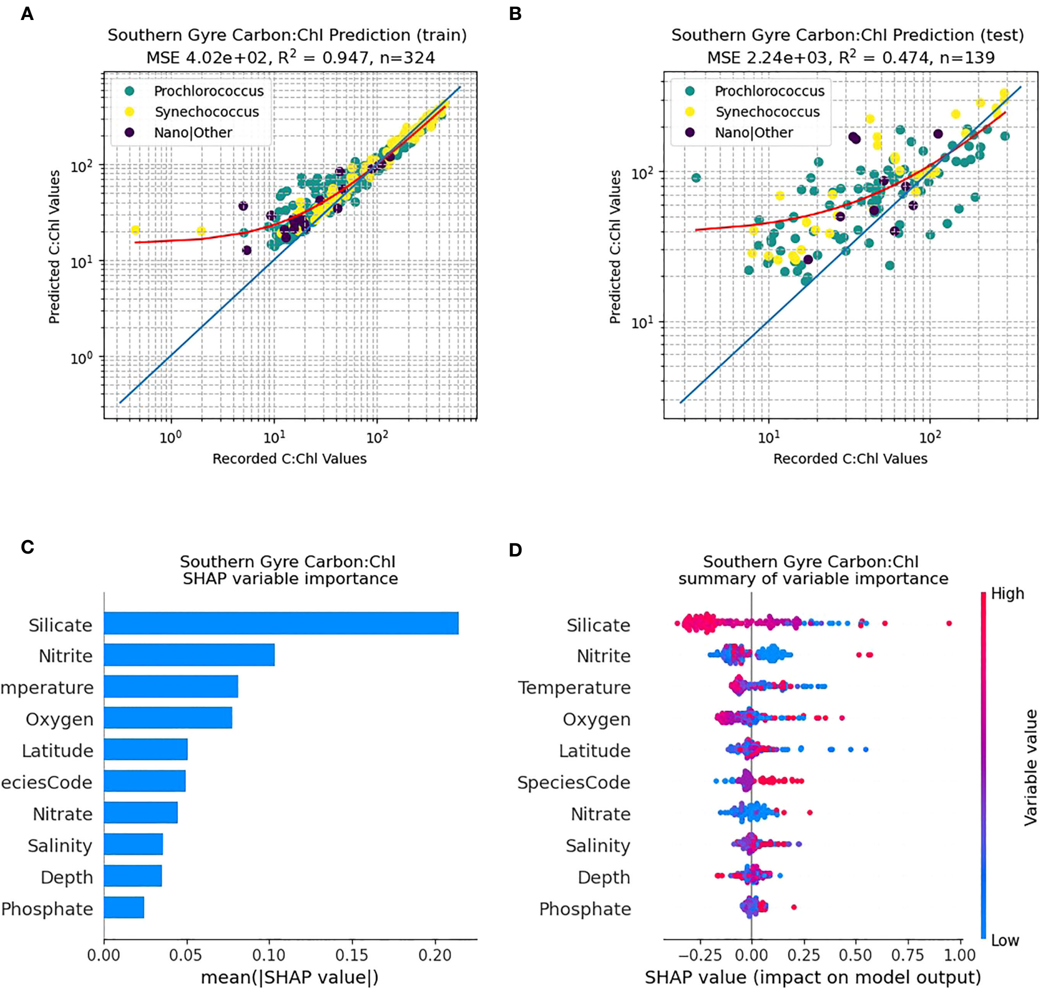

FIGURE 7
RF model prediction and analysis of C:Chl for the Southern Gyre provinces. **(A)** The RF prediction results for the training dataset, identified per species, with the red line representing the best fit and the blue line the 1:1 (perfect prediction). **(B)** The RF prediction results for the test dataset. **(C)** The SHAP variable importance of each predictor variable. **(D)** Impact of the variable on the predicted output, based on the value of the variable. The colours represent whether the variable is high or low, and the horizontal axis represents a positive or negative change on the predicted output C:Chl.

higher coefficients in our regression model may be responsible for the greater cellular content of the large-sized *Prochlorococcus* strain (Figure 1 - NAT12A) estimated by scattering (0.3 pgC) compared to that measured by elemental analysis (0.08 pgC). These findings suggest that our methodology may require further refinement to accurately assess the cellular carbon content in different phytoplankton species. As a next step, we propose to test and validate our approach not merely on cultured specimens, but also on natural phytoplankton populations using a fine-resolution size fractionation approach (Casey et al., 2019). This will provide a more comprehensive evaluation of our technique, thereby enhancing its precision and applicability.

An empirical relationship between side scatter and chlorophyll might not be expected and deserves some scrutiny as there are several confounding factors one might consider. Firstly, the chlorophyll-a molecule absorbs quite strongly (0.03 m^2 [mg chlorophyll-a]$^{-1}$) at the wavelength of the blue (488 nm) laser used for $dC_{sca}/d\Omega_4$ determinations, stronger still for the divinyl chlorophyll-a molecule synthesized by *Prochlorococcus* (0.05 m^2 [mg chlorophyll-a]$^{-1}$; Bricaud et al. (2004)). The expectation would be that, for otherwise physiologically similar cells, the scattering amplitude would decrease, rather than increase with increasing cellular chlorophyll-a concentrations. Secondly, there are potentially many overlapping absorption spectra at 488 nm due to the presence of multiple pigments, a problem compounded further by changing pigment stoichiometries associated with photoacclimation and diel cycles (Moore et al., 1995). However, we expect the magnitude of the contribution of pigment absorption to $dC_{sca}/d\Omega_4$ to be relatively small compared with the scattering amplitude, with a scattering-to-attenuation ratio of approximately 0.8 at 488 nm (Claustre et al., 2002). One rationale for the observed positive relationship between chlorophyll-a and $dC_{sca}/d\Omega_4$ is that it reflects changes in internal structure associated with both photoacclimation and photoadaptation (Ting et al., 2007). These are the thylakoid folds, the carboxysomes, and the large photosystem complexes, antennae proteins and associated membrane proteins that change within some stoichiometric bounds with light harvesting pigments. We speculate that these structural differences contribute a positive scattering component that exceeds the negative absorption component to $dC_{sca}/d\Omega_4$, resulting in the overall positive empirical relationship we observed in our cultures. Nevertheless, higher order processes and variability in photophysiology in a dynamic ocean may complicate our interpretation of $dC_{sca}/d\Omega_4$ as a proxy for chlorophyll-a content.

A completely contained methodology to quantify cellular chlorophyll concentration still requires a multi-staged approach, which we describe in this paper, with the introduction of errors when assigning a given chlorophyll concentration to an individual species group. This may possibly be solvable by using calibrated fluorescence beads, with a rigorous calibration methodology against such standards on a daily basis (Smyth et al., 2019). Simultaneous measurements of the real and imaginary parts of the cellular refractive index - can be empirically related to the carbon and chlorophyll content respectively (Stramski, 1999; DuRand et al., 2002; Agagliate et al., 2018). As we have previously reported (Smyth et al., 2019) our calibrated technique only returns the real refractive index which stymies further determination of C:Chl. However, the strong empirical relationships, albeit individual detector specific (Figure 1), between FACS measured forward and side scatter and carbon and (normalized) fluorescence respectively would appear to offer more potential than a technique based on the determination of refractive index.

Our reported ranges of C:Chl (Table 3) are broadly consistent with other literature values: Graff et al. (2015) reported C:Chl, albeit for a limited portion and depth (20 m) of the Atlantic Ocean, between a range of 35 – 408 (median, 99) for all phytoplankton types. Veldhuis and Kraay (2004) give a range of 93 – 122 for *Prochlorococcus*, and 38 – 58 for *Synechococcus* which is within range of the values reported here. The range of 9 - 499 for *Prochlorococcus* reported by Phongphattarawat et al. (2023), based on a pigment-based analysis of a global dataset that included AMT data, is close to the range reported here. Figure 8 shows an intercomparison of *Prochlorococcus* C versus Chl between this work and previous literature values. When data points are selected based on the dominant type present in the sample [i.e., >50% of the chlorophyll concentration can be attributable to *Prochlorococcus* (Figure 2)] regression statistics of slope: 0.672 ± 0.039, intercept: 1.392 ± 0.045, R^2: 0.219 are obtained. This compares with slope: 0.843, intercept: 1.711, R^2: 0.41 for Phongphattarawat et al. (2023) using 49 fg C $cell^{-1}$ (Cailliau et al., 1996) and slope: 0.788, intercept: 1.798, R^2: 0.47 for Phongphattarawat et al. (2023) using 52 and 158 fg C $cell^{-1}$ for euphotic and sub-euphotic populations, respectively (Casey et al., 2013). Our values tend towards C:Chl = 145 (Sathyendranath et al., 2009) at low values (~0.01 mg m^{-3}) of Chl, and diverge away (below) this at higher (~1 mg m^{-3}) Chl.

Prochlorococcus is well known to have distinct adaptions to environmental factors such as light intensity, temperature and nutrient concentrations (Partensky et al., 1999) with well-defined ecotypes (Rocap et al., 2003; Zinser et al., 2006; Chandler et al., 2016) as well as remarkable genetic and physiological diversity

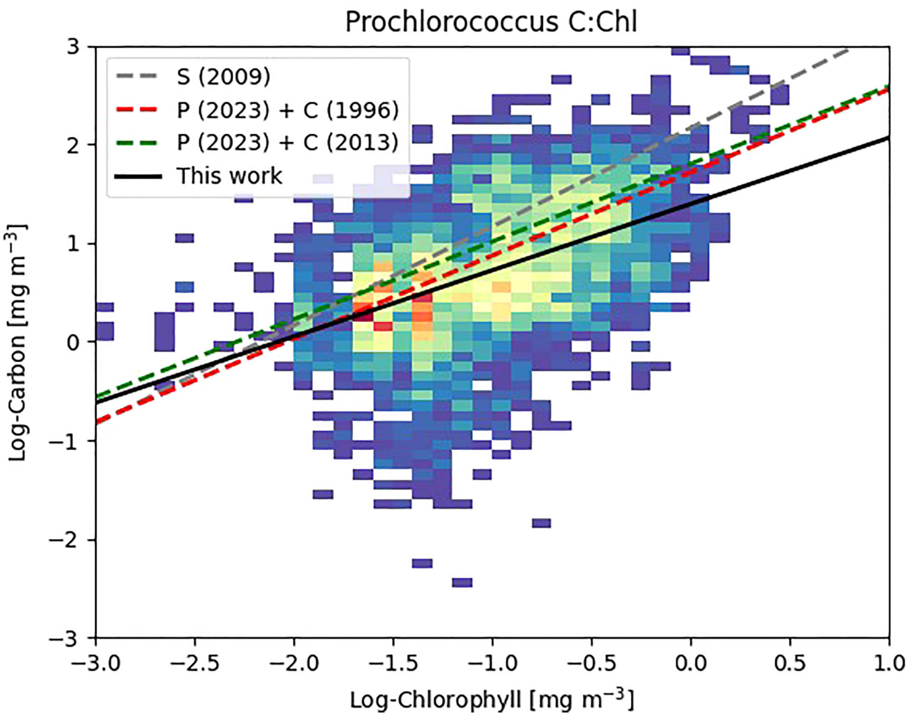

FIGURE 8
Density plot of Log Carbon vs. Log Chlorophyll for *Prochlorococcus* where *Prochlorococcus* >50% of the calculated chlorophyll content of the individual sample (Figure 2). Warmer colors denote greater number of data points. Previous literature values denoted as S (2009) - Sathyendranath et al. (2009); P (2023) + C (1996) - Phongphattarawat et al. (2023) using Cailliau et al. (1996); P (2023) + C (2013) - Phongphattarawat et al. (2023) using Casey et al. (2013).

(Rocap et al., 2003). Qualitatively Figure 4 shows such patterns with regards to scatter ($dC_{sca}/d\Omega_3$, $dC_{sca}/d\Omega_4$), carbon, nFl and C:Chl ratio. For the RF model results (Figures 5C, 6C, 7C), silicate is consistently shown to be an important variable for predicting C:Chl ranking first in the two gyres (Figures 6C, 7C) and third for all AMT ocean provinces (Figure 5C); however much of the Atlantic is deficient in silicate (Smyth et al., 2017) particularly at depths between 50 – 150 m. The SHAP value, which is a measure of impact, is negative (Figures 5D, 6D, 7D) which may reflect the silicate deficit.

Different *Prochlorococcus* ecotypes have been observed to use the nitrogen species that is most prevalent at the light levels to which they are best adapted which is ammonium in the surface waters and nitrite at depth (Rocap et al., 2003), which can explain why nitrite is a strong driver in predicting C:Chl (Figure 5C). There is also a species difference between *Synechococcus* and *Prochlorococcus* as to which nitrogen source is utilized (Moore et al., 2002) and it is known that some *Prochlorococcus* ecotypes are unable to use nitrate (Bouman et al., 2006) because of their lack of nitrate reductase (Rocap et al., 2003). However, there is evidence that some *Prochlorococcus* strains are able to utilize nitrate (Berube et al., 2015). This somewhat equivocal behaviour may explain why nitrate is not one of the dominant drivers of *Prochlorococcus* C:Chl (Figures 5–7).

The hemispheric nuances in predicting C:Chl (Figure 6 cf. Figure 7), particularly for some of the weaker predictor variables such as nitrate and phosphate (Figure 6C cf. Figure 7C), may be explicable by the wider inorganic nutrient stoichiometry of the Atlantic Ocean; and the known deficit (Redfield, 1958) of N:P which is particularly pronounced (Smyth et al., 2017) in the southern gyre. All these driving factors are manifested in the changing efficiencies in CO_2 fixation by *Prochlorococcus*, which is already known to be highly efficient - (Hartmann et al., 2014).

Conclusion

Using flow-cytometry we have shown robust relationships between forward scatter and phytoplankton cellular carbon content, as well as between side scatter and a measure of chlorophyll content for cultures of multiple phytoplankton species. This appears to be robust across several orders of magnitude in scatter and is replicated, albeit with different calibration regression coefficients, for multiple instruments. When applied to the decadal time-scale AMT expeditions, the analysis revealed that *Prochlorococcus* cellular carbon and chlorophyll vary with depth and latitude throughout the Atlantic basin, with higher values encountered at the deep chlorophyll maximum (DCM). A machine learning analysis approach has revealed that the dominant drivers of the C:Chl ratio in the Atlantic basin are silicate and nitrite, with some hemispheric differences between the gyral provinces.

Measurement of phytoplankton carbon in natural oceanographic environments has been notoriously difficult, with many existing methods relying on per-cell carbon content for different phytoplankton cells estimated based on laboratory culture experiments, e.g., Phongphattarawat et al. (2023), or on expensive and labour-intensive ship-board measurements, e.g., Graff et al. (2015). The method developed here employs differences in the scattering properties of cells, which can account for intra-species and inter-species differences in per-cell scattering and is demonstrated to function across multiple models of flow cytometers. When combined with per-cell chlorophyll information, also derived from scattering properties, it became possible to study the natural variability in C:Chl ratio in the decade-long AMT database.

Despite the C:Chl ratio being a key parameter in ecosystem models (Blackford et al., 2004), as well as being widely used in satellite algorithms of productivity and photo-acclimation (Sathyendranath et al., 2009; Sathyendranath et al., 2020), it is still a relatively poorly-understood phytoplankton property. The methodology presented here allows the rapid assessment of C:Chl for a large number of samples over a wide range of biogeochemical provinces. This represents a significant step forward in progressing towards a convergence of species-specific values and variability in C:Chl, as well as the ratio's controlling physical and biogeochemical factors.

Data availability statement

The raw data supporting the conclusions of this article will be made available by the authors, without undue reservation.

Author contributions

TS was the originator of the concept, wrote the original analysis code and led the writing of the manuscript. DM designed the Machine Learning approaches and produced the corresponding figures. GT generated the original AMT FACS datasets as well as the analysis of the laboratory cultures and was instrumental in developing the original concept of the study. FR carried out laboratory analysis of the phytoplankton cultures. TS, DM, GT, FR, JC, SS all contributed to the various iterations of the manuscript by giving intellectual insight and critical analysis. All authors contributed to the article and approved the submitted version.

Funding

This work was funded by the UK Natural Environment Research Council through its National Capability Long-term Single Centre Science Programme, Climate Linked Atlantic Sector Science, grant number NE/R015953/1, and is a contribution to the Atlantic Meridional Transect and Theme 1.3 – Biological Dynamics. This work was supported by the Simons Collaboration on Computational Biogeochemical Modeling of Marine Ecosystems/CBIOMES (Grant ID: 549947,SS).

Acknowledgments

This study contributes to the international IMBeR project and is contribution #396 of the AMT programme. The authors thank the NERC Earth Observation Data Acquisition and Analysis Service (NEODAAS) for access to compute resources for this study.

Conflict of interest

The authors declare that the research was conducted in the absence of any commercial or financial relationships that could be construed as a potential conflict of interest.

Publisher's note

Supplementary material

The Supplementary Material for this article can be found online at: https://www.frontiersin.org/articles/10.3389/fmars.2023.1191216/full#supplementary-material

References

Ackleson, S. G., and Spinrad, R. W. (1988). Size and refractive-index of individual marine particulates - a flow cytometric approach. *Appl. Optics* 27 (7), 1270–1277. doi: 10.1364/ao.27.001270

Agagliate, J., Rottgers, R., Twardowski, M. S., and McKee, D. (2018). Evaluation of a flow cytometry method to determine size and real refractive index distributions in natural marine particle populations. *Appl. Optics* 57 (7), 1705–1716. doi: 10.1364/ao.57.001705

Behrenfeld, M. J., Boss, E., Siegel, D. A., and Shea, D. M. (2005). Carbon-based ocean productivity and phytoplankton physiology from space. *Global Biogeochem. Cycles* 19, GB1006. doi: 10.1029/2004GB002299

Berube, P. M., Biller, S. J., Kent, A. G., Berta-Thompson, J. W., Roggensack, S. E., Roache-Johnson, K. H., et al. (2015). Physiology and evolution of nitrate acquisition in prochlorococcus. *ISME J.* 9 (5), 1195–1207. doi: 10.1038/ismej.2014.211

Blackford, J. C., Allen, J. I., and Gilbert, F. J. (2004). Ecosystem dynamics at six contrasting sites: a generic modelling study. *J. Mar. Sys.* 52, 191–215. doi: 10.1016/j.jmarsys.2004.02.004

Bohren, C. F., and Huffman, D. R. (1983). *Absorption and scattering of light by small particles* (New York: Wiley).

Bouman, H. A., Ulloa, O., Scanlan, D. J., Zwirglmaier, K., Li, W. K. W., Platt, T., et al. (2006). Oceanographic basis of the global surface distribution of *Prochlorococcus* ecotypes. *Science* 312 (5775), 918–921. doi: 10.1126/science.1122692

Breiman, L. (2001). Random forests. *Mach. Learn.* 45 (1), 5–32. doi: 10.1023/a:1010933404324

Bricaud, A., Claustre, H., Ras, J., and Oubelkheir, K. (2004). Natural variability of phytoplanktonic absorption in oceanic waters: influence of the size structure of algal populations. *J. Geophysical Research: Oceans* 109 (C11). doi: 10.1029/2004JC002419

Burbage, C. D., and Binder, B. J. (2007). Relationship between cell cycle and light-limited growth rate in oceanic prochlorococcus (MIT9312) and synechococcus (WH8103) (cyanobacteria). *J. Phycology* 43 (2), 266–274. doi: 10.1111/j.1529-8817.2007.00315.x

Cailliau, C., Claustre, H., Vidussi, F., Marie, D., and Vaulot, D. (1996). Carbon biomass, and gross growth rates as estimated from 14C pigment labelling, during photoacclimation in prochlorococcus CCMP 1378. *Mar. Ecol. Prog. Ser.* 145, 209–221. doi: 10.3354/meps145209

Casey, J. R., Aucan, J. P., Goldberg, S. R., and Lomas, M. W. (2013). Changes in partitioning of carbon amongst photosynthetic pico- and nano-plankton groups in the Sargasso Sea in response to changes in the north Atlantic oscillation. *Deep-Sea Res. Part Ii-Topical Stud. Oceanography* 93, 58–70. doi: 10.1016/j.dsr2.2013.02.002

Casey, J. R., Bjorkman, K. M., Ferron, S., and Karl, D. M. (2019). Size dependence of metabolism within marine picoplankton populations. *Limnology Oceanography* 64 (4), 1819–1827. doi: 10.1002/lno.11153

Chandler, J. W., Lin, Y. J., Gainer, P. J., Post, A. F., Johnson, Z. I., and Zinser, E. R. (2016). Variable but persistent coexistence of prochlorococcus ecotypes along temperature gradients in the ocean's surface mixed layer. *Environ. Microbiol. Rep.* 8 (2), 272–284. doi: 10.1111/1758-2229.12378

Claustre, H., Bricaud, A., Babin, M., Bruyant, F., Guillou, L., Le Gall, F., et al. (2002). Diel variations in prochlorococcus optical properties. *Limnology Oceanography* 47, 1637–1647. doi: 10.2307/3096536

Collos, Y., Mornet, F., Sciandra, A., Waser, N., Larson, A., and Harrison, P. J. (1999). An optical method for the rapid measurement of micromolar concentrations of nitrate in marine phytoplankton cultures. *J. Appl. Phycology* 11 (2), 179–184. doi: 10.1023/a:1008046023487

DuRand, M. D., Green, R. E., Sosik, H. M., and Olson, R. J. (2002). Diel variations in optical properties of micromonas pusilla (Prasinophyceae). *J. Phycology* 38 (6), 1132–1142. doi: 10.1046/j.1529-8817.2002.02008.x

DuRand, M. D., Olson, R. J., and Chisholm, S. W. (2001). Phytoplankton population dynamics at the Bermuda Atlantic time-series station in the Sargasso Sea. *Deep Sea Res. Part II: Topical Stud. Oceanography* 48 (8), 1983–2003. doi: 10.1016/S0967-0645(00)00166-1

Garrison, D. L., Gowing, M. M., Hughes, M. P., Campbell, L., Caron, D. A., Dennett, M. R., et al. (2000). Microbial food web structure in the Arabian Sea: a US JGOFS study. *Deep Sea Res. Part II: Topical Stud. Oceanography* 47 (7), 1387–1422. doi: 10.1016/S0967-0645(99)00148-4

Geider, R. J. (1987). Light and temperature-dependence of the carbon to chlorophyll-a ratio in microalgae and cyanobacteria - implications for physiology and growth of phytoplankton. *New Phytol.* 106 (1), 1–34. doi: 10.1111/j.1469-8137.1987.tb04788.x

Graff, J. R., Westberry, T. K., Milligan, A. J., Brown, M. B., Dall'Olmo, G., van Dongen-Vogels, V., et al. (2015). Analytical phytoplankton carbon measurements spanning diverse ecosystems. *Deep-Sea Res. Part I-Oceanographic Res. Papers* 102, 16–25. doi: 10.1016/j.dsr.2015.04.006

Green, R. E., Sosik, H. M., Olson, R. J., and DuRand, M. D. (2003). Flow cytometric determination of size and complex refractive index for marine particles: comparison with independent and bulk estimates. *Appl. Optics* 42 (3), 526–541. doi: 10.1364/ao.42.000526

Grob, C., Ulloa, O., Claustre, H., Huot, Y., Alarcón, G., and Marie, D. (2007). Contribution of picoplankton to the total particulate organic carbon concentration in the eastern south pacific. *Biogeosciences* 4 (5), 837–852. doi: 10.5194/bg-4-837-2007

Guillard, R. R. L., Smith, W. L., and Chanley, M. H. (1975). "Culture of phytoplankton for feeding marine invertebrates," in *Culture of marine invertebrate animals.* Eds. W. L. Smith and M. H. Chanley (New York: Plenum Press), 29–60.

Hartmann, M., Gomez-Pereira, P., Grob, C., Ostrowski, M., Scanlan, D. J., and Zubkov, M. V. (2014). Efficient CO2 fixation by surface prochlorococcus in the Atlantic ocean. *ISME J.* 8 (11), 2280–2289. doi: 10.1038/ismej.2014.56

Jakobsen, H. H., and Markager, S. (2016). Carbon-to-chlorophyll ratio for phytoplankton in temperate coastal waters: seasonal patterns and relationship to nutrients. *Limnology Oceanography* 61 (5), 1853–1868. doi: 10.1002/lno.10338

Jassby, A. D., and Platt, T. (1976). Mathematical formulation of the relationship between photosynthesis and light for phytoplankton. *Limnology Oceanography* 21 (4), 540–547. doi: 10.4319/lo.1976.21.4.0540

Johnson, Z. I., Zinser, E. R., Coe, A., McNulty, N. P., Woodward, E. M. S., and Chisholm, S. W. (2006). Niche partitioning among prochlorococcus ecotypes along ocean-scale environmental gradients. *Science* 311 (5768), 1737–1740. doi: 10.1126/science.1118052

Landry, M. R., and Kirchman, D. L. (2002). Microbial community structure and variability in the tropical pacific. *Deep Sea Res. Part II: Topical Stud. Oceanography* 49 (13), 2669–2693. doi: 10.1016/S0967-0645(02)00053-X

Longhurst, A., Sathyendranath, S., Platt, T., and Caverhill, C. (1995). An estimate of global primary production in the ocean from satellite radiometer data. *J. Plankton Res.* 17 (6), 1245–1271. doi: 10.1093/plankt/17.6.1245

Lundberg, S. M., and Lee, S. I. (2017). "A unified approach to interpreting model predictions," in *31st annual conference on neural information processing systems (NIPS)* (57 Morehouse Lane, Hook, NY, United States: Curran Associates Inc.).

Marie, D., Rigaut-Jalabert, F., and Vaulot, D. (2014). An improved protocol for flow cytometry analysis of phytoplankton cultures and natural samples. *Cytometry Part A* 85 (11), 962–968. doi: 10.1002/cyto.a.22517

Menden-Deuer, S., and Lessard, E. J. (2000). Carbon to volume relationships for dinoflagellates, diatoms, and other protist plankton. *Limnology Oceanography* 45 (3), 569–579. doi: 10.4319/lo.2000.45.3.0569

Mie, G. (1908). Contribution to the optical properties of turbid media, in particular of colloidal suspensions of metals. *Ann. Phys. (Leipzig)* 25, 377–452. doi: 10.1002/andp.19083300302

Moore, L. R., Coe, A., Zinser, E. R., Saito, M. A., Sullivan, M. B., Lindell, D., et al. (2007). Culturing the marine cyanobacterium prochlorococcus. *Limnology Oceanography: Methods* 5 (10), 353–362. doi: 10.4319/lom.2007.5.353

Moore, L. R., Goericke, R., and Chisholm, S. W. (1995). Comparative physiology of synechococcus and prochlorococcus: influence of light and temperature on growth, pigments, fluorescence and absorptive properties. *Mar. Ecol. Prog. Ser.* 116 (1/3), 259–275. doi: 10.3354/meps116259

Moore, L. R., Post, A. F., Rocap, G., and Chisholm, S. W. (2002). Utilization of different nitrogen sources by the marine cyanobacteria prochlorococcus and synechococcus. *Limnology Oceanography* 47 (4), 989–996. doi: 10.4319/lo.2002.47.4.0989

Olson, R. J., Shalapyonok, A., Kalb, D. J., Graves, S. W., and Sosik, H. M. (2017). Imaging FlowCytobot modified for high throughput by in-line acoustic focusing of sample particles. *Limnology Oceanography-Methods* 15 (10), 867–874. doi: 10.1002/lom3.10205

Pallon, J., Elfman, M., Kristiansson, P., Malmqvist, K., Graneli, E., Sellborn, A., et al. (1999). Elemental analysis of single phytoplankton cells using the Lund nuclear microprobe. *Nucl. Instruments Methods Phys. Res. Section B-Beam Interact. Materials Atoms* 158 (1-4), 312–316. doi: 10.1016/s0168-583x(99)00372-9

Partensky, F., Hess, W. R., and Vaulot, D. (1999). Prochlorococcus, a marine photosynthetic prokaryote of global significance. *Microbiol. Mol. Biol. Rev.* 63 (1), 106–127. doi: 10.1128/MMBR.63.1.106-127.1999

Phongphattarawat, S., Bouman, H. A., Lomas, M. W., Sathyendranath, S., Tarran, G. A., Ulloa, O., et al. (2023). Ecophysiological basis of spatiotemporal patterns in picophytoplankton pigments in the global ocean. *Front. Mar. Sci.* 10. doi: 10.3389/fmars.2023.1112177

Redfield, A. C. (1958). The biological control of chemical factors in the environment. *Am. Sci.* 46 205–221. doi: 10.1002/bmb.20717

Rees, A. P., Nightingale, P. D., Poulton, A. J., Smyth, T. J., Tarran, G. A., and Tilstone, G. H. (2017). The Atlantic meridional transect programme (1995-2016). *Prog. Oceanography* 158, 3–18. doi: 10.1016/j.pocean.2017.05.004

Ribalet, F., Berthiaume, C., Hynes, A., Swalwell, J., Carlson, M., Clayton, S., et al. (2019). SeaFlow data v1, high-resolution abundance, size and biomass of small phytoplankton in the north pacific. *Sci. Data* 6. doi: 10.1038/s41597-019-0292-2

Riemann, B., Simonsen, P., and Stensgaard, L. (1989). The carbon and chlorophyll content of phytoplankton from various nutrient regimes. *J. Plankton Res.* 11 (5), 1037–1045. doi: 10.1093/plankt/11.5.1037

Rocap, G., Distel, D. L., Waterbury, J. B., and Chisholm, S. W. (2002). Resolution of prochlorococcus and synechococcus ecotypes by using 16S-23S ribosomal DNA internal transcribed spacer sequences. *Appl. Environ. Microbiol.* 68 (3), 1180–1191. doi: 10.1128/AEM.68.3.1180-1191.2002

Rocap, G., Larimer, F. W., Lamerdin, J., Malfatti, S., Chain, P., Ahlgren, N. A., et al. (2003). Genome divergence in two prochlorococcus ecotypes reflects oceanic niche differentiation. *Nature* 424 (6952), 1042–1047. doi: 10.1038/nature01947

Sathyendranath, S., Platt, T., Kovac, Z., Dingle, J., Jackson, T., Brewin, R. J. W., et al. (2020). Reconciling models of primary production and photoacclimation invited. *Appl. Optics* 59 (10), C100–C114. doi: 10.1364/ao.386252

Sathyendranath, S., Stuart, V., Nair, A., Oka, K., Nakane, T., Bouman, H., et al. (2009). Carbon-to-chlorophyll ratio and growth rate of phytoplankton in the sea. *Mar. Ecol. Prog. Ser.* 383, 73–84. doi: 10.3354/meps07998

Shalapyonok, A., Olson, R. J., and Shalapyonok, L. S. (2001). Arabian Sea Phytoplankton during southwest and northeast monsoons 1995: composition, size structure and biomass from individual cell properties measured by flow cytometry. *Deep Sea Res. Part II: Topical Stud. Oceanography* 48 (6), 1231–1261. doi: 10.1016/S0967-0645(00)00137-5

Smyth, T., Quartly, G., Jackson, T., Tarran, G., Woodward, M., Harris, C., et al. (2017). Determining Atlantic ocean province contrasts and variations. *Prog. Oceanography* 158, 19–40. doi: 10.1016/j.pocean.2016.12.004

Smyth, T. J., Tarran, G. A., and Sathyendranath, S. (2019). Marine picoplankton size distribution and optical property contrasts throughout the Atlantic ocean revealed using flow cytometry. *Appl. Optics* 58 (32), 8802–8815. doi: 10.1364/ao.58.008802

Smyth, T. J., Tarran, G. A., and Sathyendranath, S. (2021). Sub-Micron picoplankton shape, orientation, and internal structure combined to preferentially amplify the forward scatter. *Optics Express* 29 (2), 2014–2024. doi: 10.1364/OE.413576

Stramski, D. (1999). Refractive index of planktonic cells as a measure of cellular carbon and chlorophyll a content. *Deep-Sea Res. Part I-Oceanographic Res. Papers* 46 (2), 335–351. doi: 10.1016/s0967-0637(98)00065-x

Tarran, G. A., Heywood, J. L., and Zubkov, M. V. (2006). Latitudinal changes in the standing stocks of eukaryotic nano- and picophytoplankton in the Atlantic ocean. *Deep-Sea Res. II* 53, 1516–1529. doi: 10.1016/j.dsr2.2006.05.004

Thomas, M. K., Fontana, S., Reyes, M., and Pomati, F. (2018). Quantifying cell densities and biovolumes of phytoplankton communities and functional groups using scanning flow cytometry, machine learning and unsupervised clustering. *PloS One* 13 (5). doi: 10.1371/journal.pone.0196225

Ting, C., Hsieh, C., Sundararaman, S., Mannella, C., and Marko, M. (2007). Cryo-electron tomography reveals the comparative three-dimensional architecture of prochlorococcus, a globally important marine cyanobacterium. *J. bacteriology* 189, 4485–4493. doi: 10.1128/JB.01948-06

Veldhuis, M. J. W., and Kraay, G. W. (2004). Phytoplankton in the subtropical Atlantic ocean: towards a better assessment of biomass and composition. *Deep Sea Res. Part I: Oceanographic Res. Papers* 51 (4), 507–530. doi: 10.1016/j.dsr.2003.12.002

Volk, T., and Hoffert, M. I. (1985). Ocean carbon pumps: analysis of relative strengths and efficiencies in ocean-driven atmospheric CO2 changes. *Carbon Cycle Atmospheric CO2: Natural Variations Archean to Present* 99–110. doi: 10.1029/GM032p0099

Welschmeyer, N. A. (1994). Fluorometric analysis of chlorophyll-a in the presence of chlorophyll-b and pheopigments. *Limnology Oceanography* 39 (8), 1985–1992. doi: 10.4319/lo.1994.39.8.1985

Worden, A. Z., Nolan, J. K., and Palenik, B. (2004). Assessing the dynamics and ecology of marine picophytoplankton: the importance of the eukaryotic component. *Limnology Oceanography* 49 (1), 168–179. doi: 10.4319/lo.2004.49.1.0168

Zinser, E. R., Coe, A., Johnson, Z. I., Martiny, A. C., Fuller, N. J., Scanlan, D. J., et al. (2006). Prochlorococcus ecotype abundances in the north Atlantic ocean as revealed by an improved quantitative PCR method. *Appl. Environ. Microbiol.* 72 (1), 723–732. doi: 10.1128/aem.72.1.723-732.2006

Frontiers in Marine Science

TYPE Original Research
PUBLISHED 15 August 2023
DOI 10.3389/fmars.2023.1241333

OPEN ACCESS

EDITED BY
Andrew Paul Rees,
Plymouth Marine Laboratory,
United Kingdom

REVIEWED BY
Luis Manuel Bolaños,
University of Exeter, United Kingdom
Maria Vila-Costa,
Spanish National Research Council (CSIC),
Spain

*CORRESPONDENCE
Michael Cunliffe
✉ micnli@mba.ac.uk

†These authors have contributed equally to this work

RECEIVED 16 June 2023
ACCEPTED 28 July 2023
PUBLISHED 15 August 2023

CITATION
Allen R, Bird KE, Murrell JC and Cunliffe M (2023) Latitudinal variation in the potential activity of Atlantic Ocean bacterioplankton revealed through 16S rRNA and 16S rRNA gene metabarcoding.
Front. Mar. Sci. 10:1241333.
doi: 10.3389/fmars.2023.1241333

Latitudinal variation in the potential activity of Atlantic Ocean bacterioplankton revealed through 16S rRNA and 16S rRNA gene metabarcoding

Ro Allen[1†], Kimberley E. Bird[1,2†], J. Colin Murrell[2] and Michael Cunliffe[1,3*]

[1]Marine Biological Association, The Laboratory, Citadel Hill, Plymouth, United Kingdom, [2]School of Environmental Sciences, University of East Anglia, Norwich, United Kingdom, [3]School of Biological and Marine Sciences, University of Plymouth, Plymouth, United Kingdom

The activities of bacterioplankton sustain open ocean biogeochemical and ecological processes, however, little is known about the activity of specific bacterioplankton, especially related to their biogeography across oceanic scales. The Atlantic is the second largest of the world's oceans and has an essential role in the global carbon cycle. Here, we show congruence in the structure of 16S rRNA and 16S rRNA gene derived bacterioplankton communities throughout the Atlantic Ocean from temperate to tropical regions. We used 16S rRNA:16S rRNA gene ratios as a phylogenetically resolved proxy for potential activity, demonstrating ocean-scale patterns of putative oligotrophy and copiotrophy in major bacterioplankton groups, with spatial niche partitioning being evident at single-nucleotide resolution within some groups, including the *Flavobacteria* and SAR86. This study examines the potential structure of the active microbiome of the Atlantic Ocean, providing novel insights into the ecology and life history strategies of both well-known and currently understudied bacterioplankton taxa.

KEYWORDS

16S rRNA, bacterioplankton, biogeography, microbial activity, Atlantic Ocean

1 Introduction

Bacterioplankton regulate biogeochemical and ecological processes in the oceans at local and global scales (Falkowski et al., 2008). For example, approximately 50% of global primary production occurs in the marine environment (Field et al., 1998), a large fraction of which is converted to dissolved organic matter (DOM) that is processed by heterotrophic bacterioplankton through the microbial loop (Azam and Malfatti, 2007). Important ecological interactions in planktonic ecosystems depend on the activity of bacterioplankton, including the production and exchange of metabolites (Kazamia et al., 2016), growth inhibiting compounds (Van Tol et al., 2017), and the provision of 'public-good' functions (Reintjes et al., 2019). Despite their established functional importance, the diversity and distribution of active open ocean bacterioplankton remain poorly understood.

High-throughput sequencing of 16S rRNA genes amplified from genomic DNA (gDNA) is a standard approach to survey the diversity and distribution of bacterioplankton in the marine environment (Sunagawa et al., 2015). However, in addition to metabolically-active cells, 16S rRNA gene surveys capture dormant cells (i.e. metabolically-inactive), dead cells, and cell-free DNA. A large proportion of bacterioplankton are dormant in oceanic ecosystems (Lennon and Jones, 2011), ranging from ~50–95% of cells in oligotrophic regions (Del Giorgio and Scarborough, 1995; Longnecker et al., 2010; Alonso-Sáez et al., 2012), and cell-free DNA can accumulate in substantial concentrations in seawater, despite rapid turnover rates (Taylor et al., 2018). Consequently, the recovery of dormant cells, dead cells, and cell-free DNA from 16S rRNA gene surveys can mask important patterns in the diversity and distribution of the active bacterioplankton that underpin biogeochemical and ecological processes.

High-throughput sequencing of complementary DNA (cDNA) synthesised from 16S rRNA is an approach used to characterize the active components of bacterial communities, whilst minimizing the influence of dormant cells, dead cells, and cell-free DNA as outlined above (Bowsher et al., 2019). While dormant cells still contain some ribosomes (Chambon et al., 1968; Sukenik et al., 2012), 16S rRNA concentrations generally correlate with growth rates in cultured marine bacteria (Kemp et al., 1993; Kerkhof and Ward, 1993; Worden and Binder, 2003; Lin et al., 2013; Salter et al., 2015). However, the relationship between 16S rRNA and growth rate is often non-linear and can differ substantially between taxa (Kerkhof and Kemp, 1999; Blazewicz et al., 2013; Lankiewicz et al., 2016). Despite these caveats, 16S rRNA surveys can provide a more refined view of active bacterial communities than DNA-based 16S rRNA gene surveys. Furthermore, the ratio of 16S rRNA to 16S rRNA genes (hereafter 16S rRNA:16S rRNA gene ratios) can act as an *in situ* proxy for the protein synthesis potential (potential activity) of specific bacterial populations (Jones and Lennon, 2010; Campbell et al., 2011).

In the South China Sea, cDNA derived bacterioplankton communities display stronger coupling to prevailing environmental conditions than gDNA derived communities (Zhang et al., 2014). This suggests that 16S rRNA surveys may reduce stochasticity introduced by dormant cells, dead cells, and cell-free DNA, to more accurately resolve the relationships between bacterioplankton communities and their environment. In coastal waters, 16S rRNA:16S rRNA gene ratios have been used to demonstrate that large proportions of bacterioplankton operational taxonomic units (OTUs) cycle between states of high and low potential activity (Campbell et al., 2011). Whilst at the Hawaii Ocean Time-Series station ALOHA, 16S rRNA:16S rRNA gene ratios indicated that some rare populations display high potential activity, suggesting that they contribute disproportionately to biogeochemical processes relative to their abundance (Hunt et al., 2013). Importantly, these studies were focused on local or regional environments, and employed 97% similarity clustering of OTUs which is does not resolve ecologically relevant microdiversity within bacterioplankton communities (Needham et al., 2017). The biogeographic relationship between active and total bacterioplankton communities, and the potential activity of specific bacterioplankton populations at high phylogenetic resolution, remain poorly understood across oceanic basin.

The Atlantic is the second largest oceanic basin on Earth, and plays a major role in the global carbon cycle (Hoppe et al., 2002; Tilstone et al., 2017). The Atlantic is a net sink for atmospheric CO_2 and is responsible for the drawdown of approximately 0.5 Pg C yr^{-1} (Landschützer et al., 2014). The biogeochemical function of the Atlantic Ocean is primarily modulated by the balance between phytoplankton primary production and the metabolic activity of heterotrophic bacterioplankton (Hoppe et al., 2002). Current understanding of the structure and function of Atlantic Ocean bacterioplankton communities is primarily founded on DNA-based 16S rRNA gene surveys (Milici et al., 2016a; Milici et al., 2016b; Logares et al., 2020; Bolaños et al., 2021) and *in situ* estimates of secondary production and respiration (Hoppe et al., 2002; García-Martín et al., 2017). The biogeography of potentially active bacterioplankton is poorly understood across the Atlantic, limiting efforts to comprehensively link bacterioplankton community structure and function across this regionally and globally important ocean.

Here, we present an ocean-scale survey of cDNA and gDNA derived bacterioplankton communities, from samples collected across three variable depths dependent on light levels (97%, 55% and 1% photosynthetically active radiation; PAR) throughout the Atlantic Ocean during the Austral spring. We show congruence in the structure of cDNA and gDNA derived communities across oceanic scales, which was greatest in the nutrient-rich waters of the Southwest Atlantic Shelves where cDNA and gDNA derived bacterioplankton diversity also converge. We then explore the use 16S rRNA:16S rRNA gene ratios to examine patterns in the protein synthesis potential (potential activity) of bacterioplankton groups and populations through space. Based on 16S rRNA:16S rRNA gene ratios, we speculate on possible signatures of putative oligotrophy and copiotrophy in biogeochemically important bacterioplankton groups, and propose how spatial niche partitioning underlies broad-scale patterns in potential activity and distribution.

2 Methods

2.1 Sample collection

Seawater sampling was conducted between 18th September and 4th November 2015 aboard the *RRS James Clark Ross* during the Atlantic Meridional Transect (AMT) research voyage from the UK to the Falkland Islands (AMT25/JR15001). Forty eight seawater samples were collected from 16 stations spanning 8 oceanographic provinces, ranging from the North Atlantic Drift to the South Subtropical Convergence and Southwest Atlantic Shelves (Reygondeau et al., 2013) (Figure 1A; Supplementary Figure 1). At each station, 9 litre seawater samples were collected from three

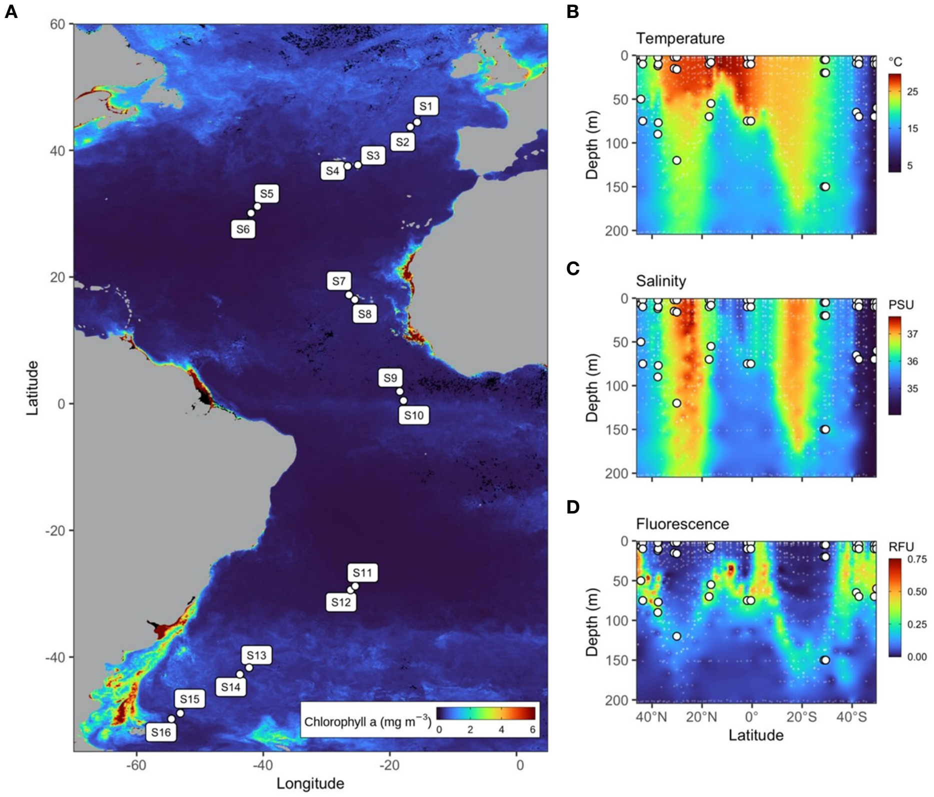

FIGURE 1

(A) Map of 16 stations sampled during the AMT25 latitudinal transect of the Atlantic Ocean during the Austral spring of 2015. Colour represents MODIS-Aqua satellite-derived chlorophyll-*a* concentration averaged from 21/09/2015 to 21/12/2015 at 4 km resolution. **(B–D)** Temperature, salinity, and fluorescence depth profiles throughout the Atlantic Ocean measured using the Sea-Bird SBE 911plus CTD and Aquatracka III Fluorometer, respectively.

light-dependent depths (97%, 55%, and 1% PAR) using Niskin bottles attached to a CTD rosette system. Seawater samples were immediately filtered through 0.2 µm cellulose nitrate filters and transferred to sterile 2 ml microcentrifuge tubes containing 1 ml of RNAlater (Merck, Germany) before storage at −80°C. Filtration took on average 2hr 22 min (range 1hr11 to 3hr11).

Depth profiles for temperature (Figure 1B) and salinity (Figure 1C) were measured using a Sea-Bird SBE 911 plus CTD (Sea-Bird Scientific, USA), and dissolved oxygen was measured using a Sea-Bird SBE 43 dissolved oxygen sensor. Fluorescence (Figure 1D) was measured using an Aquatracka III Fluorometer (Chelsea Technologies, United Kingdom) and PAR was measured using a QCD-905L sensor (Biospherical Instruments, USA). Inorganic nutrient (nitrate NO_3^-, nitrite NO_2^-, phosphate PO_4^{3-} and silicate SiO_2) concentrations were measured onboard from discrete water samples using an AutoAnalyzer 3 (Bran+Luebbe, Germany) according to GO-SHIP protocols and determined according to standard analytical techniques (Hydes et al., 2010).

2.2 Nucleic acid extraction and sequencing

Filters were thawed on ice and transferred to sterile 2 ml FastPrep Lysing Matrix B tubes (MP Biomedicals, USA) before being snap frozen in liquid nitrogen and fragmented using a sterile pellet pestle. GTC lysis buffer (700 µl) (Omega Bio-Tek, USA) was added to the filters followed by further mechanical disruption using a Mini-BeadBeater-8 (BioSpec, USA) for 3 minutes at maximum speed. RNA and DNA were co-extracted from the lysate using the E.Z.N.A. DNA/RNA isolation kit (Omega Bio-Tek, USA) according to the manufacturer's instructions, including an on-column DNase digestion with RNase-Free DNase (Omega Bio-Tek, USA). cDNA was synthesised from 200 ng of extracted RNA using the Omniscript Reverse Transcription kit (Qiagen, Germany) according to the manufacturer's instructions, with the primer PROK1492R (GGWTACCTTGTTACGACTT) (Suzuki et al., 2000).

Sequencing libraries were constructed from gDNA and the raised cDNA according to protocols described in Comeau et al. (2017). In brief, the V4–V5 regions of the 16S rRNA gene were PCR amplified in duplicate using the primers 515F-Y (GTGYCAGCMGCCGCGGTAA) and 926R (CCGYCAATTYMTTTRAGTTT) (Parada et al., 2016) modified to include Illumina Nextera adaptors and indices. Pooled duplicate PCR products were purified and normalised in one-step using the SequalPrep 96-well plate kit (Invitrogen, USA) according to manufacturer's instructions and then pooled to generate a single library, which was quantified using the Qubit dsDNA High Sensitivity Assay (ThermoFisher Scientific, USA). Sequencing was performed on the Illumina MiSeq platform using the V3 reagent kit, yielding 2 × 300 bp paired-end reads (Illumina, USA).

2.3 Bioinformatics

A total of 7,997,448 paired-end reads were recovered from 96 samples (48 cDNA, 48 gDNA) and were processed according to the Bioconductor workflow (Callahan et al., 2016; Bioconductor version 3.11). Primer sequences were trimmed (forward reads: position 19, reverse reads: position 20), low-quality bases were truncated (forward reads: position 270, reverse reads: position 210), and reads with greater than 2 expected errors were removed, using the 'filterandtrim' function in the R package DADA2 (Callahan et al., 2016; DADA2 version 1.18). The DADA2 algorithm was used to resolve amplicon sequence variants (ASVs) at single-nucleotide resolution. Paired-end reads were merged using the 'mergePairs' function, and chimeras were removed using the 'removeBimeraDenovo' function in DADA2. Taxonomy was assigned according to the SILVA version 132 database (Quast et al., 2013) using the RDP naïve Bayseian classifier (Wang et al., 2007). Read count, taxonomic and sample data, were assembled as a single object in the R package phyloseq (McMurdie and Holmes, 2013). ASVs not classified as bacteria were excluded. Samples were rarefied to a depth of 15,973 reads, resulting in the exclusion of two samples (Station 5, 1% PAR, cDNA and gDNA). ASVs which did not account for a minimum of 0.01% of reads in at least one sample were excluded from the total dataset prior to downstream analysis.

2.4 Statistical analyses

The effect of latitude (continuous), light-dependent depth (categorical: 1%, 55%, or 97% PAR), and nucleic acid type (categorical: cDNA or gDNA) on bacterioplankton community composition was tested using a permutational multivariate analysis of variance (PERMANOVA) (Anderson, 2001) based on Bray-Curtis dissimilarity, implemented through the R package vegan (Oksanen et al., 2014). Principal coordinates analysis (PCoA) based on Bray-Curtis dissimilarity was then conducted for cDNA and gDNA communities independently, to visualize the structuring of these communities across latitudes and light-dependent depths. To examine congruence in potentially active and total community structure throughout the Atlantic Ocean, the first two principal coordinates were extracted from each PCoA and subjected to Procrustes analysis (Peres-Neto and Jackson, 2001). Procrustes analysis is a form of multivariate correlation analysis that aims to minimize the sum of squared deviations between samples in two multivariate matrices, through translation, rotation, and dilation of one matrix to match the other. Significance testing was performed using a procrustean randomization test (PROTEST) (Peres-Neto and Jackson, 2001). Procrustes residuals were then extracted and used to examine the effect of latitude and light-dependent depth on the congruence between communities using a generalised additive model (GAM) implemented using the R package mgcv (Wood, 2012) and ANOVA with Tukey's HSD, respectively. Chao1 richness (Chao, 1984) and Pielou's evenness (Pielou, 1966) were calculated as components of alpha diversity. The effect of light-dependent depth and nucleic acid type on richness and evenness was compared using a two-way ANOVA with Tukey's HSD. The relationship between cDNA and gDNA richness and evenness was further examined using a linear model.

As a proxy for *in situ* potential activity (that is, protein synthesis potential), 16S rRNA:16S rRNA gene ratios were calculated by dividing the cDNA read count by corresponding gDNA read count for each ASV in each sample (Bowsher et al., 2019). For a given ASV in each sample, if the cDNA read count was equal to or greater than 1, but the gDNA read count was 0, 1 was added to gDNA read count prior to ratio calculation. Based on 16S rRNA:16S rRNA gene ratios, trends in the potential activity of biogeochemically and ecologically significant bacterioplankton groups, selected to represent a range from known copiotrophs (e.g. *Flavobacteriaceae*) to known oligotrophs (e.g. SAR11) and taxa with understudied life history strategies (e.g. SAR86), are described in detail. All statistical analyses were performed in R (version 3.3.6) (R-Core-Team, 2017). Maximum likelihood trees were constructed in RAxML using the GTRGAMMA model (Stamatakis, 2014), based on 16S ASV sequences.

3 Results and discussion

3.1 Bacterioplankton community structure

cDNA and gDNA derived bacterioplankton community composition was surveyed at sixteen stations across three light-dependent depths throughout the Atlantic Ocean during the Austral spring 2015 (Figure 1A) by sequencing cDNA synthesised from 16S rRNA, and the 16S rRNA gene, respectively. Bacterioplankton community composition significantly differed between nucleic acid types (i.e. cDNA versus gDNA; PERMANOVA; $R^2 = 0.05$, $p < 0.001$), latitudes ($R^2 = 0.13$, $p < 0.001$), and light-dependent depths ($R^2 = 0.09$, $p < 0.001$) throughout the Atlantic Ocean, with no significant interaction between these variables ($p > 0.05$). Independent principal coordinates analyses for cDNA and gDNA communities revealed distinct clustering according to latitude and light-dependent depth (Figures 2A, B). Northern temperate regions (S1–S2), southern temperate regions (S13–S16), the fringe of the North Atlantic Gyre and South Atlantic Gyre (S3–S4 and S11–S12), and the centre of the North Atlantic Gyre and tropical North Atlantic (S5–S10) each formed distinct clusters (Figures 2A, B), reflecting the different environmental regimes of these provinces (Figure 1A). In stratified waters, bacterioplankton communities at 1% PAR were distinct from those at 55% PAR and 97% PAR, and displayed less variation across the transect (S3–S12). In temperate regions where 1% PAR fell within the mixed layer, this trend was less pronounced (S1–S2, S13–S16; Figures 2A, B).

The structure of cDNA and gDNA communities was highly congruent throughout the Atlantic Ocean (PROTEST; $r = 0.98$, $p < 0.001$; Figure 2C). Procrustes residuals were extracted to examine the effect of latitude and light-dependent depth on congruence

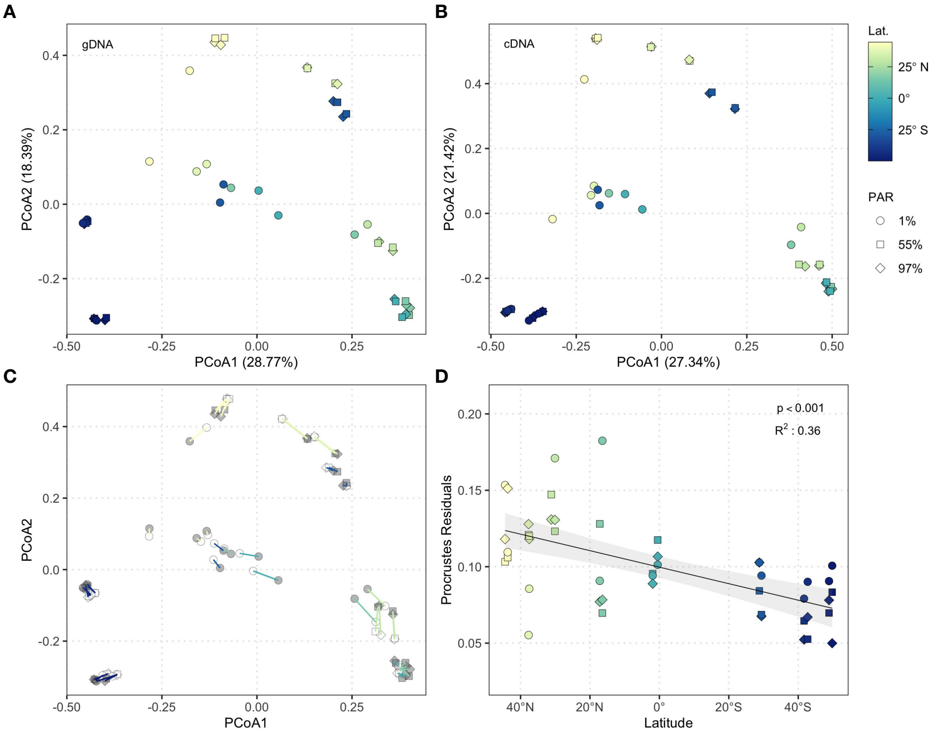

FIGURE 2
Principle coordinates analysis of **(A)** gDNA (n = 47) and **(B)** cDNA (n = 47) community structure based on Bray-Curtis dissimilarity. Shapes represent light-dependent depth (squares = 97% PAR, diamonds = 55% PAR, circles = 1% PAR), colours indicate latitude. **(C)** Procrustes superimposition of cDNA data onto gDNA data. Segments connect pairs of cDNA and gDNA samples and represent Procrustes residual values. Point colours indicate nucleic acid (grey: gDNA, white: cDNA), segment colours correspond to latitude. **(D)** Generalised additive model of Procrustes residuals against latitude (n = 47). Shading represents 95% confidence interval.

between cDNA and gDNA community structure, revealing a significant linear decrease from temperate Northern hemisphere latitudes to temperate Southern hemisphere latitudes (GAM; adjusted $R^2 = 0.36$, $p < 0.001$; Figure 2D). Congruence between cDNA and gDNA derived communities was greatest in the productive South Subtropical Convergence and Southwest Atlantic Shelves (S13–S16; Figure 1A). These data align with a survey of the Indian sector of the Southern Ocean, which suggested that cDNA and gDNA bacterioplankton communities display similar structuring in highly productive waters (Liu et al., 2019).

Comparisons of cDNA and gDNA bacterioplankton biogeography across basin scales are scarce. However, distinct biogeographic patterns in cDNA and gDNA bacterioplankton communities have been shown on regional scales in the South China Sea, where cDNA bacterioplankton communities were structured predominantly by prevailing environmental conditions, whilst gDNA communities were comparatively more influenced by water mass identity (Zhang et al., 2014). Thus, differences in the relative importance of environmental and spatial processes at a regional scale underpinned the distinct biogeography of cDNA and gDNA bacterioplankton communities. The congruence between cDNA and gDNA bacterioplankton communities demonstrated in this study across the Atlantic basin indicates that similar processes structure cDNA and gDNA bacterioplankton communities across oceanic scales (Supplementary Figure 2), suggesting that the relationship between these communities may be scale-dependent in the marine environment. Our data show that the structure of both cDNA and gDNA bacterioplankton communities reflects the oceanographic province from which samples were collected (Reygondeau et al., 2013).

3.2 Bacterioplankton richness and evenness

The overall richness of gDNA communities was greater than of cDNA communities (ANOVA; $p < 0.005$; Supplementary Figure 3), and pairwise comparisons revealed that gDNA community richness and evenness were greater than cDNA community richness evenness at each light-dependent depth (Tukey's HSD; $p < 0.05$; Supplementary Figure3). cDNA communities consisted of a subset of the gDNA community, dominated by a small cohort of ASVs with high potential activity that are apparently able to capitalize on prevailing environmental conditions. Both richness and evenness were greater at 1% PAR, which closely tracked the position of the deep chlorophyll maximum over the transect (Figure 1D), than at 55% or 97% PAR (Tukey's HSD; $p < 0.001$).

cDNA and gDNA community richness were significantly related (linear model; slope = 0.50, $R^2 = 0.56$, $p < 0.001$; Figure 3A) but displayed a shallow slope indicating that as gDNA community richness increased, the disparity between cDNA and gDNA community richness also increased. cDNA and gDNA

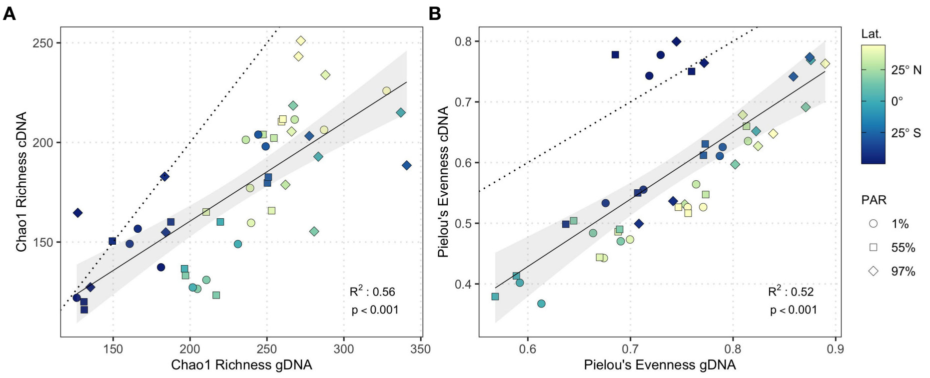

FIGURE 3
Linear model of **(A)** Chao1 Richness and **(B)** Pielou's evenness from gDNA (n = 47) and cDNA (n = 47) samples. Solid line represents linear model fit, shading represents 95% confidence interval. Dotted guideline represents 1:1 cDNA:gDNA ratio. Shapes represent light-dependent depth.

community evenness displayed a stronger relationship (linear model; slope = 1.11, R^2 = 0.52, $p < 0.001$; Figure 3B) including a slope of ~1. cDNA and gDNA community richness and evenness converged in nutrient-rich waters of the Southwest Atlantic Shelves where large phytoplankton dominate primary production (Marañón et al., 2000; Marañón et al., 2001; Tilstone et al., 2017). This convergence was driven by the high relative abundance and potential activity of copiotrophic bacterioplankton (see below), which likely capitalize on phytoplankton-derived organic carbon and nutrient availability.

3.3 Potential activity of bacterioplankton groups and populations

The potential activity and relative abundance of selected biogeochemically and ecologically important bacterioplankton groups was structured by both latitude and light-dependent depth (Figure 4). An inverse relationship between the potential activity of the cyanobacteria *Prochlorococcus* and *Synechococcus* was evident throughout the transect. *Prochlorococcus* displayed high potential activity north of the South Subtropical Convergence, whilst *Synechococcus* displayed high potential activity at the South Subtropical Convergence and Southwest Atlantic Shelves (S13–S16), aligning with their characteristically distinct thermal niches (Flombaum et al., 2013). Interestingly, the potential activity of *Synechococcus* was highest at the Southwest Atlantic Shelves despite low relative abundance, which may suggest that local environmental conditions are optimal for the growth of *Synechococcus*, but that top-down controls, such as viral infection (Suttle, 2007) and grazing (Apple et al., 2011), constrain relative abundance. However, these data must be interpreted carefully as the relationship between growth rate and cellular 16S rRNA content is non-linear in *Synechococcus* (Binder and Liu, 1998; Worden and Binder, 2003).

The filamentous diazotrophic cyanobacteria *Trichodesmium* displayed high potential activity in the tropical North Atlantic (S7–S8; Figure 4), corresponding to areas of known iron supply from atmospheric dust deposition (Fernández et al., 2010). These data underscore the crucial role that *Trichodesmium* play in nitrogen fixation in this region and suggest that they may contribute disproportionately to biogeochemical function relative to their abundance. Conversely, the unicellular diazotroph UCYN-A (*Candidatus Atelocyanobacterium thalassa*) were restricted to surface water masses, and displayed high potential activity in the South Atlantic Subtropical Gyre (S11–S12) (Figure 4), illustrating latitudinal switching in the potential activity of the two major nitrogen fixing cyanobacteria in the Atlantic Ocean.

The potential activity of NS4, NS5, NS9, and NS10 marine group *Flavobacteria* was enhanced at the Southwest Atlantic Shelves (S15–S16; Figure 4) and was related to nutrient availability (Supplementary Figure 4). The observed pattern of enhanced potential activity in nutrient-rich waters where large phytoplankton dominate primary production likely reflects the copiotrophic life history strategy of these taxa, which possess physiological adaptations to capitalize on the availability of phytoplankton-derived organic carbon (Buchan et al., 2014) and are frequently associated with diatom blooms (Teeling et al., 2012; Teeling et al., 2016). Possible niche partitioning was indicated between phylogenetically coherent clusters of active NS4 and NS5 marine group *Flavobacteria* ASVs, aligning with evidence of ecologically distinct units within these groups (Díez-Vives et al., 2019). ASVs displaying the highest potential activity at the Southwest Atlantic Shelves were largely absent from subtropical and tropical latitudes. In contrast, ASVs distributed throughout the subtropical and tropical Atlantic were absent at the Southwest Atlantic Shelves (Figure 5A). These findings indicate that the cosmopolitan distribution of NS4 and NS5 Marine Groups throughout the Atlantic Ocean (Figure 4) is underpinned by ecological niche partitioning between specific ASVs (Figure 5A) and highlights the value of detailed phylogenetic resolution when investigating bacterioplankton ecology.

The ubiquitous SAR86 are proteorhodopsin-containing *Gammaproteobacteria* with streamlined genomes that lack biosynthesis pathways for key vitamins, cofactors, and amino acids (Dupont et al., 2012). As SAR86 have only relatively recently been cultivated, significant questions remain about their ecology and life history strategies. We show that SAR86 are

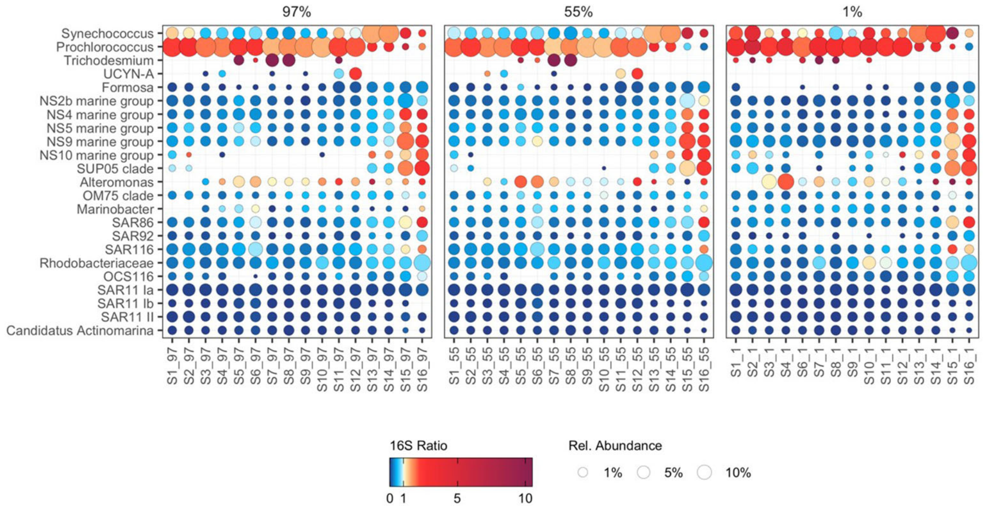

FIGURE 4

The potential activity and abundance of major bacterioplankton groups. Point size represents the average relative abundance in cDNA and gDNA derived bacterioplankton communities. Colours represent 16S rRNA:16S rRNA gene ratios, a proxy for protein synthesis potential (potential activity). 16S rRNA:16S rRNA gene ratios greater than 10 are represented by a dark plum colour (e.g. in *Trichodesmium*).

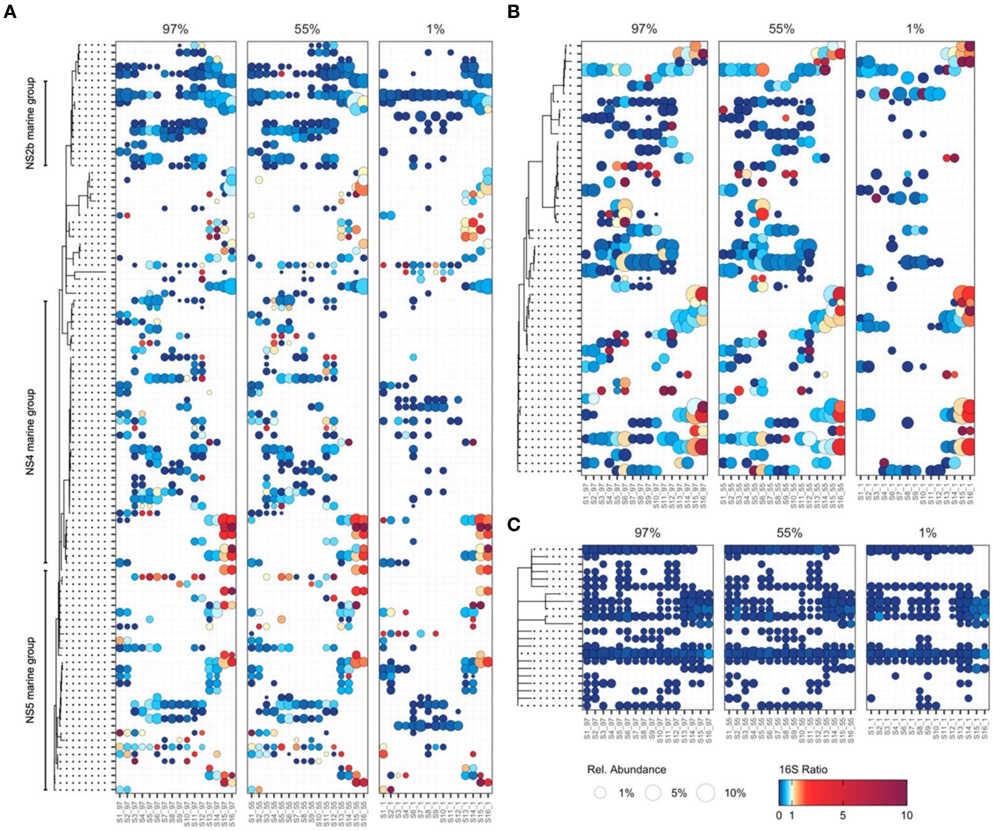

FIGURE 5

The potential activity and abundance of bacterioplankton ASVs at single-nucleotide resolution within **(A)** *Flavobacteriaceae*, **(B)** SAR86, and **(C)** SAR11 Ia. Point size represents the average relative abundance in cDNA and gDNA derived bacterioplankton communities. Colours represent 16S rRNA:16S rRNA gene ratios, a proxy for protein synthesis potential (potential activity). 16S rRNA:16S rRNA gene ratios greater than 10 are represented by a dark plum colour.

cosmopolitan in their distribution throughout the Atlantic Ocean yet display enhanced potential activity at the Southwest Atlantic Shelves (Figure 4). Group-level patterns in the potential activity of SAR86 resemble those of typical copiotrophic bacterioplankton, suggesting that SAR86 are capable of substantially upregulating potential activity in response to resource availability. Recent evidence indicates that SAR86 can be subdivided into ecotypes based on functional gene content, and that these ecotypes possess distinct biogeographic distributions (Hoarfrost et al., 2020). In this study, niche partitioning was indicated between SAR86 ASVs, which were typically constrained to either tropical and subtropical latitudes, or temperate latitudes (Figure 5B). A cohort of SAR86 ASVs displayed enhanced potential activity in the Southwest Atlantic Shelves, suggesting that they may play an important role in processing phytoplankton-derived organic carbon. Many SAR86 ASVs were restricted to surface water masses (97% and 55% PAR) in oligotrophic tropical and subtropical regions (Figure 5B). We speculate that this trend may relate to the role of proteorhodopsins, a light-driven proton pump, which contributes to cellular energy budget of SAR86 in these regions (Beja et al., 2000; Sabehi et al., 2004). Single-cell and metagenomic evidence indicates substantial variation in organic carbon utilization capabilities and proteorhodopsin content within SAR86 (Hoarfrost et al., 2020), suggesting that a wide array of life history strategies may coexist within the group. Here, we provide ocean scale insights into the potential activity of SAR86, revealing distinct clusters putatively adapted to oligotrophic surface waters and nutrient-rich waters, respectively (Figure 5B).

The *Gammaproteobacteria* clade SUP05 play an important role in open ocean sulfur metabolism (Moran and Durham, 2019), degrading algal-derived dimethylsulphoniopropionate (DMSP), and utilising energy generated from sulfur oxidation to drive autotrophic carbon fixation (Walsh et al., 2009; Spietz et al., 2019). Heterotrophic carbon metabolism has also been demonstrated in the SUP05 clade member *Thioglobus singularis* strain PS1, indicative of their ability to utilise diatom cell lysate to support heterotrophic growth (Spietz et al., 2019). To date, most studies of SUP05 are related to the deep ocean and oxygen minimum zones (Walsh et al., 2009; Shah et al., 2019), though viable SUP05 cells have been cultivated from surface waters (Marshall and Morris, 2013). Here we show that SUP05 display high potential activity at the Southwest Atlantic Shelves (Figure 4) where large phytoplankton dominate primary production (Marañón et al., 2000; Marañón et al., 2001; Tilstone et al., 2017). The high potential activity of SUP05 may be underpinned by the production of DMSP and associated organic sulfur compounds by diatoms and other large phytoplankton. Alternatively, the high potential activity of SUP05 may be resultant of heterotrophic growth fuelled by phytoplankton primary production. Regardless of mechanism, these data suggest that SUP05 play an important role in biogeochemical cycling during phytoplankton blooms in these regions, highlighting the need for further investigation to elucidate the role of this enigmatic group.

SAR11 clades Ia, Ib, and II generally displayed uniform relative abundance and low potential activity throughout the Atlantic Ocean (Figure 4). Similar uniformity in activity and abundance of SAR11 has been demonstrated across the Atlantic Ocean using flow-cytometry and ^{35}S-methionine uptake (Mary et al., 2006). These trends may emerge from the generally limited ability of SAR11 to respond to transient increases in substrate availability, and their survival through scavenging widespread labile organic compounds and nutrients present at low background concentrations (Cottrell and Kirchman, 2016; Giovannoni, 2017). SAR11 Ia ASVs displayed distinct distribution patterns, despite minimal variability in potential activity (Figure 5C). Interestingly, we identified a minor increase in the potential activity of a small cluster of SAR11 Ia ASVs at the Southwest Atlantic Shelves (Figure 5C), suggesting that these populations possess some capacity for metabolic upregulation. We speculate that this may be the result of differences between carbon-source utilization pathways in SAR11 genomes (Schwalbach et al., 2010), which may elicit subtle responses to phytoplankton-derived organic carbon for some specialised ASVs. Some SAR11 populations can be particle-associated and therefore may occupy alternative niches other than the generalized archetypical free-living oligotroph (Yeh and Fuhrman, 2022). Our findings provide additional evidence supporting the paradigm that SAR11 generally maintain a consistent state of low metabolic activity across oceanic scales, but some SAR11 have the ability to respond to changes in environmental conditions or substrate availability (Brown et al., 2012; Bolaños et al., 2021; Bolaños et al., 2022). Given that the 16S rRNA gene has limited taxonomic resolution for SAR 11 (Eren et al., 2013) we should be cautious in interpretation of these data and complementary approaches to assess SAR11 diversity should also considered.

4 Summary

This study provides an investigation of the relationship between cDNA and gDNA derived bacterioplankton communities on an oceanic scale. We showed congruence in cDNA and gDNA community structure throughout the Atlantic Ocean, indicating that similar processes structure these communities across oceanic scales. We used 16S rRNA:16S rRNA gene ratios to explore patterns in the potential activity of bacterioplankton groups, from which cyanobacteria, copiotrophic, and oligotrophic bacterioplankton could be broadly distinguished. Furthermore, we provide ASV-level investigation of potential activity in the marine environment, demonstrating possible niche partitioning of *Flavobacteria* and SAR86 ASVs that underlie the cosmopolitan distribution of these taxa. While potential activity derived through 16S rRNA:16S rRNA gene ratios are indirect indicators of metabolic activity, they are possible proxies of protein synthesis potential providing important ecological insights at detailed phylogenetic resolution which can be used to guide the development of hypotheses for further investigation (Blazewicz et al., 2013). Integrating 16S rRNA:16S rRNA gene ratios with other molecular tools such as metatranscriptomics, which offers insights into the transcription of specific genes within a community but does not directly indicate translation, and metaproteomics, which offers insights into the realised expression of proteins but do not directly indicate the activity of these proteins, are clear avenues for developing a more holistic understanding of bacterioplankton metabolic activity on the community level. Combined, the findings of this study shed light on the active microbiome of the Atlantic Ocean and provide insights towards the ecology and life history strategies of biogeochemically and ecologically significant bacterioplankton.

Data availability statement

The datasets presented in this study can be found in online repositories. The names of the repository/repositories and accession number(s) can be found below: https://www.ebi.ac.uk/ena/browser/view/PRJEB38834.

Author contributions

KB and MC conceived and designed the study. KB conducted the fieldwork, seawater sample processing, DNA/RNA extraction and initial data analysis. RA performed further data and statistical analysis. All authors contributed to the interpretation of the results. RA wrote the first draft of the manuscript working with MC and KB. All authors contributed to manuscript revision, read, and approved the submitted version. All authors contributed to the article and approved the submitted version.

Funding

KB was supported by the UKRI Natural Environment Research Council (NERC) Environment East (EnvEast) Doctoral Training Partnership (grant number NE/L002582/1). Sampling was supported by NERC National Capability funding for Atlantic Meridional Transect (AMT) Programme to Plymouth Marine Laboratory. AMT is funded by the NERC through its National Capability Long-term Single Centre Science Programme, Climate Linked Atlantic Sector Science (grant number NE/R015953/1).

Acknowledgments

We are indebted to the all the scientists, the captain and crew of the *RRS James Clark Ross* AMT25 who helped make this work happen, especially those who contributed metadata (nutrients, etc.) used in this study and helped with sampling.

Conflict of interest

The authors declare that the research was conducted in the absence of any commercial or financial relationships that could be construed as a potential conflict of interest.

Publisher's note

Supplementary material

The Supplementary Material for this article can be found online at: https://www.frontiersin.org/articles/10.3389/fmars.2023.1241333/full#supplementary-material

SUPPLEMENTARY FIGURE 1
Map of 16 stations sampled during the AMT25 latitudinal transect of the Atlantic Ocean during the Austral spring of 2015 with Longhurst oceanographical spatial codes (NADR, North Atlantic Drift; NASTE, Northeast Atlantic subtropical gyral; NASTW, Northwest Atlantic subtropical gyral; NATR, North Atlantic tropical gyral; ETRA, Eastern Tropical Atlantic; SATL, South Atlantic gyral; SSTC, South subtropical convergence; FKLD, Southwest Atlantic shelves).

SUPPLEMENTARY FIGURE 2
Canonical correspondence analysis (CCA) of **(A)** gDNA (n = 47) and **(B)** cDNA (n = 47) derived bacterioplankton community composition. Vectors represent statistically significant environmental variables ($p < 0.01$).

SUPPLEMENTARY FIGURE 3
(A) Chao1 Richness and **(B)** Pielou's evenness at each light-dependent depth from gDNA (n = 47; white) and cDNA (n = 47; grey) samples. Crossbar represents median value.

SUPPLEMENTARY FIGURE 4
The relative activity (16S ratio) of copiotrophic (top row), oligotrophic (middle row) and understudied (bottom row) ASVs against nitrate/nitrite concentration (n = 38). Black lines indicate significant linear model fits ($p < 0.05$), shaded areas represent 95% confidence intervals. Red guidelines indicate threshold above which ASVs are considered active (16S ratio ≥ 1).

References

Alonso-Sáez, L., Sánchez, O., and Gasol, J. M. (2012). Bacterial uptake of low molecular weight organics in the subtropical Atlantic: Are major phylogenetic groups functionally different? *Limnology Oceanography* 57, 798–808. doi: 10.4319/lo.2012.57.3.0798

Anderson, M. J. (2001). A new method for non-parametric multivariate analysis of variance. *Austral Ecology* 26 (1), 32–46. doi: 10.1111/j.1442-9993.2001.01070.pp.x

Apple, J. K., Strom, S. L., Palenik, B., and Brahamsha, B. (2011). Variability in protist grazing and growth on different marine Synechococcus isolates. *Appl. Environ. Microbiol.* 77, 3074–3084. doi: 10.1128/AEM.02241-10

Azam, F., and Malfatti, F. (2007). Microbial structuring of marine ecosystems. *Nat. Rev. Micro* 5, 782–791. doi: 10.1038/nrmicro1747

Beja, O., Aravind, L., Koonin, E. V., Suzuki, M. T., Hadd, A., Nguyen, L. P., et al. (2000). Bacterial rhodopsin: evidence for a new type of phototrophy in the sea. *Science* 289, 1902–1906. doi: 10.1126/science.289.5486.1902

Binder, B. J., and Liu, Y. C. (1998). Growth rate regulation of rRNA content of a marine *Synechococcus* (Cyanobacterium) strain. *Appl. Environ. Microbiol.* 64, 3346–3351. doi: 10.1128/AEM.64.9.3346-3351.1998

Blazewicz, S. J., Barnard, R. L., Daly, R. A., and Firestone, M. K. (2013). Evaluating rRNA as an indicator of microbial activity in environmental communities: limitations and uses. *ISME J.* 7, 2061–2068. doi: 10.1038/ismej.2013.102

Bolaños, L. M., Choi, C. J., Worden, A. Z., Baetge, N., Carlson, C. A., and Giovannoni, S. (2021). Seasonality of the microbial community composition in the north atlantic. *Front. Mar. Sci.* 8. doi: 10.3389/fmars.2021.624164

Bolaños, L. M., Tait, K., Somerfield, P. J., Parsons, R. J., Giovannoni, S. J., Smyth, T., et al. (2022). Influence of short and long term processes on SAR11 communities in open ocean and coastal systems. *ISME Commun.* 2, 116. doi: 10.1038/s43705-022-00198-1

Bowsher, A. W., Kearns, P. J., and Shade, A. (2019). 16S rRNA/rRNA gene ratios and cell activity staining reveal consistent patterns of microbial activity in plant-associated soil. *mSystems* 4, e00003–19. doi: 10.1128/msystems.00003-19

Brown, M. V., Lauro, F. M., Demaere, M. Z., Muir, L., Wilkins, D., Thomas, T., et al. (2012). Global biogeography of SAR11 marine bacteria. *Mol. Syst. Biol.* 8, 595–595. doi: 10.1038/msb.2012.28

Buchan, A., Lecleir, G. R., Gulvik, C. A., and González, J. M. (2014). Master recyclers: features and functions of bacteria associated with phytoplankton blooms. *Nat. Rev. Microbiol.* 12, 686–698. doi: 10.1038/nrmicro3326

Callahan, B. J., McMurdie, P. J., Rosen, M. J., Han, A. W., Johnson, A. J. A., and Holmes, S. P. (2016). DADA2: High-resolution sample inference from Illumina amplicon data. *Nature Methods* 13, 581–583. doi: 10.1038/nmeth.3869

Campbell, B. J., Yu, L., Heidelberg, J. F., and Kirchman, D. L. (2011). Activity of abundant and rare bacteria in a coastal ocean. *Proc. Natl. Acad. Sci. U.S.A.* 108, 12776–12781. doi: 10.1073/pnas.1101405108

Chambon, P., Deutscher, M. P., and Kornberg, A. (1968). Biochemical studies of bacterial sporulation and germination. X. Ribosomes and nucleic acids of vegetative cells and spores of *Bacillus megaterium*. *J. Biol. Chem.* 243, 5110–5116. doi: 10.1016/S0021-9258(18)91998-8

Chao, A. (1984). Nonparametric estimation of the number of classes in a population. *Scandinavian J. Stat* 11, 265–270. Available at: https://www.jstor.org/stable/4615964.

Comeau, A. M., Douglas, G. M., and Langille, M. G. (2017). Microbiome helper: a custom and streamlined workflow for microbiome research. *mSystems* 2, e00127–16. doi: 10.1128/mSystems.00127-16

Cottrell, M. T., and Kirchman, D. L. (2016). Transcriptional control in marine copiotrophic and oligotrophic bacteria with streamlined genomes. *Appl. Environ. Microbiol.* 82, 6010–6018. doi: 10.1128/AEM.01299-16

Del Giorgio, P. A., and Scarborough, G. (1995). Increase in the proportion of metabolically active bacteria along gradients of enrichment in freshwater and marine plankton: implications for estimates of bacterial growth and production rates. *J. Plankton Res.* 17, 1905–1924. doi: 10.1093/plankt/17.10.1905

Díez-Vives, C., Nielsen, S., Sánchez, P., Palenzuela, O., Ferrera, I., Sebastián, M., et al. (2019). Delineation of ecologically distinct units of marine Bacteroidetes in the Northwestern Mediterranean Sea. *Mol. Ecol.* 28, 2846–2859. doi: 10.1111/mec.15068

Dupont, C. L., Rusch, D. B., Yooseph, S., Lombardo, M. J., Richter, R. A., Valas, R., et al. (2012). Genomic insights to SAR86, an abundant and uncultivated marine bacterial lineage. *ISME J.* 6, 1186–1199. doi: 10.1038/ismej.2011.189

Eren, A. M., Maignien, L., Sul, W. J., Murphy, L. G., Grim, S. L., Morrison, H. G., et al. (2013). Oligotyping: differentiating between closely related microbial taxa using 16S rRNA gene data. *Methods Ecol. Evol.* 4, 1111–1119. doi: 10.1111/2041-210X.12114

Falkowski, P. G., Fenchel, T., and Delong, E. F. (2008). The microbial engines that drive Earth's biogeochemical cycles. *Science* 320, 1034–1039. doi: 10.1126/science.1153213

Fernández, A., Mouriño-Carballido, B., Bode, A., Varela, M., and Marañón, E. (2010). Latitudinal distribution of *Trichodesmium* spp. and N_2 fixation in the Atlantic Ocean. *Biogeosciences* 7, 3167–3176. doi: 10.5194/bg-7-3167-2010

Field, C. B., Behrenfeld, M. J., Randerson, J. T., and Falkowski, P. (1998). Primary production of the biosphere: integrating terrestrial and oceanic components. *Science* 281, 237–240. doi: 10.1126/science.281.5374.237

Flombaum, P., Gallegos, J. L., Gordillo, R. A., Rincon, J., Zabala, L. L., Jiao, N., et al. (2013). Present and future global distributions of the marine Cyanobacteria *Prochlorococcus* and *Synechococcus*. *Proc. Natl. Acad. Sci. U.S.A.* 110, 9824–9829. doi: 10.1073/pnas.1307701110

García-Martín, E. E., Aranguren-Gassis, M., Hartmann, M., Zubkov, M. V., and Serret, P. (2017). Contribution of bacterial respiration to plankton respiration from 50° N to 44°S in the Atlantic Ocean. *Prog. Oceanography* 158, 99–108. doi: 10.1016/j.pocean.2016.11.006

Giovannoni, S. J. (2017). SAR11 bacteria: the most abundant plankton in the oceans. *Annu. Rev. Mar. Sci.* 9, 231–255. doi: 10.1146/annurev-marine-010814-015934

Hoarfrost, A., Nayfach, S., Ladau, J., Yooseph, S., Arnosti, C., Dupont, C. L., et al. (2020). Global ecotypes in the ubiquitous marine clade SAR86. *ISME J.* 14, 178–188. doi: 10.1038/s41396-019-0516-7

Hoppe, H. G., Gocke, K., Koppe, R., and Begler, C. (2002). Bacterial growth and primary production along a north-south transect of the Atlantic Ocean. *Nature* 416, 168–171. doi: 10.1038/416168a

Hunt, D. E., Lin, Y., Church, M. J., Karl, D. M., Tringe, S. G., Izzo, L. K., et al. (2013). Relationship between abundance and specific activity of bacterioplankton in open ocean surface waters. *Appl. Environ. Microbiol.* 79, 177–184. doi: 10.1128/AEM.02155-12

Hydes, D., Aoyama, M., Aminot, A., Bakker, K., Becker, S., Coverly, S., et al. (2010). Determination of dissolved nutrients (N, P, Si) in seawater with high precision and inter-comparability using gas-segmented continuous flow analysers. In *The GO-SHIP repeat hydrography manual : a collection of expert reports and guidelines*. IOCCP Report No 14, ICPO Publication Series No. 134, version 1, 2010 (UNESCO/IOC). Available at: https://archimer.ifremer.fr/doc/00020/13141/.

Jones, S. E., and Lennon, J. T. (2010). Dormancy contributes to the maintenance of microbial diversity. *Proc. Natl. Acad. Sci. U.S.A.* 107, 5881–5886. doi: 10.1073/pnas.0912765107

Kazamia, E., Helliwell, K. E., Purton, S., and Smith, A. G. (2016). How mutualisms arise in phytoplankton communities: building eco-evolutionary principles for aquatic microbes. *Ecol. Lett.* 19, 810–822. doi: 10.1111/ele.12615

Kemp, P. F., Lee, S., and Laroche, J. (1993). Estimating the growth rate of slowly growing marine bacteria from RNA content. *Appl. Environ. Microbiol.* 59, 2594–2601. doi: 10.1128/aem.59.8.2594-2601.1993

Kerkhof, L., and Kemp, P. (1999). Small ribosomal RNA content in marine *Proteobacteria* during non-steady-state growth. *FEMS Microbiol. Ecol.* 30, 253–260. doi: 10.1111/j.1574-6941.1999.tb00653.x

Kerkhof, L., and Ward, B. B. (1993). Comparison of nucleic acid hybridization and fluorometry for measurement of the relationship between RNA/DNA ratio and growth rate in a marine bacterium. *Appl. Environ. Microbiol.* 59, 1303–1309. doi: 10.1128/aem.59.5.1303-1309.1993

Landschützer, P., Gruber, N., Bakker, D. C. E., and Schuster, U. (2014). Recent variability of the global ocean carbon sink. *Global Biogeochemical Cycles* 28, 927–949. doi: 10.1002/2014GB004853

Lankiewicz, T. S., Cottrell, M. T., and Kirchman, D. L. (2016). Growth rates and rRNA content of four marine bacteria in pure cultures and in the Delaware estuary. *ISME J.* 10, 823–832. doi: 10.1038/ismej.2015.156

Lennon, J. T., and Jones, S. E. (2011). Microbial seed banks: the ecological and evolutionary implications of dormancy. *Nat. Rev. Microbiol.* 9, 119–130. doi: 10.1038/nrmicro2504

Lin, Y., Gazsi, K., Lance, V. P., Larkin, A. A., Chandler, J. W., Zinser, E. R., et al. (2013). *In situ* activity of a dominant *Prochlorococcus* ecotype (eHL-II) from rRNA content and cell size. *Environ. Microbiol.* 15, 2736–2747. doi: 10.1111/1462-2920.12135

Liu, Y., Debeljak, P., Rembauville, M., Blain, S., and Obernosterer, I. (2019). Diatoms shape the biogeography of heterotrophic prokaryotes in early spring in the Southern Ocean. *Environ. Microbiol.* 21, 1452–1465. doi: 10.1111/1462-2920.14579

Logares, R., Deutschmann, I. M., Junger, P. C., Giner, C. R., Krabberød, A. K., Schmidt, T. S. B., et al. (2020). Disentangling the mechanisms shaping the surface ocean microbiota. *Microbiome* 8, 55. doi: 10.1186/s40168-020-00827-8

Longnecker, K., Lomas, M. W., and Van Mooy, B. A. (2010). Abundance and diversity of heterotrophic bacterial cells assimilating phosphate in the subtropical North Atlantic Ocean. *Environ. Microbiol.* 12, 2773–2782. doi: 10.1111/j.1462-2920.2010.02247.x

Marañón, E., Holligan, P. M., Barciela, R., González, N., Mouriño, B., Pazó, M. J., et al. (2001). Patterns of phytoplankton size structure and productivity in contrasting open-ocean environments. *Mar. Ecol. Prog. Ser.* 216, 43–56. doi: 10.3354/meps216043

Marañón, E., Holligan, P. M., Varela, M., Mouriño, B., and Bale, A. J. (2000). Basin-scale variability of phytoplankton biomass, production and growth in the Atlantic Ocean. *Deep Sea Res. Part I: Oceanographic Res. Papers* 47, 825–857. doi: 10.1016/S0967-0637(99)00087-4

Marshall, K. T., and Morris, R. M. (2013). Isolation of an aerobic sulfur oxidizer from the SUP05/Arctic96BD-19 clade. *ISME J.* 7, 452–455. doi: 10.1038/ismej.2012.78

Mary, I., Heywood, J., Fuchs, B., Amann, R., Tarran, G., Burkill, P., et al. (2006). SAR11 dominance among metabolically active low nucleic acid bacterioplankton in surface waters along an Atlantic meridional transect. *Aquat. Microbial Ecol.* 45, 107–113. doi: 10.3354/ame045107

McMurdie, P. J., and Holmes, S. (2013). phyloseq: an R package for reproducible interactive analysis and graphics of microbiome census data. *PloS One* 8, e61217. doi: 10.1371/journal.pone.0061217

Milici, M., Tomasch, J., Wos-Oxley, M. L., Decelle, J., Jáuregui, R., Wang, H., et al. (2016a). Bacterioplankton biogeography of the Atlantic Ocean: a case study of the distance-decay relationship. *Front. Microbiol.* 7, 590. doi: 10.3389/fmicb.2016.00590

Milici, M., Tomasch, J., Wos-Oxley, M. L., Wang, H., Jáuregui, R., Camarinha-Silva, A., et al. (2016b). Low diversity of planktonic bacteria in the tropical ocean. *Sci. Rep.* 6, 19054. doi: 10.1038/srep19054

Moran, M. A., and Durham, B. P. (2019). Sulfur metabolites in the pelagic ocean. *Nat. Rev. Microbiol.* 17, 665–678. doi: 10.1038/s41579-019-0250-1

Needham, D. M., Sachdeva, R., and Fuhrman, J. A. (2017). Ecological dynamics and co-occurrence among marine phytoplankton, bacteria and myoviruses shows microdiversity matters. *ISME J.* 11, 1614–1629. doi: 10.1038/ismej.2017.29

Oksanen, J., Blanchet, F. G., Kindt, R., Legendre, P., Minchin, P. R., O'Hara, R. B., et al. (2014). Vegan: Community Ecology Package. R Package Version 2.2-0. Available at: http://CRAN.Rproject.org/package=vegan.

Parada, A. E., Needham, D. M., and Fuhrman, J. A. (2016). Every base matters: assessing small subunit rRNA primers for marine microbiomes with mock communities, time series and global field samples. *Environ. Microbiol.* 18, 1403–1414. doi: 10.1111/1462-2920.13023

Peres-Neto, P. R., and Jackson, D. A. (2001). How well do multivariate data sets match? The advantages of a Procrustean superimposition approach over the Mantel test. *Oecologia* 129, 169–178. doi: 10.1007/s004420100720

Pielou, E. C. (1966). The measurement of diversity in different types of biological collections. *J. Theor. Biol.* 13, 131–144. doi: 10.1016/0022-5193(66)90013-0

Quast, C., Pruesse, E., Yilmaz, P., Gerken, J., Schweer, T., Yarza, P., et al. (2013). The SILVA ribosomal RNA gene database project: improved data processing and web-based tools. *Nucleic Acids Res.* 41, D590–D596. doi: 10.1093/nar/gks1219

R-Core-Team (2017). *R: A language and environment for statistical computing* (Vienna, Austria: R Foundation for Statistical Computing). Available at: https://www.R-project.org/.

Reintjes, G., Arnosti, C., Fuchs, B., and Amann, R. (2019). Selfish, sharing and scavenging bacteria in the Atlantic Ocean: a biogeographical study of bacterial substrate utilisation. *ISME J.* 13, 1119–1132. doi: 10.1038/s41396-018-0326-3

Reygondeau, G., Longhurst, A., Martinez, E., Beaugrand, G., Antoine, D., and Maury, O. (2013). Dynamic biogeochemical provinces in the global ocean. *Global Biogeochemical Cycles* 27, 1046–1058. doi: 10.1002/gbc.20089

Sabehi, G., Béjà, O., Suzuki, M. T., Preston, C. M., and Delong, E. F. (2004). Different SAR86 subgroups harbour divergent proteorhodopsins. *Environ. Microbiol.* 6, 903–910. doi: 10.1111/j.1462-2920.2004.00676.x

Salter, I., Galand, P. E., Fagervold, S. K., Lebaron, P., Obernosterer, I., Oliver, M. J., et al. (2015). Seasonal dynamics of active SAR11 ecotypes in the oligotrophic Northwest Mediterranean Sea. *ISME J.* 9, 347–360. doi: 10.1038/ismej.2014.129

Schwalbach, M. S., Tripp, H. J., Steindler, L., Smith, D. P., and Giovannoni, S. J. (2010). The presence of the glycolysis operon in SAR11 genomes is positively correlated with ocean productivity. *Environ. Microbiol.* 12, 490–500. doi: 10.1111/j.1462-2920.2009.02092.x

Shah, V., Zhao, X., Lundeen, R. A., Ingalls, A. E., Nicastro, D., and Morris, R. M. (2019). Morphological plasticity in a sulfur-oxidizing marine bacterium from the SUP05 clade enhances dark carbon fixation. *mBio* 10, e00216–19. doi: 10.1128/mbio.00216-19

Spietz, R. L., Lundeen, R. A., Zhao, X., Nicastro, D., Ingalls, A. E., and Morris, R. M. (2019). Heterotrophic carbon metabolism and energy acquisition in Candidatus *Thioglobus singularis* strain PS1, a member of the SUP05 clade of marine *Gammaproteobacteria*. *Environ. Microbiol.* 21, 2391–2401. doi: 10.1111/1462-2920.14623

Stamatakis, A. (2014). RAxML version 8: a tool for phylogenetic analysis and post-analysis of large phylogenies. *Bioinformatics* 30, 1312–1313. doi: 10.1093/bioinformatics/btu033

Sukenik, A., Kaplan-Levy, R. N., Welch, J. M., and Post, A. F. (2012). Massive multiplication of genome and ribosomes in dormant cells (akinetes) of *Aphanizomenon ovalisporum* (Cyanobacteria). *ISME J.* 6, 670–679. doi: 10.1038/ismej.2011.128

Sunagawa, S., Coelho, L. P., Chaffron, S., Kultima, J. R., Labadie, K., Salazar, G., et al. (2015). Structure and function of the global ocean microbiome. *Science* 348 (6237). doi: 10.1126/science.1261359

Suttle, C. A. (2007). Marine viruses—major players in the global ecosystem. *Nat. Rev. Microbiol.* 5, 801–812. doi: 10.1038/nrmicro1750

Suzuki, M. T., Taylor, L. T., and Delong, E. F. (2000). Quantitative Analysis of Small-Subunit rRNA Genes in Mixed Microbial Populations via 5′-Nuclease Assays. *Appl. Environ. Microbiol.* 66, 4605–4614. doi: 10.1128/AEM.66.11.4605-4614.2000

Taylor, J. D., Bird, K. E., Widdicome, C. E., and Cunliffe, M. (2018). Active bacterioplankton community response to dissolved 'free' deoxyribonucleic acid (dDNA) in surface coastal marine waters. *FEMS Microbiol. Ecol.* 94, fiy132–fiy132. doi: 10.1093/femsec/fiy132

Teeling, H., Fuchs, B. M., Becher, D., Klockow, C., Gardebrecht, A., Bennke, C. M., et al. (2012). Substrate-controlled succession of marine bacterioplankton populations induced by a phytoplankton bloom. *Science* 336, 608–611. doi: 10.1126/science.1218344

Teeling, H., Fuchs, B. M., Bennke, C. M., Kruger, K., Chafee, M., Kappelmann, L., et al. (2016). Recurring patterns in bacterioplankton dynamics during coastal spring algae blooms. *Elife* 5, e11888. doi: 10.7554/eLife.11888

Tilstone, G. H., Lange, P. K., Misra, A., Brewin, R. J. W., and Cain, T. (2017). Micro-phytoplankton photosynthesis, primary production and potential export production in the Atlantic Ocean. *Prog. Oceanography* 158, 109–129. doi: 10.1016/j.pocean.2017.01.006

Van Tol, H. M., Amin, S. A., and Armbrust, E. V. (2017). Ubiquitous marine bacterium inhibits diatom cell division. *ISME J.* 11, 31–42. doi: 10.1038/ismej.2016.112

Walsh, D. A., Zaikova, E., Howes, C. G., Song, Y. C., Wright, J. J., Tringe, S. G., et al. (2009). Metagenome of a versatile chemolithoautotroph from expanding oceanic dead zones. *Science* 326, 578–582. doi: 10.1126/science.1175309

Wang, Q., Garrity, G. M., Tiedje, J. M., and Cole, J. R. (2007). Naive Bayesian classifier for rapid assignment of rRNA sequences into the new bacterial taxonomy. *Appl. Environ. Microbiol.* 73, 5261–5267. doi: 10.1128/AEM.00062-07

Wood, S. N. (2012). *mgcv:Mixed GAM Computation Vehicle with GCV/AIC/REML smoothness estimation*. Available at: https://researchportal.bath.ac.uk/en/publications/mgcv-mixed-gam-computation-vehicle-with-gcvaicreml-smoothness-est.

Worden, A. Z., and Binder, B. J. (2003). Growth regulation of rRNA content in *Prochlorococcus* and *Synechococcus* (marine cyanobacteria) measured by whole-cell hybridization of rRNA-targeted peptide nucleic acids. *J. Phycology* 39, 527–534. doi: 10.1046/j.1529-8817.2003.01248.x

Yeh, Y.-C., and Fuhrman, J. A. (2022). Contrasting diversity patterns of prokaryotes and protists over time and depth at the San-Pedro Ocean Time series. *ISME Commun.* 2, 36. doi: 10.1038/s43705-022-00121-8

Zhang, Y., Zhao, Z., Dai, M., Jiao, N., and Herndl, G. J. (2014). Drivers shaping the diversity and biogeography of total and active bacterial communities in the South China Sea. *Mol. Ecol.* 23, 2260–2274. doi: 10.1111/mec.12739

Frontiers in Marine Science

TYPE Original Research
PUBLISHED 23 August 2023
DOI 10.3389/fmars.2023.1197727

*CORRESPONDENCE
Ian J. Brown
ib@pml.ac.uk

RECEIVED 31 March 2023
ACCEPTED 09 August 2023
PUBLISHED 23 August 2023

CITATION
Brown IJ, Kitidis V and Rees AP (2023) Simultaneous high-precision, high-frequency measurements of methane and nitrous oxide in surface seawater by cavity ring-down spectroscopy.
Front. Mar. Sci. 10:1197727.
doi: 10.3389/fmars.2023.1197727

Simultaneous high-precision, high-frequency measurements of methane and nitrous oxide in surface seawater by cavity ring-down spectroscopy

Ian J. Brown*, Vassilis Kitidis and Andrew P. Rees

Plymouth Marine Laboratory, Plymouth, United Kingdom

An automated system was developed using commercially available Cavity Ring-Down Spectroscopy (CRDS) technology (Picarro LTD., G2508) which was interfaced to a custom-made system which automated the equilibration and analysis of seawater dissolved nitrous oxide (N_2O) and methane (CH_4). The combined system was deployed during two research cruises in the Atlantic Ocean, which combined covered 16,500 kms, one on a west to east transect between the United States and Europe at approximately 24°N, the second was a north to south transect which covered approximately 70° of latitude between the Tropic of Cancer and the Southern Ocean. Semi-continuous measurements using the CRDS (Approx. 73,000) were compared to discretely collected samples (n=156) which were analysed using gas chromatography (GC) with flame ionisation detection for CH_4 and electron capture detection for N_2O. Excellent agreement between the two approaches, though with an increase in analytical precision offered by CRDS compared to GC gives great confidence in the applicability of the CRDS system, whilst the significant (2 to 3 orders of magnitude) increase in measurement frequency offer an opportunity to greatly increase the number of dissolved N_2O and CH_4 data that are currently available. Whilst identifying a number of small-scale features, deployment during this study showed that whilst the surface of large areas of the Atlantic Ocean were in-balance with the overlying atmosphere with respect to N_2O, the most of this region was offering a source of atmospheric CH_4.

KEYWORDS

nitrous oxide, methane, cavity ring-down spectroscopy, gas chromatography, Atlantic Meridional Transect (AMT), Atlantic Ocean

1 Introduction

Greenhouse gases (GHG's) absorb infrared radiation which increases atmospheric temperature and contributes to global warming. Although anthropogenic emissions of carbon dioxide (CO_2) contribute most to GHG induced warming, other long lived gases such as methane (CH_4) and nitrous oxide (N_2O) affect climate for decades to millennia, influencing climate change and stratospheric chemistry (Montzka et al., 2011). Atmospheric concentrations of these long lived GHG's have been increasing rapidly over the last century, mainly in association with human activities, leading to an overall warming of the earth's climate system (IPCC, 2021). The oceans play a major role in controlling atmospheric greenhouse gases, though consumption and production processes are not homogenously distributed so that on a regional scale the ocean may act as source or sink. N_2O concentration in most of the surface of the ocean is in close equilibrium with the atmosphere (Nevison et al., 1995) and global emissions from the open ocean and coastal waters contribute 35–39% of the total natural sources of N_2O (Tian et al., 2020) though there is a fine balance between the ocean acting as net producer or consumer of N_2O and an increase in the number and frequency of measurements provides our motivation to better constrain the uncertainty in absolute exchange rates. The world's oceans are also a natural source of CH_4 though this source makes only a minor contribution to the global atmospheric budget. The open ocean and coastal waters account for 7 to 12% of total natural sources and approximately 4% of global emissions (Saunois et al., 2020) with estuarine and coastal waters accounting for approximately 75% of the total marine source (Weber et al., 2019).

Large coordinated efforts are in place to determine the role of the ocean in removing atmospheric CO_2 and which include the Surface Ocean CO_2 Atlas (SOCAT) and the Integrated Carbon Observing System (ICOS). Despite their importance the same isn't in place for CH_4 and N_2O, and vast areas of the ocean remain under investigated with regard to their role in emissions (Bange et al., 2019; Yang et al., 2020). Temporal and spatial studies are sparse due to constraints posed by existing discrete and semi-continuous methods, combined with the difficulties operating in remote parts of the oceans. This has led to the oceanic emission estimates of both gases being poorly quantified which highlights the need for better spatial distributions of long lived GHG measurements. The most common technique for N_2O and CH_4 determination involve the injection of the gas phase into a gas chromatograph fitted with an electron capture detector and flame ionisation detector for N_2O and CH_4 respectively following either purge and trap of dissolved gases or equilibration of seawater with a gas of known N_2O/CH_4 content (Wilson et al., 2018). These methods are labour intensive and thereby limit the temporal resolution of data. There is therefore a need for development and implementation of cost-effective methods for underway measurements which offer the potential to extend the spatial coverage and temporal resolution of ship-based observations (Arévalo-Martínez et al., 2013; Wilson et al., 2020). Over the last decade or so, a number of technologies (including cavity ring-down spectroscopy and off-axis integrated cavity-output spectroscopy), have evolved to determine these gases at high frequency and high precision. Use of these systems is dominated by atmospheric measurements e.g. (Crosson, 2008; Yang et al., 2019; Ganesan et al., 2020) though several approaches have been taken to extract and introduce gases dissolved in fresh and seawater to the gas analyser, though in the main for N_2O or CH_4 individually or in concert with CO_2 (Arévalo-Martínez et al., 2013; Nicholson et al., 2018; Zhan et al., 2021). To date there are limited reports of simultaneous measurements of both N_2O and CH_4 (Troncoso et al., 2018).

Here we present a system which interfaces Picarro G2508 analyser (Picarro Inc., USA) to a custom-made equilibration unit which allows N_2O and CH_4 gases to be measured continuously from ship-based underway water with concurrent atmospheric measurements. This new method was compared with discrete samples measured using established gas chromatography methods.

2 Materials and methods

2.1 Equilibrator principle

As in discrete analysis using GC and headspace equilibrium approaches, the principle of continuous analysis involves equilibrating air (gas phase) with seawater (aqueous phase) and determining the concentration of the target species in the gas phase. This method eliminates the potential of phase partitioning and potential detector sensitivity considerations (Upstill-Goddard et al., 1996). However continuous analysis requires re-circulation of the air phase through the detector and its return to the water phase in a closed circulation loop in order to maintain equilibrator pressure and full equilibration. A shower head type equilibrator was used to obtain an equilibrated gas phase similar to the one described by (Kitidis et al., 2012). Due to the different solubilities and diffusivities of CH_4 and N_2O (Wiesenberg and Guinasso, 1979; Weiss and Price, 1980) and to ensure complete equilibration of each gas, separate equilibrators were used, set to different water flow rates. CH_4 solubility is lower and is therefore likely to require a longer residence time for full equilibration, this was achieved by utilising a lower flow rate. A water flow of 1.6 L min^{-1} and 1.2 L min^{-1} was maintained for the N_2O and CH_4 equilibrators respectively. Initially two equilibrators were utilised however it was determined that N_2O was fully equilibrated from the lower flow of the CH_4 equilibrator. Figure 1 shows a schematic setup of the equilibrator and were the same as previously used with the PML-Dartcom *Live*pCO_2 system which compared favourably with other equilibrators (Ribas-Ribas et al., 2014).

2.2 Equilibration conditions

The equilibrators were supplied with a continuous supply of seawater from an intake at the ship's hull, approximately 5 m below the surface. The equilibrators consist of an outer acrylic tube (diameter 135 mm) with an inner acrylic chamber (Diameter 98mm). The outer chamber was filled with a continuous flow of surface water to act as a thermal insulator in order to maintain the inner and a stable equilibration chamber temperature. The water in the inner chamber passed through a Sprinkler head (BETE® N series nozzle) to increase the surface area available for gas exchange and thus decreasing equilibration times. A trap vent with a vent to the atmosphere creates a lower water phase which is isolated from the headspace and maintains a constant water volume which is

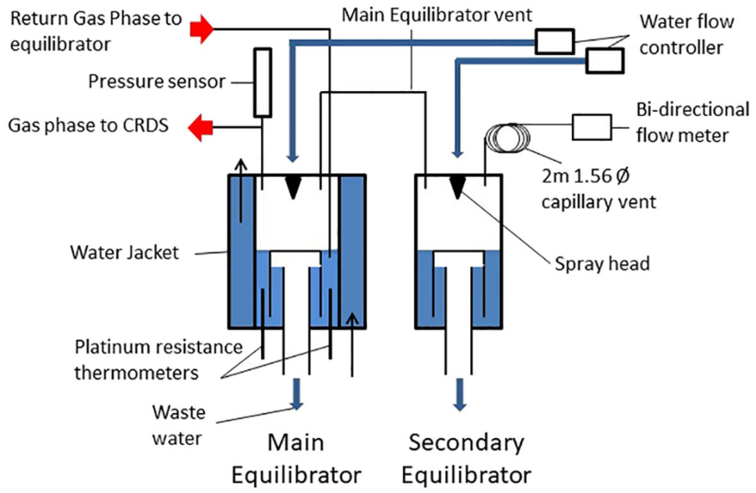

FIGURE 1
Design of seawater-air equilibrator during this study.

continuously renewed from the ships underway water supply system. Each equilibrator is connected via a 6.25 mm Teflon tube to a smaller secondary equilibrator through which underway seawater also flows through a Sprinkler head (BETE® W series nozzle). The secondary equilibrator allows for compensation of potential air volume changes caused by humidity removal, solubility changes due to warming or cooling of the water or disequilibrium of one of the main dissolved gases e.g. oxygen (Schneider et al., 2007) or pressure changes due to water flow variations. The secondary equilibrator is in turn vented via a 2m 1.56 mm stainless steel tube to minimise atmospheric exchange and to maintain atmospheric pressure. Any small pressure fluctuations inside the main equilibrator are thereby eliminated, buffered by the secondary equilibrator and 2 m vent. At the end of this vent line is a bi-directional flow meter (Honeywell AWM3303V bi-directional mass flow sensor) to measure any exchange of air through the vent to the atmosphere. The water flow is regulated with a proportional solenoid (Burket series 6240) with an electronic control (Burket Type 8611 eControl) which maintains the desired water flow under variable flow conditions from the underway seawater supply. A pressure sensor (Druck X7517-05A-3257) is located on the gas re-circulation loop close to the equilibrator to monitor the equilibrator pressure.

During the water phase sampling operation, the headspace gas to me measured is continuously drawn from the equilibrator and passed through a Peltier dryer, cooled to -20°C, which is fitted with a water watcher switch (Honeywell Phototransistor Level Switch, LLE102000) to automatically protect the electronics and detector from flooding in case of water ingress. The dried air is then directed through the detector and then passes through a valve tray where a series of solenoids (Peter Paul 52N8DGB) select the appropriate equilibrator to send the return air flow to the inner chamber below the surface of the residual water.

A 6.25 mm Decabon® line was set up from the meteorological platform at the bow of the ship to allow atmospheric air to be pumped directly into the lab for atmospheric measurements.

2.3 Sampling, calibration and data logging

Seawater was continuously supplied from the ships underway system from approximately 5m depth. The intake temperature was recorded and compared to that at the equilibration point to account for changes in temperature as the water passes through the ship. A gas phase sampling schedule was set up allowing each equilibrator and marine air to be sampled sequentially. Each equilibrator was sampled for 60 minutes before switching to the next equilibrator, also for 60 minutes. This cycle was completed 4 time before switching to marine air. This allows time for adequate flushing of the analyser and ensures a stable base line. Flushing times for N_2O and CH_4 at 1.6 and 1.2 L min^{-1} were determined as 15 and 30 minutes for CH_4 for equilibrators 1 and 2 respectively. The analysis protocol involved determination of three mixed reference gas standards (Air Products Ltd.) with mixing ratios 317.4, 406.4, 496.7 ppbv N_2O and 1.009, 2.058, 3.04 ppmv CH_4 in synthetic air which had been calibrated against National Oceanic and Atmospheric Administration (NOAA) primary gas standards. These were run for approximately 45 minutes each at the start and end of the day. The system was synchronised to the ship's navigation and underway logging system to acquire positional and ancillary data (date, time, seawater temperature, salinity) every 10 seconds. The data were logged with 6 readings averaged to give one measurement per minute. The software R was used to integrate and process the data, (see data processing equations in Supplementary Material). The first 30 minutes of each equilibrator cycle were removed to ensure full equilibration of water and gas phases.

2.4 Automation

The sampling schedule and processes were controlled electronically by custom-built software based on the PML Dartcom *Livep*CO_2 system (Kitidis et al., 2017). Solenoids (Peter Paul 52N8DGB) controlled the gas flow through an automated manifold in order to select the particular gas source to be measured (equilibrator 1 or 2, atmospheric air or standards) and a recirculation loop allowed for the return to the equilibrators. Gases within the tray associated with the equilibrator were monitored with appropriate sensors for pressure (Druck X7517-05A-3257), temperature and humidity (Farnell HIH-4602-C), and flow rate (Honeywell AWM3303V) at both the input and output of the valve tray. Humidity and pressure were monitored in the gas stream before and after passing through the CRDS. The programme allows for the independent setting of the equilibrators and standards to enable adequate flushing time and frequency of analysis. The schematic setup of the analytical system is shown in Figure 2. The Picarro CRDS is sensitive to strong pressure differences that may arise following the total closure of all gas lines resulting in zero flow though the analyser, which have the potential to damage the in-built laser. A default position was therefore programmed in case moisture develops in the equilibrator lines in which all valves automatically align to enable atmospheric air flow through the CRDS unit. A water watcher switch (Honeywell Phototransistor Level Switch, LLE102000) triggers the default position in the event that water is detected in a gas drying unit (Figure 2).

2.5 CRDS principle

The CRDS allows for the simultaneous measurement of molar fractions of N_2O and CH_4 with precision at sub-parts per billion (ppb) levels. The device is based upon the technology described in full by (Maity et al., 2020) and briefly summarised here. Gas concentrations are measured from a single frequency laser diode in a 25cm long cavity defined by 3 mirrors which increase the effective path length to over 20km. The laser is abruptly turned off once the photodetector signal reaches a threshold level, typically this is achieved in a few tens of microseconds. The light continues to pass between the mirrors which have a 99.99% reflectivity; the intensity steadily decays to zero the “ring down”. The time difference in this decay, to that of an empty cavity, is directly proportional to the near infra-red absorption of the gas-phase molecules at known wavelengths for the target gases.

During sampling air is pumped continuously by a recirculation pump A0702 (Picarro Research Inc., USA) which simultaneously achieves the sub-atmospheric pressure required for the cavity and provides a re-circulatory air supply to the equilibrator loop (Figure 2). The CRDS cell temperature and pressure are very precisely and continually recorded by the instrument and used as part of the gas molar fraction calculations. The gas flow is dried in a purpose-built Peltier dryer unit prior to analysis which reduces the moisture content to <15%. The CRDS measures the H_2O molar fraction along with N_2O and CH_4, this allows the calculation of the dry mole fractions and allows for potential bias in partial pressure due to the water vapour content and negates the need to completely dry the sample air. To calculate the dry mole fractions of N_2O and CH_4 the Picaro software applies the following calculation:

$$[x(gas)]\_dry = [x(gas)]\_wet/((1-(xH_2O)/10^6))$$

Where x(gas) dry and x(gas) wet are the mole fractions of the corresponding gas after and before correction respectively and xH_2O is the measured molar fraction of water vapour correction.

2.6 Gas chromatography reference method

Discrete seawater samples were collected at 5m using clean Tygon® tubing into 500 ml borosilicate bottles either from the ship's continuous seawater supply or from Niskin bottles on a CTD rosette. Bottles were overfilled with three times the bottle volume to eliminate air bubbles and poisoned with 200 µl of a saturated mercuric chloride solution. They were then transferred to a water bath at 25 ± 0.1°C and temperature equilibrated for a minimum of one hour before analysis. Samples were analysed for CH_4 and N_2O by single-phase equilibration gas chromatography using a flame ionisation detector and Electron Capture detector and similar to that described by (Upstill-Goddard et al., 1996). Samples were typically analysed within 8 hours of collection and calibrated with the same 3 certified standards (Air Products Ltd.; mixing ratios 317.4, 406.4, 496.7 PPBv N_2O and 1.009, 2.058, 3.04 PPMv CH_4 in synthetic air; calibrated against NOAA primaries). The PPMv and

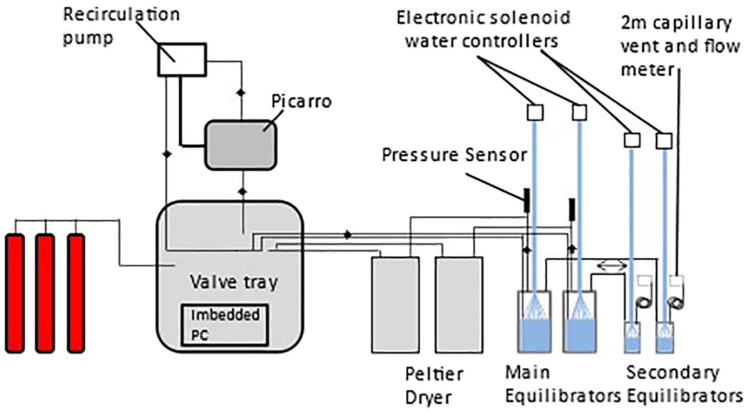

FIGURE 2
Schematic of integrated equilibrator and analysis system.

PPBv mixing ratios correspond to the gas phase concentration. All other concentrations are converted to nmol L^{-1} to allow accurate comparison to discrete GC samples.

Air measurements were made at each oceanographic station and were collected into Tedlar® gas sample bags from a position at the ships bow. These were analysed and calibrated against the same reference gases and used for calculating atmospheric mixing ratios. Aqueous CH_4 and N_2O concentrations were calculated from the solubility tables of (Wiesenberg and Guinasso, 1979; Weiss and Price, 1980) respectively.

The CRDS and gas chromatography (GC) systems were both deployed during two oceanographic campaigns in the Atlantic during RRS Discovery cruise DY040 as part of the RAGNARoCC (Radiatively Active Gases from the North Atlantic Region and Climate Change) between Florida and the Canary Islands (6th December 2016 – 22nd January 2015) and during RRS Discovery cruise DY084 AMT27 as part of the Atlantic Meridional Transect programme (23 September – 5th November 2017) between the UK and Falkland Islands (Figure 3). 156 discrete surface measurements were made using GC on DY040 and 100 on DY084.

3 Results and discussion

The performance of the CRDS N_2O/CH_4 analyser system in the field was evaluated by comparison with the established GC method (Upstill-Goddard et al., 1996; Rees et al., 2011; Brown et al., 2014) using discrete CTD and underway sea surface discrete samples for N_2O and CH_4 analysis (Figure 4). The cruise track of DY084 (Figure 3) traverses more than 100 degrees of latitude along the length of the Atlantic with analyses for the purpose of this study used between 11.5° North and 55.5° South and through several different biogeographic provinces from the temperate north Atlantic, the tropics, south Atlantic and on to the productive waters of the Antarctic circumpolar current and the waters around South Georgia. This provided a variety of water masses and a greater range of gas concentrations suitable for a comparison. DY040 traveling from west to east across the north Atlantic Gyre offers a large geographical area of relatively low concentrations and variability suitable for comparing the re-producibility of the CRDS.

Dissolved concentrations determined on discrete samples collected during DY040 showed a very limited range for both gases: 5.97 – 7.51 nmolL^{-1} (Mean ± 1 sd = 6.56 ± 0.37 nmol L^{-1}) for N_2O and 2.03 to 3.76 nmolL^{-1} for (2.20 ± 0.27 nmol L^{-1}) for CH_4 (n=156). N_2O and CH_4 saturations were 102.62% and 117.56% respectively which on balance reflects equilibrium with the atmosphere for N_2O and the ocean offering a source of CH_4. The highest CH_4 concentration of 3.76 nmol L^{-1} was equivalent to a saturation value of 169% and was determined at the eastern side of the transect in proximity to the African coast. Dissolved concentrations determined on discrete samples during DY084 ranged from 5.31 to 15.28 and 1.74 to 8.21 nmol L^{-1} for N_2O and CH_4 respectively (n=100) (Figure 4) with the maximum values being recorded in Cumberland Bay, South Georgia during DY084 on day 304 and which were likely influenced by nearby elephant seal and king penguin colonies. Mean saturations indicate that for much of this area N_2O was generally in equilibrium with the atmosphere (100.9% ± 1.2%) whilst there was a potential source of CH_4 from the ocean to the atmosphere (110.5% ± 26.9%). The higher uncertainty in the CH_4 saturations can be attributed to the larger range of saturations particularly when in close proximity to South Georgia.

A correlation and regression analysis of discrete and underway N_2O and CH_4 measurements collected within 30 minutes of a CRDS measurement during both cruises show a significant linear agreement between the two analytical approaches for both gases (Figure 5). Correlation coefficients for the two approaches using 153

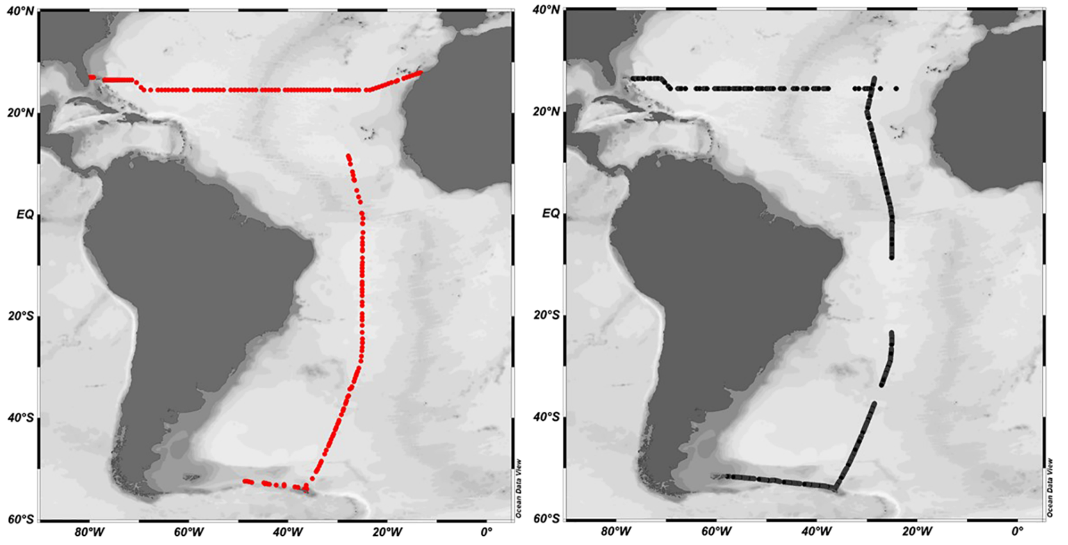

FIGURE 3
DY040 and DY084 cruise tracks. DY040 transacted West to East along 24.5°N, DY084 followed the AMT track from North to South. Black dots indicate CRDS measurements. Red dots indicate CTD stations and underway measurements analysed by gas chromatography.

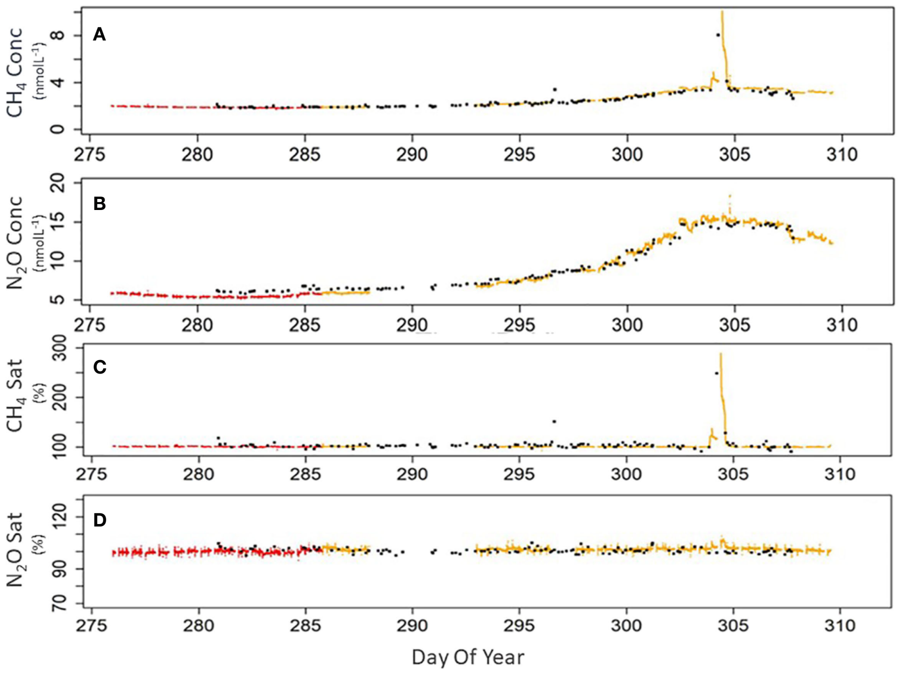

FIGURE 4
Comparison of GC and CRDS data collected during cruise DY084 (AMT27) in 2017. Panels **(A)** methane concentration (nmol L^{-1}), **(B)** nitrous oxide concentration (nmol L^{-1}), **(C)** methane saturation (%), **(D)** nitrous oxide saturation (%). All panels, CRDS using equilibrator 1 (red dots), CRDS using equilibrator 2 (yellow dots), GC from underway and CTD measurements (black dots).

pairs of observations determined over the two research expeditions were $r^2 = 0.9871$, $p<0.001$ and $r^2 = 0.9839$, $p<0.001$ for N_2O and CH_4 respectively. The derived regressions showed that N_2O-CRDS = ((N_2O-GC * 1.03549 ± 0.01) - 0.522472 ± 0.09) and CH_4-CRDS = ((CH_4-GC * 1.09041 ± 0.29) - 0.255484 ± 0.09). A T test on the same data shows values of -0.153 and 1.616 $P \leq 0.05$ (DF153) for N_2O and CH_4 respectively, again showing no significant difference between the GC and CRDS data. The limit of detection of the CRD is far below our 300ppb/1ppm N_2O/CH_4 standard which were always lower than our measured samples. The response of the instrument is linear between the range of standards used.

During the majority of both expeditions the saturations of N_2O and CH_4 were generally close to atmospheric equilibrium with concentrations largely determined by seawater temperature. (Figure 4). This suggests strong physical processes that determine and regulate surface concentrations throughout much of the surface Atlantic Ocean. The CH_4 data shows some small variability between the GC and CRDS which is greater in the South Atlantic region where the concentrations are higher and have larger variability. There were no systematic trends in this change suggesting that these can be attributed to heterogeneity in collected samples. The significant statistical agreement between both approaches for both gases, the stringent calibration of both approaches and our engagement in a previous community intercalibration exercise for GC analysis (Wilson et al., 2018) indicates that the methods are statistically proven to be in good agreement, giving great confidence in the use

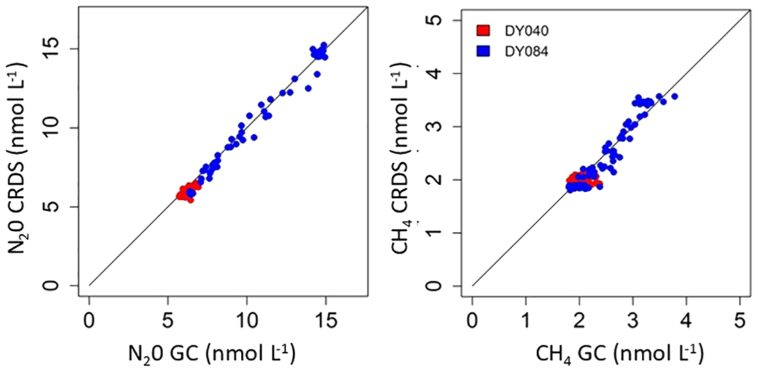

FIGURE 5
Discrete and underway N_2O and CH_4 samples collected on DY040 and DY084 within 30 minutes of a CRDS measurement.

of either approach. It is evident though that the CRDS system provides not only great advantage in terms of frequency of measurement but also in analytical precision, (DY040 CH_4 Ave concentration 1.99 nmol L^{-1} RSD 0.03% and N_2O 5.87 nmol L^{-1} RSD 0.04% n=45202). The discrete samples analysed by GC involved additional handling and measuring procedures which contribute to larger uncertainties in the analysis and increased variability compared to that of the high frequency autonomous measurement using CRDS. During the period 20 to 23 October (days 293 to 296 Figure 4) 2017 (DY084) 27294 measurements were made using the CRDS system which gave averages values of 2.17 ± 0.07 nmol L^{-1} (3% variability) and 7.37 ± 0.38 nmol L^{-1} (5% variability) for CH_4 and N_2O respectively. In the same period 22 GC measurements gave concentrations of 2.54 ± 0.21 nmol L^{-1} (8% variability) and 7.63 ± 0.47 (6% variability) nmol L^{-1} for CH_4 and N_2O respectively.

4 Conclusion

The CRDS underway system was used to provide an accurate and precise data set of nearly 200,000 N_2O and CH_4 measurements and has the potential to offer greater spatial and temporal coverage of surface waters than previously achievable when deployed using the approach presented here. Due to near continuous measurement offered by the CRDS approach, features and gradients in dissolved gas distribution were highlighted which discrete sampling and GC analysis failed to resolve. CRDS measurements proved to be stable in tropical, temperate, and polar waters and have compared favourably to traditional techniques whilst offering better spatial and temporal resolution with a fraction of the manual effort required by GC methodology. The CRDS system as described here is applicable to coastal and open ocean studies offering the potential to improve our understanding of these climatically important gases. The current set-up has the potential to be used continuously not only onboard research vessels but also on voluntary observing ships, this is currently limited to some extent by the cost of instrumentation but further by the current requirement for manual intervention should there be an ingress/build-up of water downstream of the equilibrators.

Data availability statement

The raw data supporting the conclusions of this article will be made available by the authors, without undue reservation.

Author contributions

IB: Led the design of instrumentation and construction of instrumentation and project design. VK: Led R script development. AR: Led Research direction. Manuscript preparation led by IB with full input from VK and AR. All authors contributed to the article and approved the submitted version.

Funding

This work benefitted from funding and contributed to the outputs of UK NERC funded projects RAGNARRoCC - Radiatively active gases from the North Atlantic Region and Climate Change (NERC: NE/K002511/1) and the Atlantic Meridional Transect (AMT) through National Capability Long-term Single Centre Science Programme, Climate Linked Atlantic Sector Science (NE/R015953/1).

Acknowledgments

We would like to extend our thanks to the officers and crew on RRS Discovery during both research cruises. This study contributes to the international IMBeR project and is contribution number 392 of the AMT programme. We would also like to offer our thanks to Dartcom Ltd our partners in the development of system software and electronic manifold control.

Conflict of interest

The authors declare that the research was conducted in the absence of any commercial or financial relationships that could be construed as a potential conflict of interest.

Publisher's note

Supplementary material

The Supplementary Material for this article can be found online at: https://www.frontiersin.org/articles/10.3389/fmars.2023.1197727/full#supplementary-material

References

Arévalo-Martínez, D. L., Beyer, M., Krumbholz, M., Piller, I., Kock, A., Steinhoff, T., et al. (2013). A new method for continuous measurements of oceanic and atmospheric N_2O, CO and CO_2: performance of off-axis integrated cavity output spectroscopy (OA-ICOS) coupled to non-dispersive infrared detection (NDIR). *Ocean Sci.* 9, 1071–1087. doi: 10.5194/os-9-1071-2013

Bange, H. W., Arevalo-Martinez, D. L., de la Paz, M., Farias, L., Kaiser, J., Kock, A., et al. (2019). A harmonized nitrous oxide (N_2O) ocean observation network for the 21st century. *Front. Mar. Sci.* 6. doi: 10.3389/fmars.2019.00157

Brown, I. J., Torres, R., and Rees, A. P. (2014). The origin of sub-surface source waters define the sea-air flux of methane in the Mauritanian Upwelling, NW Africa. *Dynamics Atmospheres Oceans* 67, 39–46. doi: 10.1016/j.dynatmoce.2014.06.001

Crosson, E. R. (2008). A cavity ring-down analyzer for measuring atmospheric levels of methane, carbon dioxide, and water vapor. *Appl. Phys. B* 92, 403–408. doi: 10.1007/s00340-008-3135-y

Ganesan, A. L., Manizza, M., Morgan, E. J., Harth, C. M., Kozlova, E., Lueker, T., et al. (2020). Marine nitrous oxide emissions from three eastern boundary upwelling systems inferred from atmospheric observations. *Geophys. Res. Lett.* 47, e2020GL087822. doi: 10.1029/2020GL087822

IPCC (2021). *Climate change 2021: the physical science basis. Contribution of working group I to the sixth assessment report of the intergovernmental panel on climate change* (Cambridge, United Kingdom and New York, NY, USA: Cambridge University Press), In press.

Kitidis, V., Brown, I., Hardman-Mountford, N., and Lefèvre, N. (2017). Surface ocean carbon dioxide during the Atlantic Meridional Transect, (1995–2013); evidence of ocean acidification. *Prog. Oceanography* 158, 65–75. doi: 10.1016/j.pocean.2016.08.005

Kitidis, V., Hardman-Mountford, N. J., Litt, E., Brown, I., Cummings, D., Hartman, S., et al. (2012). Seasonal dynamics of the carbonate system in the Western English Channel. *Continental Shelf Res.* 42, 30–40. doi: 10.1016/j.csr.2012.04.012

Maity, A., Maithani, S., and Pradhan, M. (2020). "Chapter 3 - Cavity ring-down spectroscopy: recent technological advances and applications," in *Molecular and laser spectroscopy*. Eds. V. P. Gupta and Y. Ozaki (Elsevier), 83–120.

Montzka, S. A., Dlugokencky, E. J., and Butler, J. H. (2011). Non-CO_2 greenhouse gases and climate change. *Nature* 476, 43–50. doi: 10.1038/nature10322

Nevison, C. D., Weiss, R. F., and Erickson, D. J. (1995). Global oceanic emissions of nitrous-oxide. *J. Geophysical Research-Oceans* 100, 15809–15820. doi: 10.1029/95JC00684

Nicholson, D. P., Michel, A. P. M., Wankel, S. D., Manganini, K., Sugrue, R. A., Sandwith, Z. O., et al. (2018). Rapid mapping of dissolved methane and carbon dioxide in coastal ecosystems using the chemYak autonomous surface vehicle. *Environ. Sci. Technol.* 52, 13314–13324. doi: 10.1021/acs.est.8b04190

Rees, A. P., Brown, I. J., Clark, D. R., and Torres, R. (2011). The Lagrangian progression of nitrous oxide within filaments formed in the Mauritanian upwelling. *Geophys. Res. Lett.* 38, L21606. doi: 10.1029/2011GL049322

Ribas-Ribas, M., Rérolle, V. M. C., Bakker, D. C. E., Kitidis, V., Lee, G. A., Brown, I., et al. (2014). Intercomparison of carbonate chemistry measurements on a cruise in northwestern European shelf seas. *Biogeosciences* 11, 4339–4355. doi: 10.5194/bg-11-4339-2014

Saunois, M., Stavert, A. R., Poulter, B., Bousquet, P., Canadell, J. G., Jackson, R. B., et al. (2020). The global methane budget 2000-2017. *Earth System Sci. Data* 12, 1561–1623. doi: 10.5194/essd-12-1561-2020

Schneider, B., Sadkowiak, B., and Wachholz, F. (2007). A new method for continuous measurements of O2 in surface water in combination with pCO_2 measurements: Implications for gas phase equilibration. *Mar. Chem.* 103, 163–171. doi: 10.1016/j.marchem.2006.07.002

Tian, H. Q., Xu, R. T., Canadell, J. G., Thompson, R. L., Winiwarter, W., Suntharalingam, P., et al. (2020). A comprehensive quantification of global nitrous oxide sources and sinks. *Nature* 586, 248–24+. doi: 10.1038/s41586-020-2780-0

Troncoso, M., Garcia, G., Verdugo, J., and Farías, L. (2018). Toward high-resolution vertical measurements of dissolved greenhouse gases (Nitrous oxide and methane) and nutrients in the Eastern South Pacific. *Front. Mar. Sci.* 5. doi: 10.3389/fmars.2018.00148

Upstill-Goddard, R. C., Rees, A. P., and Owens, N. J. P. (1996). Simultaneous high-precision measurements of methane and nitrous oxide in water and seawater by single phase equilibration gas chromatography. *Deep-Sea Res. Part I-Oceanographic Res. Papers* 43, 1669–1682. doi: 10.1016/s0967-0637(96)00074-x

Weber, T., Wiseman, N. A., and Kock, A. (2019). Global ocean methane emissions dominated by shallow coastal waters. *Nat. Commun.* 10, 4584. doi: 10.1038/s41467-019-12541-7

Weiss, R. F., and Price, B. A. (1980). Nitrous-oxide solubility in water and seawater. *Mar. Chem.* 8, 347–359. doi: 10.1016/0304-4203(80)90024-9

Wiesenberg, D. A., and Guinasso, N. L. (1979). Equilibrium solubilities of methane, carbon monoxide, and hydrogen in water and sea water. *J. Chem. Eng. Data* 24, 356–360. doi: 10.1021/je60083a006

Wilson, S. T., Al-Haj, A. N., Bourbonnais, A., Frey, C., Fulweiler, R. W., Kessler, J. D., et al. (2020). Ideas and perspectives: A strategic assessment of methane and nitrous oxide measurements in the marine environment. *Biogeosciences* 17, 5809–5828. doi: 10.5194/bg-17-5809-2020

Wilson, S. T., Bange, H. W., Arevalo-Martinez, D. L., Barnes, J., Borges, A. V., Brown, I., et al. (2018). An intercomparison of oceanic methane and nitrous oxide measurements. *Biogeosciences* 15, 5891–5907. doi: 10.5194/bg-15-5891-2018

Yang, M., Bell, T. G., Brown, I. J., Fishwick, J. R., Kitidis, V., Nightingale, P. D., et al. (2019). Insights from year-long measurements of air–water CH_4 and CO_2 exchange in a coastal environment. *Biogeosciences* 16, 961–978. doi: 10.5194/bg-16-961-2019

Yang, S., Chang, B. X., Warner, M. J., Weber, T. S., Bourbonnais, A. M., Santoro, A. E., et al. (2020). Global reconstruction reduces the uncertainty of oceanic nitrous oxide emissions and reveals a vigorous seasonal cycle. *Proc. Natl. Acad. Sci.* 117, 11954–11960. doi: 10.1073/pnas.1921914117

Zhan, L. Y., Zhang, J. X., Ouyang, Z. X., Lei, R. B., Xu, S. Q., Qi, D., et al. (2021). High-resolution distribution pattern of surface water nitrous oxide along a cruise track from the Okhotsk Sea to the western Arctic Ocean. *Limnol. Oceanogr.* 66, S401–S410. doi: 10.1002/lno.11604

frontiers | Frontiers in Marine Science

TYPE Original Research
PUBLISHED 30 October 2023
DOI 10.3389/fmars.2023.1222895

OPEN ACCESS

EDITED BY
Vanda Brotas,
University of Lisbon, Portugal

REVIEWED BY
Stella Psarra,
Hellenic Centre for Marine Research (HCMR), Greece
Presentación Carrillo,
University of Granada, Spain

*CORRESPONDENCE
Pablo Serret
pserret@uvigo.es

RECEIVED 15 May 2023
ACCEPTED 13 October 2023
PUBLISHED 30 October 2023

CITATION
Serret P, Lozano J, Harris CB, Lange PK, Tarran GA, Tilstone GH, Woodward EMS and Zubkov MV (2023) Respiration, phytoplankton size and the metabolic balance in the Atlantic gyres.
Front. Mar. Sci. 10:1222895.
doi: 10.3389/fmars.2023.1222895

Respiration, phytoplankton size and the metabolic balance in the Atlantic gyres

Pablo Serret[1]*, Jose Lozano[1], Carolyn B. Harris[2], Priscila K. Lange[3], Glen A. Tarran[2], Gavin H. Tilstone[2], E. Malcolm S. Woodward[2] and Mikhail V. Zubkov[4]

[1]Centro de Investigación Mariña da Universidade de Vigo, Departamento de Ecoloxía e Bioloxía Animal, Vigo, Spain, [2]Plymouth Marine Laboratory, Plymouth, United Kingdom, [3]Universidade Federal do Rio de Janeiro, Rio de Janeiro, Brazil, [4]Scottish Association for Marine Science, Oban, United Kingdom

The balance between plankton photosynthesis (GPP) and community respiration (CR) in the euphotic zone (net community production, NCP) is an essential driver of the biological carbon pump. Deficient datasets and a lack of knowledge of the mechanisms regulating CR cause poor empirical models and oversimplified parameterisations that maintain NCP as one of the most important unknowns for projections of the carbon pump. One important unresolved issue is the unexpected lack of empirical relationships between CR and the biomass or size-structure of the phytoplankton, which undermines the use of remotely sensed observations to predict net community metabolism. Here we analyse the spatial variation of plankton metabolism, chlorophyll a concentration (Chla), pico- and nanophytoplankton abundance and size-fractionated primary production (^{14}CPP) along a latitudinal (49°N–46°S) transect of 73 stations across the Atlantic Ocean (AMT-22 cruise). The use of depth-weighted rates (rates integrated to the depth of 0.1% PAR, divided by the regionally varying depth of integration) markedly improved the depiction of latitudinal patterns and the significance of relationships, over volumetric or integrated rates. Depth-weighted CR showed clear and consistent latitudinal patterns with relevance for the distribution of NCP. Depth-weighted Chla and CR exhibited a significant relationship ($CR_Z=1.42Chla_Z-0.21$, $r^2 = 0.69$, N=37, $p<0.001$) with potential for the difficult prediction of CR. A general ratio of 1.42 mmolO_2 mgChla^{-1} d^{-1} and a threshold Chla for net heterotrophy of ca. 0.25 mgChla m^{-3} can be tentatively proposed for the Atlantic, although further analyses of spatial and seasonal variation are necessary. We observed unusually positive NCP rates in the central part of the N gyre, due to a marked decrease of CR in a patch of high *Synechococcus* spp. abundance and high ^{14}CPP by large phytoplankton. However, no relationship was observed between size-fractionated ^{14}CPP and CR or the GPP : CR ratio during the cruise, contradicting the hypothesis that food web functioning is determined by the phytoplankton size structure. Such independence, together with the persistence of distinct GPP : CR and ^{14}CPP : NCP relationships in distinct biogeographic provinces suggest a resilience of trophic dynamics and the existence of alternative ecosystem states, whose implications for projections of the metabolic state of the ocean are discussed.

KEYWORDS

plankton, respiration, photosynthesis, net community production, phytoplankton size structure, ecosystem state, prediction

1 Introduction

Marine organisms play a key role in CO_2 storage in the ocean, mainly through the biological carbon pump (BCP), where the sinking of organic carbon produced in the illuminated upper ocean leaves a deficit of dissolved CO_2 near the surface that is compensated by air-sea diffusion of atmospheric CO_2 (e.g., Boyd et al., 2019). The BCP accounts for around 90% of the vertical dissolved inorganic carbon gradient in the ocean and in its absence, the atmospheric CO_2 concentration would be double its current value (Boyd et al., 2019). There is consensus that the BCP will change due to the alteration of nutrient fluxes and the combined effects of three interconnected drivers of change in the ocean: warming, deoxygenation and acidification. However, the magnitude and even direction of these changes are highly uncertain, partly due to knowledge gaps in the representation of the biological contribution to the BCP (Bindoff et al., 2019; Wilson et al., 2022).

The primary driver for the BCP is the accumulation of organic carbon in the surface ocean, whose magnitude and efficiency are determined by two key biological processes: photosynthesis and respiration. Photosynthesis by the phytoplankton is responsible of virtually all the production of organic matter in the ocean. However, not all the organic carbon photosynthesised in the euphotic layer (gross primary production: GPP) sinks to depth. The maintenance, growth and activity of the phytoplankton and of the heterotrophs that directly or indirectly feed upon them require metabolic energy that is mostly supplied through respiration, thus reducing the net amount of organic matter available. By determining the rate at which the sinking organic matter is lost, the respiration of the entire plankton community (CR, the aggregated respiration of the phytoplankton and heterotrophic organisms) regulates the efficiency of the BCP. The balance of these processes in the euphotic layer is net community production (NCP=GPP-CR), which represents the potential BCP, i.e. the net amount of GPP in the euphotic zone that is ultimately available for sinking to the deep ocean or for transfer through food webs. Despite its importance, the magnitude and variation of NCP over regional scales remains poorly resolved, especially in the oligotrophic open ocean (e.g., Ducklow and Doney, 2013), which is particularly important due to its current extent (~ 56% of the ocean´s surface) and projected climate change-related increases in area and oligotrophication (Signorini et al., 2015, and references therein).

Accurate projections of NCP would require validated empirical models or robust parameterisations of CR or NCP, based on knowledge of their controlling mechanisms. None of these is available. GPP : CR relationships used to extrapolate and predict the metabolic state of the epipelagic ocean (e.g., del Giorgio et al., 1997; Duarte and Agusti, 1998; Williams, 1998; Serret et al., 2009; Westberry et al., 2012; Regaudie-de-Gioux and Duarte, 2013; Tilstone et al., 2015; Ford et al., 2021) produced conflicting results that maintained a heated debate of >15 years about the metabolic state (auto- vs. heterotrophic) of the oligotrophic ocean (Ducklow and Doney, 2013). The analysis of data from ten Atlantic Meridional Transect (AMT) cruises subsequently revealed that the oligotrophic ocean is neither auto- nor heterotrophic, but functionally diverse (Serret et al., 2015), however the different GPP : CR relationships observed in the North (heterotrophic) and South (autotrophic) Atlantic gyres have little predictive power.

Regarding parameterisation, in stark contrast to knowledge on controls and feedbacks on primary production (e.g., Falkowski et al., 1998), the biogeochemical processes controlling CR and NCP are largely undetermined. A recent review of field and experimental studies from 1991 to 2020 found only 36 publications with some empirical information about plankton respiration regulation (Wikner et al., 2023), where temperature, followed by primary production and DOC appear as unique controlling factors. Temperature dependence is the main, if not the only controlling factor of respiration in coupled climate-carbon cycle models in the oxygenated ocean (Wilson et al., 2022; Pasquier et al., 2023). Higher temperature undoubtedly increases the kinetics of respiration, as it does with any chemical reaction, including photosynthesis (Morel et al., 1996; Behrenfeld and Falkowski, 1997; Bouman et al., 2005; Smyth et al., 2005; Robinson et al., 2018). However, photosynthesis is rarely predicted from temperature alone because this physiological control is often intertwined in a complex matrix of interacting ecological constraints (e.g., nutrient availability, light, cell size, taxonomic composition, competition, predation) that covary with the environment (e.g., stratification, circulation, wind patterns, distance to the coast, etc.), thus reducing the relevance of the chemically-driven impact of temperature. Similarly, it is also very unlikely that real-world rates of CR in the ocean are controlled by temperature alone, although respiration is certainly expected to increase with higher temperature. The root of this oversimplified parameterisation of CR compared to PP is our poor empirical knowledge of the biogeochemical processes that interact with temperature to determine respiration rates *in situ*.

One important reason for this poor knowledge on empirical patterns and models of CR and NCP on the one hand, and on controlling processes of CR and NCP on the other hand, is the very poor database of measurements in the ocean (Robinson and Williams, 2005; Regaudie-de-Gioux and Duarte, 2013). Two main approaches exist to measure NCP in the ocean: methods based on *in situ* changes in budgets of chemical tracers in the water column, and methods based on *in vitro* changes in O_2 concentration after incubations of small seawater samples.

In situ methods are greatly improving the spatial and temporal coverage of NCP measurements, especially after the growing fleet of sensors mounted on autonomous platforms (e.g., Claustre et al., 2020). Target accuracy and precision of oxygen concentration determination from optodes (~1 μmol kg^{-1} and 0.5 μmol kg^{-1}, respectively, Gruber et al., 2010; Bittig et al., 2018; Vikström et al., 2019), and observational bias and error (~ 3% and 6%, respectively. Johnson et al., 2017; Mignot et al., 2019) are large compared to typical NCP rates in the oligotrophic ocean ($\leq$ 0.5 mmolO_2 m^{-3} d^{-1}, Serret et al., 2015). This implies that long and large integrations of O_2 budgets are needed. These integrative NCP estimates are very necessary indeed, but ineffective to represent the rapid dynamics and spatial heterogeneity of biogeochemical processes and interactions driving the functioning of plankton ecosystems, which undermines the potential for projection of the BCP, e.g. in response to different climate change scenarios. In this regard, *in situ* budget-based NCP estimations in the euphotic zone are especially difficult. This zone, which is particularly relevant for projections of the BCP (see above), is operationally defined as the layer in the water column from the surface to the depth of the 1% of photosynthetically available light (PAR), not corresponding to any physical boundary related to the structure of the water column. This implies that the upper mixed layer may cross above and below the euphotic depth during the long periods necessary for budget calculations, causing difficulties to discern the long-term biological impact on O_2 inventories (Haskell et al., 2020). Altogether, the uncertainty in euphotic zone NCP estimations based on O_2 budgets in the upper ocean is very high (e.g. Hull et al., 2016; Hemming et al., 2022; see also Bittig et al., 2018).

Direct methods based on *in vitro* O_2 changes after 24 h incubations allow resolving scales better-suited to study the control of CR and NCP in the euphotic zone of the ocean. However, they are time-consuming and prone to manipulation biases due to lengthy sample handling protocols or potential “bottle effects” on the incubated communities. The ensuing paucity of *in vitro* data explains why large-scale and generalised patterns of plankton metabolism have been searched through meta-analyses of combined results from independent studies (e.g., Regaudie-de-Gioux and Duarte, 2013; Serret et al., 2015). Unbiased meta-analyses require datasets that are highly consistent in terms of accuracy and precision, which is a challenge for a method that combines a high potential for biases and a need for high precision to detect the minor changes in seawater O_2 concentration. For instance, measuring a rate of 0.4 $\text{mmolO}_2\ \text{m}^{-3}\ \text{d}^{-1}$, typical of the oligotrophic open ocean, requires an interval of confidence ~0.3 $\text{mmolO}_2\ \text{m}^{-3}\ \text{d}^{-1}$, especially for the critical determination of the positiveness or negativeness of NCP; this implies a coefficient of variation in the replicated measurements of oxygen concentration in the initial and incubated samples of ~0.05% (assuming a seawater concentration of 225 $\text{mmolO}_2\ \text{m}^{-3}$, 4 replicates and p=0.05). The most extensive collection of independent published and unpublished plankton metabolism data (Regaudie-de-Gioux and Duarte, 2013; http://dx.doi.org/10.20350/digitalCSIC/220) evidences that these requirements are not always met. Only 58% of the CR and NCP measurements reported (2116 out of 3634 CR data and 2226 out of 3849 NCP data) are presented with any indication of statistical dispersion. As the magnitude of the standard error (s.e.) of metabolic rates is difficult to assess, we have compared the s.e. relative to the magnitude of NCP in the 2226 data in the combined dataset of Regaudie-de-Gioux and Duarte (2013) with the 973 data points from 10 Atlantic Meridional Transect cruises (AMT11-18, AMT21-22), which resulted from the concerted effort of a small group of researchers following the same protocols (Serret et al., 2015). This comparison evidences striking differences in precision, with many data in the combined dataset whose s.e. are too large (Figure 1A), especially at low NCP values. Accuracy of NCP measurements is even more difficult to assess, because no standard exists for metabolic rates. However, absolute bounds can be derived from purely physiological constraints, based on the biomass and maximum photosynthetic efficiency of the phytoplankton. The maximum photosynthetic rate per unit chlorophyll-a (Chla) in the global ocean (~23 mmolO2 mgChla-1 d-1, assuming 10 h of light and a PQ=1.1; Falkowski, 1981; Marra, 2012) and in oligotrophic ecosystems (~5 mmolO2 mgChla-1 d-1, assuming 10 h of light and a PQ=1.1; Karl et al., 2002; Marra et al., 2007) set two such bounds for net primary production (NPP). As NCP is < NPP (NCP=NPP-heterotrophic R), NCP values considerably far from 5 mmolO2 mgChla-1 d-1 are very unlikely in the gyres, and values near or above 23 are physiologically impossible. To minimise the impact of differences in phytoplankton biomass or light and nutrient fields on photosynthetic efficiency (Laws et al., 1987), we have compared the Chla : NCP ratios in the two subsets of data from the upper 10 m in unproductive ecosystems where Chla concentration was < 0.5 mg m^{-3} within the AMT latitude-longitude ranges (Figure 1B). While most AMT data are very close to, and below the 5 line, a large dispersion is observed along a similar Chla range in the independent observations gathered in Regaudie-de-Gioux and Duarte (2013), with some data that appear highly improbable, not to say physiologically impossible. These differences in precision and accuracy translate into noticeable differences in the representations of both the variability and latitudinal trend of NCP in the Atlantic Ocean (Figures 1C, D), and may partly explain the sustained disagreements and high uncertainty in regional estimations of NCP based on *in vitro* changes in O_2 concentration (Duarte et al., 2013; Williams et al., 2013).

A further shortcoming of meta-analyses is that small-scale patterns that are necessary to decipher the dynamic, often episodic and patchy co-variation of plankton metabolism with potential controlling factors, tend to be blurred in the grand averages or general trends (e.g. GPP : CR relationships). Our joined analysis of ten AMT datasets (8-37 stations per cruise) collected over >10 years (2000 to 2012) revealed consistent differences in GPP : CR relationship and metabolic state between the similarly oligotrophic North (heterotrophic) and South (autotrophic) Atlantic gyres (Serret et al., 2015). However, it provided very little insight into the regulation of NCP and CR in the ocean. Similarly, Robinson and Williams (2005) highlighted the unexpected lack of relationship between Chla and CR, despite both maintenance respiration and heterotrophic activity being expected to increase with autotrophic biomass. Such lack of relationship, which undermines the use of remotely sensed Chla observations to predict community metabolism, was confirmed by Regaudie-de-Gioux and Duarte (2013). Moreover, these authors also found a weak Chla : GPP relationship (R^2 = 0.29, n=1111) that contrasts with the key role played by phytoplankton biomass in models of primary production in the ocean (Westberry et al., 2023 and references therein). Conceptual and mechanistic models have often predicted that phytoplankton size determines the organisation and functioning of food webs, which should reflect on GPP : CR ratios and NCP (see Smith and Kemp, 2001 and references therein). However, the relationship between CR or NCP and the phytoplankton size-structure remains unresolved (Serret et al., 2001; Smith and Kemp, 2001; Arbones et al., 2008; Soria-Píriz et al., 2017; Wang et al., 2018; Juranek et al., 2020; Lozano et al., 2021). One specific objective of this paper is to overcome the limitations of meta-analysis, studying the relationship of CR and NCP with the abundance and structure of the phytoplankton

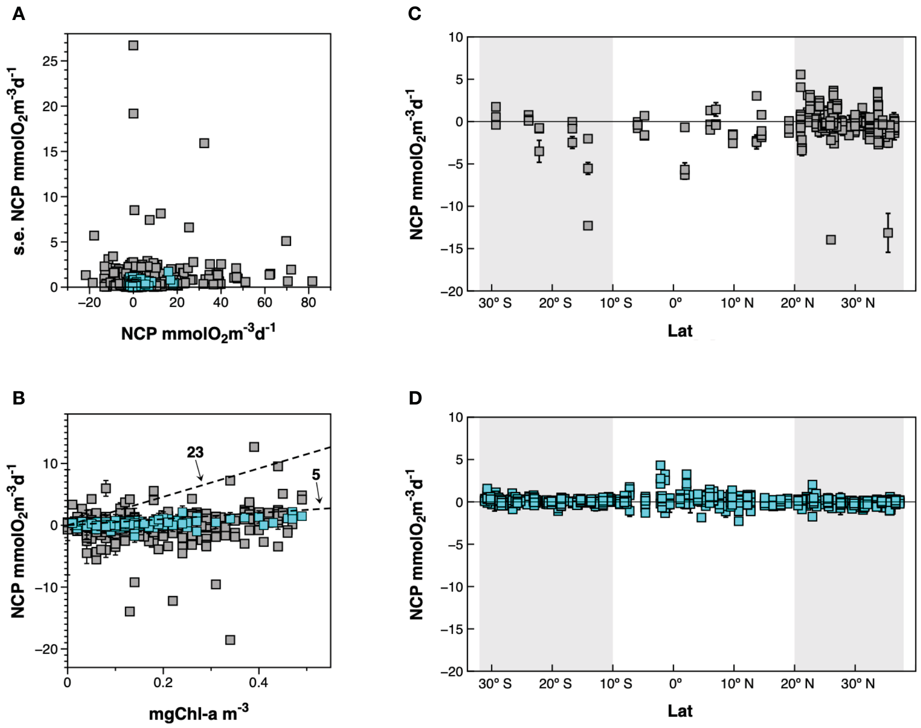

FIGURE 1

Comparison of precision and accuracy in two datasets in the Atlantic Ocean: grey squares, 25 published and unpublished records in the combined dataset of Regaudie-de-Gioux and Duarte (2013); blue squares, AMT11-22 data (Serret et al., 2015). **(A)** Comparison of standard errors relative to the magnitude of net community production. **(B)** Relationship between chlorophyll a concentration and net community production. Two physiological boundaries are identified based on the assimilation numbers that determine the maximum photosynthetic rate per unit chlorophyll a: ~23 mmol O2 mg Chla-1 d-1 for the global ocean (Marra, 2012) and ~5 mmol O2 mg Chla-1 d-1 characteristic of oligotrophic systems (Karl et al., 2002; Marra et al., 2007). NCP values considerably far from the 5 line are very unlikely in the gyres; values near or above the 23 line are physiologically impossible. **(C)** Latitudinal variation of net community production from the combined dataset in Regaudie-de-Gioux and Duarte (2013). **(D)** Latitudinal variation of NCP in Serret et al. (2015). The shadowed areas indicate the approximate location of the gyres. See text for details.

communities along a single latitudinal transect of the open Atlantic Ocean, with a focus on improved prediction.

We present here the detailed spatial variation of plankton metabolism along one selected Atlantic Meridional Transect (AMT) cruise, together with the variation of the physical and chemical environment and of the abundance and size-structure of the phytoplankton. We have selected the AMT22 cruise because, with 37 profiles of 5-6 depths down to the 0.1% PAR, including 12 stations in the Northern gyre and 9 in the Southern gyre, it is one of the most comprehensive datasets of plankton metabolism in the AMT series. Consistency of these data will be assessed by comparison with the entire AMT11-22 dataset (Serret et al., 2015) and also with a more coherent (in terms of precision and spatial coverage) subset of cruises (AMT11, 15, 21) to compare latitudinal patterns. AMT11, 15, 21 and 22 all took place during the boreal autumn; the very limited number of observations during boreal spring in the AMT11-22 dataset preclude an in-depth analysis of seasonality, however no evidence of a seasonal bias in regional patterns was observed (Serret et al., 2015). Our objectives are 1) to assess the validity of the conclusions, grand averages and general GPP : CR relationships derived from the meta-analysis of Serret et al. (2015) at ecological scales that are critical for prediction of changes in the metabolic state of the open ocean, 2) to improve the depiction of quasi-synoptic depth and latitudinal trends of GPP, CR and NCP along the Atlantic Ocean, and 3) to study the relation between community metabolism and the phytoplankton abundance, community structure and ^{14}C NPP; specifically, we will test the hypotheses that a) CR is poorly related to Chla (Robinson and Williams, 2005; Regaudie-de-Gioux and Duarte, 2013; Wikner et al., 2023, and references therein), b) CR is relatively invariant compared to GPP, meaning that the variation of NCP can be determined from GPP (Westberry et al., 2012; Duarte et al., 2013, and references therein), and c) the size-structure of phytoplankton communities determines food web functioning, reflecting on the GPP : CR ratio and NCP in the open ocean (Serret et al., 2001; Smith and Kemp, 2001 and references therein).

2 Methods

2.1 Sampling

A latitudinal (49°N–46°S) transect of 73 stations across the Atlantic Ocean (Atlantic Meridional Transect (AMT)-22 cruise) was conducted on RRS James Cook between Southampton, UK and Punta Arenas, Chile, between 10 October and 24 November 2012. Six biogeochemical provinces of the Atlantic Ocean were traversed: the mesotrophic North Atlantic Drift (NADR), Western Tropical

Atlantic (WTRA) and South Subtropical Convergence (SSTC), the oligotrophic South Atlantic Gyre (SATL), North Atlantic Tropical Gyre (NATR) and Northeast Atlantic Subtropical Gyre (NASTE) (Longhurst et al., 1995) (Figure 2). Each day, two stations were sampled at between 04:00 and 05:00 h, and between 13:00 and 14:00 h. Vertical profiles of temperature and conductivity were performed at every station using a stainless steel-framed Seabird CTD fitted to a rosette of 24x20 L Niskin bottles. The CTD system fluorometer was calibrated against extracted chlorophyll-a measurements from 250 mL seawater samples collected from the CTD Niskin bottles, following Welschmeyer (1994). Samples for nitrate concentration and abundance of pico- and nano-phytoplankton were collected at every station, while O_2 and ^{14}C-derived metabolic rates were measured only during the early morning stations, which were spaced at approximately 350 km intervals. Vertical profiles of photosynthetic active irradiance (PAR, 400-700 nm) were calculated at the 13:00-14:00 h stations from casts of an optical profiler (SeaOPS).

2.2 Nitrate concentration

Micromolar nitrate concentrations were determined using a Technicon segmented flow colorimetric autoanalyser with methodology based on Brewer and Riley (1965) employing clean sampling and handling techniques. The 60ml HDPE sample bottles were 10% acid cleaned and then Milli-Q washed before the sample water was taken from the CTD bottles into these sample bottles, wearing vinyl, powder free gloves. The sample bottle was fitted directly to the autosampler ready for analysis with no decanting of the samples to again stop any potential contamination. All samples were analysed within 90 min of sampling from the CTD-Rosette system.

2.3 Phytoplankton community structure and abundance by flow cytometry

Fresh seawater samples were collected in clean 250 mL polycarbonate bottles from the 20 L Niskin bottles from all CTD casts. Samples were stored in a refrigerator and analysed within 2 hours of collection. Fresh samples were measured using a Becton Dickinson FACSort flow cytometer which characterised and enumerated *Prochlorococcus* sp. and *Synechococcus* sp. (cyanobacteria) and pico- and nano-eucaryote phytoplankton, based on their light scattering and autofluorescence properties (Tarran et al., 2006).

2.4 Gross primary production, net community production and community respiration

At the early morning stations, gross primary production (GPP), net community production (NCP) and community respiration (CR) were determined at six depths from *in vitro* changes in dissolved O_2 after 24 h light and dark bottle incubations. Sampling and incubation were carried out at the same depths,

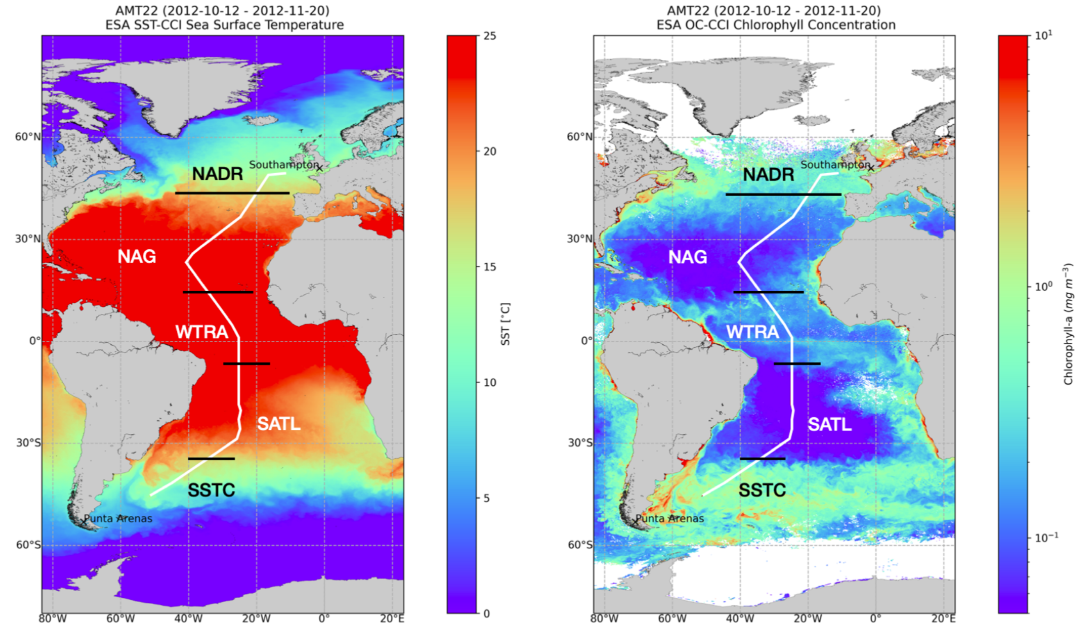

FIGURE 2
Track of Atlantic Meridional Transect 22 (AMT22) cruise, September–October 2012, overlaid on plots showing ESA Climate Change Initiative (CCI) Ocean Colour and Sea Surface Temperature data. The boundaries of biogeochemical provinces traversed (Longhurst, 1998) is shown. Each plot represents the median value for each pixel over the duration of the cruise. Earth observation data produced by the ESA Sea Surface Temperature Climate Change Initiative (SST-CCI) ESA Ocean Colour Climate Change Initiative (OC-CCI), courtesy of the NERC Earth Observation Data Acquisition and Analysis Service, the Ocean Biology Processing Group, NASA and European Space Agency.

simultaneously and under the same conditions as for ^{14}C incorporation experiments. Twelve 120 mL, gravimetrically calibrated, borosilicate glass bottles were carefully filled from each Niskin bottle using silicon tubing, overflowing by >250 mL. From each depth, four replicate 'zero-time' bottles were fixed immediately with Winkler reagents (1 mL of 3 M $MnSO_4$ and 1 mL of (8 M KOH + 4 M KI) solutions) added separately with an automatic multipipette. Two further sets of four replicates were incubated for 24 h in deck incubators. The incubators were maintained at surface temperature by pumping sea water from a depth of ~7 m through the upper light level incubators (97, 55, 33, 14, 7 & 3%) and from a chiller maintained at ±1°C of *in situ* temperature for the lower light level incubators (1 & 0.1%). One set of replicates was incubated in the dark, the other set in the equivalent irradiance to that found at the *in situ* sampling depth using various combinations of neutral density and blue plastic filters. Incubations always started at dawn and lasted 24 h. After the incubation period, the dark and light bottles were fixed with Winkler reagents. Dissolved O_2 concentration was determined with an automated Winkler titration system using potentiometric (Metrohm 716 DMS Titrino) end-point detection (Oudot et al., 1988). Aliquots of fixed samples were delivered with a gravimetrically calibrated ~50 mL overflow ("Knudsen") pipette. Fixing, storage and standardization procedures followed the recommendations by Grassoff et al. (1983). Production and respiration rates were calculated from the difference between the means of the replicate light and dark incubated bottles and zero-time analyses: NCP = ΔO_2 in light bottles (mean of $[O_2]$ in 24 h light - mean zero time $[O_2]$); CR = ΔO_2 in dark bottles (mean zero time $[O_2]$ - mean $[O_2]$ in 24 h dark); GPP = NCP + CR. The average standard error about the mean of both the NCP and CR rate measurements (which includes both experimental and biological variability) was 0.15 (n=214) $mmolO_2\ m^{-3}\ d^{-1}$. Integrated values were obtained by trapezoidal integration of the volumetric data down to the depth of 0.1% surface incident photosynthetically active irradiance, excluding volumetric data whose standard error was more than twice the magnitude of the rate. The standard error of integrated GPP, CR and NCP was calculated through propagation of the random error in the volumetric measurements.

2.5 ^{14}C primary production

Water samples were taken from pre-dawn CTD deployments from 6 depths in the euphotic zone following the methods described in Tilstone et al. (2009). The samples were transferred from Niskin bottles to black carboys and sub-sampled into three 75 mL clear polycarbonate bottles and three black polycarbonate bottles; all bottles were pre-cleaned following JGOFS protocols (IOC, 1994), to reduce trace metal contamination. Each sample was inoculated with between 185 and 740 kBq (5 - 15 µCi) $NaH^{14}CO_3$ according to the biomass of phytoplankton, which was checked using the Chla profiles from the CTD cast. The polycarbonate bottles were transferred to the same on-deck (simulated *in situ*) incubation system used for NCP and CR incubations, using neutral density and blue filters to simulate subsurface irradiance over depth to 97%, 55%, 33%, 20%, 14%, 7%, 3%, 1% or 0.1% of the surface value and incubated from local dawn to dusk (10 – 16 h). To terminate the incubations, suspended material was filtered sequentially through 0.2 µm, 2 µm and 10 µm polycarbonate filters to measure pico-, nano- and microphytoplankton production respectively. A low vaccum pressure (20 cm Hg) was used to filter the samples to ensure that there was no loss of cells from the micro- or nano- to the pico- size fractions. The filters were exposed to concentrated hydrochloric acid fumes for 8-12 h, immersed in scintillation cocktail and ^{14}C disintegration time per minute (DPM) measured on board using a Packard, Tricarb 2900 liquid scintillation counter, with external standard and the channel ratio methods applied to correct for quenching.

3 Results

3.1 Thermal structure, nitrate and chlorophyll a concentrations

Figure 3 shows the latitudinal and vertical distributions of seawater temperature, nitrate and chlorophyll a concentration in the upper 250 m along the AMT22 cruise transect, which reflect the characteristics of the provinces traversed, identified here following Longhurst (1998). Although no single criterion can determine the exact location of regional nutriclines throughout such a varying scenario, the nitracline here is broadly defined as a gradient from 1 to 5 $\mu mol\ NO_3^-\ L^{-1}$ through a vertical range of 25 m, although only the 1 $\mu mol\ NO_3^-\ L^{-1}$ isoline (the uppermost part) is presented in figures.

The transect began in the south-eastern region of the NADR, where salinity and temperature were relatively low and homogeneous and nitrate was high through the water column. In the southern part of the NADR (47-43° N), a relatively weak thermocline was observed at the bottom of a shallow (~50 m depth) nitrate-depleted surface mixed layer. A broad frontal zone marked the transition from the NADR to the North Atlantic Gyre (NAG), which includes the westerlies NAST-E province (43-30° N) and the trades NATR province (30°-15° N) (Longhurst et al., 1995). The southward deepening of the nitracline reflected the increased surface warming and stratification through the gyre. The depth of the nitracline ranged from 75-100 m at the periphery of the gyre to 150-225 m at the centre of the NATR, where nitrate concentration was <0.05 $\mu mol\ L^{-1}$ from the surface down to ca. 100 m depth, indicative of very strong oligotrophic conditions. At the southern end of the NAG, the tilting of isolines of temperature and nitrate indicated the transition to the WTRA (15° N to 5° S), where the quasi-permanent upwellings and the increased surface warming created the most intense vertical gradients in temperature and nitrate. The strongest upwelling and shallowest nitracline (50 m depth) was found at the northern part of the province (centred around 10° N), caused by the divergence between the N equatorial current and counter current. The upwelling created by the equatorial divergence at ca. 2° S was less intense, possibly due to the seasonal weakening of equatorial trade winds (Grodsky et al., 2008). The associated convergence created between the N equatorial

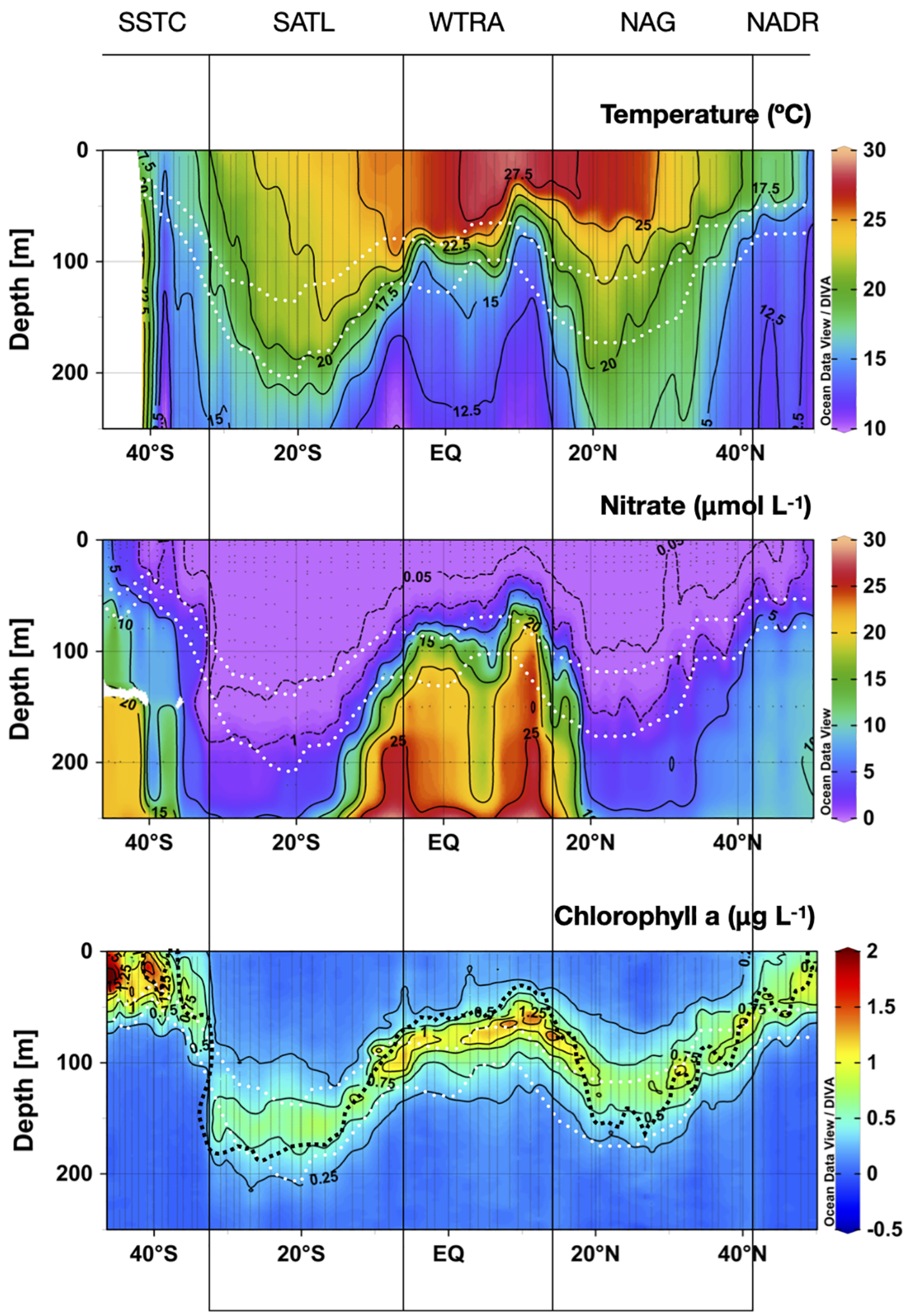

FIGURE 3
Depth-latitudinal sections of temperature, nitrate concentration and chlorophyll a concentration during the AMT22 cruise. The white dotted lines are the depths of the 1 and 0.1%PAR. The black dotted line in the chlorophyll a contour plot is the depth of the nitracline. The approximate location of biogeographic provinces (Longhurst, 1998) is presented. Figures produced using Ocean Data View (Schlitzer, Reiner, Ocean Data View, https://odv.awi.de, 2022).

counter current and the S equatorial current can be identified in the sinking of surface seawater at ~5° N. South of the equatorial upwelling, the pycnocline progressively deepened and weakened as surface seawater became more saline (data not shown) and relatively colder. The transition to the SATL (5-32° S) was marked by such a progressive cooling and deepening of the surface mixed layer, with spatial patterns of thermohaline properties mirroring the NAG-WTRA transition. In the SATL, however, surface cooling was evident from the very northern boundary. The fact that sampling was carried out during early boreal autumn in the NAG, and during early austral spring in the SATL (i.e., after long periods of surface warming and cooling, respectively) may contribute to these regional differences. The vertical gradients of temperature were weaker and more extended, and the mixed layer and nitracline reached deeper in the SATL than in the NAG. The thermocline and nitracline depths were maximum near the centre of the SATL at ~15-25° S. South of this area, a front marked the transition between the stratified waters of the SATL and the colder and well-mixed waters of the SSTC (32-45°S). The reduced stratification and intense wind in this province caused a marked increase in nitrate concentration through the water column, with the 1 $\mu molNO_3^- L^{-1}$ isoline reaching the surface.

Throughout the transect, the nitracline was always deeper relative to the light field in the gyres than in the productive provinces: it was above or near the depth of the 1% of photosynthetic available radiation (PAR) in the NADR, WATR and SSTC, but it was near the depth of the 0.1%PAR in the NAG and SATL. Such deep nutrient depletion reflects the intense oligotrophy in the gyres, and suggests relevant biological uptake of nitrate in these regions >50 m deeper than the 1%PAR.

Near-surface Chla maxima were only observed in the temperate NADR and SSTC, with almost three times higher concentration in the latter, possibly related to the higher stratification and lower nutrient concentration in the autumn NADR than in the spring SSTC. The deepening of the thermocline and nitracline into the N and S gyres was accompanied by a progressive deepening and weakening of the Chla maximum. Through both the NAG and SATL a deep Chla maximum (DCM) was observed extending 40-75 m above the nitracline. The maximum Chla concentration was lower in the SATL than in the NAG, and the absolute depth of the DCM, its vertical extent and upward distance from the nitracline were higher in the SATL than in the NAG. In the latter, the DCM was centred near the depth of the 1% PAR, as it was throughout most meso- and eutrophic environments, but the DCM in the SATL was found between the 1 and 0.1% PAR. This all indicates a higher degree of oligotrophy in the SATL, despite the fact that sampling was carried out during early boreal autumn in the NAG and during the austral spring in the SATL. Local increases in Chla concentration were observed at the DCM in the NAST-E section within the NAG (43-30° N) associated to local uplifts of the nitracline (e.g. at 32° N). Both surface and subsurface Chla concentrations increased approx. twice in the WTRA province, where the DCM followed the uplift of the thermo- and nitraclines by the regional upwelling. The shallowest DCM and highest Chla concentration were observed near the North equatorial divergence (around 10° N) where the most intense upwelling occurred.

3.2 Nano- and picophytoplankton abundance

Figure 4 shows the spatial distribution of the abundance of nano- and picoeukaryotic phytoplankton, *Synechococcus* spp. and *Prochlorococcus* spp. Abundance of nano- and picoeukaryotic cells was very high in the productive waters of the NADR, WTRA and SSTC, especially in the latter. In these provinces, the vertical distribution of cell abundance always matched the variation of Chla, with higher numbers in the surface layer of the high latitude provinces and in the DCM of the WTRA. Very low abundance of nano- and picoeukaryotic phytoplankton was observed in the two gyres, where higher numbers of picoeukaryotes were observed at the depths of the DCM; nanoeukaryotic phytoplankton was more abundant in the SATL than NAG and very low numbers were found in both gyres at the DCM.

The abundance of *Synechococcus* spp. was also very high in the Chla-rich surface NADR and SSTC, and in the upwelling system of the WTRA, but higher concentrations in the latter were observed above the DCM. Along the two gyres, the abundance of *Synechococcus* spp. was very low, especially at the DCM. An exception to these general patterns was observed in the central part of the NAG at around 23-28° N, where relatively high *Synechococcus* spp. numbers were observed in the upper 75 m.

The abundance of *Prochlorococcus* spp. was very low in high latitudes, especially in the highly productive SSTC, where it was practically absent. The highest abundances were found above the DCM in the WTRA, and relatively high numbers were observed in the upper part of the DCM within the two gyres (above the 1% PAR depth), where its distribution mirrored that of *Synechococcus* spp.

These observations agree with the general patterns in the Atlantic of higher abundance of *Synechococcus* spp. and eukaryotic phytoplankton in mesotrophic regions, and dominance of *Prochlorococcus* spp. in the gyres (Zubkov et al., 2000).

3.3 Plankton O_2 metabolism

3.3.1 Gross photosynthesis

3.3.1.1 Volumetric rates

GPP ranged from 0.01 ± 0.12 $mmolO_2 m^{-3} d^{-1}$ at the bottom of the euphotic layer in the NAG to 9.83 ± 0.34 $mmolO_2 m^{-3} d^{-1}$ near the surface at about 46° South (SSTC) (Figure 5). Throughout the transect, higher rates were always measured near the surface, with the highest values in the Chla-rich surface waters of the SSTC and NADR (>6 and >2 $mmolO_2 m^{-3} d^{-1}$, respectively), and relatively high rates above the DCM in the WTRA (>1.5 $mmolO_2 m^{-3} d^{-1}$).

GPP was also ≥1 $mmolO_2 m^{-3} d^{-1}$ near the surface in the transition zones at the periphery of the gyres, and decreased rapidly towards their centres, especially in the NAG. GPP at the DCM in the N and S gyres was very low, but measurable at most stations down to the depth of the 0.1%PAR (the average rates at the 0.1% PAR in the NAG and SATL were 0.18 ± 0.09 and 0.30 ± 0.06 $mmolO_2 m^{-3} d^{-1}$, respectively; and the average standard error of measurements at that depth were 0.13 and 0.15 $O_2 m^{-3} d^{-1}$, respectively). In the NAG, GPP values ≤ 0.5 $mmolO_2 m^{-3} d^{-1}$ were measured between ~32° and 25° N through the euphotic layer, including the DCM. South of ~26°N, GPP rates >0.5 $mmolO_2 m^{-3} d^{-1}$ were observed again in both the upper 50 m and at the DCM. Despite its lower Chla concentration and higher degree of oligotrophy, GPP was higher and less variable in the SATL than in the NAG, with rates typically ≥0.5 $mmolO_2 m^{-3} d^{-1}$ from the surface to the DCM. These values are in agreement with the average GPP rates at the NAG and SATL in the combined AMT11-22 dataset (Table 1).

3.3.1.2 Integrated rates

The average integrated GPP was highest in the SSTC (196.6 ± 7.3 $mmolO_2 m^{-2} d^{-1}$), followed by the WTRA, SATL, NAG and NADR provinces (114.0 ± 15.6, 95.5 ± 26.2, 58.3 ± 19.6, 46.9 ± 6.3 $mmolO_2 m^{-2} d^{-1}$ respectively) (Figure 6A). These results, where higher integrated GPP is observed in the oligotrophic SATL than in

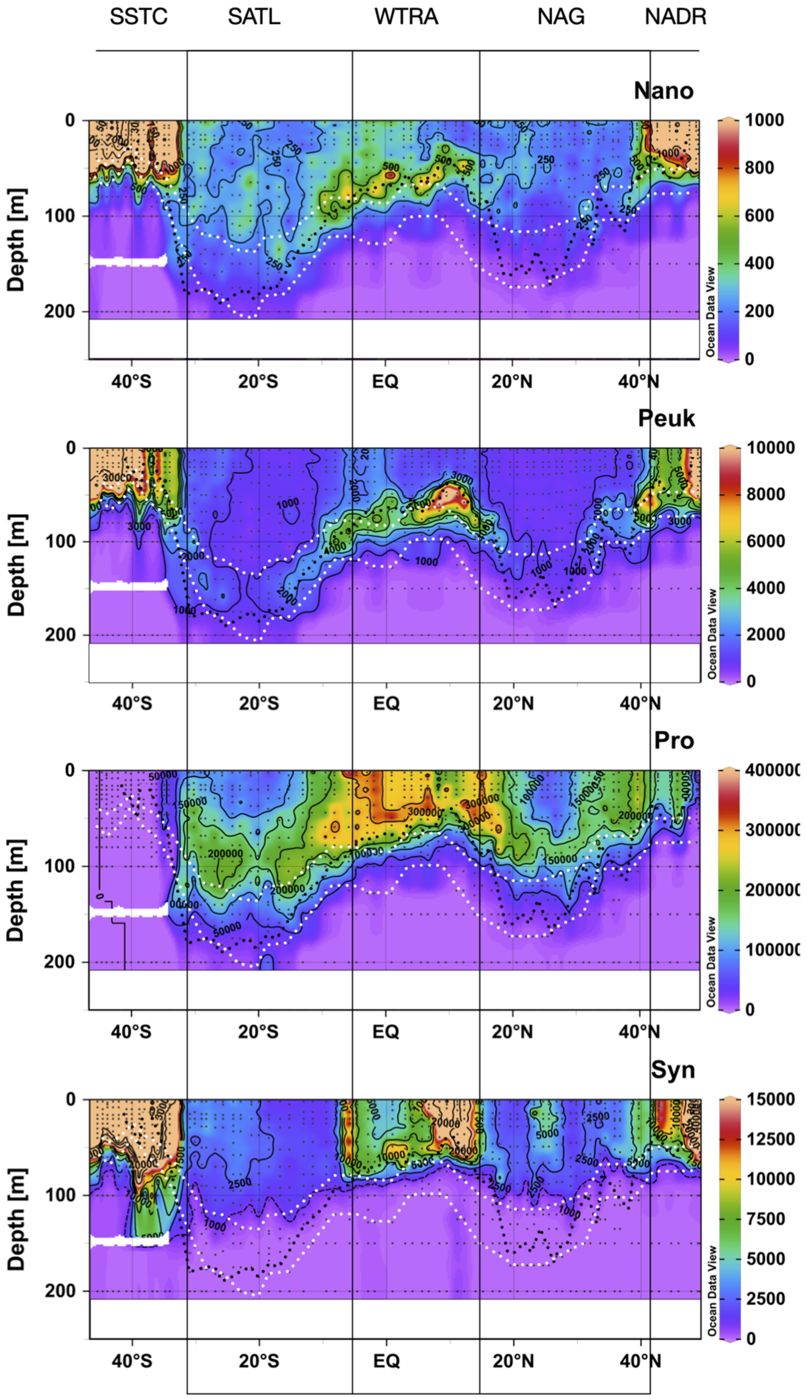

FIGURE 4
Depth-latitudinal sections of abundance (cells mL-1) of nanoeukaryotic and picoeukaryotic phytoplankton, *Prochlorococcus* spp. and *Synechococcus* spp. during the AMT22 cruise. The white dotted lines are the depths of the 1 and 0.1%PAR. The black dotted line is the depth of the nitracline. The approximate location of biogeographic provinces (Longhurst, 1998) is presented. Figures produced using Ocean Data View (Schlitzer, Reiner, Ocean Data View, https://odv.awi.de, 2022).

the mesotrophic NADR, partly result from the regional differences in depth of integration, i.e., in the depth at which the incident light reached the 0.1% in each biogeographic province (see Figure 5). When integrated rates are divided by the depth of integration at the respective sampling stations, the spatial variation of the depth-weighted GPP (GPP_Z, which represents the average GPP rate across the euphotic layer) conforms well with the expectations based on the general productivity of the provinces: the highest average GPP_Z was measured in the SSTC (2.78 ± 0.16 mmolO_2 m^{-3} d^{-1}), followed by the WTRA, NADR, SATL and NAG (1.20 ± 0.19, 0.99 ± 0.15, 0.63 ± 0.16, 0.5 ± 0.16 mmol O_2m^{-3} d^{-1} respectively). Depth-weighting of integrated GPP also brings the magnitude and variation of AMT22 rates very close to those in previous AMT cruises (Figure 6B). For this comparative exercise we have selected

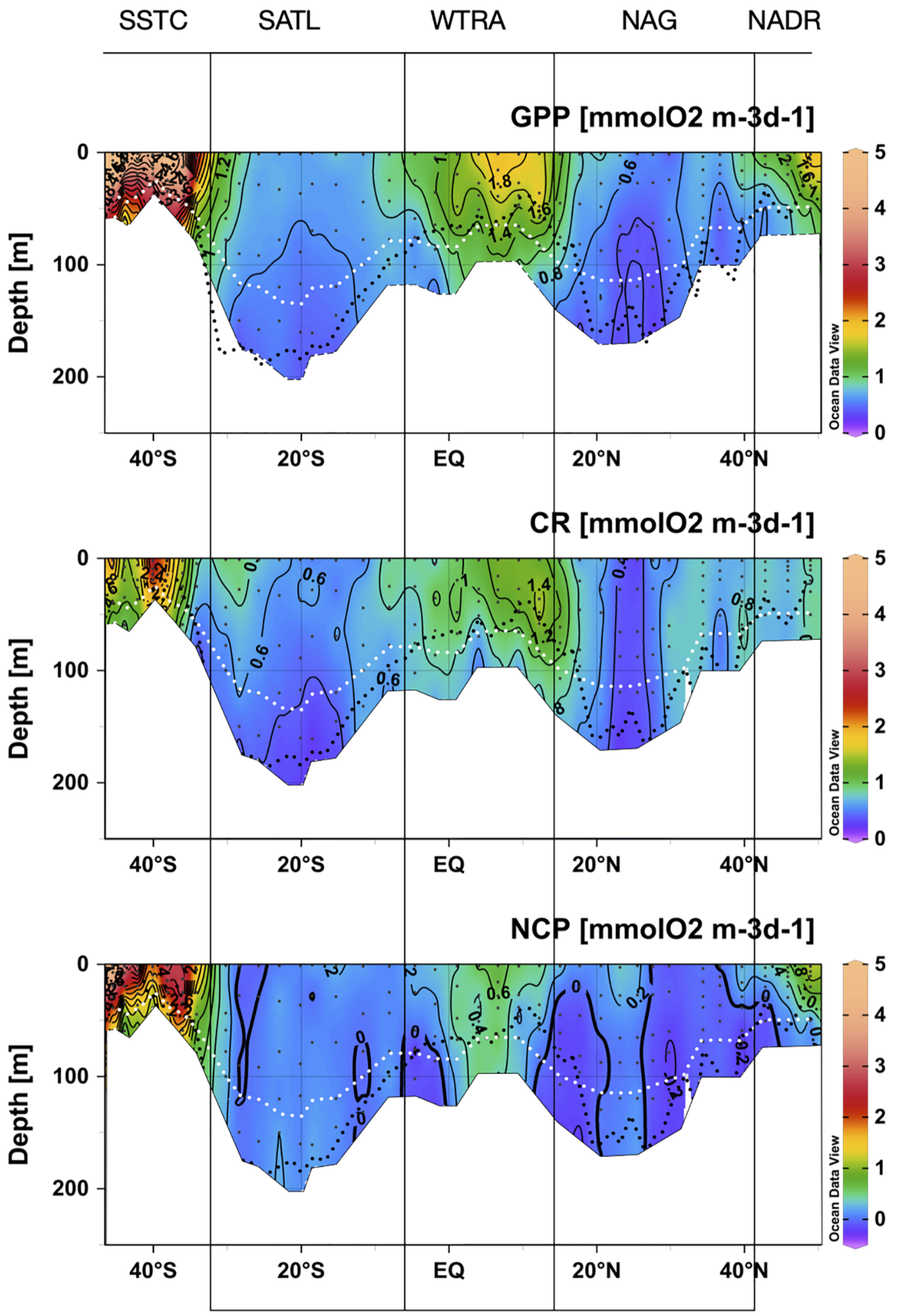

FIGURE 5
Depth-latitudinal sections of gross primary production, community respiration and net community production during the AMT22 cruise. The black dotted line is the depth of the nitracline. The white dotted line is the depth of the 1%PAR. The blanked area is the location of the deepest sample of each profile, at the depth of the 0.1%PAR. The approximate location of biogeographic provinces (Longhurst, 1998) is presented. Figures produced using Ocean Data View (Schlitzer, Reiner, Ocean Data View, https://odv.awi.de, 2022).

from the AMT11-22 dataset, those cruises with a continuous record of data through the regions studied here (AMT11-15-21), which ensures the consistency of zonal averages. GPP_Z rates in the AMT22 and the AMT11-15-21 datasets depict very similar W-shaped latitudinal trends, in a much better agreement with the latitudinal variation of the nitracline than the variation of GPPint, with more sensible differences between meso- and oligotrophic regions and lesser differences between the two gyres (Figures 6A, B). Moreover, the relationship between depth-weighted Chla and GPP (GPP_Z=4.53$Chla_Z$-0.59; r^2 = 0.88; n=37) markedly improved over the poor volumetric (not shown) and integrated relationships (Figures 7A, B), confirming the value of representing biogeographic patterns with depth-weighted, rather than volumetric or integrated variables. The significant $Chla_Z$: GPP_Z relationship shows little regional differences, despite the marked differences in euphotic, pycnocline, nitracline and DCM depths that

TABLE 1 Average (± s.e.) integrated (mmolO2 m-2 d-1) and depth-weighted (mmolO2 m-3 d-1) metabolic rates in the NAG and SATL in the combined AMT11-22 dataset (Serret et al., 2015) and in the AMT22 alone.

	NAG		SATL	
	Serret et al. (2015) autumn	AMT22	Serret et al. (2015) spring	AMT22
GPP_{int}	55.7 ± 3.2	71.17 ± 9.24	70.8 ± 2.6	116.1 ± 6.63
CR_{int}	72.0 ± 3.5	74.26 ± 10.49	58.4 ± 3.7	93.15 ± 2.69
NCP_{int}	-16.3 ± 2.5	-3.27 ± 5.77	12.3 ± 2.4	23.98 ± 6.93
GPP_Z	0.56 ± 0.02	0.56 ± 0.06	0.55 ± 0.02	0.69 ± 0.06
CR_Z	0.68 ± 0.03	0.59 ± 0.07	0.48 ± 0.02	0.55 ± 0.04
NCP_Z	-0.12 ± 0.02	-0.03 ± 0.04	0.06 ± 0.02	0.14 ± 0.04

reflect on differences in phytoplankton composition and community structure (see above). This strong relationship allows the estimation of a general daily assimilation number (ratio of photosynthetically O_2 produced per mg Chla per day) of 4.35 $mmolO_2\ mgChla^{-1}\ d^{-1}$, which is near but below the maximum 5 $mmolO_2\ mgChla^{-1}\ d^{-1}$ characteristic of oligotrophic systems (Karl et al., 2002; Marra et al., 2007; assuming 10 h of light and PQ=1.1) and agrees well with values measured during stratification periods in coastal temperate ecosystems (4.15 ± 1.23 $mmolO_2\ mgChla^{-1}\ d^{-1}$ in the Ría de Vigo during the summer; Lozano et al., 2021).

3.3.2 Community respiration

3.3.2.1 Volumetric rates

CR was less variable than GPP, ranging from 0.10 ± 0.18 $mmolO_2\ m^{-3}\ d^{-1}$ below the DCM in the central SATL to 3.51 ± 0.20 $mmolO_2\ m^{-3}\ d^{-1}$ near the surface at about 40° South (SSTC)

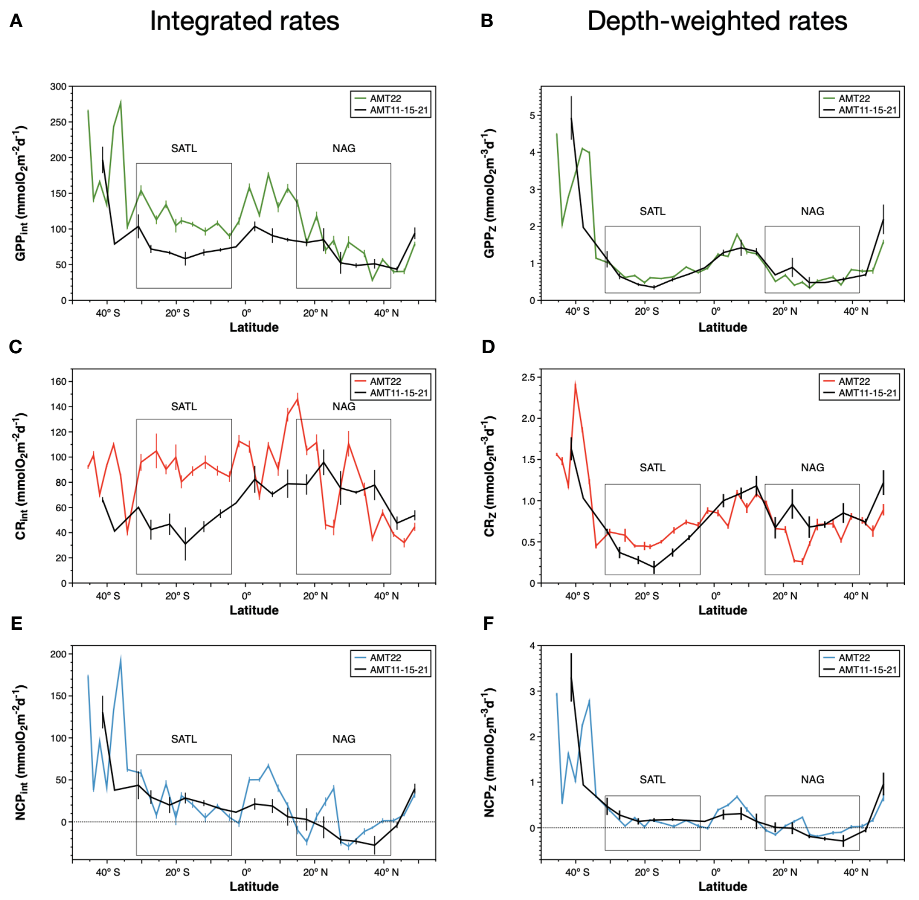

FIGURE 6
Integrated rates of **(A)** gross photosynthesis, **(C)** community respiration and **(E)** net community production during the AMT22 cruise. Depth-weighted rates in the euphotic zone of **(B)** gross photosynthesis, **(D)** community respiration and **(F)** net community production along the AMT22 cruise. The variation of integrated and depth-weighted rates during the AMT11, 15 and 21 cruises is presented, averaged in sections of 5o of latitude. Error bars are standard errors. Note the different scale for GPP, CR and NCP rates.

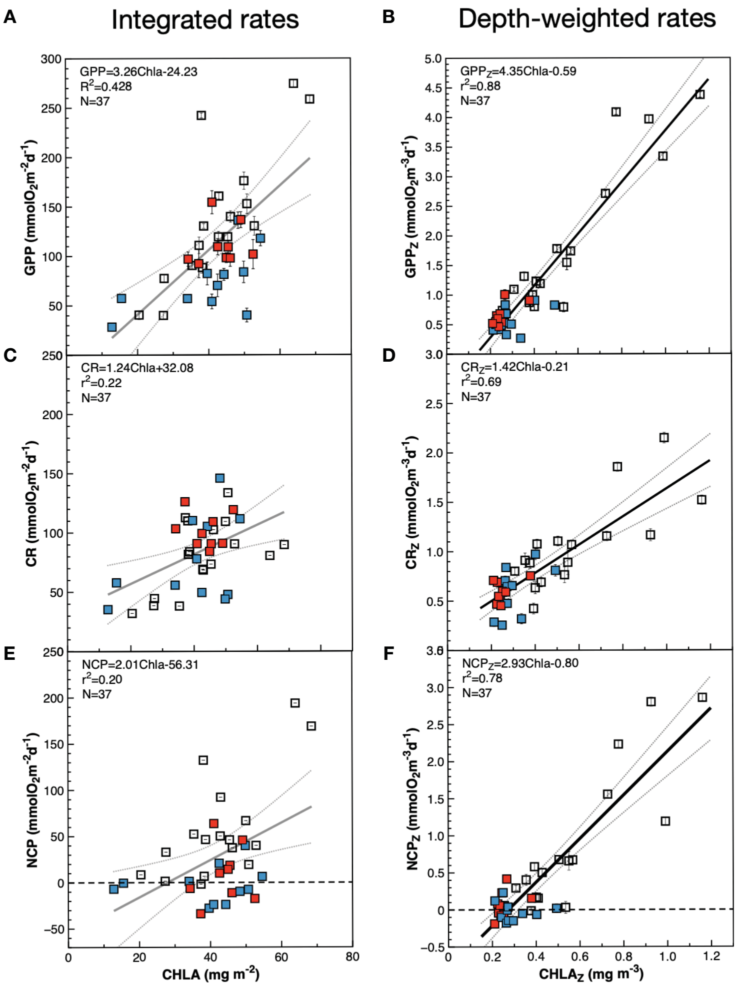

FIGURE 7
Relationships between chlorophyll a concentration and metabolic rates in the euphotic zone during the AMT22 cruise. Blue symbols are data from the NAG, red symbols are data from the SATL, open symbols are data from other provinces. **(A, C, E)**, integrated values; **(B, D, F)**, depth-weighted values calculated dividing the integrated values by the depth of integration (0.1% PAR depth). Results of general OLS regression analyses are always presented for comparison, despite the poor fit with integrated values (poorly fitted lines are presented in grey). The dotted lines are the 95% confidence interval. Error bars are standard errors.

(Figure 5). As with GPP, CR was high (≥ 1 mmolO$_2$ m^{-3} d^{-1}) in the SSTC and also in the WTRA, particularly in its northern sector (approx. 15°-5°N) above the DCM. However, in surface areas of the NADR with similar GPP and Chla values, low CR rates were observed. The lowest respiration was measured in the gyres, with values near 0.5 mmolO$_2$ m^{-3} d^{-1} and very little depth or latitudinal variation through most of the S gyre. These values agree well with the SATL average of 0.48 ± 0.02 mmolO$_2$ m^{-3} d^{-1} in the AMT11-22 dataset (Table 1). The NAG showed similarly low depth variation, but higher latitudinal variation than the SATL, with very low CR rates (0.09 ± 0.15 to 0.45 ± 0.13 mmolO$_2$ m^{-3} d^{-1}, average 0.25 ± 0.03 mmolO$_2$ m^{-3} d^{-1}) in the central region of the gyre (26-23° N) where high abundances of *Synechococcus* spp. were observed (see above). These low rates are less than half the CR measured elsewhere in the NAG (>0.6 mmolO$_2$ m^{-3} d^{-1}), the latter agreeing with the average NAG CR in the AMT11-22 dataset (0.68 ± 0.03 mmolO$_2$ m^{-3} d^{-1}; Table 1).

3.3.2.2 Integrated rates

The small range of volumetric CR is reflected in a weaker (if appreciable) regional variation of integrated CR (CR_{int}) compared to integrated GPP (Figures 6A, C; note differences in the Y scale). If any, lower CR_{int} was observed in the NADR and the NAG, although with too high a variation within this province to discern regional patterns. This would concur with the general agreement on the relative constancy of CR compared to GPP in the ocean (Karl et al., 2003; Williams et al., 2004; del Giorgio and Williams, 2005; Robinson and Williams, 2005; Carlson et al., 2007; Duarte et al., 2013; Regaudie-de-Gioux and Duarte, 2013). However, such a constancy partly results here from the regional differences in the depth of the euphotic zone: when CR_{int} rates are divided by the depth of integration (0.1% PAR) a clear W-shaped latitudinal pattern emerges (Figure 6D), resembling the GPP_Z trend. Special attention deserves to be paid to the low CR region in the NAG at 26-23° N, which is clearly observable in both the volumetric, integrated and depth-weighted CR rates (Figures 5, 6). In addition to improved spatial patterns, CR_Z also markedly improves the relationship with Chla over the poor $Chla_{int}$: CR_{int} relationship (Figures 7C, D).

3.3.3 Net community production and GPP: CR relationship

3.3.3.1 Volumetric rates

NCP ranged between -1.50 ± 0.16 $mmolO_2\ m^{-3}\ d^{-1}$ near the bottom of the euphotic layer at 44 °S, to 7.02 ± 0.15 $mmolO_2\ m^{-3}\ d^{-1}$ near the surface at about 45.5° S, both at the SSTC (Figure 5). NCP was >0.4 $mmolO_2\ m^{-3}\ d^{-1}$ in the Chla-rich, high GPP waters of the NADR, WTRA and SSTC. Strong vertical gradients of NCP developed in the periphery of the NADR and WTRA, where negative rates were measured in subsurface waters including the DCM. Low and mostly positive NCP was measured through the SATL (-0.48 ± 0.11 to 0.59 ± 0.11 $mmolO_2\ m^{-3}\ d^{-1}$, average 0.13 ± 0.04 $mmolO_2\ m^{-3}\ d^{-1}$), with very little vertical or latitudinal variation. A similar range was observed in the NAG (-0.43 ± 0.11 to 0.48 ± 0.05 $mmolO_2\ m^{-3}\ d^{-1}$), however, both the average (-0.01 ± 0.03 $mmolO_2\ m^{-3}\ d^{-1}$) and distribution of NCP were different, with a general prevalence of net heterotrophy (NCP<0) except throughout the euphotic zone at the low CR region in the central part of the gyre (26-23° N).

3.3.3.2 Integrated rates

As with GPP and CR, depth-weighted NCP rates (NCP_Z) improve the representation of latitudinal patterns compared to integrated rates: the difference between the oligotrophic gyres and the productive provinces (especially the NADR) is increased, the difference between the two gyres is reduced and a W-shaped latitudinal trend emerges (Figures 6E, F). Such a trend, which agrees with the latitudinal variation of the nitracline, is flattened compared to GPP_Z due to the enhanced respiration in the permanent upwelling systems of the WTRA, and asymmetric due to the lower NCP_Z in the NAG than in the SATL (caused by the higher CR_Z in the former). This NCP_Z trend also compares well with the average latitudinal variation of NCP_Z in the AMT11-15-21 dataset, and greatly improves the significance of the relationship of NCP with Chla (Figures 7E, F), with the average Chla in the euphotic zone ($Chla_Z$) explaining 78% of the variation of NCP_Z.

3.3.3.3 GPP: CR relationships

The depth and latitudinal covariation observed between volumetric and integrated CR and GPP rates during the AMT22 (Figures 5, 6) is reflected in significant GPP : CR relationships (Figure 8). Volumetric rates depict a single GPP : CR relationship, with no differences between mesotrophic and oligotrophic provinces, contrasting with different system-dependent relationships previously observed (Serret et al., 2009; Serret et al., 2015; Lozano et al., 2021). The generalised GPP : CR relationship has a slope <1 and a threshold GPP for net heterotrophy (GPP<CR) of 0.63 $mmolO_2\ m^{-3}\ d^{-1}$. This is a lower threshold than the 1.26 $mmolO_2\ m^{-3}\ d^{-1}$ in Regaudie-de-Gioux and Duarte (2013), but would still predict net heterotrophy through extensive areas of the NAG and SATL where net autotrophy was observed (Figure 5), indicative of the poor predictive power of generalised relationships or derived thresholds between volumetric rates.

When integrated and depth-weighted rates are analysed, the GPP : CR relationships remain invariant for mesotrophic provinces (although a significant relationship is only observed with depth-weighted rates), but oligotrophic gyres showed a different behaviour: significant 1:1 GPP_{int} : CR_{int} and GPP_Z : CR_Z relationship were observed in the NAG, while results in the SATL did not show any significant trend. Although the different GPP : CR relationships between meso- and oligotrophic provinces agree with

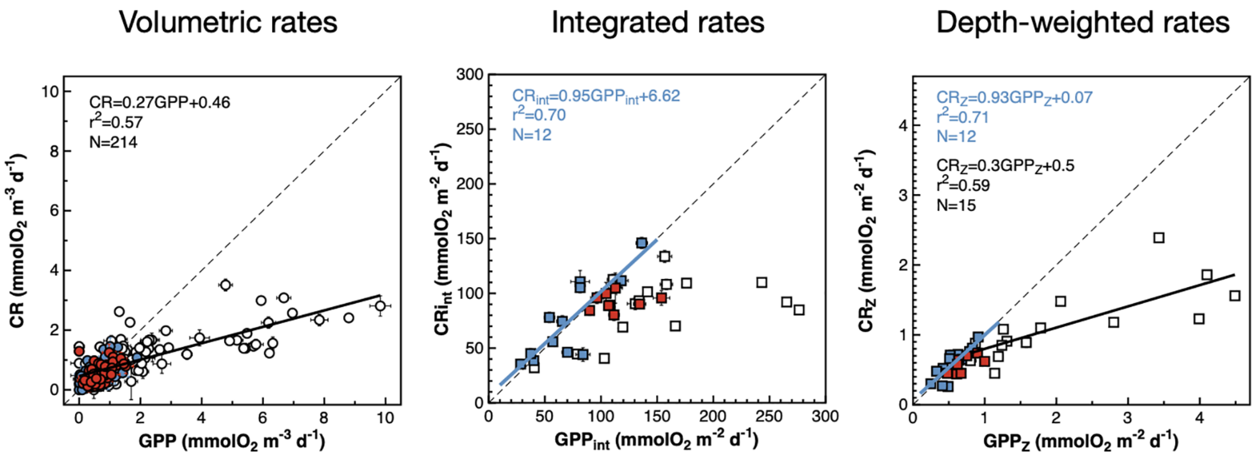

FIGURE 8

Relationships between volumetric, integrated and depth-weighted rates of gross photosynthesis and community respiration. Blue symbols are data from the NAG, red symbols are data from the SATL, open symbols are data from other provinces. Results of OLS regression analyses are presented when the r2 > 0.5. The blue line is the regression line with NAG data. Black lines are regression lines with non-gyral data. Error bars are standard errors. The dotted lines are 1:1 lines. Error bars are standard errors.

previous observations (Serret et al., 2009), the relationships in the gyres disagree with observations in the AMT11-22 dataset, where a 1:1 relationship was observed in the SATL while the slope in the NAG was 0.76 (Serret et al., 2015). This conflict between the analysis of results from a single cruise and the meta-analysis of results from ten cruises over >10 years puts into question the scalability of the relationships and conclusions from such a meta-analysis and will be discussed in the next section.

3.4 Particulate ^{14}C primary production

The highest rates of particulate organic carbon production (^{14}CPP) were measured in the surface layer of the SSTC and, to a lesser extent, of the NADR and WTRA, and the lowest rates were measured in the SATL (Figure 9). In the productive temperate provinces, the vertical distribution of ^{14}CPP was tightly coupled to that of Chla, while in the equatorial upwelling province (WTRA) and in the stratified oligotrophic gyres, ^{14}CPP was always higher near the surface, detached from the deep maxima in Chla and nano- and picophytoplankton abundances. Higher rates were observed in the NAG than in the more oligotrophic SATL.

The depth and latitudinal variation of ^{14}CPP and O_2 GPP were very similar. The relationship between GPP and ^{14}CPP is described by the equation GPP (mmolO_2 m^{-3} d^{-1}) = 1.83^{14}CPP (mmolC m^{-3} d^{-1}) + 0.42, n = 198, $r^2 = 0.88$, $p<0.01$, which agrees with the 1.94 slope observed in the AMT11 dataset (Serret et al., 2006) and with the results in Bender et al. (1999) where 24-h ^{14}CPP rates were ca. 45% of O_2 GPP in the equatorial Pacific, but are lower than the GPP to ^{14}CPP ratio of 7.1 ± 0.1 in the meta-analysis of Regaudie-de-Gioux and Duarte (2013). Excluding negative values, the relationship of net community production (NCP) with ^{14}CPP is described by the equation NCP (mmolO_2 m^{-3} d^{-1}) = 1.3 ^{14}CPP (mmolC m^{-3} d^{-1}) + 0.07, n=135, $r^2 = 0.70$, $p<0.01$, which is between the theoretical photosynthetic quotients of 1.4 ± 0.1 and 1.1 ± 0.1 for new and recycled production (Laws, 1991), and concurs with the 1.4 slope obtained by Marra (2009) from the regression between ^{14}C assimilation and O_2 NCP data from 4 JGOFS process studies.

Picophytoplankton was the size-fraction dominating the photosynthetic production of particulate carbon throughout the transect, followed by the nanoplankton (Figure 9). The relative contribution of the nanoplankton to total ^{14}CPP was higher near the surface and decreased markedly with depth in the gyres, reaching <20% at the DCM. The contribution of the picophytoplankton was higher at depth, particularly in the gyres, where it represented >60% throughout the DCM and reached >80% especially in the SATL. A marked decrease in the percentage of ^{14}CPP by the picoplankton was observed near the centre of the NAG (at around 25° N), just below the layer where high numbers of *Synechococcus* spp. cells were observed together with reduced CR rates. Such a decrease resulted from an almost five times increase in the rate of ^{14}CPP by cells >10 µm, reaching 121.74 ± 18.06 mgC m^{-2} d^{-1} (vs. a regional average, excluding this station, of 25.04 ± 16.14 mgC m^{-2} d^{-1}). Despite the relative importance, overall range and regional variation of the percentage of ^{14}CPP by the picophytoplankton, no relationship was observed with either GPP, CR or the GPP/CR ratio (Figure 10).

4 Discussion

Community respiration is a relatively slow variable that integrates the energy-producing process that supports the maintenance, activity and growth of most auto- and heterotrophic organisms in the oxygenated ocean. All three components of respiration depend on the availability of organic matter, which should reflect on tight relationships between CR and the biomass and production of autotrophic organisms (Robinson and Williams, 2005). However, the faster response of photosynthesis to environmental forcing implies that photosynthesis and respiration are not always tightly connected, especially at the community level and in the dynamic ocean. Sinking, trophic processes (e.g., lability or stoichiometric constraints on heterotrophy), or community dynamics (e.g., different population growth or loss rates of auto- and heterotrophs) mean that, even in a theoretically isolated water column, the respiration of organic matter may occur with some delay or deeper than when/where it was produced. To cope with these differences in scale, Williams (1998) proposed to use depth-integrated GPP and CR rates to obtain “a more accurate picture of the distribution of the balance of autotrophy and heterotrophy in the oceans”. Integrated values are certainly useful when we are interested in pooled balances (e.g., the bulk net production of a region summarizes the total amount of organic matter available for export to depth or transfer to higher trophic levels). However all trophic processes require the interaction between particles, which depends on encounter rates that are governed more by concentration than areal magnitude (e.g., nitrate uptake kinetics, DOM respiration or predation). Hence, depth-weighted values (which represent average concentrations or rates) not only improve the comparison between regions differing largely in euphotic depth, but they also provide a more accurate representation of the interaction between fast and slow trophic processes across the whole layer of interest. Our results confirm that both the representation of the distribution of the balance of autotrophy and heterotrophy in the oceans, and the relationships between plankton metabolism and environmental variability across different ecosystems improve when a) the surface layer of interest reaches from the surface to the depth of 0.1% PAR ($Z_{0.1\%PAR}$) and b) depth-weighted, rather than volumetric or integrated values are used.

4.1 The euphotic zone depth for GPP and CR interaction is the depth of 0.1% PAR

Based on calculations of the compensation depth, Marra et al. (2014) found that the base of the euphotic zone was consistently deeper than the 1%PAR ($Z_{1\%PAR}$), and concluded that it occurs “at a depth that encompasses the depth range of all, or nearly all, autotrophic biomass”. In our study, the depth encompassing

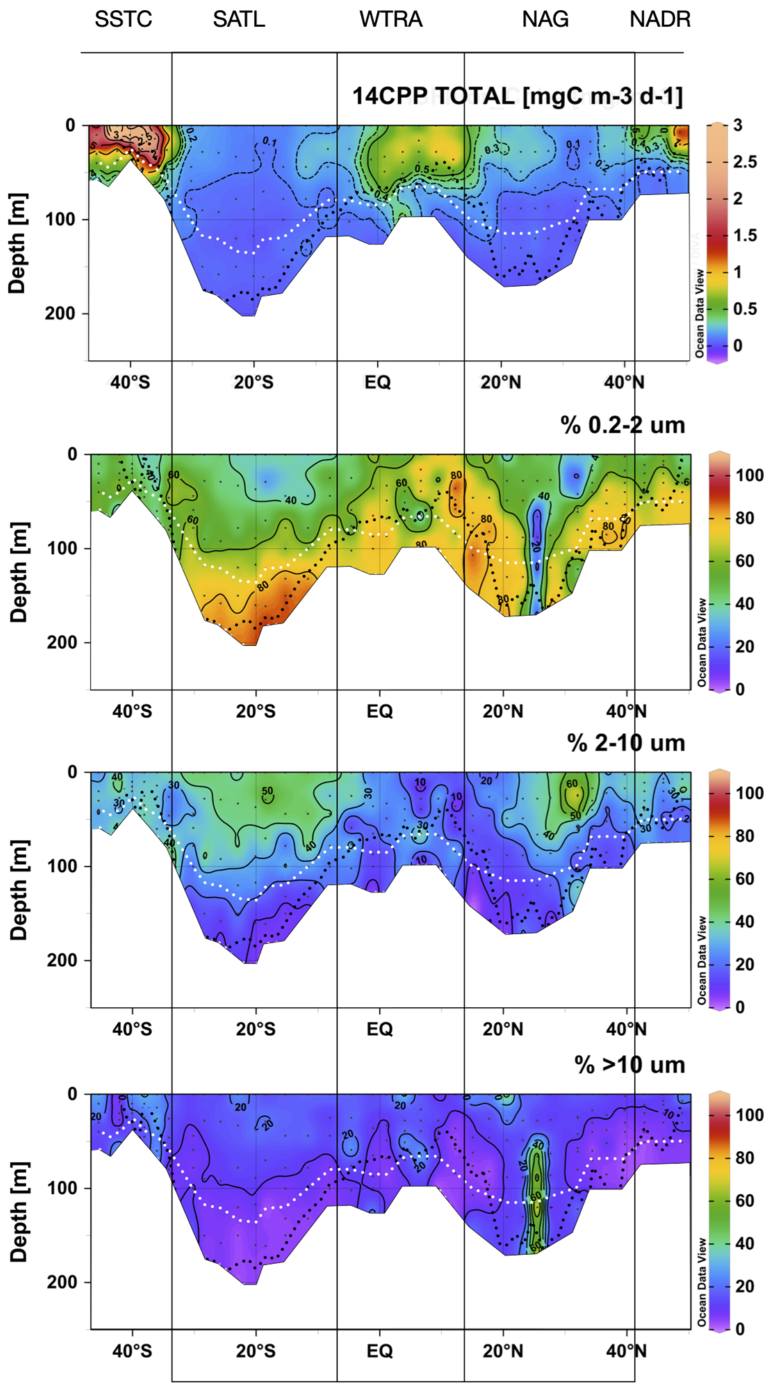

FIGURE 9
Depth vs. latitude sections of total and size-fractionated 14C primary production during the AMT22 cruise. The white dotted lines are the depths of the 1 and 0.1%PAR. The black dotted line is the depth of the nitracline. The blanked area is the location of the deepest sample of each profile, at the depth of the 0.1%PAR. The approximate location of biogeographic provinces (Longhurst, 1998) is presented. Figures produced using Ocean Data View (Schlitzer, Reiner, Ocean Data View, https://odv.awi.de, 2022).

nearly all Chla is $Z_{0.1\%PAR}$ (see Figure 3), where average GPP was 0.18 ± 0.09 and 0.30 ± 0.06 mmolO_2 m^{-3} d^{-1} in the NAG and SATL, respectively. Moreover, the biological depletion of nitrate in both the NAG and SATL reached depths exceeding the $Z_{1\%PAR}$, so that the nitracline was up to 50 m deeper, near the $Z_{0.1\%PAR}$. All this confirms that the $Z_{1\%PAR}$ is too shallow a boundary for the euphotic zone, which agrees with the observations of Laws et al. (1987) in the N Pacific gyre, where the contribution of photosynthesis below the $Z_{1\%PAR}$ to integrated rates was estimated to be 14%. In a recent comprehensive meta-analysis of optical and biological determinants of the euphotic zone depth, Wu et al. (2021) concluded that the depth of $Z_{1\%PAR}$ is often too shallow compared to the compensation depth, but also found that the $Z_{0.1\%PAR}$ was too deep. This, however, reinforces our conclusion because Wu et al. (2021) identified the

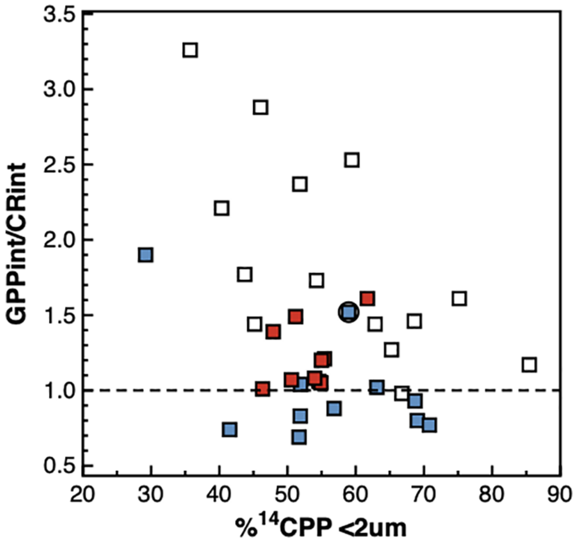

FIGURE 10
Relationship between the integrated percentage of 14C primary production by phytoplankton cells < 2 µm and the ratio of integrated gross photosynthesis to community respiration. Blue symbols are data from the NAG, red symbols are data from the SATL, open symbols are data from other provinces. The dotted line is the GPP/CR=1 line that marks the transition between net auto- and net heterotrophy.

base of the euphotic zone with the compensation depth, "where the rate of photosynthesis equals that of autotrophic respiration, that is, NPP = 0". Our interest in community metabolic balances (GPP and CR) justifies the extension of the euphotic zone to the deeper layer where GPP (rather than NPP) becomes undetectable, with the $Z_{0.1\% \mathrm{PAR}}$ as a reliable proxy.

4.2 The variation of CR_Z in the oligotrophic ocean is systematic and relevant for the metabolic state

The existence of important differences in $Z_{0.1\%\mathrm{PAR}}$, both between and within provinces, produces some biases or difficult to understand patterns of integrated community metabolism (e.g., higher GPP_{int} in the oligotrophic NAG than in the mesotrophic NADR, higher CR_{int} in the low biomass NAG than in the high biomass SSTC. Figure 6), which are cancelled out when the integrated rates are divided by their respective depth of integration. CR_Z and GPP_Z, which are the average rates through the euphotic zone, compensate potential transient/local imbalances in volumetric rates caused by the different scale of the relatively fast photosynthesis and the relatively slow respiration. Hence, they concur with integrated rates at providing a better representation of the plankton community metabolic interactions and balances (Williams, 1998), while avoiding the bias caused by regional differences in depth of integration. The use of depth-weighted rates produces sensible latitudinal W-shaped patterns of GPP, in line with the variation of nutrient availability in the euphotic zone (see Results). More importantly, it produces the emergence of unusually clear CR patterns that were blurred by the biased spatial variability of CR_{int} (Figure 6). The asymmetric W-shaped latitudinal variation of CR_Z compares very well with the average CR_Z trend in the AMT11-15-21 dataset, and with the higher average CR in the NAG than in the SATL in Serret et al. (2015) (Table 1). This suggests that these are characteristic, biogeographic, features of the Atlantic Ocean, which challenges the minor importance attributed to CR on the variation of metabolic balances in the oligotrophic ocean. Such irrelevance is based on the observation of a relative constancy of CR compared to the large variation of primary productivity (Karl et al., 2003; Williams et al., 2004; del Giorgio and Williams, 2005; Robinson and Williams, 2005; Carlson et al., 2007; Duarte et al., 2013; Regaudie-de-Gioux and Duarte, 2013). We conclude that such relative constancy partly resulted from the analysis of volumetric or integrated rates. Our results show that the variation of CR_Z in the oligotrophic ocean is systematic and relevant for regional patterns of NCP_Z, implying that the variation of NCP cannot be determined from the variation of GPP alone (as in e.g. Westberry et al., 2012; Duarte et al., 2013).

4.3 CR_Z covaries with $Chla_Z$ over the Atlantic Ocean

Significant volumetric and integrated GPP : CR relationships have often been obtained (Robinson and Williams, 2005; Regaudie-de-Gioux and Duarte, 2013; Serret et al., 2015, and references therein) and used to predict NCP at regional-global scales (e.g., Duarte and Agusti, 1998; Westberry et al., 2012). As heterotrophic respiration is supported by autotrophic biomass, not by GPP, and biomass is a slower variable than GPP, one would expect stronger Chla : CR relationships. However, individual studies and meta-analyses have failed to obtain significant empirical evidence of a relationship of CR with total Chla, or with the autotrophic community structure. For instance, of the 18 individual studies analysed by Robinson and Williams (2005), in only 50% was the r^2 of the Chla : CR relationship greater than 0.3, and these were studies in shelf seas with ranges of Chla (0.2-50 mg m^{-3}) and CR (1-53 mmolO_2 m^{-3} d^{-1}) that are 18 and 17 times larger than our open ocean ranges. The meta-analysis of Regaudie-de-Gioux and Duarte (2013) obtained a similarly poor relationship (R^2 = 0.29, p<0.05) with the 1111 pairs of data included. And the recent review of processes regulating CR by Wikner et al. (2023) reported only two significant Chla : CR relationships, both based on integrated values in coastal embayments with very large magnitude and variability of Chla and CR (Smith and Kemp, 2001, Chesapeake Bay; Olesen et al., 1999, Gulf of Riga -although Figure 9 in the latter puts into question the consistency of this relationship). Altogether, the very little evidence on the influence of Chla on plankton respiration leads to Chla being not included or removed from empirical models of CR (Wikner et al., 2023), which undermines the potential for the Earth observation of CR. Our volumetric and integrated CR and Chla data concur with this lack of relationship (the r^2 of the $Chla_{int}$: CR_{int} relationship was 0.22, agreeing with previous studies), however, a significant relationship emerges when depth-weighted data are analysed (CR_Z=1.42$Chla_Z$-0.21, r^2 = 0.69, N=37, p<0.001)

(Figure 7). Given the paucity of previous observations, this is an important result with potential for the difficult prediction of CR from a variable that can be estimated remotely. A general ratio of 1.42 mmolO_2 mgChla^{-1} d^{-1} can be tentatively proposed for the Atlantic, although further analyses of spatial and temporal variation are necessary (note that all our observations were made during the boreal autumn). From the x-intercept of the significant Chla$_Z$: NCP$_Z$ relationship (Figure 7), a threshold Chla for net heterotrophy of ca. 0.25 mgChla m^{-3} can be derived. This is lower than the 0.35 mgChla m^{-3} in Regaudie-de-Gioux and Duarte (2013), thus reducing the magnitude of extrapolated heterotrophy in the global open ocean, although such a threshold is a broad generalization, not useful for actual prediction of metabolic rates in specific communities.

4.4 Revisiting meta-analysis of AMT data

The practical value of using depth-weighted rates is further evidenced by the examination of the disagreement between the variation of metabolic rates in the AMT22 vs. the AMT11-22 datasets, which puts into question the validity of the GPP : CR relationships in Serret et al. (2015) to represent and predict the actual variation of NCP in the oligotrophic Atlantic (see section 3.3.3.3 above). The combined AMT11-22 dataset depicted differences in average NCP and in the GPP$_{int}$: CR$_{int}$ relationship between the two gyres (slopes were 1 in the SATL and 0.7 in the NAG) indicative of the prevalence of heterotrophy only in the NAG, which agrees with its higher liability to inputs of allochthonous organic matter (e.g., Reynolds et al., 2014). No such differences exist in the AMT22 dataset: average NCP was not negative in either the SATL or the NAG, and average GPP$_Z$ and CR$_Z$ rates were not significantly different between the NAG and SATL (GPP$_Z$: t-Value=1.58, df=19, P=0.13; CR$_Z$: t-Value=0.28, df=19, P=0.78) (Table 1); moreover, a 1:1 GPP : CR relationship was observed only in the NAG (P<0.001) (Figure 8). The analysis of integrated rates would indicate that the cause for such a disagreement in the NAG was its higher GPP$_{int}$ in the AMT22, as average CR$_{int}$ remained invariant (Table 1). However, depth-weighted rates, which are pertinent because integration in Serret et al. (2015) only reached the $Z_{1\%PAR}$ vs. $Z_{0.1\%PAR}$ here, shows that it was average GPP$_Z$ that remained invariant and the unusual metabolic balance in the NAG was due to the lower than usual average CR$_Z$ rates in the AMT22 compared to the AMT11-22 series (Table 1; Figure 6).

A closer inspection shows however, that, except at the low CR region in the central part of the gyre (26-23° N), negative NCP did actually prevail through the NAG (Figures 5, 6), agreeing with both the regional average in Serret et al. (2015) and with the latitudinal variation in the spatially coherent AMT11-15-21 subset. Such a locally anomalous region is the cause of the disagreements in the NAG presented above: the average NCP$_{int}$ and NCP$_Z$ in the NAG outside that region are -12.17 ± 3.69 mmolO_2 m^{-2} d^{-1} and -0.08 ± 0.02 mmolO_2 m^{-3} d^{-1}, respectively, not different to the NAG averages in Serret et al. (2015) (Table 1). And the GPP$_Z$: CR$_Z$ relationship excluding the two anomalous data from 26-23° N is the same as the autumn NAG equation in Serret et al. (2015) (Figure 11). This exception thus actually confirms the general validity of the GPP : CR relationships from the aggregated AMT11-22 data at ecologically relevant scales.

4.5 Phytoplankton size-structure does not regulate the relationship and balance of GPP and CR

Such a region of anomalously low CR and positive NCP coincided with the area of anomalously high abundance of *Synechococcus* spp. and >4 times increase in ^{14}CPP by cells >10 µm (^{14}CPP$_{>10}$). This agrees with conceptual and mechanistic models that highlight the role of phytoplankton size in the organisation of aquatic food webs (Legendre and Le Fevre, 1989; Kiørboe, 1993). These models emerge from the cell size-dependency of factors regulating growth and loss rates of phytoplankton

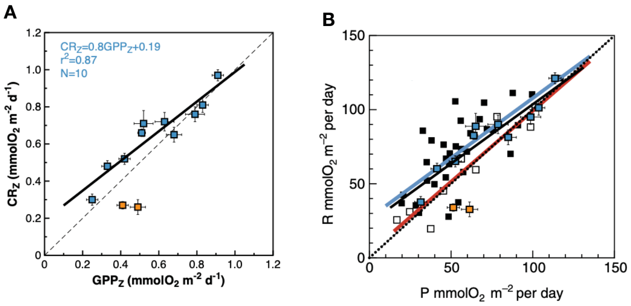

FIGURE 11
Relationship between the depth-weighted rates of gross primary production and community respiration in the N Atlantic gyre. **(A)** AMT22 data. Orange squares are the data from 26-23° N; blue squares are the rest of the data in the NAG. Results of OLS regression analysis with data outside the 26-23° N region are presented. See text for details. The dashed line is the 1:1 line that marks the transition between net auto- and net heterotrophy. **(B)** AMT22 data and regression line (black line) overlaid on Figure 7A of Serret et al. (2015), depicting the relationship between the integrated rates of gross primary production and community respiration in the NAST and SATL in autumn (coinciding with the time of the year of the AMT22 cruise). The blue line is the regression line for the NAST data: CR = 0.80GPP + 26.9, R2 = 0.54, n = 33. The red lines is the regression line for the SATL data: CR = 0.96GPP + 3.56; R2 = 0.87; n = 9 The dotted line indicates the 1:1 line. Error bars are standard errors.

populations (competitive advantage for light or nutrients, photosynthetic efficiency, sinking or grazing rates). The size selectivity of predators for prey would then shape the size structure of the entire food web, causing that transitions in the relative importance of trophic pathways (from the herbivorous food web to the microbial loop) are ultimately controlled by the relative dominance of large vs. small phytoplankton (e.g., Finkel, 2007 and references therein). According to this paradigm, the relationship between GPP and CR would be largely regulated by the size structure of the community, so that higher GPP : CR ratios and NCP rates are expected in communities dominated by large phytoplankton and herbivorous food webs (Smith and Kemp, 2001). These expectations are met in the comparison of the patch of high $^{14}CPP_{>10}$ at 23-26 °N with the rest of the NAG, although the high GPP : CR ratios (1.9) and positive NCP_Z were not accompanied by concurrent increases in either Chla, total ^{14}CPP or GPP, but resulted entirely from a marked decrease in CR_Z (Figure 6). These results confirm the relevance of the variation of CR_Z in the oligotrophic ocean, not only for the regional differences in metabolic state (see above), but also for local/transient variations of NCP_Z driven by changes in community structure within provinces. This evidences the importance of improving the parameterisation of respiration for realistic projections of the biological carbon pump. The significant CR_Z : $Chla_Z$ relationship observed here (see above) and the sharp change in CR_Z associated with a patch of high *Synechococcus* spp. abundance and $^{14}CPP_{>10}$ indicate that the biomass and structure of phytoplankton communities are important overlooked parameters regulating CR that need to be incorporated in predictive models.

A wider analysis however disputes the generality of the relationship between phytoplankton size and the degree of heterotrophy predicted by food web models. These models have been mostly validated based on the relative abundances and growth rates of different trophic compartments (e.g., Armengol et al., 2019), size fractionated primary production and autotrophic biomass (e.g., Tremblay and Legendre, 1994) or vertical flux of particles (e.g., Guidi et al., 2009). However, there is very little empirical confirmation of a relationship between direct measurements of the energy transfer efficiency or the degree of heterotrophy (e.g. GPP : CR ratio) and the phytoplankton size-structure, and only in coastal embayments and strong transition zones, and with unclear results (Serret et al., 2001; Smith and Kemp, 2001; Arbones et al., 2008; Soria-Píriz et al., 2017; Wang et al., 2018; Juranek et al., 2020; Lozano et al., 2021). Such a relationship is an important validation for these models because it does not entail the improbable assumption that population and energy dynamics are tightly connected over nested spatial and temporal scales in the non-steady state pelagic ecosystem. Our AMT22 results show no significant relationship between GPP : CR ratios and the percentage of ^{14}CPP in any size fraction. Within a given $\%^{14}CPP_{<2}$ between ~40 and 70%, the full range of GPP : CR ratios can be observed; while the same value of the GPP : CR ratio may be observed through the full range of $\%^{14}CPP_{<2}$ (Figure 10). More significantly, a biogeographic pattern emerges from this relationship: at any $\%^{14}CPP_{<2}$, the lowest GPP : CR ratios were always observed in the NAG, intermediate values were observed in the SATL, and the highest GPP : CR ratios were always observed in mesotrophic provinces (Figure 10). This all indicates that the phytoplankton size structure is a poor predictor of regional differences in the functioning of food webs and in the trophic state of the pelagic ecosystem. This spatial analysis of variation concurs with the temporal observations of Lozano et al. (2021) over a twice-monthly seasonal study in the temperate coastal upwelling system of the Ría de Vigo. Results there only conformed to predictions of models when highly contrasting situations were compared (the highly autotrophic microphytoplankton-dominated upwelling vs. the almost in balance pico- and nanophytoplankton-dominated winter mixing period), similar to the comparison of AMT22 data from the contrasting 26-23° N patch vs. the rest of the N gyre. However, both the AMT22 dataset and the seasonal variation in the Ría de Vigo revealed the absence of a systematic relationship between phytoplankton size and the degree of heterotrophy, thus refuting the hypothesis that cell size determines food web functioning. This also agrees with observations of high NCP in communities dominated by small phytoplankton in the Southern Ocean (Cassar et al., 2015) and tropical estuaries (Soria-Píriz et al., 2017), and with the weak relationship between taxonomy and NCP in low-production waters of the NW Atlantic (Wang et al., 2018). The idea that higher respiration per unit biomass or primary production should occur in a consumer-controlled and complex microbial food web where heterotrophic activities and remineralisation play key roles for the maintenance of the community, and the biomass of heterotrophs exceeds that of autotrophs (Gasol et al., 1997), than in simpler, resource-controlled herbivore food webs, seems irrefutable (Legendre & Le Fevre, 1989; Kiørboe, 1993; Legendre & Rassoulzadegan, 1996). However, our results show that such a theoretical connection is not always realised in the ocean, either because it is short-circuited by the differences in scale between population and trophic dynamics, or because other size-independent processes regulating GPP or CR have a larger impact on community metabolism patterns (for instance the higher inputs of allochthonous organic matter in the NAG, e.g., Reynolds et al., 2014; Serret et al., 2015).

4.6 Alternative ecosystem states constrain prediction of NCP in the upper ocean

The discussion above highlights the importance of the biogeographic component in the variation of plankton CR and NCP in the Atlantic Ocean, agreeing with the system dependency observed in ^{14}CPP : NCP relationships (Serret et al., 2009). These are potentially useful relationships for prediction, because of the methodological independence of the variables and the large global dataset of ^{14}CPP measurements and Earth observation algorithms. Two such distinct models in the Atlantic represented productive +isolated oligotrophic ecosystems (AMT11 model) and productive +subsidised oligotrophic ecosystems (AMT6 model), respectively (for details, see Serret et al., 2009). To explore the consistency of this spatial partition, we have analysed the seasonal variation in the Ría de Vigo in Lozano et al. (2021), where two distinct periods were identified: winter-spring, when heterotrophy was locally sustained by relatively low productive situations, thus resembling the AMT11 model; and summer, when episodes of strong organic matter accumulation driven by short upwelling events were followed by periods of stratification and increased heterotrophy representing temporally subsidised oligotrophic systems similar to those in the AMT6 spatial model. The striking similarity observed in the ^{14}CPP : NCP relationships in donor- (AMT6, summer upwelling) vs. locally controlled ecosystems (AMT11, winter spring) across the Atlantic Ocean and through the year in the Ría de Vigo (Figure 12A) is a robust validation of the system dependency of empirical relations of community metabolism, and confirms that NCP can be accurately predicted in the ocean. However, such prediction remains challenging in practice, because our poor knowledge on respiration variation and control implies that determining which system-dependent relationship will suit a particular ecosystem is difficult. For instance, the AMT22 dataset included oligotrophic data from the remote SATL (as the AMT11 model), but also included data from the supposedly subsidised NAST-E (as the AMT6 model). Yet the AMT22 ^{14}CPP : NCP relationship including all these data tightly corresponds to the AMT11 model only (Figure 12B), which agrees with the unusual GPP : CR relationship and overall metabolic balance observed in the NAG during the AMT22 (see above). Even for the region of the open ocean whose metabolic balance has been more thoroughly studied (the NAST-E; see Regaudie-de-Gioux and Duarte, 2013 and Serret et al., 2015), prediction of NCP at ecological scales remains elusive because of the difficulty to determine which empirical model to use.

The persistence of distinct GPP : CR and ^{14}CPP : NCP relationships within types of ecosystems, and the independence of

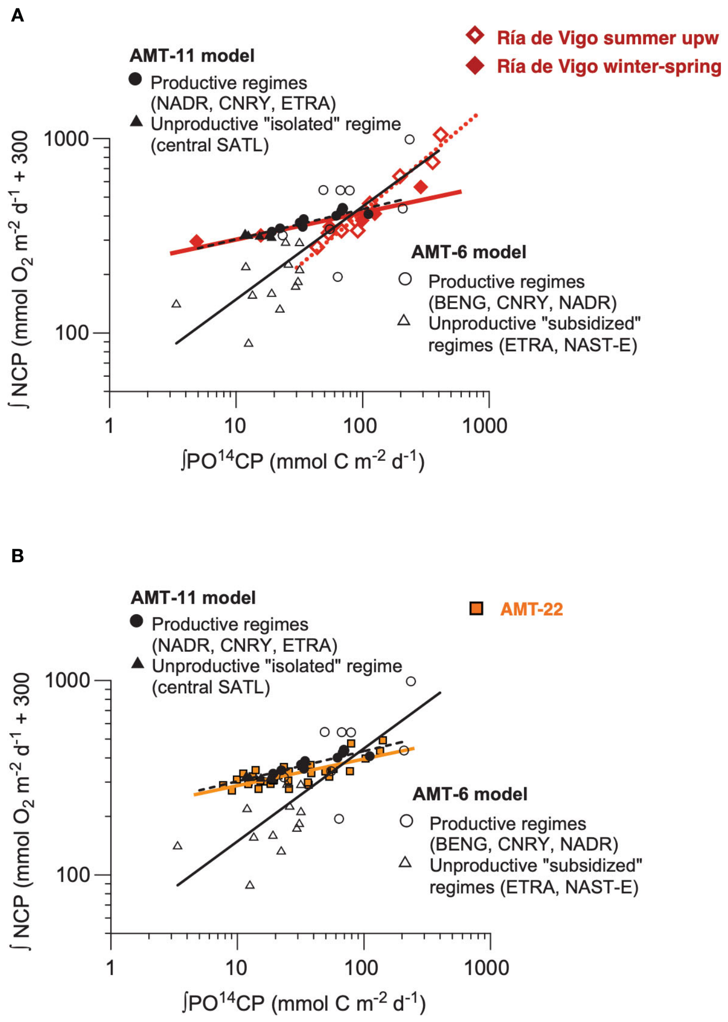

FIGURE 12
Relationship between the integrated rates of 14C primary production and net community production in **(A)** a seasonal study in the Riía de Vigo (Lozano et al., 2021) (red symbols and lines) and **(B)** the AMT22 (orange squares and line), both overlaid on Figure 2 from Serret et al. (2009) for comparison with the AMT6 (open symbols and black continuous line) and AMT11 (black filled symbols and black dashed line) models from Serret et al., 2009. The red continuous line is the OLS regression line with the winter-spring data in the Riía de Vigo (14CPPint = 0.80GPP + 26.9, R2 = 0.54, n = 33. The equations are NCPint = 212.0114CPP - 300, r2 = 0.85, n = 15, p < 0.001 (AMT11, black dashed line), NCPint = 49.5314CPP - 300, r2 = 0.61, n = 21, p < 0.001 (AMT6, black continuous line), NCPint = 219.2014CPP - 300, r2 = 0.82, n = 6, p < 0.001 (Riía de Vigo, winter-spring, red continuous line), NCPint = 33.0314CPP - 300, r2 = 0.95, n = 9, p < 0.001 (Riía de Vigo, summer, red dotted line), and NCPint = 209.1614CPP - 300, r2 = 0.58, n = 35, p < 0.001 (AMT22, orange continuous line).

community metabolism from the size-structure of the phytoplankton evidence the existence of alternative ecosystem states (e.g., Holling, 1973; Beisner et al., 2003; Carpenter et al., 2022) emerging from a trophic resilience that overcomes regional and seasonal differences in community composition and structure in the upper ocean. This implies that strong perturbations of the community structure are necessary to shift the trophic functioning (e.g., at 26-23° N during the AMT22, during upwelling in the Ría de Vigo), which reflects on the observed lack of a general relationship between the degree of heterotrophy and the phytoplankton size (Lozano et al., 2021, this work) or taxonomic composition (Wang et al., 2018). On the other hand, a biogeographic perspective emerges from the responsiveness of state variables (such as the metabolic state and the GPP : CR relationships) to changes in environmental parameters (such as inputs of allochthonous organic matter or the dynamics of inorganic nutrients) that vary systematically between regions and along seasons. Identifying which are all those meaningful parameters and how they vary in the ocean would allow one to define domains for NCP prediction just as biogeographic provinces are used to define domains for PP models (e.g., Longhurst, 1998). In these models, photosynthetic parameters are assigned "on the basis of ecological provinces of the ocean" (Kulk et al., 2020), classified based on the hydrodynamic conditions, supply of nutrients and average irradiance. An analogous biogeography based on CR regulation is necessary to develop a global NCP prediction that is urgently needed for projections of carbon storage in a changing ocean. The system-dependency of empirical models is a suitable tool to identify some domains for NCP prediction, but global prediction requires understanding trophic resilience and determining thresholds for transitions between alternative ecosystem states, which demands a better knowledge of the processes regulating community metabolism in the ocean (especially CR) and their interaction with both community organisation and the variation of environmental parameters. This calls for a very substantial improvement of the global dataset of reliable measurements of plankton metabolism in the euphotic zone.

Data availability statement

The original contributions presented in the study are included in the article/Supplementary Material. Further inquiries can be directed to the corresponding author. The complete data set of all the physical, chemical and biological variables is available at the British Oceanographic Data Centre (http://www.bodc.ac.uk/projects/uk/amt). The conditions under which the data may be used are in line with the NERC Data Policy (http://www.nerc.ac.uk/research/sites/data/policy/), and will be explained following a request, before the delivery of data.

Author contributions

PS conceptualized this study, analyzed the results and wrote the manuscript, which was reviewed and edited by coauthors. PS and JL measured plankton metabolism. CH and EMSW provided the nutrients data. PL and GHT provided the ^{14}CPP data. GAT and MZ provided cell counts data. All authors contributed to the article and approved the submitted version.

Funding

The Atlantic Meridional Transect is funded by the UK Natural Environment Research Council through its National Capability Long-term Single Centre Science Programme, Climate Linked Atlantic Sector Science (grant number NE/R015953/1). This study contributes to the international IMBeR project and is contribution number 398 of the AMT programme. The Spanish MICINN grant Scaling, monitoring and predicting marine plankton metabolism in a changing ocean CTM2011-29616 awarded to PS partly funded this study.

Acknowledgments

We thank all personnel on board during the AMT22 cruise (RRS James Cook JCO79). Special thanks to Rob Thomas for chlorophyll a measurements used to calibrate the CTD fluorescence sensor. We acknowledge the comments by the reviewers, which improved the paper.

Conflict of interest

The authors declare that the research was conducted in the absence of any commercial or financial relationships that could be construed as a potential conflict of interest.

The handling editor VB declared a past collaboration with the authors EMSW and GHT.

Publisher's note

References

Arbones, B., Castro, C. G., Alonso-Perez, F., and Figueiras, F. G. (2008). Phytoplankton size structure and water column metabolic balance in a coastal upwelling system: the Ría de Vigo, NW Iberia. *Aquat. Microb. Ecol.* 50, 169–179. doi: 10.3354/ame01160

Armengol, L., Calbet, A., Franchy, G., Rodríguez-Santos, A., and Hernández-León, S. (2019). Planktonic food web structure and trophic transfer efficiency along a productivity gradient in the tropical and subtropical Atlantic ocean. *Sci. Rep.* 9, 2044. doi: 10.1038/s41598-019-38507-9

Behrenfeld, M. J., and Falkowski, P. G. (1997). Photosynthetic rates derived from satellite-based chlorophyll concentration. *Limnol. Oceanogr.* 42, 1–20. doi: 10.4319/lo.1997.42.1.0001

Beisner, B. E., Haydon, D. T., and Cuddington, K. (2003). Alternative stable states in ecology. *Front. Ecol. Environ.* 1 (7), 376–382. doi: 10.1890/1540-9295(2003)001[0376:ASSIE]2.0.CO;2

Bender, M. L., Orchardo, J., Dickson, M. L., Barber, R., and Lindley, S. (1999). *In vitro* O2 fluxes compared with 14C production and other rate terms during the JGOFS Equatorial Pacific experiment. *Deep-Sea Res.* 46, 637–654. doi: 10.1016/S0967-0637(98)00080-6

Bindoff, N. L., Cheung, W. W. L., Kairo, J. G., Arístegui, J., Guinder, V. A., Hallberg, R., et al. (2019). "Changing ocean, marine ecosystems, and dependent communities," in *IPCC Special Report on the Ocean and Cryosphere in a Changing Climate*. Eds. H.-O. Pörtner, D. C. Roberts, V. Masson-Delmotte, P. Zhai, M. Tignor, E. Poloczanska, K. Mintenbeck, A. Alegría, M. Nicolai, A. Okem, J. Petzold, B. Rama and N. M. Weyer (Cambridge University Press, Cambridge, UK and New York, NY, USA), 447–587.

Bittig, H. C., Körtzinger, A., Neill, C., van Ooijen, E., Plant, J. N., Hahn, J., et al. (2018). Oxygen optode sensors: principle, characterization, calibration, and application in the ocean. *Front. Mar. Sci.* 4. doi: 10.3389/fmars.2017.00429

Bouman, H., Platt, T., Sathyendranath, S., and Stuart, V. (2005). Dependence of light-saturated photosynthesis on temperature and community structure. *Deep-Sea Res. I.* 52, 1284–1299. doi: 10.1016/j.dsr.2005.01.008

Boyd, P. W., Claustre, H., Levy, M., Siegel, D. A., and Weber, T. (2019). Multi-faceted particle pumps drive carbon sequestration in the ocean. *Nature* 568, 327–335. doi: 10.1038/s41586-019-1098-2

Brewer, P. G., and Riley, J. P. (1965). The automatic determination of nitrate in sea water. *Deep Sea Res. Oceanographic Abstracts* 12 (6), 765–772. doi: 10.1016/0011-7471(65)90797-7

Carlson, C. A., del Giorgio, P. A., and Herndl, G. J. (2007). Microbes and the dissipation of energy and respiration: from cells to ecosystems. *Oceanography* 20 (2), 89–100. doi: 10.5670/oceanog.2007.52

Carpenter, S. R., Arani, B. M. S., Van Nes, E. H., Scheffer, M., and Pace, M. L. (2022). Resilience of phytoplankton dynamics to trophic cascades and nutrient enrichment. *Limnol. Oceanogr.* 67, S258–S265. doi: 10.1002/lno.11913

Cassar, N., Wright, S. W., Thomson, P. G., Trull, T. W., Westwood, K. J., de Salas, M., et al. (2015). The relation of mixed-layer net community production to phytoplankton community composition in the Southern Ocean. *Global Biogeochem. Cycles* 29, 446–462. doi: 10.1002/2014GB004936

Claustre, H., Johnson, K. S., and Takeshita, Y. (2020). Observing the global ocean with biogeochemical-Argo. *Annu. Rev. Mar. Sci.* 12, 23–48. doi: 10.1146/annurev-marine-010419-010956

del Giorgio, P. A., Cole, J. J., and Cibleris, A. (1997). Respiration rates in bacteria exceed phytoplank- ton production in unproductive aquatic systems. *Nature* 385, 148–151. doi: 10.1038/385148a0

del Giorgio, P. A., and Williams, P. (2005). "The global significance of respiration in aquatic eco- systems: From single cells to the biosphere," in *Respiration in Aquatic Ecosystems*. Eds. P. A. d. Giorgio and P. Williams (New York: Oxford University Press, New York), 267–303.

Duarte, C. M., and Agusti, S. (1998). The CO2 balance of unproductive aquatic ecosystems. *Science* 281 (5374), 234–236. doi: 10.1126/science.281.5374.234

Duarte, C. M., Regaudie-de-Gioux, A., Arrieta, J. M., Delgado-Huertas, A., and Agusti, S. (2013). The oligotrophic ocean is heterotrophic. *Ann. Rev. Mar. Sci.* 5, 551–569. doi: 10.1146/annurev-marine-121211-172337

Ducklow, H. W., and Doney, S. C. (2013). What is the metabolic state of the oligotrophic ocean? *A. Debate. Ann. Rev. Mar. Sci.* 5, 525–533. doi: 10.1146/annurev-marine-121211-172331

Falkowski, P. G. (1981). Light-shade adaptation and assimilation numbers. *J. Plankt Res.* 3 (2), 203–216. doi: 10.1093/plankt/3.2.203

Falkowski, P. G., Barber, R. T., and Smetacek, V. (1998). Biogeochemical controls and feedbacks on ocean primary production. *Science* 281 (5374), 200–206. doi: 10.1126/science.281.5374.200

Finkel, Z. V. (2007). "Does phytoplankton cell size matter? The evolution of modern marine food webs," in *Evolution of Aquatic Photoautotrophs*. Eds. P. G. Falkowski and A. H. Knoll (Academic Press, San Diego), 333–350.

Ford, D., Tilstone, G. H., Shutler, J. D., Kitidis, V., Lobanova, P., Schwarz, J., et al. (2021). Wind speed and mesoscale processes drive net autotrophy in the South Atlantic Ocean. *Remote Sens. Env.* 260, 112435. doi: 10.1016/j.rse.2021.112435

Gasol, J. M., del Giorgio, P. A., and Duarte, C. M. (1997). Biomass distribution in marine planktonic communities. *Limnol. Oceanogr.* 42 (6), 1353–1363. doi: 10.4319/lo.1997.42.6.1353

Grassoff, K., Erhardt, M., and Kremlin, M. (1983). *Methods of seawater analysis. 2nd edn* (Verlag Chemie, Weinheim), 419.

Grodsky, S. A., Carton, J. A., and McClain, C. R. (2008). Variability of upwelling and chlorophyll in the equatorial Atlantic. *Geophysical Res. Lett.* 35 (3), 1–6. doi: 10.1029/2007GL032466

Gruber, N., Doney, S. C., Emerson, S. R., Gilbert, D., Kobayashi, T., Körtzinger, A., et al. (2010). "Adding oxygen to argo: developing a global *in situ* observatory for ocean deoxygenation and biogeochemistry," in *Proceedings of OceanObs'09: Sustained Ocean Observations and Information for Society*, Venice, Italy, 21-25 September 2009, Vol. 2, 12 (ESA Publication WPP-306), Paris, France, European Sace Agency. doi: 10.5270/OceanObs09.cwp.39

Guidi, L., Stemmann, L., Jackson, J. A., Ibanez, F., Claustre, H., Legendre, L., et al. (2009). Effects of phytoplankton community on production, size and export of large aggregates: A world-ocean analysis. *Limnol. Oceanogr.* 54 (6), 1951–1963. doi: 10.4319/lo.2009.54.6.1951

Haskell, W. Z. II, Fassbender, A. J., Long, J. S., and Plant, J. N. (2020). Annual net community production of particulate and dissolved organic carbon from a decade of biogeochemical profiling float observations in the Northeast Pacific. *Global Biogeochem. Cycles* 34, e2020GB006599. doi: 10.1029/2020GB006599

Hemming, M. P., Kaiser, J., Boutin, J., Merlivat, L., Heywood, K. J., Bakker, D. C. E., et al. (2022). Net community production in the northwestern Mediterranean Sea from glider and buoy measurements. *Ocean Sci.* 18, 1245–1262. doi: 10.5194/os-18-1245-2022

Holling, C. S. (1973). Resilience and stability of ecological systems. *Annu. Rev. Ecol. Syst.* 4, 1–23. doi: 10.1146/annurev.es.04.110173.000245

Hull, T., Greenwood, N., Kaiser, J., and Johnson, M. (2016). Uncertainty and sensitivity in optode-based shelf-sea net community production estimates. *Biogeosciences* 13, 943–959. doi: 10.5194/bg-13-943-2016

Intergovernmental Oceanographic Commission (1994). Protocols for the joint global ocean flux study (JGOFS) core measurements. Paris, France, UNESCO-IOC, 170pp. (Intergovernmental oceanographic commission manuals and guides: 29). *JGOFS Rep.* 19. doi: 10.25607/OBP-1409

Johnson, K. S., Plant, J. N., Coletti, L. J., Jannasch, H. W., Sakamoto, C. M., Riser, S. C., et al. (2017). Biogeochemical sensor performance in the SOCCOM profiling float array. *J. Geophys. Res. Oceans* 122, 6416–6436. doi: 10.1002/2017JC012838

Juranek, L. W., White, A. E., Dugenne, M., Henderikx Freitas, F., Dutkiewicz, S., Ribalet, F., et al. (2020). The importance of the phytoplankton "middle class" to ocean net community production. *Global Biogeochem. Cycles* 34, e2020GB006702. doi: 10.1029/2020GB006702

Karl, D. M., Bidigare, R. R., and Letelier, R. M. (2002). "Sustained and aperiodic variability in organic matter production and phototrophic microbial community structure in the North Pacific Subtropical Gyre," in *Phytoplankton Productivity: Carbon Assimilation in Marine and Freshwater Ecosystems*. Eds. P. J. B. Williams, D. N. Thomas and S. Colin (New York: Reynolds Blackwell Publishing Ltd), 222–264.

Karl, D. M., Laws, E. A., Morris, P., Williams, P., and Emerson, S. (2003). Metabolic balance of the open sea. *Nature* 426, 32. doi: 10.1038/426032a

Kiørboe, T. (1993). Turbulence, phytoplankton cell size and the structure of pelagic food webs. *Adv. Mar. Biol.* 29, 1–72. doi: 10.1016/S0065-2881(08)60129-7

Kulk, Platt, T., Dingle, J., Jackson, T., Jönsson, B. F., Bouman, H. A., et al. (2020). Primary production, an index of climate change in the ocean: satellite-based estimates over two decades. *Remote Sens.* 12, 826. doi: 10.3390/rs12050826

Laws, E. A. (1991). Photosynthetic quotients, new production and net community production in the open ocean. *Deep-Sea Res. I.* 38 (1), 143–167. doi: 10.1016/0198-0149(91)90059-O

Laws, E. A., DiTullio, G. R., and Redalje, D. G. (1987). High phytoplankton growth and production rates in the North Pacific subtropical gyre. *Limnol. Oceanogr.* 32 (4), 905–9.18. doi: 10.4319/lo.1987.32.4.0905

Legendre, L., and Le Fevre, J. (1989). "Hydrodynamical singularities as controls of recycled versus export production in oceans," in *Productivity of the Oceans: Present and Past*. Eds. W. H. Berger, V. S. Smetacek and G. Wefer (John Wiley & Sons), 49–63.

Legendre, L., and Rassoulzadegan, F. (1996). Food-web mediated export of biogenic carbon in oceans: environmental control. *Mar. Ecol. Prog. Ser.* 145, 179–193. doi: 10.3354/meps145179

Longhurst, A. (1998). *Ecological Geography of the Sea* (Academic Press).

Longhurst, A., Sathyendranath, S., Platt, T., and Caverhill, C. (1995). An estimate of global primary production in the ocean from satellite radiometer data. *J. Plank. Res.* 17 (6), 1245–1271. doi: 10.1093/plankt/17.6.1245

Lozano, J., Aranguren-Gassis, M., García-Martín, E. E., González, J., Herrera, J. L., Hidalgo-Robatto, B., et al. (2021). Seasonality of phytoplankton cell size and the relation between photosynthesis and respiration in the Ría de Vigo (NW Spain). *Mar. Ecol. Prog. Ser.* 664, 43–58. doi: 10.3354/meps13669

Marra, J. (2009). Net and gross productivity: weighing in with 14C. *Aquat. Microb. Ecol.* 56, 123–131. doi: 10.3354/ame01306

Marra, J. (2012). Comment on "Measuring primary production rates in the ocean: Enigmatic results between incubation and non-incubation methods at Station ALOHA. *Global Biogeochem. Cycles* 26 (2). doi: 10.1029/2011GB004087

Marra, J., Trees, C. C., and O'Reilly, J. E. (2007). Phytoplankton pigment absorption: A strong predictor of primary productivity in the surface ocean. *Deep-Sea Res. I.* 54, 155–163. doi: 10.1016/j.dsr.2006.12.001

Marra, J. F., Lance, V. P., Vaillancourt, R. D., and Hargreaves, B. R. (2014). Resolving the ocean's euphotic zone. *Deep-Sea Res. I* 83, 45–50. doi: 10.1016/j.dsr.2013.09.005

Mignot, A., D'Ortenzio, F., Taillandier, V., Cossarini, G., and Salon, S. (2019). Quantifying observational errors in Biogeochemical-Argo oxygen, nitrate, and chlorophyll a concentrations. *Geophysical Res. Lett.* 46, 4330–4337. doi: 10.1016/S0924-7963(99)00054-8

Morel, A., Antoine, D., Babin, M., and Dandonneau, Y. (1996). Measured and modeled primary production in the northeast Atlantic (EUMELI JGOFS program): the impact of natural variations in photosynthetic parameters on model predictive skill. *Deep-Sea Res. I.* 43, 1273–1304. doi: 10.1016/0967-0637(96)00059-3

Olesen, M., Lundsgaard, C., and Andrushaitis, A. (1999). Influence of nutrients and mixing on the primary production and community respiration in the Gulf of Riga. *J. Mar. Sys.* 23, 127–143. doi: 10.1016/S0924-7963(99)00054-8

Oudot, C., Gerard, R., Morin, P., and Gningue, I. (1988). Precise shipboard determination of dissolved oxygen (Winkler procedure) for productivity studies with a commercial system. *Limnol. Oceanogr.* 33, 146–150. doi: 10.4319/lo.1988.33.1.0146

Pasquier, B., Holzer, M., Chamberlain, M. A., Matear, R. J., Bindoff, N. L., and Primeau, F. W. (2023). Optimal parameters for the ocean's nutrient, carbon, and oxygen cycles compensate for circulation biases but replumb the biological pump. *Biogeosciences* 20, 2985–3009. doi: 10.5194/egusphere-2023-363

Regaudie-de-Gioux, A., and Duarte, C. M. (2013). Global patterns in oceanic planktonic metabolism. *Limnol. Oceanography* 58 (3), 977–986. doi: 10.4319/lo.2013.58.3.0977

Reynolds, S., Mahaffey, C., Roussenov, V., and Williams, R. G. (2014). Evidence for production and lateral transport of dissolved organic phosphorus in the eastern subtropical North Atlantic. *Global Biogeochem. Cycles* 28. doi: 10.1002/2013GB004801

Robinson, A., Bouman, H. A., Tilstone, G. H., and Sathyendranath, S. (2018). Size class dependent relationships between temperature and phytoplankton photosynthesis-Irradiance parameters in the Atlantic Ocean. *Front. Mar. Sci.* 4. doi: 10.3389/fmars.2017.00435

Robinson, C., and Williams, P. (2005). "Respiration and its measurement in surface marine waters," in *Respiration in Aquatic Ecosystems*. Eds. P. A. d. Giorgio and P. Williams (New York: Oxford University Press, New York), 147–180.

Serret, P., Fernández, E., Anadón, R., and Varela, M. (2001). Trophic control of biogenic carbon export in Bransfield and Gerlache Straits, Antarctica. *J. Plank. Res.* 23 (12), 1345–1136. doi: 10.1093/plankt/23.12.1345

Serret, P., Fernandez, E., Robinson, C., Woodward, E. M. S., and Perez, V. (2006). Local production does not control the balance between plankton photosynthesis and respiration in the open Atlantic Ocean. *Deep-Sea Res. II* 53 (14–16), 1611–1628. doi: 10.1016/j.dsr2.2006.05.017

Serret, P., Robinson, C., Aranguren-Gassís, M., García-Martín, E. E., Gist, N., Kitidis, V., et al. (2015). Both respiration and photosynthesis determine the scaling of plankton metabolism in the oligotrophic ocean. *Nat. Commun.* 6, 6961. doi: 10.1038/ncomms7961

Serret, P., Robinson, C., Fernández, E., Teira, E., Tilstone, G., and Pérez, V. (2009). Predicting plankton net community production in the Atlantic Ocean. *Deep-Sea Res. Part II* 56, 941–953. doi: 10.1016/j.dsr2.2008.10.006

Signorini, S. R., Franz, B. A., and McClain, C. R. (2015). Chlorophyll variability in the oligotrophic gyres: mechanisms, seasonality and trends. *Front. Mar. Sci.* 2. doi: 10.3389/fmars.2015.00001

Smith, E. M., and Kemp, W. M. (2001). Size structure and the production/respiration balance in a coastal plankton community. *Limnol. Oceanogr.* 46 (3), 473–485. doi: 10.4319/lo.2001.46.3.0473

Smyth, T. J., Tilstone, G. H., and Groom, S. B. (2005). Integration of radiative transfer into satellite models of ocean primary production. *J. Geophys. Res. Oceans* 110, C10014. doi: 10.1029/2004JC002784

Soria-Píriz, S., García-Robledo, E., Papaspyrou, S., Aguilar, V., Seguro, I., Acuña, J., et al. (2017). Size fractionated phytoplankton biomass and net metabolism along a tropical estuarine gradient. *Limnol. Oceanogr.* 62, S309–S326. doi: 10.1002/lno.10562

Tarran, G. A., Heywood, J. L., and Zubkov, M. V. (2006). Latitudinal changes in the standing stocks of eukaryotic nano- and picophytoplankton in the Atlantic Ocean. *Deep-Sea Res. II* 53 (14-16), 1516–1529. doi: 10.1016/j.dsr2.2006.05.004

Tilstone, G. H., Smyth, T. J., Poulton, A., and Hutson, R. (2009). Measured and remotely sensed estimates of primary production in the Atlantic Ocean from 1998 to 2005. *Deep Sea-Res. II* 56 (15), 918–930. doi: 10.1016/j.dsr2.2008.10.034

Tilstone, G. H., Xie, Y., Robinson, C., Serret, P., Raitsos, D. E., Powell, T., et al. (2015). Satellite estimates of net community production indicate predominance of net autotrophy in the Atlantic Ocean. *Remote Sens. Environ.* 164, 254–269. doi: 10.1016/j.rse.2015.03.017

Tremblay, J. E., and Legendre, L. (1994). A model for the size-fractionated biomass and production of marine phytoplankton. *Limnol. Oceanogr.* 39 (8), 2004–2014. doi: 10.4319/lo.1994.39.8.2004

Vikström, K., Tengberg, A., and Wikner, J. (2019). Improved accuracy of optode-based oxygen consumption measurements by removal of system drift and nonlinear derivation. *Limnol. Ocenagr.: Methods* 17, 179–189. doi: 10.1002/lom3.10297

Wang, S., Lin, Y., Gifford, S., Eveleth, R., and Cassar, N. (2018). Linking patterns of net community production and marine microbial community structure in the western North Atlantic. *ISME J.* 12, 2582–2595. doi: doi. 10.1038/s41396-018-0163-4

Welschmeyer, N. A. (1994). Fluorometric analysis of chlorophyll a in the presence of chlorophyll b and pheopigments. *Limnol. Oceanogr.* 39, 1985–1992. doi: 10.4319/lo.1994.39.8.1985

Westberry, T. K., Silsbe, G. M., and Behrenfeld, M. J. (2023). Gross and net primary production in the global ocean: An ocean color remote sensing perspective. *Earth-Sci. Rev.* 237, 104322. doi: 10.1016/j.earscirev.2023.104322

Westberry, T. B., Williams, P.J. B., and Behrenfeld, M. J. (2012). Global net community production and the putative net heterotrophy of the oligotrophic oceans. *Global Biogeochem. Cycles.* 26, GB4019. doi: 10.1029/2011GB004094

Wikner, J., Vikström, K., and Verma, A. (2023). Regulation of marine plankton respiration: A test of models. *Front. Mar. Sci.* 10. doi: 10.3389/fmars.2023.1134699

Williams, P.J. B. (1998). The balance of plankton respiration and photosynthesis in the open oceans. *Nature* 394, 55–57. doi: 10.1038/27878

Williams, P.J. B., Morris, P., and Karl, D. M. (2004). Net community production and metabolic balance at the oligotrophic ocean site, station ALOHA. *Deep-Sea Res. I.* 51, 1563–1578. doi: 10.1016/j.dsr.2004.07.001

Williams, P. B., Quay, P. D., Westberry, T. K., and Behrenfeld, M. J. (2013). The oligotrophic ocean is autotrophic. *Ann. Rev. Mar. Sci.* 5, 535–549. doi: 10.1146/annurev-marine-121211-172335

Wilson, J. D., Andrews, O., Katavouta, A., de Melo Viríssimo, F., Death, R. M., Adloff, M., et al. (2022). The biological carbon pump in CMIP6 models: 21st century trends and uncertainties. *PNAS* 119 (29), e2204369119. doi: 10.1073/pnas.2204369119

Wu, J., Lee, Z., Xie, Y., Goes, J., Shang, S., Marra, J. F., et al. (2021). Reconciling between optical and biological determinants of the euphotic zone depth. *J. Geophysical Res.: Oceans* 126, e2020JC016874. doi: 10.1029/2020JC016874

Zubkov, M., Seligh, M. A., Burkill, P. H., and Leakey, R. J. G. (2000). Picoplankton community structure on the Atlantic Meridional Transect: a comparison between seasons. *Prog. Oceanography* 45, 369–386. doi: 10.1016/S0079-6611(00)00008-2

frontiers | Frontiers in Marine Science

TYPE Original Research
PUBLISHED 03 November 2023
DOI 10.3389/fmars.2023.1229692

EDITED BY
Takafumi Hirata,
Hokkaido University, Japan

REVIEWED BY
Jesús M. Mercado,
Spanish Institute of Oceanography (IEO),
Spain
Haimanti Biswas,
Council of Scientific and Industrial
Research (CSIR), India
Willem Hendrik Van De Poll,
University of Groningen, Netherlands

*CORRESPONDENCE
Vanda Brotas
✉ vbrotas@fc.ul.pt

RECEIVED 26 May 2023
ACCEPTED 16 October 2023
PUBLISHED 03 November 2023

CITATION
Brotas V, Ferreira A, Veloso V, Tracana A, Guerreiro CV, Tarran GA, Woodward EMS, Ribeiro L, Netting J, Clewley D and Groom SB (2023) Assessing phytoplankton community composition in the Atlantic Ocean from *in situ* and satellite observations.
Front. Mar. Sci. 10:1229692.
doi: 10.3389/fmars.2023.1229692

Assessing phytoplankton community composition in the Atlantic Ocean from *in situ* and satellite observations

Vanda Brotas[1]*, Afonso Ferreira[1], Vera Veloso[1], Andreia Tracana[1], Catarina V. Guerreiro[1], Glen Adam Tarran[2], E. Malcolm S. Woodward[2], Lourenço Ribeiro[1], Jane Netting[2], Daniel Clewley[2] and Steve B. Groom[2]

[1]Marine and Environmental Science Centre (MARE) / Aquatic Research Network (ARNET), Faculdade de Ciências, Universidade de Lisboa, Lisbon, Portugal, [2]Plymouth Marine Laboratory (PML), Plymouth, United Kingdom

The Atlantic Meridional Transect (AMT) program (www.amt-uk.org) provides the perfect opportunity to observe the phytoplankton community size structure over a long latitudinal transect 50°N to 50°S, thereby covering the most important latitude-related basin-scale environmental gradients of the Atlantic Ocean. This work presents cell abundance data of phytoplankton taxa recently collected during cruises AMT28 and 29 (in 2018 and 2019, respectively) using flow cytometer and microscope observations, as well as the pigment composition of the community, to assess the abundance and spatial distribution of taxonomic groups across the Atlantic. The community size structure showed a clear consistency between cruises at large spatial scale, with a dominance of picoplanktonic Cyanobacteria in oceanic gyres, an increase in all groups in the equatorial upwelling region, and high biomass of microplankton size class at higher latitudes. Phytoplankton carbon biomass for oceanographic provinces, ranged from median values of 10 to 47 mg Carbon m^{-3}, for the oligotrophic gyres, and South Atlantic (45°S-50°S), respectively. Satellite images of total chlorophyll *a* (as a proxy for phytoplankton biomass) as well as the relative contribution of the three phytoplankton size classes were produced for both cruises, and despite the small number of matchups, statistically agreed well with *in situ* size classes estimated as carbon biomass, constituting the first attempt in the literature to match satellite size classes with *in situ* data derived from cell abundance. The comparison of community structure between recent cruises (2019, 2018, 2015) and earlier ones (1995-1998) indicates a decrease in the number of diatom-bloom forming species, and an increase in Dinoflagellates, whereas nitrogen-fixing *Trichodesmium* abundance in tropical Atlantic remains constant. Within the recent period, a relative increase in the median values of picoplankton fraction was seen in SATL region, counterbalanced by a decrease in both nano- and microplankton fractions. Additionally, this study includes a database of species identified by microscopy, which had been interrupted for 20 years, providing a basis for long-term series of phytoplankton species.

KEYWORDS

phytoplankton taxonomic groups, Atlantic Meridional Transect, carbon, ocean colour, size classes

Introduction

The effect of climate change on the environment and biota should no longer be denied. The scientific community is thus strongly committed to evaluating the consequences of global warming on the interaction between atmospheric drivers and the fate and diversity of biological communities. In the ocean, phytoplankton is the basis of most trophic chains; it is responsible for sequestering as much atmospheric CO_2 as the terrestrial vegetation by photosynthesis, hence, playing a major role in the carbon cycle (Field et al., 1998). Phytoplankton comprises microscopic organisms from diverse phylogenetic evolutionary lines, with different cell sizes (cell biovolume spanning along seven orders of magnitude), different nutrient and light requirements (Reynolds, 2006), and yet not completely understood diverse trophic strategies (Glibert and Mitra, 2022). Phytoplankton communities respond rapidly to environmental changes due to fast turnover rates, often with a shift between species, due to inter-specific competition for resources. Changes in the community composition may have drastic cascading consequences for the other levels of the marine trophic chain (e.g. Reynolds, 2006). Hence, it is essential, yet complex, to understand whether such community shifts and diversity changes are due to natural response to environmental drivers or due to changes arising from climate change. Databases of long temporal series are vital to address these questions, as multiple sets of observations of species variability over a range of different time and space scales could contribute to our better understanding of species dynamics and characterisation of deviations.

The scientific knowledge on phytoplankton communities in the open ocean is considerably lower than in coastal and high-productivity zones (Buitenhuis et al., 2013) not least due to the practicality and cost of sampling away from the coast. Assessing phytoplankton diversity, studying taxonomic composition, cell size, or trophic strategy is mandatory to comprehend the ocean and the response of biological communities to climate change. Moreover, a better knowledge of phytoplankton functional types (PFTs) is key to understanding biogeochemical cycles (Le Quéré et al., 2005). PFTs were defined to link phytoplankton taxonomic classes with specific biogeochemical functions, enabling the development of ocean-ecosystem biogeochemistry models (Nair et al., 2008). The PFT concept originally evolved from a vegetation recognition approach, based on the functional associations of species in plankton (Reynolds et al, 2002). The number of defined PFT varies according to the scientific question being addressed; in the present work, we considered the same PFTs as in Brotas et al. (2022), ie picoautotrophs, calcifiers (coccolithophores), silicifiers (diatoms), diazotrophs (filamentous Cyanobacteria and symbiontic diatoms), autotrophic dinoflagellates, heterotrophic dinoflagellates and mixed nanoeukaryotes.

Satellite observations of near-surface Chl-*a* concentration, the proxy for phytoplankton biomass, has been defined by the Global Climate Observing System (GCOS) as an Essential Climate Variable and has been widely used in the literature addressing the response of oceanic phytoplankton to climate indicators (e.g., Brewin et al., 2012); hence, within this context, the terms remote sensing or Earth Observation (EO) are used in the literature to describe this technique (Sathyendranath et al., 2019a). Algorithms to assess phytoplankton functional types (PFTs) from space have also been developed (e.g., Xi et al., 2023), and the need to have complementary approaches to study phytoplankton dynamics has been stressed by IOCCG (2014) and acknowledged by the scientific community (Bracher et al., 2017). Hence, for effective understanding of changes at a global scale, spatio-temporal observations provided by satellites, including Chl*a* , size structure, and carbon dynamics (Sathyendranath et al., 2020), coupled with *in situ* observations are essential.

Phytoplankton size classification (Sieburth et al., 1978) considers three size classes: microplankton (Equivalent Spheric Diameter, ESD > 20 μm), nanoplankton (2 to 20 μm) and picoplankton (<2 μm). The phytoplankton size classes (PSC) can be assessed from pigment concentration using the method proposed by Vidussi et al. (2001), and further developed by Uitz et al. (2006), which differentiates the fractions of the three size classes in relation to total Chl*a* (TChl*a*), using the concentration of seven diagnostic pigments, belonging to the major marine taxonomic groups. The sum of these seven pigments is weighted by specific coefficients derived from extensive *in situ* databases. The fraction of each size class is then determined by the sum of its diagnostic pigments divided by the sum of all seven pigments, and the value of Chl*a* attributed to each size class fraction can be then computed by multiplying it by the total Chl*a* value. This methodology, in spite of the lack of a one-to-one correspondence between diagnostic pigments and most microalgal taxonomic classes, has proven to be adequate to represent phytoplankton size classes composition over large spatial scales, and it is widely used with remote sensing studies of phytoplankton (Nair et al., 2008, IOCCG, 2014; Bracher et al., 2017; Sun et al., 2023, amongst others).

The Atlantic Meridional Transect (AMT) is a multi-disciplinary research program that sampled the Atlantic Ocean on a transect from 50°N to 50°S, biannually from 1995 to 2000, and annually from 2000 onwards. Phytoplankton has been a major focus, along with the carbon biogeochemical cycle. The breadth and quality of scientific investigation which has resulted from AMT is impressive (see Rees et al., 2017), and has already shown changes which occurred probably due to climate change, e.g., Aiken et al. (2017), who found that the area of the north and south Atlantic gyres are expanding.

Species composition by microscope of the phytoplankton community was thoroughly assessed during AMTs 1 to 10 (from 1995-2000), but was discontinued in subsequent cruises with the exception of a short-term coccolithophore study covering the period 2003-2005 (Poulton et al., 2017). Hence, this paper presents a resumption of species composition by microscopy, continuing our previous work on AMT25 (Brotas et al., 2022) and provides the database as supplementary material.

This work aims to contribute to the following main goals of the AMT programme (stated in Rees et al., 2017): i) "building multi-decadal ocean time series" and ii) "quantifying the nature of ecological and biological variability in planktonic systems". The specific objectives of this paper are: 1) to characterise spatial patterns of biomass and community composition variability on a

~50°N to ~50°S transect on the Atlantic in two recent cruises, applying complementary *in situ* and satellite observations, focusing on biomass estimation (converted into carbon) of the phytoplankton taxonomic groups; and 2) to investigate and compare the most abundant phytoplankton species (within diatoms, dinoflagellates, filamentous Cyanobacteria) in earlier AMT cruises from the late 1990s with those from recent years (2015, 2018 and 2019).

Methodology

Sampling

This work comprises data collected on two AMT cruises: AMT28, on board *RRS James Clark Ross*, which took place from 23rd September to 30th October 2018, and AMT29 onboard *RRS Discovery*, from 13th October to 25th November 2019. The full reports of the cruises are available at https://www.amt-uk.org/Cruises.

Seawater samples were taken from 24 x 20 litre OTE (Ocean Test Equipment) CTD bottles mounted on a stainless steel rosette frame and a Seabird CTD system. The samples were taken from the predawn and noon CTD casts. Chl*a*-Fluorescence was obtained from the CTD sensor Wet Labs ECO-AFL/FL Fluorometer. Samples for Flow Cytometer analyses of phytoplankton groups and HPLC analyses of the concentration of photosynthetic pigments were taken at the surface for 63 stations in AMT28 and 52 in AMT29. Nutrient samples were collected at every depth from each CTD cast according to GO-SHIP protocols. For microscopic enumeration of phytoplankton, surface samples were taken from a water depth between 2-7m for both cruises at all sampling stations. Additionally, Deep Chlorophyll Maximum (DCM) samples for microscopy were also taken at 19 stations for AMT28, and 18 for AMT29, located in northern latitudes in the North and South, and in the area of the Equatorial upwelling. The DCM was assessed during sampling by observing the profile of Chl*a* Fluorescence obtained through the CTD.

Nutrients

To measure the concentration of nutrients, water samples taken at each CTD cast were sub-sampled into clean (acid-washed) 60 mL HDPE (Nalgene) sample bottles, which were rinsed three times with sample seawater prior to filling and capping.

For AMT28, samples were analysed on the ship as soon as possible after sampling and were not stored or preserved, whereas for AMT29, samples were analysed at Plymouth Marine Laboratory (PML). Samples were kept at -20° C during the cruise. For both cruises Micro-molar nutrient analysis was carried out using a four-channel SEAL analytical AAIII segmented flow nutrient auto-analyser.

The colourimetric analysis methods used were: Nitrate (Brewer and Riley, 1965, modified), Nitrite (Grasshoff, 1976), and Phosphate and Silicate (Kirkwood, 1989). The detection limit for Silicate was 0.02 µm and for the three others was 0.01µm. Sample handling and protocols were carried out where possible according to GO-SHIP protocols (Becker et al., 2020).

Microscope cell identification and counting

For each site, a sample of 200 mL was put in amber glass bottles and fixed with acid Lugol's iodine solution (2% final concentration). In the laboratory, observations were carried out with a Zeiss Axiovert 200 inverted microscope with 10x40 magnification. Cells > 10 µm were counted in a 50 mL chamber, following the Utermöhl method (Utermöhl, 1958), aiming to count at least a total number of 400 cells; when this value was not reached, a second chamber was counted. Species from the following divisions/classes were identified and counted: Bacillariophyceae (diatoms), Dinophyceae, separated into Autotrophic (ADinos) and Heterotrophic dinoflagellates (HDinos), Prasinophyceae, filamentous Cyanobacteria, and the genus *Phaeocystis*. For *Trichodesmium* spp (filamentous Cyanobacteria), the number of cells was estimated for each filament, giving an average number of 100 cells per filament.

These groups were defined according to work carried out on AMTs 1 to 10, from which a database of taxa identified by microscopy was published (Sal et al., 2013), and restarted in AMT25 by Brotas et al. (2022).

Coccolithophore species > 10 µm were not assessed by microscopy, as this community was the object of another paper in this special issue (Guerreiro et al., 2023). Hence in this work, coccolithophore species were only assessed by Flow Cytometry. Taxonomic names were checked against the World Register of Marine Species (WoRMS).

Flow cytometer cell analysis

Sea water samples were collected in clean 250 mL polycarbonate bottles from the CTD system, stored in a refrigerator and analysed within 2 hours of collection. Fresh samples were analysed using a Becton Dickinson FACSort flow cytometer. Within the analysis window, six different groups were enumerated: *Prochlorococcus*, *Synechococcus*, pico-eukaryotes (PEUK), coccolithophores within 5-10 µm (COCCOS), Cryptophytes (CRYPTO) and other nanophytoplankton (NEUK), following the methodology described in Tarran et al. (2006).

Flow cytometery targets the smaller component of phytoplankton cells, from ESD of < 1 µm up to *ca* 10 µm, whereas microscopy may identify cells with ESD ≥ 10 µm.

Carbon content of Phytoplankton community

Cell numbers of each taxon were converted into carbon concentration (mg Carbon m^{-3}). For phytoplankton cells counted by microscopy, the Cell Carbon content was obtained either from the AMT database published by Sal et al. (2013) or from species biovolume, which was then converted into carbon using the conversion factors of Menden-Deuer and Lessard (2000), as detailed in Brotas et al., 2022 (see Table S1 in Supplementary Material, which has the values of pg Carbon per cell for all microplanktonic species identified).

For taxa measured by flow cytometry, cell numbers of *Prochlorococcus* and *Synechococcus* were converted to Cell Carbon by applying conversion factors of 32 and 110 fg Carbon Cell^{-1}, respectively, following Tarran et al. (2001). Cell Carbon content factors for PEUK, NEUK, CRYPTO, and COCCOS were 0.44, 3.53, 23.66 and 33.37 pg Carbon Cell^{-1}, respectively (Tarran et al., 2006).

Photosynthetic Pigments and size class pigment classification

In order to analyse the concentration in photosynthetic pigments, a volume of 2 to 6 L of seawater was vacuum-filtered through 25 mm diameter GF/F filters onboard, immediately after sampling. Filters were folded into 2 mL cryovials and stored immediately in the -80°C freezer.

Phytoplankton pigments were determined later in the laboratory using High Performance Liquid Chromatography (HPLC). The chromatographic separation of pigments is based on the C8 method developed by Zapata et al. (2000), and adapted by Mendes et al. (2007). This method is based on a reverse-phase and a pyridine-containing mobile phase. Filters are extracted with 3 ml of 95% cold-buffered methanol (2% ammonium acetate) in a polypropylene test tube. An internal standard, trans-β-apo-8'-carotenal at a concentration of 0.005 mg L^{-1}, is included in the extraction solvent, for posterior correction of pigment concentrations. The equipment used is a Shimadzu Prominence – I Plus® Lc 2030C 3D Plus, with a monomeric octysilica (OS) C8 column Symmetry® (150mm x 4.6mm dimensions, 100 Å pore size, 3.5 µm particle size, 335 m^2 g^{-1} surface area and 12% carbon load). The solvent gradient has a flow rate of 1 mL min^{-1} and a run of 40 min; the sample injection volume is 100 µL. The composition of the solvents is the following: A – Methanol: Aqueous pyridine: Acetonitrile (50:25:25 v/v/v) and B - Methanol: Acetonitrile: Acetone (20:60:20v/v/v).

The HPLC was calibrated using a suite of standards purchased from DHI (Denmark). Pigments were identified based on retention time and spectral match using a photo-diode array.

The three size classes' abundance was estimated according to Uitz et al. (2006). The weight of each diagnostic pigment followed Brewin et al. (2017), who investigated the pigment ratios and the influence of ambient light on a vast *in situ* dataset in the Atlantic, updating the initial coefficients proposed by Uitz et al. (2006). Hence, the weighted sum of all diagnostic pigments, equivalent to total Chlorophyll *a* was computed from the expression $C = \sum W_i P_i$, where W (weight) = {1.65, 1.04, 0.78, 1.19, 3.14 1.27, 1.02}, and P, (pigments) = {fucoxanthin, peridinin, 19'hexanoyloxyfucoxanthin, 19'butonoyloxyfucoxanthin, alloxanthin, chlorophyll *b* + divinyl chlorophyll *b* and zeaxanthin}.

Microplankton class was determined by the sum of fucoxanthin and peridinin (diagnostic pigments diatoms and dinoflagellates, respectively), nanoplankton encompassed coccolithophores, Cryptophytes, and a non-differentiated assemblage of nano-eukaryotes (represented by 19'hexanoyloxyfucoxanthin, 19'butonoyloxyfucoxanthin, alloxanthin), and chlorophyll *b* + divinyl chlorophyll *b* and zeaxanthin were used to estimate picoplankton fraction (dominated by the small Cyanobacteria *Prochlorococcus* and *Synechoccocus*).

The filamentous Cyanobacteria (which contain the cyanobacteria diagnostic pigments) did not fit into the size class approach, as according to their size, they should be considered microplankton and not picoplankton.

Satellite data

Satellite data analysis was undertaken by the UK NERC Earth Observation Data Acquisition and Analysis Service (NEODAAS). For sea-surface temperature (SST), the UK Met Office reprocessed OSTIA global foundation SST was used, obtained from the Copernicus Marine Environment Monitoring Service (https://data.marine.copernicus.eu/product/SST_GLO_SST_L4_REP_OBSERVATIONS_010_011/description). The OSTIA level 4 product uses a combination of satellite data, from both infrared and microwave radiometers, and *in situ* data, to provide daily, global, 0.05 x 0.05 degree resolution, gap-filled images (Good et al., 2020). Chl*a* data were obtained from the ESA ocean colour climate change initiative (OC-CCI portal: www.oceancolour.org/portal) at daily, 4km resolution and comprised version 6. The OC CCI dataset is a multi-sensor product with inter-sensor bias correction. Each pixel is classified in terms of fuzzy (or partial) membership of optical water types (OWT) and the Chl*a* is computed as a function of the memberships and the best performing algorithm per OWT (Sathyendranath et al., 2019a). Aerosol optical thickness (AOT) at 550nm was obtained from the NOAA Suomi VIIRS sensor at daily, 4 km resolution. Composite images were produced as simple averages of all daily data for the duration of each cruise.

In order to obtain the Chl*a* contribution of each size class as well as, separately, of diatoms and dinoflagellates, to total satellite-derived Chl*a*, the model of Brewin et al. (2017) was used, which incorporates SST-dependency of the model parameters. This is a development of the three-component model of PSC of Brewin et al., (2010) which assumes that TChl*a* derives from the sum of Chl*a* from each size-class (Micro-, nano- and picoplankton), and uses two exponential functions to calculate Chl*a* of nano+picoplankton, and Chl*a* from picoplankton as a function of TChl*a*. The parameters of these functions are from the statistical correlation of pigment ratios in extensive *in situ* databases. Linking model parameters to SST in addition to Chl*a* resulted in only slight improvement to regression statistics (RMSE and bias) but incorporated variations in model parameters that are not captured in the Chl*a*-only fixed-parameter model (Brewin et al., 2017). Size class specific Chl*a* was computed using the daily Chl*a* and SST data.

Daily matchups were obtained between the satellite results and contemporaneous *in situ* sampling of biomass for AMT28 and AMT29.

Comparison of microplankton most abundant species with earlier AMTs

A comparison of diatom and dinoflagellate and filamentous Cyanobacteria species from AMT1, 3, 5, 7 (which occurred in boreal autumn in 1995, 1996, 1997 and 1998, respectively), AMT25 and the present AMT28 and 29 was undertaken. The routes of the seven AMTs are shown in Figure 1, whereas Table 1 specifies the dates and number of stations for each cruise. Data from earlier AMTs were gathered from Sal et al. (2013), and AMT25 data were published in the BODC database (Brotas and Veloso, 2022) and analysed by the same person as the samples for AMT28 and AMT29. Only results from surface samples were considered (2 to 7 m).

Statistical data analysis

Regression analyses were performed of the matchups of satellite-derived size class Chl*a* and the *in situ* carbon biomass of the three size classes, estimated from the cellular carbon content described above. A matchup was between the *in situ* data and the satellite retrievals for the same location and the same day; obviously, these were limited by cloud cover masking the sea-surface from the satellite sensor. Microplankton was computed as the sum of diatoms and dinoflagellates, nanoplankton as the sum of coccolithophores, Cryptophyte and other NEUK, and picoplankton the sum of *Prochlorococcus, Synechococcus* and PEUK. There were a total of 15 matchups for AMT28 and 17 for AMT29. All Chl*a* data were logarithm 10 transformed prior to analysis.

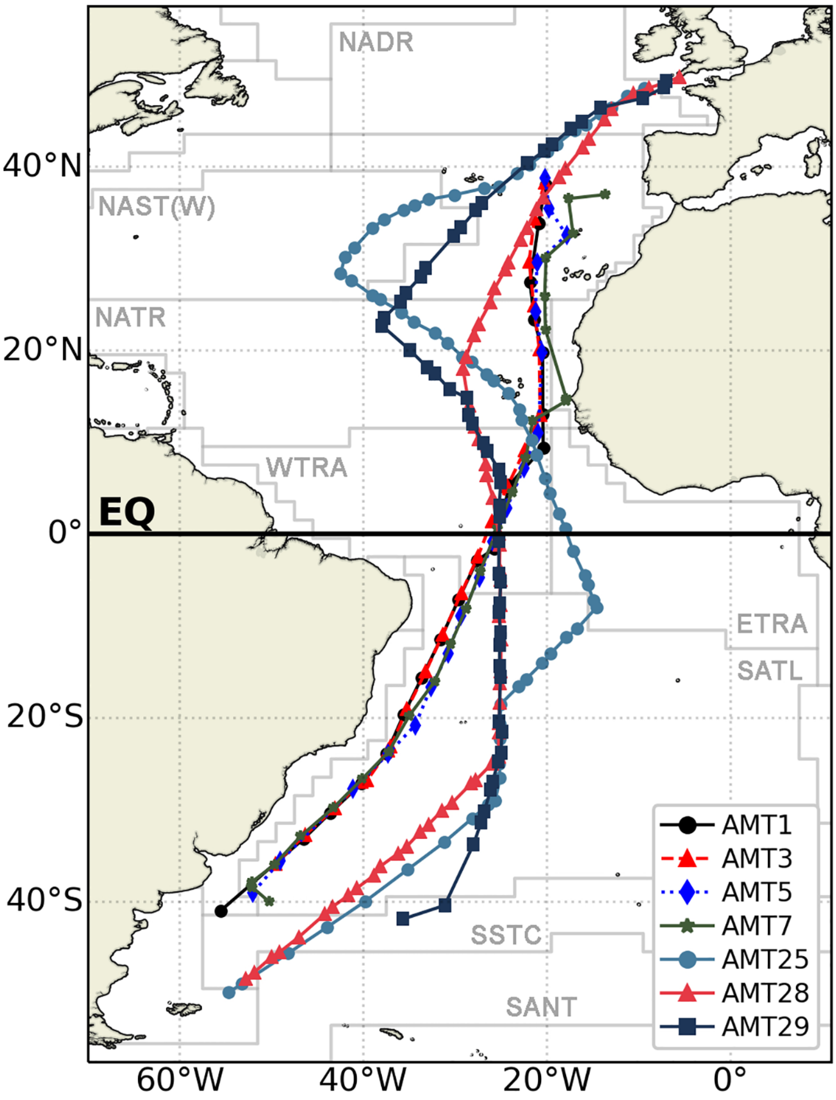

FIGURE 1
Map of AMTs tracks. AMT1,3,5,7, 25, 28, 29, superimposed on the Longhurst provinces.

TABLE 1 Dates for the AMT cruises considered for comparison of species, number of stations with microscopy observations.

AMT Cruise	Initial Date	Final Date	Stations (n)
AMT1	21-09-1995	24-10-1995	19
AMT3	22-09-1997	25-10-1997	21
AMT5	14-09-1997	17-10-1997	19
AMT7	14-09-1998	25-10-1998	26
AMT25	15-09-2015	3-11-2015	57
AMT28	25-09-2018	27-10-2018	66
AMT29	16-10-2019	18-11-2019	55

A Bray-Curtis analysis (Bray and Curtis, 1957) was performed to determine the similarity/dissimilarity between regions sampled in all AMTs. Data on species from AMTs 1, 3, 5, 7, 25, 28 and 29 with concentrations higher than $1x10^4$ cells L^{-1} were gathered; the Bray-Curtis analysis was performed on non-transformed data. To better visualise these relationships, a classification analysis was made using hierarchical agglomerative clustering of the samples and group-average linking (Field et al., 1982). During the construction of the dendrogram, the significant difference of every group of samples was tested by the similarity profile routine (SIMPROF, Clarke et al., 2008). Calculated for every node, the SIMPROF analysis is a permutation test of the null hypothesis that the set of samples below any given node of the dendrogram does not differ from each other or show any significant multivariate structure. For each test, 1000 permutations were applied to calculate a mean similarity profile, with a chosen significance level of 5%. The taxa mainly responsible for the average Bray-Curtis dissimilarity between the *a posteriori* significantly different clusters of samples, as well as intra-group similarity, were selected and sorted by SIMPER analysis (Clarke, 1993). All these analyses and routines were performed using tools found in PRIMER® 6 software package (PRIMER-E, Plymouth, UK).

A principal component analysis (PCA) was performed to understand how environmental patterns (Chl*a*, SST, salinity, macronutrients, depth of the nutricline) shaped the surface distribution of taxonomic groups, using data from both cruises (n=111). Data were standardized (value-average divided by standard deviation) prior to running the analysis. The PCA was run using the sklearn module in python 3.8.8 (Pedregosa et al., 2011).

Results

Environmental data

The tracks of AMT28 and AMT29 across the Atlantic Ocean, plotted over cruise-averaged images of Chl*a*, SST and AOT) are shown in Figure 2. SST showed the expected latitudinal distribution and was very similar between cruises, in fact, the one-month lag difference is only noticeable around 40°N. The Chl*a* showed similar patterns for AMT 28 and 29 with low Chl*a* in the oligotrophic gyres in the north and south Atlantic, though with a larger extent on AMT29 reflecting the later timing of this cruise (and, hence, later in austral Spring). Higher Chl*a* values appeared at higher northerly or southerly latitudes while enhanced values north of the equator are probably associated with equatorial upwelling and the extension offshore to the west of Africa due to eastern boundary upwelling. The AOT 550nm cruise composite data were markedly different between the cruises, with Saharan dust plumes extending offshore between 10°N and 22°N during AMT28 and lower values on AMT29.

Figure 3 shows the nutrient concentration between the surface and 200m depth along the transects. The Nutricline was plotted as the isoline of NO_x = 1µmol L^{-1}, following Moore et al. (2009). The North-South nutrient distribution followed the same general pattern in both cruises, with higher concentrations reaching the surface at the higher latitude regions of both hemispheres (from 40°-50°N and 40°-50°S) but more notably in the South Atlantic. The highest concentrations of all macronutrients were observed at greater water depths between 18°N-10°S, where the nutricline was shallower (reaching its shallowest position to the north of the equator ~40 m water depth at 5-15°N) and at the equator (70-80 m water depth). At the higher-latitude regions during both AMTs, enhanced mixing-induced nutrient supply to the surface was more notable in the southern hemisphere, possibly linked to the Malvinas Current.

Community composition

Phytoplankton relative composition for AMT28 and AMT29 for ten groups, along with the concentration of Chl*a* is illustrated in Figure 4. Biomass (derived from cell concentration) was expressed as mg Carbon m^{-3}, to allow for a comparison of the various groups, hence, it should be highlighted here that values of carbon content per cell are strongly dependent on the cell biovolume. Cell biovolume ranged from 0.11 (*Prochlorococcus*) to 1.23×10^6 μm^3 (the large diatom *Rhizosolenia styliformis*) hence, spanning 7 orders of magnitude. For diatoms, ADinos, HDinos, and filamentous Cyanobacteria, cell abundance was determined by microscopy, whereas for coccolithophores < 10 µm, NEUK, Cryptophytes, PEUK, *Prochlorococcus* and *Synechococcus* it was determined by Flow Cytometry. It should be noted that AMT29, due to bad weather conditions, had fewer sampling stations in the South Atlantic Gyre (SATL) province and none in South Atlantic Subtropical Convergence (SSTC).

Other taxa were counted by microscope, namely the Haptophyte *Phaeocystis*, and species from the classes Prasinophyceae and Euglenophyceae, but with very low biomass values across the transect, (always less than 1% of total biomass), and were excluded from the plots. Coccolithophores abundance only accounted for the cells enumerated by flow cytometry; hence, the biomass contribution of this group in the figure is underestimated.

The spatial distribution of the different phytoplankton groups in AMT28 and AMT29 presented the same general pattern with

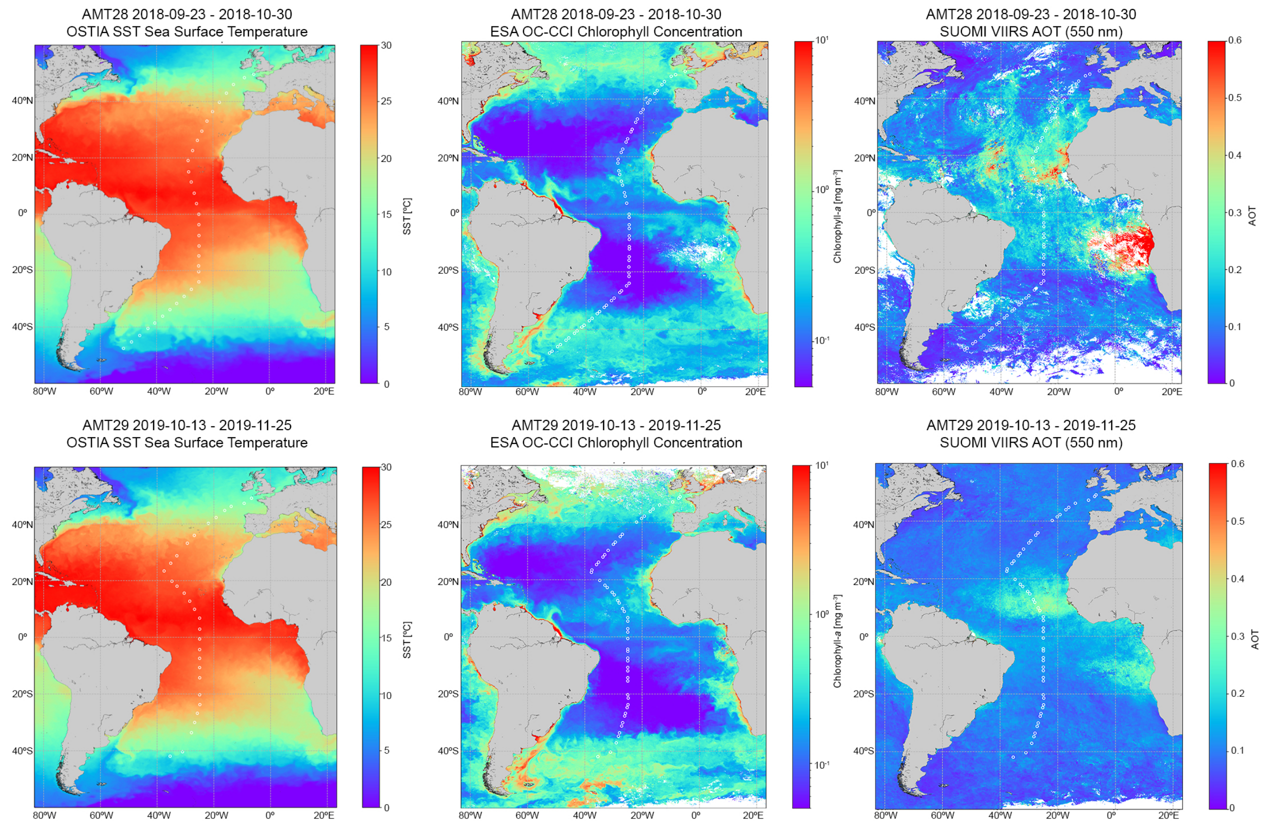

FIGURE 2

Composite images of Sea Surface Temperature (SST), (left): Chla mg m^{-3} (middle): Aerosol Optical Thickness (AOT), (right) for AMT28 (top) and AMT29 (bottom), for the entire cruise period.

high abundance of diatoms and dinoflagellates (higher than 10^3 cells L^{-1}) in higher latitudes, and picoplankton carbon biomass (comprising PEUK, *Synechococcus* and *Prochlorococcus*) over 40% of total biomass from 20°N to 40°S on both cruises. Also, in both cruises, a clear increase in Chl*a* was noticeable in the region around the Equator (where nutrient concentrations increased within the photic zone, and above the nutricline). The dominance of picoplankton is clear in the ocean gyres, where *Prochlorococcus* is the most abundant taxa in the majority of the stations, and it was replaced by *Synechococcus* when the NO_x values were above ~0.1 µmol L^{-1}; PEUK had similar distribution and abundance to *Synecoccocus*. COCCOS, HDinos and NEUK were the least important groups in terms of carbon contributions, and did not show a clear meridional distribution, i.e., occurring both in the oligotrophic gyres where *Prochlorococcus* dominated, but also in the more productive regions where diatoms and ADinos were more abundant.

There are differences in the relative abundance between the two AMTs, regarding diatoms and dinoflagellates, as whilst diatoms are more abundant in AMT28, both ADinos and HDinos presented clearly higher biomass in AMT29, with ADinos being the dominant taxa north of 20°N. Another major difference was the occurrence of the bloom of the autotrophic dinoflagellate *Prorocentrum cordatum*, with 1.9 x10^6 cells L^{-1}, contributing to a Chl*a* value of 2.83 mg m^{-3}, located in the northern station of AMT28 (49.63°N), and absent in AMT29.

Non-heterocystous filamentous Cyanobacteria included two species: *Trichodesmium erythraeum* and *Oscillatoria limosa*, the former was largely more abundant, appearing in both cruises in the Tropical region north of the Equator, on AMT28, from 22°N to 7°N, and on AMT29, from 5°N to 25°N, in the surface samples, but also at the DCM (Figure 5), although in low quantities.

The biomass results (in mg Carbon $m^{-}3$) obtained for diatoms, ADinos, HDinos and filamentous Cyanobacteria, for the stations sampled in surface and DCM, are plotted in Figure 5, superimposed on the integrated Chl*a* profile (measured by CTD fluorescence) down to 200m depth, and showed that biomass of each group was higher at the surface than at the DCM, in most stations, which allowed for a more detailed analysis of the more abundant species in surface samples only.

Spatial variability in Phytoplankton Size classes

The pigment approach to derive phytoplankton size classes has been extensively used in oceanographic studies, and it is presented here as a complementary analysis to the cell enumeration data

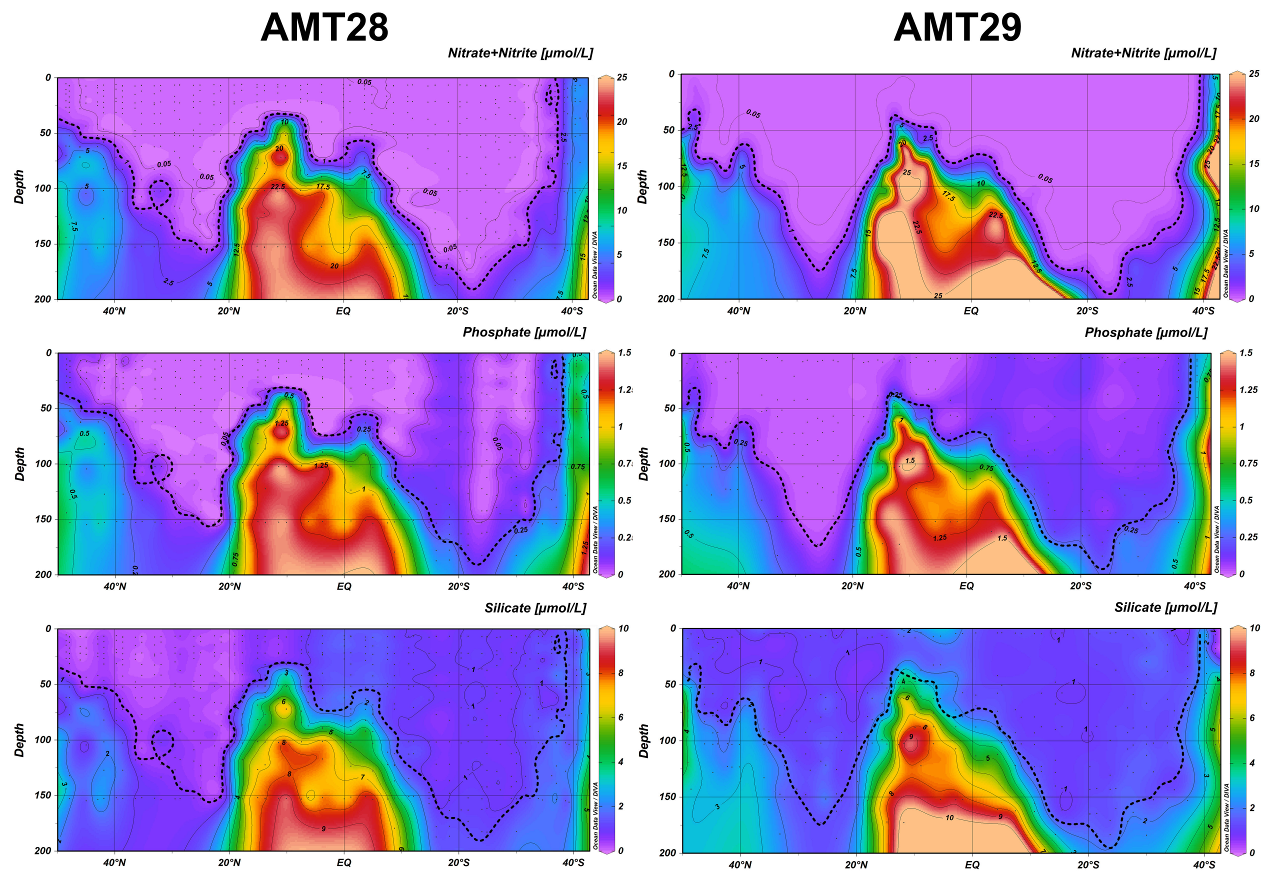

FIGURE 3
Concentration of nitrate+nitrite, phosphate and silicate for AMT28 (Left) and AMT29 (Right). The isoline of 1 µmol L^{-1} NO_x is plotted in all graphs.

presented in Figures 4 and 5. Figures 6A, B show the community composition in terms of size classes, for surface samples, for both AMT28 and AMT29. All size classes (pico-, nano-, microplankton) increased in the higher-latitude regions during both expeditions. Picoplankton was the group increasing the most between 10°N and 10°S, whilst micro- and nanoplankton were more important at higher latitudes (i.e., > 40°N and > 30°S). Whereas the values for TChl*a* and TCarbon for AMT 28 and AMT29 surface samples are displayed in Figures 6C, D. The common patterns between the two cruises were: i) the overall distribution of Chla, with highest values in higher Northern and Southern latitudes, very low values in oceanic gyres, and an increase in the equatorial region (10°N to 10°S): ii) in higher latitudes, both micro-and nanoplankton contributed to the high Chl*a* values, whereas, within the region between 15°N to 10°S, the several small peaks observed are mostly due to an increase in the nanoplankton fraction, iii) the median values in both cruises were almost the same: 0.092 and 0.091 mg Chl*a* m^{-3} for AMT28 and AMT29, respectively.

The main difference was the high Chl*a* value in AMT28 at 49°N, due to the *Prorocentrum cordatum* bloom in the English Channel, which reached of 326 mg Carbon m^{-3}.

The taxonomical structure of the community determined by cell enumeration and expressed as carbon biomass was fitted into the three size-class classification as described above. Table 2 discriminates the median values for TCarbon, and the relative distribution of the total community by size classes through the oceanic provinces determined as above. Interestingly, the overall median for both cruises gave the same result: 17 mg Carbon m^{-3}. The results evidence the spatial distribution of phytoplankton community along the North-South track in the Atlantic, with values of 10-15 in the oceanic gyres, and above 18 in North Atlantic Drift (NADR). The highest median value of 47 mg Carbon m^{-3} was observed for the SATL region in AMT28, where microplankton carbon biomass fraction reached almost 70%; we split the vast SATL region into two areas, at latitude 27°S, separating the gyre from the more productive southern SATL. The minimum values observed in both cruises were similar: 8 mg Carbon m^{-3} for AMT28 at 12°S and 7 mg Carbon m^{-3} for AMT29 at 15°S.

Satellite assessment of size classes

Using satellite imagery, the following products were derived: the relative contribution of micro-, nano- and picoplankton, as well the contribution of diatoms and dinoflagellates, according to Brewin et al. (2017). Cruise composite images of Chl*a* (mg m^{-3}) for each size class, for the total period of the cruises are displayed in Figure 7. The large-scale nutrient distribution affects all three size classes, as all classes present higher abundance in high-latitude regions and lower in oligotrophic gyres. However, the response of cells to

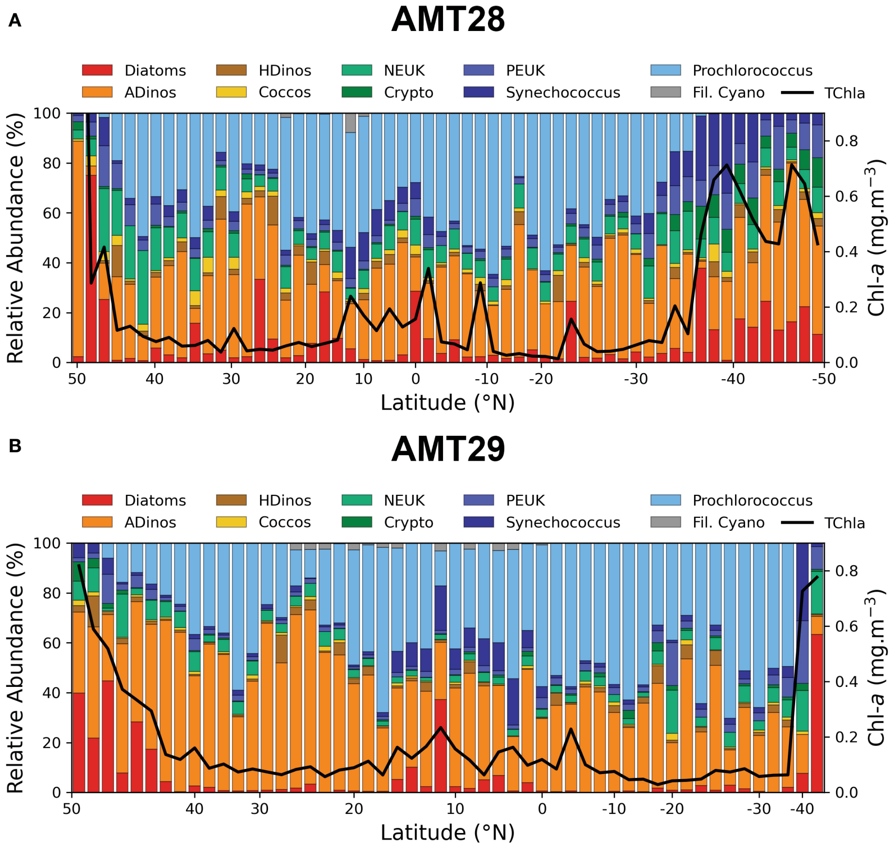

FIGURE 4
Relative abundance of major phytoplankton groups in surface samples, enumerated by FC (Prochlorococcus, Synecoccocus, PEUK, NEUK, Cryptophytes, or microscopy (diatoms, dinoflagellates and filamentous Cyanobacteria) and estimated in mg Carbon m^{-3}, along the AMT transect (N-S), Chla mg m^{-3} value is also plotted. The correspondence between groups and size classes is given by the colour code: Picoplankton – blue tones, Nanoplankton – yellow and green, Microplankton – Red and Brown. Note that Chla in the 1st station of AMT28 is not plotted as the value was 2.89 mg m^{-3}. Note that AMT29 was sampled only until 35°S. AMT28 (top), AMT29 (bottom).

nutrient enrichment scales up according to cell size. Picoplankton was present in all latitudinal regions, becoming dominant in low-nutrient gyres, where micro- and nanoplankton attain minimum values. Nanoplankton taxa biomass increased in tropical Atlantic and higher latitudes, whereas Microplankton fraction presented high values only in high northern and southern latitudes.

The number of daily matchups between satellite and *in situ* data found was 15 for AMT28 and 17 for AMT29, so the comparison analysis was made on samples of the two cruises together. For the *in situ*, the total carbon of the three size classes was computed as described above. The results in Table 3 showed significant correlation values (r^2) for the three size classes, as well as when considering diatoms and dinoflagellates separated.

Analysis of microplankton fraction and bloom identification

A total of 30 diatom taxa, 156 dinoflagellate taxa and three filamentous Cyanobacteria taxa were identified during AMT28 and AMT29 (see Supplementary Material, Table 1). Our taxonomic criteria followed as much as possible those presented by Sal et al. (2013), in order to compare phytoplankton species occurrence and abundance with previous AMT studies.

Data from diatoms, dinoflagellates and filamentous Cyanobacteria obtained during AMT28, AMT29 presented here were compared to data from AMT25 (Brotas et al., 2022) and from the earlier AMT1, 3, 5, 7, all of which also took place during boreal Autumn. While all cruises followed the same general meridional latitudinal track, AMT25 and AMT28 extended further south compared to the other cruises (Figure 1). In terms of longitude, significant track differences occurred in the northern part of NATR, with AMT25 and AMT29 being ca 20° displaced to the east compared to the other track cruises, and thereby following a more open-ocean route, AMT29 being the furthest east.

The present analysis is focused only on the most abundant species in these seven cruises, i.e., only species which "bloomed" (where a bloom was considered when the cell concentration was higher than 10^4 cells L^{-1}); it should be noted that for *Trichodesmium* spp. the bloom was defined not by the number of filaments, but by the number of cells L^{-1}.

These species are enumerated in Table 4 and were used in the cluster analysis. The table classified each diatom and dinoflagellate species according to two simple criteria, namely size (greater or

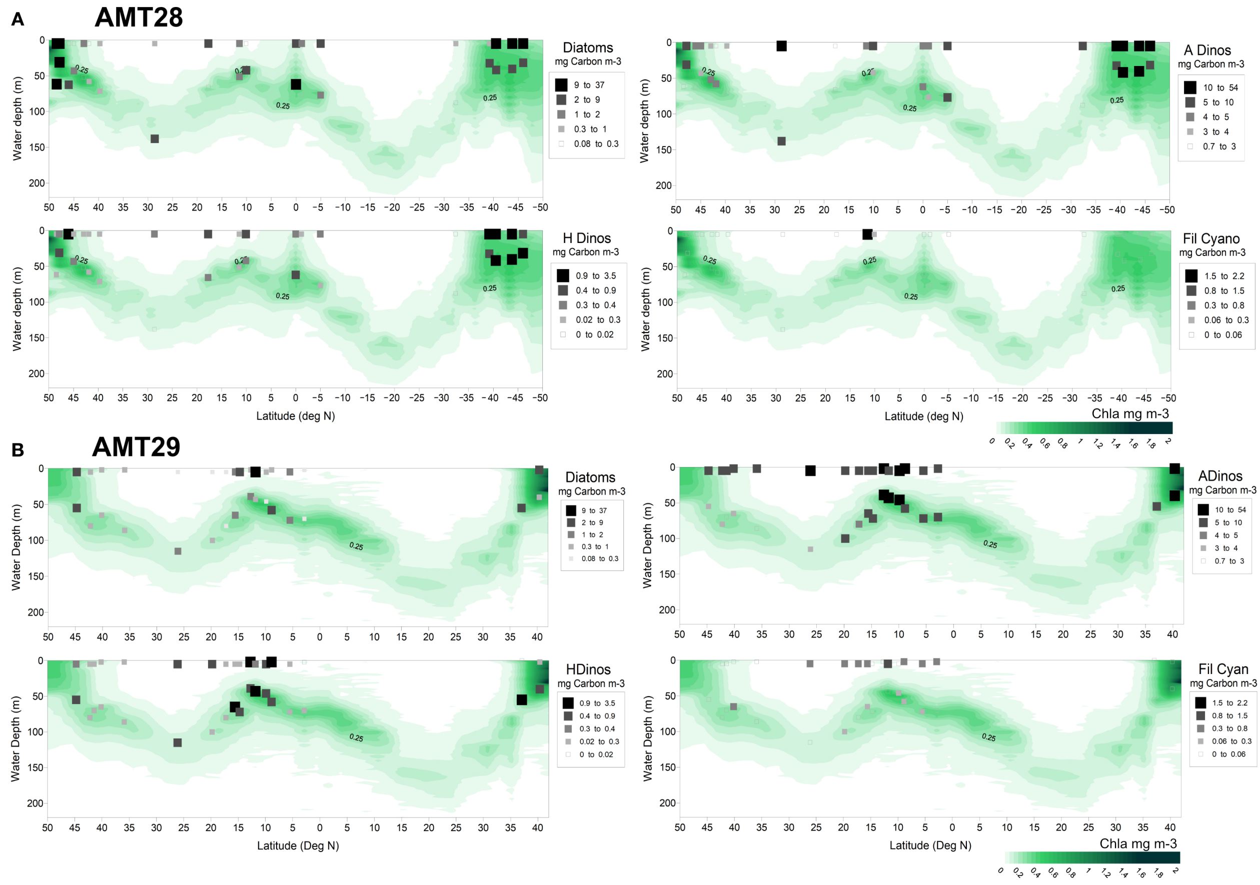

FIGURE 5
Surface and DCM carbon biomass (mg Carbon m^{-3}) of microplankton taxa plotted over Chla values (measured with CTD fluorometer). AMT28 **(A)**, AMT29 **(B)**.

lesser than 17.5 µm ESD, thus separating species belonging to nano or microplankton size fraction, respectively), and colonial versus unicellular/short chains. For diatoms, species were also classified as centric or pennate (thus belonging to the order *Centrales* or *Pennales*, respectively). Categories such as Pennate group (10-30 µm), or Athecate dinoflagellates, where the genus is not discriminated, are present in Sal et al. (2013), and were also frequently observed in our samples.

Cluster analysis, with the SIMPROF test (Figure 8), identified six groups of samples, which were statistically distinct (at the 5% level). SIMPER analysis determined the taxon or group of taxa that mostly contributed to each group's average similarity. The largest group (D) clustered the tropical Atlantic (NATR and WTRA) from AMT1, 7, 25, 28 and 29, being defined by the presence of *Trichodesmium* blooms. Spanning also from earlier to recent AMTs, Group C's average similarity was mainly due to Athecate dinoflagellates. Groups B and E, were exclusive of earlier AMTs, and cluster latitudinal regions where up to 6 different species of diatoms were observed. Group A was defined by the *Prorocentrum cordatum* blooms that occurred twice in the NADR region in AMT28, and at an *ad-hoc* station of AMT25; both blooms occurred in the English Channel, in September, with this species attaining 99 % of the total cell abundance of the microplankton fraction. Finally, group F contained two blooms that share no similarities with other assemblages, namely *Gymnodinium galeaeforme* (AMT1) and Pennate diatoms (> 40µm), in AMT28.

Furthermore, a common feature between all AMTs, in the North Atlantic Subtropical Gyre (NAST), and SATL North regions, which comprise a significant part of the North and South Atlantic oligotrophic gyres, respectively, was that no blooms were observed, except for Athecate dinoflagellates and "Pennate group (10-30 µm)" in AMT3.

Discussion

Phytoplankton community variability patterns in the Atlantic regions

The large-scale relative abundance of phytoplankton groups in Longhurst biogeographic provinces, was comparable, in terms of the dominant groups for each region. The comparison of the median values of TCarbon over the provinces gave very similar results for AMT28, AMT29, and AMT25 (Brotas et al., 2022, their Table 3). Ocean gyres presented median values of 10-15 mg Carbon m^{-3}, whereas higher latitudes registered higher variability, and median values between 25-47 mg Carbon m^{-3}.

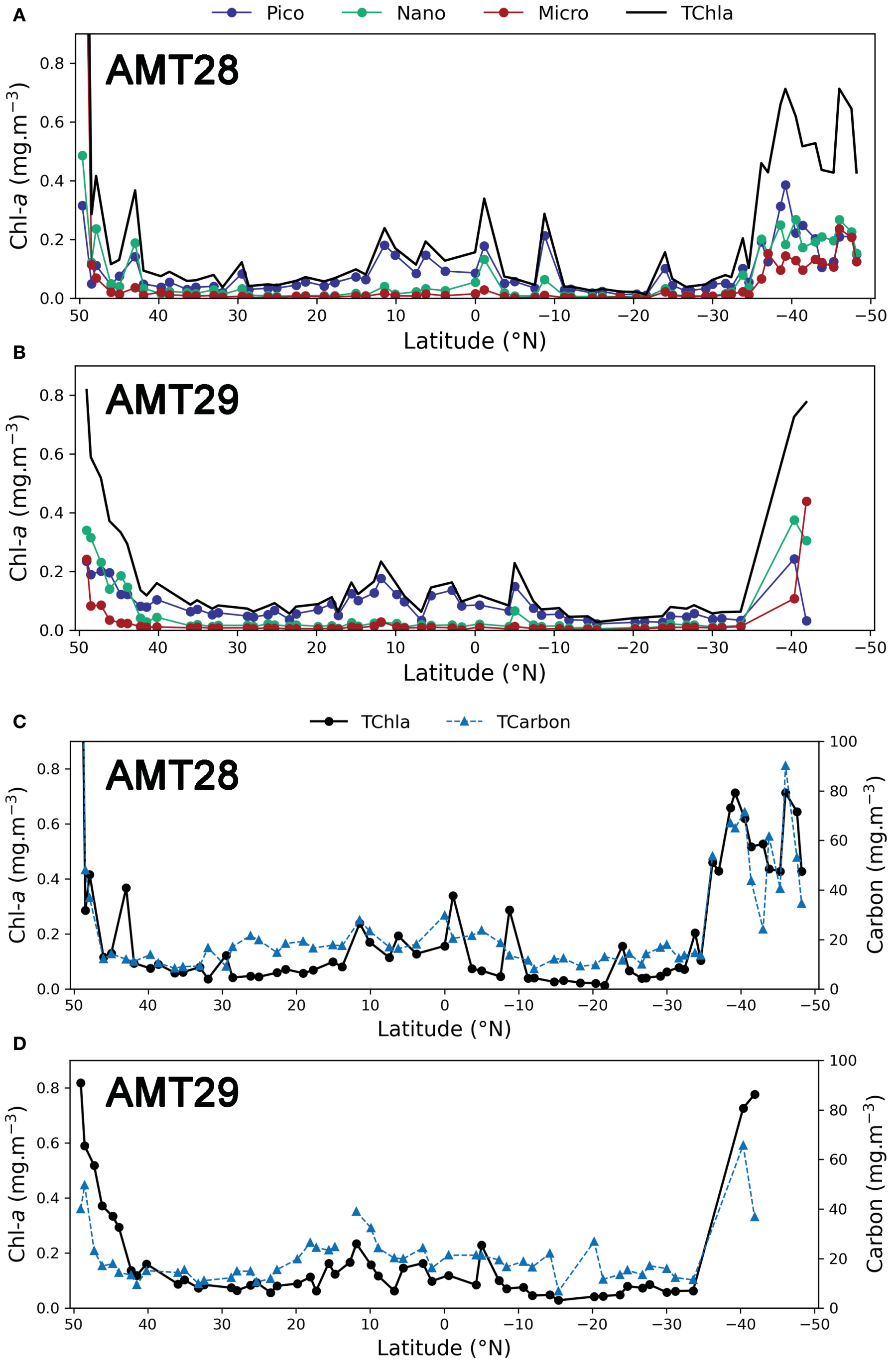

FIGURE 6
Distribution of TChla (mg m^{-3}) and Chla for each size class: pico-, nano- and microplankton determined by pigment's concentration for surface stations. AMT28 **(A)** and AMT29 **(B)**. TChla and TCarbon (mg m^{-3}), determined by cell enumeration. AMT28 **(C)**, AMT29 **(D)**.

We used three complementary methodological approaches to study phytoplankton composition, two of them based on *in situ* data, photosynthetic pigments and cell enumeration, and the third using satellite observations. All three approaches showed a similar pattern for the spatial distribution of phytoplankton community composition in the Atlantic regions for the two cruises, suggesting that environmental conditions of each region play a major role in shaping the relative composition of phytoplankton communities.

With the goal of strengthening this observation, and in order to identify the main drivers for the observed spatial distribution of the taxonomic groups, a Principal Component Analysis was performed on AMT28 and AMT29 data. The environmental factors considered were the surface concentration of nutrients (nitrates+nitrites, phosphates and silicates), depth of the nutricline, Temperature, Salinity and TChl*a*, versus the ten taxonomic groups considered in this study. The resulting PCA, shown in Figure 9, plots the dominant taxa in the two components, which explain 79% of the

TABLE 2 Median values of TCarbon, in mg m^{-3}, and median values of the percentage of micro- nano- and pico-plankton for each biogeographic oceanic province, for AMT28 and AMT29.

Regions	Stations (N)	TCarbon (mg m^{-3})	Size Classes Fraction (%) Micro-Nano-Pico	AMT
NADR, North Atlantic Drift, 56°N-42°N	6	25	44-17-29	28
NADR, North Atlantic Drift, 56°N-42°N	7	18	73-9-19	29
NAST, North Atlantic Subtropical Gyre, 42°N-30°N	7	10	37-18-45	28
NAST, North Atlantic Subtropical Gyre, 42°N-30°N	6	13	52-7-41	29
NATR, North Atlantic Tropical Gyre, 30°N-10°N	12	18	40-9-49	28
NATR, North Atlantic Tropical Gyre, 30°N-10°N	13	20	58-4-34	29
WTRA, Western Tropical Atlantic, 10°N-10°S	9	19	41-10-51	28
WTRA, Western Tropical Atlantic, 10°N-10°S	11	21	43-4-52	29
SATL, South Atlantic Gyre, 10°S-27°S	10	12	34-9-56	28
SATL, South Atlantic Gyre, 10°S-27°S	9	15	35-6-60	29
SATL, South Atlantic Gyre, 27°S-45^0 S	15	24	45-17-39	28
SATL, South Atlantic Gyre, 27°S-45°S	6	17	31-9-57	29
SSTC, South Subtropical Convergence, 45°S-50°S	4	47	67-16-16	28
SSTC, South Subtropical Convergence, 45°S-50°S	NS	NS	NS	29

SATL was subdivided into two sub-regions. NS, not sampled.

total variability. *Prochlorococcus* was clearly linked with low nutrients and low Chl*a* values, and the diatoms were located in the opposite situation. *Synecchoccoccus* appeared only twice as the dominant group, linked with high Chl*a* and high nutrients, as indeed, all regions with high values of picoplankton (Figure 6) were dominated by *Prochlorococcus*. The group ADinos appeared scattered throughout the space defined by both axes, with values on the right end of axis 1 linked with high Chl*a* and high nutrient values. Furthermore, the Bray-Curtis analysis focused only on microplankton species, clustering the same regions from all the AMT cruises, rather than clustering the earlier AMTs versus the recent ones, reinforcing the above conclusions, i.e., the phytoplankton community composition is shaped by the strong gradients of the environmental conditions.

The presence of diazotrophic Cyanobacteria within the same latitudinal range in both AMT28 and 29, was probably related to iron and phosphate supplied by Saharan dust deposition in the region, and would lead to enhanced N_2-fixation rates (Smyth et al., 2017; Guerreiro et al., 2023, this issue). AOT data from AMT29 (Oct-Nov 2019) showed lower averaged values than AMT28 (Sep-Oct 2018) (Figure 2C). However, a broader latitudinal range of N_2-fixing *Trichodesmium* was observed in AMT29, in comparison to AMT28 (Figure 5). This may be related to the fact that dust deposition was occasionally slightly higher during AMT29 compared to AMT28, as indicated by *in-situ* measurements of Mn concentrations (pmol m-3) measured from dust samples collected *in situ* during the cruises (data not shown, personal commun. published)."

The effect of Saharan dust input of nutrients such as iron, promotes the growth of not only the filamentous Cyanobacteria, but also the diazotrophic diatom, *Hemiaulus hauckii* species (Nair et al., 2008), which was observed in this region, in both cruises (as well in AMT25, Brotas et al., 2022). Although the total biomass of nitrogen-fixing species did not attain high values (Figure 5), the ubiquitous presence of diazotrophic species in the North Atlantic gyre in response to dust deposition has been reported to contribute to an increase in carbon sequestration in the region (Pabortsava et al., 2017).

The increase of Autotrophic dinoflagellates carbon biomass in AMT29, in comparison to AMT28, can have two possible interpretations. It can be due to the natural community seasonal evolution, from an earlier stage, with diatoms dominating, to a later stage, with a higher abundance of dinoflagellates, as AMT29 was one month later than AMT28, or it could be an indicator of an effective shift in the community occurring independent of the seasonality. In fact, when we compare the overall median values of dinoflagellates in AMT25, AMT28 and AMT29 (which were 1.57, 5.66 and 8.04 mg Carbon m^{-3}, respectively), a trend in biomass increase appeared. Hence, this aspect should be investigated in future AMTs, as more data are needed to evaluate whether there is a consistent shift or not.

It should also be pointed out that we applied the distinction of Autotrophic and Heterotrophic, following Sal et al. (2013). However, dinoflagellates species can have a variety of trophic strategies; other authors, such as Barton et al. (2013), categorised as either mixotrophic or heterotrophic the dinoflagellates species observed in North Atlantic, implying that there are not pure autotrophic species. Also, the relevance of mixotrophic or predator protists in marine microbial cycles has been highlighted (Worden et al., 2015; Glibert and Mitra, 2022), specifying that dinoflagellates can be major grazers of diatoms.

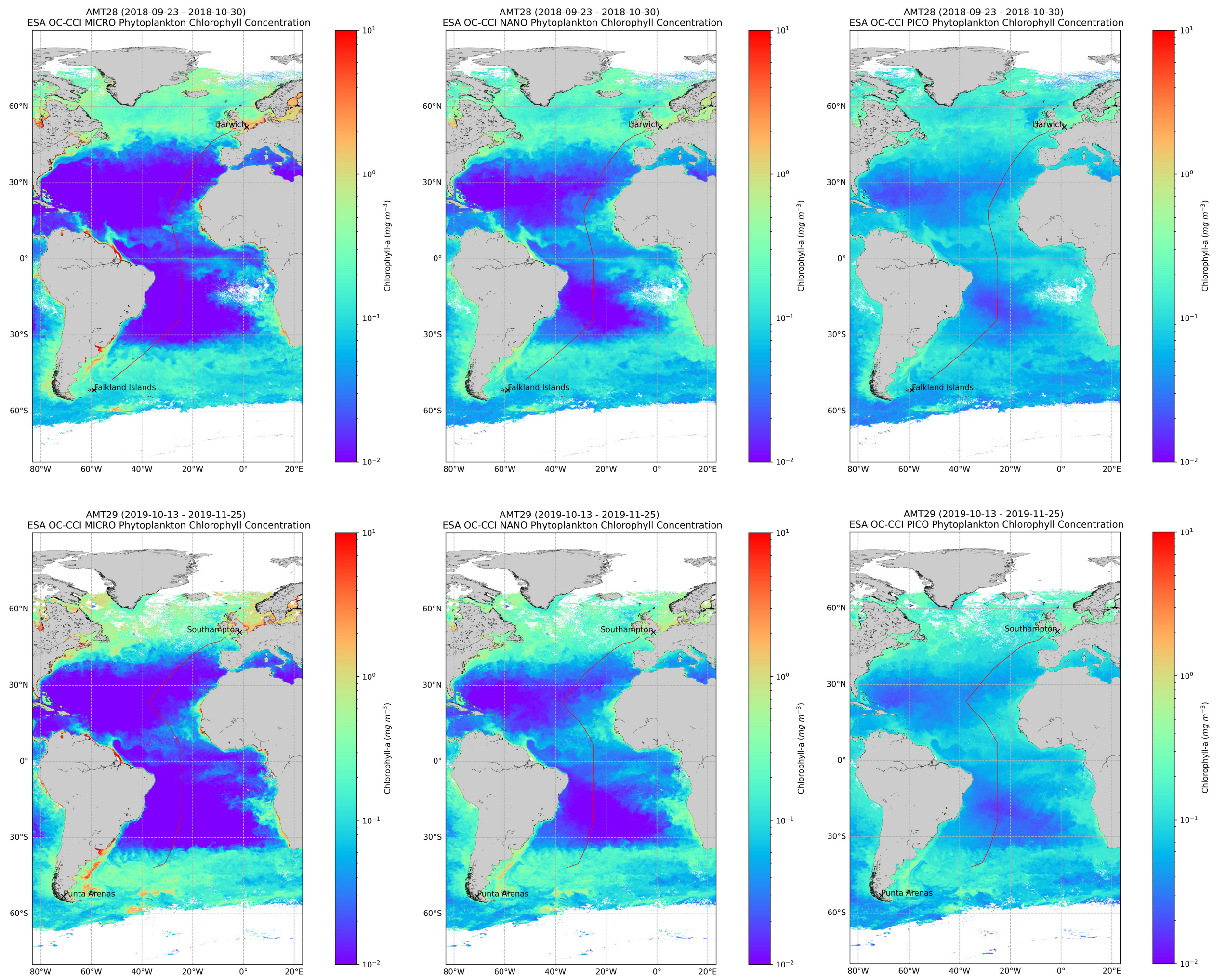

FIGURE 7

Concentration of phytoplankton size classes, obtained from OCCCI 1 km version 6, average for the cruise period. Composite image of Chla (mg m^{-3}) for each size class, for AMT28 (top) and AMT29 (bottom).

Coccolithophores span a wide range of ESD and can be observed in light microscopy, as well as counted in flow cytometry, but in the present work, we only considered the enumeration by flow cytometry. Therefore, the contribution of this group to the total biomass was underestimated. Coccolithophores constitute the functional type calcifiers which play a key role in biogeochemical cycles, presenting higher biomass in higher oceanic Northern and Southern latitudes (Le Quéré et al., 2005). The average contribution to total biomass was 2% and 1% for AMT28 and AMT29, respectively; whereas in our previous AMT25 work, where coccolithophores were enumerated both by Flow cytometer and light microscopy, the average was 3.6%, and it was estimated that at least 40% of the total coccolithophores carbon biomass was due to species with ESD > 10 µm (Brotas et al., 2022).

TABLE 3 Results of linear regression Type II in log-transformed data of satellite products (Brewin et al., 2017) and *in situ* carbon, in 31 match-ups for AMT28 and AMT29, for size classes Micro-, Nano- and Picoplankton and for the diatoms and dinoflagellates.

X - in situ	Y - satellite	RMSE	r^2	p-value
Micro Carbon (diatoms + dinoflagellates	Micro Sat	2.93	0.56	<0.001
Nano Carbon (COCOS, CRYPTO; NEUK)	Nano Sat	1.80	0.47	<0.001
Pico Carbon (*Prochloroccocus*, *Synechoccoccus*, PEUK)	Pico Sat	2.20	0.15	<0.05
Diatoms carbon	Diatoms Sat	1.84	0.50	<0.001
Dinoflagellates Carbon	Dinoflagellates Sat	3.54	0.41	<0.001

The taxonomic groups for each size class are indicated. RMSE, Root Mean Square Error.

TABLE 4 Species/Taxa which presented abundances > 10^4 cell L^{-1}, in the different Longhurst regions, in AMT 1, 3, 5, 7, 25, 28 and 29.

	NADR 56°N - 42°N	NAST 42°N - 30°N	NATR 30°N - 10°N	WTRA 10°N - 10°S	SATL 10°S - 27°S	SATL 27°S - 45°S	SSTC 45°S - 57°S
AMT_1	NS		*Gymnodinium galeaeforme* 5 ⊙ ▲ F	*Trichodesmium* 5 D		*Bacteriastrum* spp. 4 ▪ ● *Chaetoceros* spp. 4 ▪ ● ⊙ *Fragilariopsis* spp. 4 ◆ ● *Pseudo-nitzschia* spp. 4 ◆ ● E	NS
AMT_3	NS	Athecate Dinoflagellates 4 ⊙ C	*Bacteriastrum* spp. 4 ▪ ● B *Dactyliosolen phuketensis* 4 ▪ ⊙ ✚ *Guinardia striata* 5 ▪ ⊙ ✚ *Leptocylindrus* spp. 4 ▪ ● *Rhizosolenia chunii* 6 ▪ ⊙ ✚ *Rhizosolenia hebetata* 4 ▪ ⊙ ✚ Athecate Dinoflagellates 4 ⊙	Pennate group (10-30µm) 4 ◆ ⊙ C	Pennate group (10-40µm) 4 ◆ ⊙ Athecate Dinoflagellates 4 ⊙ C	Centric group (20µm) 4 ▪ ● *Chaetoceros* spp. 5 ▪ ● ⊙ *Fragilariopsis* spp. 5 ◆ ● Pennate group (10-40µm) 4 ◆ ⊙ E	NS
AMT_5	NS		*Cylindrotheca closterium* 4 ◆ ⊙ *Dactyliosolen phuketensis* 4 ▪ ⊙ ✚ *Leptocylindrus* spp. 4 ▪ ● *Pseudo-nitzschia* spp. 5 ◆ ● *Trichodesmium* 4. E			*Chaetoceros* spp. 4 ▪ ● ⊙ *Rhizosolenia* spp. 4 ▪ ⊙ ✚ E	NS
AMT_7	NS		*Leptocylindrus* spp. 4 ▪ ● *Pseudo-nitzschia* spp. 4 ◆ ● Athecate Dinoflagellates 4 ⊙ *Trichodesmium* 4 D	*Trichodesmium* 4 D		*Bacteriastrum* spp. 5 ▪ ● C Centric group (10µm) 4 ▪ *Cylindrotheca closterium* 4 ◆ ⊙ Pennate group (10-40µm) 4 ◆ ⊙ *Pseudo-nitzschia* spp. 4 ◆ ● Athecate Dinoflagellates 4 ⊙	NS
AMT_25	*Prorocentrum* A *cordatum* 6 ⊙		*Trichodesmium* 4. D	*Trichodesmium* 4. D			
AMT_28	Pennate group (10-40µm) 4 ◆ *Prorocentrum cordatum* 6 ⊙ A		*Trichodesmium* 4. D	*Trichodesmium* 4 D		Pennate group (40-80µm) 4 ◆ ⊙ ✚ Pennate group (> 80µm) 4 ◆ ⊙ ✚ F	Athecate Dinoflagellates 4 ⊙ *Scrippsiella* spp. 4 ⊙ ▲ C
AMT_29	Athecate C Dinoflagellates 4 ⊙			*Trichodesmium* 4 D			NS

The numbers 4, 5 and 6 indicate blooms higher than 10^4 cell L^{-1}, 10^5 cell L^{-1}, and 10^6 cell L^{-1}, respectively. The following categories were established: ▪ - Centric Diatom; ◆ - Pennate Diatom; ● - colonial species; ⊙ - single cells or short chain; ✚ - ≥ 17.5 µm Diatom; ▲ - ≥ 17.5 µm Dinoflagellate. Dinoflagellate species are in red, filamentous Cyanobacteria in blue, and diatoms in black. The letters identify the cluster groups of the SIMPROF analysis.
NS, no sampling.

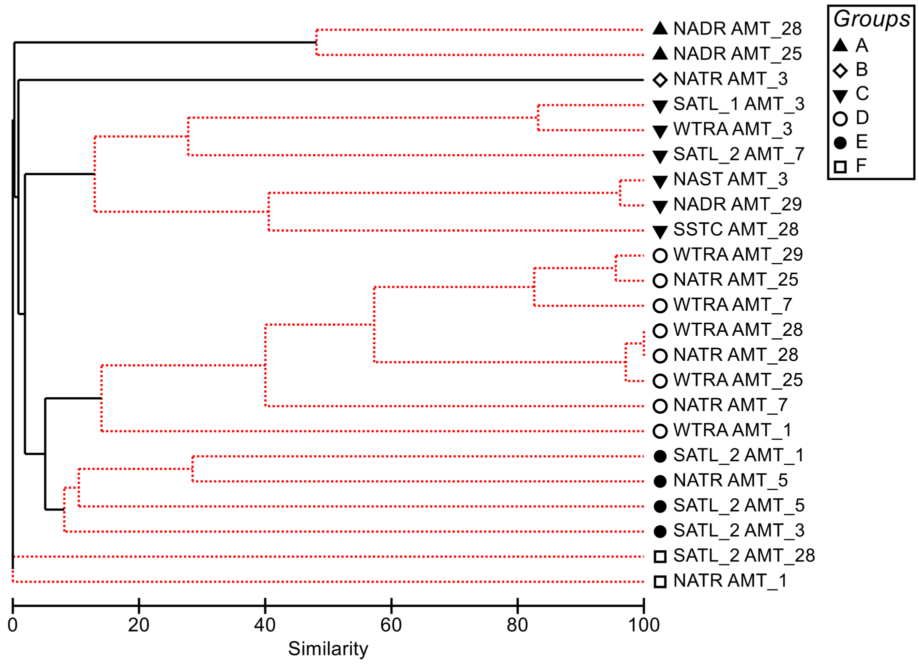

FIGURE 8

Dendrogram for hierarchical clustering of phytoplankton abundance samples using group-average linking of Bray–Curtis similarities. Only samples which presented abundances > 10^4 cell L^{-1}, in the different Longhurst regions were included and data. Red dotted lines indicate nonsignificant clustering (SIMPROF test; significance level: P < 5%).

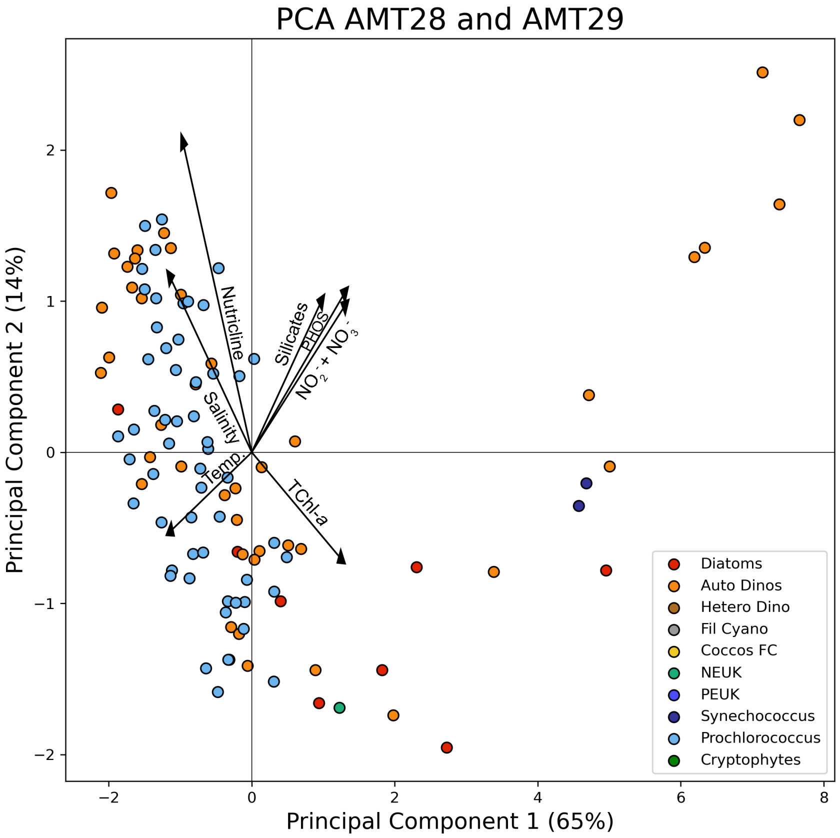

FIGURE 9

Principal Component Analysis performed on the phytoplankton taxonomic over the environmental data. The colour code represents the dominant phytoplankton taxon by carbon biomass.

A detailed study on the coccolithophores community in AMT28 Northern Hemisphere is presented by Guerreiro et al. (2023, this issue), where the maximum cell number (3.5 x 10^4 cells L^{-1}) was observed in NADR.

Complementary approaches between satellite and situ

The correspondence of size classes based on pigment chemotaxonomy and taxonomic groups may have flaws and uncertainties, however, as pointed out by Aiken et al. (2008), in spite of the reductionist approach of PSC, biological oceanography has shown that phytoplankton size classes are aligned with the environmental niches they live in, justifying the retrieval of PSC from Earth Observation. Also, the relationship between size classes and functional types using concentration of diagnostic pigments has been considered at a global scale (Hirata et al., 2011), aiming at establishing links which would allow the identification of PFTs from space, and these findings have been widely used by the ocean-colour community (Sun et al., 2023; Xi et al., 2023, amongst others). Moreover, as pointed out by Sathyendranath et al. (2020), the estimation of phytoplankton carbon size structure is crucial for our understanding of phytoplankton dynamics, but there is a lack of information regarding phytoplankton carbon content which should be addressed by the scientific community. The comparison of *in situ* PSC with cell enumeration expressed as carbon biomass had already been addressed for AMT25 in Brotas et al. (2022), who found a good agreement between both methodological approaches, although with an overestimation of the chemotaxonomic method regarding the nanoplankton fraction. In this work, to our knowledge for the first time, the comparison of *in situ* carbon measurements with satellite estimation of size classes was investigated. The validation of EO products is performed with fiducial ground truth measurements, which are limited by the cloud cover conditions. For our study, a limited number of matchups was available (31), nevertheless, the correlations obtained between the *in situ* carbon biomass and the satellite products derived from Brewin et al. (2017) model were significant, including the differentiation, within the microplankton fraction, of diatoms and dinoflagellates. It should be noted that the dinoflagellates satellite product relies on the assumption that peridinin is the diagnostic pigment for this taxonomic class, and although peridinin is only present in dinoflagellate species, not all species have this pigment.

The global warming effect on oceanic phytoplankton biomass will affect bloom phenology (Kahru et al., 2011; Racault et al., 2014, amongst others), likely with cascade effects on the trophic chain; moreover, warming is expected (Doney, 2006) to enhance stratification of the surface water layer, thus probably causing a reduction in cell growth in tropical latitudes (due to nutrient limitation) and an increase of biomass in higher latitudes, due to a shallower MLD, thus reducing light limitation (Doney, 2006; Cermeño et al., 2008). In order to properly evaluate global biomass trends in response to climate change, long-term, synoptic scale observations are crucial. For example, using the EO OCCCI Chl*a* product, Sathyendranath et al. (2019b) reported a global Chl*a* analysis showing an increasing trend in high latitudes and a decreasing trend in tropical areas.

Previous literature dealing with AMT, such as Racault et al. (2014), showed that Chl*a* concentration assessed by remote sensing did not change during the period 2003-2010, but a shift in the relative proportion of the three size classes was detected when chemotaxonomic *in situ* data was used, showing the relevance of using complementarity between EO and *in situ* approaches. Focusing only on the *in situ* data of the same period, Agirbas et al. (2015) concluded that microplankton fraction decreased in North Atlantic Tropical Gyre and SATL, with a counterbalanced increase of picoplankton fraction. Our results also showed that an increase in picoplankton fraction in SATL can be spotted, from 36% (AMT25), 50% (AMT28) and 59% (AMT29), compensated by a decrease in nano- and microplankton fractions. The average Chl*a* values for the three size classes assessed by satellite imagery for AMT28 and 29 cruises evidenced a widespread picoplankton community in all regions (Figure 7), whereas the abundance of nano- and microplankton fractions is strongly dependent on the nutrient availability, as demonstrated also by the PCA results.

Comparative analysis of occurring blooms over 25 years

Variability of phytoplankton species is an inherent and well-known characteristic of marine ecosystems, however assessing phytoplankton variability patterns and the way communities respond to changes, in terms of shift between taxa, cell size, or trophic strategy, is still a challenging research subject. As pointed out by Behrenfeld and Boss (2014), factors controlling phytoplankton blooms remain controversial despite a century of investigation.

The spatial and in-depth distribution of small cells belonging to nano- and picoplankton was characterised in previous AMTs (Tarran et al., 2006) and discussed in Phongphattarawat et al. (2023, this issue). Hence, our study is focused on microplanktonic species counted by microscopy, namely diatoms, dinoflagellates and filamentous Cyanobacteria. The comparison was focused on earlier boreal AMT cruises (1995-1998) and recent ones, namely 2015 (Brotas et al., 2022) and the cruises studied in this work, AMT28 and AMT29, thus encompassing a 25-year period.

Overall, results showed that blooms were mainly produced by diatom species, and that blooms of 10^5 or 10^6 cells L^{-1} were only observed in earlier AMTs, suggesting conditions which would favour diversity. In fact, from the total of 20 diatom species producing a bloom identified for the seven AMT cruises, only three taxa were observed in the recent ones (2015-2019), belonging to the pennate-colonial species type, (hence, constituting as well a decrease in shape diversity in relation to the earlier AMT cruises species).

The higher diversity in diatom bloom-forming species, namely in the NATR and SATL regions (up to 6 different species) registered in earlier AMTs might be due to the difference in in cruise tracks (from coastal in early years to more oceanic recently), however, the hypothesis of a decrease in the number and diversity of diatoms should be investigated in future studies. Regarding dinoflagellates, the blooms observed for *Prorocentrum cordatum*, constituting more than 90% of the total carbon biomass (Figure 4), occurred only in recent cruises (AMT25 and AMT28). This finding is in agreement with Khanaychenko et al. (2019), who stated that the toxic species *Prorocentrum cordatum* has been reported to become more widespread in recent years; hence these results constitute an alert for future studies in the English Channel.

Concerning filamentous Cyanobacteria, the abundances of *Trichodesmium* spp seem to be remarkably similar. The maxima values of *Trichodesmium* spp were 960 filaments in AMT 28 (11.45°N; -27.71°W), and 720 in AMT29 (11.85°N, 27.96°W). Tyrrell et al. (2003), in AMTs 1,3, 5 and 7 reported high filament abundances in the region between 0° and ~15°N, with a maximum value of 1040 filaments of *Trichodesmium* spp. for AMT 5. In AMT25, Brotas et al. (2022), reported a maximum of 700 filaments, and the presence of filamentous Cyanobacteria from 23°N to 2°N. Hence, not only the presence but also the abundance levels of filamentous Cyanobacteria seem to be a common feature in this area, as shown in this work, as well as in the earlier Boreal Autumn AMTs (1, 3, 5, and 7) and AMT25.

Conclusions

This work provides observations on the abundance and diversity of phytoplankton taxa on a gradient of trophic conditions in the North and South Atlantic. Our data contribute to the main goal of the AMT program, regarding the regular and long-term acquisition of a series of observations, crucial to understand the response of biological communities to ongoing climate change, whilst providing data for the development and testing of more accurate prediction models for future climatic scenarios.

The results obtained showed a common pattern from both cruises of phytoplankton biomass distribution and relative dominance of groups, across the Atlantic: the biomass values for the different biogeographic oceanic provinces were similar in both cruises, and comparable to those found in AMT25. Interannual major differences were found in high latitudes, where blooms of diatoms and dinoflagellates appeared.

This work explored complementary approaches to study phytoplankton size classes, namely *in situ* determination of size classes by chemotaxonomy, *in situ* enumeration of cell abundance of all taxonomic groups, and remote sensing of the relative contribution of the three size classes to Chl*a*. We found a good relationship between satellite determination of phytoplankton size classes with *in situ* size classes estimated as carbon biomass, albeit with a relatively small number of available matchups.

An increase in the picoplankton fraction was detected in southern Atlantic, along AMT25, 28 and 29, consistent with earlier reports (Racault et al., 2014; Agirbas et al., 2015).

In spite of the differences in route tracks between the different AMTs, the analysis of the more abundant microplankton species of diatoms, dinoflagellates and filamentous Cyanobacteria between AMT cruises from the 1990s and more recent expeditions, highlights key observations, which might be considered for future studies, namely i) *Trichodesmium* blooms are a common feature in earlier and recent AMTs, with remarkably similar abundance values, ii) the small Athecate Dinoflagellate category is also a common taxa throughout the different AMTs, iii) there is a possible indication for a shift in most abundant diatom species, as their blooms have clearly decreased, including in Southern SATL, where the nutrient concentrations are high, iv) the *Prorocentrum cordatum* dinoflagellate blooms in recent cruises may be in line with the widespread of toxic species.

Additionally, we produced a database of cell carbon content per species, and its abundance in the sampled Atlantic regions, extending the database from the late 1990s, published by Sal et al. (2013), leaving a record for future research on biodiversity.

Data availability statement

The original contributions presented in the study are included in the article/Supplementary Material. Further inquiries can be directed to the corresponding author.

Author contributions

All authors contributed to the conceptual development of the paper. Authors contributed differently to the following aspects: cruise participation (GT, AT, AF), HPLC pigment analysis (AT), microscope identification and enumeration (VV), flow cytometry analysis (GT), satellite imagery (SG, DC, JN) nutrient analysis (EW), figures and statistics (AF, LR, CG), English correction (SG). All authors contributed to manuscript revision, read, and approved the submitted version.

Funding

The Atlantic Meridional Transect is funded by the UK Natural Environment Research Council through its National Capability Long-term Single Centre Science Programme, Climate Linked Atlantic Sector Science (grant number NE/R015953/1). This study contributes to the international IMBeR project and is contribution number 393 of the AMT programme. This work received funding from the European Union's Horizon 2020 research and innovation programme under grant agreement n° 810139 Project Portugal Twinning for Innovation and Excellence in Marine Science and Earth Observation – PORTWIMS", and Interreg project Innovation in the Framework of the Atlantic Deep Ocean (iFADO). This study had the support of FCT through the strategic project UIDB/04292/2020 awarded to MARE and through project LA/P/0069/2020 granted to the Associate Laboratory ARNET. CG benefited from a Marie Sklodowska-Curie European Fellowship supported by the EU H2020-MSCA-IF-2017 (grant no. 796802) linked to project DUSTCO, and currently benefits from a research grant funded by FCT (contract CEECIND/00752/ 2018/CP1534/CT0011) linked to project CHASE (www.chase-dust.com). CG currently benefits from a research grant funded by FCT (contract CEECIND/00752/ 2018/ CP1534/CT0011) linked to project CHASE (www.chase-dust.com). AT benefited a grant from European Union's (EU) Horizon 2020 CERTO (Copernicus Evolution: Research for harmonised Transitional water Observation) project (No. 870349).

Acknowledgments

We thank the officers and crew of the British Antarctic Survey vessel RRS James Clark Ross and RRS Discovery. We are indebted to NEODAAS for processing the satellite imagery. We thank Carolina Sá and Giulia Sent for their help in AMT29. We thank the three reviewers for valuable suggestions.

Conflict of interest

The authors declare that the research was conducted in the absence of any commercial or financial relationships that could be construed as a potential conflict of interest.

Publisher's note

Supplementary material

The Supplementary Material for this article can be found online at: https://www.frontiersin.org/articles/10.3389/fmars.2023.1229692/full#supplementary-material

SUPPLEMENTARY TABLE 1
Supplementary material. List of species found in AMT28 and AMT29, with AphiaID from Worms (site), the cell biovolume (μm^3) and cell carbon content (pg Carbon Cell^{-1}).

SUPPLEMENTARY TABLE 2
Supplementary material. Species abundances, in mg Carbon m^{-3} for AMT28.

SUPPLEMENTARY TABLE 3
Supplementary material. Species abundances, in mg Carbon m^{-3} for AMT29.

References

Agirbas, E., Martinez-Vincente, V., Brewin, R. J. W., Racault, M. F., Airs, R. L., and Llewellyn, C. A. (2015). Temporal changes in total and size-fractioned chlorophyll-a in surface waters of three provinces in the Atlantic Ocean (September to November) between 2003 and 2010. *J. Mar. Syst.* 150, 56–65. doi: 10.1016/j.jmarsys.2015.05.008

Aiken, J., Brewin, R. J. W., Dufois, F., Polimene, L., Hardman-Mountford, N. J., Jackson, T., et al. (2017). A synthesis of the environmental response of the North and South Atlantic Sub-Tropical Gyres during two decades of AMT. *Prog. Oceanography* 158, 236–254. doi: 10.1016/j.pocean.2016.08.004

Barton, A. D., Finkel, Z. V., Ward, B. A., Johns, D. G. J., and Follows, M. J. (2013). On the roles of cell size and trophic strategy in North Atlantic diatom and dinoflagellate communities Limnol. *Oceanogr.* 58, (1) 254–266. doi: 10.4319/lo.2013.58.1.0254

Becker, S., Aoyama, M., Woodward, E. M. S., Bakker, K., Coverly, S., Mahaffey, C., et al. (2020). GO-SHIP repeat hydrography nutrient manual: the precise and accurate determination of dissolved inorganic nutrients in seawater, using continuous flow analysis methods. *Front. Mar. Sci.* 7. doi: 10.3389/fmars.2020.581790

Behrenfeld, M. J., and Boss, E. S. (2014). Resurrecting the ecological underpinnings of ocean plankton blooms. *Annu. Rev. Mar. Sci.* 6, 1, 167–194. doi: 10.1146/annurev-marine-052913-021325

Bracher, A., Bouman, H., Brewin, R. J. W., Bricaud, A., Brotas, V., Ciotti, A. M., et al. (2017). Obtaining phytoplankton diversity from ocean color: A scientific roadmap for future development. *Front. Mar. Sci.* 4. doi: 10.3389/fmars.2017.00055

Bray, J. R., and Curtis, J. T. (1957). An ordination of the upland forest communities of Southern Wisconsin. *Ecol. Monogr.* 27, 326–349.

Brewer, P. G., and Riley, J. P. (1965). The automatic determination of nitrate in seawater. *Deep Sea Res.* 12, 765–772. doi: 10.1016/0011-7471(65)90797-7

Brewin, R. J. W., Ciavatta, S., Sathyendranth, S., Jackson, T., Tilstone, G., Curran, K., et al. (2017). Uncertainty in ocean-colour estimates of chlorophyll for phytoplankton groups. *Front. Mar. Sci.* 4, 104. doi: 10.3389/fmars.2017.00104

Brewin, R. J. W., Hirata, T., Hardman-Mountford, N. J., Lavender, S. J., Sathyendranath, S., and Barlow, S. R. (2012). The influence of the Indian Ocean Dipole on interannual variations in phytoplankton size structure as revealed by Earth Observation. *Deep Sea Res. Part II: Topical Stud. Oceanography* 77–80, 117–127. doi: 10.1016/j.dsr2.2012.04.009

Brewin, R. J.W., Sathyendranath, S., Hirata, T., Lavender, S., Barciela, R. M., and Hardman-Mountford, N. J. (2010). A three-component model of phytoplankton size class for the Atlantic Ocean. *Ecol. Model.*, 1472–1483. doi: 10.1016/j.ecolmodel.2010. 02.014

Brotas, V., Tarran, G., Veloso, V., Brewin, R. J. W., Woodward, E. M. S., Airs, R., et al. (2022). Complementary approaches to assess phytoplankton groups and size classes on a long transect in the Atlantic Ocean. *Front. Mar. Sci.* 11. doi: 10.3389/fmars.2021.682621

Brotas, V., and Veloso, V. (2022). Phytoplankton species counts from Atlantic Ocean surface water samples collected during JR15001 (AMT25) in September-November 2015. *NERC EDS Br. Oceanographic Data Centre NOC.* doi: 10.5285/eb752e17-cd14-3889-e053-6c86abc0ec59

Buitenhuis, E. T., Vogt, M., Moriarty, R., Bednarsek, N., Doney, S. C., Leblanc, K., et al. (2013). MAREDAT: towards a world atlas of MARine Ecosystem DATa. *Earth Syst. Sci. Data* 5, 227–239. doi: 10.5194/essd-5-227-2013

Cermeño, P., Dutkiewicz, S., Harris, R. P., Follows, M., Schofield, O., and Falkowski, P. G. (2008). The role of nutricile depth in regulating the ocean carbon cycle. *PNAS* 105, (51). doi: 10.1073/pnas.0811302106

Clarke, K. R. (1993). Non-parametric multivariate analyses of changes in community structure. *Aust. J. Ecol.* 18, 117–143. doi: 10.1111/j.1442-9993.1993.tb00438.x

Clarke, K. R., Somerfield, P. J., and Gorley, R. N. (2008). Testing of null hypotheses in exploratory community analyses: similarity profiles and biota-environment linkage. *J. Exp. Mar. Biol. Ecol.* 366, 56–69. doi: 10.1016/j.jembe.2008.07.009

Doney, S. C. (2006). Plankton in a warmer world. *Nature* 444 (7120), 695–696. doi: 10.1038/444695a

Field, C. B., Behrenfeld, M. J., Randerson, J. T., and Falkowski, P. (1998). Primary production of the biosphere: integrating terrestrial and oceanic components. *Science* 281 (5374), 237–240. doi: 10.1126/science.281.5374.237

Field, J. G., Clarke, K. R., and Warwick, R. M. (1982). A practical strategy for analysing multispecies distribution patterns. *Mar. Ecol. Prog. Ser.* 8, 37–52.

Glibert, P. M., and Mitra, A. (2022). From webs, loops, shunts, and pumps to microbial multitasking: Evolving concepts of marine microbial ecology, the mixoplankton paradigm, and implications for a future ocean. *Limnol. Oceanogr.* 67, 585–597. doi: 10.1002/lno.12018

Good, S., Fiedler, E., Mao, C., Martin, M. J., Maycock, A., Reid, R., et al. (2020). The current configuration of the OSTIA system for operational production of foundation sea surface temperature and ice concentration analyses. *Remote Sens.* 12, 720. doi: 10.3390/rs12040720

Grasshoff, K. (1976). *Methods of Sea-water Analysis* (Weiheim: Verlag Chemie), 317.

Guerreiro, C. V., Ferreira, A., Cros, L., Stuut, J.-B., Baker, A. R., Tracana, A., et al. (2023). Response of coccolithophore communities to oceanographic and atmospheric processes across the North- and Equatorial Atlantic. *Front. Mar. Sci.* 10. doi: 10.3389/fmars.2023.1119488

Hirata, T., Hardman-Mountford, N. J., Brewin, R. J. W., Aiken, J., Barlow, R., Suzuki, K., et al. (2011). Synoptic relationships between surface Chlorophyll-a and diagnostic pigments specific to phytoplankton functional types. *Biogeosciences* 8, 311–327. doi: 10.5194/bg-8-311-2011

IOCCG (2014). “Phytoplankton functional types from space,” in *Reports of the International Ocean Color Coordinating Group No. 15*. Eds. S. Sathyendranath and V. Stuart (Dartmouth, NS: IOCCG).

Kahru, M., Brotas, V., Manzano-Sarabia, M., and Mitchell, B. G. (2011). Are phytoplankton blooms occurring earlier in the Arctic? *Global Change Biol.* 17 (4), 1733–1739. doi: 10.1111/j.1365-2486.2010.02312.x

Khanaychenko, A. N., Skarlato, S. O., and Telesh, I. (2019). Bloom-forming potentially toxic dinoflagellates Prorocentrum cordatum in marine plankton food webs. *Protistology* 13 (3), 95–125. doi: 10.21685/1680-0826-2019-13-3-1

Kirkwood, D. S. (1989). Simultaneous determination of selected nutrients in seawater, ICES CM 1989/C:29.

Le Quéré, C., Harrison, S. P., Prentice, I. C., Buitenhuis, E. T., Aumont, O., Bopp, L., et al. (2005). Ecosystem dynamics based on plankton functional types for global ocean biogeochemistry models. *Global Change Biol.* 11, 2016–2040. doi: 10.1111/j.1365-2486.2005.1004.x

Menden-Deuer, S., and Lessard, E. J. (2000). Carbon to volume relationships for dinoflagellates, diatoms, and other protist plankton. *Limnol. Oceanogr*. 45 (3), 569–579. doi: 10.4319/lo.2000.45.3.0569

Mendes, C. R., Cartaxana, P., and Brotas, V. (2007). HPLC determination of microalgae pigments: comparing resolution and sensitivity of a C18 and a C8 method. *Limnol. Oceanog.* 5, 363–370. doi: 10.4319/lom.2007.5.363

Moore, C. M., Mills, M. M., Achterberg, E. P., Geider, R. J., La Roche, J., Lucas, M. I., et al. (2009). Large-scale distribution of Atlantic nitrogen fixation controlled by iron availability. *Nat. Geosci.* 2 (12), 867–871. doi: 10.1038/NGEO667

Nair, A., Sathyendranath, S., Platt, T., Morales, J., Stuart, V., Forget, M.-H., Devred, E., et al (2008). Remote sensing of phytoplankton functional types. Remote Sens. *Environ.* 112, 3366–3375.

Pabortsava, K., Lampitt, R., Benson, J., Crowe, C., McLachlan, R., Le Moigne, F. A. C., et al. (2017). Carbon sequestration in the deep Atlantic enhanced by Saharan dust. *Nat. Geosciences* 10 (3), 189–194. doi: 10.1038/ngeo2899

Pedregosa, F., Varoquaux, G., Gramfort, A., Michel, V., Thirion, B., Grisel, O., et al. (2011). Scikit-learn: machine learning in python. *J. Mach. Learn. Res.* 12, 2825–2830.

Phongphattarawat, S., Bouman, H. A., Lomas, M. W., Sathyendranath, S., Tarran, G. A., Ulloa, O., et al. (2023). Ecophysiological basis of spatiotemporal patterns in picophytoplankton pigments in the global ocean. *Front. Mar. Sci*. doi: 10.3389/fmars.2023.1112177

Poulton, A. J., Holligan, P. M., Charalampopoulou, A., and Adey, T. R. (2017). Coccolithophore ecology in the tropical and subtropical Atlantic Ocean: New perspectives from the Atlantic meridional transect (AMT). *Prog. Oceanography* 158, 150–170. doi: 10.1016/j.pocean.2017.01.003

Racault, M-F., Platt, T., Sathyendranath, S., Agirbas, E., Martinez Vicente, V., and Brewin, R. J. W. (2014). Plankton indicators and ocean observing systems: support to the marine ecosystem state assessment. *J. Plankton Res.* 36 (3), 621–629. doi: 10.1093/plankt/fbu016

Rees, A. P., Nightingale, P. D., Poulton, A. J., Smyth, T. J., Tarran, G. A., and Tilstone, G. H. (2017). The atlantic meridional transect programme, (1995-2016). *Prog. Oceanography* 158, 3–18. doi: 10.1016/j.pocean.2017.05.004

Reynolds, C. (2006). *Ecology of Phytoplankton* (Cambridge: Cambridge University Press).

Reynolds, C. S., Huszar, V., Kruk, C., Naselli-Flores, L., and Melo, S. (2002). Towards a functional classification of the freshwater phytoplankton. *J. Plankton Res.* 24, 417–428. doi: 10.1093/plankt/24.5.417

Sal, S., López-Urrutia, Á., Irigoien, X., Harbour, D. S., and Harris, R. P. (2013). Marine microplankton diversity database. *Ecology* 94 (7), 1658. doi: 10.1890/13-0236.1

Sathyendranath, S., Brewin, R.J.W., Brockmann, C., Brotas, V., Calton, B., Chuprin, A., et al. (2019a). An ocean-colour time series for use in climate studies: the experience of the ocean-colour climate change initiative (OC-CCI). *Sensors* 19 (19), 4285. doi: 10.3390/s19194285

Sathyendranath, S., Pardo, S., Benincasa, M., Brando, V., Brewin, R. J.W., Mélin, F., et al. (2019b). Copernicus marine service ocean state report. *J. Operational Oceanography* 11 (sup1), S1–S142. doi: 10.1080/1755876X.2018.1489208

Sathyendranath, S., Platt, T., Kovač, Ž., Dingle, J., Jackson, T., Brewin, R. J. W., et al. (2020). Reconciling models of primary production and photoacclimation. *Appl. Opt* 59, C100–C114. doi: 10.1364/AO.386252

Sieburth, J. M., Smetacek, V., and Lenz, J. (1978). Pelagic ecosystem structure: heterotrophic compartments of the plankton and their relationship to plankton size fractions. *Limnol Oceanogr* 23, 1256–1263.

Smyth, T., Quartly, G., Jackson, T., Tarran, G., Woodward, M., Harris, C., et al. (2017). Determining Atlantic Ocean province contrasts and variations. *Prog. Oceanography* 158, 19–40. doi: 10.1016/j.pocean.2016.12.004

Sun, X., Brewin, R. J. W., Sathyendranath, S., Dall’Olmo, G., Airs, R., Barlow, R., et al. (2023). Coupling ecological concepts with an ocean-colour model: Phytoplankton size structure. *Remote Sens. Environ.* 285, 113415. doi: 10.1016/j.rse.2022.113415

Tarran, G. A., Heywood, J. L., and Zubkov, M. V. (2006). Latitudinal changes in the standing stocks of nano- and picoeukaryotic phytoplankton in the Atlantic Ocean. *Deep-Sea Res. Part II: Topical Stud. Oceanography* 53, 1516–1529. doi: 10.1016/j.dsr2.2006.05.004

Tarran, G. A., Zubkov, M. V., Sleigh, M. A., Burkill, P. H., and Yallop, M. (2001). Microbial community structure and standing stocks in the NE Atlantic in June and July of 1996. *Deep-Sea Res. Part II: Topical Stud. Oceanography* 48 (4–5), 963–985. doi: 10.1016/s0967-0645(00)00104-1

Tyrrell, T., Maranon, E., Poulton, A. J., Bowie, A. R., Harbour, D. S., and Woodward, E. M. S. (2003). Large-scale latitudinal distribution of Trichodesmium spp. *Atlantic Ocean. J. Plankton Res.* 25, 405–416. doi: 10.1093/plankt/25.4.405

Uitz, J., Claustre, H., Morel, A., and Hooker, S. B. (2006). Vertical distribution of phytoplankton communities in open ocean: An assessment based on surface chlorophyll. *J. Geophysical Res.* 111, CO8005. doi: 10.1029/2005jc003207

Utermöhl, H. (1958). Zur Vervolkommung der quantitativen Phytoplankton: methodik. Mitteilungen Internationale Vereinigung f̈r Theoretische und Angewandte. *Limnologie* 9, 1–39.

Vidussi, F., Claustre, H., Manca, B. B., Luchetta, A., and Marty, J. (2001). Phytoplankton pigment distribution in relation to upper thermocline in the eastern Mediterranean Sea during winter. *J. Geophysical Res.* 106, 19939–19956. doi: 10.1029/1999JC000308

Worden, A. Z., Follows, M. J., Giovannoni, S. J., Wilken, S., Zimmerman, A. E., and Keeling, P. J. (2015). Environmental science. Rethinking the marine carbon cycle: factoring in the multifarious lifestyles of microbes. *Science* 347 (6223), 1257594. doi: 10.1126/science.1257594

Xi, H., Bretagnon, M., Losa, S. N., Brotas, V., Gomes, M., Peeken, I., et al. (2023). Satellite monitoring of surface phytoplankton functional types in the Atlantic Ocean over 20 years (2002–2021). *State Planet* 1-osr7, 5. doi: 10.5194/sp-1-osr7-5-2023

Zapata, M., Rodriguez, F., and Garrido, J. L. (2000). Separation of chlorophylls and carotenoids from marine phytoplankton: a new HPLC method using a reversed phase C8 column and pyridine-containing mobile phases. *Mar. Ecol. Prog. Ser.* 195, 29–45. doi: 10.3354/meps195029

Frontiers in Marine Science

TYPE Original Research
PUBLISHED 29 November 2023
DOI 10.3389/fmars.2023.1197753

EDITED BY
Vanda Brotas,
University of Lisbon, Portugal

REVIEWED BY
Rajani Kanta Mishra,
Ministry of Earth Sciences, India
John T. Bruun,
University of Exeter, United Kingdom
Emmanuel Boss,
University of Maine, United States

*CORRESPONDENCE
Graham D. Quartly
✉ gqu@pml.ac.uk

RECEIVED 31 March 2023
ACCEPTED 06 November 2023
PUBLISHED 29 November 2023

CITATION
Quartly GD, Aiken J, Brewin RJW and Yool A (2023) The link between surface and sub-surface chlorophyll-a in the centre of the Atlantic subtropical gyres: a comparison of observations and models. *Front. Mar. Sci.* 10:1197753.
doi: 10.3389/fmars.2023.1197753

The link between surface and sub-surface chlorophyll-a in the centre of the Atlantic subtropical gyres: a comparison of observations and models

Graham D. Quartly[1]*, Jim Aiken[1], Robert J. W. Brewin[2] and Andrew Yool[3]

[1]Plymouth Marine Laboratory, Plymouth, United Kingdom, [2]Centre for Geography and Environmental Science, University of Exeter, Penryn, United Kingdom, [3]Marine Systems Modelling, National Oceanography Centre, Southampton, United Kingdom

Satellite observations have given us a clear idea of the changes in chlorophyll in the surface ocean on both a seasonal and interannual basis, but repeated observations at depth are much rarer. The permanently-stratified subtropical gyres in the Atlantic are highly oligotrophic, with most production centred on a deep chlorophyll maximum (DCM) just above the nitracline. This study explores the variations in this feature in the core of both gyres, considering both seasonal and interannual variations, and the linkages between changes at the surface and sub-surface. The *in situ* observations come from the Atlantic Meridional Transect (AMT), a long-running UK monitoring programme, and also from biogeochemical Argo floats. AMT provides measurements spanning more than 25 years directed through the centres of these gyres, but samples only 2 to 4 months per year and thus cannot resolve the seasonal variations, whereas the profiling floats give coverage throughout the year, but without the rigid spatial repeatability. These observational records are contrasted with representation of the centres of the gyres in two different biogeochemical models: MEDUSA and ERSEM, thus fulfilling one of AMT's stated aims: the assessment of biogeochemical models. Whilst the four datasets show broadly the same seasonal patterns and that the DCM shallows when surface chlorophyll increases, the depth and peak concentration of the DCM differ among datasets. For most of the datasets the column-integrated chlorophyll for both gyres is around 19 mg m^{-2} (with the AMT fluorescence-derived values being much lower); however the MEDUSA model has a disparity between the northern and southern gyres that is not understood. Although the seasonal increase in surface chlorophyll is tied to a commensurate decrease in concentration at depth, on an interannual basis years with enhanced surface levels of chlorophyll correspond to increases at depth. Satellite-derived observations of surface chlorophyll concentration act as a good predictor of interannual changes in DCM depth for both gyres during their autumn season, but provide less skill in spring.

KEYWORDS

chlorophyll, subtropical gyre, Atlantic Meridional Transect, BGC-Argo, deep chlorophyll maximum, seasonal, interannual, model validation

1 Introduction

The patterns of ocean productivity are set by physical processes and chemical resources. The Earth's orbit around the sun and thus the changing solar zenith angle produces an annual cycle in the main forcing terms: solar irradiance (SI) incorporating both photosynthetically available radiation (PAR) and the infra-red components that raise sea surface temperature (SST), increase stratification and, as shown by Levitus (1982), lead to a shallowing of the mixed layer depth (MLD). There is, of course, a daily cycle of heating and night-time cooling, with the latter creating convectional mixing at the top of the water column that disperses those plankton that exist there throughout a seasonal mixed layer. Whilst coastal and well-mixed high-latitude seas have a plentiful nutrient supply, large regions in the tropics are permanently stratified leading to nutrient depletion in the surface waters. This unique environment, controlled by both growth and loss (grazing) processes, leads to low surface concentrations of phytoplankton, with a vertical profile marked by a deep chlorophyll-a maximum (DCM). In this region light levels are very low (typically of order ~1% of that at the surface), but there is sufficient supply of the essential nutrients from a reservoir below. Since growth rates of phytoplankton are fast (doubling time of the order of 1 day), these population profiles must usually be considered as in a quasi-steady state, balancing predation and other loss terms against individuals' reproduction, noting that the conditions of light and nutrients at the DCM are able to support a larger standing stock of phytoplankton.

Within the Atlantic there are two main oligotrophic regions corresponding to the centres of the northern subtropical gyre (NSTG) and the southern subtropical gyre (SSTG). Each of these gyres occupies about 5% of the Earth's surface (Aiken et al., 2017), and although low in surface chlorophyll-a they are an important area for research as they may contribute significantly to carbon drawdown. Furthermore, several climate change predictions suggest greater stratification for larger areas of the Earth's subtropical ocean, so those ecological implications need to be assessed. This study examines the seasonal and interannual variations in the DCM within these gyres, taking particular advantage of the Atlantic Meridional Transect (AMT) programme, which has provided *in situ* measurements spanning more than two decades. Our goal is in line with a core aim of AMT to provide essential data for global ecosystem model development and validations (Rees et al., 2015). As the timing of these cruises has been tied to the resupply of the UK's Antarctic bases e.g. Rothera, the cruises have mainly been in September/October to November and in April to May/June (see Figure 1). As the dynamics of the NSTG and SSTG may be somewhat different, we keep the analyses for these two regions separate and are thus considering four seasonal "modes":

- Boreal spring (northward leg through NSTG) when PAR and SST are increasing
- Austral autumn (northward leg through SSTG) when PAR and SST are declining
- Boreal autumn (southward leg through NSTG) when PAR and SST are declining
- Austral spring (southward leg through SSTG) when PAR and SST are increasing

These analyses are augmented by profiles from biogeochemical (BGC) Argo floats, which do not provide spatially homogeneous coverage, but allow us to look more clearly at seasonal variations. Additionally we look at output from two numerical biological models to assess how well they replicate the seasonal changes in the DCM, and whether they can give us insight into the causal connections between changes in surface and sub-surface properties.

The aim of this paper is to look at the connectivity between surface manifestations of chlorophyll and the developments at the deep chlorophyll maximum, using both *in situ* and model data. Surface chlorophyll affects distribution below, as it modifies the light penetration at depth. There are clear seasonal variations, because of the annual cycles in forcing, but the challenge is whether sub-surface interannual variations can be inferred from observing the surface only.

2 Data

In this paper, we focus on the use of chlorophyll as an indicator of phytoplankton biomass. This follows standard biological oceanography practice, as it is an easily recorded consistent measure with global standards (see Table 1 of Sathyendranath et al., 2023) and is also one of the currencies used by most biological models, including the two that we had access to for this paper. However, a number of factors do affect the reliability of this measure of plankton biomass along the vertical dimension, including changes in plankton community structure and photoacclimation, viz. phytoplankton's change in Chl-a content per cell in response to light saturation/starvation (Cullen, 1982; Kitchen and Zaneveld, 1990).

This paper makes use of two sources of *in situ* data, and output from two different biogeochemical models, plus satellite observations to give the wider context. Note that the *in situ* measurements detailed in these first two sub-sections are strictly measurements of chlorophyll-a (hereafter denoted Chl-a), both monovinyl and divinyl forms, as they respond to the fluorescence associated with those specific molecules, whereas the fields in the models refer to total chlorophyll (i.e. model fields do not differentiate between the different types of chlorophyll pigment). High Performance Liquid Chromatography (HPLC) for these core regions within the Atlantic gyres indicates that the concentration of Chl-a exceeds that of other chlorophyll molecules (e.g. Chl-b and Chl-c) by almost a factor of ten (Aiken et al., 2017). Furthermore these HPLC measurements showed good agreement with satellite (SeaWiFS) data, suggesting it is reasonable to intercompare these subtly different measurements.

2.1 Cruise data from the Atlantic Meridional Transect programme

The AMT programme provides long-term monitoring of changes in the whole of the Atlantic Ocean by surveying physical and

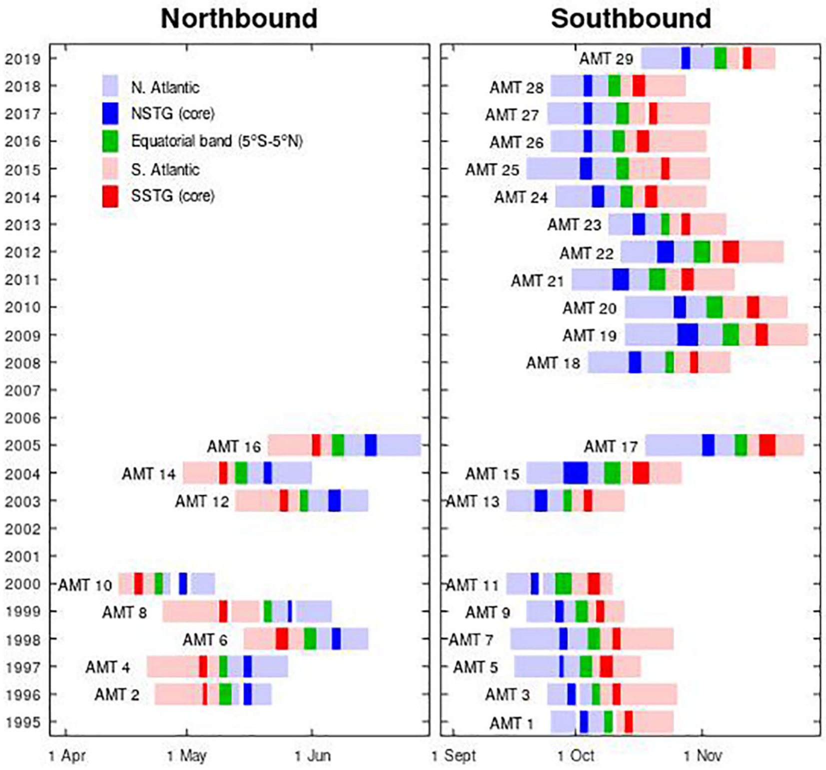

FIGURE 1
Timelines of the AMT cruises, showing that up to 2006 there were equal numbers in each half of the year, but since then cruises 18-29 have all been southbound (boreal autumn; austral spring). [Image based on Figure 2 of Aiken et al. (2017)].

biological properties in the Atlantic Ocean on a roughly yearly basis. The AMT programme has been operational since 1995, and makes use of the need for an Antarctic supply vessel to travel from the UK to the research bases, for example, at Rothera on the Antarctic Peninsula. This endeavour is unique in its scope of sampling a wide range of Longhurst provinces ranging from productive coastal waters to the centre of the oligotrophic gyres. Much of the section is along the 25°W meridian, but there are variations from year to year according to other scientific or logistical needs. In particular, the route used in the 1990s stayed close to Africa in the northern hemisphere, but was adapted to sample better the NSTG from 2003 onwards (see Figure 1 of Rees et al., 2017).

Each cruise incorporates many CTD (conductivity-temperature-depth) stations, where along with those three essential measurements of physical properties, there are other chemical or biological profiles taken using fluorometers, light sensors and assays of chemical constituents. Here we make use of the estimated chlorophyll-a concentration obtained by a fluorometer attached to the CTD frame. Although efforts are made to calibrate the fluorometer for each cruise, it was noted that in some cases the value at depth was distinctly different from zero. In this paper our focus is on the permanently-stratified oligotrophic gyres, where interannual changes may be small. Data from a number of the earlier cruises are omitted due to concerns about the calibration of the fluorometers. For the remaining ones the average over 250-300 m is calculated and removed from all other measurements, assuming it to be a fluorometer measure of detritus or dissolved substances and/or a calibration error.

The majority of cruises have been on the southbound route to Antarctica during the period September to November; these cruises measured the NSTG during boreal autumn and the SSTG during austral spring. However, in the first phase, several cruises were done on the return leg heading northbound to the UK in April to May, thus sampling the SSTG in austral autumn and the NSTG in boreal spring. A clear depiction of the periods sampled is shown in Figure 1). In our analysis, these two sets of cruises are kept separate, so that we assess the variations in Chl-a profile in the oligotrophic gyres through four different modes: NSTG in boreal spring and autumn, and SSTG in austral spring and autumn. Although one might expect some similarities in behaviour for the northern and southern hemispheres, the currents bounding them do differ e.g. the NSTG will contain some waters from the deep Mediterranean outflow, whilst the SSTG is traversed by Agulhas Rings carrying Indian Ocean water (Nencioli et al., 2018). There are also hemispheric differences in the availability of dissolved organic nitrogen (Clark et al., 2022). Smyth et al. (2017) also illustrate the differences in seasonal forcing for these two gyres. The AMT observations thus allow us some insight into annual variations albeit from just two seasons of the year.

2.2 BGC-Argo profiling floats

Argo profiling floats have been providing temperature and salinity data in the world ocean for approximately 20 years (Wong et al., 2020), with the target of 3000 floats sampling every 10 days reached in 2007. Biogeochemical (BGC) sensors have been added to a small but growing number of floats, but their deployment and operation has been driven more by individual research projects, rather than the aim of establishing quasi-global coverage. Therefore there may be a series of floats in one region with frequent (daily or sub-daily) sampling, whilst others regions have had few floats. We use here the data-field termed "CHLA_ADJUSTED" as Roesler et al. (2017) have pointed out that the data from the factory calibration typically lead to an overestimate of the amount of chlorophyll by a factor of two on average. We also make some correction (see below) using the estimated Chl-a values at depth. In the present work we have considered measurements representative of the SSTG if they are within 5° longitude and 5° latitude of 25°W, 20°S and have a surface chlorophyll value less than 0.1 mg m^{-3}, with a similar-sized box around 38°W, 24°N for the NSTG. There are profiles in these regions for all years since 2012 (see Figure 2), but not always in all seasons.

As the floats are generally not recovered and recalibrated, there can be issues with a drift in performance, especially for fluorometers. Thus, similar to the approach for the AMT CTDs, we consider the mean derived Chl-a concentration in the interval 251-300 m as a base value to be subtracted from the rest of the profile. Although in some regions, such as near the Equator there may be falling detritus, higher concentrations of dissolved substances and downwelling of plankton leading to significant real values at depth, we assume this is not the case within these gyres. If the base value is outside the range [-0.05, 0.05] mg m^{-3} the data are discarded on the assumption that a linear adjustment may no longer be valid.

2.3 NEMO/MEDUSA model

MEDUSA (Model of Ecosystem Dynamics, nutrient Utilisation, Sequestration and Acidification) is an intermediate complexity biological model (Yool et al., 2011) that has been embedded in the physical model NEMO (Nucleus for European Modelling of the Ocean, Madec and NEMO team, 2015). This configuration of NEMO is a global model with 75 vertical layers, with a thickness of ~1 m at the surface and ~14 m at 130 m (the mean depth of the DCM in this model). The horizontal resolution is 1/12°, allowing realistic representation of eddies and currents (Quartly et al., 2013). The marine biogeochemistry component used here, MEDUSA, is "intermediate complexity", with a dual size-class nutrient-phytoplankton-zooplankton-detritus (NPZD) structure. The plankton are described as two size classes, with "small" representing prokaryotic phytoplankton and protistan zooplankton, and "large" encompassing eukaryotic phytoplankton – specifically diatoms – and metazoan zooplankton. These different plankton functional types (PFTs) produce small, slow-sinking and large, fast-sinking detritus particles with separate remineralization pathways and profiles. Together with dissolved components, the model represents the biogeochemical cycles of nitrogen, silicon, iron, carbon, alkalinity and oxygen. This "intermediate complexity" requires only 15 model tracers, facilitating MEDUSA's use in simulations of long duration or high resolution (as here). A full description of the model is given in Yool et al. (2013). This has meant that it was one of the first biological models that could be implemented on high-resolution global models spanning several decades.

We obtained model output at 5-day intervals for two locations in the Atlantic, corresponding to the two subtropical gyres. The fields provided comprised both diatom and non-diatom chlorophyll; for these locations the latter category had values typically an order of magnitude greater than that for diatoms. In this work we just sum the two components together to give a measure of chlorophyll, similar to the undifferentiated values from the other sources, and do not discuss the particular PFTs. The model output was provided over a 25x25 pixel array centred on the chosen location; the majority of our analysis simply utilises the values at the central points (typical of the point sampling by AMT and BGC-Argo), but the appendix does explore the issue of spatial variability.

2.4 ERSEM model

For comparison, we obtained data from a special run of the ERSEM (European Regional Seas Ecosystem Model). This was a 1-D simulation of the SSTG, with the model forced by air temperature, wind stress, atmospheric pressure, cloudiness, humidity and surface values of PAR (photosynthetically available radiation). Physical processes such as heating and mixing were controlled by the General Ocean Turbulence Model (Burchard et al., 1999), but there was also assimilation of temperature profiles from the Smith and Haines (2009) reanalysis to make some allowance for physical features migrating through the domain – see Hardman-Mountford et al. (2013) for further details. This is a more complicated model than MEDUSA, encompassing eight different phytoplankton functional types (4 phytoplankton, 3 zooplankton and heterotrophic bacteria to facilitate the decomposition). Accounting is done for separate reservoirs of carbon, nitrogen, silicon, phosphorous and chlorophyll, so the model is able to accommodate species and processes that are not bound by the classical Redfield ratios that summarise the bulk concentrations of these constituents in the ocean. Consequently, this allows the recycling of detritus in the water column to vary according to the actual carbon-nitrogen-phosphorous proportions (Baretta et al., 1995). However, the ERSEM model was developed for European shelf seas (Hardman-Mountford et al., 2013), rather than the relatively unproductive Atlantic gyres.

The run of the model was from Jan 1995 to Aug. 2007, with daily files produced, but here we use the summary output available every 7 days. The data from the first year showed strong spin-up effects, so are ignored here.

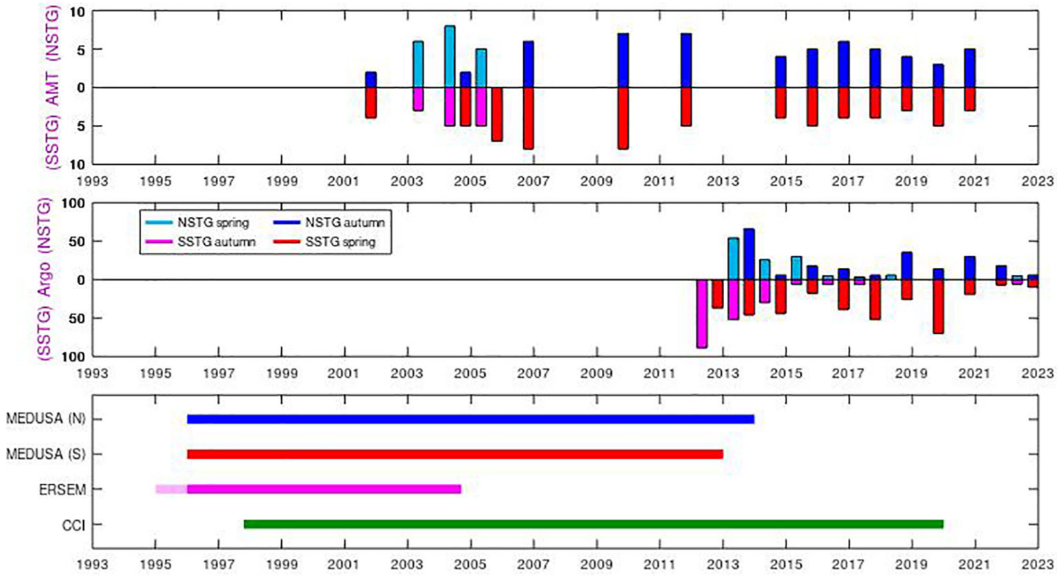

FIGURE 2
Time span of the various datasets. The AMT cruises occur in Apr-May or Sept-Nov, with a tendency in the last 15 years for observations in the latter period as the ship heads southbound to supply the Antarctic bases. However, not all cruises make measurements in the NSTG or SSTG, depending on their route. The BGC-Argo data are very heterogeneous, according to the research interests of the institutions deploying them; tallies of profiles in NSTG and SSTG are only shown here for Apr-May and Oct-Nov for comparison with AMT. The model and satellite (CCI) data are continuous and uniform, with the coloured lines simply indicating the extent of these various datasets.

2.5 Satellite observations

We also make use of satellite observation of surface Chl-a concentration, as these can provide context for the *in situ* measurements of AMT and BGC-Argo. The dataset we use is CCI v6.0, a merged compilation of measurements from all available ocean colour sensors, produced by Plymouth Marine Laboratory under the auspices of the Climate Change Initiative project (Sathyendranath et al., 2019). These data span from Sept. 1997 onwards, reflecting the period of continuous ocean colour coverage. The dataset we use contains 5-day composites at a resolution of 1/12°, which we then average to 0.5° resolution and apply a little temporal smoothing to minimise gaps due to persistent cloud. Data were extracted for 20 complete years (1998-2017).

The periods of data utilised for the various datasets do not fully coincide (see Figure 2); we are not aiming to study individual events in detail, but rather look at the dependencies between surface and sub-surface properties in both models and observations, noting common themes.

3 Seasonal and interannual variations

3.1 Selection of *in situ* data

Most of the AMT cruises went close to 20°S, 25°W, so all stations within 4° latitude of this point and with a surface Chl-a less than 0.1 mg m^{-3} were used. There was greater variation in the routes in the North Atlantic, with 38°W, 24°N being chosen as the nominal point with a similar latitudinal span around it used. Although the core Argo float array has been operational for nearly 20 years with quasi-uniform coverage, the deployment of BGC-Argo floats is much more heterogeneous, as the focus to-date has been more on the particular research interests of the relevant institutions than on creating a spatially balanced array. Thus although the BGC Argo floats provide measurements throughout all seasons of the year, the extent of the "area of interest" was extended slightly (to within 5° of nominal location) in order to obtain sufficient profiles for meaningful statistical analysis. However we also include the constraint that the BGC-Argo's surface Chl-a value should be less than 0.1 mg m^{-3} to ensure that float profiles on the edge of the gyres are not included.

3.2 Depth of DCM

The AMT CTD stations and BGC Argo profiles provide measurements with a vertical resolution of a few metres or less; as these are noisy due to the inherent challenges in recording fluorescence, some smoothing is applied in the vertical dimension. On the other hand, there is no such high-frequency depth variation in the model values, as these are assigned uniform chlorophyll values within cells of order 10-20 m high. To achieve a more precise determination of the depth of the sub-surface chlorophyll maximum, we fit a parabola to the five depth cells spanning the peak (see Figure 3) and use the location of the apex to define our best estimate of the location of the deep chlorophyll maximum.

Figure 4 shows the chlorophyll concentration data for the SSTG from the ERSEM model. It is clear that the values at the DCM are an order of magnitude greater than at the surface, and that strong

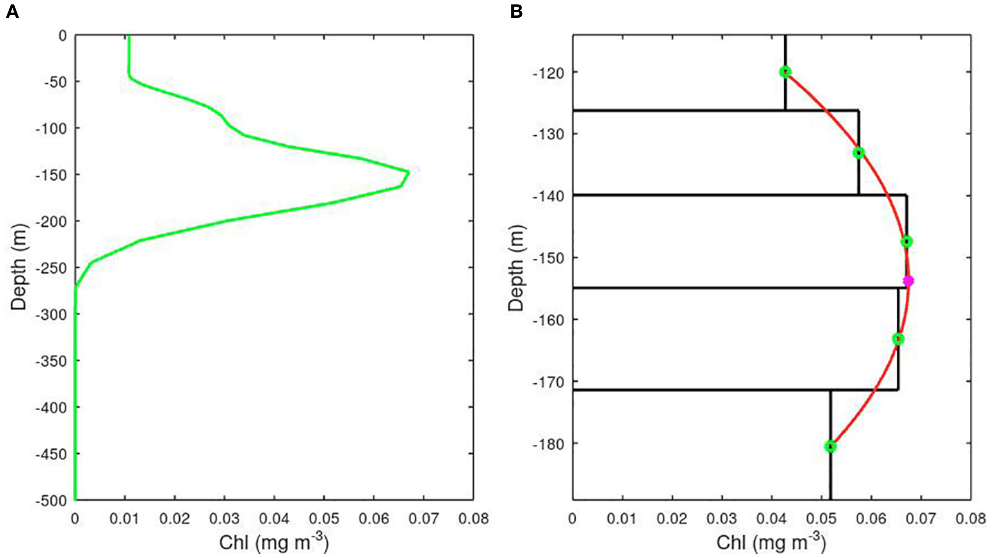

FIGURE 3
The precision of the depth of a model's Deep Chlorophyll Maximum is improved by fitting a parabola to the values for the 5 layers bracketing the largest value. **(A)** The complete profile over 500 m. **(B)** Zoom in on the peak, with the derived depth of the peak shown by the pink asterisk. (Example is from MEDUSA's representation of SSTG).

seasonal variations can be seen in both the depth of the DCM and in the concentration at the surface, with peak surface concentrations in May-June, although with significant interannual variation. The total column-integrated chlorophyll shows much weaker seasonal variations, with the annual modulation of the total being only about ±5% of the mean. A slight minimum occurs at the middle of the year, which is when the surface signature is strongest. However, that does not necessarily imply a causal connection, as the total

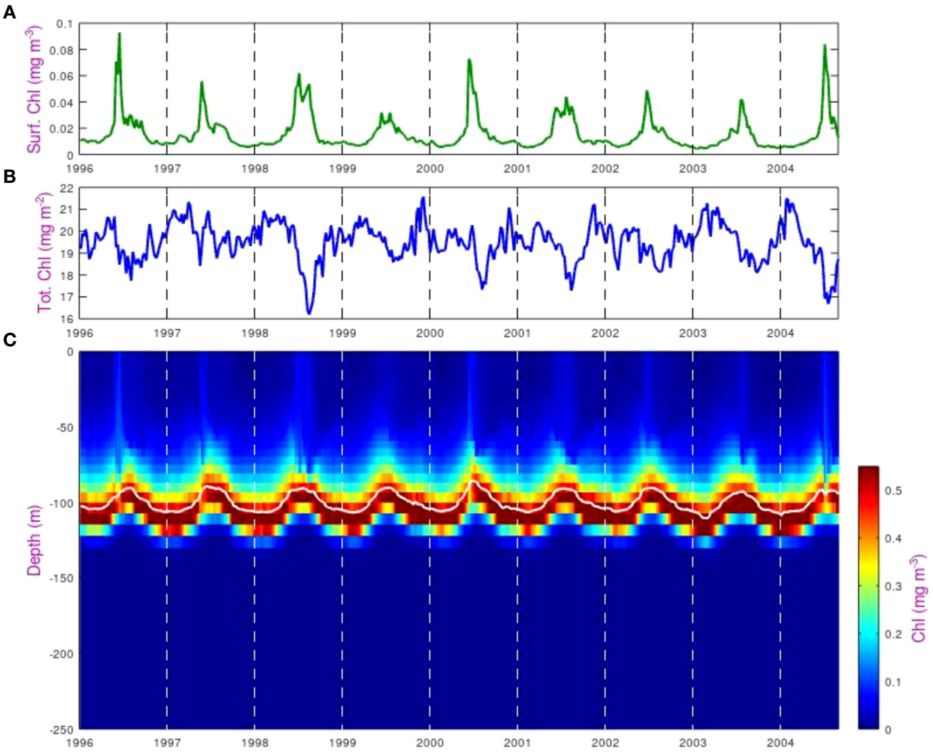

FIGURE 4
Variations in chlorophyll concentration at the SSTG within the ERSEM model. **(A)** Value in the surface layer, **(B)** Total column-integrated chlorophyll, **(C)** Value in each depth bin, showing the variation in depth of the DCM peak (highlighted by the solid white line).

chlorophyll could be responding to many different factors having a seasonal variation.

3.3 Seasonal variations

Figure 5 shows the differences in mean values and seasonal variation for the various *in situ* datasets and for the numerical models. Although numerical biogeochemical models perform well at getting the broad patterns of surface chlorophyll variation correct (e.g. Figure 11 of Yool et al., 2011), it is often challenging to get the magnitudes correct. This is particularly the case at the extremes (highly productive and oligotrophic regions).

The surface chlorophyll concentration shows strong seasonal modulation for all the continuous datasets (both CCI and models), with that for the NSTG peaking in February-March and the SSTG reaching its maximum sometime between June and August. This agrees with prior satellite analysis by McClain et al. (2004) and Aiken et al. (2017). The timing of the AMT cruises puts them outside these periods of maximum surface chlorophyll, implying the cruises are not suitable for a detailed seasonal examination; however it does also mean that two or three weeks difference between the time of year of various cruises should not lead to apparent interannual variation.

The SSTG surface bloom for ERSEM occurs three months earlier than in MEDUSA, and also lasts longer. That evidenced by the satellite data has a peak slightly earlier than in MEDUSA and a much longer duration than in either model. A similar picture is seen for the NSTG: the heightened chlorophyll values in the CCI dataset peak a month earlier than in MEDUSA and have a longer duration. The temporal pattern revealed by BGC-Argo matches well that of CCI, but both *in situ* sources (AMT and Argo) have much lower values. This is possibly due to non-photochemical quenching, which is discussed later.

When considering total chlorophyll in the water column we note that there is no clear pattern. The two models disagree in the magnitude of the total for the SSTG by a factor of two, although both show slightly higher values for March-May (autumn) than for July-August (winter), so there is slightly less in total when values are higher in the surface layer, confirming this anti-correlation in seasonality noted by Hardman-Mountford et al. (2013). This pattern is clearer for MEDUSA's representation of the NSTG, with ~20% more total chlorophyll outside the peak months for surface chlorophyll.

The values from BGC-Argo floats are of a very similar magnitude to those produced by the models, with the Argo-derived values at SSTG matching the seasonal variation shown by ERSEM and those for the NSTG being close to those for MEDUSA. However, that model has much lower values for the SSTG, which appear to be roughly matched with AMT values at both sites. All the datasets with year-round coverage show total chlorophyll to be at its smallest during the winter period for that site.

Finally, we consider the seasonal variations in the depth of the DCM. The value at any particular time may not fully reflect the state of the ecosystem, as physical features (e.g. eddies or internal waves) may raise or lower the level quite considerably. However, we use point values for DCM depth from the model rather than some large-scale average (see Appendix) because the *in situ* measurements are discrete point measurements. Figure 4 showed that for the SSTG ERSEM had a regular gently varying DCM depth; this translates into a smooth climatological signal varying around 100 m (Figure 5C), with a decrease at the time of the peak surface concentrations (typical of 1-D simulations). MEDUSA has a much wider variation of values, due to the physical features passing through, but on average the depth at the SSTG is much deeper (130-140 m). The decreases in DCM depth in MEDUSA both coincide with increased surface values. For the SSTG, the BGC-Argo profiles show a seasonal variation matching ERSEM, but with typical depth values agreeing with MEDUSA; Argo's DCM depth variation for the NSTG is, as might be expected, roughly the reverse of that for the SSTG, whereas the MEDUSA variation is more complicated and less clearly linked to surface changes.

3.4 Interannual variations

Within the climatological means illustrated previously there is often a great range of individual values. Figure 6 shows probability distribution functions (p.d.f.) of the depth of DCM and the total columnar chlorophyll. In this case, data are shown separately for the two seasons for which AMT observations exist. As noted before ERSEM shows a shallower DCM than the other datasets, but does agree that for the SSTG the DCM is generally slightly higher in austral autumn than in spring. AMT and BGC-Argo also show a slightly higher DCM for NSTG in boreal autumn than in spring, but this is not the case for MEDUSA. In MEDUSA both spring sets of observations show a pronounced minority of shallow DCM events, possibly related to passing physical features having advected nutrients up from deeper layers (but also note the issue of spatial variation discussed in the Appendix).

When considering the p.d.f.s of total chlorophyll (second row of Figure 6) we note that there is a large variation in the values. MEDUSA for SSTG and AMT for both sites yield values of order 10 mg m^{-2}, but MEDUSA for NSTG and ERSEM and ARGO estimate the totals as of order 20 mg m^{-2}. The spring/autumn variation is weak, with AMT and MEDUSA datasets showing increased values for both regions during Oct-Nov compared with Apr-May, whereas ARGO shows the reverse and for ERSEM the distributions for the two periods are similar. However the periods under consideration represent the transition times at the end or start of the peak surface chlorophyll period, and so the relative change between Apr-May and Oct-Nov is sensitive to when the surface values intensify in these datasets. We also note that the AMT Apr-May sections mainly occurred early in the programme, whereas Oct-Nov transects have taken place more evenly throughout the AMT programme (Figure 1), so the seasonal difference noted for AMT may partially reflect an increasing trend in surface chlorophyll noted in Figures 15 and 16 of Aiken et al. (2017).

Table 1 summarises the statistics describing the chlorophyll profiles in all four datasets. ERSEM has a much larger amplitude for the DCM peak than the other datasets; however as it's DCM is

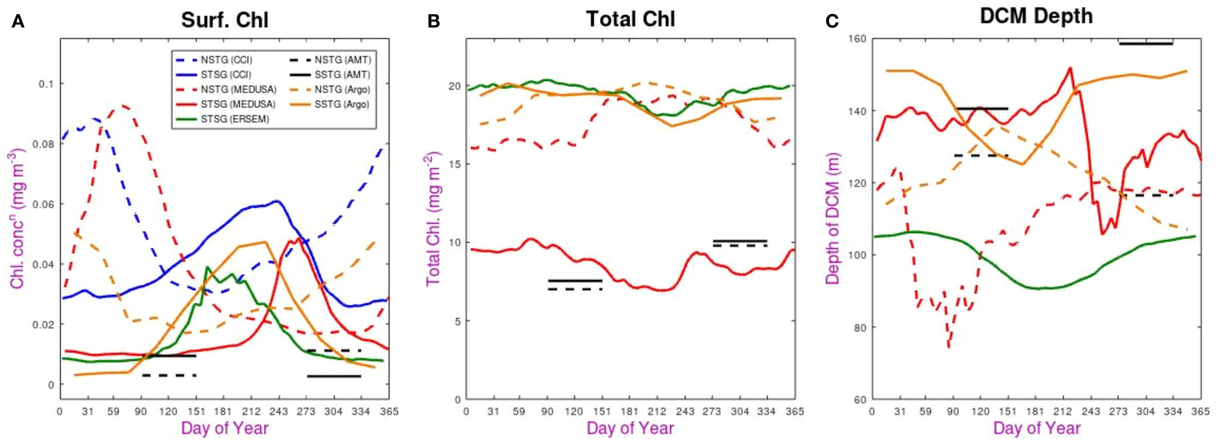

FIGURE 5
Seasonal variations in the various datasets. **(A)** chlorophyll concentration in the surface layer, **(B)** Total column integrated chlorophyll, **(C)** Depth of DCM. In all cases the solid line shows observation for the SSTG and the dashed line for the NSTG. The satellite (CCI) dataset only provides surface measurements, and the AMT data are simply shown as averages over the two distinct periods when the transects took place.

typically shallower and less wide than in the other datasets, it returns a total chlorophyll value in line with most of the others. The seasonal change in amplitude of peak chlorophyll is generally opposite to that of the width of the DCM, so that the total chlorophyll has a weaker variation than either (see Figure 5B). Aiken et al. (2017) show output from the biological model of Brewin et al. (2017), which also gives values of total chlorophyll in the middle of the gyres of around 22 mg m^{-2}, with a seasonal variation of only ~5%.

3.5 Significant connections?

A great many physical and biological properties exhibit a seasonal cycle so that significant correlations may be found, especially with the assumption that one value may lag another by several weeks. However, no causal connection should be inferred because each may be responding to different solar-related drivers e.g. cloudiness, sea temperature, windiness etc. However if we

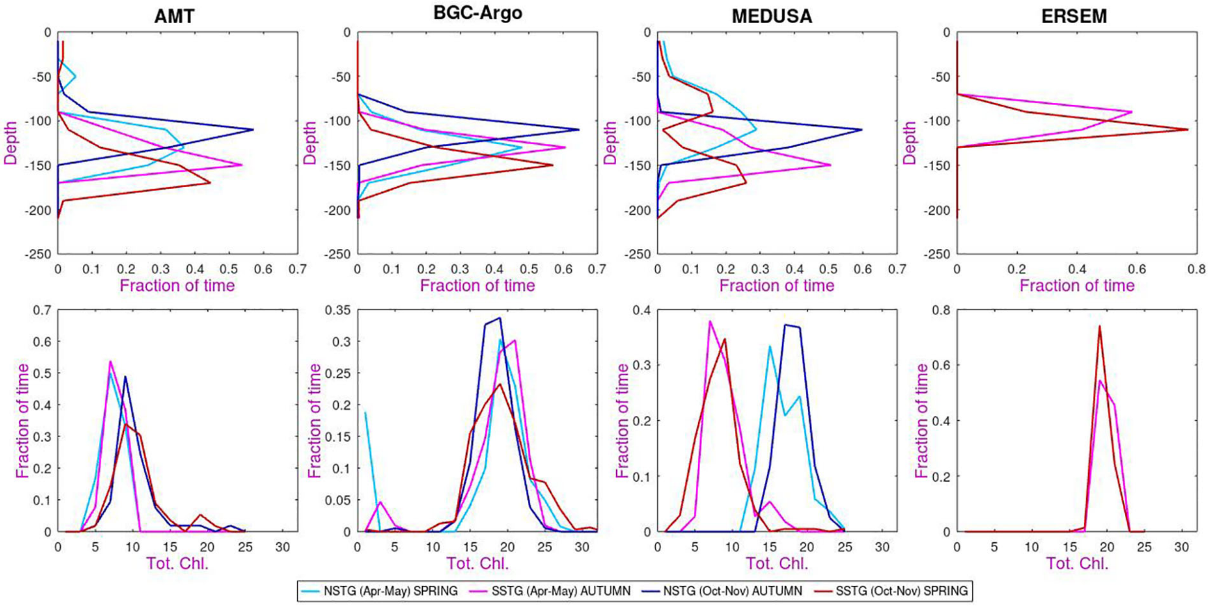

FIGURE 6
Probability distribution functions of (top row) depth of DCM (second row) total chlorophyll. The same colour legend applies to all panels. [The binning intervals are 20 m in depth (top row) and 2 mg m^{-2} for total chlorophyll (bottom row), with “fraction of time” indicating that all histograms are normalized to unity].

TABLE 1 Characteristics of the NSTG and SSTG chlorophyll profiles derived from the various datasets.

	Gyre (Time)	N	Surf Chl (mg m^{-3})	Peak Chl (mg m^{-3})	DCM depth (m)	DCM width (m)	Total Chl (mg m^{-2})
AMT	N (Apr-May)	19	0.003	0.10	128	62	7.0
	S (Apr-May)	13	0.009	0.10	141	67	7.5
	N (Oct-Nov)	56	0.011	0.14	114	79	9.8
	S (Oct-Nov)	65	0.003	0.17	156	56	10.1
BGC-Argo	N (Apr-May)	129	0.018	0.29	132	44	19.3
	S (Apr-May)	214	0.017	0.27	132	50	19.4
	N (Oct-Nov)	190	0.034	0.24	111	61	18.2
	S (Oct-Nov)	330	0.010	0.29	149	52	18.9
MEDUSA	N (Apr-May)	216	0.05	0.18	100	57	16.5
	S (Apr-May)	229	0.009	0.10	143	68	8.5
	N (Oct-Nov)	204	0.02	0.31	119	51	18.6
	S (Oct-Nov)	216	0.003	0.06	148	74	7.8
ERSEM	S (Apr-May)	78	0.012	0.53	99	27	20.0
	S (Oct-Nov)	69	0.009	0.61	102	25	19.5

A median is given as that is insensitive to extreme values calculated from anomalous profiles. N details the number of observations used, but they are not all independent, being in some cases successive CTDs in a cruise or profiles of a float or model profiles at short time separation. The width (computed as full width at half maximum, FWHM) is a measure of the depth range of the deep chlorophyll maximum for each profile, rather than a measure of the uncertainty in the depth of the maximum.

consider anomalies from the average for that time of year, then it may be more significant if some extreme of a surface value presages the variation at depth.

In Figure 7 we examine the co-occurrence of anomalies in surface chlorophyll with those in total chlorophyll or depth of DCM. The colour scheme reflects the four different sampling regimes, since the connection may not be the same for all such "modes". Firstly we note that there is a great deal of scatter – once the regular seasonal variations are removed, there are potentially many causes for the weaker remaining variations, so that a connection between anomalies in surface and sub-surface properties will be much weaker. Conversely a unique event in the MEDUSA representation of the NSTG for Oct-Nov produced large anomalies in various properties leading to a significant correlation value without necessarily being indicative of a causal relationship occurring throughout the rest of the time series.

Assigning confidence intervals to these correlations is challenging, as consecutive CTD casts or Argo profiles will not

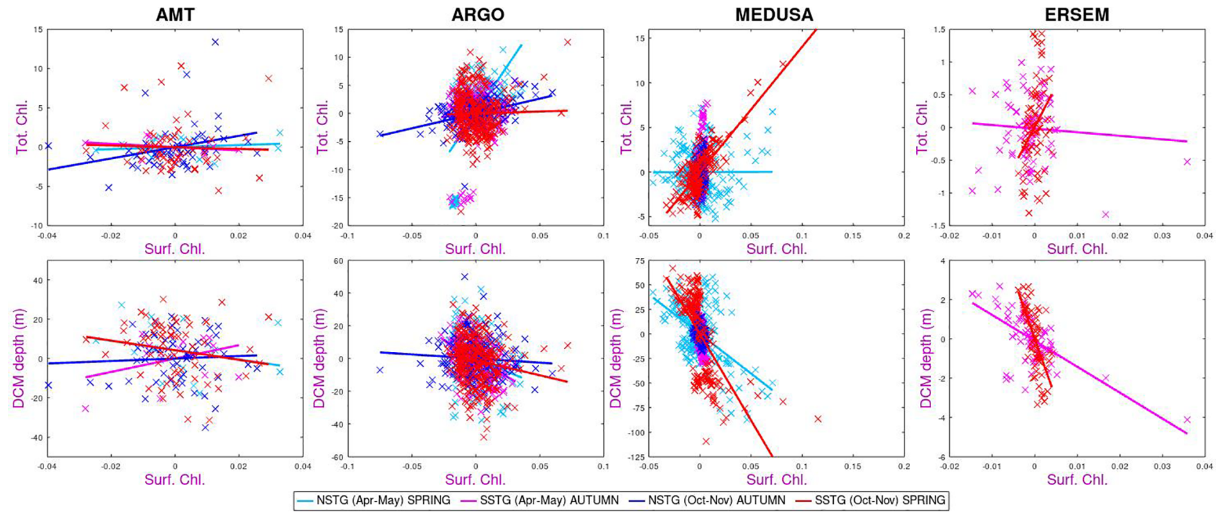

FIGURE 7
Correlation of anomalies in surface chlorophyll with values at depth, with no lag. The plot compares behaviour at NSTG and SSTG for the two parts of the year sampled by AMT. MEDUSA's anomalies for the NSTG in Oct-Nov are dominated by one large event in the 18-year time series.

be independent, so instead here we look for common themes spanning various datasets or common to both gyres for the same season.

Regions with enhanced upwelling tend to have lower SST but higher surface chlorophyll, due to nutrient supply, leading to negatively correlated spatial patterns of these two properties. Figure 8 shows that the year-to-year variation in these two surface terms are also usually negatively correlated, which would be consistent with changes in mixing affecting these two aspects coherently. However this is not borne out for AMT sampling of the NSTG. We hypothesise that this may be due to the wide variation in the route traversed in the northern hemisphere, especially during the first decade that provided most of the Apr-May transects. Thus a variation in the locations being compared may be the cause of the positive correlation noted between SST and surface chlorophyll. Similarly warmer than average SST tends to be associated with a shallower MLD and so a negative correlation, with the exception also being in the behaviour noted for the AMT observations of the NSTG.

Continuing on to the sub-surface biological properties we note that both models show a strong negative correlation between amount of surface chlorophyll and the depth of the DCM. This is as expected due to increased surface chlorophyl reducing the amount of PAR reaching depth. However, this expectation is not borne out by the AMT measurements of one of the modes (SSTG in Apr-May), which instead shows a high positive correlation. The surface chlorophyll value is generally positively correlated with the columnar total, however for the SSTG in Apr-May three of the datasets (AMT, Argo and ERSEM) agree that the correlations are close to zero.

With regards to the overall pattern of correlations shown in Figure 8, there is a good correspondence between those for MEDUSA and ERSEM. Both are, of course, numerical models and thus can only show patterns corresponding to the result of those biogeochemical interactions that have been modelled. However they are very different models, with MEDUSA being a full 3-D fine resolution grid with features being advected through and ERSEM being a 1-D implementation of conditions in the SSTG, but with more nuanced biological components. The analysis of the AMT data shows some agreement with that from analysing the models, but there are many differences. These could be due to the real world having interannual variations in forcing conditions or biological interactions not simulated in the models; however it could also be partially due to the Apr-May occupations being principally in the first half of the period analysed in the models and there also being much spatial variation in the tracks occupied then, so complicating the calculation of anomalies in various properties.

3.6 Delayed response?

In winter PAR is lowest, and the reduced light flux to the DCM results in reduced growth of phytoplankton there. Consequently the nutrient gradient enables more nutrients to be entrained into the sub-surface mixed layer above the DCM, increasing chlorophyll values near the surface. A positive feedback can be established, with the increased chlorophyll production at the surface further reducing light flux to the DCM and so enhancing surface production. As the seasons progress from low-light winter to spring the higher PAR flux penetrates to the DCM, increasing chlorophyll production there and cutting down the nutrient flux to the surface. [Letelier et al. (2004) note that for the NSTG in the Pacific, the isolumes (contours of equal illumination) are displaced by as much as 31m between winter and summer].

For the biological response, the chlorophyll signal at depth may possibly lag behind the changes at the surface, if there is vertical variability in growth and loss rates between layers. Alternatively, if most of the anomalies (relative to the average for that time of year) are due to mesoscale features advecting through, then the changes at

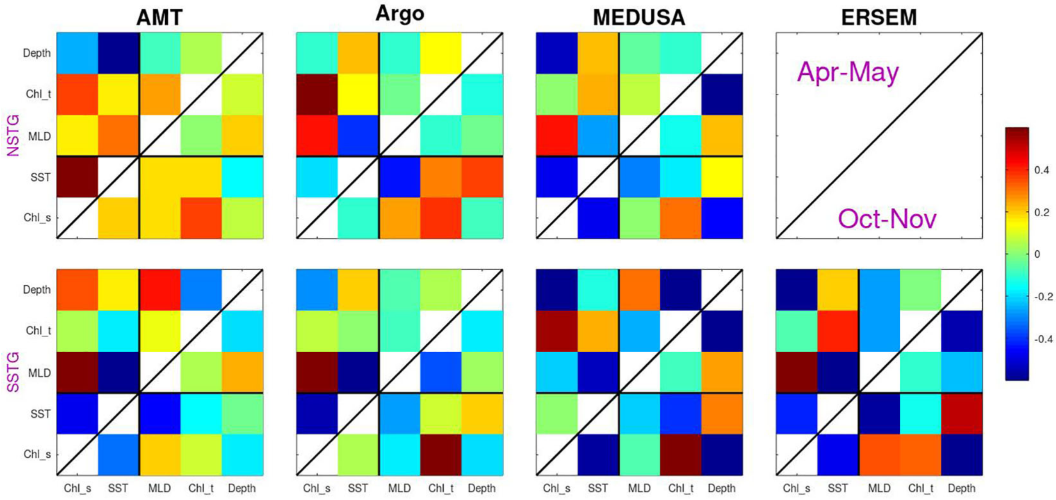

FIGURE 8
The correlation between various properties calculated using anomalies relative to the mean for that time of year. The values analysed comprise two surface properties (surface chlorophyll and SST) and three sub-surface values (MLD, total chlorophyll and depth of DCM), with the colour indicating the correlation. Analysis is for both gyres and the two periods sampled by AMT (with Apr-May above the diagonal line and Oct-Nov below it).

surface and depth are likely to be coherent. To investigate these issues we explore the correlation between anomalies in surface and sub-surface features, looking at lags of the order of weeks.

For the AMT sub-surface measurements there are no *in situ* samples a few weeks prior to the CTD casts, so the AMT estimates of the DCM have to be contrasted with earlier satellite observations of the surface from the CCI project (Figure 9). These satellite-derived products have been well-validated on AMT (Brewin et al., 2016; Tilstone et al., 2021). The dataset being used provided 5-day composites every 5 days, so we investigate lags from 0 to 25 days. The MEDUSA model had a time step of 5 days and ERSEM was at steps of 7 days, so these were used in the lag analysis. Only positive lags were considered, as we do not expect the sub-surface changes to lead those at the surface.

Figure 10 shows the results of the lag analysis, indicating to what degree prior information on surface chlorophyll concentrations could be used to predict either total depth-integrated chlorophyll or the depth of the DCM. For total chlorophyll. the correlations are of order ±0.25. MEDUSA shows similar patterns for NSTG and SSTG, with a negative response in Apr-May peaking at ~15 days, whilst there is a positive correlation in Oct-Nov that is maximum at zero lag. This is surprising given these periods correspond to different community growth/decline conditions at the two sites. For the SSTG, ERSEM also shows a positive correlation but peaking at ~14 days.

Larger correlations are noted for the DCM depth and they are nearly all negative. One particular point of interest is the low correlation for AMT with *in situ* measurements of surface chlorophyll, but high correlations (approaching -0.8 for autumn)

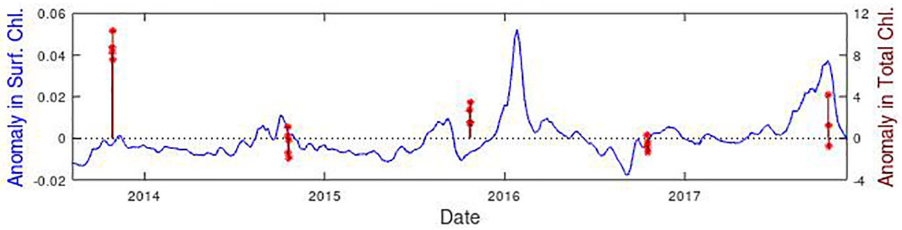

FIGURE 9
Time series of surface chlorophyll concentration at the SSTG observed by CCI (in blue) and AMT estimates of total chlorophyll (in dark red). Both datasets are expressed as anomalies relative to the mean value for that time of year, with 4 or 5 independent CTDs taking place within the specified region for each cruise. Note both datasets cover 2001-2020, with this panel simply providing a zoom to show the details.

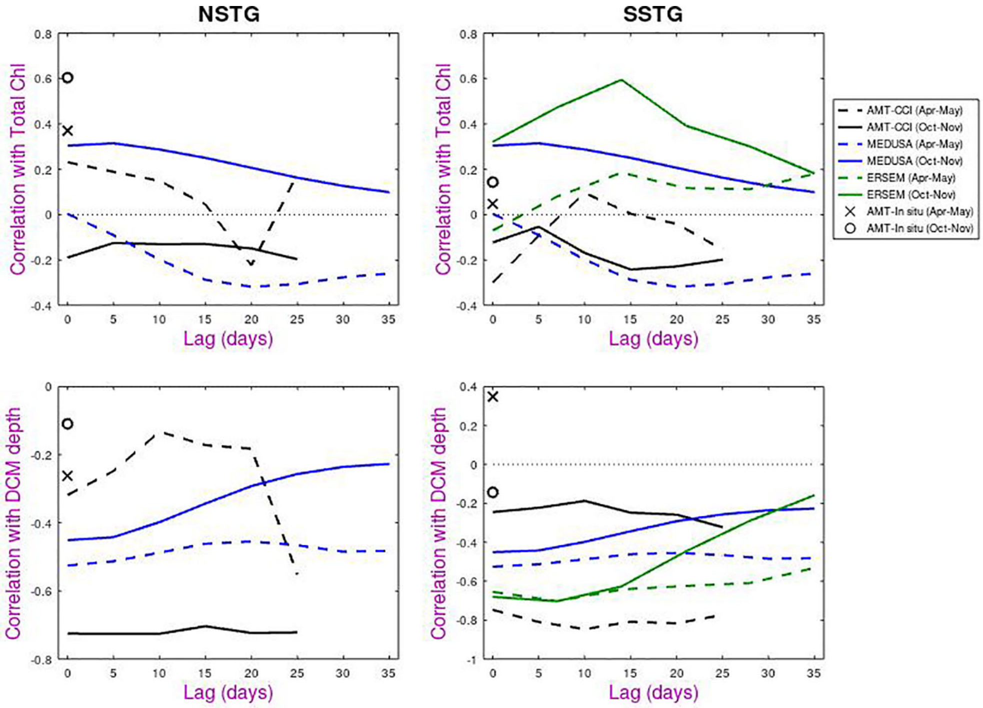

FIGURE 10
Lagged correlations of total chlorophyll and depth of DCM against surface chlorophyll measurements for all datasets (AMT, MEDUSA, ERSEM) on the same axes. Dashed lines and cross are for Apr-May and solid lines and circle are for Oct-Nov.

when compared with satellite-derived chlorophyll. The low values for the *in situ* comparison are probably due to non-photochemical quenching i.e that plankton in the sunlit ocean have adjusted their chlorophyll response to dissipate excess energy and thus give a low response to fluorometers. (More accurate values of *in situ* chlorophyll can be obtained by HPLC of collected samples, but these are only available for discrete depths).

Whilst the AMT-CCI analyses for the two gyres show similar response for boreal and austral autumn and also for boreal and austral spring, both models tend to show a flat response for Apr-May for NSTG and SSTG, and a response that peaks at zero lag for Oct-Nov. These flat responses may indicate that the DCM depth in the models is not so much responding to the amount of surface chlorophyll present at that time, but to the underlying environmental conditions that have led to that year having more or less surface chlorophyll than normal.

4 Discussion and conclusions

4.1 Seasonality observed by *in situ* sensors

The biogeochemical monitoring of the Atlantic through the Atlantic Meridional Transect programme has been ongoing for almost 30 years. There are many individual research cruises that sample some highly productive Longhurst province during a major bloom, but AMT is unprecedented in its deliberate inclusion of measurements in the centre of the Atlantic's subtropical gyres. Although these regions are much lower in chlorophyll concentration, they are of large expanse. Models and BGC-Argo profiles show that there is seasonality within these gyres, with variation not only at the surface but also at depth. However for logistical reasons the AMT cruises have always been in April-May or October-November (with most cruises in the last decade in the latter interval) and so the seasonal variation cannot be easily explored from these hydrographic measurements. On the other hand, the sampling at these times of year better enables long-term trends to be analysed, compared with the variation between midwinter and midsummer.

Profiles from drifting biogeochemical Argo floats offer some insight into the seasonal variations at depth in the real ocean. For the SSTG, there is a simple near-sinusoidal variation in the average depth of the deep chlorophyll maximum, and in the total column-integrated chlorophyll, with the minimum in the middle of the year coinciding with the peak in surface chlorophyll. For the NSTG, BGC-Argo shows a minimum in depth of DCM and in total chlorophyll for November-February; which mirrors Argo's observation of surface properties, and aligns with the temporal variation of the CCI product (Figure 5A). However the satellite product yields values consistently higher than our *in situ* estimates.

HPLC measurements are usually considered as the most trustworthy records of chlorophyll concentration. HPLC data for 3 recent AMT cruises suggest the low values in the centre of the gyres are only about 0.04 mg m^{-3} (Figure 2 of Tilstone et al., 2021). As stated in the data description (sections 2.1 and 2.2), the chlorophyll profiles recorded by AMT's CTD casts and the BGC-Argo floats do not always go to zero at depths below 250 m, but have small values both positive and negative. This has been interpretted here as a slight offset in the sensor calibrations and this deep value subtracted from the whole profile. However there may be a real small bias, where there is actually some fluorescence from detrital particles, non-viable phytoplankton and coloured dissolved organic matter (Xing et al., 2017). This could explain why the AMT and Argo values for surface chlorophyll are smaller than most other records, including the CCI data from satellites. A reduction in the base value subtracted from each whole profile would also lead to an increase in the columnar total. Brewin et al. (2017) also suggest that total chlorophyll values calculated from AMT's water samples yield a higher value than those calculated from the fluorometer alone. Analysis of flow cytometry data for two earlier AMT cruises showed that the dominant plankton in such nutrient-depleted waters was *Prochlorococcus*, and also showed that the DCM peak was ~0.1 mg m^{-3}, with its depth being deeper for the SSTG than NSTG (see Figure 3 of Tarran et al., 2006), in keeping with our fluorometer analysis detailed in Table 1.

4.2 Oligotrophic gyres in numerical biogeochemical models

Although numerical biological models can readily produce the spatial patterns of chlorophyll variation (e.g. Figure 11 of Yool et al., 2011), as that is modulated by the physics, achieving the correct magnitudes is more challenging. This is particularly so in low productivity regions, where some models may implement tuning or use non-linear loss rates in order to enable a standing stock of phytoplankton to overwinter without dying out. There may also be issues with supply of nutrients at the base of the mixed layer, as such effects have to be parameterised to allow for submesoscale physical processes that are not resolved by typical basin- or global-scale models. Many authors (e.g. Figure 1 of Signorini et al., 2015) have shown the regions of low surface chlorophyll and the presence of a DCM are linked to regions with a deep nitracline, with the resupply of nutrients from below being essential for the maintenance of these sub-surface features.

Both ERESM and MEDUSA produce a clear sub-surface chlorophyll maximum, but in the case of the 1-D run of ERSEM this is well-constrained to depths in the range 90-110 m (see Figure 4), with a peak concentration at depth of ~0.6 mg m^{-3}, leading to a total chlorophyll of ~20 mg m^{-2} (Figure 5B) that is much higher than noted by AMT's CTD data. The large peak values in the DCM are partially offset by the narrowness of the sub-surface chlorophyll peak (~25 m, see Table 1), which may suggest insufficient vertical diffusion of nitrates in the model. ERSEM also shows the simple seasonal variation borne out by the BGC-Argo analysis.

For the SSTG, MEDUSA produces a DCM at ~120-150 m with a width of ~70 m (FWHM), more in keeping with the AMT and Argo values, and its associated total chlorophyll is only 10 mg m^{-2}, agreeing broadly with AMT (but not Argo). For the NSTG, it has a shallower DCM with a higher chlorophyll concentration at its peak (0.2 mg m^{-3}, as opposed to 0.1 mg m^{-3} for SSTG), leading to a significantly higher total chlorophyll. In portraying the NSTG as having a shallower DCM, higher total chlorophyll and higher surface chlorophyll than the SSTG, MEDUSA agrees with the differences noted for both AMT and Argo.

Figure 11 of Aiken et al. (2017) show that the model of Brewin et al. (2017) produces a DCM at a depth of 85-95 m (in keeping with ERSEM) for both gyres, with values shallower in the winter period. That model also gives values of total chlorophyll of ~22 mg m^{-2}, with peaks in the winter at the time of highest surface concentration. The standard run of the COBALT biogeochemical model gave DCM depths of ~85 m in NSTG and ~60 m in SSTG, with Moeller et al. (2019) modelling grazing as a diminishing function of light intensity in order to get depths of ~135 m i.e. close to that observed in situ. Given their large spatial extent, it is crucial that models are able to portray the DCM accurately. MEDUSA appears to be one of the earliest global biogeochemical models to get the depths correct and also the integrated total for the NSTG. However the intensity of the peak for the SSTG is too weak – further work should look at the factors affecting both nutrient supply and losses in this region.

4.3 Connections between surface and sub-surface

There are many factors that affect the strength and location of the deep chlorophyll maximum within these gyres. Eddies migrating through these regions may raise or lower isopycnal surfaces, which can in turn affect the DCM. Cornec et al. (2021) noted that cyclonic eddies can provide the conditions for enhanced growth leading to a “deep biomass maximum”, whereas anticyclonic eddies forcing the plankton down encourage increased chlorophyll production within the plankton (“deep photoacclimation maximum”) in order to harvest enough light. However by collating data from a large number of CTD stations and BGC-Argo profiles we hope to average over such effects, but these transient phenomena will reduce the observed correlations.

The majority of other environmental factors have a direct or indirect link to the annual cycle of solar irradiation e.g. solar zenith angle, stratification, wind fields, cloudiness, and so it is expected that there will be seasonal cycles in SST, mixed layer depth, surface chlorophyll, depth of DCM and total chlorophyll. Some of these conditions, such as SST, will lag the solar cycle, so not all properties will peak at the same time. To get some insight into causal connections we have examined anomalies in various properties relative to their means for that time of year.

The seasonal cycles of SST are not shown, but, in general, northern hemisphere sites (including NSTG) will peak in Sept-Oct, and southern ones in Mar-Apr. Thus cool SST values partially precede the annual decrease in DCM depth (Figure 5C). Examination of anomalies relative to the seasonal average shows that higher than normal SST values are generally associated with a shallower than normal mixed layer, but with a deeper DCM. (The exception is the AMT observations of the NSTG, where the diversity of routes, as shown in Rees et al. (2015), may be a major factor.) The observed correlations could be related to reduced levels of surface chlorophyll that allow light to penetrate slightly deeper and promote the DCM, or to shallower mixing being unable to entrain higher nutrient concentrations at depth and nutrient-starving the surface. This is another question that could benefit from extended investigation with model simulations, especially as models permit individual processes such as mixing and diffusion to be selectively turned off in order to ascertain their impact.

The seasonal cycle of total column-integrated chlorophyll only varies slightly (~10%), with its minimum and that for the depth of the DCM occurring roughly when the surface chlorophyll is a maximum (Figure 5). However, when considering interannual variations, increased surface chlorophyll is associated with a shallower DCM, but is positively correlated with increases in total chlorophyll (Figure 8). SST also appears to be negatively correlated with DCM depth in Apr-May but positively correlated in Oct-Nov for both NSTG and SSTG, indicating that different factors are relevant in the two locations.

Some of the strongest correlations are between surface chlorophyll and the depth of DCM, with increased surface concentrations leading to a shallower DCM, as noted by others e.g. McClain et al. (2004). Mignot et al. (2011) collated observations from many geographically diverse regions and showed a high correlation (r^2 = 0.81), whilst Mignot et al. (2014) showed this connectivity between surface chlorophyll and DCM depth for 4 individual BGC-Argo floats monitoring the seasonal cycle in 4 separate low productivity regions. Similarly, Uitz et al. (2006) have shown a positive correlation between surface and depth-integrated chlorophyll values, with their selection of stratified waters having a large spatial variation and encompassing a wide range of surface chlorophyll values. We have extended those observations to interannual timescales, showing that once seasonal cycles are removed there is still a clear anti-correlation i.e. that an exceptionally strong surface signal leads to a less pronounced and shallower DCM than normal.

This is particularly pronounced for satellite observations of surface chlorophyll with AMT measurements of DCM depth during boreal and austral autumn (Figure 10), with the connection being much weaker in the spring seasons. The lagged correlations in Figure 10 show that the effects of anomalies in surface chlorophyll on the DCM persist for many weeks. This suggests that satellite observations can provide some skill in predicting sub-surface conditions in at least some seasons. AMT does not provide observations for winter or summer, but as the models show reasonable agreement for the DCM depth in the SSTG, it may be fruitful to consider what correlations they offer in those seasons.

At present it is not clear if this is just a biological response, or whether physical factors (such as slowly passing eddies or Rossby waves) are causing coherent variations in these measures of biology. A much more expansive analysis of MEDUSA could address this issue by studying a much wider spatial extent than used here and assessing and, if necessary, removing the effect of eddies to leave the biological response of a quiescent ocean.

4.4 Use of chlorophyll concentration as a proxy for biomass

Throughout this paper we have used estimates of chlorophyll as an indicator of biomass. Although widely used for pragmatic reasons (see Table 1 of Sathyendranath et al., 2023), there are potential biases arising from assuming a simple correspondence between chlorophyll and biomass.

Firstly, the chlorophyll to carbon (or mass) ratio varies with individual species. As different ecological niches favour different plankton functional types there will be changes in this ratio, both laterally and vertically. Figure 4C of Graff et al. (2016) displays the change in the ratio for surface waters, with the oligotrophic gyres being marked by chlorophyll content being less than half of that in other regions. Tarran et al. (2006) and Heywood et al. (2006) noted that picoeukaryotes were the most abundant plankton group within these gyres and also contributed the most biomass in the DCM. Of these, *Prochlorococcus* is far more abundant than *Synechoccus* (Zubkov et al., 1998), so even though the latter has a greater size and thus fluorescence per cell its contribution to the overall chlorophyll signal remains small (van den Engh et al., 2017).

Secondly, many plankton groups respond to low-light conditions by increasing the concentration of chlorophyll within them. Such photoacclimation processes typically occur within a few hours (Lewis et al., 1984), so the biological community readily adapts to environmental changes as internal waves or eddies propagate through the region. These changes mean that for an individual species within these gyres the pigment to particle volume ratio increases with depth towards the DCM and then stabilises or decreases below that (Kitchen and Zaneveld, 1990; Fennel and Boss, 2003). However, Figures 6 and 7 of van den Engh et al. (2017) show that the DCM in the North Pacific oligotrophic gyre does correspond to both a peak in abundance of *Prochlorococcus* as well as in its fluorescence signal. The increase in chlorophyll is not always marked by a proportional increase in fluorescence due to “packaging”, which describes the degree to which chlorophyll concentration within the cell affects its ability to absorb light and then fluoresce (Cullen, 1982). However the strong diurnal mixing present in these calm low-latitude regions implies a degree of uniformity within the small standing stock present in the seasonal mixed layer, and thus a less pronounced photoacclimation change near the surface.

Chlorophyll is the common currency for these comparisons of models and observations. Whilst the variable stoichiometric ratios used by the ERSEM model enables it to accommodate photoacclimation, the model output that we have obtained only corresponds to chlorophyll. Many of the AMT cruises have obtained water samples at various depths throughout the transect, but their vertical resolution is coarse. The BGC Argo floats, however, do offer an alternative high-resolution record of plankton through measurement of backscatter at 700 nm (different from the wavelength used for the fluorescence response). This normalised backscatter, termed b_{bp700}, is often related to the concentration of particulate organic carbon (POC), which is an amalgam of phytoplankton, zooplankton, detritus and other non-viable material, and thus can be difficult to interpret solely as an index of phytoplankton biomass. It is also not a variable directly reproduced by most ecosystem models and thus not the focus of this study. Nonetheless future work could make use of these data for testing how well ecosystem models can reproduce photoacclimation processes. The backscatter for phytoplankton corresponds to their cross-sectional area, rather than their chlorophyll content.

A typical b_{bp700} profile within these gyres is shown in Figure 11. The backscatter is fairly constant above the DCM, beyond which it decreases to its noise floor for deep waters. The values in the top 150 m are due to a range of particulates, many of which lack a fluorescence signal. These could be detritus or plankton in a non-active state due to nutrient depletion. We extracted the depth at which b_{bp700} values reduced to midway between surface and deep values and compared that with the depth below the DCM where chlorophyll fluorescence values were halved. The two measures were correlated ($r^2 = 0.42$ for NSTG, $r^2 = 0.56$ for STSG) but we did not feel these represented a useful measure of biological depth, as the b_{bp700} value was always lower and may simply indicate a physical feature such as the depth of maximal vertical stability noted in Figure 9 of Agusti and Duarte (1999).

An attendant issue is the assumption of proportionality between chlorophyll content and fluorescence response, which is the basis for fluorometer measurements from AMT and BGC-Argo. Petit et al. (2022) note that there are two main factors affecting the fluorescence yield: the light level and the fluorescence quantum yield of the particular phytoplankton present. In near-surface waters plankton may produce auxiliary pigments to reduce the radiation being absorbed by the chlorophyll and thus preventing heat stress to the organism. (Note, the CHLA_ADJUSTED field of the Argo data had already had a correction applied for non-photochemical quenching). Figure 2 of Petit et al. (2022) shows that chlorophyll estimation via fluorescence compared with HPLC analysis can vary by a factor of six, with the fluorometers significantly overestimating for communities of micro- rather than the smaller nano- and pico-plankton. As the oligotrophic gyres are dominated by the smaller classes of plankton throughout the water column, this effect, associated with plankton community structure, does not affect this study, but could be an important issue for more productive locations with a changing size population through the water column.

The work of Roesler et al. (2017) suggests that the fluorometer-derived chlorophyll estimates from BGC-Argo floats should not simply be corrected by a uniform factor everywhere; however, there is, as yet, no spatially-varying correction that is robust enough for the standard processing chain (Catherine Schmechtig, pers. comm., 2023). The data in Table 2 of Roesler et al. (2017) suggest the correction factor should be 50% larger for SSTG than NSTG, which would reduce the chlorophyll estimates of the former (surface, peak of DCM and integrated value) by a third. If implemented this would increase the disparity between the NSTG and SSTG. Likewise, the fluorometer calibrations for each AMT cruise are determined on a cruise-wide basis, since there are too few measurements to explore any regional variation in the fluorescence-chlorophyll relationship.

Thus, although there are reservations about the use of chlorophyll fluorescence as a proxy for phytoplankton biomass, we note that in these oligotrophic gyres the effects of depth-varying community structure and photoacclimation do not mask the

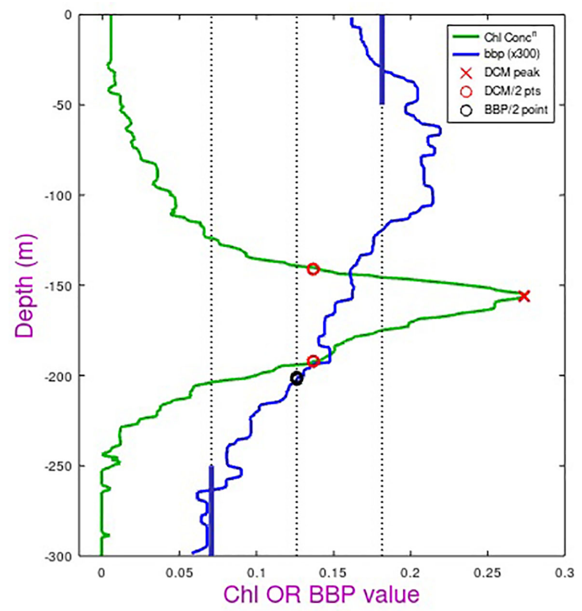

FIGURE 11
Schematic showing the definitions of the bottom depth of the biomass layer (note backscatter values have been multiplied by 300 to allow them to be displayed on the same scale). Chl-a (in mg m^{-3}) is derived from fluorescence, with a peak value and locations of half peak concentration (red circles) defined. BBP (in m^{-1}) is the optical backscatter observed at 700 nm wavelength. After despiking and application of a median filter, average surface and deep values are defined (thick blue bars) and the depth with the backscatter value midway between these selected (black circle).

development of deep concentrations of certain species such as *Prochlorococcus*, and that other sensors such as optical backscatter fail to shed adequate light on this phenomenon.

5 Overall summary

The AMT programme has generated a long-term dataset of surface and sub-surface measurements through many Longhurst provinces, with its repeated sampling within the oligotrophic gyres being almost unique. These ecosystems are representative of the ocean's largest ocean biome by area, and exhibit characteristic deep chlorophyll maxima at depths > 100m where nutrient concentrations are high enough to support primary production. These AMT data enable us to establish that the DCM for the STSG (NSTG) lies at ~145m (~120m), and is slightly deeper in the spring season than autumn for that hemisphere. As AMT only sampled two periods in the year, data from the BGC-Argo array are needed to elucidate the full annual cycle, confirming that seasonally the DCM is shallowest around the months of highest surface concentration. Interannual variations echoed this with higher than normal surface values coinciding with a shallower than normal DCM. Lagged correlations showed considerable persistence of this effect. This paper also demonstrated how AMT provides an effective dataset for validation of the portrayal of oligotrophic gyres in biogeochemical models, opening the door to exploration of the underlying biological dynamics of these regions using the models that best represent them.

This investigation focussed on the permanently stratified regions in the Atlantic, due to the availability of long time series of data within them. However, it is expected that the chlorophyll characteristics found here for these Atlantic subtropical gyres will also be manifest in the equivalent gyres in the North and South Pacific and in the South Indian Ocean. A potential extension of this work would be to explore surface/sub-surface relationships in the seasonally stratified temperate gyres found poleward of the subtropical gyres, since once the "spring bloom" has exhausted the surface nutrients a DCM develops persisting throughout summer and autumn until convectional mixing resumes. As these regions enjoy episodic (annual) injections of nutrients rather than just slow upward mixing, the relationships in these regions may be subtly different.

Data availability statement

The data collected during the Atlantic Meridional Transect programme are hosted at https://www.bodc.ac.uk/data/hosted_data_systems/amt/ and the 5-day composites of satellite-derived chlorophyll were from the ESA CCI programme, with the earlier (v5) dataset available at https://www.oceancolour.org. BGC-Argo data were obtained from https://biogeochemical-argo.org/data-access.php. These data were collected and made freely available by the International Argo Program and the national programs that contribute to it. (https://argo.ucsd.edu, https://www.ocean-ops.org). The Argo Program is part of the Global Ocean Observing System. The files containing the selected model output can be obtained from the author upon request.

Author contributions

The original research concept was by JA, with GQ expanding the aims. GQ carried out all the research, produced the figures and wrote the original draft. This was modified in response to ideas and comments from all authors. All authors contributed to the article and approved the submitted version.

Funding

The author(s) declare financial support was received for the research, authorship, and/or publication of this article. The work was supported by UK Natural Environment Research Council (NERC) National Capability funding for AMT to Plymouth Marine Laboratory, with the time for Graham Quartly also supported by funding from the National Centre for Earth Observation (NCEO) and European Union's Interreg Atlantic Area programme (grant agreement EAPA_165/2016 of the project iFADO: Innovation in the Framework of the Atlantic Deep Ocean). AMT is funded by the NERC through its National Capability Long-term Single Centre Science Programme, Climate

Linked Atlantic Sector Science (grant number NE/R015953/1). This study contributes to the international IMBER project, the work of NCEO and is contribution number 399 of the AMT programme. RB is supported by a UKRI Future Leader Fellowship (MR/V022792/1).

Acknowledgments

We thank Arnold Taylor for insightful discussions to prompt this study. We are grateful to the many people who have helped make the data available: John Stephens and Tim Smyth for collecting and collating all the AMT CTD data and Luca Polimene for providing the ERSEM output, and acknowledge the help provided by Glen Tarran and Shubha Sathyendranath in understanding the plankton community structure and the role of auxiliary pigments. We acknowledge the support of NEODAAS for the data storage and processing resources.

Conflict of interest

The authors declare that the research was conducted in the absence of any commercial or financial relationships that could be construed as a potential conflict of interest.

The reviewer JB declared a shared affiliation with the author RB to the handling editor at the time of review.

Publisher's note

References

Agusti, S., and Duarte, C. M. (1999). Phytoplankton chlorophyll a distribution and water column stability in the central Atlantic Ocean. *Oceanologica Acta* 22 (2), 193–203. doi: 10.1016/S0399-1784(99)80045-0

Aiken, J., Brewin, R. J. W., Dufois, F., Polimene, L., Hardman-Mountford, N. J., Jackson, T., et al. (2017). A synthesis of the environmental response of the North and South Atlantic Sub-Tropical Gyres during two decades of AMT. *Prog. Oceanogr.* 158, 236–254. doi: 10.1016/j.pocean.2016.08.004

Baretta, J. W., Ebenhöh, W., and Ruardij, P. (1995). The European regional seas ecosystem model, a complex marine ecosystem model. *Netherlands J. Sea Res.* 33, 233–2246. doi: 10.1016/0077-7579(95)90047-0

Brewin, R. J. W., Dall'Olmo, G., Pardo, S., van Dongen-Vogels, V., and Boss, E. S. (2016). Underway spectrophotometry along the Atlantic Meridional Transect reveals high performance in satellite chlorophyll retrievals. *Rem. Sens. Env.* 183, 82–97. doi: 10.1016/j.rse.2016.05.005

Brewin, R. J. W., Tilstone, G., Cain, T., Miller, P., Lange, P., Misra, A., et al. (2017). Modelling size-fractionated primary production in the Atlantic Ocean from remote-sensing. *Prog. Oceanogr.* 158, 130–149. doi: 10.1016/j.pocean.2017.02.002

Burchard, H., Bolding, K., and Villareal, M. (1999). *GOTM: a general ocean turbulence model. Theory, applications and test cases* (Brussels, Belgium: European Commission). Available at: https://www.researchgate.net/publication/258127949_GOTM_a_general_ocean_turbulence_model_Theory_implementation_and_test_cases (Accessed 16 Mar 2023). Technical Report EUR 18745 EN.

Clark, D. R., Rees, A. P., Ferrera, C. M., Al-Moosawi, L., Somerfield, P. J., Harris, C., et al. (2022). Nitrite regeneration in the oligotrophic Atlantic Ocean. *Biogeosci* 19, 1355–1376. doi: 10.5194/bg-19-1355-2022

Cornec, M., Claustre, H., Mignot, A., Guidi, L., Lacour, L., Poteau, A., et al. (2021). Deep chlorophyll maxima in the global ocean: Occurrences, drivers and characteristics. *Glob. Biogeo. Cycles* 35, e2020GB006759. doi: 10.1029/2020GB006759

Cullen, J. J. (1982). The deep chlorophyll maximum: Comparing vertical profiles of chlorophyll a. *Can. J. Fish Aquat. Sci.* 39 (5), 791–803. doi: 10.1139/f82-108

Fennel, K., and Boss, E. (2003). Subsurface maxima of phytoplankton and chlorophyll: Steady-state solutions from a simple model. *Limn. Oceanogr.* 4, 1521-1534. doi: 10.4319/lo.2003.48.4.1521

Graff, J. R., Westberry, T. K., Milligan, A. J., Brown, M. B., Dall'Olmo, G., Reifel, K. M., et al. (2016). Photoacclimation of natural phytoplankton communities. *Mar. Ecol. Prog. Ser.* 542, 51–62. doi: 10.3354/meps11539

Hardman-Mountford, N. J., Polimen, L., Hirat, T., Brewin, R. J. W., and Aiken, J. (2013). Impacts of light shading and nutrient enrichment geo-engineering approaches on the productivity of a stratified, oligotrophic ocean ecosystem. *J. R. Soc Interface.* 10, 9. doi: 10.1098/rsif.2013.0701

Heywood, J. I., Zubkov, M. V., Tarran, G. A., Fuchs, B. M., and Holligan, P. M. (2006). Prokaryoplankton standing stocks in oligotrophic gyre and equatorial provinces of the Atlantic Ocean: evaluation of inter-annual variability. *Deep Sea Res. II* 53 (14), 1530–1547. doi: 10.1016/j.dsr2.2006.05.005

Kitchen, J. C., and Zaneveld, J. R. V. (1990). On the noncorrelation of the vertical structure of light scattering and chlorophyll α in case I waters. *J. Geophys. Res.* 95 (C11), 20237–20246. doi: 10.1029/JC095iC11p20237

Letelier, R. M., Karl, D. M., Abbott, M. R., and Bidigare, R. R. (2004). Light driven seasonal patterns of chlorophyll and nitrate in the lower euphotic zone of the North Pacific Subtropical Gyre. *Limnol. Oceanogr.* 49 (2), 508–519. doi: 10.4319/lo.2004.49.2.0508

Levitus, S. (1982). *Climatological atlas of the world ocean* (Rockville, Md, USA: NOAA Professional Paper 13).

Lewis, M. R., Cullen, J. J., and Platt, T. (1984). Relationships between vertical mixing and photoadaptation of phytoplankton: Similarity criteria. *Mar. Ecol. Prog. Ser.* 15 (1-2), 141–149. doi: 10.3354/meps015141

Madec, G. and NEMO team. (2015). *NEMO ocean engine*. Available at: https://www.nemo-ocean.eu/wp-content/uploads/NEMO_book.pdf (Accessed 13 Mar. 2023).

McClain, C. R., Signorini, S. R., and Christian, J. R. (2004). Subtropical gyre variability observed by ocean-color satellites. *Deep Sea Res.* 51, 281–301. doi: 10.1016/j.dsr2.2003.08.002

Mignot, A., Claustre, H., D'Ortenzio, F., Xing, X., Poteau, A., and Ras, J. (2011). From the shape of the vertical profile of in *vivo* fluorescence to Chlorophyll-a concentration. *Biogeosciences* 8 (8), 2391–2406. doi: 10.5194/bg-8-2391-2011

Mignot, A., Claustre, H., Uitz, J., Poteau, A., D'Ortenzio, F., and Xing, X. (2014). Understanding the seasonal dynamics of phytoplankton biomass and the deep chlorophyll maximum in oligotrophic environments: a Bio-Argo float investigation, Global Biogeochem. *Cycles* 28, 856–876. doi: 10.1002/2013GB004781

Moeller, H. V., Laufkötter, C., Sweeney, E. M., and Johnson, M. D. (2019). Light-dependent grazing can drive formation and deepening of deep chlorophyll maxima. *Nat. Commun.* 10, 1978. doi: 10.1038/s41467-019-09591-2

Nencioli, F., Dall' Olmo, G., and Quartly, G. D. (2018). Agulhas ring transport efficiency from combined satellite altimetry and Argo profiles. *J. Geophys. Res.* 123, 5874–5888. doi: 10.1029/2018JC013909

Petit, F., Uitz, J., Schmechtig, C., Dimier, C., Ras, J., Poteau, A., et al. (2022). Influence of the phytoplankton community composition on the in *situ* fluorescence signal: Implication for an improved estimation of the chlorophyll-a concentration from BioGeoChemical-Argo profiling floats. *Front. Mar. Sci.* 9. doi: 10.3389/fmars.2022.959131

Quartly, G. D., de Cuevas, B. A., and Coward, A. C. (2013). Mozambique Channel Eddies in GCMs: a question of resolution and slippage. *Ocean Model.* 63, 56–67. doi: 10.1016/j.ocemod.2012.12.011

Rees, A. P., Nightingale, P. D., Poulton, A. J., Smyth, T. J., Tarran, G. A., and Tilstone, G. H. (2017). The atlantic meridional transect programme, (1995-2016). *Prog. Oceanogr.* 158, 3–18. doi: 10.1016/j.pocean.2017.05.004

Rees, A., Robinson, C., Smyth, T., Aiken, J., Nightingale, P., and Zubkov, M. (2015). 20 years of the atlantic meridional transect—AMT. *Limnol. Oceanogr. Bull.* 24, 101–107. doi: 10.1002/lob.10069

Roesler, C., Uitz, J., Claustre, H., Boss, E., Xing, X., Organelli, E., et al. (2017). Recommendations for obtaining unbiased chlorophyll estimates from *in-situ* chlorophyll fluorometers: a global analysis of WET Labs ECO sensors. *Limnol Oceanogr. Methods* 15, 572–585. doi: 10.1002/lom3.10185

Sathyendranath, S., Brewin, R. J. W., Brockmann, C., Brotas, V., Calton, B., Chuprin, A., et al. (2019). An ocean-colour time series for use in climate studies: the experience of the Ocean-Colour Climate Change Initiative (OC-CCI). *Sensors* 19, 4285. doi: 10.3390/s19194285

Sathyendranath, S., Brewin, R. J. W., Ciavatta, S., Jackson, T., Kul, G., Jönsson, B., et al. (2023). Ocean biology studied from space. *Surv Geophys.* 44, 1287–1308. doi: 10.1007/s10712-023-09805-9

Signorini, S. R., Franz, B. A., and McClain, C. R. (2015). Chlorophyll variability in the oligotrophic gyres: Mechanisms, seasonality and trends. *Front. Mar. Sci.* 2. doi: 10.3389/fmars.2015.00001

Smith, G., and Haines, K. (2009). Evaluation of the S(T) assimilation method with the Argo dataset. *Q. J. R. Meteorol. Soc.* 135, 739–7756. doi: 10.1002/qj.395

Smyth, T., Quartly, G., Jackson, T., Tarran, G., Woodward, M., Harris, C., et al. (2017). Determining Atlantic Ocean province contrasts and variations. *Prog. Oceanogr.* 158, 19–40. doi: 10.1016/j.pocean.2016.12.004

Tarran, G. A., Heywood, J. L., and Zubkov, M. V. (2006). Latitudinal changes in the standing stocks of eukaryotic nano- and picophytoplankton in the Atlantic Ocean. *Deep-Sea Res. II* 53 (14-16), 1516–1529. doi: 10.1016/j.dsr2.2006.05.004

Tilstone, G. H., Pardo, S., Dall'Olmo, G., Brewin, R. J. W., Nencioli, F., Dessailly, D., et al. (2021). Performance of ocean colour chlorophyll a algorithms for Sentinel-3 OLCI, MODIS-Aqua and Suomi-VIIRS in open-ocean waters of the Atlantic. *Rem. Sens. Env.* 260, 112444. doi: 10.1016/j.rse.2021.112444

Uitz, J., Claustre, H., Morel, A., and Hooker, S. B. (2006). Vertical distribution of phytoplankton communities in open ocean: An assessment based on surface chlorophyll. *J. Geophys. Res.* 111, C08005. doi: 10.1029/2005JC003207

van den Engh, G. J., Doggett, J. K., Thompson, A. W., Doblin, M. A., Gimpel, C. N. G., and Karl, D. M. (2017). Dynamics of prochlorococcus and synechococcus at station ALOHA revealed through flow cytometry and high-resolution vertical sampling. *Front. Mar. Sci.* 4. doi: 10.3389/fmars.2017.00359

Wong, A. P. S., Wijffels, S. E., Riser, S. C., Pouliquen, S., Hosoda, S., Roemmich, D., et al. (2020). Argo Data 1999-2019: Two million temperature-salinity profiles and subsurface velocity observations from a global array of profiling floats. *Front. Mar. Sci.* 7 (700). doi: 10.3389/fmars.2020.00700

Xing, X., Claustre, H., Boss, E., Roesler, C., Organelli, E., Poteau, A., et al. (2017). Correction of profiles of *in-situ* chlorophyll fluorometry for the contribution of fluorescence originating from non-algal matter, Limnol. *Oceanogr.-Meth.* 15, 80–93. doi: 10.1002/lom3.10144

Yool, A., Popova, E. E., and Anderson, T. R. (2011). MEDUSA -1.0: a new intermediate complexity plankton ecosystem model for the global domain. *Geosci. Model. Dev.* 4, 381–417. doi: 10.5194/gmd-4-381-2011

Yool, A., Popova, E. E., and Anderson, T. R. (2013). MEDUSA-2.0: An intermediate complexity biogeochemical model of the marine carbon cycle for climate change and ocean acidification studies. *Geosci. Model. Dev.* 6, 1767–1811. doi: 10.5194/gmd-6-1767-2013

Zubkov, M. V., Sleigh, M. A., Tarran, G. A., Burkill, P. H., and Leakey, R. J. G. (1998). Picoplanktonic community structure on an Atlantic transect from 50°N to 50°S. *Deep Sea Res. I* 45 (8), 1339–1355. doi: 10.1016/S0967-0637(98)00015-6

Appendix

Correlated spatial variations

The aim of this paper has been to look at sub-surface changes associated with changes in the general environmental conditions. Changes at the surface may be expected to lead to the gradual evolution of properties at depth. However there is a complication in that spatial variations, due to meandering currents or eddies may migrate through the region, giving a short-term coherent change at surface and depth. With BGC-Argo and AMT CTDs we only have limited point measurements with great separations in space, so the significance of these spatial variations in hard to assess. The MEDUSA output were provided as 25x25 points centred on the desired locations, which allows us to see the spatial variations.

Figure A1 shows a snapshot of various properties at a date in November. There are only weak spatial changes in physical condition such as SST, MLD and sea surface height (latter not shown), but quite marked changes in the biology. The surface chlorophyll levels are low, but do vary by a factor of two within this area, and the total chlorophyll changes by about a factor of 1.8 in a strikingly similar pattern. However, the large positive correlation

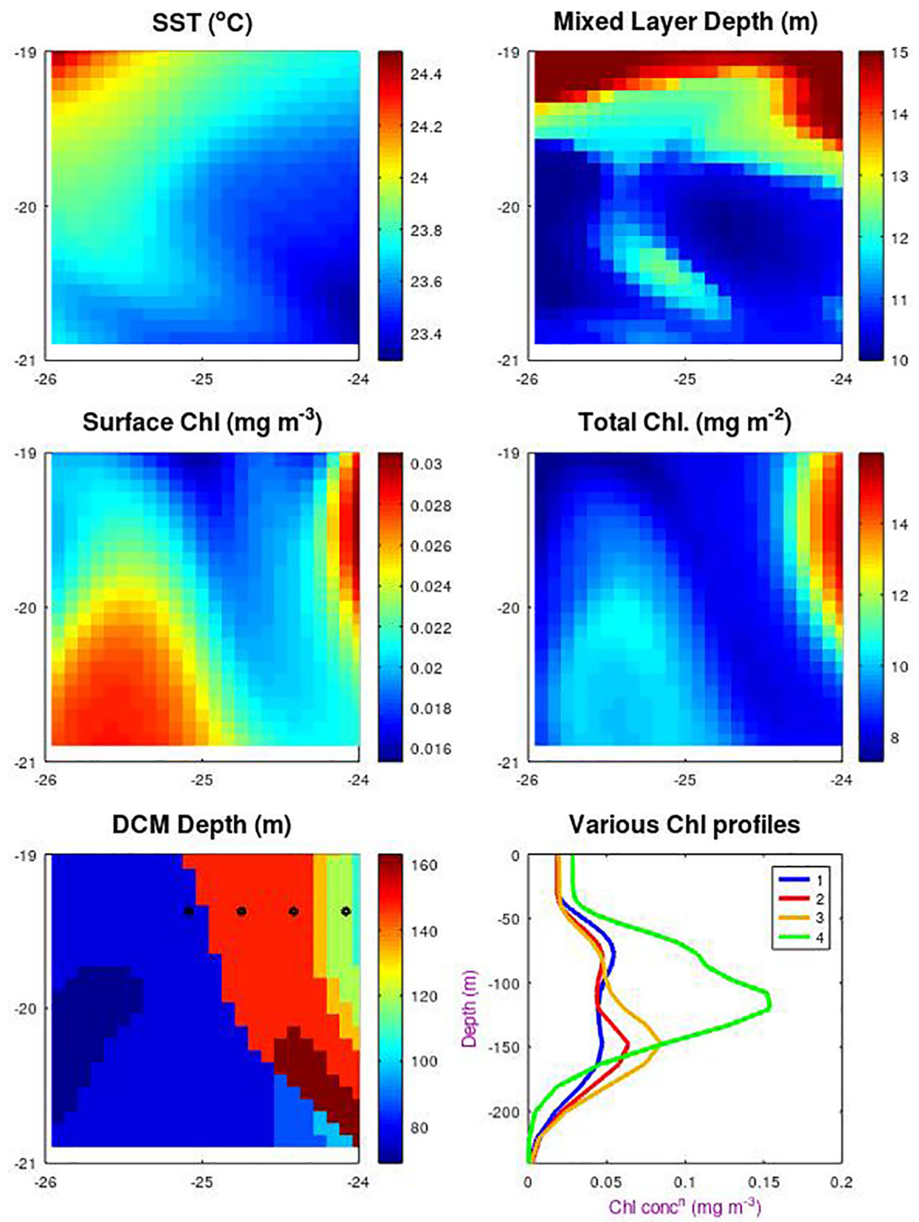

FIGURE A1
Spatial variations around SSTG within the MEDUSA model. Data are for a 2°x2° square in Nov. 1998, with the top row showing sea surface temperature and mixed layer depth as indicators of the physical features present. Subsequent plots show the surface chlorophyll and the total column-integrated chlorophyll and the depth of the layer of maximum chlorophyll. The sixth plot shows the chlorophyll profiles at the 4 locations indicated by dots, showing how there can be a step change in the apparent DCM layer between the first two locations indicated by the blue and red profiles.

observed for this case is very different from the weak or negative correlations noted for the seasonal variations of surface and total chlorophyll for MEDUSA (Figures 5A, B). This serves as an indication that a number of profiles taken quickly within a region over a short time e.g. from a rapidly-profiling BGC-Argo float will give very different correlations to measurements in that box spanning many years.

We also note that the definition of depth of DCM is inherently non-linear. The bottom two panels show the depth of the DCM and four of the vertical profiles. Moving gradually from west to east there is a point where the maximum ceases to be in the 80 m layer (as shown by the blue profile) and is now in the 150 m layer (shown in red). Although the line showing where 150 takes over from 80 m does align with the surface pattern, it would be hard to infer which depth was appropriate for the central point (the nominal location for all the other analyses). This indicates how hard it would be to predict the DCM depth at a point merely from surface observations.

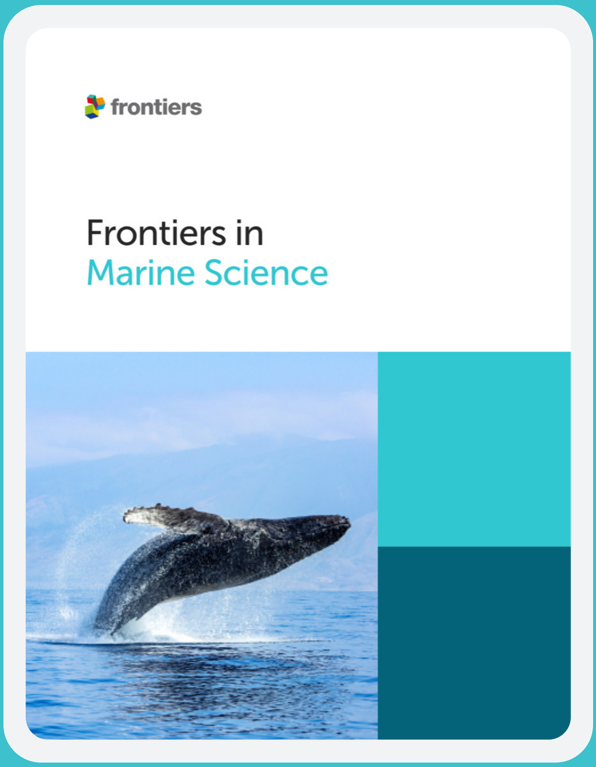

frontiers

Frontiers in
Marine Science

Frontiers

Avenue du Tribunal-Fédéral 34
1005 Lausanne, Switzerland
frontiersin.org

Contact us

+41 (0)21 510 17 00
frontiersin.org/about/contact